BURNETT, R 1996. *Transient current analysis for fault detection in large induction motors*. Robert Gordon University, PhD thesis. Hosted on OpenAIR [online]. Available from: https://doi.org/10.48526/rgu-wt-2807311

Transient current analysis for fault detection in large induction motors.

BURNETT, R.

1996

Transient Current Analysis for Fault Detection in Large Induction Motors

RONALD BURNETT

B.Eng. (Hons)

A thesis submitted in partial fulfilment of the requirements of
The Robert Gordon University
for the degree of Doctor of Philosophy

This research programme was carried out in collaboration with
Scottish Nuclear Ltd

August 1996

Acknowledgements

I, the author, wish to express my sincere gratitude to Scottish Nuclear Ltd (SNL) for providing the financial support which made this research project possible. Kind thanks must go to Mr. K. Ingle and Mr. B. Urquhart, both SNL, for the interest and co-operation which they showed throughout the project and for the assistance given by SNL power station personnel, in particular, Mr. P. Beaumont.

Thanks are also greatly expressed to my supervisor, Dr. J.F. Watson, for his invaluable advice in both the planning and problem solving areas of the project, and for his patience and general approachability throughout the last three years. I would also wish to thank the other members of the Electrical Machine Monitoring Group at The Robert Gordon University (RGU), for the assistance and knowledge which they shared with myself, in particular, Prof. W.T. Thomson, Dr. D.G. Dorrell and Dr. S. Elder.

Finally, I must thank the RGU technical staff for the construction of various experimental test-rigs and their general technical support throughout the period of the project.

Abstract

The majority of modern day health monitoring systems for polyphase squirrel cage induction machines, which employ the motors supply current as the diagnostic parameter, require the motor under investigation to be operating under fully loaded, steady state conditions before any useful information may be obtained.

The aim of the following research project was to develop a practical and portable monitoring system which would allow diagnostic information of both laboratory, and more importantly, industrially operated motors, to be obtained via information contained within the motors supply current transient. Thus making redundant the constraining operating conditions of previous current monitoring diagnostic systems.

Using the induction motors supply current transient, an electrical phenomenon which exists for a finite period of time during the motors initial acceleration, both historical and modern day signal processing techniques were investigated in order to attain their individual suitability for extracting the required diagnostic information.

The signal processing techniques employed were further used to investigate the possibility of extracting more information from the current transient, in particular, the location of a rotor fault within the squirrel cage rotor of the motor under investigation. To support this work a three phase Squirrel Cage Induction Motor with inverted geometry was commissioned. This motor allowed simpler monitoring access to the individual rotor bar currents, without the necessity for intrusive search coil mechanisms to be present between the stationary and rotating circuits. In conjunction with these investigations, the laboratory based inverted motor also allowed, due to its inherent design, an investigation into the flow of rotor bar currents to be undertaken, particularly when under faulty rotor conditions.

Using the findings from the above work a portable motor health monitoring system was successfully developed. The system, still in a prototype stage, contains both data acquisition and analysis sections and has been proven to give good diagnostic results both in the controlled laboratory and more variable industrial environments.

Research Objectives

Industrial operators of polyphase induction machines are constantly investing in new procedures and diagnostic tools which will enable them to reduce their overall running costs and reduce costly machine down-times. With this in mind many of these machine operators now employ *Condition Monitoring* techniques which allow them to monitor the health of their prime movers, thus ensuring that they operate safely and in the most economical and efficient manner.

One such diagnostic technique used by many operators, in particular the electricity generating industries, is the monitoring of supply current whilst the machine is operating under fully loaded, steady state conditions. This technique has been widely used in industry for many years. Industrial operators have reported, however, that the requirement for a suitably large current flowing within the rotor circuit, and that the motor under investigation must be operating under steady state conditions, limits the practical situations to which the diagnostic technique may successfully be employed.

As a result of these observations, and in particular those from the projects sponsors, the primary objective of the research project was agreed to be the development of a portable, stand-alone, (three phase Squirrel Cage Induction Motor supply current transient), diagnostic system based on the health of the motor being displayed in an easily interpretable format. The diagnostic system developed would be required not only to successfully monitor laboratory based motors, but also the far larger motors, both in terms of physical size and parameter ratings, which are found in many industrial applications.

The capability of the developed system to form detailed health histories on motors via 'Finger Printing' methods, and the creation of data knowledge bases was also noted to be advantageous by the industrial project sponsors.

As a sub-part to the above objective, various signal processing techniques were investigated in order to ascertain the most relevant and suitable for extracting the required diagnostic information from the motors supply current transient.

A second, but equally important objective to the project, was the investigation into the detection of further information from the motor via its supply current transient. In particular, the possibility of obtaining the physical location of any rotor bar fault within the rotor of the machine. It was felt that if this were found to be practically possible, it would greatly increase the rate of successful physical location of rotor bar faults when the motor is removed from service, and hence, reduce the length of costly machine down-times.

The final objective of the project, inherently linked to the pre-decessing objectives, was an investigation into the nature of rotor bar currents within the induction motor, particularly when the motor is operated under fault conditions. In order to implement this investigation an inverted geometry induction motor was designed, thus allowing far greater monitoring access to the individual rotor bar currents than if the more traditional layout of the motor had been used.

To My Parents

Contents

1 **The Induction Motor . . . 1**

1.0 A Historical Background . . . 1

1.1 The Modern Induction Motor and Common Faults Within . . . 2

1.2 Condition Monitoring Techniques . . . 8

1.2.1 Steady State Monitoring . . . 8

1.2.2 Transient Monitoring . . . 12

1.3 Frequency Components Indicative of Broken Squirrel Cage Rotor Bars . . . 14

1.4 Induction Motor Simulation Techniques . . . 15

1.5 Analysis of Squirrel Cage Induction Motor Rotor Bar Currents . . . 16

1.5.1 Access to Rotor Bar Current . . . 16

1.5.2 Rotor Current - Harmonic Content, Distribution and Interbar Currents . . . 18

1.6 Conclusions . . . 21

2 **The Utilisation of Supply Current as a Condition Monitoring Technique . . . 22**

2.0 Introduction . . . 22

2.1 Steady State Operation - Frequency Components Indicative of Broken Squirrel Cage Rotor Bars . . . 22

2.2 Steady State Operation - Present Non-Invasive Monitoring Techniques . . . 26

2.3 Transient Operation - Frequency Components Indicative of Broken Squirrel Cage Rotor Bars . . . 31

2.3.1 Transient versus Steady State Monitoring . . . 31

2.3.2 Typical Transient Current Signal . . . 31

2.3.3 Rotor Fault Components Present within Transient Signal . . . 32

2.4 Transient Operation - Present Non-Invasive Monitoring Techniques . . . 34

2.5 Conclusions . . . 35

3 **Signal Processing Strategies** **37**
3.0 Introduction 37
3.1 Short Time Fourier Transforms 37
3.2 The Wigner Distribution 40
3.3 Signal Analysis by Decomposition 45
3.4 The Exponential Distribution 47
3.4.1 The Choi-Williams Distribution 47
3.5 Encoding of Signal Processing Strategies 49
3.5.1 Software Development Environment 49
3.5.2 The Spectrogram 49
3.5.3 The Analytic Signal 49
3.5.4 The Wigner Ville Distribution 49
3.5.5 Wavelet Decomposition 50
3.5.6 Choi-Williams Distribution 50
3.6 Evaluation of Signal Processing Techniques using Synthesised Test Data 57
3.6.1 Description of Synthesised Test Data 57
3.6.2 The Spectrogram 57
3.6.2.1 Mono-Component Signals (Hamming Window) 57
3.6.2.2 Mono-Component Signals (Kaiser Window) 60
3.6.2.3 Multi-Component Signals (Hamming Window) 61
3.6.2.4 Non-Stationary Signals (Hamming Window) 62
3.6.3 The Wigner Ville Distribution 65
3.6.3.1 Mono-Component Signals 65
3.6.3.2 Multi-Component Signals 65
3.6.4 The Smoothed Wigner Ville Distribution 66
3.6.4.1 Mono-Component Signals 66
3.6.4.2 Multi-Component Signals 67
3.6.4.3 Non-Stationary Signals (Kaiser Window) 68
3.6.5 Wavelet Decomposition 70
3.5.6.1 Mono-Component Signals 70

3.5.6.2 Multi-Component Signals 70
3.6.5.3 Non-Stationary Signals 71
3.6.6 The Exponential Distribution 73
3.7 Evaluation of Signal Processing Techniques with Real Motor Data 76
3.7.1 Rotor Fault Component Detection using Wavelet Decomposition 81
3.8 Conclusions 85

4 Transient Monitoring Diagnostic Tool (The Current Analysis Program) 86
4.0 Introduction 86
4.1 Monitoring System (Hardware) 86
4.1.1 The PC 87
4.1.2 The Data Acquisition Card 87
4.1.3 Three Phase Synchronous Sampling 87
4.1.4 Current Transducers 91
4.2 Monitoring System (Software) 92
4.2.1 Description of Main Program Tasks 92
4.2.1.1 Three / Single Phase Synchronous Data Acquisition 93
4.2.1.2 Data Pre-Processing / Analysis 94
4.2.1.3 Display Diagnostic Information 95
4.2.1.4 Parameter Modification 96
4.2.2 Software Design 97
4.2.3 Essential Model 105
4.2.4 Essential Model - Function List 108
4.3 Monitoring Results 109
4.3.1 Description of Laboratory Test-Rig 109
4.3.2 Laboratory Results 111
4.3.2.1 Data Sampling 111
4.3.2.2 Full Load, Zero Broken Rotor Bars 113
4.3.2.3 Full Load, Two Broken Rotor Bars 113
4.3.2.4 No Load, Three Broken Rotor Bars 118
4.3.2.5 No Load, Ten Broken Rotor Bars 118
4.3.2.6 Sideband Amplitude Levels versus Rotor Fault Level 120

4.3.3 Industrial Verification of Monitoring Technique 124
4.3.3.1 Description of Testing Procedure 124
4.3.3.2 Case Study No. 1. 125
4.3.3.3 Case Study No. 2. 127
4.3.3.4 Case Study Deduction 127
4.4 Conclusions 131

5 Analysis of Transient Fault Component Amplitudes 132
5.0 Introduction 132
5.1 Review of Simulation Technique Employed 133
5.2 Investigation into Sideband Amplitudes 136
5.2.1 Review of Transient Monitoring 136
5.2.2 Sideband Amplitude Phenomenon 136
5.2.3 Investigation of Machine Parameters via Simulation 138
5.2.4 Investigation of Transient Current via Simulation 139
5.2.5 Location of Peak Amplitude 144
5.3 Conclusions 156

6 The Physical Location of Rotor Bar Faults 157
6.0 Introduction 157
6.1 Rotor Fault Location Theories 158
6.1.1 Relationship Between Complex Damping Factor and
Motor Slip 159
6.1.2 Locus of Complex Damping Factor 165
6.2 Theoretical Prediction of Rotor Bar Fault Location Technique 170
6.2.1 Detection of Location Frequency Components 170
6.2.2 Methodology Behind Broken Bar Location Detection 170
6.3 Conclusions 172

7 Results of Location Work 173
7.0 Introduction 173
7.1 Correlation of Supply Current Signals 173
7.1.1 Correlation Results 174
7.1.2 Correlation Results - Conclusions 177
7.2 Pre-Filtering of Supply Current Signal 183

7.3 Detection of Positional Components under Steady State Conditions 185
7.4 Location of Stator Coil Slots within SCIM 191
7.5 Location of Fault Positional Components 195
7.6 Detection of Fault Location Frequency Components 200
7.6.1 5th Harmonic 200
7.6.2 7th Harmonic 200
7.6.3 11th Harmonic 201
7.6.4 13th Harmonic 201
7.6.5 Single Scan Analysis Peak Timings 207
7.7 Obtaining Acceleration Information From Fault Detection Plots 214
7.8 Conclusions 216

8 The Inverted Geometry Induction Motor 218
8.0 Introduction 218
8.1 Construction of Inverted Geometry Induction Machine Test-Rig 219
8.2 IGM - Method of Operation 223
8.3 Determination of Rated Supply to IGM 225
8.4 Physical Tests to Determine Inverted Geometry Machine Parameters 229
8.4.1 Light Load Test 229
8.4.2 Blocked Rotor Test 229
8.4.3 Measurement of IGM Primary Winding Resistance 231
8.4.4 Verification of Non Saturation Motor Operation 232
8.5 IGM - DC Generator Load 234
8.6 Rotor Bar Current - Harmonic Content 236
8.6.1 Harmonics Present within Rotor Bar Current 237
8.7 Rotor Bar Transducer - Calibration and Formation 239
8.7.1 Calibration of Coil 239
8.7.2 Formation of Coil Former 241
8.7.3 Transfer of Transducer Signal 242
8.7.4 Rogowski Coil Integration 243
8.8 Results of IGM Investigations 245
8.8.1 Initial IGM Starting Problems 245
8.8.2 Rotor Bar Current under Normal and Faulted Conditions 250
8.8.3 Typical Rotor Bar Current Frequency Spectrum 252
8.8.4 Effects on Rotor Bar Current Frequency Content due to Single

Broken Rotor Bar . . . 255
8.8.5 Rotor Bar Current Transient Analysis . . . 260
8.9 Conclusions . . . 263

9 Project Conclusions and Future Work . . . 264
9.1 Prototype '*finger-printing*' Exercise . . . 268

10 References . . . 273

Appendix I
Frequency Components Present due to Rotor Asymmetries . . . A-I-i

Appendix II
Frequency Components Present due to the Effects of Torque Variations . . . A-II-i

Appendix III
Modulation due to Fault Component Third Harmonic . . . A-III-i

Appendix IV
Fault Frequency Component Induction and Interaction . . . A-IV-i

Appendix V
The Generalised Expression . . . A-V-i

Appendix VI
Three Phase Simulation Model . . . A-VI-i

Appendix VII
The Rogowski Coil . . . A-VII-i

Appendix VIII
Rotor Bar Current Acquisition . . . A-VIII-i

Appendix IX
Published Papers . . . A-IX-i

Principal Symbols

Induction Motor

SCIM . . . . Squirrel Cage Induction Motor.

UMP . . . . Unbalanced Magnetic Pull.

MMF . . . . Magneto Motive Force.

PSH . . . . Principal Slot Harmonics.

$F_{deleroi}$ . . . . Rotor Fault Location Frequency Component.

f_s. . . . . Supply Frequency Fundamental Component.

k. . . . . Harmonic Integer (k = 1, 2, 3 ...).

p. . . . . Number of Pole-Pairs.

s. . . . . Motor Slip.

ω_s. . . . . Supply Angular Fundamental Frequency.

ω_r . . . . Rotor Angular Rotation.

EMF . . . . Electro Motive Force.

m, M . . . . MMF and Peak MMF Respectively.

θ, λ . . . . Space and Time Rotation.

R . . . . Number of Cage Rotor Slots.

N . . . . Number of Cage Rotor Bars.

n . . . . Estimated Number of Broken Rotor Bars.

N_{db} . . . . dB Difference Between Lower Sideband and Mains Component.

F_{LSB} . . . . Frequency of Lower Sideband Harmonics.

F_{USB} . . . . Frequency of Upper Sideband Harmonics.

F_{PSH} . . . . Frequency of Principal Slot Harmonics.

n' . . . . Harmonic Index (n = 1, 2, 3 ...).

Equivalent Circuit Parameters (per phase)

V_{ph} . . . . Supply Voltage.
R_c . . . . Core Loss Resistance.
X_m . . . . Magnetising Reactance.
I_m . . . . Magnetising Current.
I_c . . . . Core Loss Current.
I_o . . . . No Load Current.
R_1 . . . . Stator Winding Resistance.
X_1 . . . . Stator Winding Leakage Reactance.
I'_2 . . . . Rotor Current Referred to Stator.
I_2 . . . . Rotor Current.
R_2 . . . . Rotor Winding Resistance.
X_2 . . . . Rotor Winding Leakage Reactance.
E_2 . . . . Induced Voltage.
$N_1 : N_2$ . . . . Stator : Rotor Turns Ratio.

Signal Processing

FFT . . . . Fast Fourier Transform.
FTA . . . . Fourier Transform Algorithm.
DFT . . . . Discrete Fourier Transform.
STFT . . . . Short Time Fourier Transform.
WD . . . . Wigner Distribution.
PWD . . . . Psuedo Wigner Distribution.
WVD . . . . Wigner Ville Distribution.
SWVD . . . . Smoothed Wigner Ville Distribution.
ED . . . . Exponential Distribution.
F(k) . . . . STFT Spectral Point.
k . . . . Harmonic Index (k = 1, 2, 3...).
n . . . . Harmonic Number (n = 1, 2, 3...).
N . . . . Total Number of Samples.
w(nT) . . . . Sampled Smoothing Window.
f(nT) . . . . Sample of Signal under Analysis.

rMT . . . . Length of Overlap between successive STFT's.

$s(t,\omega)$ . . . . Spectrogram.

R . . . . Length of Time Window.

w() . . . . Time Window.

h() . . . . Frequency Window.

$x_a()$ . . . . Analytic Signal.

$x_a^*()$ . . . . Complex Conjugate of Analytic Signal.

t . . . . Time Axis.

ω . . . . Frequency Axis.

σ . . . . Constant.

τ . . . . Shift Variable.

Inverted Geometry Induction Motor

IGM . . . . Inverted Geometry Induction Motor.

N_{SR} . . . . Turns Ratio.

m_1 , m_2 . . . . Number of Phases.

k_{w1} , k_{w2} , k_w . . . . Winding Factors.

P_m . . . . Mechanical Power.

P_o . . . . Output Power.

ω . . . . Angular Rotation.

T . . . . Torque Developed.

B . . . . Flux Density within Air-gap.

ϕ . . . . Flux per Pole.

D . . . . Diameter of Rotor.

l . . . . Axial Length.

A . . . . Axial Rotor Current Sheet.

n'' . . . . Rotor Speed.

N_{ph} . . . . Turns per Phase.

f_0, f_1, f_2 . . . . Integrator Frequency Range Bands.

Z_1, Z_2 . . . . Number of Stator, Rotor Slots Respectively.

Miscellaneous

dq . . . . Direct / Quadrature.

USB . . . . Upper Sideband.

LSB . . . . Lower Sideband.

ADC. . . . . Analog to Digital Converter.

DAC. . . . . Digital to Analog Converter.

S/H . . . . Sample and Hold.

FSD. . . . . Full Scale Deflection.

CAPro . . . . Current Analysis Program.

FL10BB . . . . Full Load, 10 Broken Rotor Bars.

FL3BB . . . . Full Load, 3 Broken Rotor Bars.

FL2BB . . . . Full Load, 2 Broken Rotor Bars.

NL10BB . . . . No Load, 10 Broken Rotor Bars.

NL3BB . . . . No Load, 3 Broken Rotor Bars.

IS . . . . Initial (energy) Surge.

M_{ss} . . . . Mutual Inductance Stator - Stator.

M_{RR} . . . . Mutual Inductance Rotor - Rotor.

L_{SS} . . . . Leakage Inductance Stator - Stator.

L_{RR} . . . . Leakage Inductance Rotor - Rotor.

M_{SR} . . . . .Mutual Inductance Stator - Rotor.

R_F . . . . Rotor Imbalance.

$I_{A,B,C,D,E,F}$ . . . . .Simulated Currents.

$F_{A,B,C}$ . . . . Simulated Force Component.

$F_X[6]$ . . . . Simulated Current Sub-Component.

Z_1 . . . . End-Ring Impedance.

Z_2 . . . . Rotor Bar Impedance.

R_e . . . . End-Ring Resistance.

R_b . . . . Rotor Bar Resistance.

X_e . . . . End-Ring Inductance.

X_b . . . . Rotor Bar Inductance.

I_{Fault} . . . . Fault Current.

$I_{R1,N}$ . . . . Mesh Current.

Z_{Total} . . . . Total Mesh Impedance.

X_r . . . . Mutual Inductance.

A . . . . Complex Ratio of Mesh Impedances, Z_1 / Z_2.

d . . . . Complex Damping Factor.

Z_{FNb} . . . . Stator - Rotor Coupling Impedances.

Z_{NbF} . . . . Rotor - Stator Coupling Impedances.

Z_{FF} . . . . Stator - Stator Coupling Impedance.

Z_{BB} . . . . Stator - Stator Coupling Impedance (negative sequence).

Z_{EE} . . . . Rotor - Rotor Coupling Impedance.

I_f . . . . Positive Sequence Currents.

I_b . . . . Negative Sequence Currents.

I_{nb} . . . . Rotor Bar Currents.

Chapter 1

The Induction Motor

1.0 A Historical Background

The technique of utilising a rotating magnetic field, in order to develop a torque upon the rotor of a machine, was first investigated by Faraday [1] in his experiments involving a metallic cube. In his investigations Faraday placed a metallic cube in the centre of a rotating magnetic field, and found that the cube experienced such forces as to allow it to rotate in the direction of field rotation. The cube's rotation being due to forces developed by the interaction between the induced currents flowing within the cube and the moving field. Faraday stated that the cube would rotate regardless of whether the rotating field was achieved by rotating electro-magnets, energised via direct currents, or by means of alternating currents producing field rotation when suitably displaced in both time and space. The currents induced within the metallic cube due to the rotating field, however, were found to be small in magnitude, resulting in similar levels of torque being developed upon the cube. This method of electro-magnetic induction via rotating magnetic fields forms the basic rudiments of the earliest '***Induction Motor***'.

Ferraris [2] in 1885 developed a motor which consisted of a solid copper cylinder placed within an appropriate structure. This allowed two alternating magnetic fields to interact with one another in both space and time at an angle of 90°, thus enabling a rotating magnetic field to pass over the cylinder in a similar manner to that of Faraday's cube. The torque developed by this motor was similarly low, due to the hysteresis and eddy currents present within the cylinder, hence, a method of increasing the levels of developed torque within such a 'Hysteresis Motor' was required.

During this period in history, the Yugoslav, Nicolia Tesla, was also investigating the principle of employing rotating magnetic fields to induce currents as a means of developing rotor torque. On graduating from '*The Technical Institute of Graz*', Austria, Tesla began his life-long research into brushless AC machines at '*The Central Telegraph Office*' in Budapest, continuing his research when he moved to '*The Continental Edison Company*' in Strasbourg. It was whilst employed here that he was encouraged to demonstrate his new theories in America, and thus, in 1884 moved to the USA and by 1887 had established '*The Tesla Electric Company*'.

Around 1886 Tesla's version of Faraday's cube, which consisted of a mechanism that allowed three alternating magnetic fields to interact with one another at 120°, in space and time, was deemed to be a more practical form of motor than that developed by Ferraris, and hence, after a lengthy period of litigation between the two inventors, Tesla's patent was upheld by the law courts.

1.1 The Modern Induction Motor and Common Faults Within

Tesla's [3] lecture to the American Institute of Electrical Engineers in 1888, entitled, '*A New System of Alternating Current Motors and Transformers*', has long been described as a major milestone within electro-mechanical technology and is agreed by many worthy academics to be the true beginning of what we now know today as '***The Polyphase Induction Motor***', Figure [1.1.1].

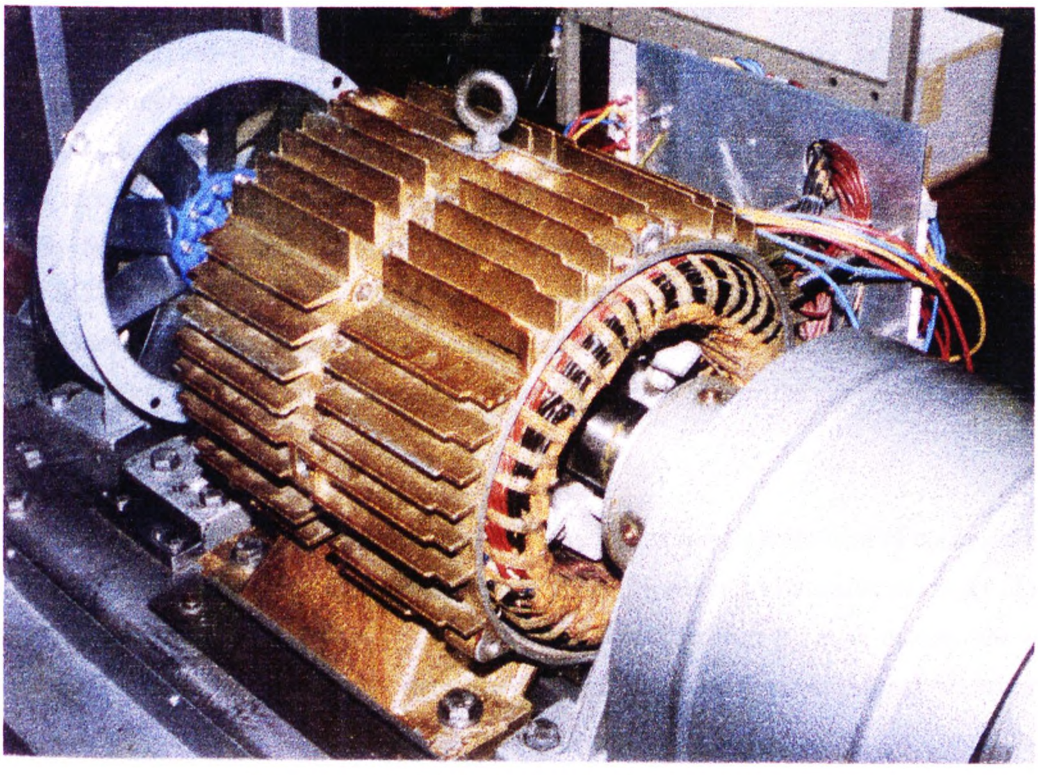

Figure [1.1.1] The Polyphase Induction Motor.

The development of the induction motor over the past 100 years has allowed the design of the motor to belong to one of two main formats, namely, those with 'Squirrel Cage' or 'Wire Wound ' rotors.

In order to develop appreciable levels of torque from that developed by the Ferraris cylinder, large induced currents must be present within a strong magnetic field. To obtain this magnetic field the non-magnetic medium which lies within the path of the motors flux must be made as short as possible, thus introducing the concept of the cylindrical stator and rotor being separated by a small air-gap. If the copper cylinder rotor developed by Ferraris is replaced by numerous copper conductors, or 'bars', which are then sunk into holes around the circumference of the rotor and short-circuited at either end by copper rings, known as 'end-rings', Figure [1.1.2], far higher levels of rotor torque are produced. This design of rotor was first described and patented by Dobrowolsky [4] in 1889. If the copper structure is removed from the rotor, as is undertaken by Armour and Walley [5] using acid to remove the iron core, the remaining cage resembles that used to exercise squirrels in the late 1800's, and hence, the class of induction motor which uses this form of rotor has since been known as the '**Squirrel Cage Induction Motor**', or SCIM. In a '**Wire Wound Induction Motor**', the rotor is comprised of a three phase star or delta connected wire winding which is terminated by external resistance's via a slip-ring mechanism to the motor supply, Figure [1.1.3]. Commonly, the cage rotor is referred to as a 'brushless machine' and the wound rotor as a 'slip-ring machine'.

The polyphase SCIM is by far the most commonly used AC prime mover in modern industry. Whether fed from single or three phase supplies, its relatively simple, rugged construction and overall ability to withstand arduous duty with minimum attention makes it almost the 'ideal machine', and ensures its use in a wide variety of industries. Small induction motors may be found in a multitude of everyday household appliances, ranging from that of refrigerators through to washing machines. Larger SCIM's are to be found operated by industry and are commonly fed from three phase supplies. Uses for such motors may include auxiliary drives within the electricity generating industries and as gas compressors, sea water injection and oil exporting pumps within the oil and gas exploration industries.

As mentioned previously, a significant reason for the induction motors wide span of operation is the high level of robustness, due to the motors inherent design. However, as industrial operators of these motors, such as, Rankin [6], Nailen [7], Gaydon [8] et al. and Bonnett [9] et al. discuss, the SCIM when operated under normal steady state conditions is under considerable thermal, electrical and

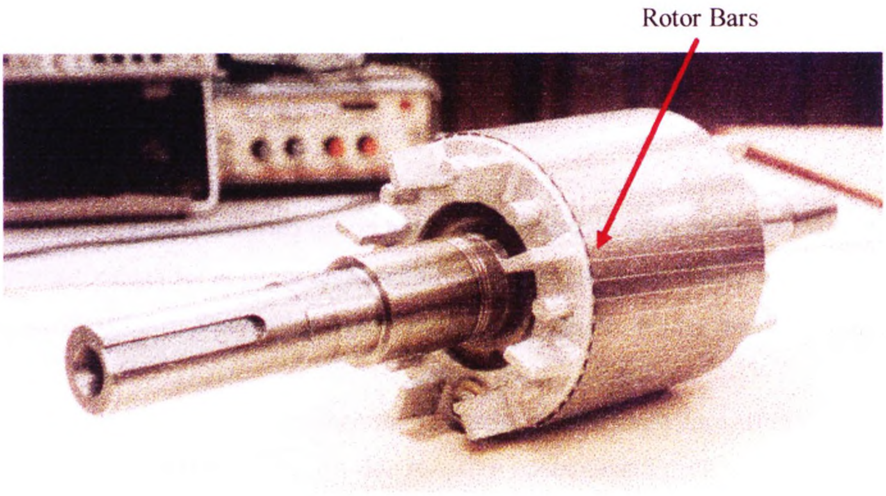

Figure [1.1.2] The Squirrel Cage Rotor.

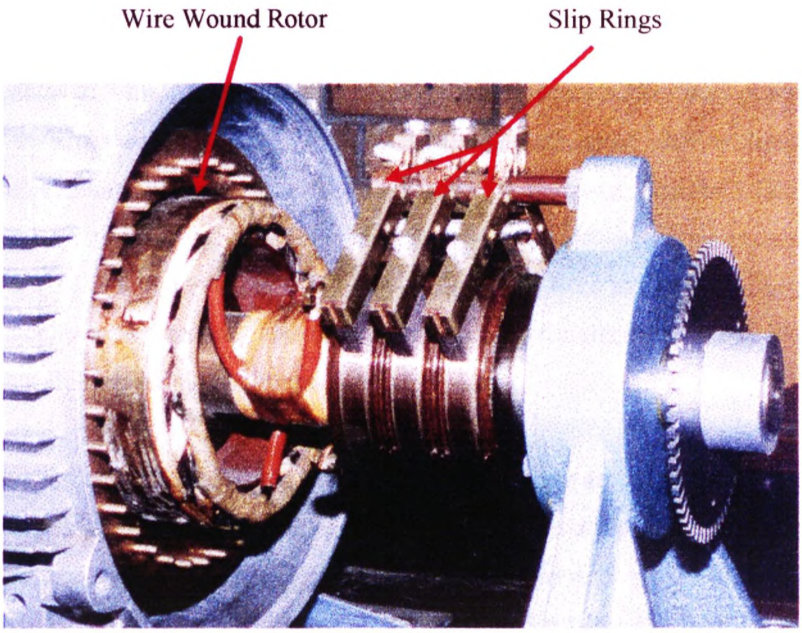

Figure [1.1.3] The Wire Wound Rotor.

mechanical stress. These stresses are particularly prominent when the SCIM is operated under abnormal and / or transient conditions. Such transient conditions being a regular feature in certain applications, with the resultant stresses leading to potentially catastrophic failures should any developing fault not be detected and corrected within time.

From the results of a survey carried out on numerous industrial SCIM operators, Thomson [10] et al. found four main categories of motor faults within an industrial SCIM. These faults are reported to be: *Inter-turn winding faults*; *Static rotor / stator eccentricity*; *Single phasing* and *Broken rotor bars*.

Inter turn winding faults [11] occur when the insulation of one single turn within a coil of the stator winding mechanism suffers breakdown due to either contamination, thermal ageing or vibrational stresses. This initial breakdown process causes increased heating within the entire winding, resulting in a change in the overall current distribution within the winding, and hence, leads to a complete insulation failure within the motor if not detected and repaired.

Static rotor / stator eccentricity [12] occurs when the axial centres of both the rotor and stator are no longer in line with each other. This being a result of either axial bearing wear or incorrect alignment during the commissioning period. The effect of the eccentricity results in a strong magnetic attraction between the stator and rotor at a particular point on the stator circumference, producing a resultant force known as 'Unbalanced Magnetic Pull', or UMP. The effects of UMP within the motor are to cause increased amounts of motor vibration, thus placing yet more stress on the SCIM.

Single phasing [13] is found to occur when one of the supply lines to the motor, or a stator winding conductor, becomes open circuited. This fault condition is potentially very serious as it results in high levels of current flowing within the motor.

Rankin [6] and Nailen [7] state that the bars within a SCIM rotor are subjected to high levels of stress during normal operation. Both mechanical and thermal stresses are prevalent within the SCIM rotor bar, due to the increased levels of current flowing through the rotor circuit under loaded conditions and at initial start-up, when the rotor current may be upto 5-6 times the fully loaded value. Typical start-up periods may last from between 1-15 seconds depending on the physical size and rating of the machine, and as Gaydon [8] et al. state, it is during these starting periods, which may be frequent in the case of auxiliary motors within power stations, that problems may occur due to the minimal cooling and maximum vibratory forces present. The result of these increased electro-magnetic and electro-mechanical stresses is that a rotor bar may physically crack and eventually break due to the overheating, frequently to the order of 200°C in large motors [14], which occurs around the location of the crack, thus causing the bars situated next to it to carry more current which, in time, will cause these bars to weaken and latterly fail. Examples of typical rotor faults may be seen within Figure [1.1.4] and Figure [1.1.5]. In extreme cases this may eventually cause mechanical failures within the rotor, resulting in debris being thrown into the stator windings, increasing the possibility of a catastrophic winding failure in addition to potential injury to both personnel and surrounding machinery.

Williamson and Smith [15] describe how imbalances and ultimately rotor cage faults occur within the cage due to imperfect manufacturing processes. The authors state that many of the cage faults are caused during the manufacture of the rotor through defective casting in the case of die cast rotors, or poor jointing in the case of brazed or welded end-rings. The authors discuss that although these types of problems are relatively simple to detect before installation, the faults are not easily detected once the motor is in operation, and that it is in fact during normal operation when such problems are amplified due to the high levels of electro-mechanical and electro-magnetic stresses.

Thomson [10] et al. conclude that industrial operators of SCIM's will always strive to minimise the costs of their maintenance procedures, time-outs of plant and the general loss of revenue caused by such motor faults. Consequently, numerous techniques have been developed over the past years which monitor specific motor parameters related to the SCIM and enable the general health of the motor to be diagnosed, thus allowing the operator to detect and determine the severity of any machine fault, and to plan cost effective maintenance schedules from the diagnostic information obtained.

Many techniques are in existence for both on-line and off-line health monitoring of SCIM's, whereby unnecessary plant failures and consequential damage together with loss of revenue may be avoided. Such techniques being all examples of what has become known as '***Condition Monitoring***'.

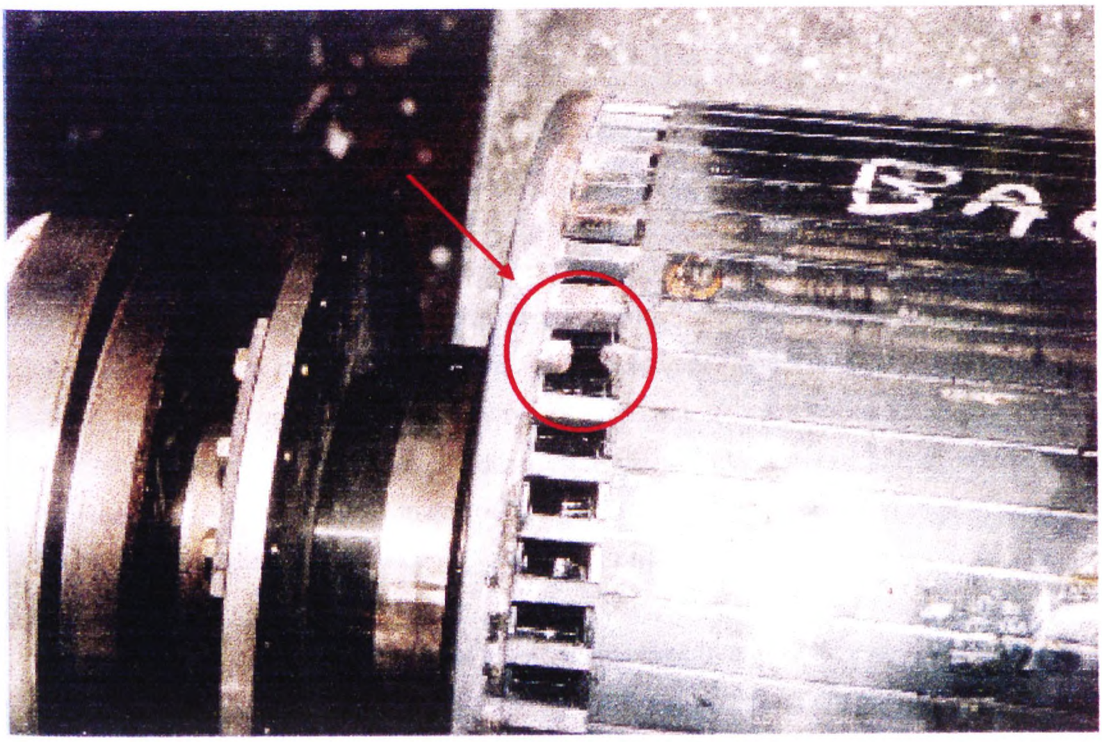

Figure [1.1.4] Broken Rotor Bar.

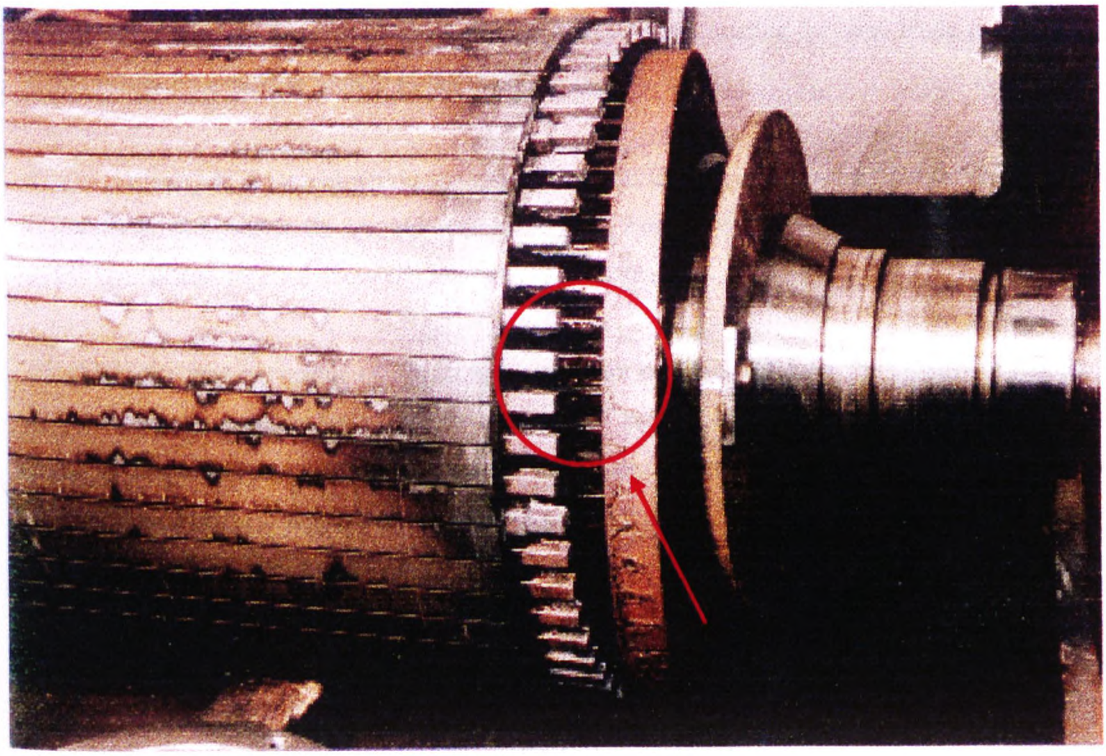

Figure [1.1.5] Broken End Ring.

1.2 Condition Monitoring Techniques

1.2.1 Steady State Monitoring

It can be shown that any specific '*Condition Monitoring*' technique originates from either one of two main categories. Those which are '**Invasive**' and those which are '**Non-Invasive**' in nature. 'Invasive' monitoring involves a motors complete removal from operation and / or disassembling in order to position transducers, or to physically carry out an inspection in order to obtain the required health information. Bhattacharyya [16] et al. discuss the various physical bench tests which may be implemented on a motor in order to determine the condition of both stator and rotor. Two common examples of these being the 'Growler' and 'Single Phasing' tests.

The 'Growler' test requires the rotor to be physically removed from the motor and placed onto an iron core test-coil arrangement. With the rotor cradled upon the pole-faces of the iron core, a magnetic circuit is obtained containing both the iron core and the rotor. When the test-coil arrangement is energised a strong magnetic field is transferred through the iron core into the rotor. Using a steel component, such as a common workshop hacksaw blade, in parallel across each rotor slot in turn, normal rotor bars are detected by the magnetic field patterns causing the steel blade to vibrate, and hence, produce an audible 'growl' as the rotor is turned by hand.

When a broken bar is present within the rotor, due to the change in magnetic field caused by the lack of current flowing within the bar, the steel blade is no longer able to lie flat against the rotor surface, and in fact will be repelled above the rotor slot in question.

The 'Growler' test is capable of detecting broken bars but does not have the sensitivity required to detect the presence of bar faults in their early stages, such as hairline fractures. It has been found, however, that if this bench test is ran over a considerable time period, then due to the increase in rotor temperature, hairline fractures are commonly found to increase in size and will ultimately be detected by the technique.

With 'Single Phasing', a single phase power source is applied to any two of the three phase stator windings of the motor. Due to the lack of a three phase signal within these windings, a rotating field within the air-gap of the motor is not created, hence, the rotor is unable to rotate by itself. However, when the rotor is manually turned slowly, the line current is found to fluctuate as a broken rotor bar passes under the winding connected to the power source. This technique, however, has many shortcomings, not least that the indication of a faulty rotor bar is not always reliable. 'Single Phasing' has also been shown not to possess the required accuracy to indicate hairline fractures within a rotor bar as the test is usually run under cold operating conditions.

The 'Growler' test is carried out on a dismantled motor whereas 'Single Phasing' is carried out on an assembled but non-operational motor. Hence, as Kliman [17] et al. state, the monitoring technique has become invasive in that the motor has had to be removed from normal operation.

As 'Invasive' monitoring involves the removal from normal operation, and hence, loss of revenue to the machine operator, a variety of research projects have been conducted within the area of 'Non-invasive' monitoring. This category of monitoring, as the name suggests, allows health information on the motor to be obtained whilst the motor is still in operation, and thus, does not involve any delays and loss of revenue to the operator.

Hargis [18] et al. show how due to MMF variations caused by rotor imbalances, a cyclic variation within the current produces torque variations which occur at twice motor slip frequency, and hence, cause a variation within the speed of the motor. Gaydon [19] uses this phenomenon to develop a monitoring system which via an oscilloscope and simple electronics, monitors the fluctuations of the rotational period of the motor using a shaft position detector. Morita [20] uses small search coils within the air-gap between the stator and rotor to detect amplitude changes within the harmonic components of air-gap flux. Morita states that it is possible to detect broken bars and end-ring faults, but the necessity to install search coils limits the 'non-invasive' scenario of the technique. Earlier Kliman [17] et al. found that if flux were the parameter to be monitored then the external leakage flux was a far more practical signal to monitor and still contained the necessary health information. Penman [21] et al. show how health information may be obtained from the axial leakage flux produced from both the stator and rotor windings as a result of winding currents. Penman discusses his monitoring system and concludes that many types of fault may be detected via the amplitude of certain frequency components within the flux spectral content. The authors state that although a true motor should never produce any axial leakage flux, in practice, minor abnormalities will be present within a rotor and stator due to errors within the manufacturing processes. As a result harmonic components will be ever present within the leakage flux. The authors indicate, however, that when the motor is run with asymmetries present, far more harmonic components are present within the axial leakage flux. The authors state that it is these higher harmonics which may be related to machine abnormalities, with the components having a relatively small magnitude under normal operation but becoming increasingly significant with the presence of fault conditions.

Carr [22] et al. discuss the stray field monitoring system marketed under the name of '*Motor Watch*'. Carr states that if the frequency content of flux is analysed between the frequencies of 10 to 1 kHz, *Supply*, *Winding*, *Rotor bar* and *Mechanical* faults may be successfully detected.

Leonard and Thomson [23] show how due to forces proportional to air-gap flux, changes within the flux spectrum will be observed within the vibration spectrum of the motor. Leonard discusses how if the vibration of the motor is monitored from an optimum sensing point, using an accelerometer positioned on the body frame of the motor, *unbalanced supplies* along with *inter-turn winding* faults may be detected from a frequency analysis of the signal. Thomson [10] et al. analyse the vibration signal around the Principal Slot Harmonics, PSH. The authors conclude that faults such as broken bars and high resistance end-rings increase the amplitude of the sidebands around these harmonics. Thomson [24] et al. discuss how the vibration signal analysed around the PSH will detect the presence of a single broken bar, however, Thomson does state that the effects of a broken bar and that of high resistance end-rings are similar, and hence, determination between the two faults would be difficult.

Cameron [25] et al. develop an expression for the calculation of the unique frequency components within the vibration signal which appear as a result of rotor eccentricity. Cameron analyses the vibration signals of several motors around these unique values and concludes that it is possible to detect eccentricity from this parameter. In particular, static eccentricity may be detected by amplitude changes within the vibration PSH and dynamic eccentricity, by the appearance of unique frequency components within the vibration and current signals.

Gaylard [26] et al. analyse the acoustic levels of the motor which occur due to these vibrations. In particular the authors are interested in the detection of loose stator windings within the motor. The authors describe how by monitoring the acoustic levels emanating from several motors via precision sound level metering and the use of neural networks, data was obtained from motors on different occasions. On comparing the audio spectra from a motor on different running occasions the authors suspected that discernible differences would be present when mechanical faults were present over and above that of electrical faults. The authors, however, conclude that no such differences were found. They also indicate that as this technique can only quantify the condition of the machines winding via long term trending and that as the noise from one motor is different from that of another with different size or geometry, care should be taken when comparisons are made with the acoustic spectra from separate machines.

Marques Cardoso and Sousa Saraiva [27] use the three phase stator supply currents to detect fault information by transforming the three phase currents into a two dimensional system, using the transformation technique known as 'Park's Vectors'. With this transformation, the authors found that under normal balanced operating conditions the transformed supply currents, when applied to the relevant inputs of an oscilloscope, give the visual representation of a circle centred at the origin. The authors found that on the introduction of common motor faults, the original relationship within the transformation does not hold and the shape which is formed on the screen is no longer of circular orientation. The authors show that they can successfully detect several common faults when the motor is run under no load conditions. Such faults include: *open circuit stator*, *short circuited stator* and *open wound rotor*. The authors conclude that using such a transformation technique gives suitable results for the detection of a number of motor defects, is a good technique for visual identification, as non-technical personnel can interpret the results, and is 'non-invasive' in nature thus permitting the detection of faults within operating motors.

Alger [28] shows how the air-gap flux within a SCIM is composed of seven principal rotating fields. Taking note of these fields, a general equation for the slot harmonics may be derived [24]. Using the theory stated by Jones [29], that upper and lower sidebands occur at $\pm 2s$ around the fundamental, where 's' represents the slip of the motor, equations may be formed for the slot harmonic frequencies for a rotor with asymmetry. Cameron [25] uses this to develop equations which predict the slot harmonics within the current signal that are representative of eccentricity. Thomson [10] et al. use the expressions [28] developed for rotor asymmetry to obtain the motor slot harmonics which are then monitored. In conjunction with the slot harmonics, the authors also monitor the supply fundamental frequency and report that the amplitude of the sidebands located at $\pm 2s$ around the fundamental also increase with increasing severity of broken bars, see Appendices I, II and III.

Monitoring the SCIM supply current frequency components acts as a window into the air-gap flux, and as is stated by Kliman [30], although line current may not contain as much information as the air-gap flux, it is far more readily accessible. This technique has also been studied by other researchers over the years and many case studies have been reported which show its reliability as a successful condition monitoring technique [6][31][32].

Modern methods of *Condition Monitoring* now involve the techniques of neural networks [33] and fuzzy logic [34] to create expert systems which give clear and precise diagnoses for the motor under investigation. With these techniques faults are no longer required to be modelled mathematically, as the decision on whether a fault has indeed occurred is made through a series of pattern recognition processes. Before a neural network can be used as a diagnostic tool, however, it must first be trained. In order to accomplish this, data must be gathered from a wide range of operating conditions as well as examples from the particular fault condition to which the network is required to identify.

In all of the above examples the monitoring of motor parameters, be it vibration, axial flux or supply current, has been done whilst the machine under investigation is operated under loaded conditions during steady state operation.

In some particular cases it may not be possible, nor desirable, for the motor under test to be run under loaded conditions for significant periods of time. This being the situation when the motor is operated under no load conditions, or has been removed to the workshop environment where loaded conditions are no longer practical nor achievable. Furthermore, in many applications a motor experiences several start-ups within the normal duty cycle, hence, research was undertaken to investigate if practical diagnostic information could be obtained from the above motor parameters, in particular supply current, during the initial transient period of motor operation when the parameters are at a natural increased level in amplitude.

1.2.2 Transient Monitoring

Elder [35] et al. and Jianguo [36] et al. report that they have both successfully located the presence of rotor faults within the transient signals obtained from a three phase SCIM. In both cases the frequency content of the transient supply current signal to the SCIM was analysed, although work investigating the transient vibrational response [37] has also been carried out.

During the initial acceleration of an induction motor from stand-still to normal operating speeds, a large supply current flows for a relatively long period of time, even when the motor is operated under no load conditions. This phenomenon happens particularly if the motor is started direct on line, a common practice within offshore facilities. Elder [35] et al. have shown how the sidebands which occur at $\pm 2s$ around the fundamental of the supply frequency, in a steady state analysis of the supply current, are non-stationary in nature during the transient, this being due to the motor slip changing from unity to near zero during the start-up period, Figure [1.2.2.1].

Elder employed the speech processing technique of a 'Speech Vocoder' to filter a wide range of frequencies around the fundamental. From the vocoder's output Elder reports that non-stationary frequency components can be observed. Elder [38] et al. were able to filter around an optimum frequency and have shown that by measuring the value of the sideband amplitude, it is possible to detect the presence of broken rotor bars using the no load supply current transient of the motor.

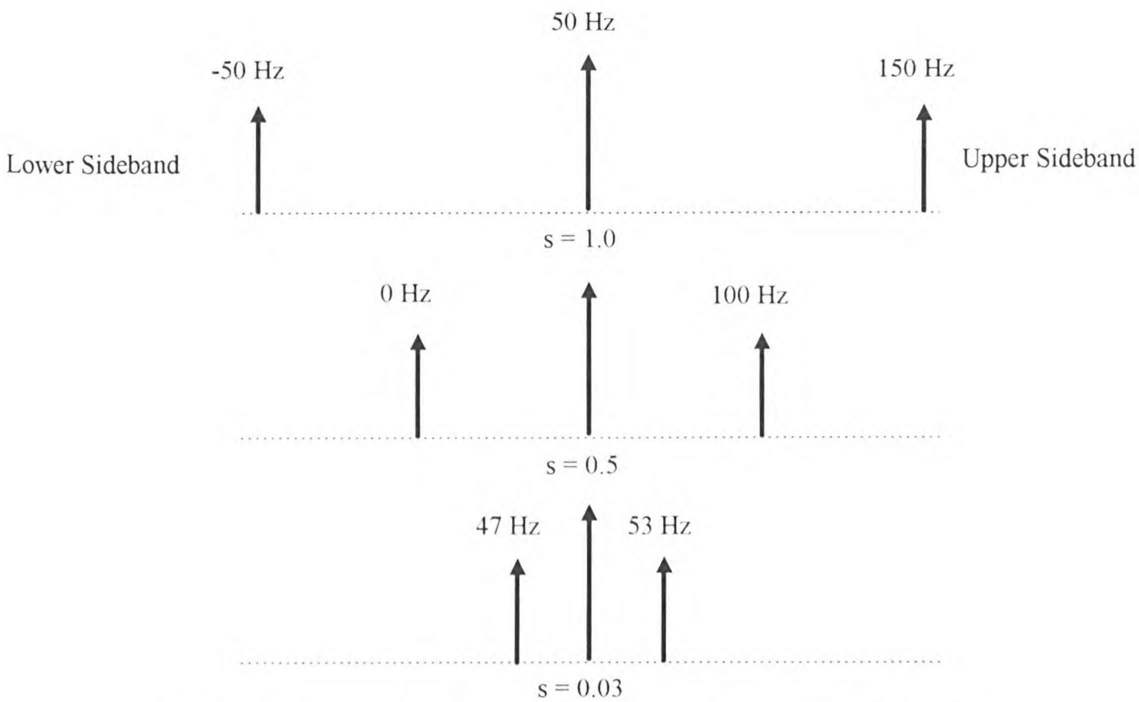

Figure [1.2.2.1] Non-Stationary Components within Typical Transient Signal.

Static eccentricity was found not to alter the amplitudes of the sidebands significantly along with machine temperature. The time at which the sideband passes through the filter however, was found to be variable upon the rotor starting position although Elder states that this may be due to the switching angle of the supply effecting the result. Jianguo [36] et al. have also observed the non-stationary frequency components within the current transient. Again, the supply current transient is passed through a signal processing technique. The authors use what is known as The Wigner Ville Distribution to produce a time-frequency representation of the transient signal. Using this technique Jianguo et al. found that the amplitude of the moving components increases with the severity of broken rotor bars, but do not give any reasons as to why this should be the case in their publications.

1.3 Frequency Components Indicative of Broken Squirrel Cage Rotor Bars

Deleroi [39] discusses how when a broken bar exists within a SCIM, an air-gap field curl is produced around the bar sending field waves into the air-gap of the motor in both directions from the bar in question. The extent to which the effects of this rotor anomaly are transmitted within the air-gap and the degree of any damping obtained are, as Deleroi states, dependant upon the rotor geometry. The damping factor is shown to be variable in that it increases with motor slip, hence, with a high value of damping factor the rotor anomaly becomes particularly localised around the broken bar. The frequencies of the induced voltages within the stator winding from this field curl effect are reported by Deleroi to be defined by eq. (1.3.1).

$$F_{deleroi} = fs\,(k / p - s\,(k / p \pm 1))\ \text{Hz} \qquad \textbf{(1.3.1)}$$

Kliman [30] uses eq. (1.3.1) to construct a prediction of the air-gap flux spectrum observed from the stator during the steady state operation for a typical SCIM motor with a single broken bar. The amplitude of the components being calculated from the expression given by Deleroi [40]. Using this prediction Kliman superimposes, as directed by Deleroi [39], the spectrum with a prediction of a normal stator current spectrum based upon the same SCIM which gave the faulted air-gap flux spectrum. The resulting spectrum shows how the low harmonics are swamped by other stator current harmonics and that it is only higher order harmonics, such as the 7th, 11th and 13th which will be due to Deleroi's field curl and still be observable. The examination of higher frequencies within the stator current signal of a SCIM should not be detrimental to the gathering of health information on the motor, as Kliman [17] et al. state that at higher frequencies other faults may be distinguishable from that of broken rotor bars.

Elkasabgy [41] et al. prove the existence of the frequency components given by eq. (1.3.1) during steady state operation, by modelling a three phase, 4 pole, 30 hp, SCIM using a Finite Element package. With this model they report that when the presence of broken bars are introduced, an anomalously high air-gap field rotates at rotor speed and is localised around the area of the broken bars. Their results, obtained by computation, are further verified by the experimental detection of the frequency components via search coils located physically within the air-gap of the SCIM under test, as previously undertaken by Deleroi [39].

1.4 Induction Motor Simulation Techniques

The simulation of electrical and mechanical parameters within an induction machine has greatly improved over the last 10 - 20 years due to the advent of the digital computer. The computer now allows the successful calculation of the differential equations required to describe the general nature of the motor. Previously, the majority of calculations had involved the steady state simulation of a motor. However, with increasing computing power, motor operation during the starting period, whereupon the differential equations describing the nature of the motor become non-linear due to rotor acceleration, may now be simulated.

Marques Cardoso [27] et al. discuss the method of transforming three phase parameters of a motor to a two dimensional format by using the transformation technique known as 'Park's vector'. The two dimensions are known as 'direct' and 'quadrature' and are used within the equivalent circuit, derived from the sequence components, to determine the differential equations required to define the stator parameters [42][43]. Vas [44] solves these equations by transferring the three phase components to a two phase axes via the 'dq' transformation. Smith [45] et al. and Lloyd [46] also transform the three phase equations to two phase, solving the resulting integral equations via the Runge Kutta method of integration. De Sarkar [47] et al. discuss the solution of these differential equations without the use of the two phase transformation. The authors solve the un-transformed equations via a direct solution method and compare the results obtained with those of the two phase solution. The authors report that the three phase calculation approach allows a wider class of problem to be handled than the limited historical transformation approach. Elder [35] et al. initially simulate the transiential period of a three phase wire-wound rotor induction motors parameters using the two axis 'dq' approach, but although the simulated results were found to be favourable, when compared with real motor results, the authors find that the method has a number of limitations. The limitations are stated to be that a balanced magnetic circuit is always required within the two phase transformation, and that at least one stator / rotor winding must be completely balanced at all times throughout the simulation, therefore limiting the full degree of fault simulation which may be calculated. Elder proceeds to use a similar approach to De Sarkar [47] et al., and successfully introduces the effects of magnetic saturation within the simulation. The authors report that on the mathematical introduction of saturation effects, improved results within motor parameters were obtained. In both of the above techniques, the Runge Kutta method of integration was employed to solve the non-linear differential equations in a step by step approach.

With the increase in mathematical analysis packages available on larger and ever more powerful computers, mathematical techniques such as 'Finite Differences' and increasingly, 'Finite Elements' are being used in the simulation of induction machines. Isiobashi [48] et al. report on the calculation of the flux distribution within the motor using such 'FE' techniques. Campbell [49] et al. discuss the forces which occur on the end-windings of the induction motor and use 'FE' techniques to successfully calculate the values of these forces. Both Ho [50] et al. and Williamson [51] et al. use the technique to successfully calculate the voltages and currents present within the induction machine during both transient and steady state periods of operation. Both report favourable results, with Williamson reporting that a far greater number of fault effects may be successfully modelled using this technique than had been previously possible using past techniques.

1.5 Analysis of Squirrel Cage Induction Motor Rotor Bar Currents

1.5.1 Access to Rotor Bar Current

Much research has been concentrated upon the subject of SCIM rotor bar currents. In particular the currents situated around broken bars and high resistance end-rings are of great interest. As access to the rotor of a SCIM, whilst the machine is in operation, is physically difficult, many techniques have been employed to obtain the rotor current signal. Tsuji [52] uses a twin stator induction motor with stators magnetically decoupled to monitor the rotor currents. The stators lie side by side with a common squirrel cage rotor. One stator is used in the normal way with the other being used as a current transducer. Operating the second stator as a transformer, Tsuji monitors the currents which flow in the rotor. Uenosono [53] et al. investigate the amplitude and frequency content of the individual rotor bar currents within the SCIM. The individual rotor bar currents are obtained by measuring the potential difference between two electrodes positioned at the ends of each rotor bar. This voltage, which is proportional to the rotor bar current at that point on the bar, is brought to the outside world via a slip ring mechanism. Yoshida [54] et al. obtain the rotor current by transforming the current to the magnetic field of axial direction due to the skew effect. With this set-up the rotor current is obtained from an induction motor which has had amorphous ferromagnetic ribbons installed in order that the axial flux can be sensed. The output signal obtained from this magnetometer is estimated to correspond to the rotor currents. Magureanu [55][57] et al. discuss a method of obtaining the current within the short circuiting rings of the rotor in order to calculate the parameters of the induction motor. This method involves the setting up of a Hall Effect transducer on the 'direct' and 'quadrature' axis of the rotor. The resulting voltages being proportional to the 'direct' and 'quadrature' rotor currents within the stator frame. Magureanu [56] et al. also use this technique for the optimum speed control of a SCIM. Monitoring and controlling the rotor current in order to control the rotor flux, whilst changing the speed of the motor.

Williamson [58] et al. verify their analysis of rotor bar currents under broken bar and end-ring faults by monitoring the currents using an Inverted Geometry Induction Motor. This type of machine has a stationary external bar cage and a rotating three phase winding inside the cage. With this set-up fault conditions are far easier installed and the monitoring of bar currents is easier. Williamson monitors the rotor bar current by placing two electrodes a certain distance apart on the bar under investigation in order to monitor the potential difference between the two points. This potential again being proportional to the bar current. Kliman [17] et al. use such an 'inside out' motor to investigate the accuracy of their developed condition monitoring system. Kliman does not monitor the individual rotor bar currents, but uses the motor in order to introduce bar and end-ring fault conditions in a simpler fashion than if an original SCIM configuration had been used.

Landy [59] uses the inverted machine to obtain rotor bar currents in order to evaluate the torque produced within the SCIM. In order to avoid interbar currents, straight slots were introduced and all rotor bars were insulated. The rotor bar currents are obtained by placing toroidal coils of wire, known as 'Rogowski Coils', around the bars in question. The resulting voltages from the outputs of such coils being proportional to the current flowing through the bars.

As Stoll [60] and Ellison [61] et al. state, current transformers are commonly used to measure alternating currents without physically disturbing the conducting circuit. However, CT's are prone to problems including that of physical size, operation at high frequencies and noise due to sources of magnetic fields other than that being monitored. Ellison et al. have found that out of several types of current transducer, the Rogowski Coil is the most stable over a wide bandwidth when used in their induction motor protection system. Ward [62] et al. discuss the operation of the Rogowski Coil and show that it operates using the principles of Amperes Law to develop a voltage which when integrated is proportional to the current signal that the coil is monitoring. Ward discusses the two main types of coil available: the rigid toroidal coil and the long flexible coil. Ward proceeds to discuss how the Rogowski Coil gives a linear output and is not effected by magnetic saturation, a problem which the CT is prone to [63]. The coil can also be used to monitor high frequency signals where upon the operation of the coil changes to that of self integrating, should the coil parameters allow the coil inductance to be greater than its resistance [64] [62].

1.5.2 Rotor Current - Harmonic Content, Distribution and Interbar Currents

Trickey [65] contributes the distortions which occur within the speed and torque curves of induction motors to be present due to a number of reasons. These include: harmonics rotating in the air-gap field, synchronous locking of both stator and rotor harmonics and lastly, the effects of slot openings. Trickey introduces the concept of each harmonic of the rotating MMF causing a proportional rotating flux and that the harmonics of these flux components singularly act upon the motor, with the individual harmonics producing small torques proportional to the fundamental torque. These harmonic torques, referred to as 'Parasitic Torques', introduce harm to the overall performance of the machine but may be eliminated or reduced in magnitude by careful consideration to the design of the motor. Trickey suggests that the harmonic MMF will be reduced by producing a revolving field which is as sinusoidal as possible. Parameters that control the levels of harmonics present within the air-gap, and thus, reduce the effects of torque distortions include: increasing the air-gap size in order to reduce harmonics, reducing the size of slot openings and increasing the rotor resistance. The latter, Trickey states, does not eliminate the harmonic torque but does reduce the magnitude of the fundamental torque component, and hence, the level of harmonic torques.

Gault [66] states that the current within a three phase SCIM comprises waves of a complicated form where three main components are prominent, these include: slip-frequency components, a component due to the non-uniformity of motor reluctance known as the 'Tooth' frequency component and a non-sinusoidal distribution of the stator current known as the 'Band' frequency component.

Gault concludes that high frequency components within the rotor bar current may contribute to a high portion of the stray load loss in a SCIM. By proper slot design, tooth frequency components may be controlled. The band frequency component depending upon the winding and may be decreased by considering the levels of winding pitch and number of phases.

Liwschitcz [67] discusses the complete harmonic problem within the induction motor. The author states that the overall problem involves seven different topics, three of which include: the harmonics of the stator including their amplitudes and speed, the harmonics of the rotor including their amplitudes and speed, and the rotor currents produced by the different harmonics.

Lee [68] discusses the saturation harmonics which occur within a SCIM. The saturation harmonic content, which is odd in order, is high only when the teeth of the motor are highly saturated and the core of the motor is not. Lee states that it is at no load that the majority of harmonics due to saturation occur. Lee also discusses the rotor currents induced by these components, the magnitude of which decreases under loaded conditions, since the machine is less saturated and that within a SCIM the rotor currents tend to damp out the saturation harmonics.

Lee finally indicates how the torque's produced by the flux components at certain slips are approximately proportional to the square of the amplitude of the flux wave and that the saturation harmonics, in the case of the SCIM, produce useful torque's.

Wallace [69] predicts the harmonic current magnitudes and frequencies by obtaining the machine parameters. Using a two axis transformation and the impedance matrix for a particular motor, in conjunction with the mutual inductance, the rotor currents are computed.

Together with the calculation of the rotor bar currents, the impedance matrix method used by Wallace is used to calculate the effects of unbalanced windings within the motor. Wallace states that the stator imbalance only effects the magnitude of the motor currents, in that it is not harmonic producing, although the rotor equations do contain some harmonics.

Binns [70] introduces the concept of the MMF field within the air-gap of the motor being modulated by a carrier wave. All harmonics which are present in the stator and the rotor of the induction motor are then listed. Binns states that the components due to saturation are comparatively small in magnitude and that other components may occur if the phases of the motor are not balanced, the motor is not symmetrical and as a result of secondary armature reaction.

Binns verifies the theoretical work by proving the existence of the predicted frequency components via laboratory experimentation. Binns concludes that all flux and current harmonics will be responsible for loss production within the motor and that with regards the stator, the loss making harmonics are the slot ripple components along with certain saturation harmonics, whereas for the rotor, the most significant 'lossey' components are those of the slot ripple components.

Finally, using an inverted motor to obtain the rotor bar currents, Landy [59] reports that the harmonic currents of significance have frequencies corresponding to the fundamental, the primary phase belt and the primary slot harmonic MMF's.

Uenosono [53] et al. obtain the rotor bar currents and report the results of a harmonic analysis upon these currents. The authors conclude that the results of the harmonic analysis show that under light loads the harmonic content of the current is heavier than during heavily loaded conditions. Williamson [58] et al. show that their calculated and experimental results verify that the current from a broken bar now flows within the surrounding bars. Smikál [71] discusses how that when under a faulted condition, if the bars within the rotor are un-insulated, then when the bars are analysed for the lengthways distribution of current, an unequal distribution may be found. This unequal distribution is effected by the cross currents corresponding to an axial current displacement. Smikál shows that if inter rings are placed within the rotor they give the characteristics of a deep bar or double cage SCIM. Kerszenbaum [72] et al. show via theoretical prediction and through experimental work that large inter bar currents flow between the rotor bars if there are un-insulated broken bars present. Kerszenbaum shows that the magnitude of the current flowing into the broken bar, and hence, the inter bar current, is dependant upon the value of slip. It is also shown that the magnitude of the end-ring impedance has a significant effect upon the size of the inter bar current. Kerszenbaum states that the effects of the inter bar currents on the nature of the SCIM include: no reduction of starting torque; a reduction in the pull-out torque; the development of vibrations and the possibility of burning within the laminations adjacent to the fault.

Walliser [73] et al. show how the inter bar currents should be taken into consideration when monitoring the condition of the SCIM with un-insulated rotor bars. An expression for the effect of these currents has been developed and may be introduced via the theories given by Deleroi [39]. Walliser states that the sidebands representative of broken bars will actually get smaller if inter bar currents are present. This is due to the decrease in imbalance when inter bar currents are present, hence, the author states that previous current monitoring techniques may have under estimated or not detected the fault at all if inter bar currents were not taken into account. Results are given showing the reduction of the sidebands due to inter bar currents. The results being obtained from analysing the supply currents around the fundamental and slot harmonics in order to detect any increase in sideband amplitude with fault conditions. Walliser states that in order to get a more accurate indication of broken bars the supply current should be monitored at higher frequencies away from that of the supply frequency [17]. Landy [59] et al. discuss how these inter bar currents will produce vibrations within the induction motor which may also be analysed in order to obtain the health condition of the machine [74].

1.6 Conclusions

The polyphase induction motor has been shown to be one of the most commonly used electric motors in all areas of modern life, be it within the home or industrial environments. Although inherently robust due its simple design, the motor is prevalent to cracked or broken rotor bars which occur due to the excessive stresses caused by the large electro-magnetic and electro-mechanical forces present during normal operation. As a result of this, many different '*Condition Monitoring*' techniques have been developed to monitor the health of a motor, thus giving the operator sufficient diagnostic information to enable suitable early detection of problems and early planning of cost effective maintenance schedules.

Historic fault detection techniques involved the physical invasion of the motor under investigation in order to obtain the health of the motor. However, latterly techniques have been developed which allow the diagnostic information to be obtained non-invasively. The majority of these techniques monitor either the axial leakage flux, the motor frame vibration, developed torque, rotor speed or the supply current whilst the motor is operated under fully loaded, steady state conditions. Researchers have now found that it is possible to obtain such information during the initial start-up period of the motor.

It has also been shown that researchers have located certain frequency components which rotate with the broken rotor bar. Through an improved transient monitoring system and investigations into rotor bar currents, it is hoped to be possible, via suitable signal processing techniques, to locate these components as a means to obtain a suitable detection on the location of any rotor bar anomaly within the rotor of the SCIM.

In conjunction with this an inverted geometry induction motor will be commissioned in order to complement this work and provide an opportunity to investigate the nature of rotor bar currents under both normal and faulted conditions.

Before proceeding with this, however, Chapter 2 will discuss in greater detail the relevant theories and techniques of monitoring supply current as a means of fault detection within induction motors.

Chapter 2

The Utilisation of Supply Current as a Condition Monitoring Technique

2.0 Introduction

The following chapter discusses the relevant theories behind the technique of utilising an induction motor's supply current to detect faults, including that of rotor bar faults, during both steady and transient states of operation. A review of a cross-section of monitoring techniques already in use has also been included for completeness.

2.1 Steady State Operation - Frequency Components Indicative of Broken Squirrel Cage Rotor Bars

Barton [75] et al. in their experimental work on the operation of an induction motor at one half normal operational speed, state that when a positive sequence voltage is supplied to the terminals of a symmetrical motor, a distributed magnetic field is created within the air-gap. This field is found to rotate in a forward nature relative to the motors stator at the synchronous speed of ω_s radians / sec. The authors state that this field is also found to rotate forwards relative to the rotor at $s\omega_s$ radians / sec, and it is this field which induces positive sequence currents of frequency sf_s Hz within the rotor conductors. Barton [75] et al. state that if the motor should have any form of rotor imbalance present, the flow of positive sequence currents through the rotor will generate negative sequence voltages at similar frequencies to the positive sequence. These voltages are induced into the air-gap and result in a negative sequence magnetic field being created. This negative sequence field, the authors state, is found to rotate in a backwards direction relative to the rotor with a similar velocity of $s\omega_s$ radians / sec, resulting in frequency components of $(1\text{-}2s)f_s$ Hz being generated within the stator [76][77]. Using separate equivalent circuits for both positive and negative sequence components, the authors show that the individual components produce torques which contain two separate components. The authors state that these components come from the interaction of the positive sequence MMF with negative sequence flux, and negative sequence MMF with positive sequence flux. Alternating torque's result from the interaction between the two torque components, oscillating at the relative slip frequency of the components and ultimately producing mechanical vibrations.

Russell [78] et al. state that the majority of induction motor analyses have historically been based upon traditional equivalent circuit methods, Figure [2.1.1]. Russell [78] et al. state that an alternative method to this analysis technique is to use magnetically coupled electric circuits. The authors describe how with this technique individual circuits are capable of relative motion in respect to one another. With this technique the authors state that due to the mutual inductances between the stator and rotor being dependant upon rotor position, the resulting differential equations contain time varying coefficients, which require axis transformation techniques to express the flux linkage equations within a reference frame not dependent upon rotor position. Using this technique, Russell [78] et al. solve machine equations for the steady state operation of a polyphase motor under various stator - rotor conditions.

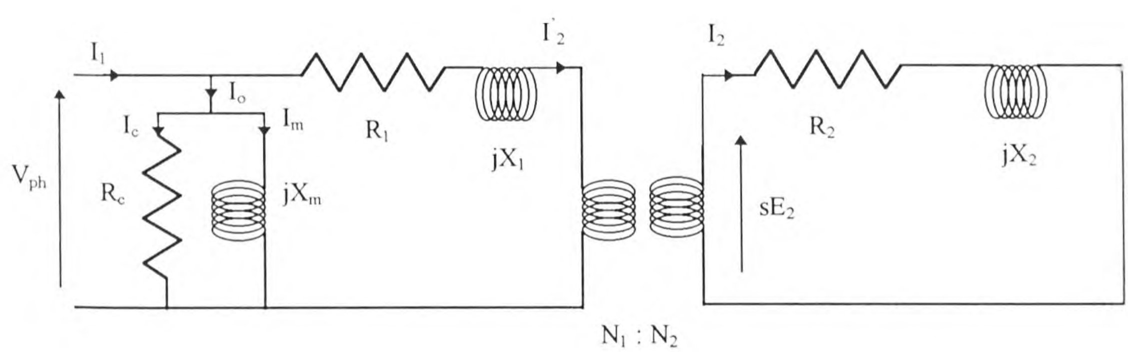

Figure [2.1.1] Traditional Induction Motor Equivalent Circuit (per phase).

For a balanced polyphase induction motor the authors formulate expressions to define the currents within the rotor. The authors show how the currents contain frequency components of sf_s and $f_s(s\text{-}2)$ Hz. As the machine is balanced, the authors state that the $f_s(s\text{-}2)$ term sums to zero leaving the sf_s

term present. The expressions for the stator currents are also defined for such a motor. These are shown to contain the frequency components f_s and $f_s(1\text{-}2s)$ Hz. Again, the $f_s(1\text{-}2s)$ component sums to zero since the motor is balanced leaving the stator current containing only the fundamental component.

In order to backup their computational analysis the authors carry out several experimental investigations. These take the form of monitoring the stator current waveform at various rotor speeds in order to observe the effects of the variable frequency components. The authors successfully show the degradation of the stator waveform at various rotor speeds and postulate that the reasoning behind such degradation is due to the above frequency component.

Williamson and Smith [58] describe the analysis technique of a mesh model of a rotor that employs the rotating field theory. The authors state that this is a general approach in that any symmetrical and more importantly, asymmetrical arrangement of rotor fault may be modelled.

The authors describe how the balanced positive sequence supply voltages applied to the stator create a forward rotating field within the air-gap. This field induces slip EMF's and therefore slip frequency currents within the rotor meshes. The authors state that the air-gap field created by these currents will include two components: a fundamentally distributed component rotating at slip speed in the forward direction with respect to the rotor; and an equal amplitude component rotating at the same speed in the backward direction. The total fundamentally distributed air-gap field being established by the ensemble of rotor currents via superposition of the individual components. The authors re-iterate that when the motor is operated under symmetrical conditions, the backwards rotating component cancels and how conversely when the motor is operated under asymmetrical conditions the resultant backward component is non-zero, a phenomenon further defined within Appendix I. This field, rotating at slip speed backwards with respect to the rotor revolves in a forwards direction at a speed of $(1\text{-}2s)$ times the synchronous speed with respect to the stator. The authors further state, that this field induces the EMF's of frequency $1\text{-}2s$ times the fundamental within the stator windings. Interestingly, the authors report that between standstill and half speed, the induced EMF's are negative sequence components; whereas from half speed through to full speed the components are reported to be positive sequence. The effects of this, the authors state, is that the mains frequency of the original stator supply current will be modulated by a variable component of twice slip frequency.

The results of these investigations are verified by the authors using a 250 hp, 8 pole machine. The authors found that the amplitude of the *(1-2s)* fault component falls to zero at a speed of 450 rev / min, which in the experimental set-up represents an operational slip of 0.5.

The authors go on to state that they would have reservations using a supply monitoring technique for rotor fault detection purposes due to the relative small amplitudes of fault component present when compared to the larger supply fundamental component. The authors point out that during their investigations under single broken bar conditions, the amplitude of the fault component over the entire speed range monitored never exceeded 1% of the supply fundamental, which itself was found to vary by less than 1% of its original symmetrical value.

Penman [21] et al. discuss how a similar effect may be observed within the axial leakage flux due to the presence of a broken rotor bar. The authors state how due to faults causing torque pulsation's, and hence, speed oscillations under faulted conditions, the stator supply current will be modulated. The level of modulation, the authors discuss, being at a frequency of $2s\omega_s$ radians / sec, thus causing the supply frequency to produce sidebands separated by $2sf_s$ Hz.

The authors conclude by verifying their theoretical predictions via a series of laboratory tests. Using a 4 kW SCIM, several faulted conditions were investigated including: *stator winding inter-turn short circuits*, *wound rotor short circuits*, *phase loss*, *eccentricity*, *supply phase sequence variation*, and *broken rotor bars*. The authors show that by monitoring axial leakage flux during steady state operation, it is possible to observe significant amplitude changes within the sidebands located at $\pm 2sf_s$ around the fundamental supply frequency. In particular, results are presented which show an increased amplitude sideband occurring under the fault condition of 1 broken rotor bar in 32. (It is noted that the increase in amplitude appears to occur mainly within the lower of the two sidebands, i.e. the component which occurs at $-2sf_s$ Hz from the supply fundamental. However, no explanation is given as to the reasoning behind such a phenomenon).

Hargis [18] et al. discuss how the impedance from the stator winding varies with a frequency of $N\omega_r$ when a normal rotor rotates. The authors discuss how if the rotor is irregular for any reason the fundamental variation of the impedance becomes $2\omega_r$. It is further shown how, by calculating an expression for the rotor MMF and modulating it with an expression describing the impedance variations of the motor, MMF components are generated as shown by eq. (2.2).

$$m = M\left[\sin(3-2s)\omega t - 3p\vartheta - \lambda + \sin(1-2s)\omega t - p\vartheta - \lambda\right] \qquad \textbf{(2.2)}$$

The authors state that it is the second of these terms which results in an EMF within the stator which is a direct measure of rotor non-uniformity. Hargis [18] et al. state that a cyclic variation within the current produces a torque variation at twice slip frequency, see Appendix II. Due to this variation, a speed fluctuation occurs producing a reduction within the magnitude of the $(1-2s)\omega_s$ current frequency component, and that a new component is found to occur at $(1+2s)\omega_s$ [76][77], which is further enhanced by any third time flux harmonic present, see Appendix III. A further discussion of how these components interact with one another in order induce other components is summarised within Appendix IV.

The authors state that if a pair of rotor bars with anomalies should occur when spaced by $\pi/2$ (elect.) radians apart, then no $(1-2s)$ component term would occur. But, as the authors state, it is generally accepted that most examples of broken bar conditions occur contiguously, due to the increased current which flows within the surrounding bars of the original fault, thus increasing the stresses present within nearby bars.

The authors finish by developing an expression, eq. (2.3), which enables the amount of broken bars to be calculated, depending upon the speed of the motor remaining constant and the broken bars being of a contiguous nature.

$$n = 2R \,/\, \left[(Ndb \,/\, 10) + 2p \right] \qquad \textbf{(2.3)}$$

Thomson [32] et al. verified the operation of this expression and concluded that it under estimates the number of broken rotor bars present. In a series of tests run by the authors, they state that the main reasoning behind the downfall of eq. (2.3) is the predictions dependence upon motor load, rotor design and general motor operating conditions [79][80].

2.2 Steady State Operation - Present Non Invasive Monitoring Techniques

Hargis [18] et al. discuss the various parameters which may be monitored within an induction motor, in particular current, speed and vibration. With respect to current, the authors state that the monitoring of a motors supply current is one of the easiest parameters to obtain. The techniques which employ this parameter are extremely 'non-invasive' in nature, as they do not require the actual supply current, since a transformed signal used for current indication within a non-hazardous control room is sufficient to obtain the required diagnostic information. The authors discuss how their system monitors the steady state supply current by initially recording the signal on a tape recorder, prior to analysis via a sufficiently high resolution spectrum analyser. The authors show how by monitoring the $(1 \pm 2s) f_s$ Hz components, the effects of a three broken bar condition and a normal rotor condition may be clearly observed via the amplitude change of the relevant frequency components. The authors state, however, that in order for an accurate detection of the motor condition, it is vital that the exact slip of the machine is obtained, in this case by monitoring the frequencies at which the principal rotor slots occur at, $\omega_s (N \pm 1)$ Hz. It is interesting to note that the authors indicate that current monitoring may also have an application within mechanical condition monitoring, as load disturbances may be quantified from the measurement of the current modulation along with some background knowledge to the mechanical parameters of the system.

Finally, the authors conclude that by using their technique there would be no obvious method of distinguishing between various possible rotor anomalies, and that current monitoring along with speed monitoring, also discussed, may in fact be liable to the under estimation of number of faulty rotor bars under certain conditions, and in extreme conditions may fail to detect the presence of any fault at all.

Steele [31] et al. discuss how with vibration monitoring, the transducers require physical access to the motor, whereas for supply current monitoring, or any other electrical line quantity, direct access to the motor is non-essential. This obviously gives significant advantages for instance, as the authors state, within industry where access is not always readily accessible.

The authors describe their prototype monitoring system which monitors supply voltage, current and power via specific electronic instrumentation connected directly to the supply current circuit. The signal processing used within the system includes a Fast Fourier Transform spectrum analyser capable of monitoring a wide frequency range, the authors quote *0 - 20 kHz*. The authors further discuss the signal processing technique of obtaining a signal cepstrum. This technique, the authors state, should be used when the signal contains a large number of harmonics / sidebands which may be difficult to interpret. The authors describe how the production of the cepstrum is obtained by further processing the signal in question. The logarithm of the spectrum being obtained and a Fourier analysis run on the results. The cepstrum, the authors state, has the effect of separating the sidebands from the source spectrum and differentiating between sets of harmonics or sidebands.

The authors proceed to report on the findings of their monitoring system. They run several tests in the detection of numerous faults within various drive units including that of defective top bearings and broken rotor bars.

The authors discuss how in the detection of broken rotor bars, such a fault was simulated by the introduction of a drilled hole through the rotor bar / end-ring connection. With this simulated fault, the authors monitoring system, it is reported, was able to detect an observable increase within the amplitude of certain sidebands of the electrical signals frequency spectrum. In particular the sidebands located at either side of the fundamental supply frequency by $2sf_s$ Hz.

The authors conclude that this method has been demonstrated to give successful fault diagnostic information, but requires further work in order to fully explain the spectrum obtained during fault conditions, and to produce a fully commercially viable diagnostic product.

Rankin [6] states that there are numerous off-line and on-line testing procedures in existence which have well proven track records in the successful detection of motor faults. Such techniques range from visual inspection, where the obvious drawbacks of such a technique are evident, to three phase current observations, where fluctuations are observed within the voltage signal when the motor is operated under faulted conditions. Rankin, however, introduces one more, that of phase current analysis, which the author states has attractive features over techniques already in existence. This technique, as the author states, may be achieved from within a motor switch-room without any form of production loss or motor downtime, and involves monitoring the supply current sidebands which exist at ±2s around the supply fundamental frequency, the amplitudes of which supply the necessary diagnostic information [81]. Rankin states that combining the results of this current analysis technique, along with background knowledge of the materials used within the construction of the motor, it is possible to determine the condition of the rotor, and hence, make suitable judgements on the continuation of motor operation. The author also indicates that it is possible to detect the presence of any air-gap eccentricities which may exist within the motor system [25].

Rankin [82] notes that only two quantities affect the magnitude of the sideband components around the fundamental supply frequency. These quantities, the author states, being the number or severity of broken bars together with the load present upon the motor, where variations on the load not only alter the magnitudes of the components, but also alter the fundamental frequency of the component. It is interesting to note that the author concludes that the expression developed by Hargis [18] et al. to calculate the severity of broken cage bars present within the rotor, is only applicable when the machine is operated under fully loaded conditions and, as the author states, has extreme limitations within the industrial environment as the expression tends to under estimate the severity of rotor faults due to the current spectra being a function of the rotor winding fault, mechanical load variations, rotor design and in some cases, the actual mechanical load.

Rankin [6] states that this technique has been well proven by testing, at the time of publication, over 2,000 motors. The author reports that this technique has been implemented on a software package specifically developed to use special routines which diagnose the motor problems on-line. The system, which makes use of an expert system, reads the current spectrum produced from a normal high resolution spectrum analyser and eliminates any extraneous factors present within the frequency spectrum, before forming a concise conclusion on the motors condition.

The author concludes, via two published case studies, that using the developed monitoring system over 20 % of the monitored motors have been found to contain problems related to cracked / broken rotor bars, high resistance joints, or air-gap eccentricities.

The author discusses that the creation of an on-line computer based diagnostic system was undertaken in order to eliminate previously required manual operations, obtain professional expertise in analysis and provide diagnosis reporting facilities. The author describes how the system contains two databases, one which allows ancillary information on the motor under investigation to be entered and stored, in order for record keeping facilities to be up-kept, and another which allows the spectrum of the motor, obtained from a normal spectrum analyser, to be stored. The system contains a third section, the diagnostic section, whereby the information on the condition of the motor is obtained from the frequency spectrum via spectral processing at relevant frequencies. Diagnostic algorithms have been created within the system which determine the severity of the fault, if any, and allows the on-board expert system to interpret the results and present concise recommendations on the condition of the motor to the operator in a clear, non-technical format.

Kliman [30] indicates that there may be a real possibility where such a current monitoring system with sufficient sensitivity to detect a single broken bar, may actually detect manufacturing and / or other asymmetries, thus giving rise to erroneous fault indications. In this case, the author suggests that the examination of higher harmonic amplitudes may give rise to such asymmetries being eliminated from that of broken bars. The author suggests that the harmonics which should be monitored instead of the fundamental component should in fact be those of the 5th, 7th, 11th and 13th. Any harmonics greater than this being indistinguishable due to their small amplitudes.

Kliman [30] proceeds to describe the software based monitoring system developed. The system samples supply current at the rate of *2 kHz* for a period of 30 seconds, before converting the time based data into the frequency domain utilising a FFT method. With this system the author monitors the frequency components characteristic to rotor anomalies. In order to do this, the values of speed and slip are obtained. This is achieved in this case by monitoring the axial flux. Since the system uses axial leakage flux, the author states that this parameter may be taken as a secondary parameter in the event of coming to a conclusion on the condition of a motor, [83][84]. The author also states that the system developed has sufficient software flexibility to allow other motor parameters to be sampled and used within the developed fault decision algorithm.

Kliman [30] gives experimental results on the usage of the developed system. Suitable examples are given of the sidebands located at either side of the fundamental supply frequency, and the sidebands around the 13th harmonic thereof, under different fault conditions.

The author concludes that a prototype non-invasive software / hardware system has been developed which offers sufficient reliability in the detection of the existence of broken / high resistance bars within normal steady state operation.

Kliman [17] et al. report further on the use of this prototype system and in particular the detection of broken rotor bars. Results are published which show the developed systems sensitivity to detect minor rotor anomalies such as one broken rotor bar. The amplitude change with this fault being particularly prominent within the lower sideband around the fundamental harmonic of the supply frequency. A further amplitude increase occurring in the case of two broken bars, etc.

The authors further discuss the decision algorithm which exits within the system and is capable of identifying the presence, or absence, of harmonics indicative to rotor anomalies. They state that there are in fact two parts to this, one which can determine the state of the motor from past monitoring tests and secondly, an algorithm which is capable of determining suitable diagnostic information from a one-off analysis. The authors discuss that the system developed has been created entirely from '*off the shelf*' components, and designed so that the sophisticated data acquisition and signal processing within the system is transparent to the user. However, any information displayed on the screen is of such a nature that it is entirely legible to computer novices.

2.3 Transient Operation - Frequency Components Indicative of Broken Squirrel Cage Rotor Bars

2.3.1 Transient versus Steady State Monitoring

It is clear from the on-line monitoring techniques employed during steady state operation, that detection of the relevant frequency components, and hence, reliable health diagnosis, may only be achieved when substantial levels of current flow both within the stator and rotor circuits of the motor under investigation. Such levels of current are required to produce large enough field aberrations within the air-gap in order to successfully detect the relevant frequency components from the stator winding. As a result, such monitoring techniques are only suitable when the motor is operated under fully loaded conditions, when a larger level of rotor current is present.

There are certain practical situations, however, as industrial operators have indicated, where such physical requirements for reliable diagnosis of a motors condition are impractical. For instance, when the motor has been removed from service and taken to a workshop environment, or where the motor has been taken off-line, when fully loaded testing conditions are no longer practical nor physically achievable. Also, there are many applications which require a motor to undertake numerous start-ups with very little steady state operation within the motors normal duty cycle. It is obviously advantageous to the operator if such periods of operation could be monitored in addition to steady state operation.

2.3.2 Typical Transient Current Signal

Figure [2.3.2.1] presents a typical three phase supply current transient for a moderately sized induction motor started under no load conditions. In this example it may be seen that the increased amplitude continues for a finite time period before decreasing to normal steady state levels. Figure [2.3.2.2] shows a similar transient obtained from the same motor started under fully loaded conditions. Due to the increased torque required to overcome the increased rotor inertia, the increased amplitude within the transient signal is present for a longer period of time. The plots presented merely indicate the increased amplitude which is present throughout the transient period. The levels of modulation which may be observed throughout both transient signals is due to the motor in question having a certain level of rotor bar fault. However, as mentioned, it is only the increased amplitude which is of concern at the moment.

2.3.3 Rotor Fault Components Present within Transient Signal

The steady state rotor fault frequency components situated at $f_s(\ 1 \pm 2s\ )$ Hz, have been successfully located by researchers to be present within the transient supply current signal of an induction motor [35][36][37]. However, as the researchers indicate, since the value of motor slip is no longer constant, due to rotor acceleration between standstill and steady state speed, the rotor fault components are non-stationary in nature as they are dependent upon motor slip.

Figure [2.3.3.1] indicates the relationships with which the rotor fault components have with other frequency components present within the transient supply current. All frequency components were calculated for different values of slip using proven expressions. The frequencies were all calculated for a three phase, 11 kW, 4 pole, 51 slot squirrel cage rotor. For the rotor fault components, or as they are commonly known, the Upper and Lower sidebands (USB, LSB), the formula used to calculate the components was that proven by Hargis [18] et al., eq. (2.3.3.1), eq. (2.3.3.2).

$$F_{LSB} = f_s\ (\ 1\text{-}2s\ ) \tag{2.3.3.1}$$

$$F_{USB} = f_s\ (\ 1+2s\ ) \tag{2.3.3.2}$$

The Principal Slot harmonics, (PSH), caused by variations within the reluctance of the air-gap due to the presence of conductor slotting within both stator and rotor circuits of the motor, were calculated using formulae previously verified by Thomson [10] et al., eq. (2.3.3.3).

$$F_{PSH} = f_s\ (n' \pm R\ (\ 1\text{-}s\ )\ /\ p\ ) \pm 2sf_s \tag{2.3.3.3}$$

The fundamental of the supply frequency was taken to be 50 Hz, although this and other constant harmonics, in particular those of the third supply harmonic, were deliberately not indicated within Figure [2.3.3.1], they were present in the form of the frequency axes.

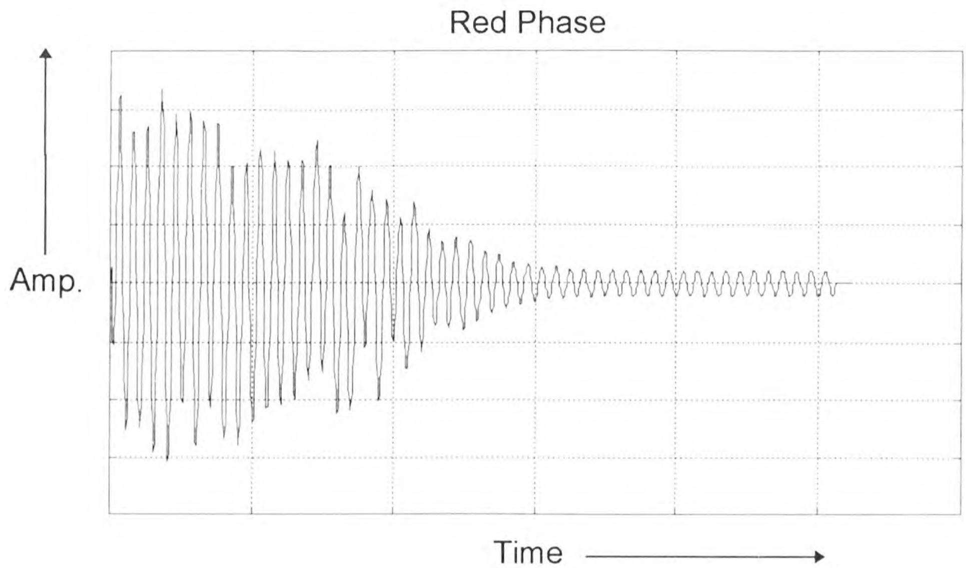

Figure [2.3.2.1] Current Transient - 11 kW Induction Motor No Load Start.

(Same Scales)

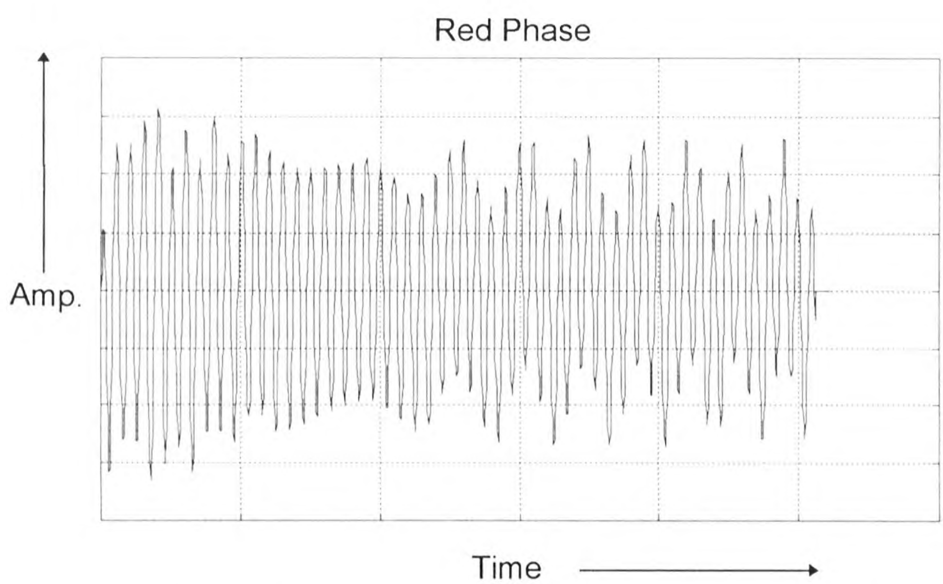

Figure [2.3.2.2] Current Transient - 11 kW Induction Motor Full Load Start.

(Same Scales)

To enable future investigations, the expression quoted by Deleroi reported to define the field curl associated with a broken cage rotor bar, eq. (1.3.1), was also indicated within the theoretical prediction of frequency components within a typical supply current transient, Figure [2.3.3.1].

$$F_{deleroi} = f_s (k / p - s (k / p \pm 1)) \qquad \textbf{(2.3.3.4)}$$

Particular note should be taken on the two sidebands indicated within Figure [2.3.3.1] by LSB and USB. These sidebands represent the theoretical locus of rotor fault frequency components defined by eq. (2.3.3.1) and eq. (2.3.3.2). It should be noted that in the case of the LSB, it is the absolute value of the component which is plotted versus slip, and not the actual value. The reason for this being that after a slip of 0.5, the LSB component becomes negative, thus indicating that the fault component has undergone a phase reversal. From Figure [2.3.3.1] it is observed that the LSB component initially starts at 50 Hz at standstill, proceeds to 0 Hz at a slip of 0.5, prior to returning to 50 Hz at near synchronous speed.

2.4 Transient Operation - Present Non-Invasive Monitoring Techniques

Elder [35][38] uses the speech phase vocoder technique to produce Spectrograms of the supply current transient signal of the motor under investigation. With this technique Elder proves that it is possible to detect broken cage rotor bars from the amplitude of the non-stationary LSB fault component. The technique uses recordings of the transient current obtained via a Store 7 data recorder. This set-up enabled laboratory, and to a lesser extent, industrial motors, to be investigated. After recording, data is transferred to a mainframe computer from where the vocoder processing technique is applied.

This technique is obviously extremely number intensive, and thus, requires a mainframe in order to handle the data to be processed within such an analysis. Although this technique was successfully tested both within laboratory and industrial environments, the necessity for such bulky recording equipment to obtain the transient data, followed by the requirement to compute the diagnosis under mainframe conditions, presents a practical hindrance and reduces the overall portability of such a monitoring technique.

2.5 Conclusions

It has been shown, in conjunction with Appendices I - IV, how past researchers have monitored the severity of broken cage rotor bars within three phase squirrel cage induction motors, using the frequency components eq. (2.3.3.1) present within the supply current. A historical review of the steady state theory was presented along with a discussion on the techniques presently employed. It was shown that out of the numerous non-invasive diagnostic techniques in operation, the technique which employs supply current, or any electrical parameter, is by far the most favourable due to the inherent flexibility and that data recordings of these parameters need not be obtained from the physical motor.

It has been indicated by researchers, however, that this technique suffers from two problems. Firstly, the results of such an analysis vary with applied load, and secondly, that the technique requires a relatively large current to be present before any reliable diagnostic information can be obtained. Due to this it was shown that under initial motor acceleration conditions, the supply current experiences a finite period of increased amplitude. This increase being anything between 5 - 8 times the steady state value. It was shown, through supply current waveforms, how the increased supply line current during this period of acceleration results in an increased level of rotor current flowing through the rotor conductors. Using this increased current, past researchers have been able to successfully locate the frequency components previously used within steady state analysis, and use them to determine the severity of cage rotor bar faults. These components being non-stationary in nature during this transiential period.

The signal processing techniques previously employed, along with recording facilities and computational requirements, created a system which enabled successful results to be attained only within an academic environment. The set-up, however, represented a non-viable approach when considered within the industrial environment.

In order to make the monitoring technique a more viable industrial concept, all aspects of the monitoring system would have to be reviewed. This involved reviewing the individual sections which go to form the data acquisition, data presentation and data processing sections of the system.

As a means to obtain a data processing technique which would be more economic in numerical operations, but still resulted in a similar level of accuracy, if not greater, than previous techniques, a collection of both historical and modern day signal processing techniques will be further discussed within Chapter 3, in order to obtain the most suited towards this particular practical application.

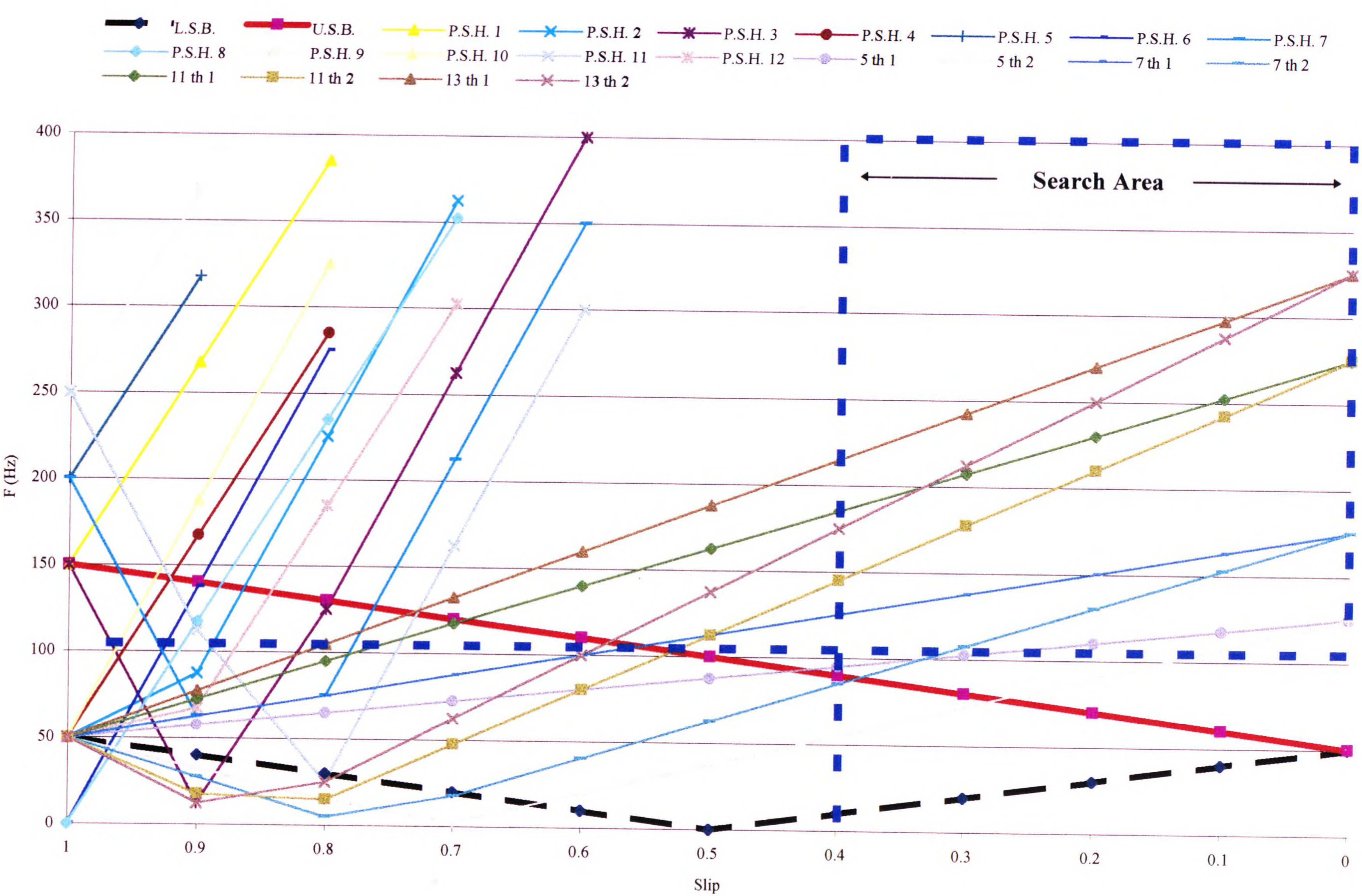

Figure [2.3.3.1] Prediction of Frequency Components Present Within Transient.

Chapter 3

Signal Processing Strategies

3.0 Introduction

Several techniques exist today which allow a signal to be represented within the Time-Frequency plane. The following chapter discusses such techniques in order to find the most suitable technique for frequency component detection within the previously described practical application. The techniques are investigated initially using synthesised mono-component, multi-component and non-stationary signals. Comparison is made on the individual techniques ability on the detection of relevant frequency components together with the effects of sample length and windowing technique used within the analysis. Finally, the techniques are investigated on their suitability towards analysing data obtained from the practical application.

In order to observe whether it would be possible to detect the non-stationary rotor fault components, as predicted by Figure [2.3.3.1], several signal processing techniques that result in the production of a signals Time-Frequency representation were investigated as a means to obtain the most efficient technique suitable for time-varying signals.

3.1 Short Time Fourier Transforms

The Spectrogram [85] is a popular method of displaying the Time-Frequency representation of a signal, a typical example of such a signal which may be analysed using a spectrogram being that of a speech signal. The spectrogram displays the Time-Frequency information of the signal by obtaining a short time spectrum of the signal via implementation of a Fourier Transform Algorithm (FTA).

If the excitation of the time varying signal under analysis is not to rapid then it may be assumed that the signal is stationary over a certain short period of time. Hence, it is possible to carry out a short time spectral analysis on the signal. The number of analyses required depending upon the total length of signal sample and the length of time window employed in partitioning the signal sample.

As the time window is increased in size it is found that the frequency resolution of the Time-Frequency representation is improved. However, as a result of this the time resolution of the display reduces. In a similar manner it is found that when the time window is reduced in size the opposite occurs.

Due to this trade off between the size of time window employed and the obtained resolution, both of time and frequency, it is common practice to utilise two such tests within one complete analysis of a signal. The first analysis would be a narrow band analysis where there is good frequency resolution but poor time resolution within the Time-Frequency representation. This would then be followed by a wide band analysis giving an improved time resolution but poorer frequency resolution within the final Time-Frequency representation.

A Spectrogram is calculated by employing a Fast Fourier Transform (FFT) algorithm, this algorithm being the most popular method of obtaining a spectrum from data within a digital computer. The FFT being a method of calculating the Discrete Fourier Transform (DFT) defined by eq. (3.1.1).

$$F(k) = \sum_{n=0}^{N-1} f(nT)\, e^{-j(2\pi / N)\, nk} \qquad \textbf{(3.1.1)}$$

F(k) represents the magnitude of the k^{th} spectral point and f(nT) represents the equally spaced samples of the analogue time signal f(t). If the sampling of the analogue signal has been carried out under Nyquist's theorem; i.e. the signal has been sampled at a rate of $2f_m$ or higher, where f_m is the highest frequency component present within the analogue time signal, it may be shown that the magnitude of F(k) is similar to the magnitude of the signal obtained at a time t = (N-1)T seconds, when the samples of the analogue signal f(t) are passed through an analogue filter with the frequency response $H(\omega)$, eq. (3.1.2).

$$H(\omega) = \sin(NT/2)(\omega - (2\pi k / NT)) / (\omega - (2k / NT)) \qquad \textbf{(3.1.2)}$$

The filter with this frequency response has a characteristic similar to that shown in Figure [3.1.1].

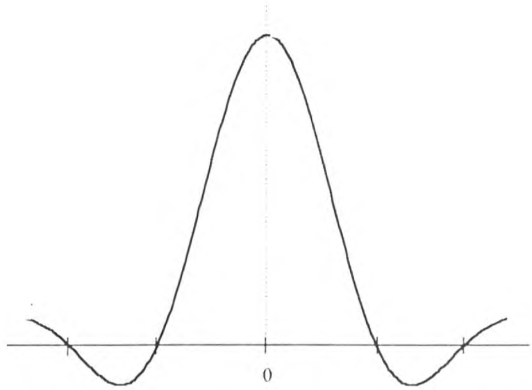

Figure [3.1.1] Filter Frequency Response Characteristic.

The data obtained from eq. (3.1.1) for values of k = 0 through to N - 1, corresponds to the output from a bank of filters each with a similar spectrum to that of Figure [3.1.1], where centre frequencies are defined by eq. (3.1.3).

$$\omega = (2\pi k) / (NT) \qquad \textbf{(3.1.3)}$$

On computation of eq. (3.1.1) only one spectral section is obtained. This being the spectrum similar to the output from the filter bank at time t = (N-1) T seconds. In order to obtain a short time spectral analysis it is necessary to repeat this computation over successive instants of time. To obtain a running spectrum of the signal under analysis eq. (3.1.1) must be modified to eq. (3.1.4). In this expression the first improvement is the addition of the window w(nT). This is done in order to improve the overall spectral characteristic when computing the DFT.

$$Fr(k) = \sum_{n=0}^{N-1} w(nT)\, f(nT + rMT)\, e^{-j(2\pi / N)nk} \qquad \textbf{(3.1.4)}$$

It should be noted that when eq. (3.1.1) is calculated on a finite amount of data, a time window is imposed onto the signal. This window is Rectangular of width, NT and it is this which results in the spectral window shown in Figure [3.1.1]. By using another type of window in eq. (3.1.4), it may be possible to obtain a far better spectral representation than that obtained from the Rectangular window. The second modification, in eq. (3.1.4), is the implementation of several spectral analyses on successive parts of the signal under analysis. Eq. (3.1.4) carries out such analyses separated in time by

MT seconds. This results in the calculation of the Short Time Fourier Transform (STFT), with the final Spectrogram being obtained from this by taking the square of the magnitude of the calculated STFT, as shown in eq. (3.1.5).

$$S(t,\omega) = |F(k)|^2 \qquad \textbf{(3.1.5)}$$

3.2 The Wigner Distribution

The Wigner Distribution (WD) of a continuous real signal is defined by Claassen and Mecklenbrauker [86] as that shown in eq. (3.2.1). x(t) represents the continuous real signal under analysis, τ represents a shift component and x^* indicates the complex conjugate of the signal x(t).

$$WD(t,\omega) = \int_{-\infty}^{\infty} x(t + \tau / 2)\, x^*(t - \tau / 2)\, e^{-j\omega\tau}\, d\tau \qquad \textbf{(3.2.1)}$$

$$WD(n,\vartheta) = 2 \sum_{m=-\infty}^{\infty} f(n + m) f^*(n - m)\, e^{-j2\pi m\vartheta} \qquad \textbf{(3.2.2)}$$

The discrete form of eq. (3.2.1) may be obtained from this equation and is again defined by Claassen and Mecklenbrauker [86] as that shown in eq. (3.2.2). In this expression the time index, n, is a discrete value with the frequency index, θ, being continuous. From this expression the WD at any time, n, depends upon the values $f(n).f^*(n)$, $f(n+1).f^*(n-1)$....., where the separation between individual samples is 2m, with m = 0,1,2,3 ....

In reality, although the integral range of eq. (3.2.2) spans from $-\infty$ to $+\infty$, only a finite data sequence will be available. Due to this a window is normally placed within the frequency domain with an automatic rectangular window being placed within the time domain due to the finite length of sequence, thus transforming eq. (3.2.2) to that of eq. (3.2.3). This form of WD is known as the Pseudo Wigner Distribution (PWD).

$$PWD(n,\theta) = 2 \sum_{m=-\infty}^{\infty} w(m) f(n + m) w^*(-m) f^*(n - m)\, e^{-j2m\vartheta} \qquad \textbf{(3.2.3)}$$

The Wigner Distribution and its many variants contain several desirable properties. These properties include: the WD of any real or complex function will be real, a time shift in the time signal will result in a time shift in the WD and the total energy in the signal is equal to the integral of the WD over the whole plane, (t, ω). However, along with these properties, the WD contains one undesirable property which limits its practical application. This property is known as the presence of 'crossterms'. The WD of two signals is a bilinear function of the original signals. This means that the sum of the two signals is not just the sum of the two WD's, but a third interference component is produced, eq. (3.2.4). The crossterms lie between the two components within the signal and are oscillatory with their frequencies increasing with increasing distance in time and frequency between the two original components. The crossterms can have peaks of up to twice that of the original components amplitude, and hence, make it difficult for component separation when analysing multi-component signals.

$$Wf + g(t,\omega) = Wf(t, \omega) + Wg(t, \omega) + 2ReWf,g(t,\omega) \qquad \textbf{(3.2.4)}$$

The method used to reduce the amplitude of crossterms is to introduce windowing. As with the PWD it is possible to window in the frequency direction in order to reduce the size of the crossterms. Types of window which give best results in the frequency direction are the Gaussian and Kaiser windows. Windowing may also be achieved within the time direction, although here a compromise must be made between crossterm attenuation and time resolution. The windows which give the best results within the time direction are the Rectangular and Gaussian windows.

The above windows all partition the data in one particular direction. Instead of windowing the data separately within the frequency direction and then the time direction, it is possible to use a two dimensional window, typically of Gaussian form, which results in a smoother version of the WD.

Another method of reducing the interference from which the WD technique suffers from is to convert the signal under analysis into its analytic form.

When a signal is analysed by the WD method, or by any variant of the technique, interference caused by aliasing within the resultant signal is reduced if Nyquists theorem is adhered to when sampling. However, regardless of the sampling rate employed there will still be low frequency components present within the WD. These components, which have no meaning in the overall frequency scan, are caused by the interaction between the positive and negative frequencies of the signal under investigation. The method of reducing the effects of these components is to make use of the Analytic version of the signal.

Consider a signal s(t) sampled at the Nyquist rate, f_s. The spectral representation of the signal is shown within Figure [3.2.1].

The analytic discrete time signal z(n) has a spectrum similar to that of Figure [3.2.2]. If a further two signals, s'(n) = s(n/2) and z'(n) = z(n/2) are then sampled at the same sampling rate, f_s, the resulting spectrums are shown in Figures [3.2.3] and [3.2.4] respectively. From these spectrums it is clear that the maximum spectral component of the signal s'(n) is now $2f_m = f_s$ and as the periodicity of the spectrum remains at f_s aliasing will occur due to the overlapping between the positive and negative frequencies.

However, with the analytic version of the signal, Figure [3.2.3], the maximum spectral component of the signal z'(n) = z(n/2) is also $2f_m = f_s$ and as the periodicity of the wave is also f_s no aliasing occurs, Figure [3.2.4].

The WD which analyses the analytic signal instead of the real signal is known as the Wigner Ville Distribution (WVD), eq. (3.2.5). The signal z(t) representing the analytic equivalent of the signal to be analysed, s(t).

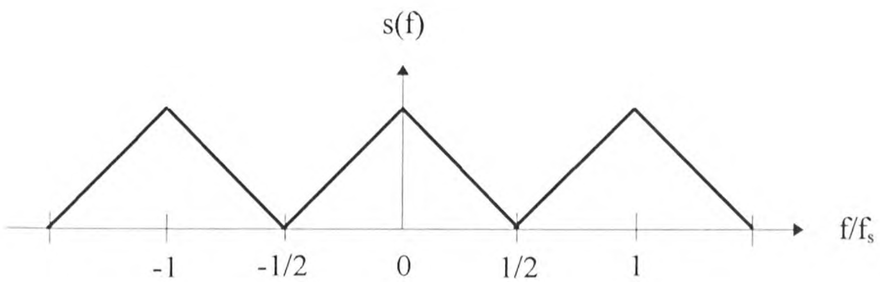

Figure [3.2.1] Spectral Representation of Signal s(t).

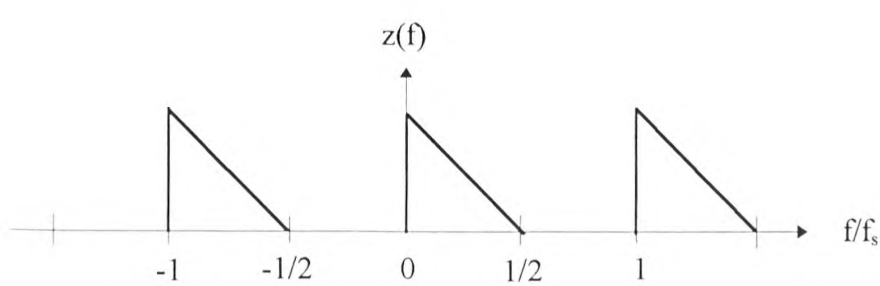

Figure [3.2.2] Analytic Discrete Spectral Representation of s(t).

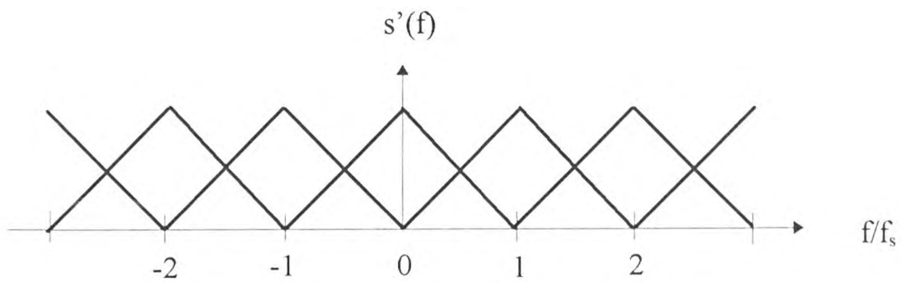

Figure [3.2.3] Spectral Representation with Aliasing.

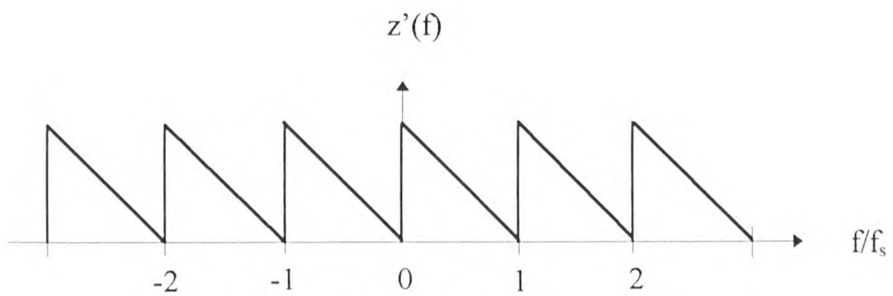

Figure [3.2.4] Analytic Representation with no Aliasing.

$$WVD(t,\omega) = \int_{-\infty}^{\infty} z(t + \tau / 2) z^*(t - \tau / 2)\, e^{-j\omega\tau}\, d\tau \qquad \textbf{(3.2.5)}$$

The analytic signal z(t) may be computed within the time domain via the Hilbert transformation, or within the frequency domain by simple multiplication.

Within the time domain the analytic signal is calculated via eq. (3.2.6).

$$z(t) = s(t) + jH[s(t)] \qquad \textbf{(3.2.6)}$$

Where H[s(t)] represents the Hilbert Transform of the signal s(t). The Hilbert Transform being calculated using eq. (3.2.7).

$$H(t) = 1 / \pi \text{ v.p. } \int [s(\tau) / (t - \tau)]\, d\tau \qquad \textbf{(3.2.7)}$$

The analytic signal z(t), however, has a frequency spectrum defined by:

$$
\begin{aligned}
Fa(\omega) &= 2.F(\omega) & \omega &> 0; \\
&= F(0) & \omega &= 0; \\
&= 0 & \omega &< 0;
\end{aligned}
$$

Hence, the analytic signal can be computed within the frequency domain in addition to the time domain. Calculation of the analytic signal in the frequency domain involves the use of the Fourier transforms of the signals s(t) and z(t), with the time domain analytic signal being recovered from z(f) via the Inverse Fourier Transform.

If the WD of a signal is assumed to be calculated by eq. (3.2.1), then if θ is made equal to $\tau / 2$, the following may be assumed.

$$WD(t,\omega) = 2 \int_{-\infty}^{\infty} s(t + \vartheta)\, s^*(t - \vartheta)\, e^{-2j\omega\vartheta}\, d\vartheta$$

(3.2.8)

$$WD(t,\omega) = \underset{\vartheta \to 2\omega}{2FT} \left[s(t + \vartheta)\, s^*(t - \vartheta) \right]$$

If the signal s(t) is assumed to be a band limited signal, s(n), which has been sampled at the Nyquist rate resulting in a sequence of duration N, then a direct application of the integral form eq. (3.2.1) to discretise eq. (3.2.8) is shown in eq. (3.2.9).

$$WD(n,m) = \underset{m \to 2k}{2\,DFT} \left[s(n + m)\, s^*(n - m) \right] \qquad \textbf{(3.2.9)}$$

The WVD in discrete form will therefore be calculated by the following manner.

$$WVD(t,f) = \underset{m \to 2k}{2\,DFT} \left[z(n + m)\, z^*(n - m) \right] \qquad \textbf{(3.2.10)}$$

The smoothed version of the WVD using windowing techniques, the SWVD, may be calculated by eq. (3.2.11).

$$SWVD(n,m) = 2 \sum_{k=-L}^{L} rn(k)\, e^{-jkm2\pi / K} \qquad \textbf{(3.2.11)}$$

$$rn(k) = \left[\sum_{i=-R}^{R} w(i)\, xa(n+i+k)\, xa^{*}(n+i-k) \right] |h(k)|^{2} \qquad \textbf{(3.2.12)}$$

Where $r_n(k)$ is referred to as the smoothed complex kernel. This kernel may be shown to be of a complex symmetrical nature; i.e. $r_n(k) = r_n(-k)$, hence, it is only necessary to compute half of the sequence as the DFT of a complex symmetrical sequence is itself real, thus the DFT of $jr_n(k)$ will be imaginary. Due to this it is possible to compute two slices of the SWVD using only one DFT calculation, combining the two complex kernels into a composite complex kernel, $R_n(k)$, eq. (3.2.13).

$$Rn(k) = rn(k) + jrn+1\,(k) \qquad \textbf{(3.2.13)}$$

The two WVD time slices thus come from both the real and imaginery parts of the composite kernel. Taking this computation property into consideration, the WD, or any variant of the WD, may be computed up to twice as fast as the STFT technique. This being one of the main reasons why the WD is used as a signal Time-Frequency representation, although for multi-component signals the technique is limited by the presence of crossterm interference.

3.3 Signal Analysis by Decomposition

One of the first Time-Frequency representations of a signal was introduced by Gabor [87]. This representation of a signal in the Time-Frequency domain was developed from the theory of quantum mechanics and is known as the Gabor Decomposition. In this decomposition, the signal under analysis, r(t), is broken down into a two variable function $R(\tau, \omega)$ and is achieved by the Gabor Decomposition expression of eq. (3.3.1).

$$R(\tau,\omega) = 1/2\pi(2\pi\sigma^{2})^{-1/4} \int_{-\infty}^{\infty} e^{(-(t-\tau)^{2}\,/\,4\sigma^{2})}\, e^{(-j\omega(t-\tau))}\, r(t)\, dt$$

(3.3.1)

On analysis of the above expression it is found that the Time-Frequency representation, $R(\tau,\omega)$, may be obtained by the convolution of the signal, r(t), with a separate signal, h(t), eq. (3.3.2). The signal, h(t), known as a wavelet may be of Gaussian format similar to that obtained from eq. (3.3.3).

$$\int_{-\infty}^{\infty} r(t)\, h(t - \tau)\, d\tau \qquad \textbf{(3.3.2)}$$

$$h(t) = 1/2\pi\, (2\pi\sigma^2)^{-1/4}\, e^{(-t^2/4\sigma^2)}\, e^{j\omega t} \qquad \textbf{(3.3.3)}$$

A phenomenon of the wavelets similar to that used within the Gabor decomposition, is that the envelope of the Gaussian wavelet has a constant time duration regardless of the frequency under investigation. This, in some cases, presents a practical limitation in that the analysis of short high frequency signals involves wavelets of broad envelope and a large number of cycles. These limitations may be overcome by the use of another Time-Frequency technique known as the Wavelet Transform. The limitation, however, is only applicable for high frequency bursts and after further investigation, was not considered to be of importance within the following applications.

In most practical cases the signals under investigation are digitised. This therefore results in a change of eq. (3.3.2) into the discrete convolution expression of eq. (3.3.4). This expression is now representitive to the characteristic of a finite impulse response filter, where the sampled points of the wavelet used within the decomposition represent the FIR filter coefficients. Eq. (3.3.4) may be implemented either by hardware or, as in the following applications, by software via the process of fast convolution.

$$r(n) = \sum_{i=-m}^{m} h(i)\, r(n - i) \qquad \textbf{(3.3.4)}$$

The decomposition of the signal under analysis may therefore be obtained by convolving the signal under investigation, via fast convolution techniques, with a Gaussian shaped wavelet similar to that described above. The wavelet must have a constant bandwidth and its centre frequency stationed upon the current frequency under investigation. A large variety of wavelet types may be used within such decomposition methods depending on the precise requirements of the application. Wavelets based on the Hamming, Hanning and Kaiser windows may all be used within the decomposition, although any Gaussian format of wavelet may be employed.

3.4 The Exponential Distribution

The Time-Frequency representations discussed previously, the STFT leading to the Spectrogram and the various versions of the Wigner Distribution may all be classed as members of a generalised Cohen class of Time-Frequency representation, see Appendix V. However, due to the inherent bilinear nature of these distributions, it has been shown that interference in the form of crossterms will reduce the effectiveness of the representations when analysing multi-component signals. The degree of interference is, however, related to the type of kernel function used, which in turn, identifies the nature of the specific distribution.

Another Time-Frequency representation which is a member of the same Cohen class of distributions is known as the Exponential Distribution or Choi Williams Distribution [88]. In this form of representation the kernel function used takes an exponential nature. The exponential kernel reduces crossterm amplitudes whilst still retaining the useful properties of the Time-Frequency distribution.

3.4.1 The Choi - Williams Distribution

The generalised Cohen distribution expression is shown in eq. (3.4.1.1).

$$Cf(t,\omega;\Phi) =$$

$$1/2\pi \int_{-\infty}^{\infty}\int_{-\infty}^{\infty}\int_{-\infty}^{\infty} e^{j(\xi\mu - \tau\omega - \xi t)}\, \Phi(\xi,\tau)\, f(\mu + \tau/2) f^*(\mu - \tau/2)\, d\mu\, d\tau\, d\xi$$

(3.4.1.1)

The Exponential Distribution (ED) uses a kernel where σ is a scaling factor. Substituting the kernel into the Generalised Expression results in the continuous form of the Exponential Distribution.

$$Ef(t,\omega) =$$

$$\int_{-\infty}^{\infty} e^{-j\omega\tau} \left[\int_{-\infty}^{\infty} 1/\sqrt{4\pi\tau^2} \;/\; \sigma\, e^{(-(\mu-\tau)^2/4\tau^2/\sigma)}\, f(\mu+\tau/2) f^*(\mu-\tau/2)\, d\mu \right] d\tau$$

(3.4.1.2)

As with the WD version of the generalised class a discrete version of eq. (3.4.1.2) may be obtained. Firstly, the generalised equation must be discretised.

$$Cf(n,\theta\ ;\ \Phi) = 2\ /\ 2\pi \sum_{\tau}\sum_{\mu} \int_{\xi=-\pi}^{\pi} e^{j(\xi\mu - 2\tau\theta - \xi n)}\ \Phi(\xi,\tau)\ f(\mu+\tau)f^{*}(\mu-\tau)\ d\xi$$

(3.4.1.3)

Where n, τ and μ are all discrete values with ξ and θ being continuous variables. Substituting the ED kernel into eq. (3.4.1.3) results in the definition of the ED for discrete time signals.

$$Ef(n,\theta) = 2 \sum_{\tau=-\infty}^{\infty} e^{-j2\theta\tau} \left[\sum_{\mu=-\infty}^{\infty} 1/\sqrt{4\pi\tau^2\ /\ \sigma}\, e^{(-(\mu-n)^2/(4\tau^2\ /\ \sigma))}\ f(\mu+\tau)f^{*}(\mu-\tau) \right]$$

(3.4.1.4)

As the real signals are of a finite length it is necessary to use windowing techniques. Using the windows $W_N(\tau)$ and $W_M(\mu)$ the expression for the Exponential Distribution for discrete signals becomes that shown in eq. (3.4.1.5).

$$Ef(n,k) =$$

$$2 \sum_{\tau=-\infty}^{\infty} WN(\tau)\, e^{-j2\pi k\tau / N} \left[\sum_{\mu=-\infty}^{\infty} WM(\mu)\ 1/\sqrt{4\pi\tau^2\ /\sigma}\, e^{(-\mu^2/4\tau^2/\sigma))} \cdot f(n+\mu+\tau)f^{*}(n+\mu-\tau) \right]$$

(3.4.1.5)

It has been found that the length and shape of window, W_N, determines the frequency resolution of the ED, whilst the length of the window, W_M determines the time resolution of the auto components. Therefore, the size of the window, W_N, determines a trade off between the high frequency resolution of the components and the smoothing of the crossterms.

The ED analyses the signal once the signal has been converted to its analytic equivalent, thus removing any potential aliasing difficulties. Eq. (3.4.1.5) shows the expression used to calculate the ED. From this it may be seen that the ED can be calculated using a Fast Fourier Transform, where 'n' represents the time index and 'k' the frequency index.

3.5 Encoding of Signal Processing Strategies

3.5.1 Software Development Environment

The investigations into which signal processing technique, and variants thereof, that would result in the most suitable Time-Frequency representation of the previously discussed practical application, were undertaken by encoding the techniques within the mathematical package, Matlab Ver. 4.0 [97]. This software package, which is windows based, enables the required encoding necessary for all three techniques to be entered and stored within user defined files, known as 'm_files', along with easy access to graphics packages required for displaying the computed Time-Frequency results, together with built in mathematical libraries resulting in easier overall implementation of the individual techniques.

3.5.2 The Spectrogram

From eq. (3.1.5) the Spectrogram is calculated by obtaining the square of the numerical series, F(k). The series F(k) represents the Short Time Fourier Transform of the data and may be computed by employing a spectral window and an FFT algorithm, eq. (3.1.4). The data flow diagram shown within Figure [3.5.2.1] presents the basic processes required to be encoded in order that a Spectrogram may be computed.

3.5.3 The Analytic Signal

As a method of removing low frequency components present within a computed Wigner Distribution, the analytic version of the signal to be analysed is used, see Section (3.2). The analytic version of a signal may be computed either within the time or frequency domains. As defined within eq. (3.2.6) and eq. (3.2.7) the technique used to obtain the analytic version of a signal within the time domain makes use of the Hilbert Transform. Computation of the analytic signal within the frequency domain, however, requires only multiplication. The data flow diagram within Figure [3.5.3.1] presents the basic procedure required to be encoded in order to calculate the analytic version of the signal.

3.5.4 The Wigner Ville Distribution

The distribution which employs the analytic version of the signal to be analysed is known as the Wigner Ville Distribution, eq. (3.2.10). The version of this distribution employed throughout the pending investigations was that of The Smoothed Wigner Ville Distribution, eq. (3.2.11) and eq. (3.2.12), where upon several different spectral windows were employed. The data flow diagram of Figure [3.5.4.1] presents the basic procedures required to be encoded in order that the SWVD of the signal may be computed.

3.5.5 Wavelet Decomposition

The Wavelet Decomposition method of producing a Time-Frequency representation of a signal requires the signal under investigation to be decomposed using a specific wavelet. The data flow diagram of Figure [3.5.5.1] shows how the wavelet was created using the Matlab software. This wavelet was then used within the Wavelet Decomposition procedure described within Figure [3.5.5.2]

3.5.6 Choi - Williams Distribution

The investigations towards the suitability of the Choi-Williams distribution as a method for both frequency component tracking within multi-component signals and, more importantly, as a technique to reduce the levels of crossterm interference, were carried out. The data diagram in Figure [3.5.6.1] shows the integral processes of the Choi - Williams m_file developed utilising the Matlab package. The code developed allowed full access to the individual parameters within the distribution technique, thus allowing a full investigation on the effects of varying these parameters.

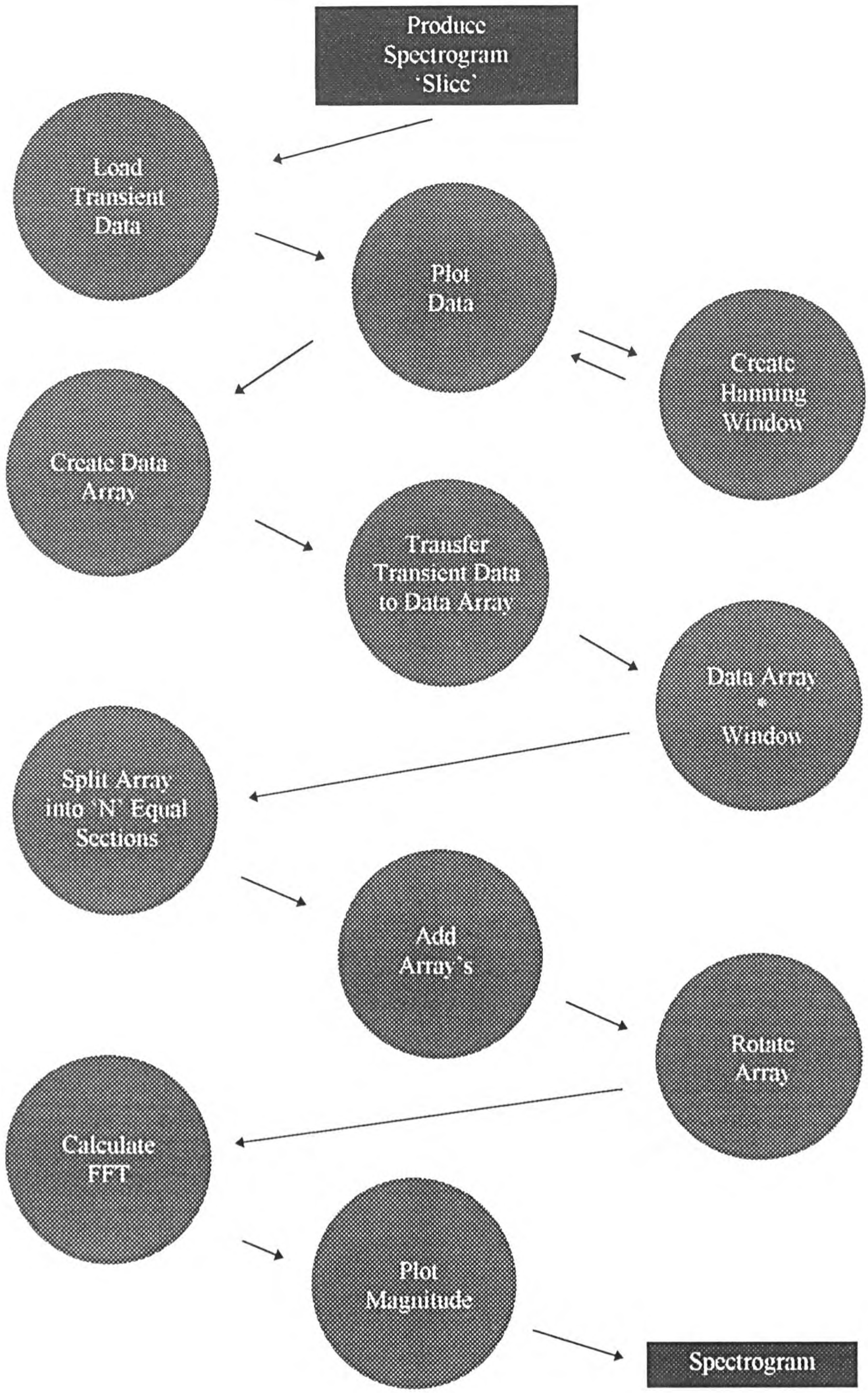

Figure [3.5.2.1] Data Flow in Spectrogram Software.

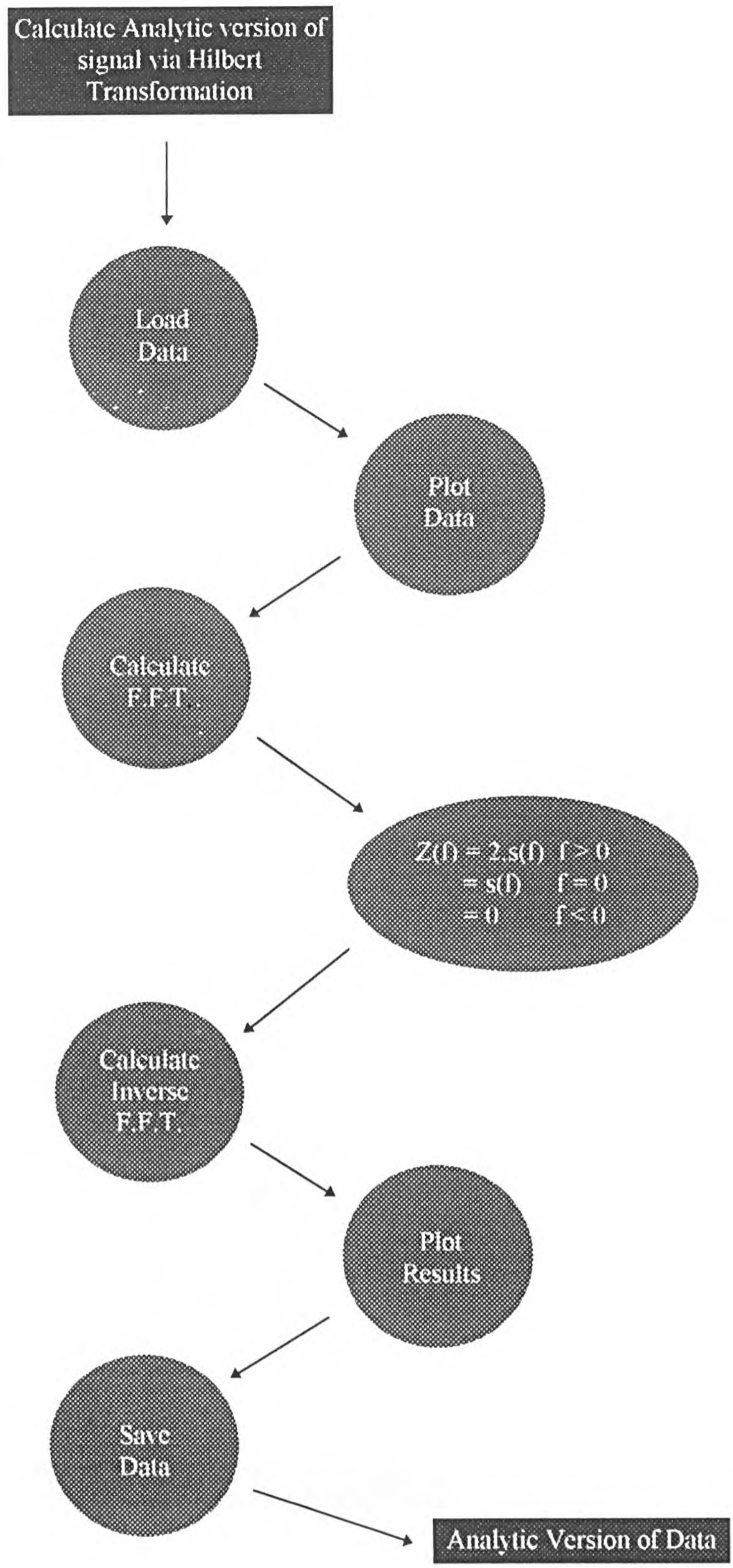

Figure [3.5.3.1] Computation of Analytic Signal.

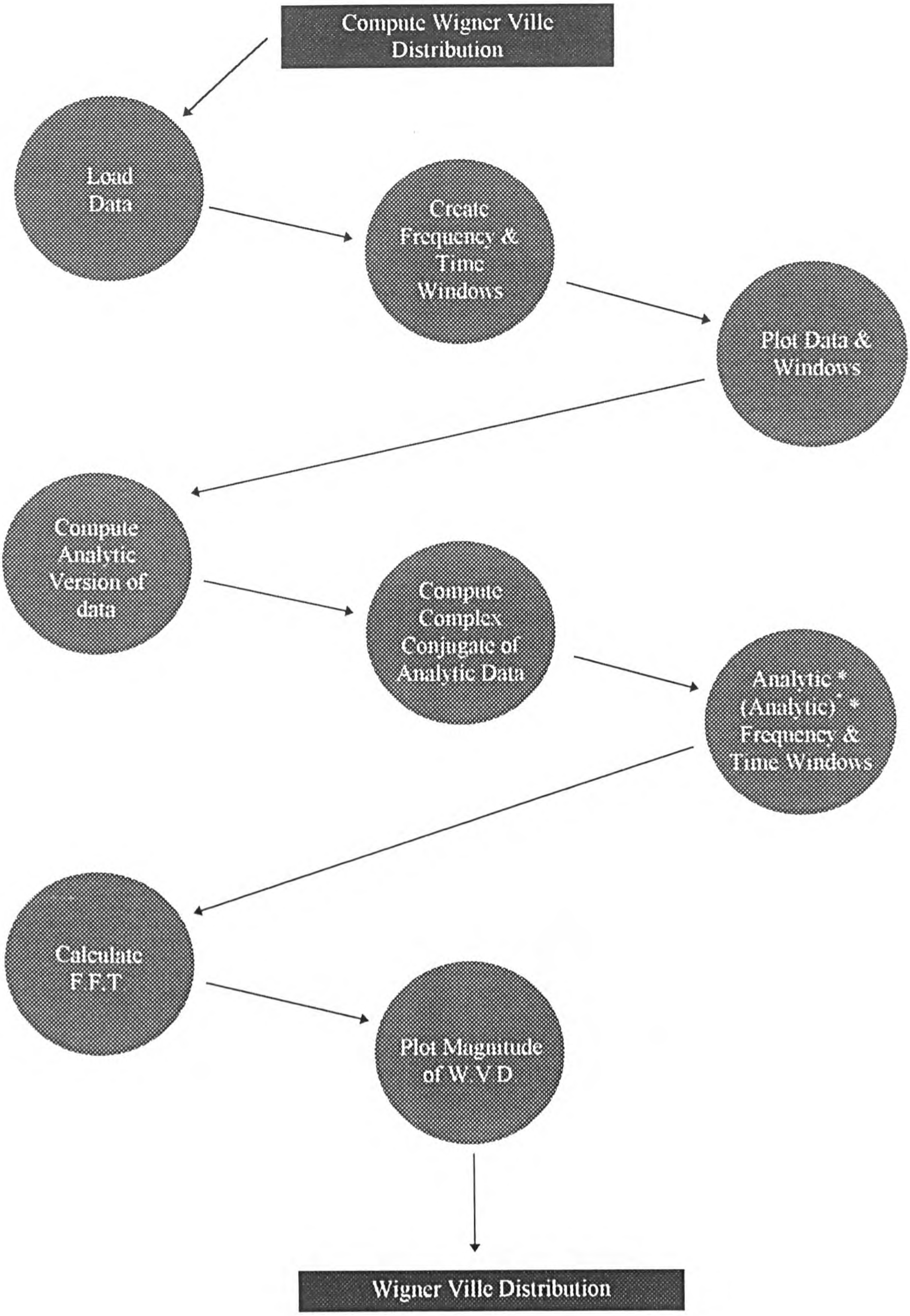

Figure [3.5.4.1] Computation within Wigner Ville Distribution M_File

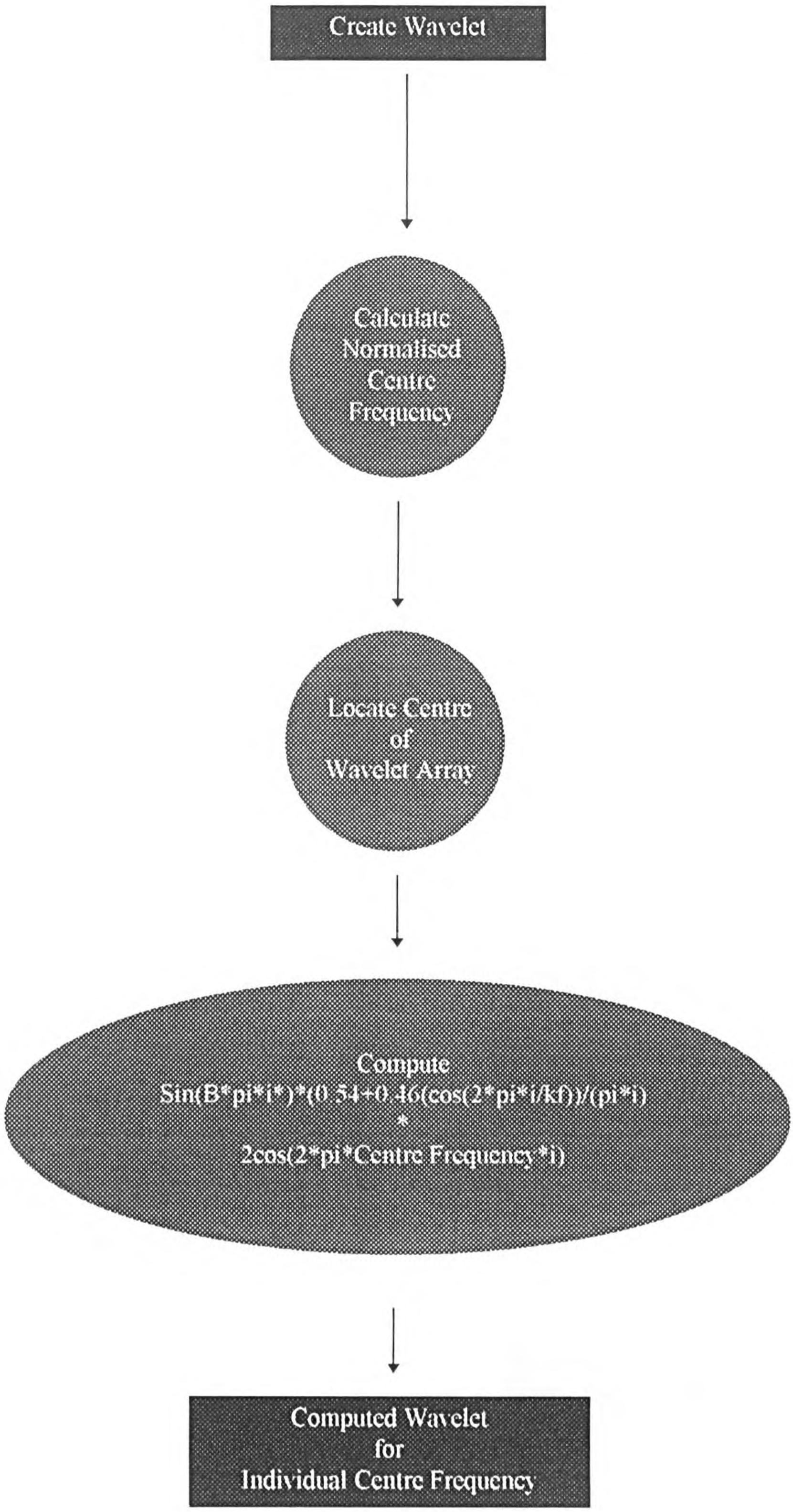

Figure [3.5.5.1] Computation of Wavelet for Wavelet Decomposition M_File

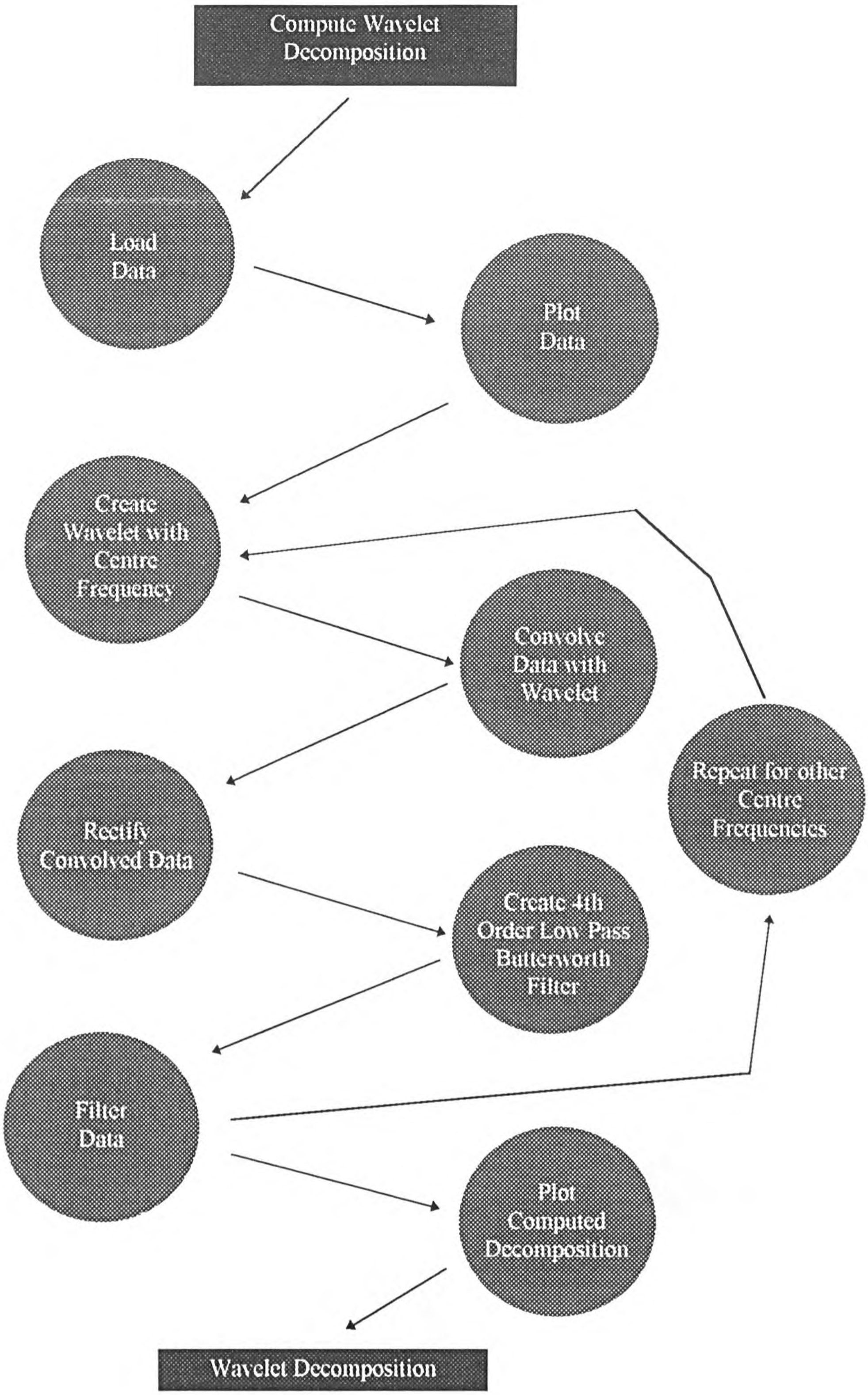

Figure [3.5.5.2] Computation Involved within Wavelet Decomposition M_File

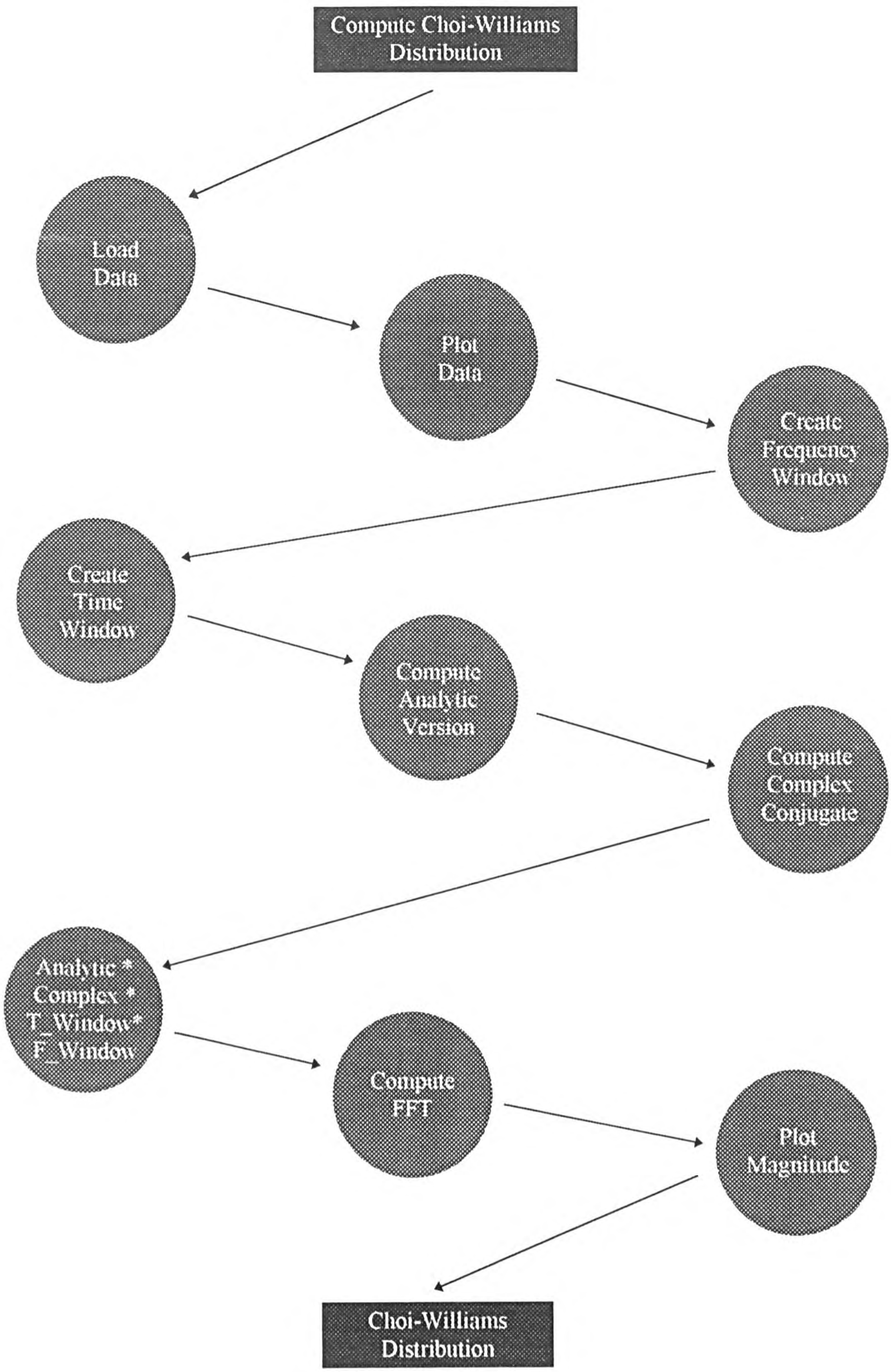

Figure [3.5.6.1] Data flow for Choi-Williams Distribution.

3.6 Evaluation of Signal Processing Techniques using Synthesised Test Data

3.6.1 Description of Synthesised Test Data

Initial investigations into the suitability of the individual signal processing techniques were carried out within the Matlab environment using several synthesised signals. The investigations were undertaken in order to evaluate the individual techniques responses to signals containing varying categories of frequency component. The synthesised signals used within the investigations comprised of four mono-component, four multi-component and a single synthetic non-stationary signal. The latter signal being a synthesised representation of the practical signals used within later investigations. Details of the individual test signals are listed within Table [3.6.1], all signals were sampled at 1 kHz.

3.6.2 The Spectrogram

3.6.2.1 Mono-Component Signals (Hamming Window)

Using synthesised signals the suitability of the STFT and Spectrogram techniques for frequency component detection were investigated. The effects on the techniques using different sample lengths and window types were also investigated.

Using a sample length, N, of 128 samples, a Hamming window of length, 2N, and a separation distance between each spectral estimation, MT, of 32 samples, test signal No. 1 was analysed. With this sample size and the sample rate of 1 kHz, the frequency resolution of the Time-Frequency analysis may be computed via eq. (3.6.2.1.1).

$$Fres = fs \ / \ N \qquad \textbf{(3.6.2.1.1)}$$

The result of the Spectrogram analysis upon test signal No. 1 may be seen in Figure [3.6.2.1.1]. From this analysis a continuous peak located at the third frequency band can be observed. From eq. (3.6.2.1.1) the frequency resolution is ***7.8125*** *Hz*, hence, the frequency of the signal under analysis is determined to be three times the resolution, i.e. test signal No. 1.

Test Signal No.	f(t)
1	f(t) = (10.Sin(2π.(**23.4375** Hz).t))
2	f(t) = (10.Sin(2π.(**15.625** Hz).t))
3	f(t) = (10.Sin(2π.(**7.8125** Hz).t) + 10.Sin(2π.(**23.4375** Hz).t))
4	f(t) = (10.Sin(2π.(**7.81255** Hz).t) + 10.Sin(2π.(**15.625** Hz).t) + 10.Sin(2π.(**23.4375** Hz).t))
5	f(t) = (10.Sin(2π.(**7.8125** Hz).t) + non-stationary sinusoid varying from **10** Hz to **100** Hz.
6	f(t) = (10.Sin(2π.(**78.125** Hz).t))
7	f(t) = (10.Sin(2π.(**78.125** Hz).t) + 10.Sin(2π.(**234.375** Hz).t))
8	f(t) = (10.Sin(2π.(**21.0** Hz).t))
9	f(t) = (10.Sin(2π.(**21.0** Hz).t) + 10.Sin(2π.(**42.0** Hz).t))

Table [3.6.1] Description of Synthesised Test Data.

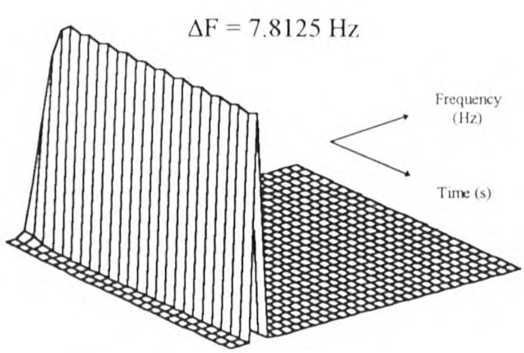

Figure [3.6.2.1.1] Spectrogram of Test Signal No. 1 (N = 128).

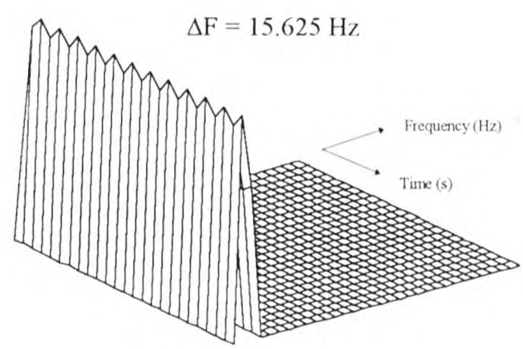

Figure [3.6.2.1.2] Spectrogram of Test Signal No. 1 (N = 64).

The effects of decreasing the sample size within the analysis were investigated. The sample length, N, was shortened to 64 and the same test signal was used in a similar analysis to that of the above. The separation between the individual STFT's and the type of spectral window used remained the same.

The result of this analysis, Figure [3.6.2.1.2], shows that as the sample length is decreased from that of the previous analysis, the frequency resolution of the analysis reduces. With the sample length, N, now reduced to 64, the resolution follows from eq. (3.6.2.1.1) to be ***15.625*** *Hz*. This results in test signal No. 1 being indicated by the analysis at frequency band 1.5, Figure [3.6.2.1.2].

Test signal No. 2 was then analysed using the Spectrogram. Using similar parameters the test signal may be observed at frequency band 1, thus indicating the frequency component of *15.625 Hz*, Figure [3.6.2.1.3].

The effects of increasing the sample length of the Spectrogram to N = 256 were found to increase the resolution of the frequency axis. From eq. (3.6.2.1.1) the frequency resolution is computed to be ***3.90625*** *Hz*. On analysing test signal No. 1 a peak is found to occur at frequency band 6. Thus indicating the correct frequency component of the test signal, Figure [3.6.2.1.4].

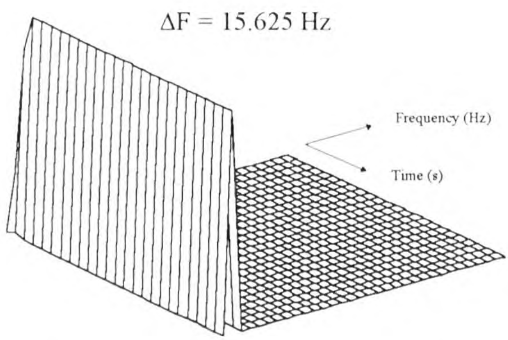

Figure [3.6.2.1.3] Spectrogram of Test Signal No. 2 (N = 64).

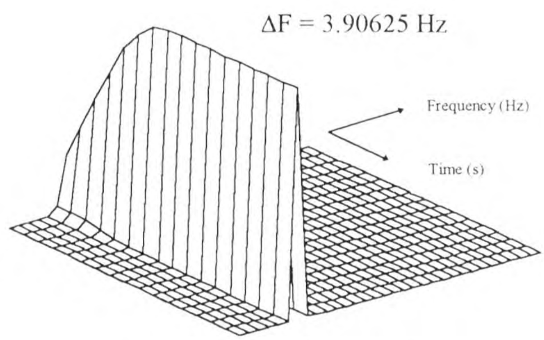

Figure [3.6.2.1.4] Spectrogram of Test Signal No. 1 (N = 256).

On comparing the Spectrogram results up to this point in time, it was noted that if the frequency resolution of the technique was varied, by changing the sample length, the time resolution of the technique varied in the opposite direction.

Investigations then proceeded onto the effects of altering the time period between successive spectral analyses, i.e. the value, M, in eq. (3.1.4) was varied.

'M' up to this point had been chosen randomly as 32. Changing this to 64 and analysing test signal No. 1 results in the frequency resolution given by eq. (3.6.2.1.1) as ***7.8125*** *Hz*. The effect of the increase in time between the individual spectral analyses may be seen to be a greater time resolution occurring in Figure [3.6.2.1.4] with a poorer time resolution occurring within Figure [3.6.2.1.5]. This clearly shows that with a smaller value of 'M', and hence, a smaller time period between the individual spectral analyses, the resolution of the analysis along the time axis is improved.

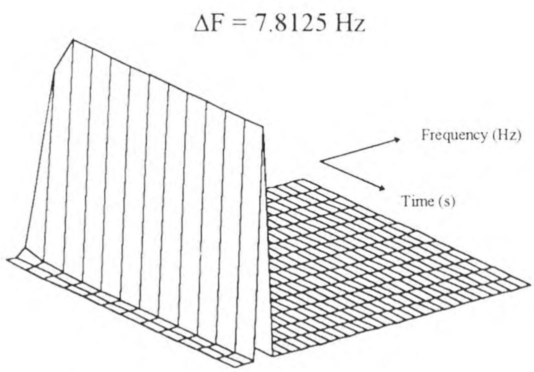

Figure [3.6.2.1.5] Spectrogram Test Signal No. 1 (M = 64).

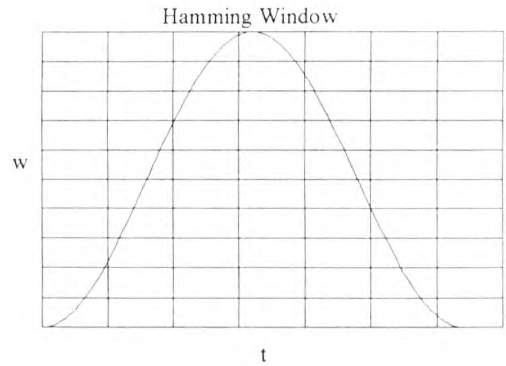

Figure [3.6.2.2.1] Example of Hamming Window used in Spectrogram.

$$w(t) = 0.54 + 0.46 \cos \frac{\pi t}{T}$$

$$(-T \leq t \leq T;\ 0 \text{ elsewhere})$$

3.6.2.2 Mono-Component Signals (Kaiser Window)

The effects of employing different windows were next investigated. As mentioned previously, the spectral window which had been used was the Hamming window, Figure [3.6.2.2.1]. Another type of window commonly used within these analyses is that of the Kaiser window, Figure [3.6.2.2.2].

There are many different variations of spectral windows, the majority of these present to the designer a particular trade-off between the width of the main spectral lobe and the side lobe levels. An exception to this is that of the Kaiser window. The major contribution of J.F. Kaiser was to suggest a window function that allowed the designer to adjust the level of trade-off between lobes.

Using test signal No. 1, an analysis was run using such a window. The sample length, N, was chosen to be 128 and the time between successive spectral analyses, M, chosen to be 32. The result of the analysis is an increase within the sensitivity of the frequency axis, Figure [3.6.2.2.3].

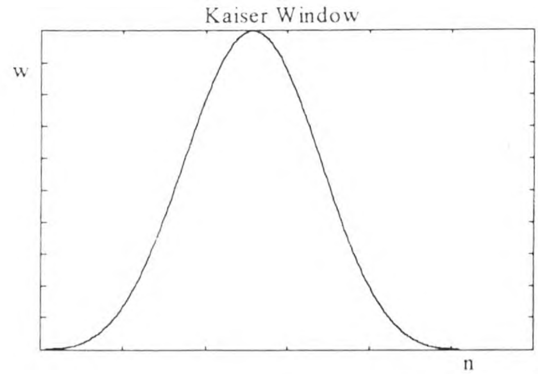

Figure [3.6.2.2.2] Example of Kaiser Window used within Spectrogram.

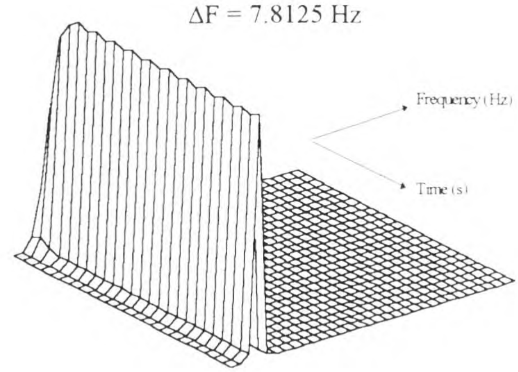

Figure [3.6.2.2.3] Spectrogram of Test Signal No. 1 (Kaiser Window).

$$w(n) = I_o\left(\alpha\sqrt{1 - (n / m)^2}\right) / I_o(\alpha)$$

$$(-m \leq n \leq m);\ 0 \text{ elsewhere}$$

3.6.2.3 Multi-Component Signals (Hamming Window)

The Spectrogram technique was next investigated using synthetic signals containing more than one frequency component. Initially, test signal No. 3 was analysed. This signal contains two separate frequency components, and hence, is an example of a multi-component signal. Using parameters, N = 128, M = 32 and a Hamming window, an analysis was executed upon the multi-component signal. The result of the analysis clearly showed two peaks at frequency levels 1 and 3, thus indicating the presence of two individual frequency components. As the resolution of the frequency axis is ***7.8125*** *Hz*, eq. (3.6.2.1.1), the peaks indicate the frequency components of ***7.8125*** *Hz* and ***23.4375*** *Hz*, i.e. test signal No. 3.

The effect of using a Kaiser window upon the analysis of the above multi-component signal was investigated. Again, this has similar effects to that of the Kaiser window upon a mono-component signal, in that it was found to increase the sensitivity of the frequency axis within the Time-Frequency representation.

Figure [3.6.2.3.1] shows the results of the Spectrogram analysis upon test signal No. 4 with similar frequency resolution to the above. This synthesised signal contains three independent frequency levels of *7.8125 Hz*, *15.625 Hz* and *23.4375 Hz*, which may be identified from the analysis, Figure [3.6.2.3.1].

ΔF = 7.8125 Hz

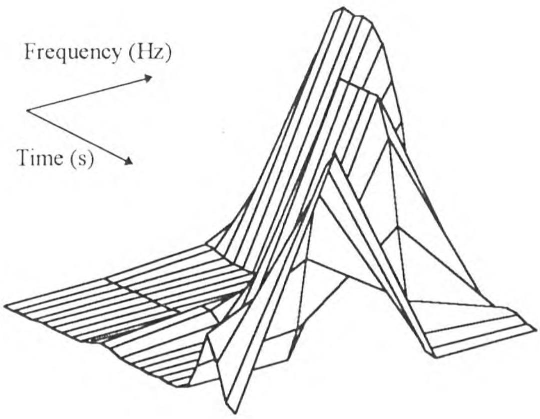

Figure [3.6.2.3.1] Spectrogram of Test Signal No. 4.

3.6.2.4 Non-Stationary Signals (Hamming Window)

In order to investigate the individual techniques ability to analyse non-stationary signals, a synthesised sinusoidal signal which varied in frequency from 10 to 100 Hz was employed. Such a test signal may be seen in Figure [3.6.2.4.1]. In addition to the non-stationary component, a component of 7.8125 Hz was also introduced into the test signal, thus producing the test signal shown within Figure [3.6.2.4.2], test signal No. 5.

When used to locate the synthesised non-stationary components within test signal No. 5, the results of the Spectrogram technique were found to be very successful, Figure [3.6.2.4.3]. In this analysis, a synthesised sample of length, N = 128 samples and a time period of 16 ms between each individual sample length was used. This results, due to eq. (3.6.2.1.1), in a frequency resolution of ***7.8125 Hz*** being obtained. From the results of the analysis, it is clear that such a technique is capable to distinguish between both the stationary and non-stationary components present within this particular test signal.

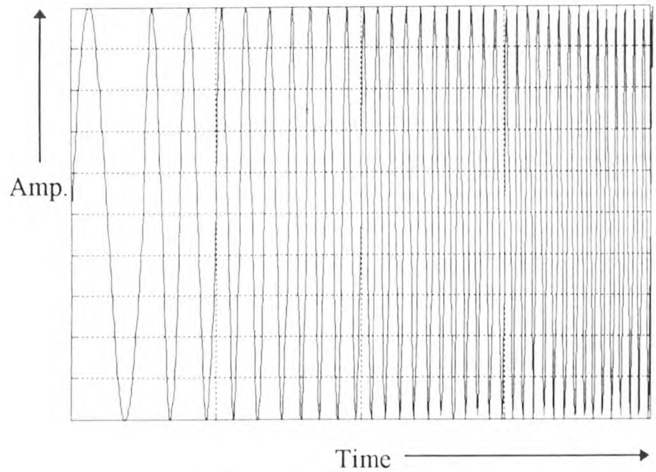

Figure [3.6.2.4.1] Non - stationary test component.

(Same Scales)

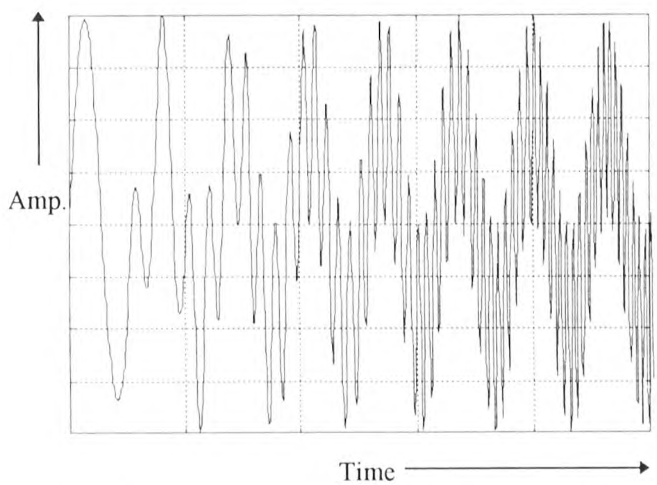

Figure [3.6.2.4.2] Non - stationary test signal No. 5.

(Same Scales)

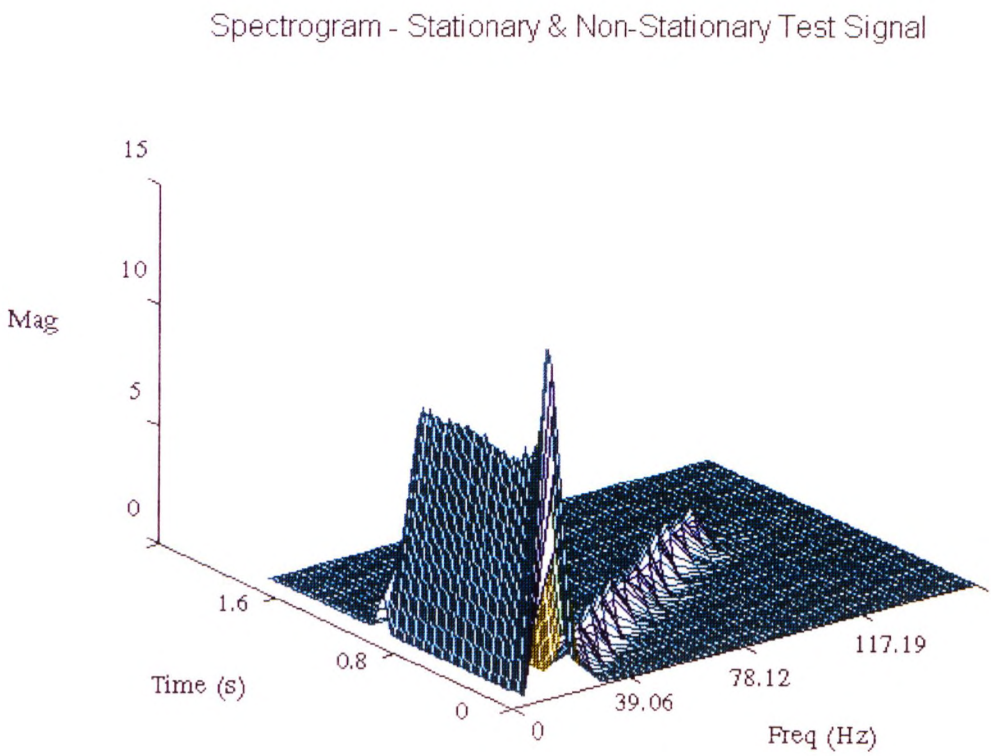

Figure [3.6.2.4.3] A Spectrogram representation of Test Signal No. 5.

3.6.3 The Wigner Ville Distribution

3.6.3.1 Mono-Component Signals

Using the basic Wigner Ville Distribution, eq. (3.1.16), the mono-component sinusoidal test signal No. 6 which has a frequency of ***78.125*** *Hz* was analysed. The test signal, sampled at the rate, f_s, of 1 kHz, has a sample length, N = 128 samples. The result of the WVD analysis being shown in Figure [3.6.2.1.1].

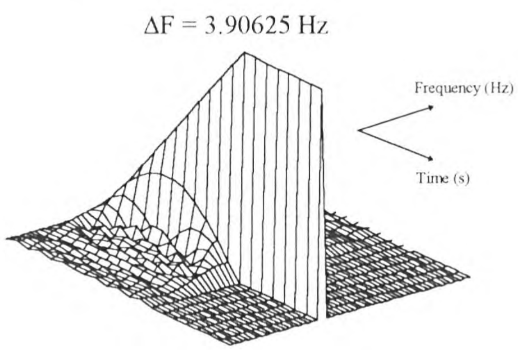

Figure [3.6.3.1.1] Wigner Ville Distribution of Mono-Component Signal No. 6.

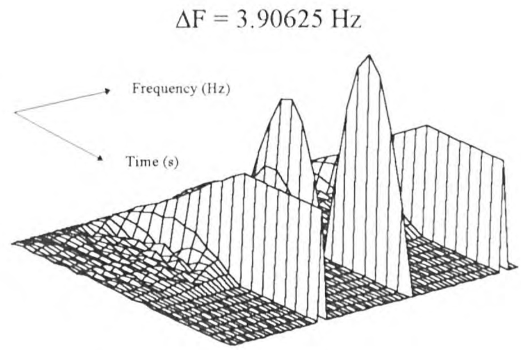

Figure [3.6.3.2.1] Wigner Ville Distribution of Multi-Component Signal No. 7.

From the Time-Frequency representation of the synthetic test signal, a frequency peak is clearly indicated at frequency band 20. As the frequency resolution of the WVD analysis is given by eq. (3.6.2.1.1), it follows that on placing the parameters of the above analysis into the expression a frequency resolution of ***3.90625*** *Hz* is obtained. This frequency resolution results in test signal No. 6 being indicated at frequency band 20, Figure [3.6.3.1.1]. It is interesting to note from the investigation that component interference may be seen within the analysis around the frequency axis of the mono-component Time-Frequency distribution.

$$Fres = fs / 2N \qquad \textbf{(3.6.3.1.1)}$$

3.6.3.2 Multi-Component Signals

The multi-component test signal No. 7 was analysed using the WVD method of eq. (3.1.6). This sinusoidal test signal comprises of two independent frequency components, namely, ***78.125*** *Hz* and ***234.375*** *Hz*. The results of the WVD analysis are shown in Figure [3.6.3.2.1].

As the sample rate and length of the sampled data sequence had not been changed from the previous mono-component analysis, the frequency resolution, eq. (3.6.3.1.1), remained the same to that of the previous analysis. With this frequency resolution, ***3.90625*** *Hz*, the Time-Frequency representation of the test signal, Figure [3.6.3.2.1], clearly indicates two frequency components at frequency bands 20 and 60. These bands correctly indicate the two frequency components of ***78.125*** *Hz* and ***234.375*** *Hz* within the multi-component test signal No. 7.

There is, however, a third frequency component indicated within Figure [3.6.3.2.1]. This frequency component is located midway between the two signal components at frequency band 40. This is an example of crossterm interference, with which this Time-Frequency technique, due to its bilinear nature, is particularly prone to when analysing multi-component signals.

3.6.4 The Smoothed Wigner Ville Distribution

3.6.4.1 Mono-Component Signals

The single frequency component test signal No. 6 was analysed using the smoothed version of the WVD, eq. (3.1.2). In this version of the Wigner Distribution, windows are employed both in the frequency and time directions. Initially, the frequency window was chosen to have a length of 128 samples and the time window a length of 32 samples. The Kaiser type of window was employed in both frequency and time directions. The result of such an analysis on test signal No. 6 being shown within Figure [3.6.4.1.1].

Again the single frequency component present in the signal is indicated at frequency band 20, due to the frequency resolution being ***3.90625 Hz***, eq. (3.6.3.1.1).

The result of using such a time window of 32 samples is to reduce the resolution of the time analysis. Reducing the time resolution thus allows more of the signal to be represented within the analysis.

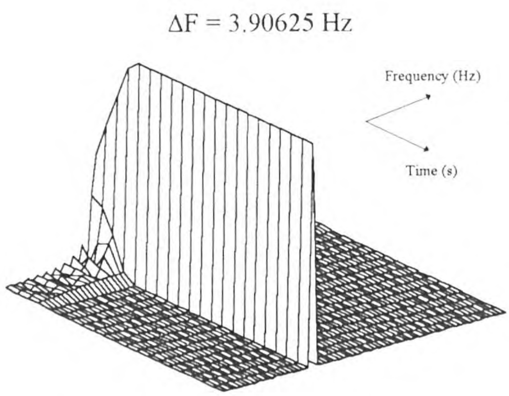

Figure [3.6.4.1.1] Smoothed Wigner Ville Distribution of Test Signal No. 6.

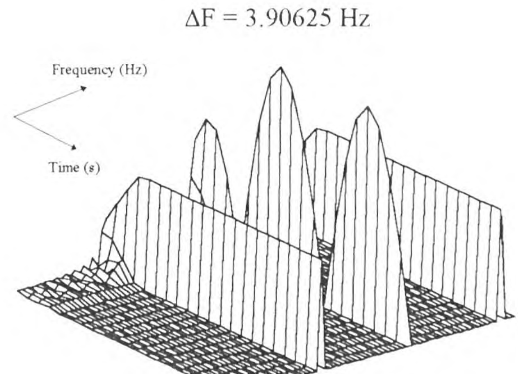

Figure [3.6.4.2.1] Smoothed Wigner Ville Distribution of Test Signal No. 7.

3.6.4.2 Multi-Component Signals

Figure [3.6.4.2.1] shows the result of using the smoothed technique on multi-component test signal No. 7. The sample lengths and types of windows used were similar to the above investigation. From Figure [3.6.4.2.1] it is clear that the two components within the test signal are correctly indicated, frequency bands 20 and 60. However, the crossterm interference situated midway between the signal components is still present.

In order to observe the effects of reducing the sizes of windows employed, the multi-component test signal was now analysed using a frequency window of sample length 128 and a time window of 16 samples.

The result of this analysis may be seen in Figure [3.6.4.2.2]. With the reduction in time window length to 16 samples, Figure [3.6.4.2.2], the time resolution of the Time-Frequency representation increases slightly. As the frequency window length remains at 128 samples, due to eq. (3.6.3.1.1), the frequency resolution remains at ***3.90625*** *Hz*, hence, the frequency components within the test signal are indicated at frequency bands 20 and 60.

The analysis was then changed so that both time and frequency windows were of length 64 samples. Due to eq. (3.6.3.1.1), as the frequency window sample length has changed, the resulting frequency resolution of the distribution alters. Using these new parameters, the frequency resolution becomes ***7.8125*** *Hz*. Since the sample length of the time window is increased the time resolution decreases considerably. The resulting Time-Frequency distribution, which still has considerable crossterm interference, may be observed within Figure [3.6.4.2.3].

Figure [3.6.4.2.4] shows the result of returning the frequency window length to 128, and changing the parameters of the Kaiser window used within the frequency direction. The Kaiser window has been made less selective in the frequency direction, hence, from the representation in Figure [3.6.4.2.4], the frequencies at which the signal components and crossterm interference occur at are less defined.

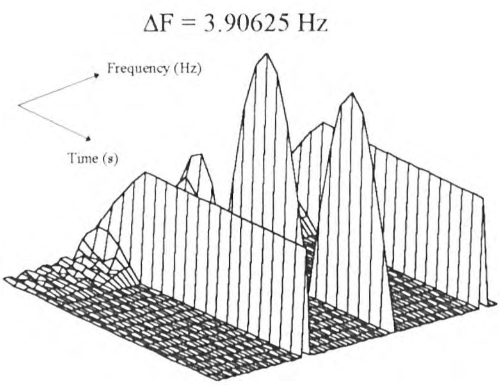

Figure [3.6.4.2.2] Smoothed Wigner Ville Distribution, N = 128.

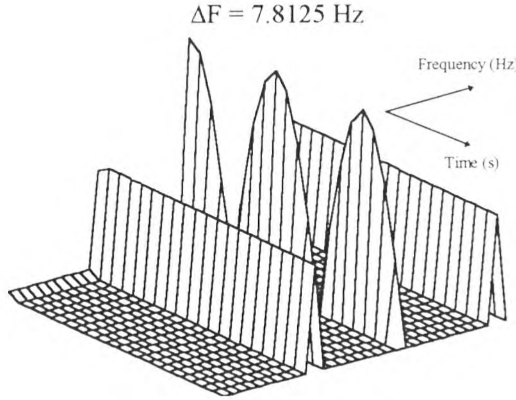

Figure [3.6.4.2.3] Smoothed Wigner Ville Distribution, N = 64.

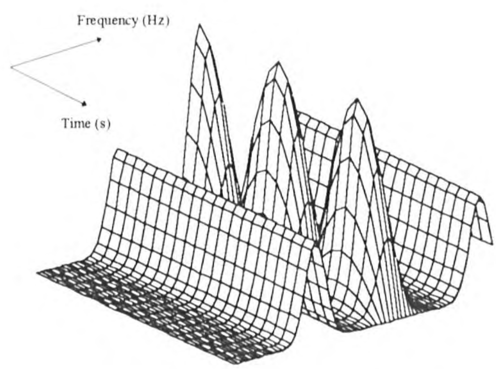

Figure [3.6.4.2.4] Smoothed Wigner Ville Distribution, N = 128.

3.6.4.3 Non-Stationary Signals (Kaiser Window)

Using a Kaiser window of 256 samples in the frequency direction, from eq. (3.6.3.1.1), the frequency resolution obtained within the SWVD analysis is ***1.953** Hz*. In conjunction with a Rectangular window of 64 samples, test signal No. 5 was analysed with the result being shown in Figure [3.6.4.3.1]. The stationary and non-stationary constituent components may clearly be seen. The crossterm interference is located midway between the components, and hence, cannot be observed within this analysis.

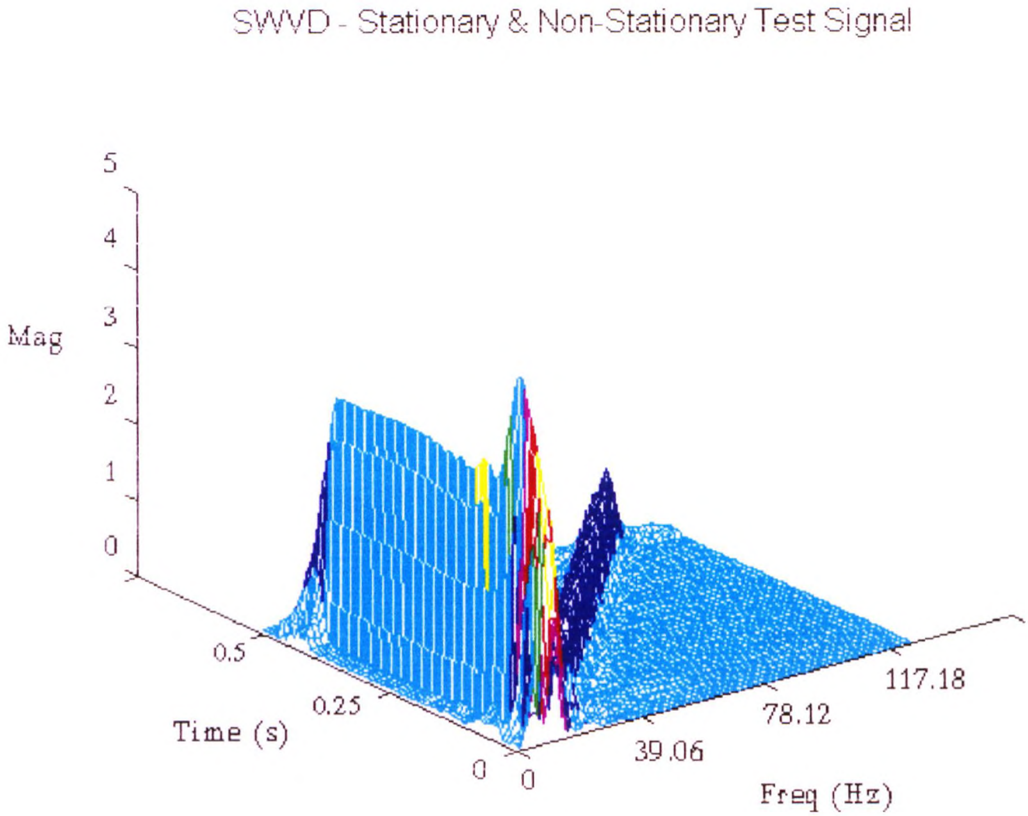

Figure [3.6.4.3.1] A Smoothed Wigner Ville Distribution of Test Signal No. 5.

3.6.5 Wavelet Decomposition

3.6.5.1 Mono-Component Signals

The Wavelet Decomposition method was initially tested using mono-component test signal No. 8. From Table [3.6.1] this signal comprises of a single 21 Hz frequency component. Utilising a Gaussian wavelet similar to that shown in Figure [3.1.1] in order to convolve the test signal over the frequency range of 1 to 50 Hz, produces the Time-Frequency representation of the test signal shown in Figure [3.6.5.1.1].

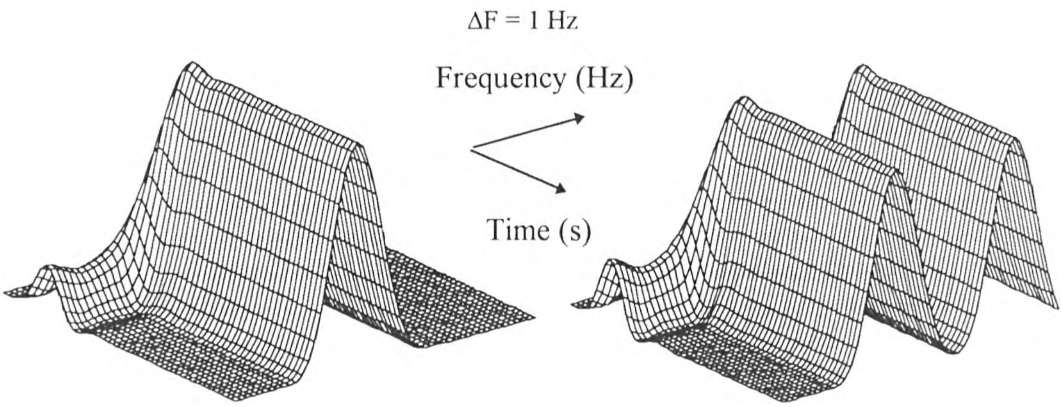

Figure [3.6.5.1.1] Wavelet Decomposition of Test Signal No. 8.

Figure [3.6.5.2.1] Wavelet Decomposition of Test Signal No. 9.

From Figure [3.6.5.1.1], a peak is found to occur at frequency band 21. As the resolution of the distribution is *1 Hz*, the resulting peak within the distribution correctly indicates the test frequency component of 21 Hz. It is noted that some interference may still be seen at the start of the analysis. This however is not in the same scale to that of previous techniques.

3.6.5.2 Multi-Component Signals

The sinusoidal multi-component test signal No. 9, Table [3.6.1], which contains two independent frequency components, 21 Hz and 42 Hz, was next investigated using the Wavelet Decomposition technique. Again, the analysis was executed over the frequency range of 1 to 50 Hz.

The result of this distribution is shown in Figure [3.6.5.2.1]. From this analysis two peaks may clearly be seen at frequency bands 21 and 42, thus indicating the presence of two frequency components within the signal, these components being 21 and 42 Hz.

The effects of varying the wavelet bandwidth used within the Wavelet Decomposition technique was next investigated. The above test was re-run with the resulting Time-Frequency representation of the same test signal being presented within Figure [3.6.5.2.2].

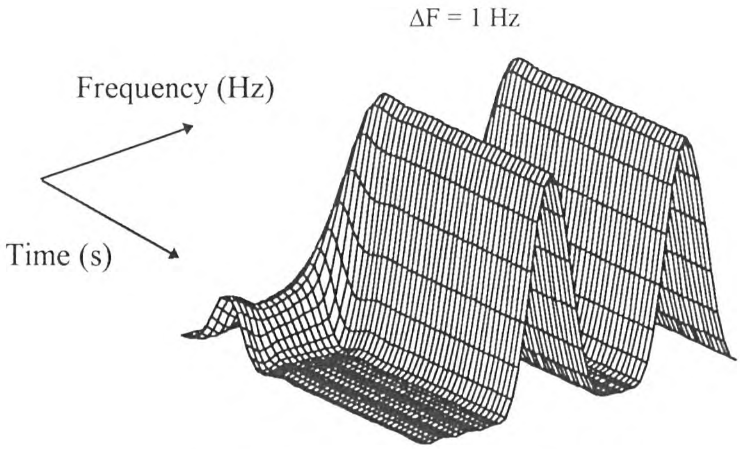

Figure [3.6.5.2.2] Wavelet Decomposition of Test Signal No. 9.

Figure [3.6.5.2.2] shows an increased selectivity within the frequency axis of the Time-Frequency representation. Thus, the reduction of the bandwidth of the wavelet used to decompose the signal under analysis improves the selectivity of the overall analysis. Again, Figure [3.6.5.2.2] shows two peaks at the correct frequency locations, thus correctly indicating the test frequency components of 21 and 42 Hz.

3.6.5.3 Non-Stationary Signals

On analysing test signal No. 5 with the Wavelet Decomposition method over the frequency range of 1 to 50 Hz, results in the Time-Frequency representation presented within Figure [3.6.5.3.1].

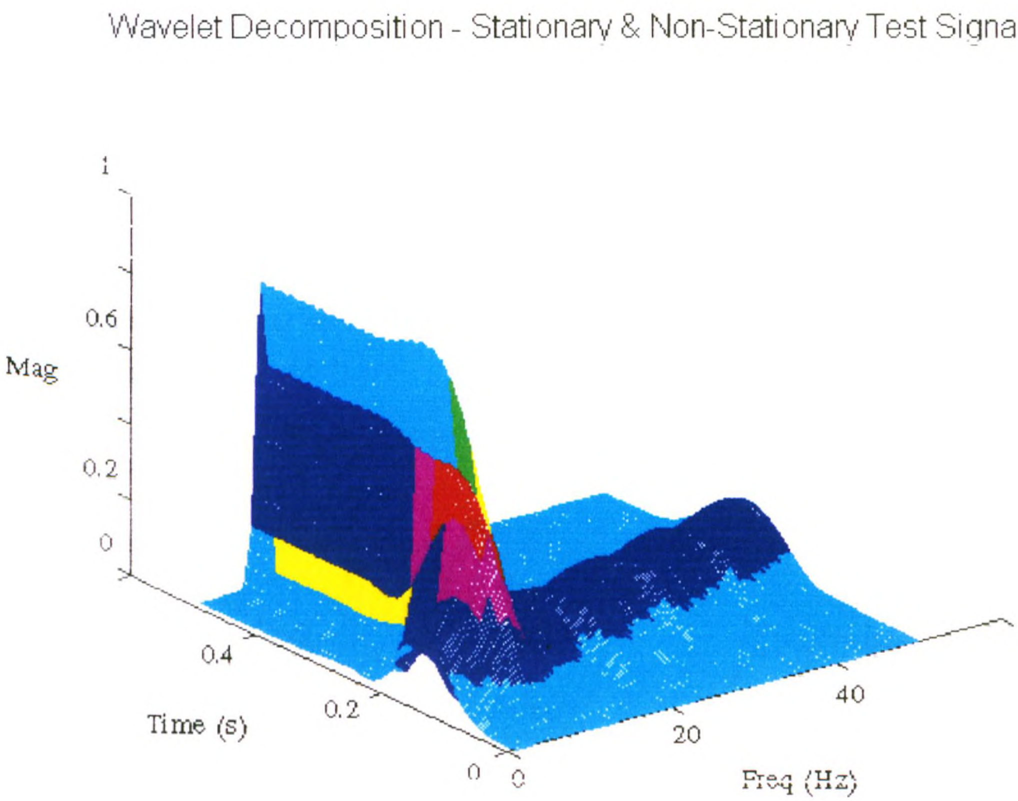

Figure [3.6.5.3.1] A Wavelet Decomposition of Test Signal No. 5.

3.6.6 The Exponential Distribution

This version of the Wigner Ville Distribution was investigated as it had been reported that it possessed certain crossterm interference reduction properties [88]. As the WVD technique had generated large crossterm interference components when analysing multi-component signals, only such multi-component synthesised sinusoidal signals were used within the following investigations. This test signal consisted of only two frequency components, namely *78.125 Hz* and *234.375 Hz*.

Initial investigations using the exponential constant $\sigma = 10^{-6}$ analysed the test signal whilst employing a frequency Kaiser window of length 64 samples and a Rectangular time window of length 64 samples, Figure [3.6.6.1].

$\Delta F = 7.8125$ Hz

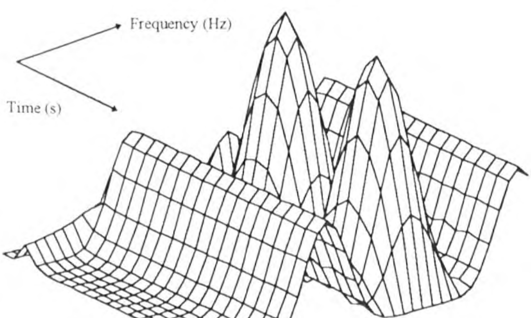

Figure [3.6.6.1] Exponential Distribution of Multi-Component Test Signal.

$\Delta F = 3.90625$ Hz

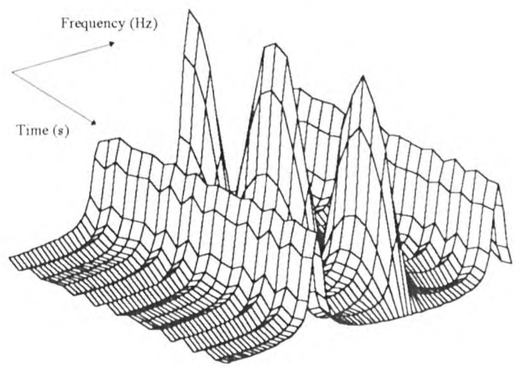

Figure [3.6.6.2] Exponential Distribution of Test Multi-Component Signal.

Using the above parameters and eq. (3.6.3.1.1) the frequency resolution of the distribution is computed to be ***7.8125** Hz*. From the result of this analysis peaks are found to occur in the frequency direction at frequency bands 10 and 30, thus representing the test frequency components of *78.125 Hz* and *234.375 Hz*. Due to the fact that the windows have relatively small sample lengths, the resolutions obtained within both directions are large.

Changing the sample length of the frequency window to 128 results in a change within the frequency resolution eq. (3.6.3.1.1) of the analysis. All other parameters of the Exponential Distribution remained unchanged except that the shape of the Kaiser window was altered so that the window became less frequency selective, Figure [3.6.6.2].

The effects on the analysis of increasing the frequency window length was to increase the frequency resolution of the distribution. The effect of making the Kaiser window less frequency selective was to introduce noise components around the areas of the peaks and crossterm interference components likewise.

Reducing the sample length of the time window to 32 samples increases the time resolution of the resulting distribution. With all other parameters remaining the same as above the effects of increasing the time resolution may be observed within the distribution presented in Figure [3.6.6.3].

ΔF = 3.90625 Hz

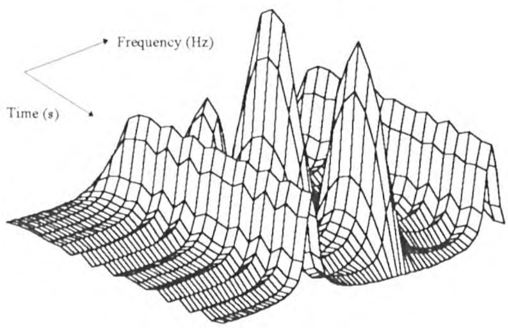

Figure [3.6.6.3] Exponential Distribution of Multi-Component Test Signal.

ΔF = 3.90625 Hz

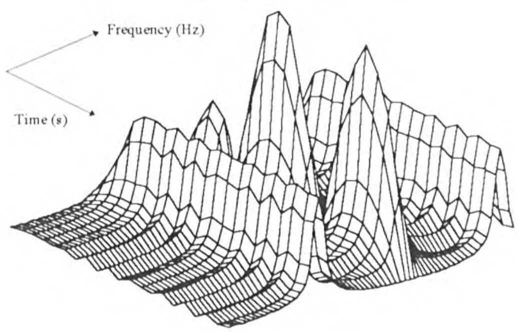

Figure [3.6.6.4] Exponential Distribution of Multi-Component Test Signal.

Crossterm interference upto this point in time was still in existence, as can be seen from the results of the individual distributions. The constant, 'σ', within the definition of the Exponential Distribution was varied in order to investigate its effects on the overall distribution. On changing the value of 'σ' to that of 1.0, using the same types of windows both in the time and frequency directions, along with similar window lengths, the test signal was re-analysed resulting in the Choi-Williams distribution shown in Figure [3.6.6.4].

From the results of this particular investigation, Figure [3.6.6.4], it may be observed that in this case no considerable alterations were observed in the amplitudes of crossterm interference.

Using similar values of window length and the same type of window as above, the frequency window was made more frequency selective. The test analysis was re-run using these new parameters and a new value of 'σ', Figure [3.6.6.5].

The results of changing these parameters are to make the frequency peaks which occur at bands 20 and 60 more prominent. This effect is advantageous to any Time-Frequency representation, however, as may be observed within the individual investigations of the technique, the effects were also present within the crossterms as well.

$\Delta F = 3.90365$ Hz

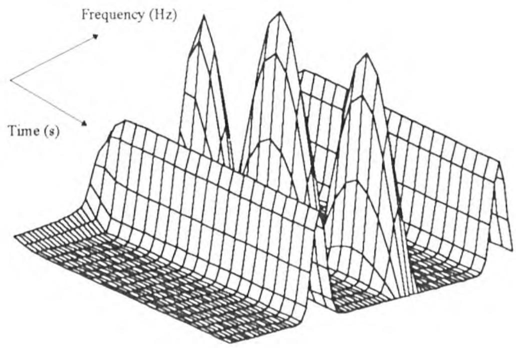

Figure [3.6.6.5] Exponential Distribution of Multi-Component Test Signal.

3.7 Evaluation of Signal Processing Techniques with Real Motor Data

As a means to determine the suitability of the individual signal processing techniques, each technique was investigated by analysing a real supply current transient from a three phase SCIM. The results of which are reported below.

A 0.5s sample of the supply current transient signal was obtained from the laboratory SCIM described further in section 4.3.1. The test-rig was run under both full and no load conditions with 10 broken bars present within the cage rotor and was analysed using the three individual signal processing techniques.

A fault condition of 10 broken bars, situated within a group on the rotor bar, was representative of an extreme fault condition used initially to observe if the fault conditions could be detected by the individual analysis methods. A more typical level of fault severity, 3 broken bars, was analysed later by the technique found to be the most suitable.

The methodology of determining which of the spectral techniques would be best suited for the detection of the rotor bar fault frequency components, eq. (2.3.3.1) and eq. (2.3.3.2), would be to obtain an analysis from a transient signal and observe which of the individual techniques best detected the locus of the Lower Sideband, Figure [2.3.3.1].

The most favourable Time-Frequency representation using the Spectrogram technique was achieved by employing a 512 sample Hamming window on a full load transient signal. Since the data was sampled at a rate of 2 kHz, from eq. (3.6.2.1.1), the frequency resolution of the Spectrogram was *7.8125 Hz*. The results shown in Figure [3.7.1] clearly show the non-stationary Lower Sideband components within the transient.

A further analysis over the frequency range 0 to 117 Hz is shown within Figure [3.7.2]. In this analysis the massive 50 Hz component, representative of the supply fundamental frequency, may clearly be observed along with the non-stationary Lower Sideband of the rotor fault component.

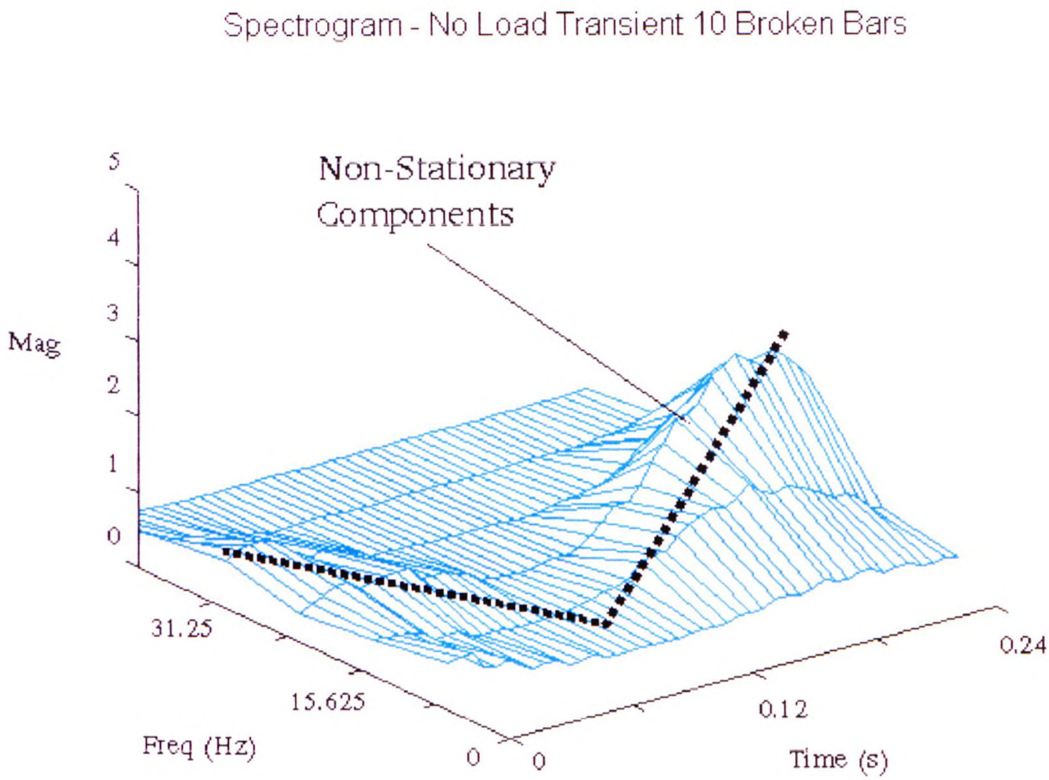

Figure [3.7.1] A Spectrogram of a No Load Transient Current Signal with 10 broken Rotor Bars.

A similar analysis was re-run upon a no-load transient obtained from the same test-rig. Again, under similar fault conditions, the supply fundamental of 50 Hz may clearly be observed together with the increased amplitude of the Lower Sideband, Figure [3.7.3].

ΔF = 7.8125 Hz

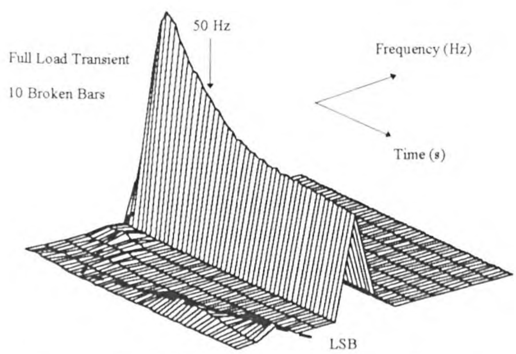

Figure [3.7.2] Spectrogram of Full Load Transient with 10 Broken Rotor Bars.

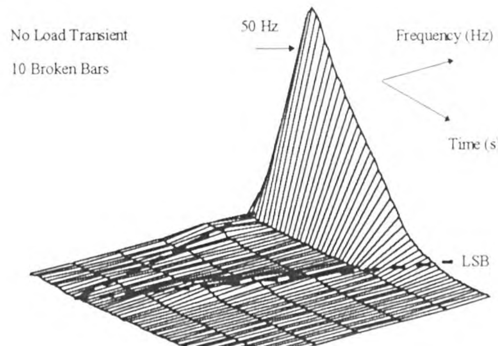

Figure [3.7.3] Spectrogram of No Load Transient with 10 broken bars present.

Figure [3.7.4] shows the results of the Smoothed Wigner Ville Distribution analysis on the same current transient. The frequency window used within this analysis was of the Kaiser type, length 256 samples, and the time window was of the Rectangular type, length 64 samples. These types and lengths of windows were found to give the best results for tracking the non-stationary components. As a result of eq. (3.6.3.1.1) the frequency resolution of the SWVD analysis was ***3.9*** *Hz*. Again, the non-stationary components within the transient signal can be observed, although the components within this technique are no longer as evident as they had been with the Spectrogram.

Figure [3.7.5] shows the result of analysing the transient signal using the Wavelet Decomposition method. In this analysis a Gaussian wavelet of bandwidth 1 Hz was convolved with the transient signal under investigation, in order to obtain the signal decomposition. Since the wavelet assumes the frequency of the investigation a frequency resolution of 1 Hz was obtained.

From the results of the three Time-Frequency representations it was clear that all three successfully detected the non-stationary components within the transient current signal. The poorest of the three investigated analyses was found to be the WVD. Although a number of crossterm interference suppression techniques were investigated within the analysis, including the SWVD and the Exponential Distribution, the presence of interference components hindered the successful detection of the non-stationary fault components.

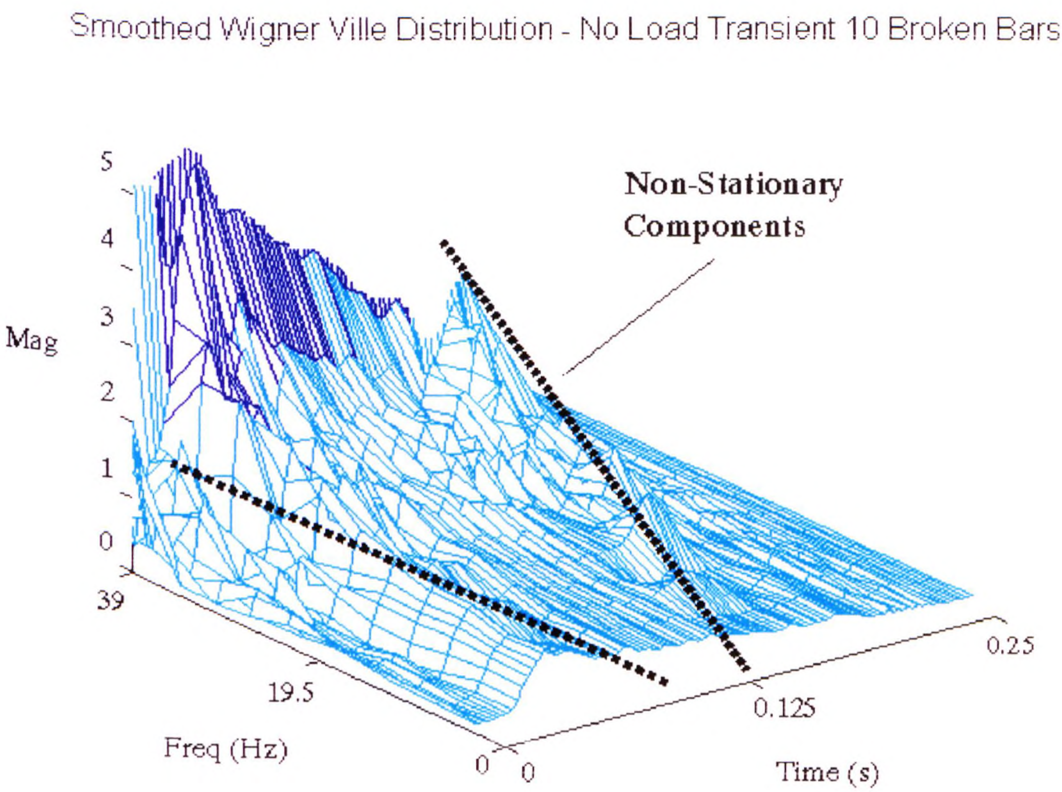

Figure [3.7.4] A Smoothed Wigner Ville Distribution of a No Load Transient Current Signal with 10 Broken Rotor Bars.

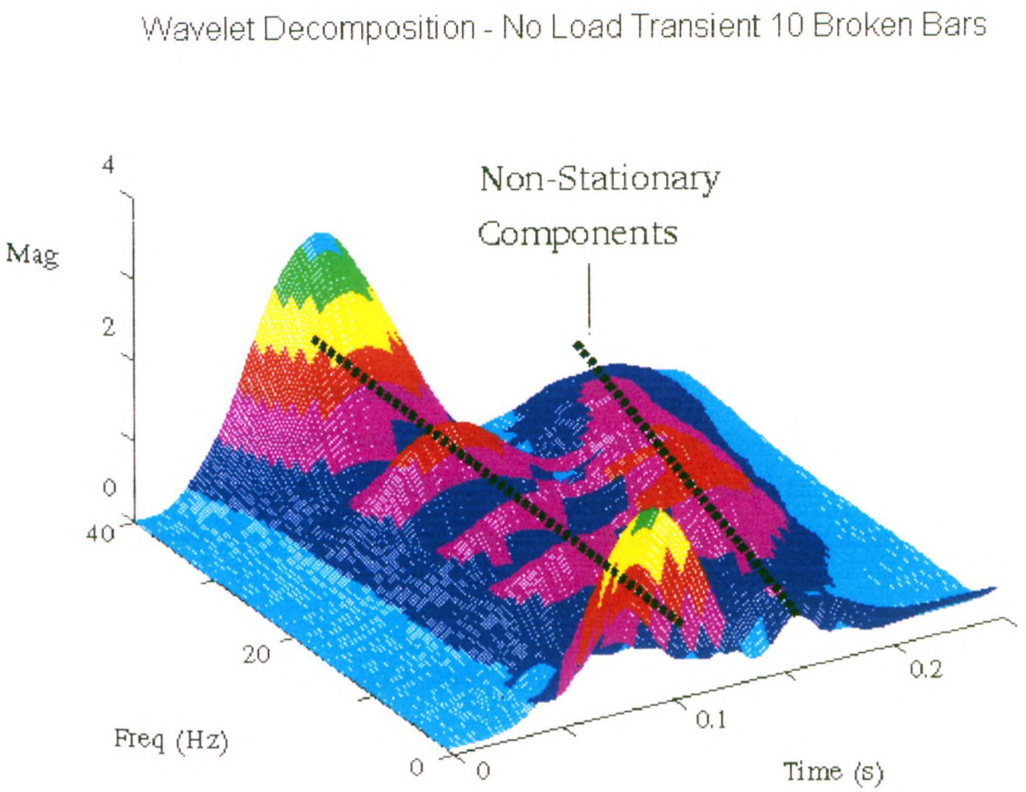

Figure [3.7.5] A Wavelet Decomposition of a No Load Transient Current Signal with 10 Broken Rotor Bars.

The next most successful technique was found to be the Spectrogram. Using this technique the non-stationary fault components were clearly located although the technique was found to suffer from a resolution problem, in that when the time resolution of the analysis was increased the frequency resolution was found to automatically reduce, and vice versa. This however, may be solved if two tests are done on the signal. The first having a high time resolution followed by a second with a high frequency resolution. This however, increases the amount of computations required to calculate a suitable analysis, and hence, indicates a numerically un-economic process.

The Time-Frequency representation technique which was found to give the best results when applied to 'actual' data obtained from the test-rig was found to be the Decomposition via a wavelet. In this technique the non-stationary fault components are clearly observable within the frequency direction. Consequently, it was this technique which would be used within future investigations, see Chapters 4, 6, 7 and 8.

3.7.1 Rotor Fault Component Detection using Wavelet Decomposition

The analysis shown in Figure [3.7.1.1] was obtained by computing the Wavelet Decomposition of the transient current data from the test-rig. The rig in this example was fitted with a 51 bar squirrel cage rotor which contains 3 broken bars. The bars again being located within a group.

The results of the analysis clearly show the non-stationary components travelling from 50 Hz at motor start up to 50 Hz during steady state operation.

Comparison of this analysis with the result of another obtained from the same motor but this time with a fault free condition, Figure [3.7.1.2], results in an obvious reduction in the amplitudes of the occurring sidebands.

Figure [3.7.1.3] clearly showing the increased amplitude within the non-stationary Lower Sidebands under the 10 broken bar fault condition.

It is this difference within the Lower Sideband amplitude which has been shown by researchers to be proportional to the degree of cage rotor bar fault severity [35][36][38].

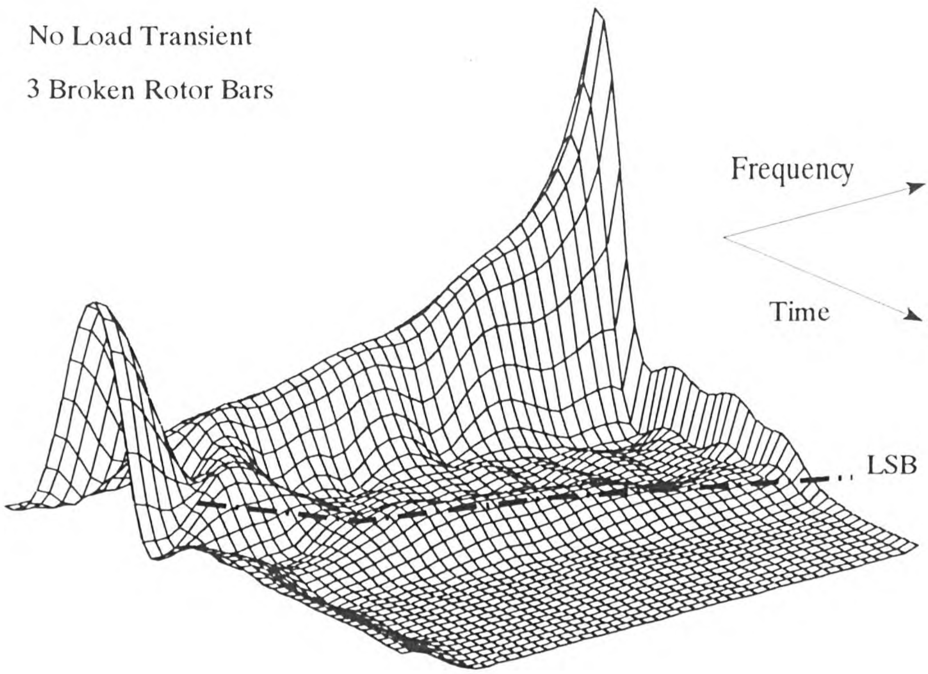

Figure [3.7.1.1] A Wavelet Decomposition of a No Load Transient with 3 Broken Rotor Bars, ΔF = 1 Hz.

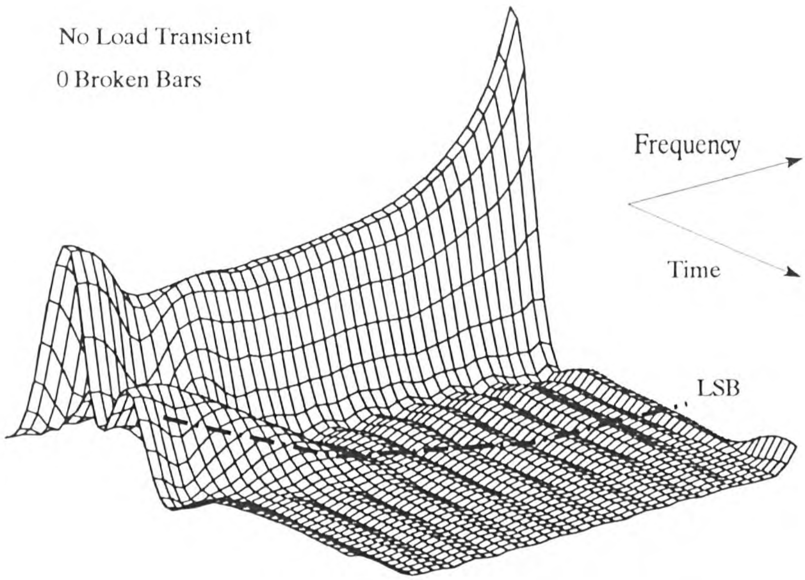

Figure [3.7.1.2] A Wavelet Decomposition of a No Load Transient with 0 Broken Rotor Bars, ΔF = 1 Hz.

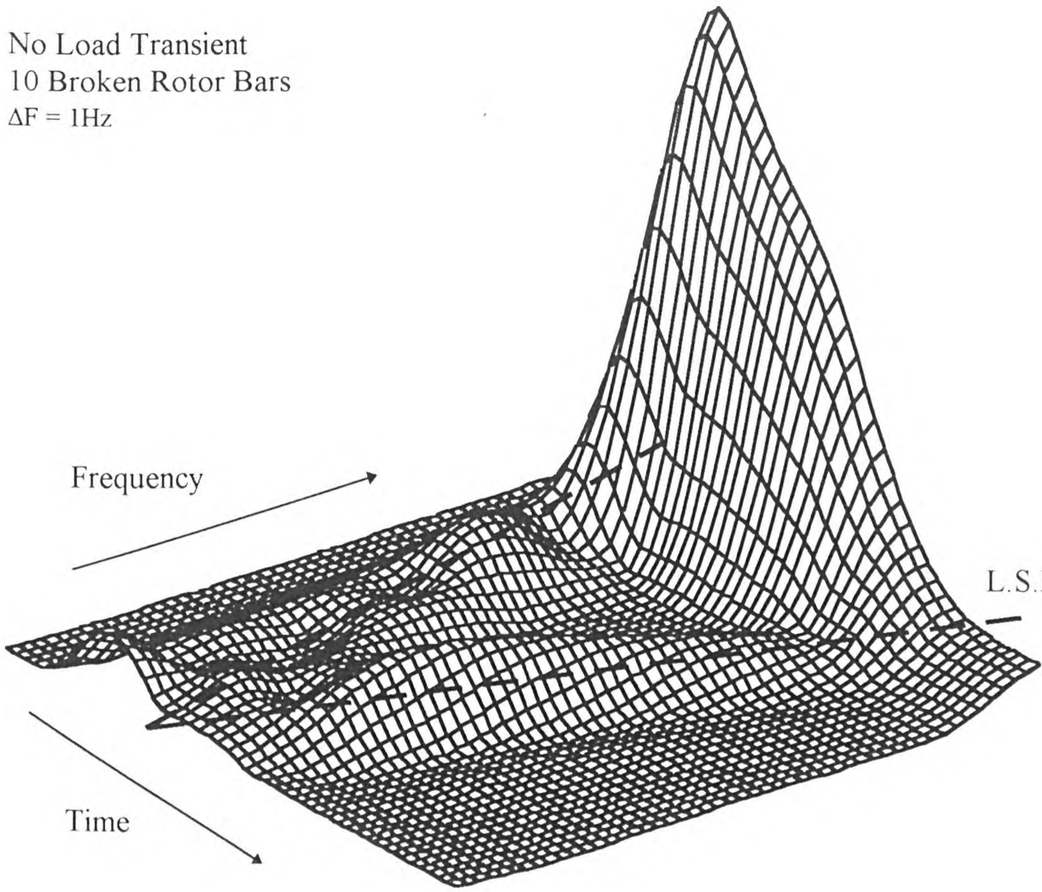

Figure [3.7.1.3] A Wavelet Decomposition of a No Load Transient with 10 Broken Rotor Bars.

3.8 Conclusions

Several signal processing techniques which result in the Time-Frequency representation of a signal were investigated as to their suitability for detecting non-stationary frequency components from the practical application previously discussed.

The Spectrogram formed via the calculation of the Short Time Fourier Transform (STFT) gave reasonable results. The technique allows average resolution control both in the time and frequency directions, and when used to locate the Lower Sidebands within a no load transient was very successful, Figure [3.7.1].

The Wigner Distribution (WD) and several of its variants were then investigated. This technique gives good control of frequency and time resolutions, however, its main disadvantage is the presence of crossterms when a multi-component signal is analysed. Several methods of crossterm reduction were investigated including that of the Exponential Distribution. These reduction techniques, however, did not successfully eliminate the presence of the crossterms within the Time-Frequency representation, so that upon tracking the Lower Sidebands within a no load transient, Figure [3.7.4], the results were not very informative.

Although the WD may be calculated in half the number of calculations of which it takes to obtain an STFT, the end results of the STFT were found to be far more useful within this application than that of the WD.

Signal analysis by means of Decomposition was then investigated. In this technique excellent time and frequency resolutions are obtained, there are no problems with interference such as crossterms, and the Lower Sidebands were successfully tracked within the no load transient, yielding the extremely clear Time-Frequency representation of Figure [3.7.5].

On summarising the results of the above investigations, the Decomposition technique of signal analysis was found, in this application, to give by far the best results when detecting the Lower Sidebands within the transient signal. It is for this reason that it was this technique which was used within the developed portable transient monitoring system, Chapter 4, and in further investigations Chapters 6, 7 and 8. The STFT and Spectrogram techniques being used as secondary analysis techniques.

Chapter 4

Transient Monitoring Diagnostic Tool

(The Current Analysis Program)

4.0 Introduction

From Chapter 2 it was shown that faults within rotor bars cause unique frequency components to occur at $(1 \pm 2s)f_s$ Hz. The following chapter discusses the portable transient monitoring system developed using the signal processing technique of Wavelet Decomposition, see Chapter 3, to enable diagnostic information to be obtained from the motor supply current. Results are presented which verify that the developed monitoring system can successfully detect various severities of cage rotor bar fault both within laboratory and industrially based motors.

4.1 Monitoring System (Hardware)

The initial transient monitoring research was conducted on laboratory based machines [35][38][89], it was obviously desirable that the theories previously developed should be tested within an industrial environment. Previous transient monitoring systems had initially required a mainframe in order to compute the relevant signal processing, with the techniques latterly being transferred to a desktop PC. It was felt that the improvements within available computing power and the readily available modern day signal processing accessories, both in hardware and software, would now permit a more useful, portable instrumentation system to be developed. A system which would then allow the diagnostic technique to be fully tested within an industrial environment.

4.1.1 The PC

As a means of centralising the control required to acquire the necessary data; running the relevant analysis signal processing software together with storing the required data and results, it was obvious that some form of processor control was in order. A 486 based PC was the best available at the time of development. Sufficient RAM was required in order to allow the data signals to be analysed using the relevant signal processing technique, hence, a 33 MHz, 4MByte RAM, Toshiba DX6400 [98] along with a National Instruments, Lab PC+ data acquisition card [99], attached to the PC's ISA adapter were employed.

4.1.2 The Data Acquisition Card

The data acquisition card used to sample the supply current was the National Instruments Lab PC+. This is a multi-function card which may be used for analog, digital and timing operations when used in conjunction with a controlling PC. The Lab PC+ card contains a 12 bit, successive approximation ADC, and may achieve conversion rates of upto 75 kHz on the 8 analog inputs which may be configured as either 8 single ended inputs or, as used in this case, 4 differential inputs.

The Lab PC+ also contains a 12 bit DAC with several voltage outputs, 24 lines of TTL compatible digital I / O, and six 16 bit counter / timer channels which all may be used in future developments.

For data acquisition purposes the Lab PC+ card was configured initially to have a single, bi-polar, differential input. This meant that the signal to be fed into the channel had to be within the voltage limits of ± 5 V. Configuration being achieved via jumpers prior to the card being fitted.

4.1.3 Three Phase Synchronous Sampling

Initially, data acquisition was designed to only capture a single phase of data, however, later versions of the monitoring system sampled all three phases of the SCIMs supply current, but with the knowledge that a slight time difference existed between the individual phase samples. This being due to the acquisition card not supporting any form of synchronous sampling facilities.

Future investigations, however, hinted that there would be a requirement for all three data phases to be sampled simultaneously, and hence, a sample and hold facility was developed as a part of the overall monitoring systems data acquisition capability.

The synchronous sampling of all three supply lines was achieved via the portable PC, in conjunction with the LAB Windows 'Lab PC +' data acquisition card and some developed hardware.

The synchronous data sampling hardware arrangement may be seen in Figure [4.1.3.1]. For reference purposes the synchronous sampling of data was achieved by the S/H facility shown within Figure [4.1.3.2].

In order to obtain synchronicity within data sampling, an external clock pulse was required to supply the conversion signal, *EXTCONV*, needed by the acquisition card. Figure [4.1.3.2] also shows the schmitt clock circuitry used to obtain this conversion pulse.

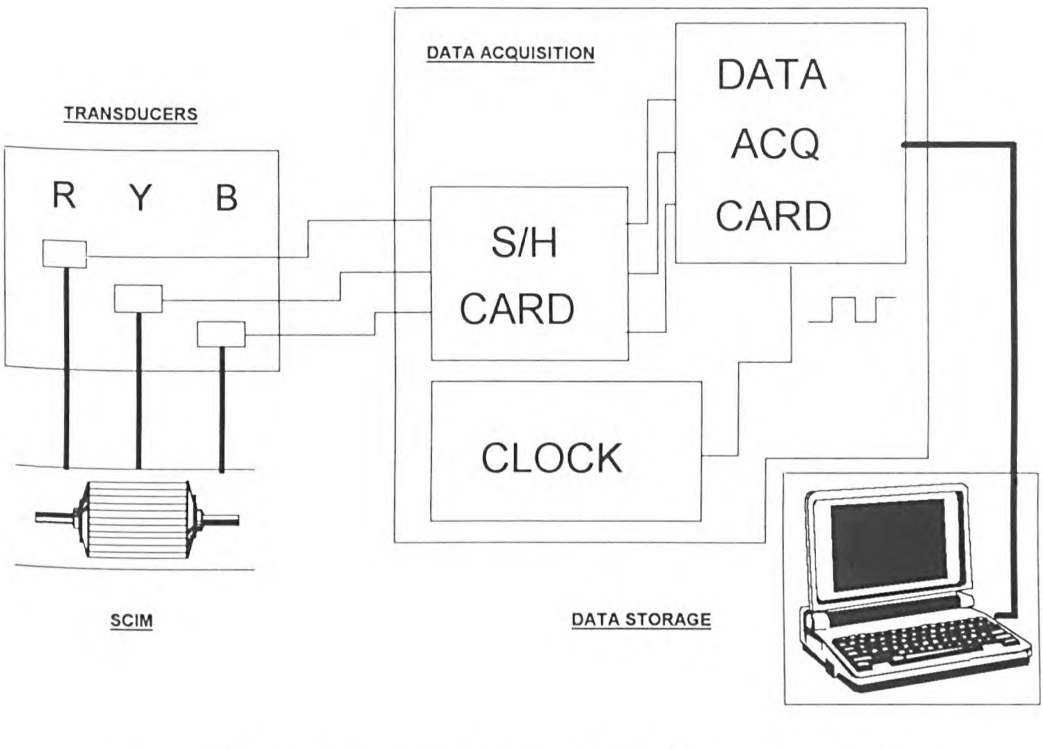

Figure [4.1.3.1] Synchronous Data Sampling Hardware Arrangement.

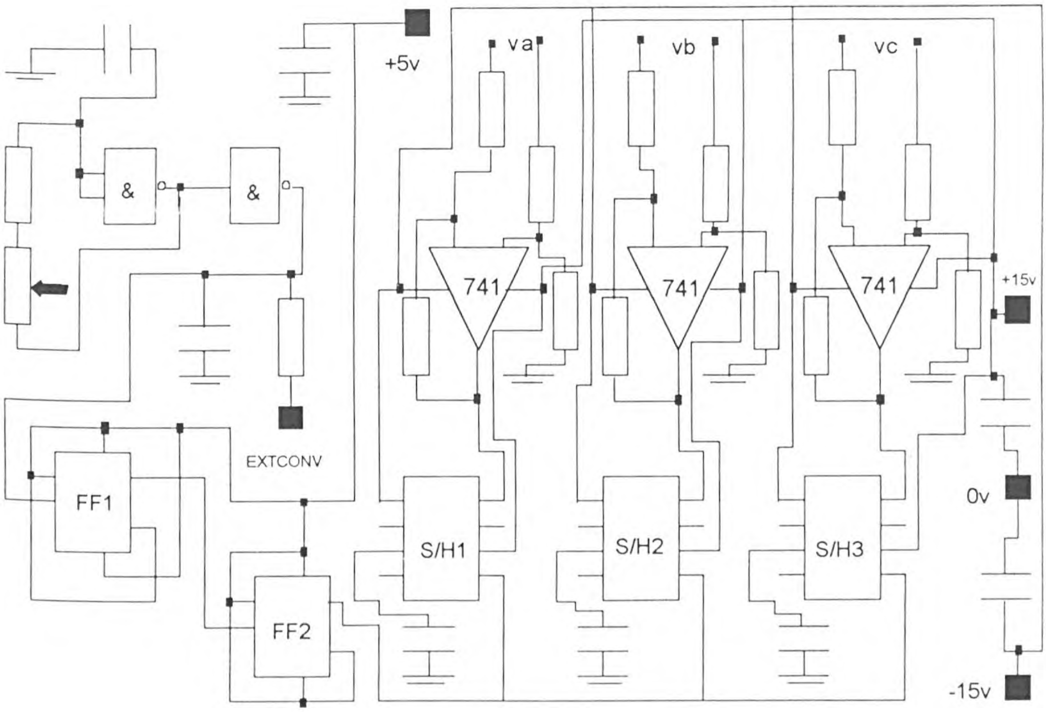

Figure [4.1.3.2] Developed S/H Facility.

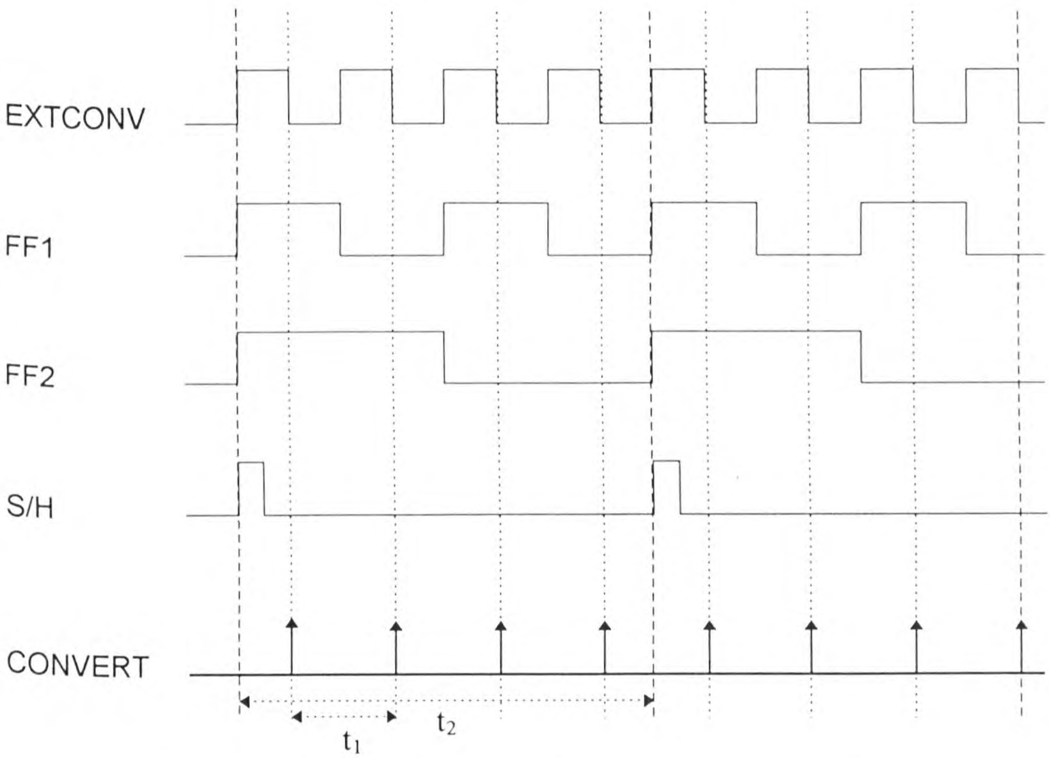

Figure [4.1.3.3] Synchronised Data Acquisition Timing Diagram.

The *EXTCONV* signal shown within Figure [4.1.3.3] has a frequency of 8 kHz. From Figure [4.1.3.1] it may be seen that this external conversion signal is fed directly into the acquisition card. Four channels are sampled altogether, t_1, resulting in every fourth channel being sampled at a rate of 2 kHz. Four channels being sampled due to a restriction within the acquisition card. The *EXTCONV* signal is also used as a trigger for the S/H circuit, t_2. The S/H circuit required a signal which was one quarter of the frequency of the *EXTCONV* signal, hence, as may be seen from Figure [4.1.3.2], the signal was passed through a series of flip-flops in order to divide the pulse to the required rate.

As the *EXTCONV* signal is external to the acquisition card, it was required to be generated from an external clock source. Several clock pulse generators were investigated in order to find the most suitable in terms of accuracy and stability. These investigations included that of the common 555 astable multi-vibrator. The 555 was found to be very susceptive to noise however, hence, the clock source used within the developed system was that of a schmitt trigger based circuit similar to that presented in Figure [4.1.3.2]. Figure [4.1.3.2] also shows the 'D' type flip-flops used to scale the clock pulse to the required frequency for the S/H circuit.

The S/H board developed therefore contains three parallel S/H IC's, each being fed form separate differential amplifiers. Alongside the S/H part of the board there is a clock generator together with the necessary clock conditioning circuitry, the board being powered by both DC +5V and ±15V sources obtained from the regulation circuit developed, Figure [4.1.3.4].

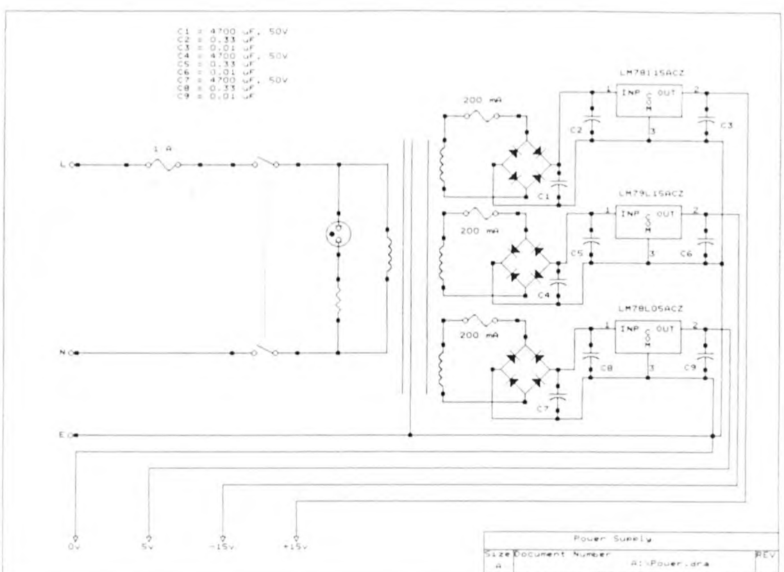

Figure [4.1.3.4] Developed DC Power Circuit.

4.1.4 Current Transducers

The current transducers used within the monitoring system were Hall Effect transducers together with their associated conditioning circuitry. These transducers utilise the 'Hall Effect' principle to produce a variable voltage signal proportional to the alternating current signal within the conductor placed through the centre of the transducer, Figure [4.1.4.1]. The Hall effect being chosen due to its linear properties within the range of currents under consideration. Three such transducers were employed to monitor the supply lines each giving a FSD of ±5V for a current range of 100A.

Figure [4.1.4.1] shows the developed portable monitoring system indicating the four main constituent parts of the system.

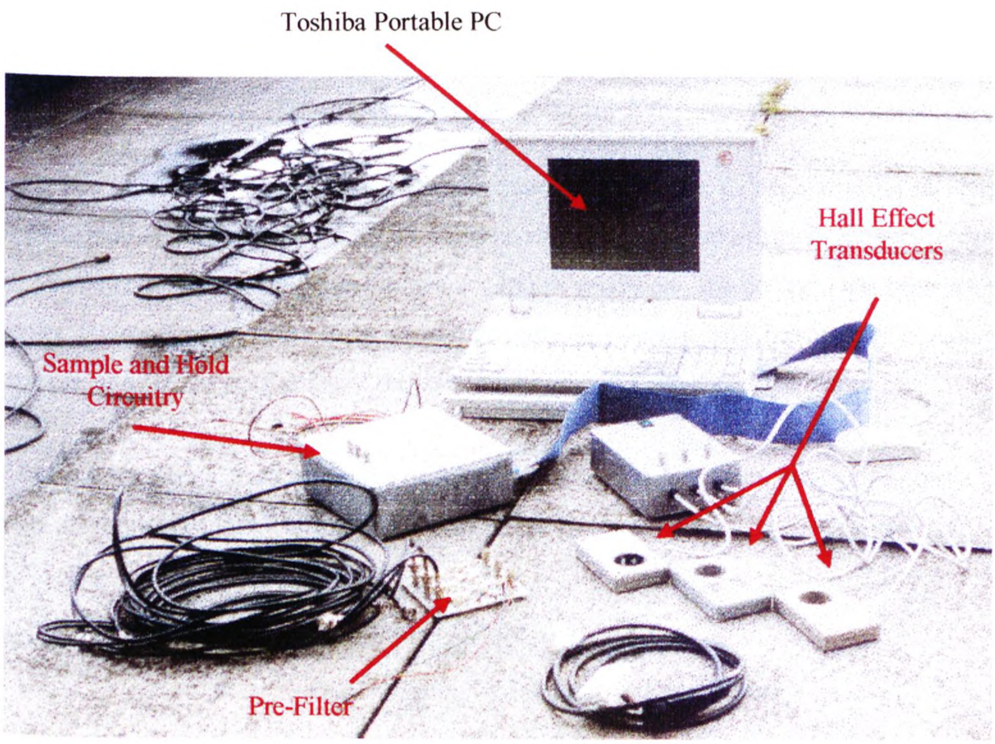

Figure [4.1.4.1] Portable Monitoring System.

4.2 Monitoring System (Software)

4.2.1 Description of Main Program Tasks

The software supplied with the data acquisition card was NI-DAQ, Ver. 2.0. It was possible to program the card to acquire data using this software, but it must be written at a very low level, as NI-DAQ allows access by the programmer to the registers within the acquisition card, hence, the individual registers of the card must be programmed in a sequential manner. In order to program at a higher level the software package LabWindows Ver. 3.0 [100] was required. This software package is produced by National Instruments as a program development environment for data acquisition and control applications when using such cards as the Lab PC +. LabWindows provides an environment for the development of structured software languages such as 'C' and more simple languages such as BASIC. The environment also gives the programmer access to an extensive range of pre-written libraries for data acquisition, instrument control, data analysis: including signal processing libraries, and graphical data presentation.

The *Current Analysis Program*, or *CAPro*, developed using Turbo C Ver 3.0 [101] in conjunction with *LabWindows* Acquisition, Advanced Analysis and Graphical Presentation libraries, contains five main functions in order to diagnose the motor's health condition. The package has been written in a windows environment in order to be as user friendly as possible, and hence, may be operated via keystrokes, or after the installation of the relevant driver, via a standard IBM mouse.

The five main software areas within the monitoring system which is menu driven and operated from a general main menu bar are listed within Figure [4.2.1.1].

- *Acquisition of Data.*
- *Pre-Processing of Data Ready For Analysis.*
- *Analysing Captured / Pre-Processed Data.*
- *Display / Record Results in a Non-Technical Format.*
- *Access to Parameters Required within Analysis / Data Acquisition.*

Figure [4.2.1.1] Five Main Functions of Current Analysis Program.

4.2.1.1 Three / Single Phase Synchronous Data Acquisition

The signals to be sampled are firstly pre-conditioned so that they fall within the range limits of ±5 V at the input of the LAB PC+ acquisition card. This is in order that the data acquisition card is not damaged, although it does have an input protection for voltages upto 45 V.

Sampling is initiated via keyboard control and may be carried out on a single named phase, or three phases simultaneously. Sampling is executed at a rate of 4 kHz for both single and three phase sampling, resulting in a sample interval of 250 μs between individual samples. Sampling continues until the total number of samples has been acquired. This has a default value of 5s of data, but may be altered by the operator to a maximum of 60s. This increased amount of data storage making use of a facility within the acquisition card known as double buffering.

The technique of double buffering allows the data buffer used to handle incoming data to be configured as a circular buffer. The NI-DAQ software divides this buffer into two separate sections which handle the flow of incoming data separately, so that when data is being written to one half of the buffer, the remaining half is stored within the defined format of file. The double buffering operation, developed by National Instruments, is shown graphically within Figure [4.2.1.1.1].

Once the required data has been obtained, it is stored within a text / binary file. A text file is used rather than a binary file as it may be necessary to transfer the sampled data to different computer systems for further analysis. Although text files require more memory space than similar files stored in binary format. Figure [4.2.1.1.2] summarises the operations available within the data acquisition section of the developed monitoring system.

- *Three Phase Data Acquisition*
- *Single Phase Data Acquisition*
- *Sample Length Selection*
- *Acquired Data Saved in User Defined Files*
- *Displays Acquired Data*

Figure [4.2.1.1.2] Summary of Data Acquisition within CAPro.

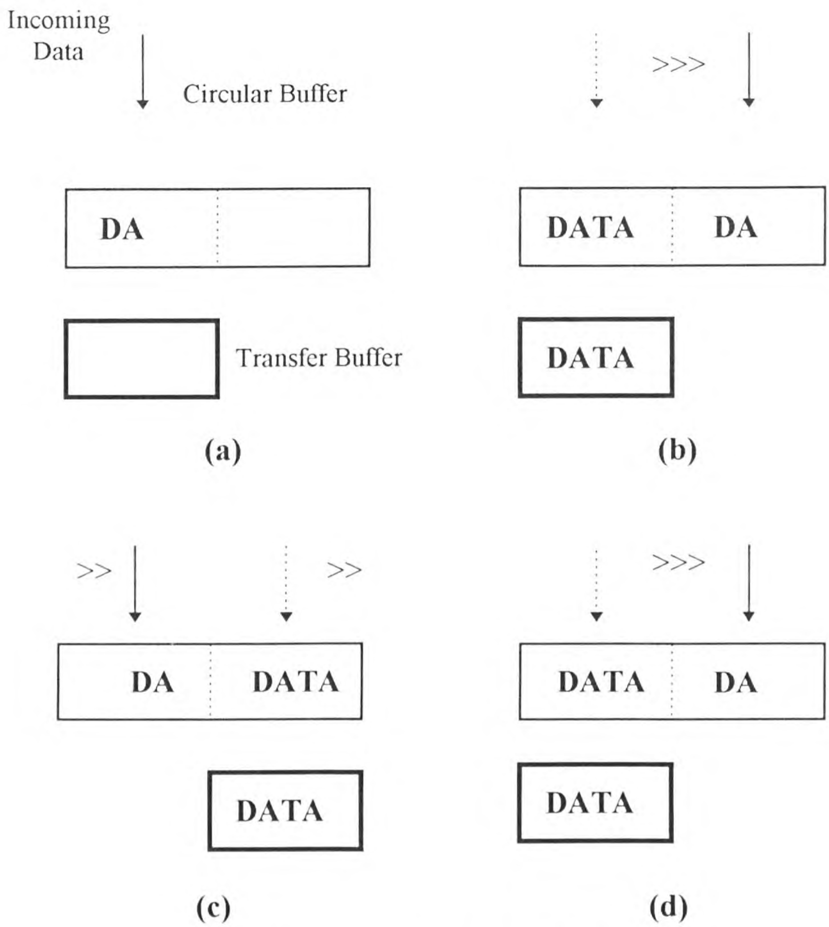

Figure [4.2.1.1.1] Double Buffering Data Storage.

4.2.1.2 <u>Data Pre-Processing / Analysis</u>

The data is sampled at 4 kHz by the data acquisition section. Prior to the data being passed to the analysis part of the developed package, it has any DC offset removed. Once this offset has been removed, the data is decimated by a factor of two. It is only after these two pre-processing operations have been completed that the data is then ready for analysis.

As the PC does not contain enough memory to compute the entire Time-Frequency representation of the current transient, the analysis which takes place within the developed package is that of the limited analysis technique [35][38]. In this analysis, only a single frequency slice of the entire Time-Frequency representation is used to determine the health of the motor. This obviously reduces the number of calculations required to derive a suitable diagnosis and will also ease the interpretation of the final diagnosis. The frequency value used to centre the frequency slice will be 21 Hz, see Section (4.3), a historic value successfully used within Elder's system [89].

Using the LabWindows software advanced analysis libraries, the data is filtered by a bandpass filter with a bandwidth of 1 Hz and a centre frequency of 21 Hz in order to decompose the data, by convolving it with the filter wavelet generated with the aid of the LabWindows software.

The decomposed data is finally rectified and passed through a low pass filter, again using the LabWindows libraries. The low pass filter being a Butterworth filter with a cut off frequency of 6 Hz.

Figure [4.2.1.2.1] summarises the individual processes available within the data pre-processing / analysing section of the monitoring system.

- *Process Binary / Text Data Files*
- *Process Single / Three Phase Data*
- *Display Processed Data*
- *Full Analysis of Data*
- *Part Analysis of Data*

Figure [4.2.1.2.1] Summary of Data Pre-Processing / Analysis.

4.2.1.3 Display Diagnostic Information

With this facility the operator may display onto the screen either the captured transient current waveform, or the results of the analysis on the captured data. The user can dictate how many data points are to be displayed on the screen and break the displaying of the completed analysis into three integral stages. These stages being the full analysis, the analysis before low pass filtering and finally, the analysed wave before rectification.

A facility is also provided which allows the data to be saved in order that the results of the analysis may be recorded for future use.

4.2.1.4 Parameter Modification

As the monitoring system is still theoretically a prototype, it was often necessary to vary certain parameters within the system during an analysis. It was also felt that the operator may in certain cases be required to adjust certain parameters whilst running the system, therefore, a parameter modification section was developed within the controlling software which allows the operator of the system to alter various values within the acquisition, analysis and display features from that of the pre-programmed default values.

Figure [4.2.1.4.1] lists a summary of the parameters which may be altered by the operator of the system.

- *Offset into Data File*
- *Bandwidth of Bandpass Filter*
- *Sample Frequency*
- *Low Pass Filter 3dB Point*
- *Low Pass Filter Order*
- *No. of Points Displayed*

Figure [4.2.1.4.1] Summary of Parameters.

4.2.2 Software Design

The following section describes the structured analysis process employed within the design of the monitoring software. Such techniques are commonly used within the design of real time programs and the following essential models / data flow diagrams are commonly used within Real Time Structured Analysis tools such as Cardtools, Cradle, Teamwork and Yourdon.

Figure [4.2.2.1] shows a glossary of common terms used within these design techniques.

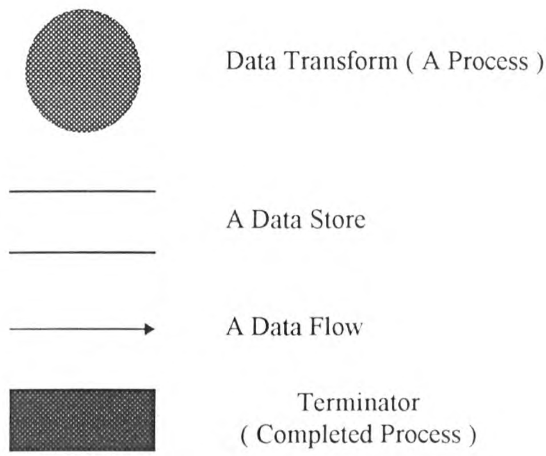

Figure [4.2.2.1] Glossary of Essential Model Terms.

The main task required of the monitoring program, Figure [4.2.2.2], was to obtain a sampled current transient from the SCIM, execute a Wavelet Decomposition upon the stored data, and record the relevant results of the analysis for future purposes.

As a means to do this, three main function areas were identified which would enable such an analysis to be undertaken. Figure [4.2.2.3] highlights these areas to be data acquisition, data analysis and parameter variation.

The first function task of 'data acquisition' was further broken-down into the individual tasks required to be encoded in order to allow successful data sampling. From Figure [4.2.2.4] it may be shown that the data acquisition function allows both three and single phase sampling to be undertaken. Figure [4.2.2.5] shows the essential model required to analyse the transients once they have been successfully recorded. It should be noted that the analysis software was written in order to analyse data which had been stored both in binary and text format. Figure [4.2.2.6] shows the various parameters which the operator of the monitoring program is capable of altering whilst running the software.

Figure [4.2.2.7] and Figure [4.2.2.8] show the low level processes of encoding required within the acquisition card in order to achieve both single and three phase data sampling.

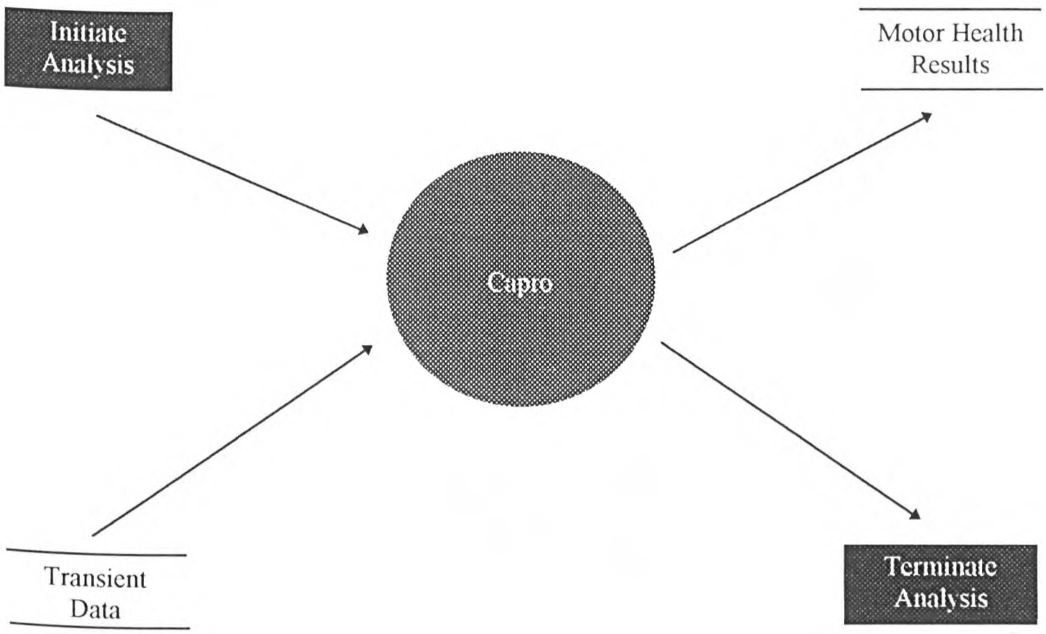

Figure [4.2.2.2] Essential Model of Monitoring Program Main Task.

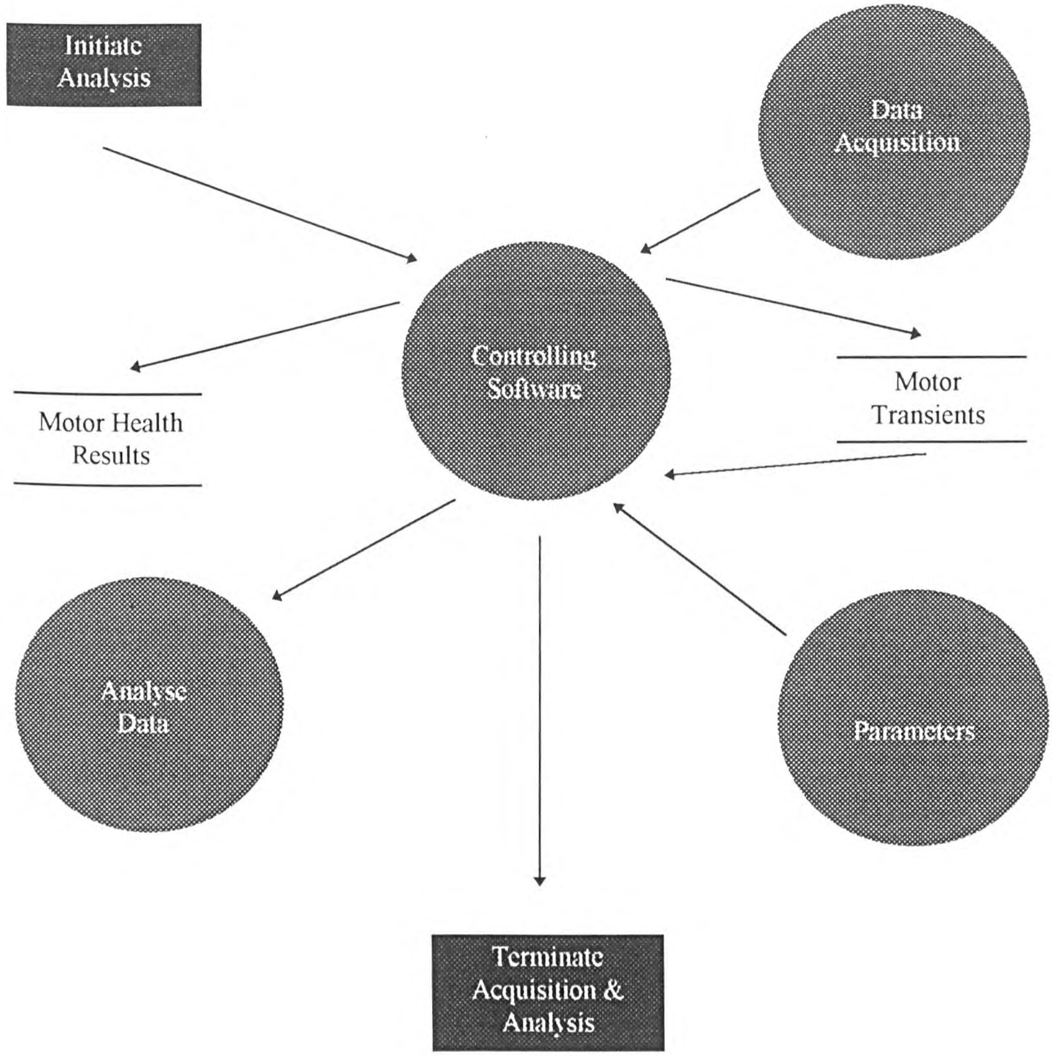

Figure [4.2.2.3] Main Task Functions within 'Capro'.

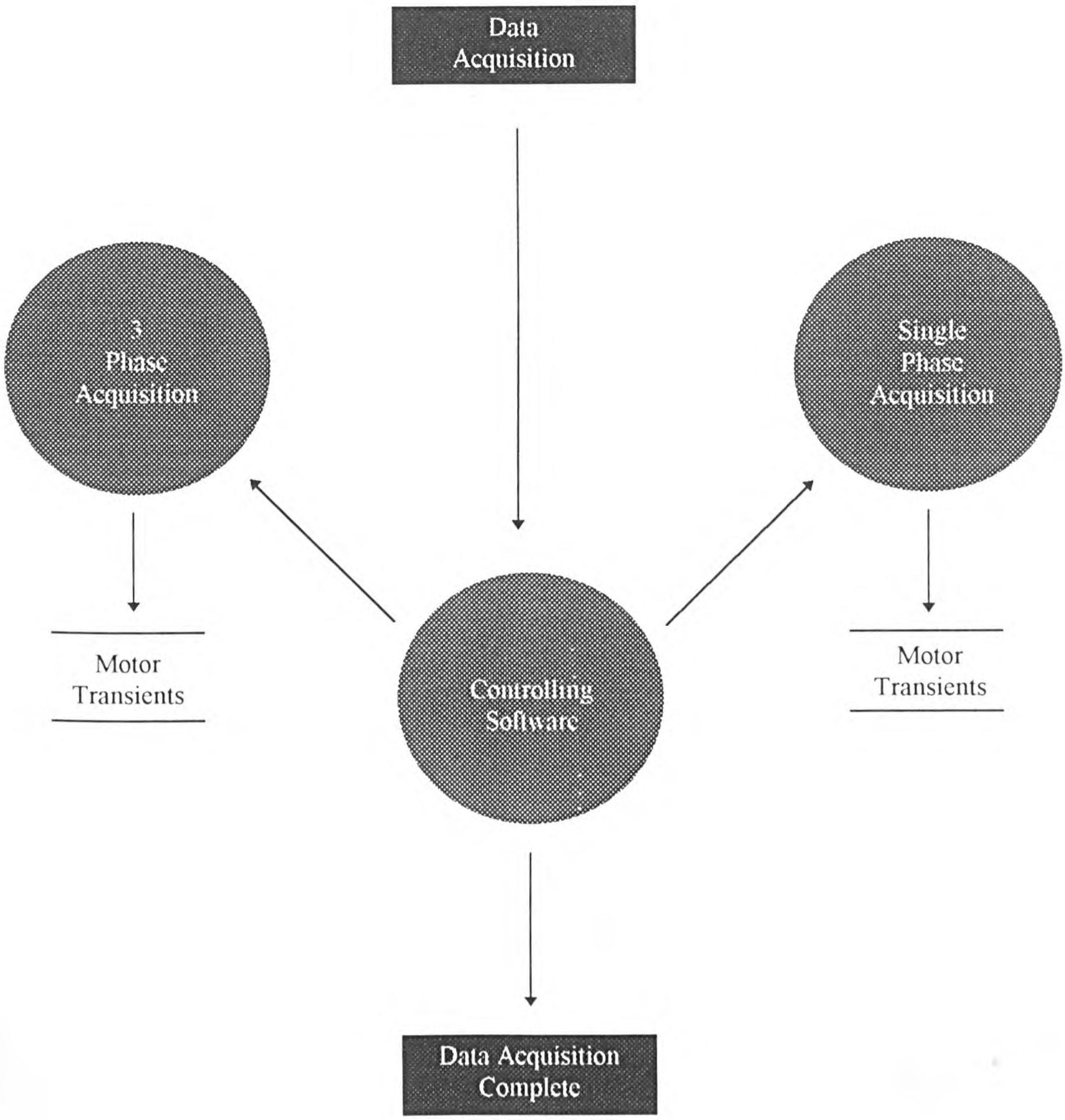

Figure [4.2.2.4] Essential Model of Data Acquisition.

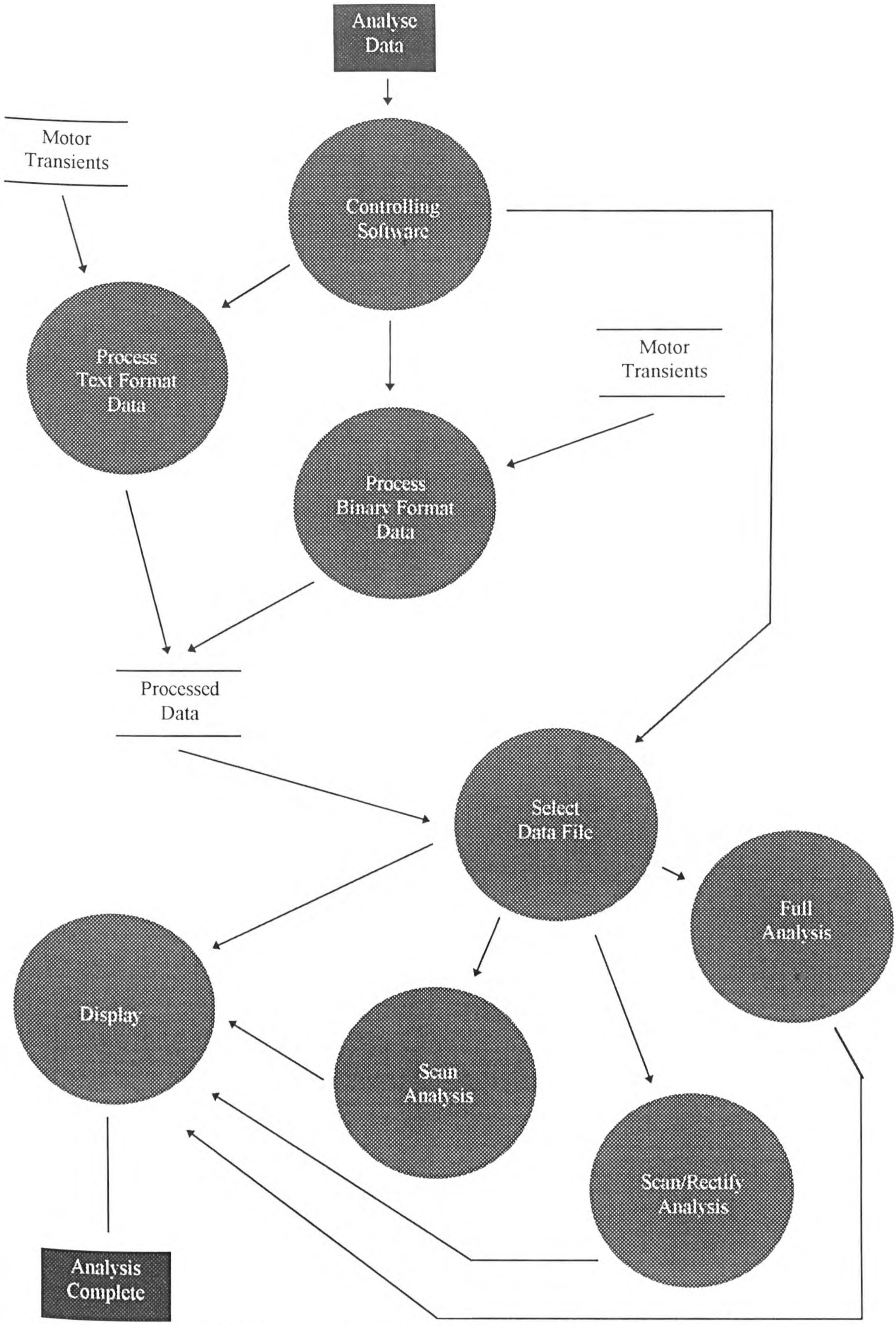

Figure [4.2.2.5] Essential Model for Data Analysis.

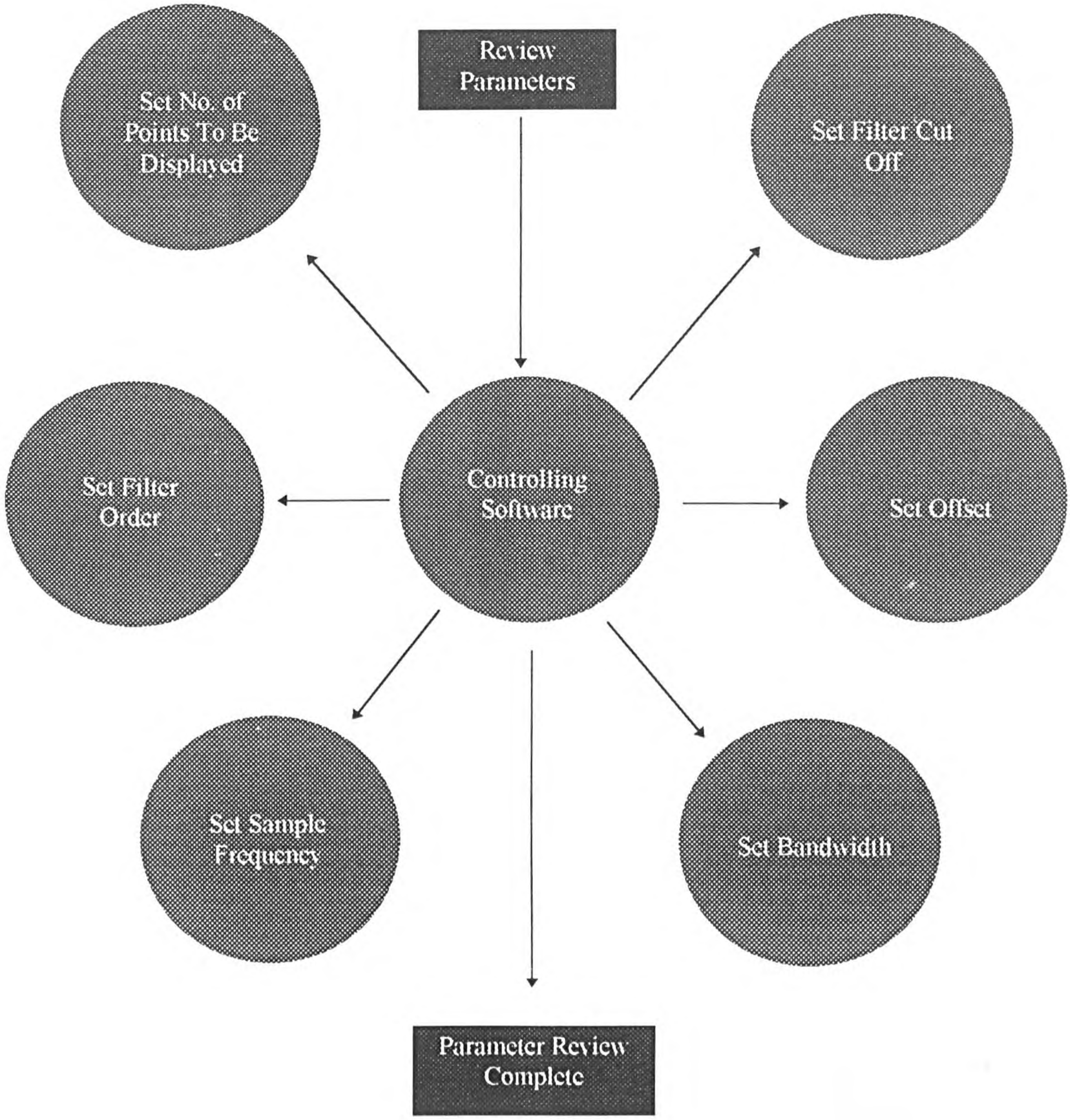

Figure [4.2.2.6] Essential Model for Parameter Variation.

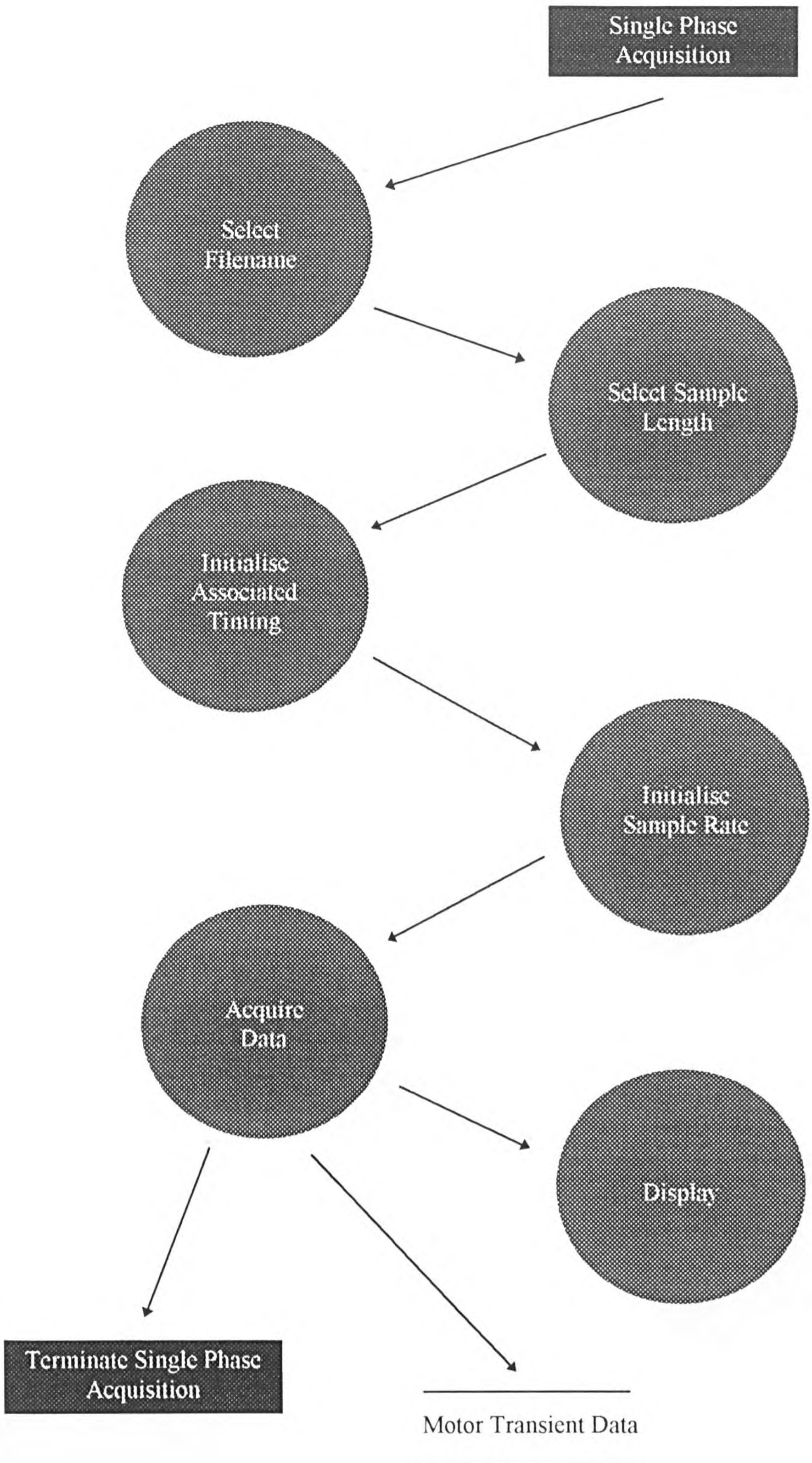

Figure [4.2.2.7] Essential Model for Single Phase Acquisition.

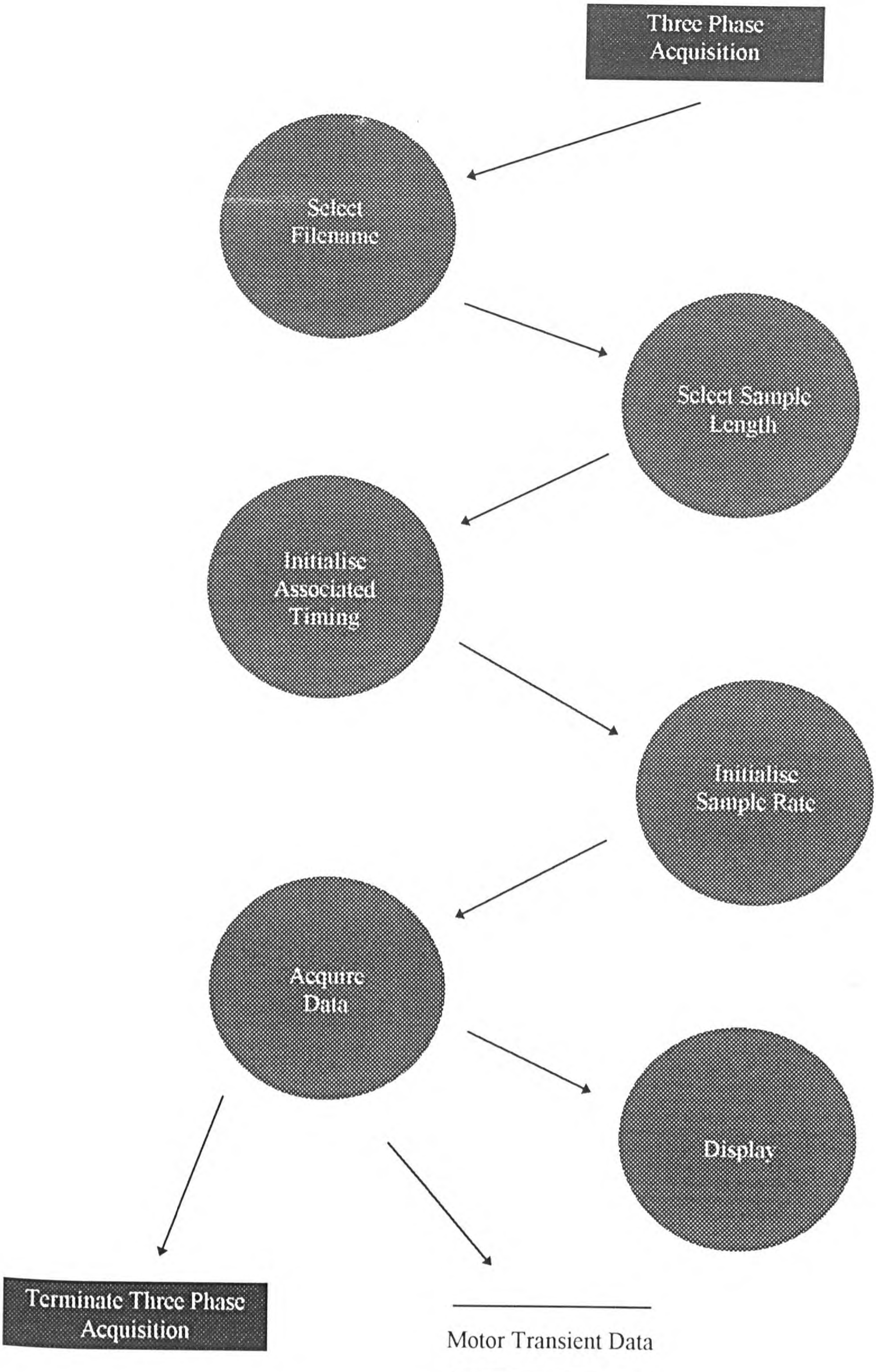

Figure [4.2.2.8] Essential Model for Three Phase Acquisition.

4.2.3 Essential Model

The essential model of the monitoring software shown in Figure [4.2.3.1] was used in the development of the monitoring system. The model, commonly referred to as the '*football field*', shows the main data flows between the individual functions which make up the entire monitoring program. For completeness the names of variables passed between the functions should be listed, but it was felt that this level of information could be omitted here, the essential model being reported as a means to give a general feeling for the software developed. A glossary of the individual functions is listed within Section (4.2.4).

Figure [4.2.3.1] /

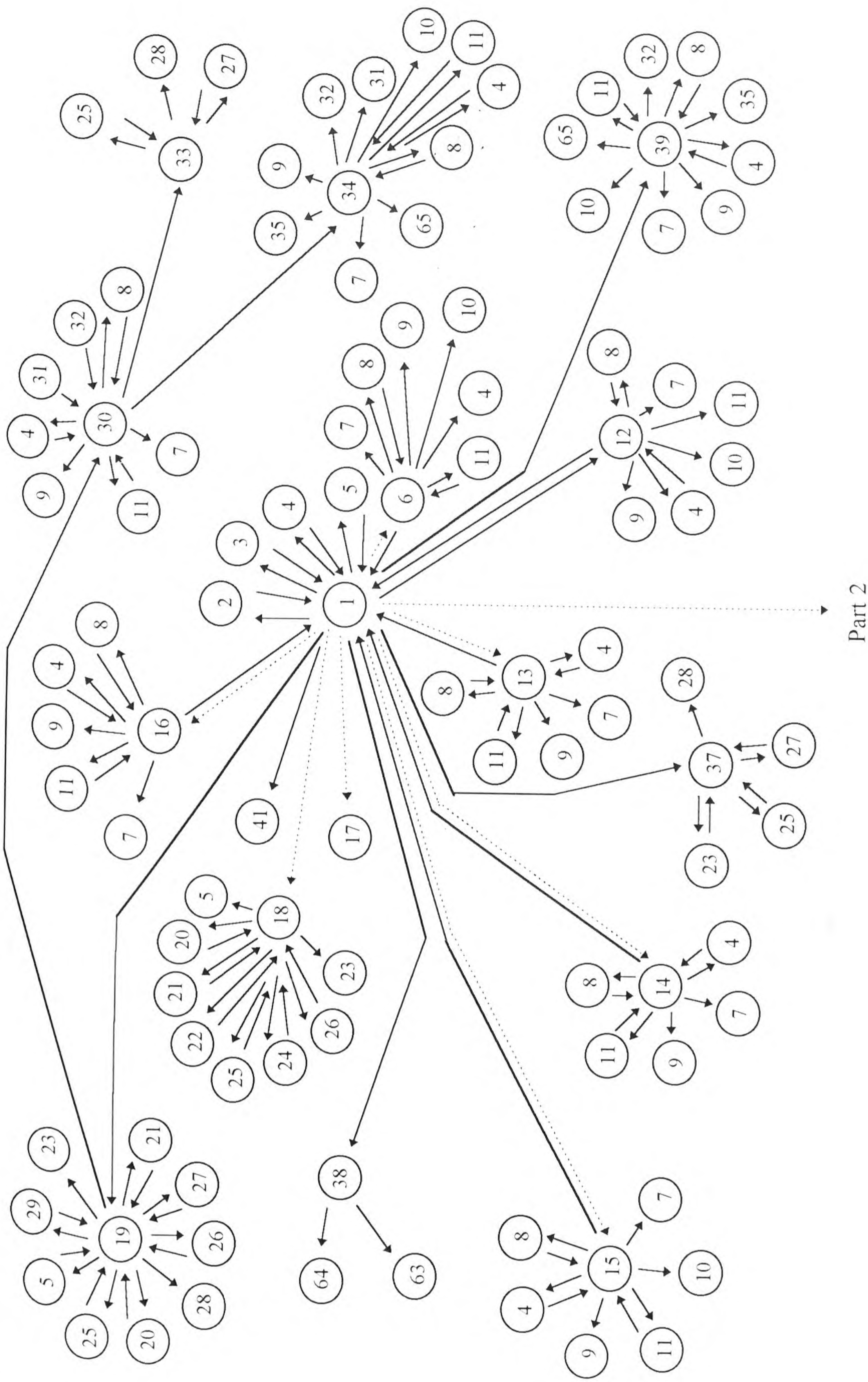
Part 2

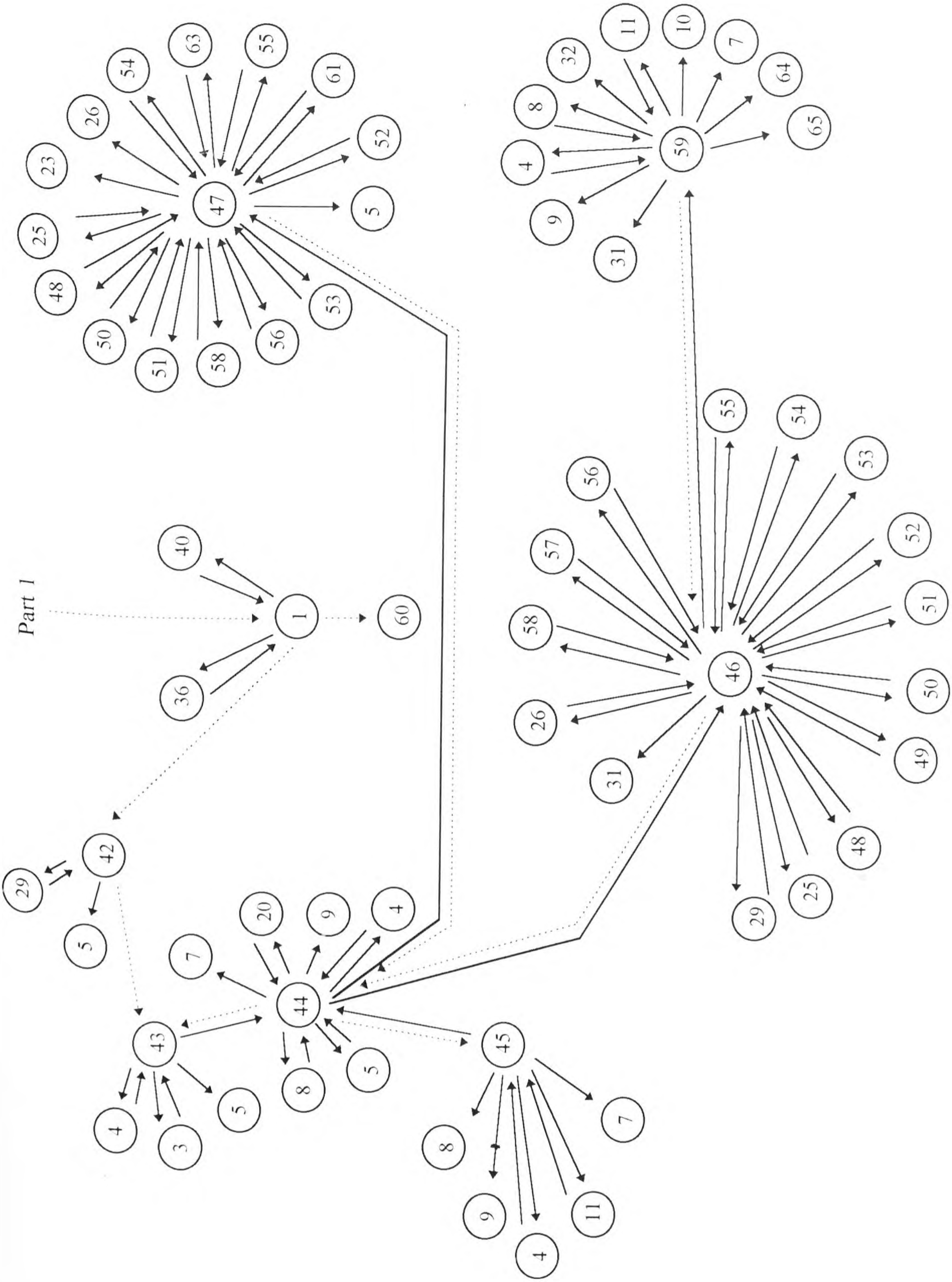
Part 1

4.2.4 Essential Model - Function List

(1) - Capro();
(2) - ConfirmPopUp();
(3) - LoadMenuBar();
(4) - GetUserEvent();
(5) - MessagePopUp();
(6) - Enter_Offset();
(7) - UnLoadPanel();
(8) - LoadPanel();
(9) - DisplayPanel();
(10) - SetInputMode();
(11) - GetCtrlVal();
(12) - Select_Bandwidth();
(13) - Select_Sample();
(14) - Cut_Off();
(15) - Enter_Point_No();
(16) - Select_Order();
(17) - UnLoadMenuBar();
(18) - Process_Data();
(19) - Process_Binary_Data();
(20) - FileSelectPopUp();
(21) - PromptPopUp();
(22) - AscDec();
(23) - Fclose();
(24) - Fgetc();
(25) - Fopen();
(26) - Fwrite();
(27) - Fread();
(28) - Fseek();
(29) - ConfirmPopUp();
(30) - Load_1_Phase();
(31) - ClearGraphicsScreen();
(32) - SetActivePanel();
(33) - LoadData();
(34) - Plot_Data();
(35) - Delete_Plots();
(36) - FileSelectPopUp();
(37) - Read_Data();
(38) - Scan_Data();
(39) - Display();
(40) - PromptPopUp();
(41) - Rectify();
(42) - Data_Acquisition();
(43) - Acquire_Menu();
(44) - Acquire_Panel();
(45) - Sample_Length();
(46) - Ph_Grab_Data();
(47) - Grab_3_Phase_Data();
(48) - AI_Configure();
(49) - AI_Mux_Config();
(50) - DAQ_Config();
(51) - DAQ_Trigger_Config();
(52) - DAQ_DB_Half_Ready();
(53) - DAQ_DB_Transfer();
(54) - DAQ_DB_Config();
(55) - DAQ_Rate();
(56) - DAQ_Vscale();
(57) - DAQ_Start();
(58) - DAQ_clear();
(59) - Ph_Display_Array();
(60) - CloseInterfaceManager();
(61) - Lab_Scan_Start();
(62) - Timeout_Config();
(63) - Wind_BPF();
(64) - Cxy();
(65) - Ploty();

4.3 Monitoring Results

4.3.1 Description of Laboratory Test-Rig

The laboratory test-rig on which all tests were carried out is shown in Figure [4.3.1.1]. The motor is a three phase 11 kW, 51 rotor bar, Squirrel Cage Induction Motor. The machine which is star / delta started may either be run in motor or generator mode but for the means of this project was operated in motor mode only. As may be seen from Figure [4.3.1.1] the induction motor is loaded via a dynamometer which may be varied to give different levels of loading. The test-rig was designed prior to its use within this project, hence, all relevant parameters were at easy access to the operator. These parameters include: line and phase currents / voltages, accessible from a wiring panel situated in front of the motor, Figure [4.3.1.1], rotor speed, via a tachometer and vibration, obtained from a suitable sensor but used within this project.

A wide range of squirrel cage rotors were available with differing degrees of fault severity, ranging from fault free rotors to those with a complete group of ten broken bars present. Bars with cracked end-rings were also available along with a rotor which had the facility of making and breaking two bars, thus creating a rotor which could represent both fault free and two broken rotor bar conditions. All rotors could be inserted into the test-rig with varying degrees of eccentricity if so desired, although in the case of this project all rotors were inserted with 0% stator / dynamic eccentricity, or as near 0% as is practically possible.

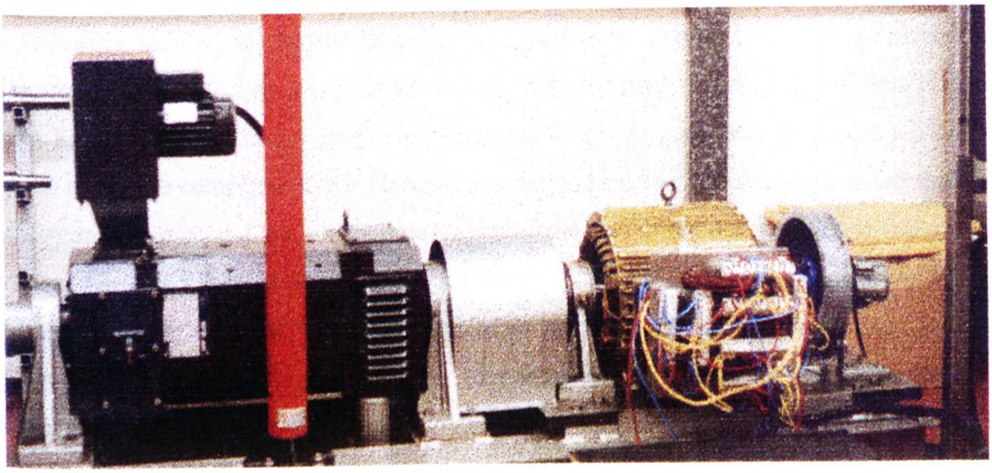

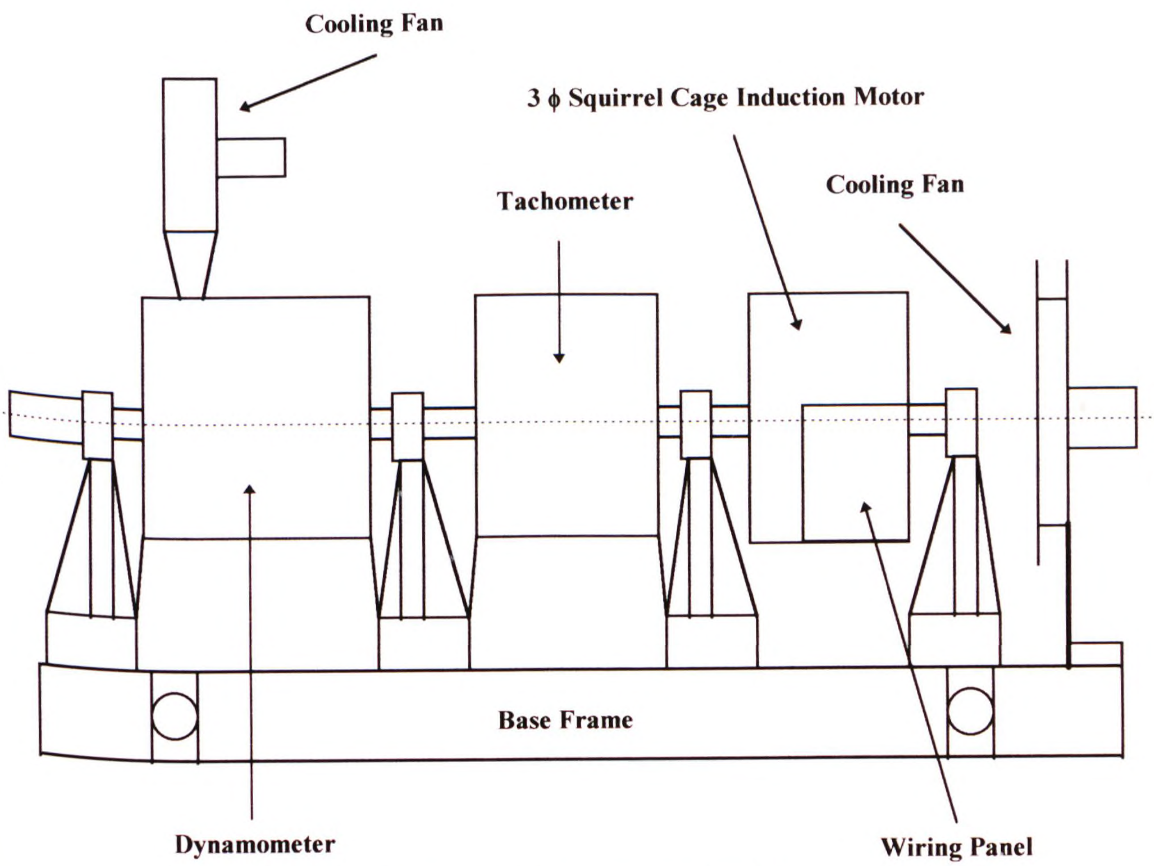

Figure [4.3.1.1] Laboratory Test Rig.

4.3.2 Laboratory Results

The following section summarises the laboratory results obtained from the developed transient monitoring system. All tests were carried out upon the test-rig described in Section (4.3.1), under various Squirrel Cage rotor bar fault conditions that included: zero, two, three and ten broken rotor bars. All tests were completed under both full and no load start-ups. It should be noted that the rotors which contained three and ten broken bars had had their bars drilled out in order to simulate the fault condition, whereas the rotor which contained the two bar fault had been designed so that the fault could be removed if required. This was achieved by insulating out of the circuit two bars within the rotor as a means to simulate the bar fault. Removing this insulation thus allowed the bars to be brought back into circuit and therefore simulate a rotor with zero bar faults. All rotor bar faults were of a contiguous nature throughout laboratory testing.

The transducers used throughout the testing were Hall Effect transducers which had a FSD of ±100A → ± 5V. This therefore results in a conversion factor within the following figures of 1V → 20A. See Section (4.1.4) for further details.

4.3.2.1 Data Sampling

The monitoring system developed allowed data to be sampled synchronously both under single phase and three phase formats. Figure [4.3.2.1.1] and Figure [4.3.2.1.2] show two such common examples of the data sampling capability within the monitoring system. Figure [4.3.2.1.1] represents the successful completion of a three phase data sample. Due to the limited RAM available onboard the PC, the amount of data capable of being captured is less than that of a single phase of data. It should be noted that the amplitude of the data within phase 'A' is approximately half of the other phases. This was due to a transducer problem and was later rectified. Figure [4.3.2.1.2] shows the results of a single phase data capture. The signals displayed are all examples of a no load, three broken bar transient.

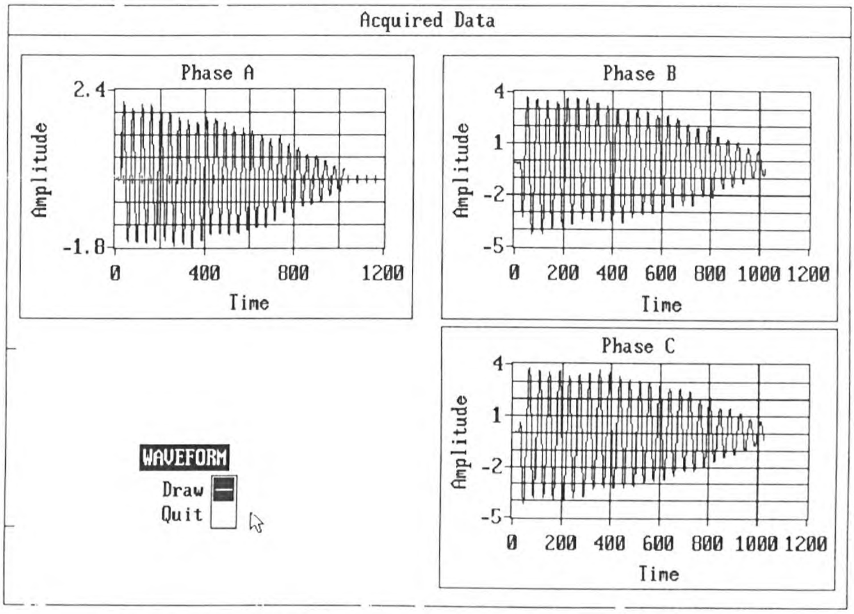

Figure [4.3.2.1.1] No Load 3 Broken Bar, 3 Phase Sample.

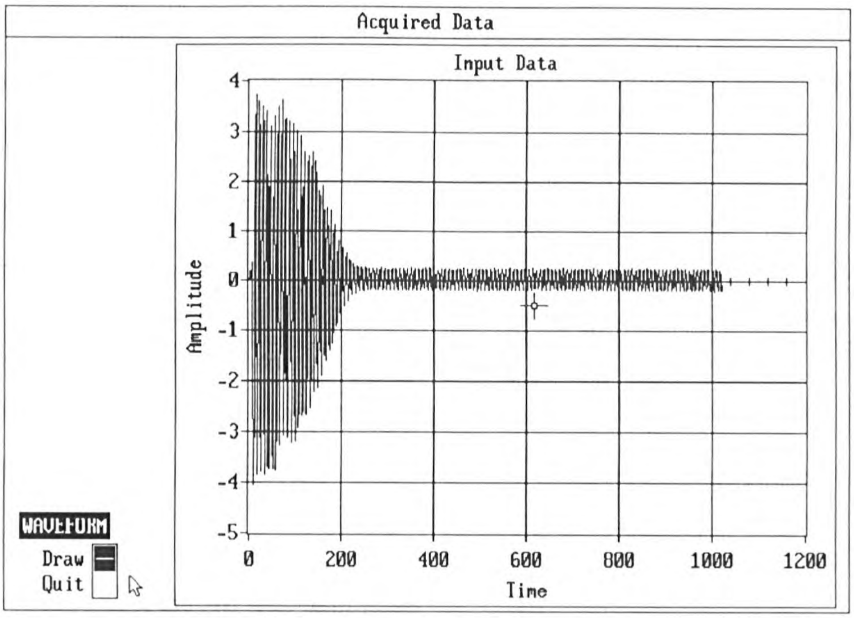

Figure [4.3.2.1.2] No Load 3 Broken Bar, Single Phase Sample.

4.3.2.2 Full Load, Zero Broken Rotor Bars

Figure [4.3.2.2.1] shows the transient signal obtained from the test-rig under full load, zero broken bar conditions. From this it may be observed that an initial transient peak of $80A_{(pk)}$ is achieved for 600ms before reducing to the full load steady state level of $25A_{(pk)}$.

Figure [4.3.2.2.2] presents the results of the full analysis carried out upon the above transient. From this plot there are three main areas to observe. These areas being the initial surge of energy at the start of the plot and the locations within the plot marked (a) and (b). It is at these points, as will be observed in later results, that the sidebands indicative to rotor faults will be present. However, as can clearly be observed within Figure [4.3.2.2.2] no 'peaks' are present, hence, this plot is clear evidence of the rotor being fault free. Figure [4.3.2.2.3] presents the result of the same analysis at a stage prior to final filtering. It was envisaged that this part analysis may be of some use during the development of the monitoring tool. From the part analysis, it may be easily observed that after the initial energy surge no further peaks of energy are present within the analysis.

4.3.2.3 Full Load, Two Broken Rotor Bars

Figure [4.3.2.3.1] presents the single phase sample of a starting transient obtained by monitoring the test-rig under a full load, two broken bar transient condition. From this it may be observed that an initial transient of $74A_{(pk)}$ is obtained for approximately 600ms, prior to the transient reducing to the full load steady state level of $24A_{(pk)}$.

Figure [4.3.2.3.2] clearly shows the result of the full analysis completed upon the above transient. Again the initial energy surge is present within the plot, but more importantly, two definite peaks can now be observed located at (a) and (b). It is these peaks which are indicative of the rotor fault sidebands passing through the monitoring systems filtering process. Figure [4.3.2.3.3] shows the part analysis and it is in this plot that interestingly the peak situated at (a) may be observed to be smaller in amplitude than the peak situated at (b).

Comparing Figure [4.3.2.3.2] to Figure [4.3.2.2.2] shows the clear difference within peak amplitudes and thus the indication of the two rotor fault levels.

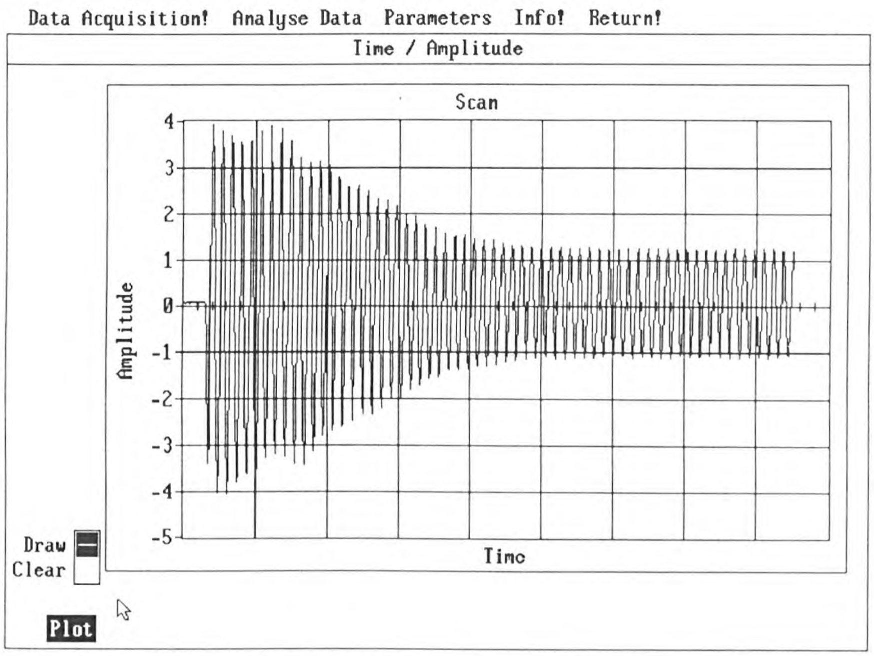

Figure [4.3.2.2.1] Full Load 0 Broken Bars, Single Phase Sample.

(Δt = 20 ms, ΔAmpl = 20 A)

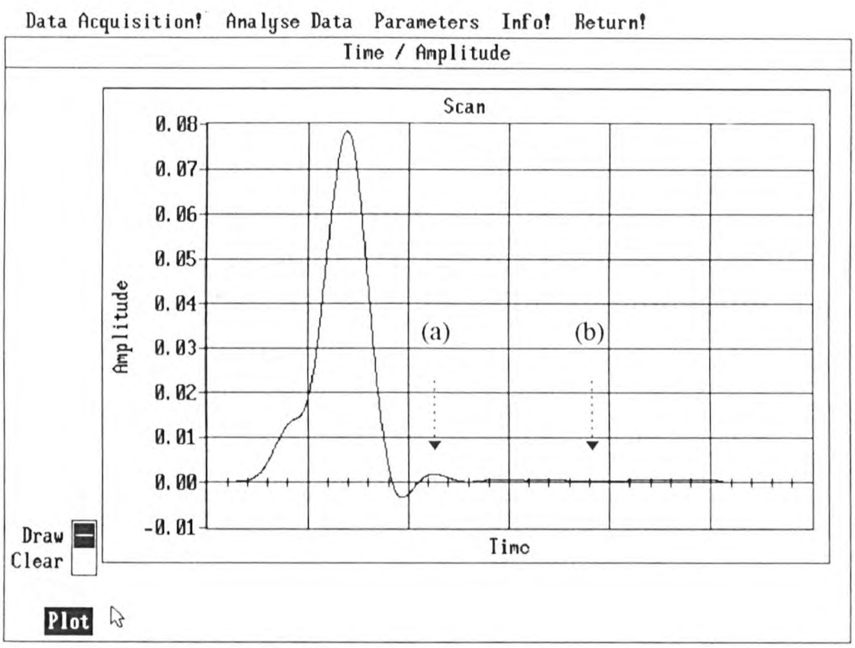

Figure [4.3.2.2.2] Full Load 0 Broken Bars, Full Analysis.

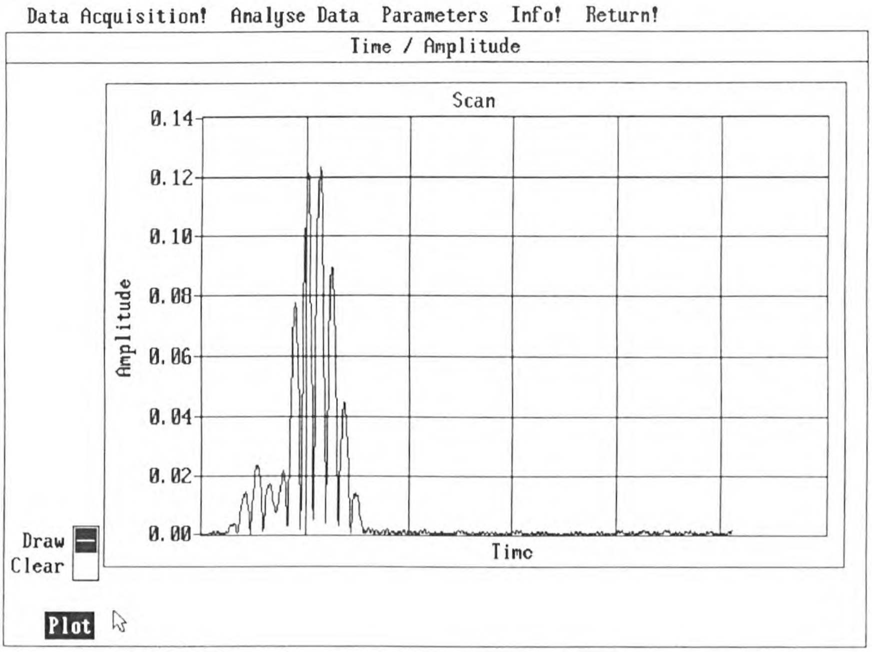

Figure [4.3.2.2.3] Full Load 0 Broken Bars, Scan / Rectify Part Analysis.

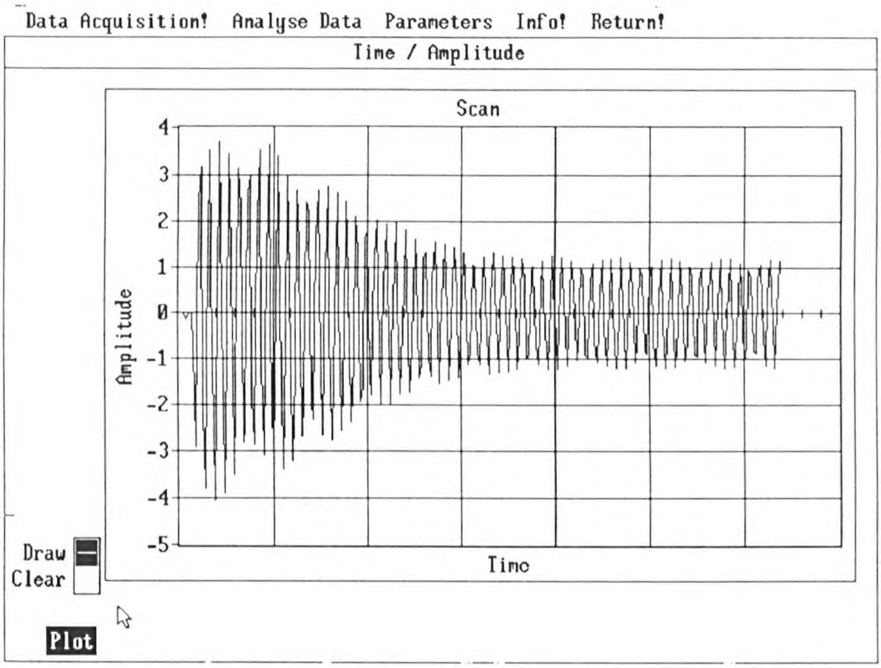

Figure [4.3.2.3.1] Full Load 2 Broken Bars, Single Phase Sample.

($\Delta t = 20$ ms, $\Delta Ampl = 20$ A)

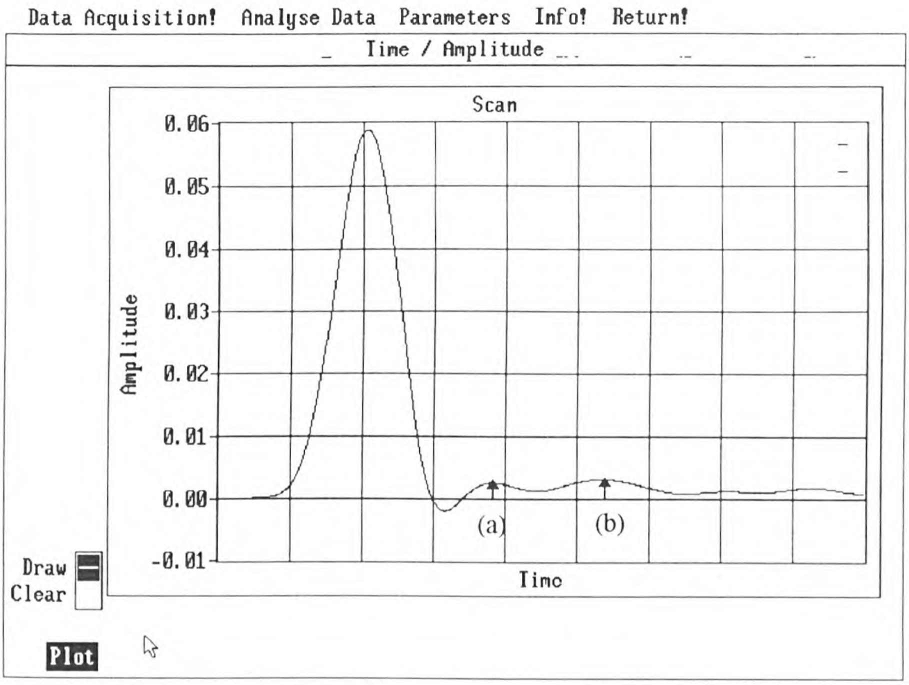

Figure [4.3.2.3.2] Full Load 2 Broken Bars, Full Analysis.

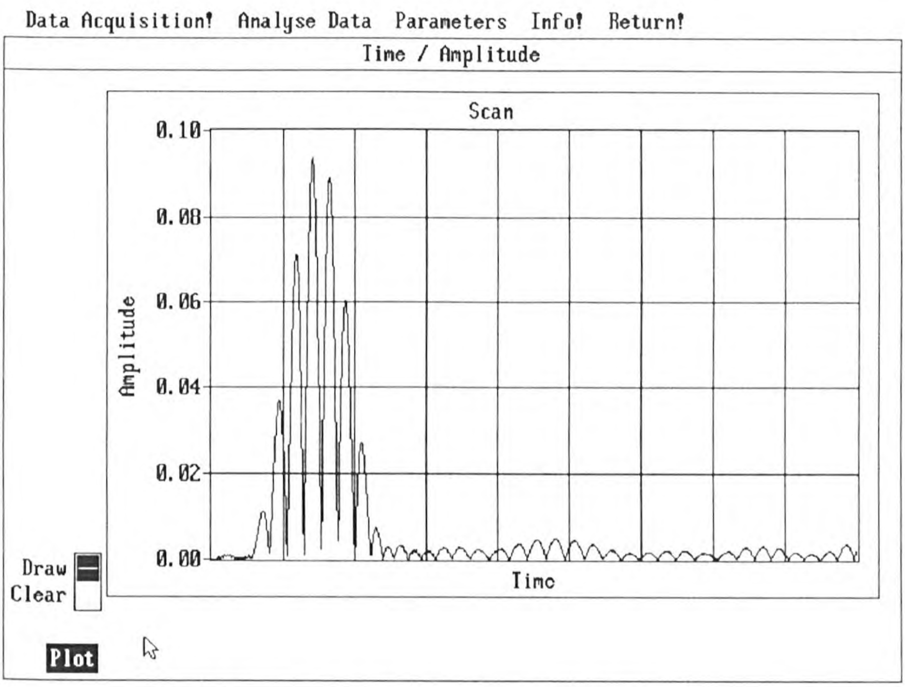

Figure [4.3.2.3.3] Full Load 2 Broken Bars, Scan / Rectify Part Analysis.

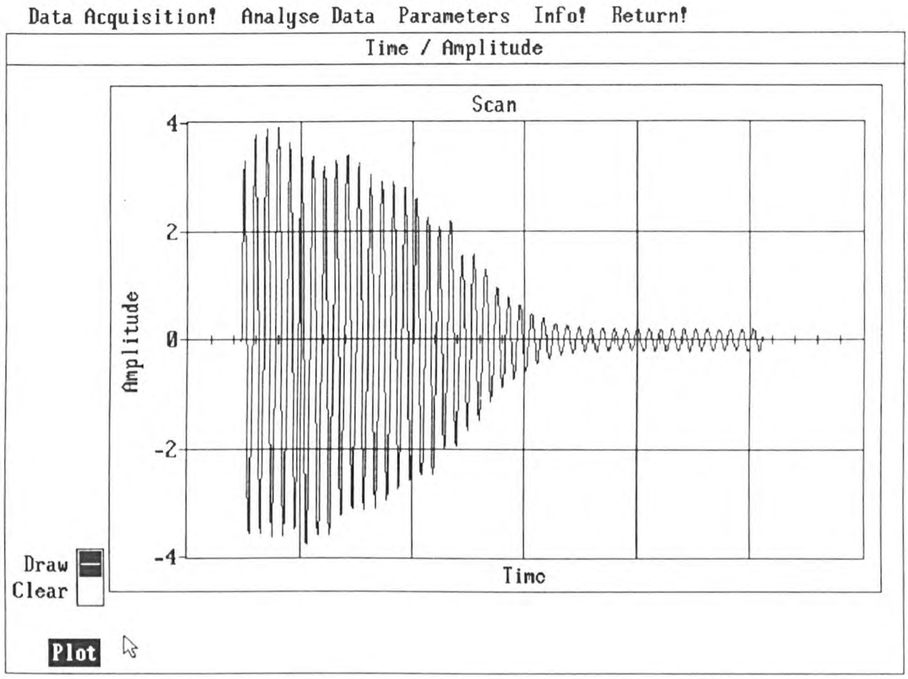

Figure [4.3.2.4.1] No Load 3 Broken Bars, Single Phase Sample.

(Δt = 10 ms, ΔAmpl = 20 A)

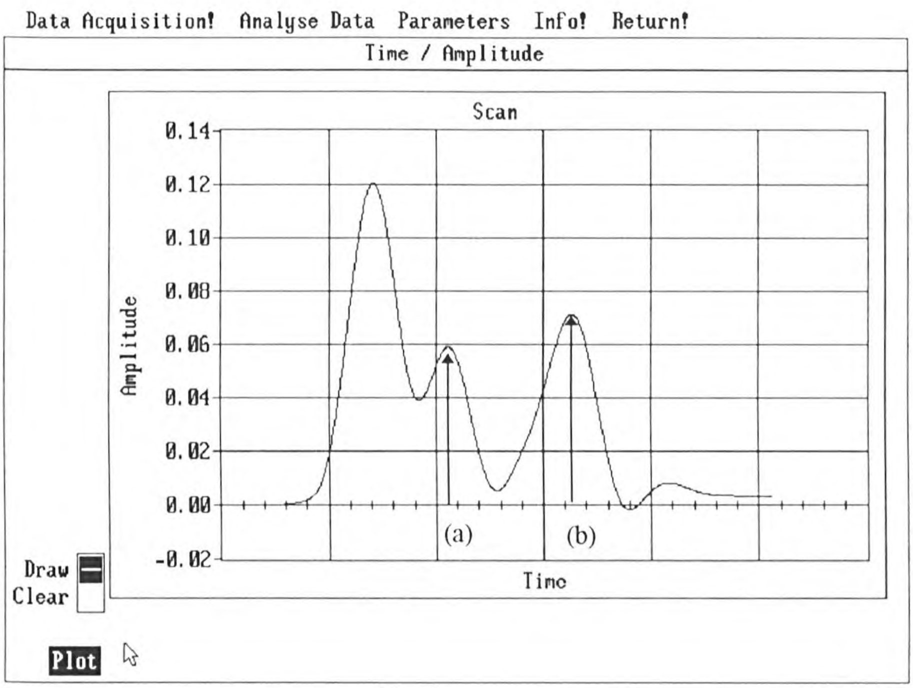

Figure [4.3.2.4.2] No Load 3 Broken Bars, Full Analysis.

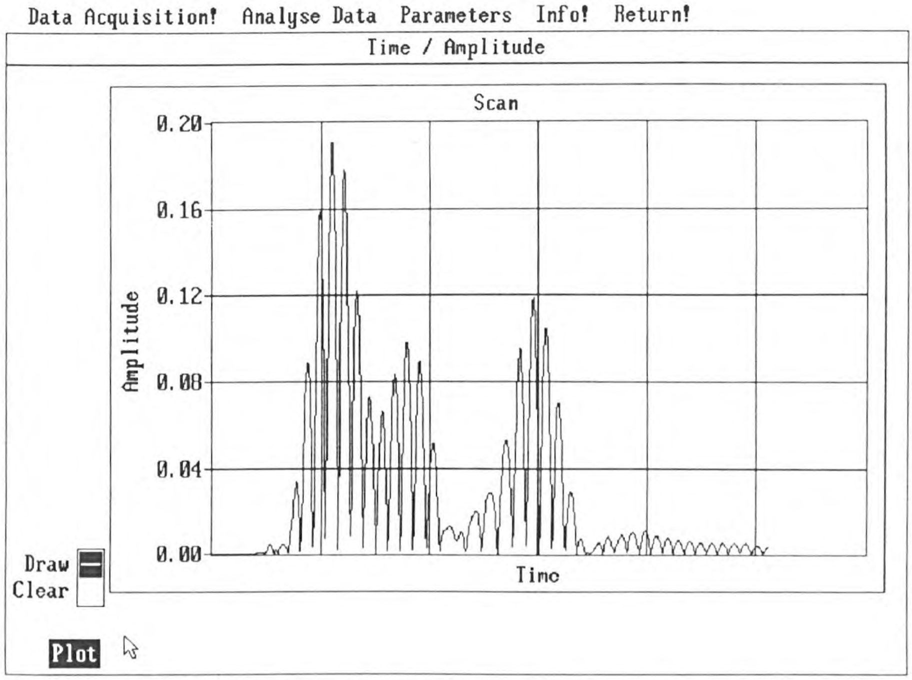

Figure [4.3.2.4.3] No Load 3 Broken Bars, Scan / Rectify Part Analysis.

4.3.2.4 No Load, Three Broken Rotor Bars

Figure [4.3.2.4.1] shows a typical transient obtained from the test-rig under no load, three broken bar conditions. Again a peak current of $78A_{(pk)}$ is obtained for approximately 300ms before reducing to the no load steady state level of $5A_{(pk)}$.

Figure [4.3.2.4.2] shows the results of a full analysis upon the no load transient. Looking at the peaks indicated by (a) and (b), it is clear to observe the sidebands obtained under this fault condition. Again it may be observed that the peak marked (b) is larger than that marked (a), with Figure [4.3.2.4.3] verifying this.

4.3.2.5 No Load, Ten Broken Rotor Bars

Figure [4.3.2.5.1] shows the single phase transient obtained from the test-rig under the exaggerated test fault condition of no load, ten broken bars. From this an initial peak transient of $70A_{(pk)}$ is observed for approximately 300ms prior to reduction to the no load steady state level of $5A_{(pk)}$.

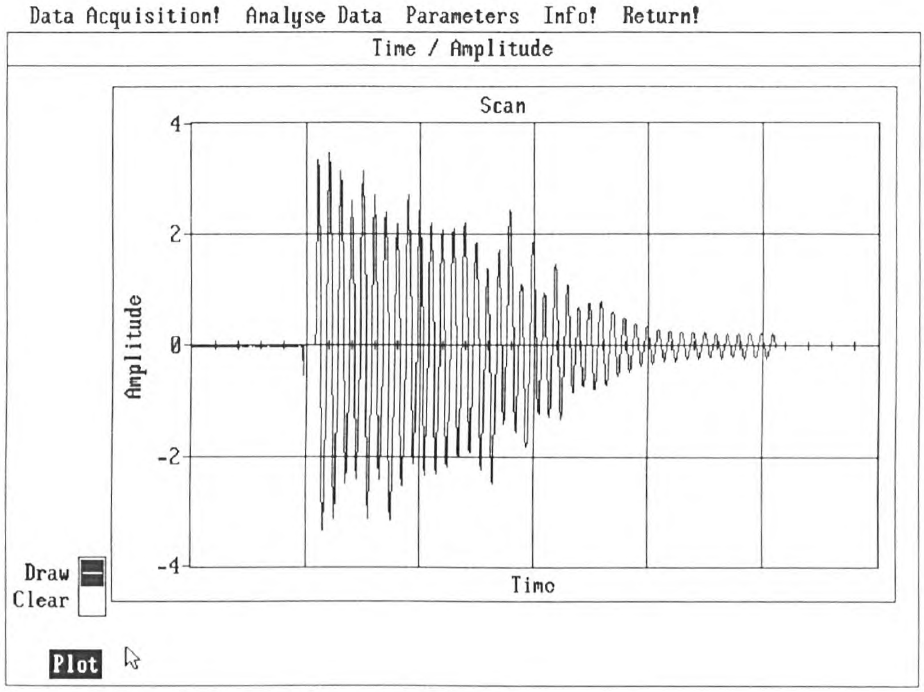

Figure [4.3.2.5.1] No Load 10 Broken Bars, Single Phase Sample.

(Δt = 10 ms, ΔAmpl = 20 A)

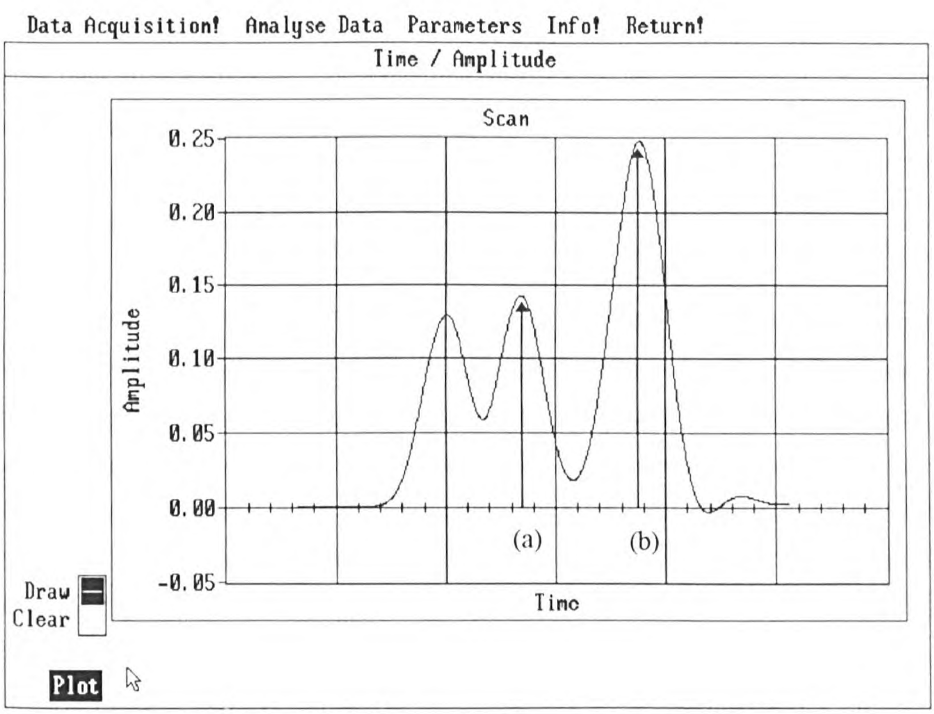

Figure [4.3.2.5.2] No Load 10 Broken Bars, Full Analysis.

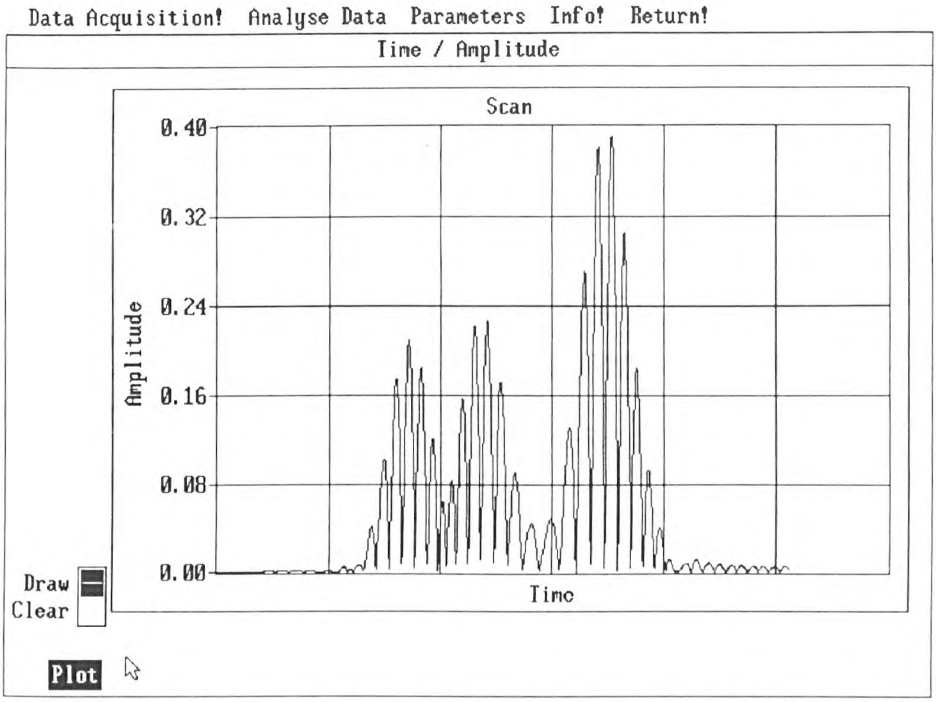

Figure [4.3.2.5.3] No Load 10 Broken Bars, Scan / Rectify Part Analysis.

Figure [4.3.2.5.2] shows the results of the full analysis completed upon the transient signal. From this it may be clearly observed that both the amplitudes of (a) and (b) have dramatically increased in amplitude as the level of rotor fault has increased. However, the relationship of (a) remaining smaller in amplitude than (b) is maintained throughout this level of rotor fault. Figure [4.3.2.5.3] confirms the increased amplitude of (b) under these fault conditions.

4.3.2.6 Sideband Amplitude Levels versus Rotor Fault Level

Figures [4.3.2.6.1] through to Figure [4.3.2.6.4] report on the results obtained from the monitoring system. In particular the amplitudes of the three main peaks within a series of full and part analyses under several rotor bar fault conditions. These peaks include the initial surge, the sideband marked (a) and finally, the sideband marked (b). Figure [4.3.2.6.1] to Figure [4.3.2.6.2] show that during both full and no load starts the initial energy surge at no point indicates any correlation to the level of rotor bar fault present. The amplitudes of these peaks occurring purely at random. The sidebands marked (a), however, in both full and no load starts may be observed to indicate a level of proportionality to the level of fault. The sidebands marked (b) in both instances has a much higher level and shows similar levels of proportionality to the level of fault. Figure [4.3.2.6.3] to Figure [4.3.2.6.4] show close correlation to the above findings with the fault amplitudes generally being slightly higher.

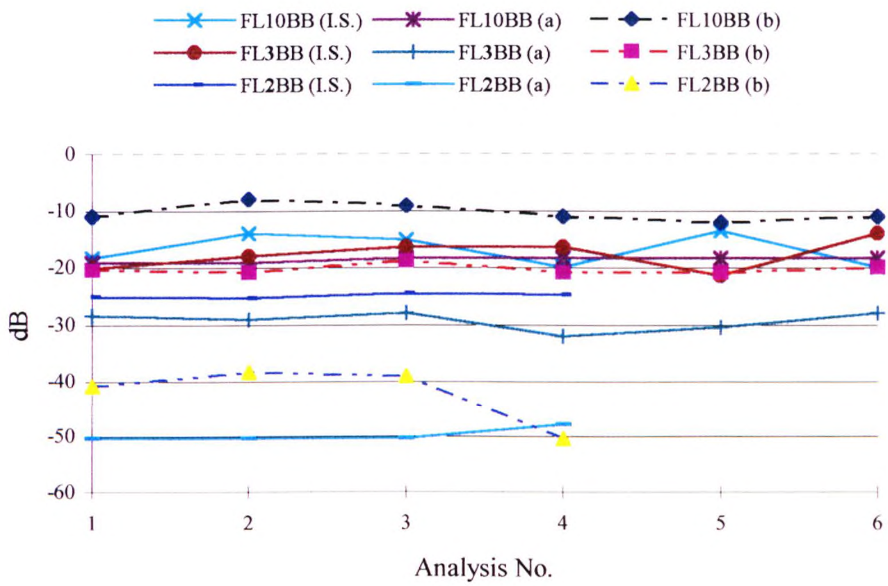

Figure [4.3.2.6.1] Full Analysis Peak Amplitudes - Full Load.

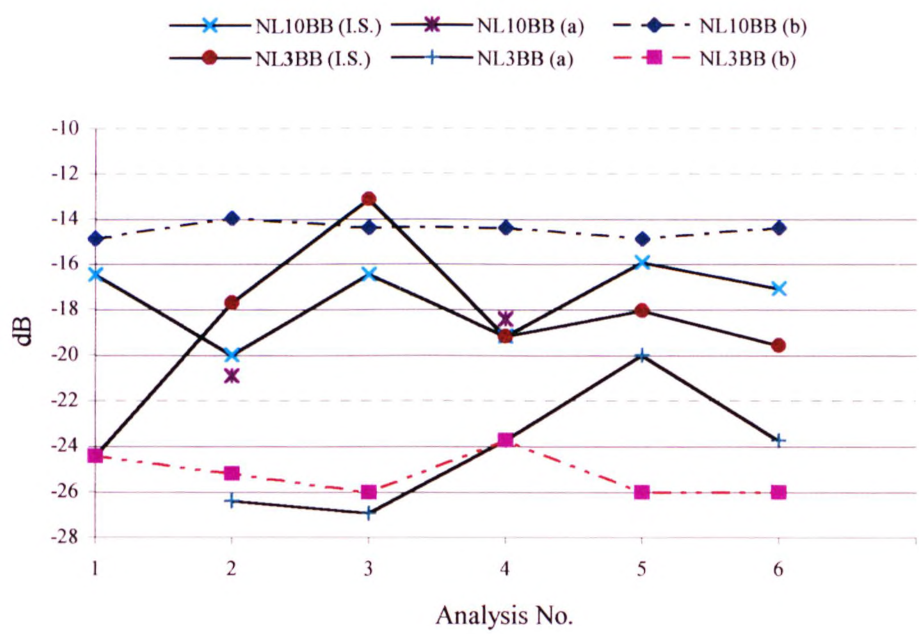

Figure [4.3.2.6.2] Full Analysis Peak Amplitudes - No Load.

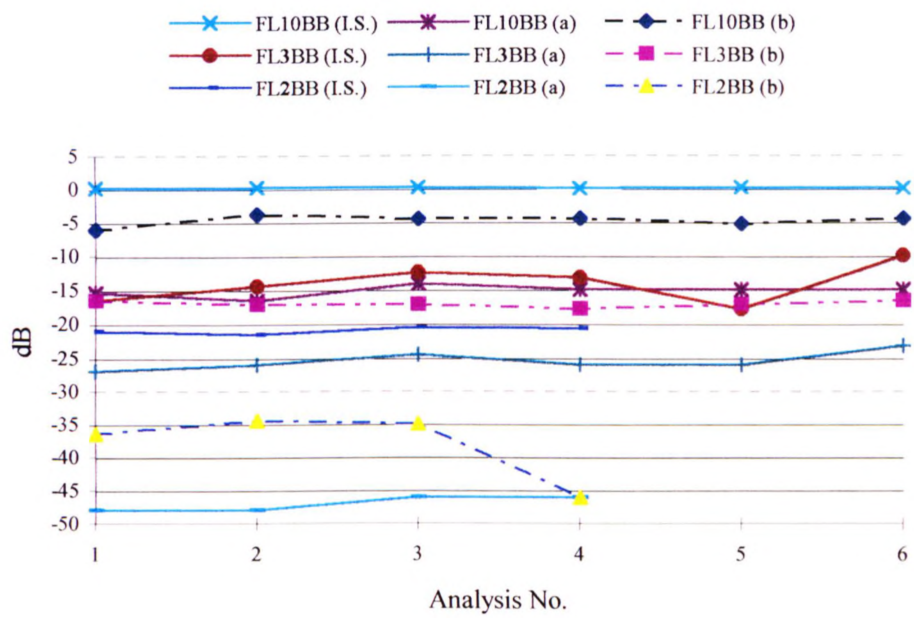

Figure [4.3.2.6.3] Part Analysis Peak Amplitudes - Full Load.

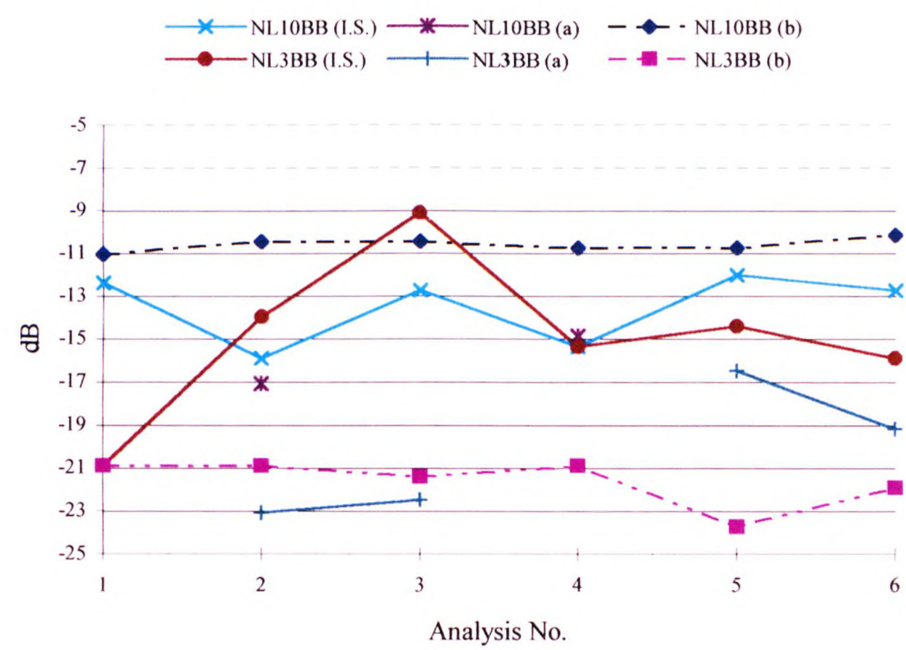

Figure [4.3.2.6.4] Part Analysis Peak Amplitudes - No Load.

The data presented in Tables [4.3.2.6.1] through to Table [4.3.2.6.4] summarises the average fault component levels for the various fault conditions. From these results it may be observed that as the level of rotor fault increases a similar increase is found within the amplitude of the monitoring system output.

This phenomenon is found to be present both within the full and no load analyses. One point to note, however, is the large increase throughout all tests in the fault level between two and three bar conditions when compared with three and ten. Although there is an increase, thus indicating a difference in fault level, there does not seem to be any linearity between the fault levels. This, however, must be as a result of the rotor used. As mentioned previously, the two broken rotor bar used throughout was not faulted in a similar manner to the other rotors. Due to the above results it must be assumed that this method did not allow a good fault condition to be simulated, in that current within the form of leakage or interbar currents was able to flow within the broken bars. Therefore, in order for any linearity work to be completed all rotor bars should have been faulted in a similar manner.

No. of Broken Rotor Bars	Average dB Level	Difference
10	-10.38	*
3	-20.34	9.96
2	-42.24	21.9

Table [4.3.2.6.1] Full Analysis, Full Load.

No. of Broken Rotor Bars	Average dB Level	Difference
10	-14.50	*
3	-25.24	10.74

Table [4.3.2.6.2] Full Analysis, No Load.

No. of Broken Rotor Bars	Average dB Level	Difference
10	-4.71	*
3	-16.99	12.28
2	-37.95	20.96

Table [4.3.2.6.3] Part Analysis, Full Load.

No. of Broken Rotor Bars	Average dB Level	Difference
10	-10.61	*
3	-21.64	11.03

Table [4.3.2.6.4] Part Analysis, No Load.

4.3.3 Industrial Verification of Monitoring Technique

As a means of verifying the laboratory based results of the monitoring software, an industrial visit was arranged in collaboration with the projects sponsoring establishment. This enabled monitoring of industrial sized machines to be undertaken, with the results indicating as to the portability of transferring the laboratory based theories behind the technique into the industrial environment.

4.3.3.1 Description of Testing Procedure

The following tests took place at one of the sponsoring establishments power stations. The motors monitored were two 11 kV, 5 MW pumps of which one was suspected to contain a rotor based problem.

The individual pumps were physically housed within a separate pump house. However, it was possible for the monitoring to be successfully completed within the switch-gear rooms of the individual motors. Here access was available to the three phase supply conductors to the motors, thus indicating the overall portability of the current based monitoring system in not requiring actual physical contact to the motor under investigation. Machine data for the two motors investigated is given within Table [4.3.3.1.1].

All three phases of the supply were monitored simultaneously using both Rogowski Coils and Current Transformers with load burdens acting as current transducers. Using both a Racal Store 7 data recorder, and the sampling facility within the monitoring software, (it was imperative to record the transient first time due to the operational limitations imposed. These limitations resulted from a motor of such physical size taking a finite period of time to come to rest, thus allowing only a few starts to be undertaken in the allocated recording time), several transients from both motors under investigation were acquired and analysed using the monitoring package. The results of which are presented within the following case studies.

Machine Nameplate Data

Manufacturer	GEC
5MW	240 Rotor Bars
36 Pole	164 RPM
Full Load Current	124 A

Typical Transient Data

Initial Peak Current	1600 A (pk)
Transient Current	600 A (pk)
Duration	5 - 6 sec.

Table [4.3.3.1.1] Machine and Transient Data.

4.3.3.2 Case Study No. 1

For motor 1 the red phase was used for analysis purposes. The motor was still coupled to the pump, and hence, was not exactly under a no load condition. This, however, was out with our control in this investigation. Using the simplified version of the analysis technique, the transient was found to give results as shown in Figure [4.3.3.2.1]. On comparing this result with previous laboratory results, the initial peak was interpreted as being due to the transient switching process. After this initial peak no subsequent peaks occur within the waveform. From laboratory results this waveform implies that the motor contains a relatively healthy rotor.

In order to confirm the validity of these results, a steady state current analysis was completed upon the motor using the industrially accepted steady state monitoring technique, 'Motormonitor'. The results of this for the above motor yielded a broken bar factor of **0.14**. This would suggest a healthy rotor. The above tests were then repeated on the motor with the suspected rotor fault. The results of which are presented within Case Study No. 2.

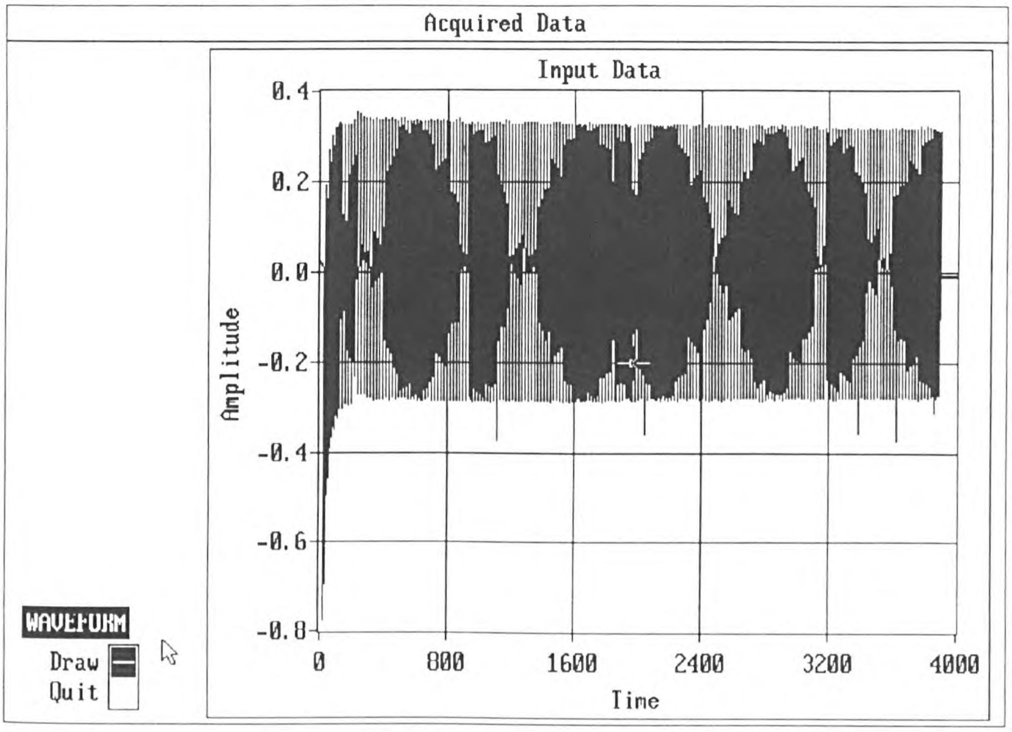

(a)

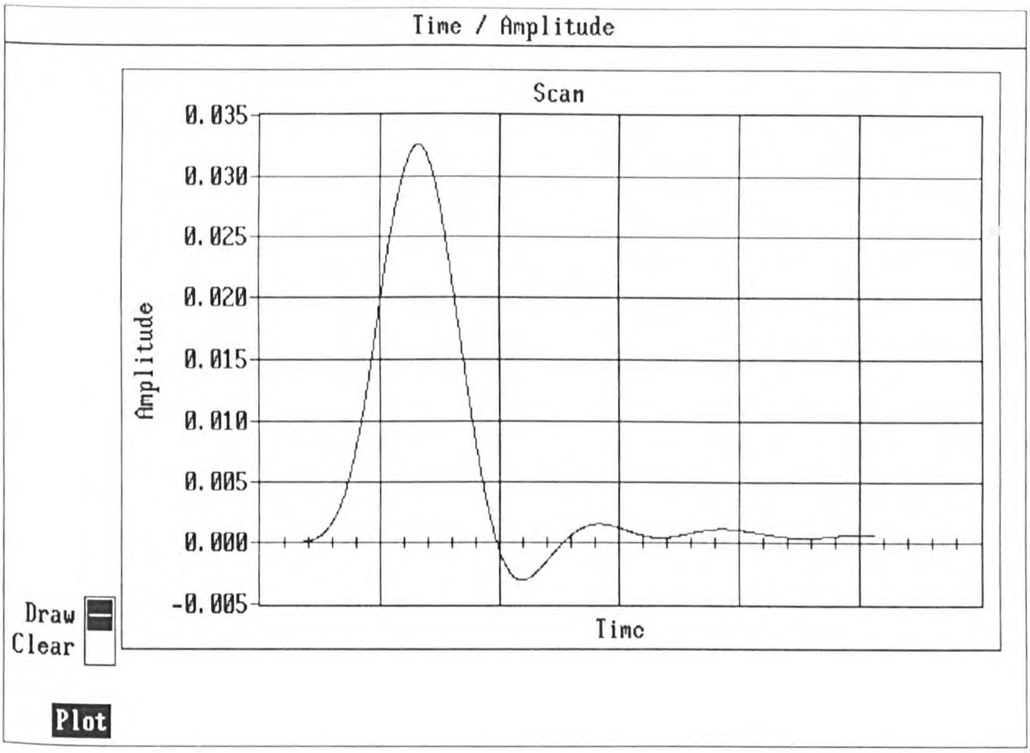

(b)

Figure [4.3.3.2.1] Red Phase Transient and Result of Analysis.

4.3.3.3 Case Study No. 2

As before, the red phase was used for the analysis. The simplified analysis technique was again run on the motor, the results of which are presented within Figure [4.3.3.3.1]. Comparing the analyses of the identical pump motors, Figure [4.3.3.2.1] and Figure [4.3.3.3.1], it can clearly be observed that two peaks, formed from the energy of the non-stationary sidebands, are present within the second analysis. This would suggest that motor 2 is suffering from a rotor circuit problem.

Verification of this technique using 'Motormonitor' resulted in the motor returning an increased broken bar factor of **1.1**.

4.3.3.4 Case Study Deduction

Comparing the two sets of results from the two identical motors suggests that the motor monitored within Case Study No. 2 does exhibit characteristics of broken rotor bars. The transient monitoring technique is still in development, hence, no absolute number of broken bars can be suggested at present, as the results purely indicate the presence of faults. Quantification of this indication being an area for future work.

The presence of faults within the motor of Case Study No. 2 was verified by running the steady state analysis package, 'Motormonitor'. Using this technique indicated the presence of a rotor bar fault in that the motor of Case Study No. 2 reported a far higher broken bar factor. This indication, which 'Motormonitor' uses to predict the severity of rotor faults, is approx. 700% higher than the motor within Case Study No. 1. It is interesting to note that the amplitude change of the transient system between the two case studies also results in an approx. 700% increase in the case of the faulted cage rotor.

These tests were carried out under semi-loaded conditions, as circumstances beyond our control prevented the tests to be run during precise no-load operation. This therefore denied any trials of the technique on no-load, one of the main attractions to the transient monitoring technique. Previous experience has shown that similar diagnoses may be obtained under loaded and non-loaded conditions, although the signal processing may be more complex in the latter due to the shorter transient.

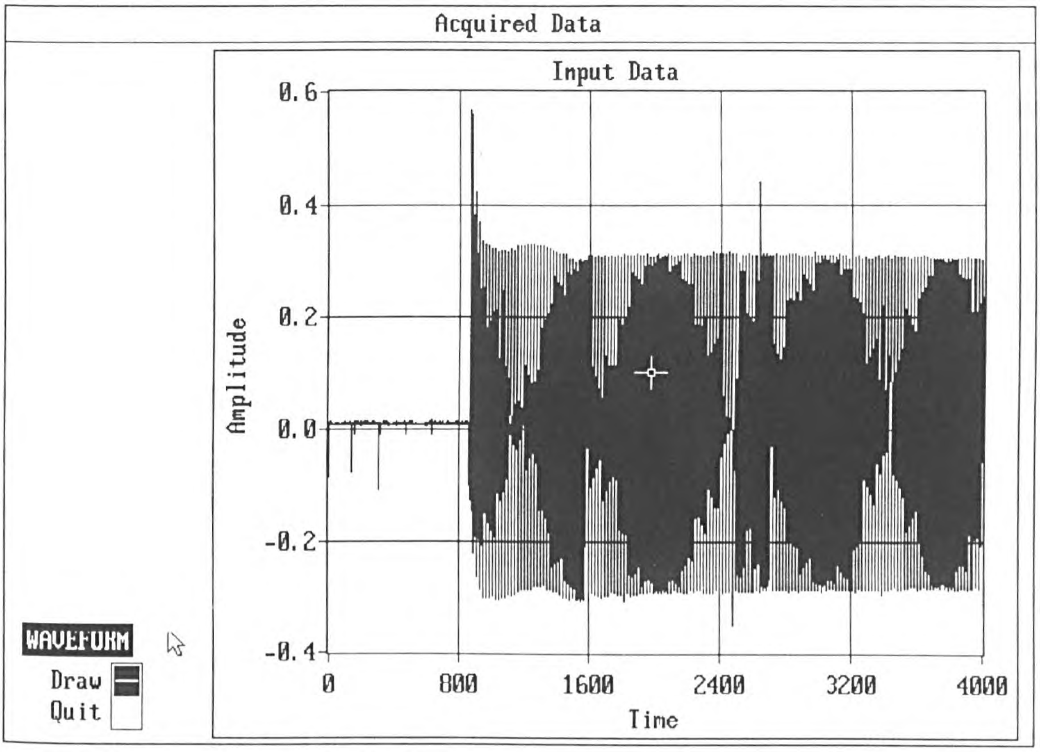

(a)

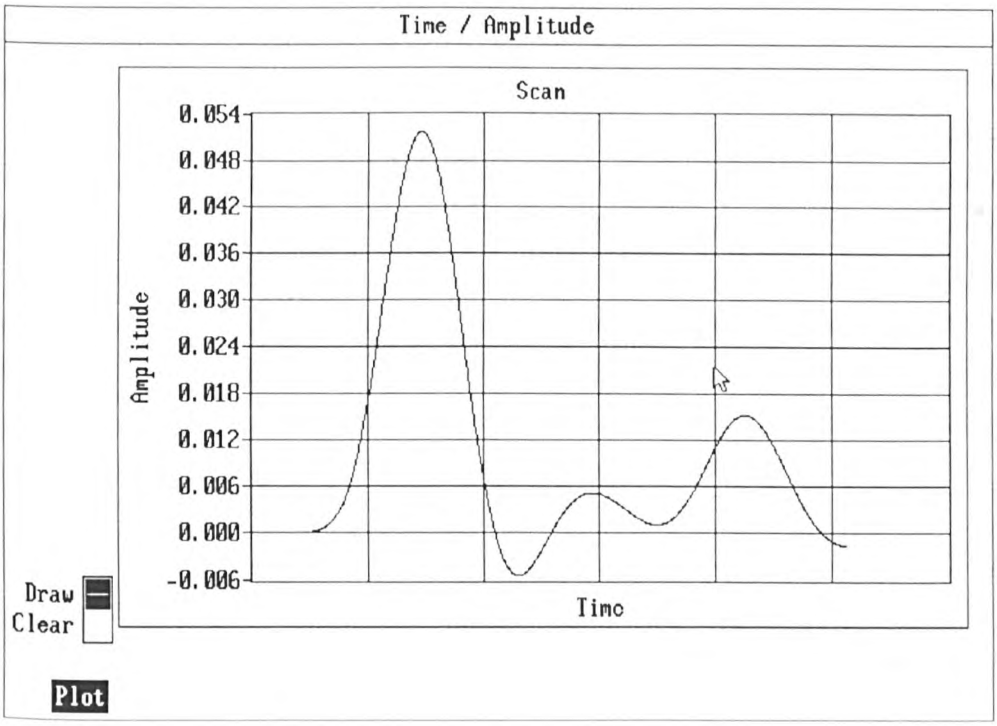

(b)

Figure [4.3.3.3.1] Red Phase Transient and Result of Analysis.

From these results and those of 'Motormonitor', the operators of the motor highlighted within Case Study No. 2 removed it from operation for a detailed physical investigation. The results of these investigations concluded that there were two rotor problems within the rotor cage. Figure [4.3.3.4.1] and Figure [4.3.3.4.2] show the faults detected from the physical investigation of the rotor within Case Study No. 2.

Figure [4.3.3.4.1] shows signs of the rotor bar brazing melting at the junctions between several rotor bars and the end-ring, see indicator. This melting was thought to have occurred due to excess heat during the brazing process.

Figure [4.3.3.4.2] however, shows a more series form of rotor fault. Again a brazing fault has caused tears to occur within joints between various bars and the end-ring, see indicator.

The above tests therefore successfully verified that it was possible to transfer the transient monitoring technique from the laboratory environment into the industrial. However, in order to further verify this technique, more industrial tests are obviously required in order to further develop the technique as a viable monitoring system.

Finally, an interesting problem occurred within the monitoring software acquisition section. The digital signals required to control the acquisition circuitry are obtained from a clock circuit which is ultimately powered from the mains supply, Section (4.1.3). Unfortunately, when a motor of this size, 5 MW, is started the mains borne electromagnetic disturbance is substantial, hence, the generated pulses are corrupted for a finite period of time. This period is long enough for the acquisition software to detect an error within the sampling pulse and terminate the entire acquisition section. In order to solve this problem, it is envisaged that two methods may be employed in the future. The first of these methods which may reduce the noise problem would be to design a filter system which would smooth out the disturbance within the digital signal. Secondly, as the disturbance is transmitted within the mains signal, it may be possible to power the clock circuitry from a power source which is not dependant upon the mains supply. One such source being that of a DC battery system.

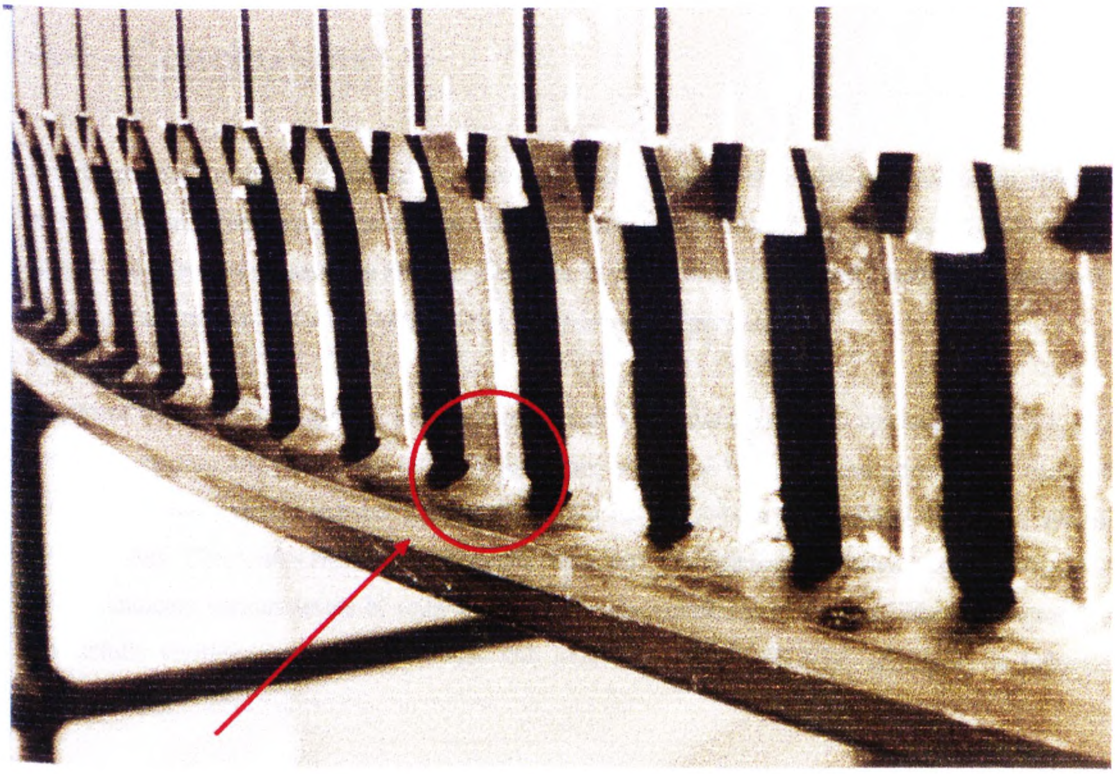

Figure [4.3.3.4.1] Rotor Brazing Melting - Case Study No. 2.

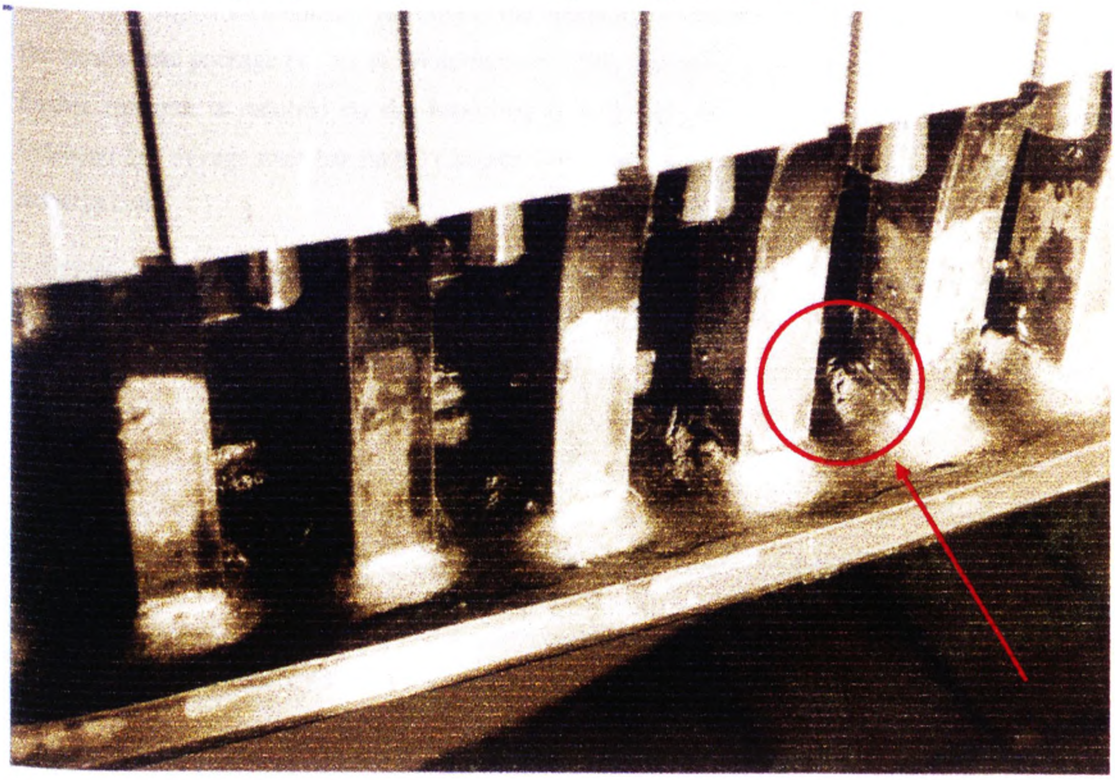

Figure [4.3.3.4.2] Rotor Brazing Tears - Case Study No. 2.

4.4 Conclusions

A new portable machine condition monitoring system which enables the operator of an induction motor to acquire the supply line current transient, process and analyse the data and finally store the results has been developed. The chapter discusses in detail the integral parts behind the monitoring system including the hardware, software and necessary transducer aspects.

Results of the monitoring system, which makes use of a Toshiba DX6400 in conjunction with a menu driven acquisition and processing program developed using LabWindows, are presented to verify the ability of the technique to indicate squirrel cage rotor bar faults both within laboratory and industrial environments. The results show that within the laboratory the monitoring system may be successfully used to indicate various levels of rotor fault. The work carried out within an industry environment successfully verifies that such a technique can indeed be transferred from laboratory to industrial applications.

Future developments of this monitoring system should incorporate a method whereby a set limit of fault would trigger an automatic warning to the operator, in a similar manner to that available within the steady state package known as 'Motormonitor' [90]. Before work on this can be started, however, further research is required on the reasoning behind such amplitude changes within the Lower Sideband due to cage rotor bar faults. Chapter 5 discusses work carried out within one aspect of this research area.

Chapter 5

Analysis of Transient Fault Component Amplitudes

5.0 Introduction

From the full transient analysis obtained from a three phase induction motor with a typical rotor bar fault, Figure [3.7.1.3], it was observed that the fault component, as it varies in frequency does not remain at a constant amplitude. As may be seen in Figure [3.7.1.3] and other examples of the full transient analysis, the amplitude of the fault component, in particular the Lower Sideband, comes to a very evident peak within the latter half of the frequency variation.

It was felt necessary to investigate the cause of this peak within the sideband energy, since this may have significance in establishing an accurate monitoring strategy. The cause is not, however, immediately obvious. The analysis of the induction motor during a starting transient is complex and it is necessary to revert to a numerical analysis of the motor in question. As a means to investigate the reasoning the induction motor simulation program, developed by Elder [35][38], was employed. This simulation allows various parameters within a motor to be varied independently, in order to observe the effects that the individual parameters have on the overall motor simulation.

5.1 Review of Simulation Technique Employed

The simulation technique employed in the following investigations was developed from that of Elder [89]. In the simulation the three phase differential equations defining motor operation are transformed from a rotating reference frame into a two phase stationary system. This transformation converts the rotating three phase current quantities of the motor into stationary two phase orthogonal currents for both the stator / rotor, and allows the operator to calculate the derivative equations by means of numerical calculation. Several methods of numerical integration were used by Elder, with the Runge Kutta technique being found to be the most suitable.

Using the two phase model, Elder found that it was possible to successfully simulate the presence of rotor imbalances within the three phase machine by replacing the rotor resistance with three individual phase resistances.

Elder found that reasonable results were obtained using this model when non-linearities such as: mutual inductance saturation, leakage inductance saturation and skin effect were included. The model, however, was found to have limiting constraints in that it was not possible to simulate a motor fed from a harmonic filled supply, and that during any one simulation either the stator or rotor had to remain balanced at all times. Elder notes that the stationary two phase model became unstable when used with reference frames other than that of the stator, although Elder suspected that the method of integration used within these reference frames was incorrect.

In order to improve the resolution and overall accuracy, Elder developed a three phase simulation. Variables related to parameters within the real motor were not required to undergo any form of transformation when applied to the model, thus reducing the risk of data corruption during the transformation process. Saturation could be applied within individual circuits, and winding imbalances were placed within the stator / rotor circuits along with the implementation of any supply voltage harmonics.

Elder reasoned that the three phase model developed could be an initial step on the expansion of the model to physically represent individual rotor bars, although for a true representation of 51 rotor bars, as Elder points out, the matrix geometry would require far greater computing power than that currently available.

Although the theory behind the simulation technique used within the following investigations is well reported within Elder [89], it is necessary for completeness at this moment that a recap of the relevant theories is given, the background theory relevant to the derivation of the three phase simulation model being presented in Appendix VI.

Elder [89] uses the above three phase model in conjunction with real motor parameters obtained from a laboratory wire-wound rotor machine. Initial investigations follow closely to the results obtained from the two phase model, and bare a close resemblance to the real machine once leakage saturation, implemented on a per phase basis, was taken into consideration. Elder states that, as with the two phase model, an unavoidable experimental error in obtaining vital motor parameters, such as leakage inductance, was thought to account for the majority of discrepancies between the real and simulated data.

Upon steady state operation the model's response was found to be similar to that of the real machine, in that the frequency of sidebands at particular steady state rotor speeds gave exact correlation between simulated and real data. However, differences between the absolute magnitudes of the sidebands were noted and were thought to be due to an over simplification within the three phase model, or an omission of some interaction occurring within the real machine.

The simulation under transient conditions was found to closely follow that of the real motor, although again there were discrepancies found between the actual amplitudes of the Lower Sideband within the simulation and that of the real motor. The Lower Sideband has, however, better correlation between the real and simulated conditions within the transient condition, and both were found to have a similar characteristic shape.

The three phase models simulation of the Upper Sideband or USB, under various levels of rotor imbalance was next investigated. The simulated USB results correlate closely to that of the real data obtained from the laboratory test-rig, and that the enhancement of the upper sideband, on the mathematical implementation of leakage saturation, agreed with the predicted responses already obtained from steady state theory.

The enhancement of the USB during the steady state period was less, however, than that observed during the simulated starting transient. This, it is thought, is due to the large levels of current which flow during the transient condition, thus effecting the magnitudes of the harmonics produced by the leakage inductance characteristics.

One of the main advantages to this simulation technique over that of the two phase model, was the ability to vary the individual supply voltages within the simulation. This allows the simulation of supply voltages with harmonics and would thus allow the simulation of an induction motor fed from an inverter source. On the simulation of a supply heavily containing third harmonics, however, Elder reports that little change was found within the model's response.

On varying the switching angle of the supply voltage to the simulation results in little variation within the simulated parameters, in addition, on varying the starting position of the rotor within the simulation, the results were completely independent. Elder does state, however, that this was in contradiction to experimental observations, in that there was a suggestion that the initial starting position of the rotor did have an influence on the timing at which the LSB reaches the maximum within the transient analysis.

Elder [89] finally reports on how this three phase simulation was altered in order to simulate the effects of a three phase cage Squirrel Cage motor. Assuming a single bar per phase, the model simulates the presence of the rotor bars by first partitioning the end-rings into as many sections as there were rotor bars. The resistance of the two end-ring sections, for a particular bar, being transformed and appended to the resistances for the bar. The transformation is required to take into account the differences between bar current and the end-ring current. On completion of this the whole rotor is suitably represented by rotor bars which now contain a portion of the end-ring resistance. The rotor resistance within the model is further transformed to take into account parameters such as stator winding factor, total number of bars and the number of series turns per phase. Elder states, however, that the three phase model shows good agreement for general trends and spectral content generated by imbalances.

However, reservations were reported by Elder on the methods whereby the model represented broken bars within the cage rotor circuit. Due to these reservations on the cage motor simulations authenticity, and that it had been previously shown that the sideband peaks were also found to occur within the wire wound simulation, it was this model which would be used within the following investigations.

5.2 Investigation into Sideband Amplitudes

5.2.1 Review of Transient Monitoring

Figure [3.7.1.2] displays the result of monitoring the supply current transient obtained from a no-load start of the laboratory test-rig with zero broken cage rotor bars.

To interpret this plot it is necessary to imagine each line as the output from a series of filters, each assigned to filter a specific frequency between the values of 0 and 50 Hz. The output from the 50 Hz filter being situated towards the rear of the plot within Figure [3.7.1.2], and similarly the output from the 0 Hz filter being situated at the front. Comparing this plot with that shown in Figure [3.7.1.3], obtained from analysing the same test-rig on no-load with ten broken cage rotor bars present, it may be clearly seen that there is a difference in amplitude between the two plots. In Figure [3.7.1.3], the non-stationary ±2sf fault component of the Lower Sideband, discussed previously, may be seen as time increases, to travel from 50 to 0 Hz as the speed of the motor nears that of half speed, followed by the same components returning to 50 Hz as the speed of the motor nears that of steady state speed. The increased amplitude of these components, in particular the components returning from 0 to 50 Hz, indicating the presence and severity of broken bars within the machine. Figure [5.2.1.1] displays the result of a similar analysis on data obtained via the three phase simulation model.

From this analysis it may be seen that there is a close similarity between the plots within Figure [3.7.1.3] and Figure [5.2.1.1], thus providing evidence on the close correlation between the real and simulated currents.

5.2.2 Sideband Amplitude Phenomenon

On comparing the results of both the simulated and real data analyses it was observed that the amplitudes of the non-stationary sidebands were non-constant, in that they come to an evident peak when the components return from 0 to 50 Hz. This noticeable peak occurs around the midway point within the transient when the motor is between half and full speed. Elder had previously found that this peak, for the laboratory based test-rig, occurred at the frequency of 21 Hz. Fault severity within a rotor thus being determined from the amplitude of the sidebands of a filter centred at this frequency alone.

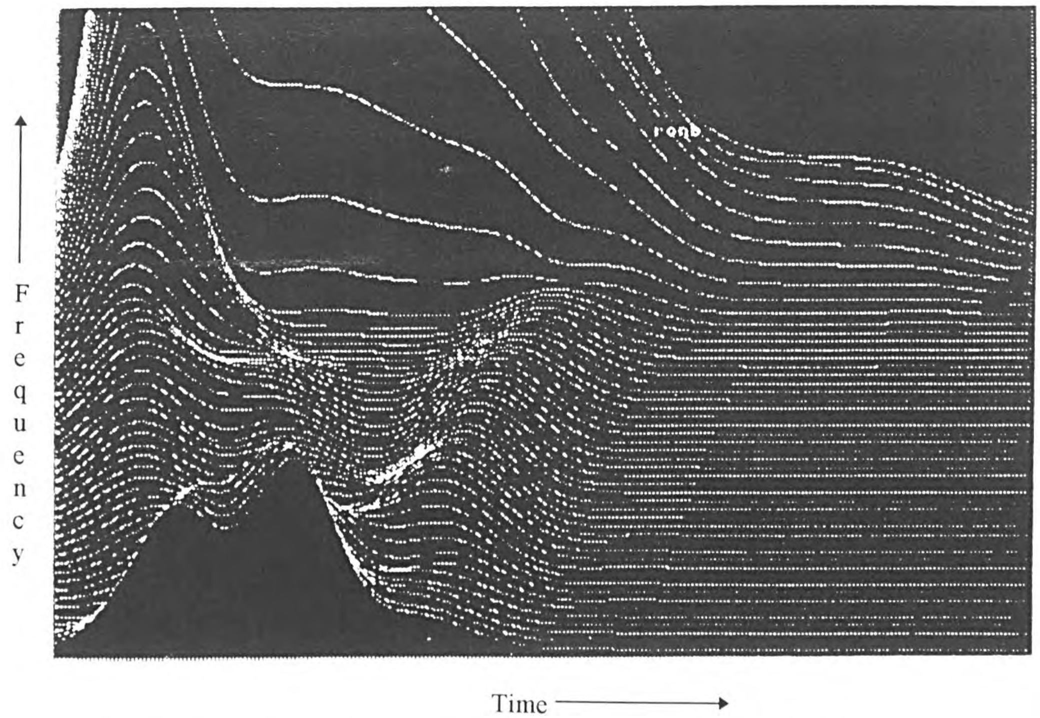

Figure [5.2.1.1] Transient Analysis of Simulated Current with Rotor Imbalance, ΔF = 1 Hz.

From the transient analysis shown in Figure [3.7.1.3], obtained from the test-rig under a ten broken cage rotor bar fault condition, the magnitude of the $(1\text{-}2s)f_s$ component is found to be non-linear. The sideband locus of the $(1\text{-}2s)f_s$ frequency component within the transient at various frequency values, Figure [5.2.2.1], provides a good example of the locus which occurs within all transient analyses be they obtained from severely faulted, minimally faulted, no load or full load analyses. From the locus it may be observed that the energy of the sideband is found to peak over the region between 0 and 50 Hz after passing through half speed, s = 0.5, when returning towards steady state frequencies, s = 0.01.

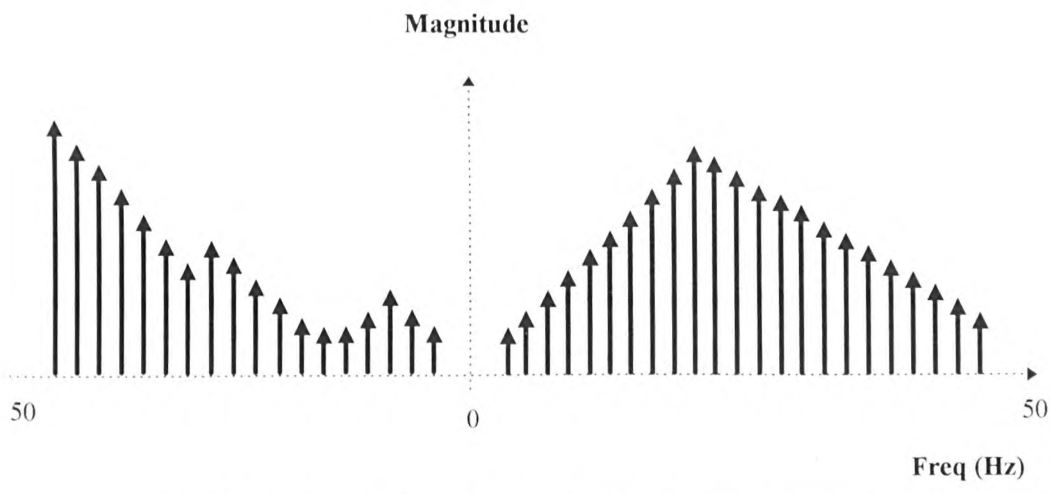

Figure [5.2.2.1] Sideband Locus of (1-2s)f_s Broken Bar Component.

Investigations were then initiated into obtaining a reasoning behind such peaks within the sideband amplitude. It was felt that the phenomenon would be due to a complex interaction between some or all of the motor parameters during the transient period. Examples of the parameters being investigated included the decreasing line current in conjunction with the simultaneously increasing torque / speed. Investigations were carried out making use of the previously mentioned three phase simulation model, as a means to isolate any parameters within the motor which may behave in such a mannerism.

5.2.3 Investigation of Machine Parameters via Simulation

The three phase simulation was used to determine the cause of the sideband peaks. Using this simulation it was possible to vary the individual parameters of the motor in order to observe if this caused any variation within the amplitude of the sidebands after execution of the transient analysis technique upon the simulated currents.

Initially the rotor electrical angle of the simulation was varied from 0° to 180°, in steps of 45°. A 60% rotor imbalance was introduced in one of the simulated rotor windings, and the transient analysis was re-run on the simulated current signals with no significant changes to the amplitudes of the sidebands being observed.

The individual parameters of the induction motor were varied in order to see if variations of the motor parameters would alter the amplitude of the fault sidebands. The parameters of the machine which could be varied via the three phase simulation program were: the stator / stator mutual inductance, the rotor / rotor mutual inductance, the stator self inductance, the rotor self inductance and the stator / rotor mutual inductance. Some of these values were found to be extremely sensitive, and resulted in a corrupted simulation if varied out with very tight limits. However, all values were varied, a little, and the transient analysis re-run upon the simulated no-load current outputs. The results of which show that the varying of motor parameters within the simulation had very little effect upon the amplitudes of the fault sidebands.

The main result of motor parameter variation was found to be a difference within the timing at which the fault sidebands passed through the filters, and the length of time that which the sidebands took to pass through the filters. Full load simulations were also carried out with similar results being observed.

5.2.4 Investigation of Transient Current via Simulation

The three phase wound rotor machine simulation was further investigated in order to see if it were possible to obtain the conditions which produce the sideband peaks from within the simulation itself. These investigations took the form of breaking down the simulation code and observing certain variables from within the code itself, during parameter variation, and re-running the transient analysis technique upon these variables in a quest to obtain some form of correlation for the reasoning behind the amplitude peaks.

From investigations on the simulation code, it was found that the simulated currents were formed from the sum of six differently calculated values. These six sub-currents were each individually analysed using the transient analysis to find that three of the sub-currents, once analysed, contained moving frequency components similar to those within the analysis of the main current component. Again the parameters of the induction machine were varied whilst running the transient analysis on the sub-currents, with similar results to the previous variations, in that no sizeable changes in sideband amplitudes were observed.

One of the above sub-currents was further broken down to find that this component was formed, in the case of the simulator code, by the multiplication of two further components. One of these components being derived from the inverted impedance matrix, used in the calculation of the differential equations employed to simulate the effects of the induction motor, and the other being calculated from the supply voltage fed to the stator. A transient analysis on each of these components individually shows that the travelling fault sideband, from 50 to 0 Hz and back to 50 Hz, is produced from one component travelling from 0 to 50 Hz and another separate component travelling from 50 to 0 Hz over the complete transient period.

On searching where these two components came from within the simulator code it was found that, as previously mentioned, one came from the calculation of the supply voltage and the other from the impedance matrix. It was also found that this latter component could be further traced back, within the code, to the changing rotor electrical angle of the simulated machine. The rotor angle changing due to the increase in speed during the motors initial acceleration period.

The diagrams within Figures [5.2.4.1] through to Figure [5.2.4.5] summarise the investigations using the three phase simulation model. These investigations led only to an explanation on how the simulator obtained the changing frequency component. It did not in any way give an indication as to the reasoning behind such peaks within the amplitude of the Lower Sideband.

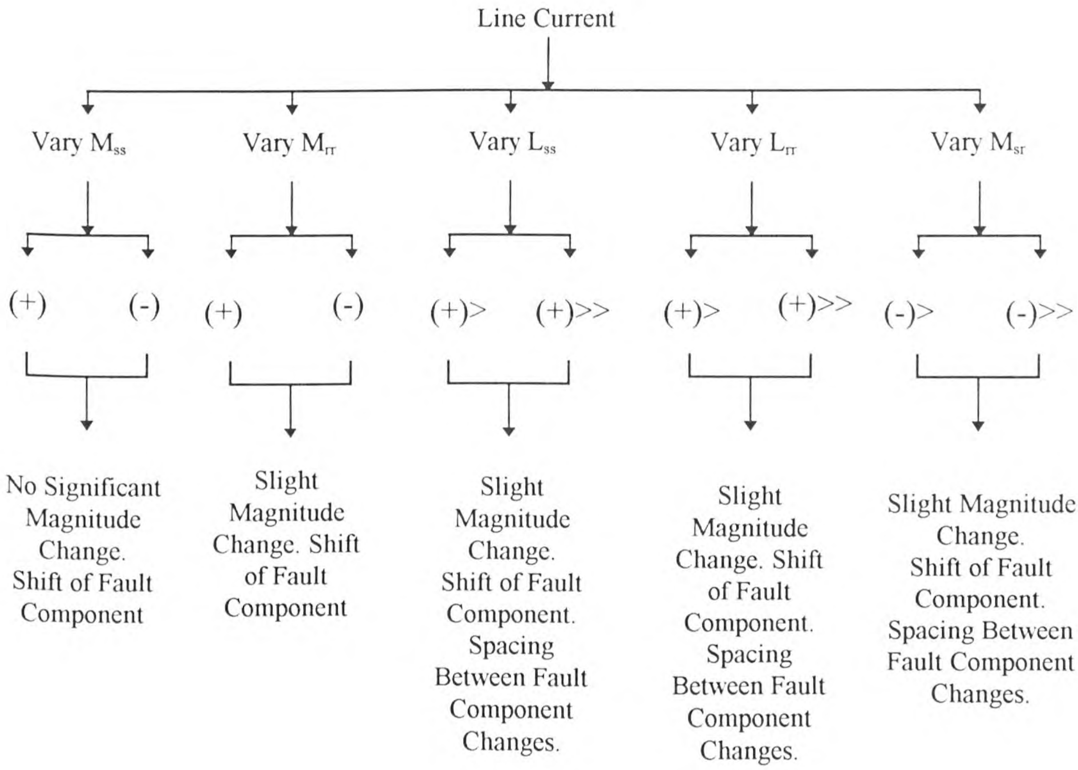

Figure [5.2.4.1] Results of Variation of Motor Parameters.

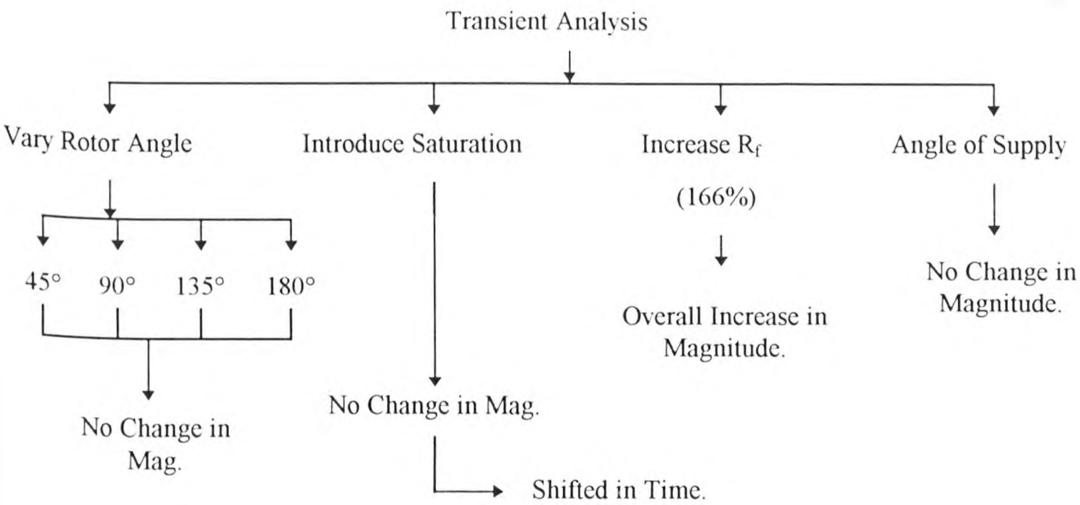

Figure [5.2.4.2] Effects on Transient Analysis of Simulated Currents.

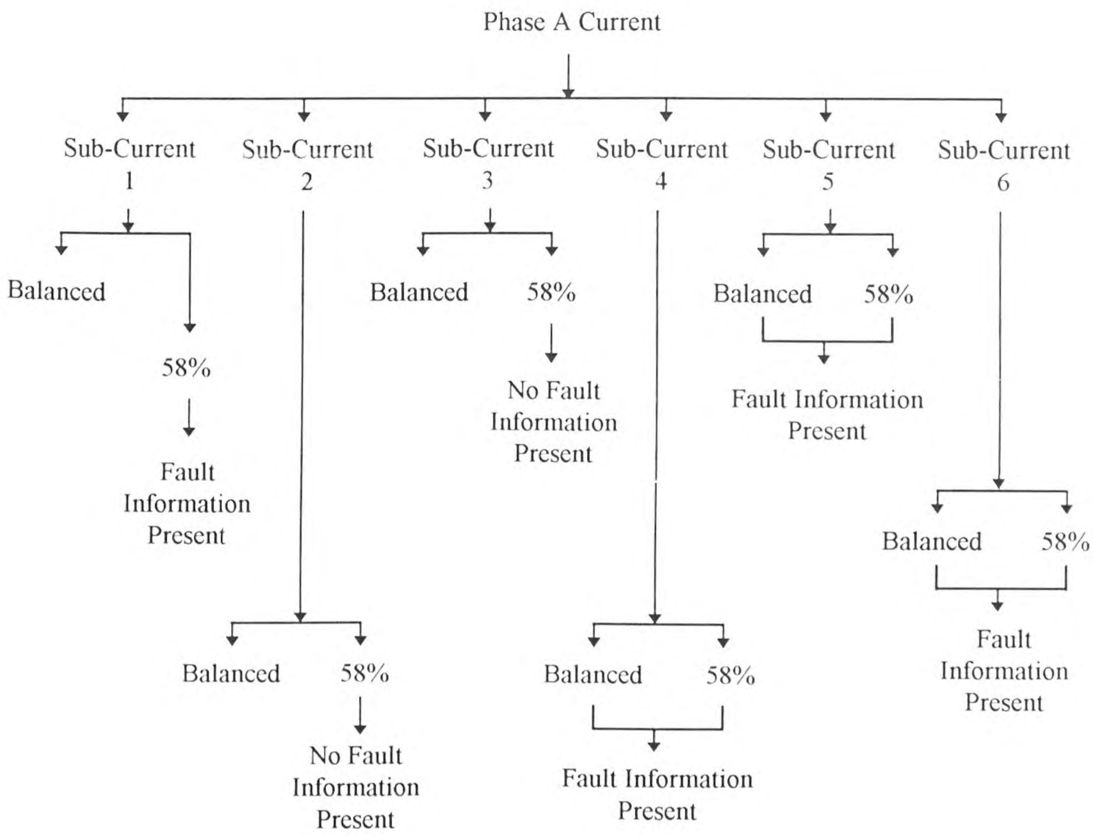

Figure [5.2.4.3] Formation of and Effects on Simulated Current.

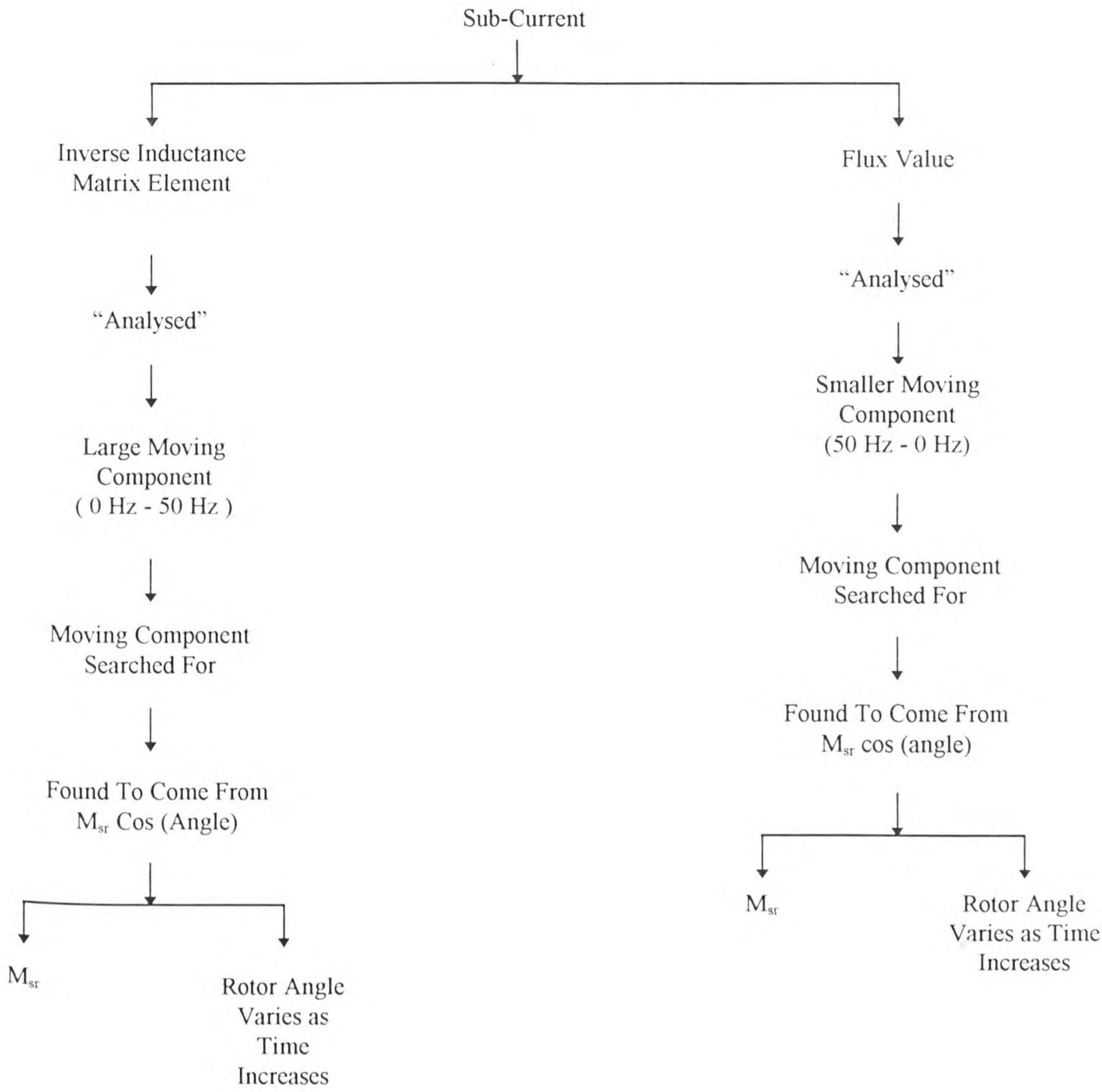

Figure [5.2.4.4] Formation of Sub Current Component.

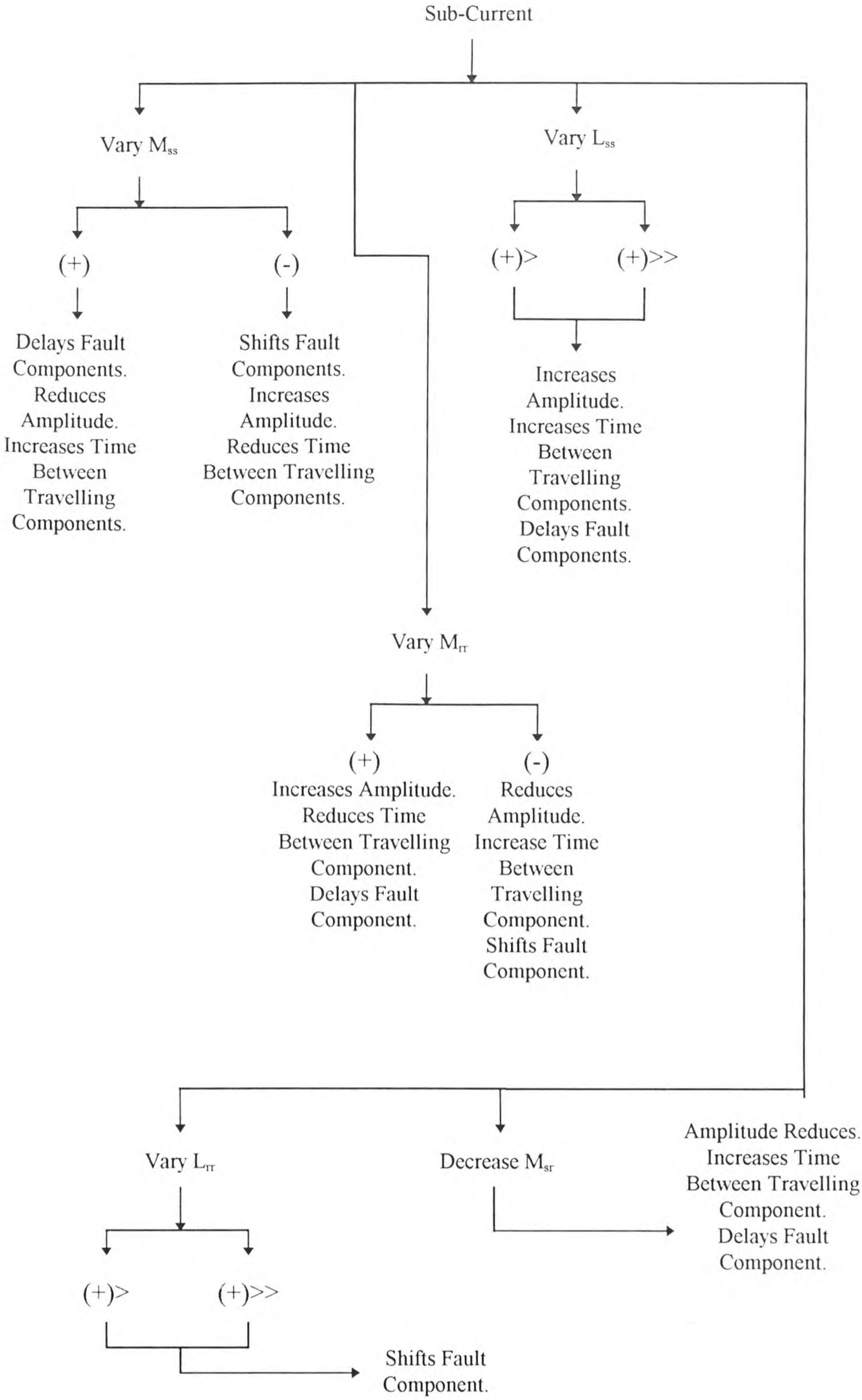

Figure [5.2.4.5] Parameter Variation of Sub-Current Component.

5.2.5 Location of Peak Amplitude

The location of the peak amplitude within the transient analysis with respect to other motor parameters was next investigated, again making full use of the three phase motor simulation. Figure [5.2.5.1] shows the occurrence of the peak sideband amplitude for several imbalance conditions over three different load torques. The results clearly show, as expected, that when the load torque of the simulated motor is increased, the time at which the peak value of the sideband occurs at increases. It can also be observed that, regardless of the load torque simulated, as the percentage of imbalance within the rotor increases, the time at which the peak of the sideband occurs reduces.

Figures [5.2.5.2] through to Figure [5.2.5.4] report the speeds at which the rotor achieves before the sideband peak value occurs. Again, three load torques are analysed for different percentages of rotor imbalance. It should be noted that the value of steady state speed which is attained for the respective load torque and level of imbalance has also been indicated. From these results it is observed that the level of speed at which the peak sideband amplitude occurs reduces as the level of load torque is increased. Over the total range of imbalances the value of speed remains fairly constant. It may be observed from the results that there is some correlation between the values which the sideband peaks and the steady state speed, for example, within Figure [5.2.5.4], as the steady state speed dips at the imbalance values of 30 and 40%, the value of rotor speed at which the sideband peaks also dips.

Figure [5.2.5.5] through to Figure [5.2.5.7] show the level of steady state rotor angle together with rotor angle at the point in time which the sideband peak occurs, again, for several load torques and rotor imbalances. From the results it may be observed that as the steady state value increases over several rotor imbalances, the level of rotor angle at which the peak amplitude occurs at within the sideband remains level. This being repeated over the entire range of load torques.

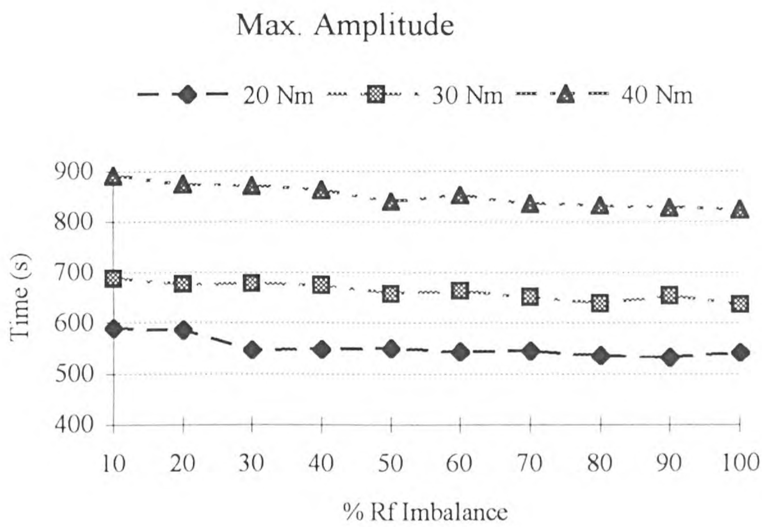

Figure [5.2.5.1] Timing of 'peak' Occurrences v.'s Rotor Imbalance.

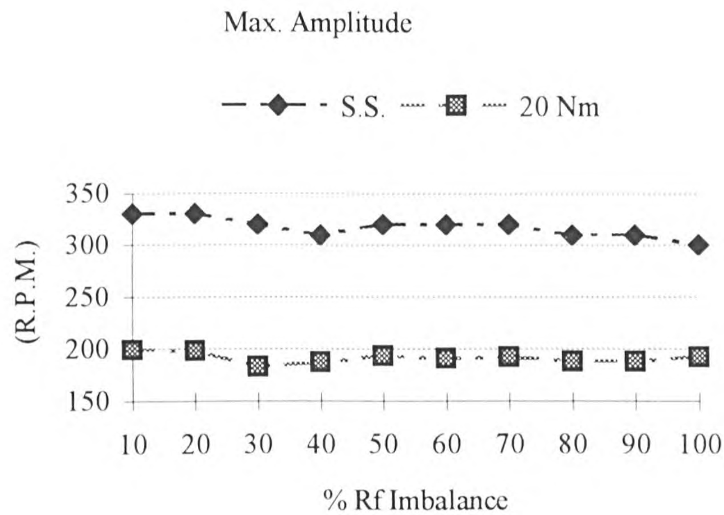

Figure [5.2.5.2] Rotor Speed, 20 Nm.

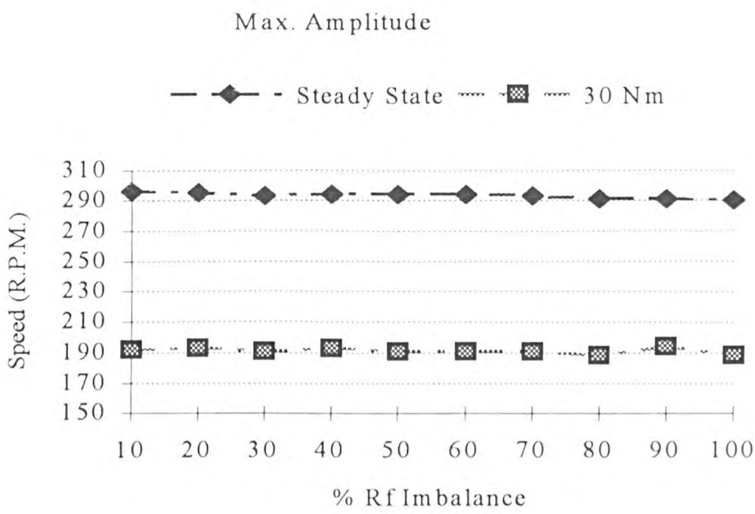

Figure [5.2.5.3] Rotor Speed, 30 Nm.

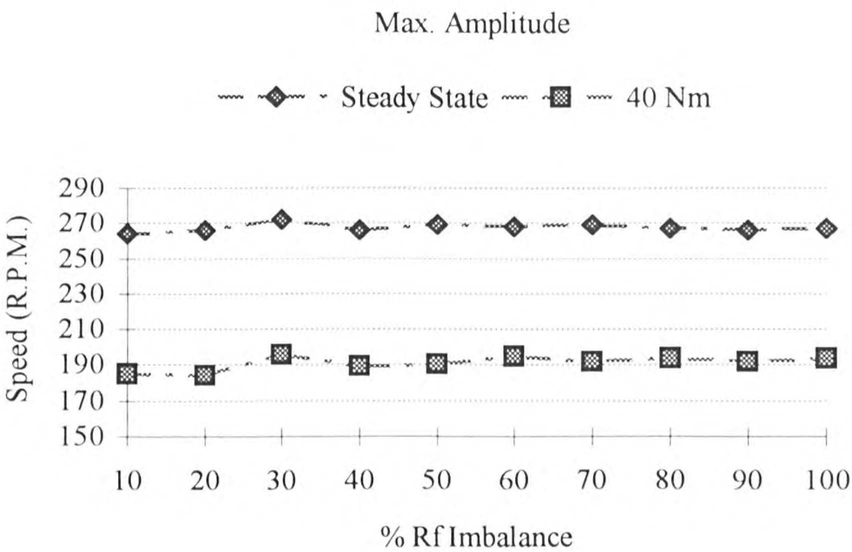

Figure [5.2.5.4] Rotor Speed, 40 Nm.

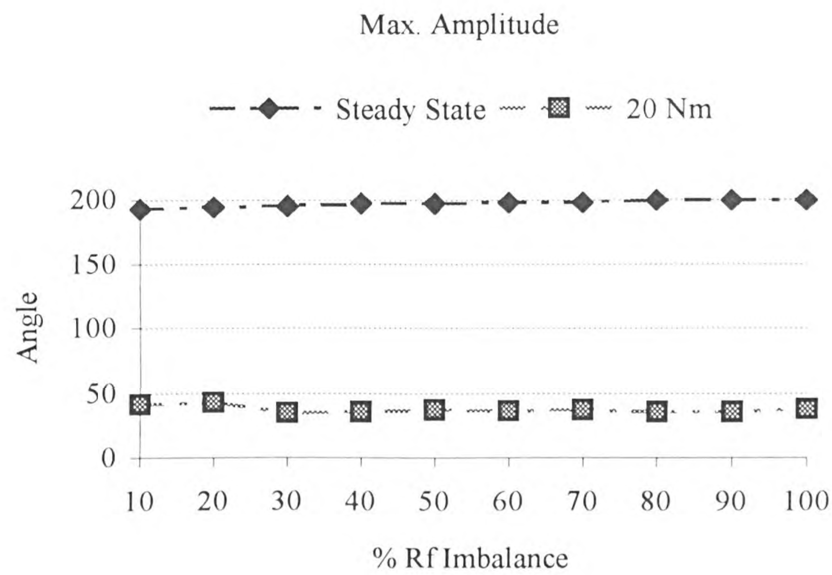

Figure [5.2.5.5] Rotor Electrical Angle, 20 Nm.

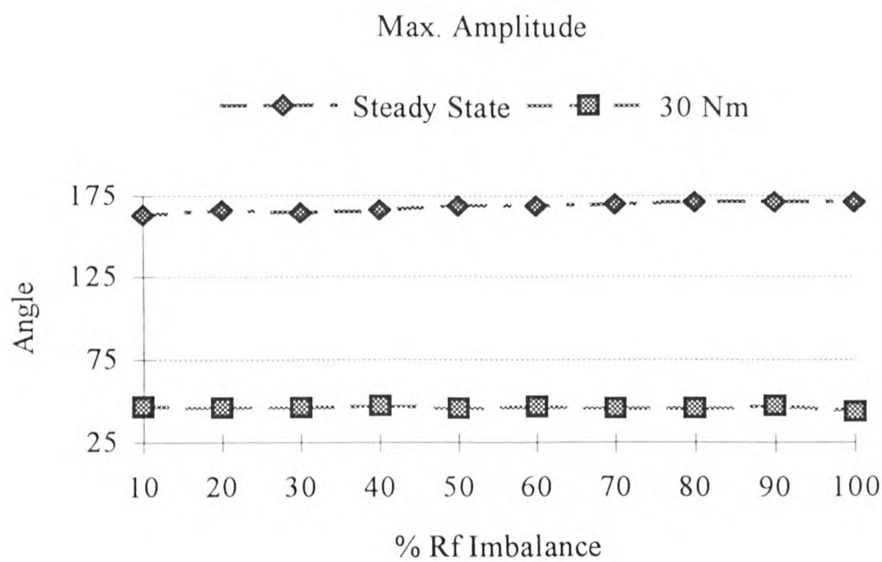

Figure [5.2.5.6] Rotor Electrical Angle, 30 Nm.

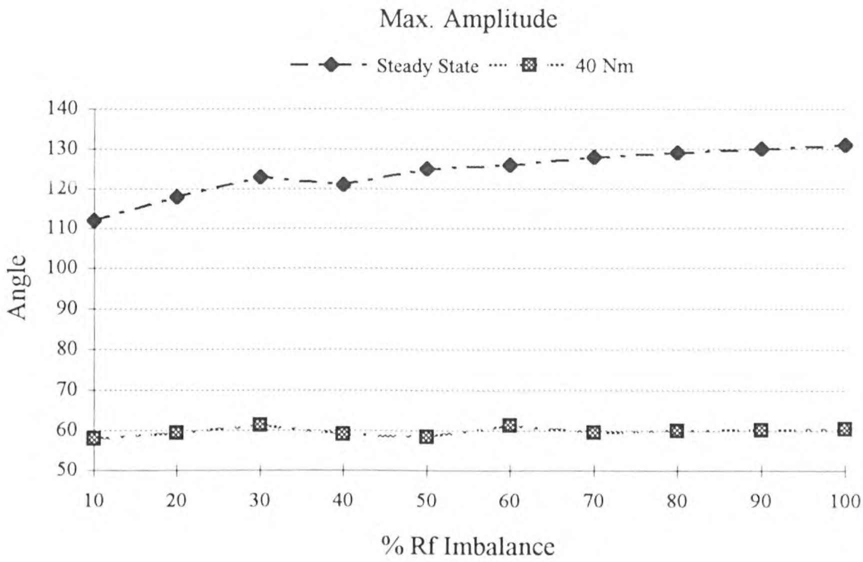

Figure [5.2.5.7] Rotor Electrical Angle, 40 Nm.

Figure [5.2.5.8] and Figure [5.2.5.9] report the percentage rotor angle and speed at which the lower sideband peak occurs at. These tests have been carried out over the load torque range of 20 to 40 Nm and cover a rotor resistance imbalance of 10 to 100%.

Tables [5.2.5.1] to Table [5.2.5.3] report the nature of the motor torque when the lower sideband peaks. It should be noted that the majority of peaks do occur when the torque is at a maximum, although several results do indicate that this is not the complete story.

Further investigations using the simulation program involved taking note on whether component values within the simulation code were at a peak value when the peak of the sideband occurred. A summary of these investigations is listed within Table [5.2.5.4] to Table [5.2.5.5], along with a similar investigation into when maximum power output was obtained within the simulation, Table [5.2.5.6].

From the results it may be observed that at low values of load torque, the majority of rotor imbalances have sideband peak values occurring whilst torque is at a maximum. However, as the load torque value increases, it is only the lower percentages of rotor imbalances which give peak values at a torque maximum.

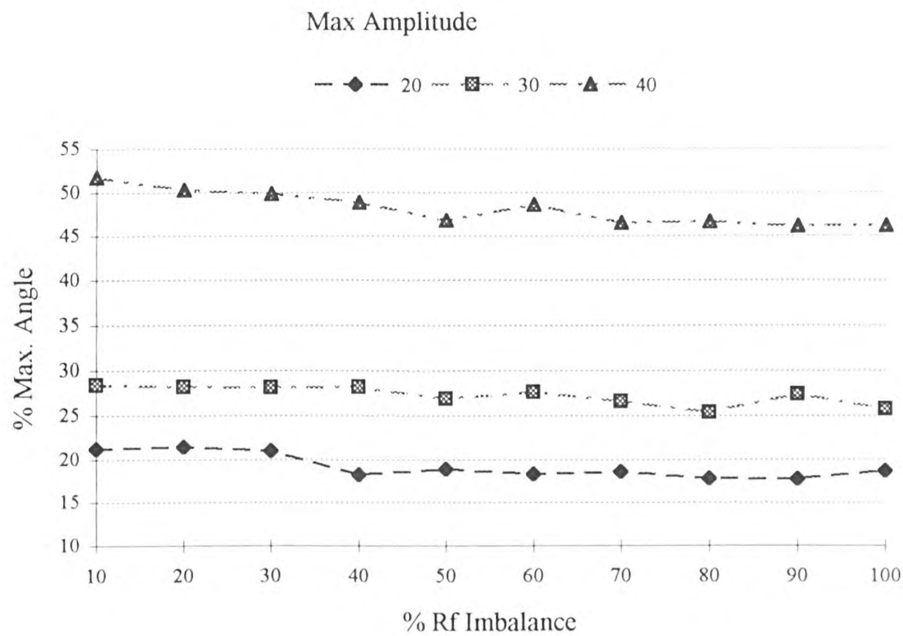

Figure [5.2.5.8] % Rotor Angle at which Peak Occurs.

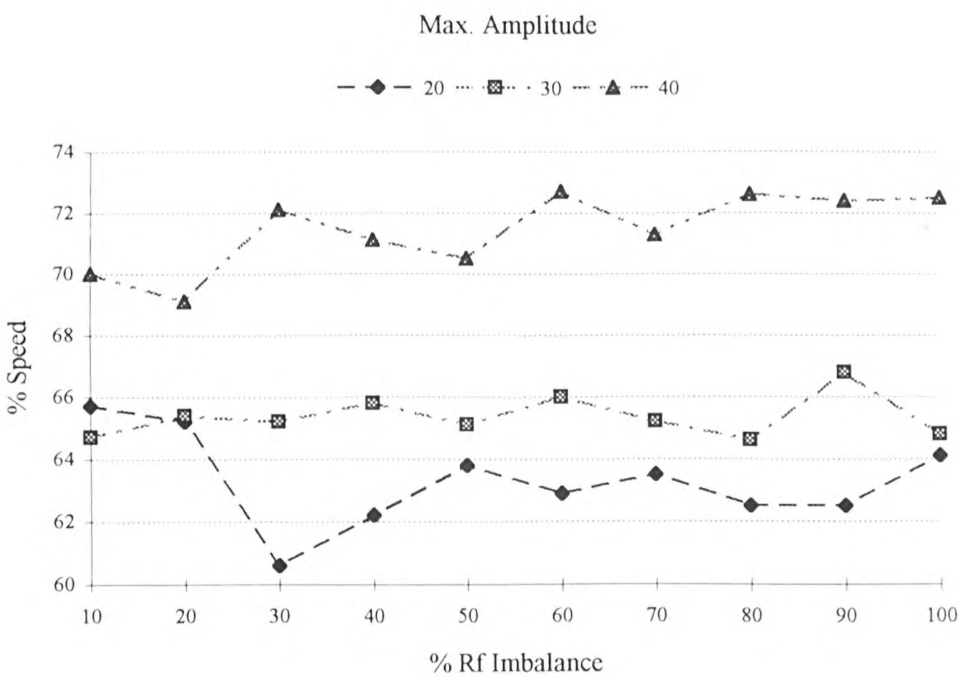

Figure [5.2.5.9] % Rotor Speed at which Peak Occurs.

For higher values of rotor imbalance the peak of the sideband amplitude occurs at an earlier point in time. The peak can be seen to occur approximately 8% faster with a 100% rotor imbalance than that with a 10% imbalance, over all torques. This reduction within the time at which the peak occurs is, however, non-linear over the remaining imbalances. It may be seen that as the load torque is increased the change within time does have an increasing linearity.

The speed at which the peak occurs remains fairly constant throughout the range of rotor imbalances even though the value of steady state speed is reducing. At high values of load torque it is noticed that as the steady state value of speed is dropping, as rotor imbalance is increasing, the speed at which the peak in the sideband occurs at is increasing.

As the speed remains fairly constant but the time at which the peak occurs is reducing, then the overall effect of adding an imbalance into the rotor must be to increase the torque achieved by the rotor.

The rotor angle at which the peak value of the sideband occurs at remains constant throughout the entire range of rotor imbalances and load torques.

From these results it is not possible to state that the maximum of the sideband amplitude, within the transient analysis of the starting current, occurs due to any one specific parameter. The above findings may only be used as clues to further investigations which may take place in the future.

Load (Nm)	Imbalance (%)	Torque at Max. when Peak Occurs
20	10	YES
20	20	YES
20	30	YES
20	40	YES
20	50	YES
20	60	YES
20	70	YES
20	80	YES
20	90	NO
20	100	YES

Table [5.2.5.1] Peak occurs at Max. Torque.

Load (Nm)	Imbalance (%)	Torque at Max. when Peak Occurs
30	10	YES
30	20	YES
30	30	YES
30	40	YES
30	50	YES
30	60	YES
30	70	NO
30	80	YES
30	90	NO
30	100	NO

Table [5.2.5.2] Peak occurs at Max. Torque.

Load (Nm)	Imbalance (%)	Torque at Max. when Peak Occurs
40	10	YES
40	20	YES
40	30	YES
40	40	YES
40	50	YES
40	60	NO
40	70	NO
40	80	NO
40	90	NO
40	100	NO

Table [5.2.5.3] Peak occurs at Max. Torque.

Load (Nm)	Imbal (%)	I_A	I_B	I_C	I_D	I_E	I_F	F_A	F_B	F_C
40	100	*Zero*	*Zero*	***Max***	*No*	*Zero*	***Max***	***Max***	***Max***	***Max***
40	90	*Zero*	***Min***	*Zero*	*Zero*	***Min***	*No*	*No*	*Zero*	*Zero*
40	80	***Max***	*Zero*	***Min***	***Max***	*Zero*	***Min***	*Zero*	***Min***	***Min***
40	70	*No*	***Max***	*Zero*	*No*	***Max***	*Zero*	***Min***	*No*	*Zero*
40	60	*No*	*Zero*	***Min***	*No*	*No*	*Zero*	*Zero*	*Zero*	*No*
30	100	*Zero*	***Max***	*Zero*	*No*	***Min***	*Zero*	***Min***	*Zero*	*No*
30	90	*Zero*	*No*	***Min***	*Zero*	*No*	*No*	***Min***	*Zero*	***Min***
30	80	***Min***	*Zero*	*Zero*	***Max***	*No*	*No*	*Zero*	*Zero*	***Min***
30	70	***Max***	*Zero*	*No*	*No*	***Max***	*Zero*	*Zero*	***Min***	*No*
30	60	*Zero*	*Zero*	***Max***	*Zero*	*No*	*No*	***Max***	***Max***	***Max***
20	100	*Zero*	*No*	***Max***	*No*	*No*	*No*	***Max***	*Zero*	***Max***
20	90	*Zero*	*No*	***Min***	***Max***	*Zero*	***Min***	***Min***	***Min***	***Min***
20	80	*No*	***Max***	*No*	*No*	*No*	*No*	*No*	***Min***	*No*
20	70	*No*	***Min***	*No*	*No*	*No*	*Zero*	*No*	***Max***	***Max***
20	60	*Zero*	*No*	*No*	*No*	*No*	*No*	***Max***	*No*	*No*
10	100	***Min***	*No*	*No*	*No*	*No*	*No*	*No*	*No*	*No*
10	90	***Min***	*No*	*No*	*No*	*No*	*No*	*No*	*No*	*Zero*
10	80	***Min***	*No*	*No*	*No*	*No*	*No*	*No*	*No*	*Zero*
10	70	*No*	***Max***	*Zero*	*No*	*No*	*No*	*No*	*Zero*	*No*
10	60	*Zero*	*No*	***Max***	*No*	*No*	*No*	***Max***	***Max***	***Max***

Table [5.2.5.4] Component Value at Max / Min when Sideband Peak Occurs.

Load (Nm)	Imbalance (%)	Max/Min
40	100	*No*
40	90	***Yes***
40	80	*No*
40	70	***Yes***
40	60	***Yes***
30	100	*No*
30	90	*No*
30	80	*No*
30	70	*No*
30	60	***Yes***
20	100	*No*
20	90	*No*
20	80	*No*
20	70	*No*
20	60	*No*
10	100	*No*
10	90	*No*
10	80	*No*
10	70	***Yes***
10	60	*No*

Table [5.2.5.5] Peak Sideband Occurs at Max/Min of Fx[6].

Load (Nm)	Imbalance (%)	Output Power Max.
30	100	*No*
30	90	*No*
30	80	*No*
30	70	*No*
30	60	*No*
20	100	*No*
20	90	*No*
20	80	*No*
20	70	*No*
20	60	*No*
10	100	*No*
10	90	*No*
10	80	*No*
10	70	*No*
10	60	*No*

Table [5.2.5.6] Peak Sideband Amplitude Occurs at Maximum Power Output.

5.3 Conclusions

Observations from the latter half of the Lower Sideband within a full analysis, see Chapter 4, indicated that the sideband amplitude did not remain constant whilst travelling towards the steady state frequency of 50 Hz. The amplitude coming to a prominent peak midway between 0 Hz and the fundamental frequency. This chapter reports on the investigations, using a field theory model of an induction motor, into obtaining a reasoning behind such a phenomenon.

Various parameters within the model were varied accordingly to observe the effects that each had on a full analysis of the simulated supply current. Parameters varied included: rotor angle, supply angle and rotor imbalance. Various inductances within the model were altered as well, the results of these variations, however, did not indicate any reasoning behind such peaks within the Lower Sidebands.

The model was then interrogated and the various parameter and inductances were again varied whilst monitoring individual 'software variables' within the code of the model. This, however, did not show any evidence towards the peaks and was thus abandoned.

Investigations using the model were then carried out on the nature of the motors physically measurable parameters when the sideband peak occurred. As one of the 'gut feelings' towards such peaks was that the phenomenon occurred due to a relationship between increasing torque and decreasing current within the motor, particular interest was paid to both current and torque values. Again, however, no concise reasoning as to the cause of these peaks was obtained.

This phenomenon is now currently being looked at by another researcher employing a more accurate model of an induction motor within a finite element environment.

Chapter 6 will now introduce, in some detail, the theory and methodology used for obtaining the location of broken rotor bars from within cage rotors.

Chapter 6

The Physical Location of Rotor Bar Faults

6.0 Introduction

Previous chapters have indicated that it is possible to determine both the presence and severity of common cage rotor bar faults, such as broken rotor bars, by means of monitoring the supply current transient of the motor under investigation. Using the monitoring system developed in Chapter 4, the operator may confidently detect whether the rotor bar has merely cracked due to the various stresses and strains present within the motor, or if in fact it has completely fractured, an altogether more serious fault situation, (see Chapter 1). In addition to this, the results obtained from the monitoring system may be used, over a period of time, to create a data-base containing historic health conditions of the prime mover.

As indicated within Chapter 1, the major loss of revenue for operators occurs at any point in time at which the motor is non-operational. It therefore makes economic sense for operators to strive to reduce the downtime, whilst faults are physically located and repaired, to a minimum. Operators have indicated that any further diagnostic methods which may be used within the workshop environment, or otherwise, as a means to aid physical location of rotor bar faults would be advantageous, since not every rotor bar fault will be a complete fracture, and hence, may not be easily identified. The majority of bar problems that are sought within the workshop will in fact be bar cracks, which by their very nature are extremely elusive to locate physically. As mentioned previously, techniques such as the 'Growler' and 'Single Phasing' tests are available to enable the location of faults to be achieved, but due to their nature are no longer practical when dealing with physically large machines.

The work discussed within the following chapters investigates the possibility of creating a monitoring system which would not only determine the presence and severity of any rotor bar faults, but also indicate to some extent, the physical location of the faulty bar.

6.1 Rotor Fault Location Theories

When a rotor cage is completely symmetrical the rotor current pattern may be assumed to be fundamentally distributed. However, should the cage obtain some form of asymmetry then additional space harmonics are produced. If the stator windings are assumed to be ideal, the rotor fields which influence the stator will be those which have the same pole numbers as the stator. Two fields are produced, the first being the normal forward rotating component which induces mains frequency EMF's within the stator and is the rotor driven field present when the cage is symmetrical, the second being the component which rotates backwards at slip speed with respect to the rotor and originates from the cage asymmetry, see Appendix I. From standstill to half speed these components form a negative sequence set whilst from half speed to synchronous they are positive in nature.

Deleroi [39] states that when a fault occurs, the distortion to the overall symmetry on the rotor may be assumed to produce a fault current within the rotor bar which contains the asymmetrical component, over and above the current which would flow under normal symmetrical conditions.

The magnetic field within the air-gap under these fault conditions may be obtained by calculating the field caused only by this additional fault current. The field around the broken bar has a fundamental component which is always two-pole and due to the abrupt nature of its radial components is rich in harmonics. The anomaly rotates at the mechanical frequency of the rotor since it is attached to the rotor bar, the rotating components pulsating at slip frequency. From a rotating observer the fundamental may be resolved into two oppositely directed travelling waves of two-pole wavelength and frequency.

Deleroi [39] shows how the ratio of the fault current within the two neighbouring meshes to the rotor bar which contains the asymmetry is equal to a constant value. This value, given the symbol 'd', is complex in nature and is independent to the number of rotor bars present within the rotor. This ratio has also been proven to occur within the air-gap flux density surrounding the bars in question, resulting in the amplitude of the flux density wave being damped in a bi-directional step-wise manner with increasing distance from the bar which contains the asymmetry.

6.1.1 Relationship Between Complex Damping Factor and Motor Slip

In order to derive the complex damping factor present within the fault current and air-gap flux density, it was necessary to derive expressions for the individual rotor bar currents surrounding the bar which contains the asymmetry. From such an expression it would then be possible to indicate the relationship between the localisation of the effect around the broken bar with a variable motor slip. In order to accomplish this the equivalent circuit for the Squirrel Cage rotor was created.

From the general equivalent circuit of the induction motor, Figure [2.1.1], three separate reactance components are included: X_1, X_2, and X_m, together with the associated phase resistances. The component X_m represents what is known as the magnetising reactance, whereas X_1 and X_2 are viewed as the overall leakage reactances due to all other elements of flux produced by the respective windings. The leakage reactance components may be further sub-divided [28] into eight distinct reactance components: (a) The Primary Slot Reactance, (b) The Secondary Slot Reactance, (c) The Zig-Zag Leakage Reactance, (d) The Reactance due to the effects of Rotor Skew, (e) The Belt Leakage Reactance, (f) The Coil End Leakage Reactance, (g) The Incremental Reactance and (h) The Peripheral Leakage Reactance. It is, however, beyond the scope of this report to further discuss these inductances. It was deemed necessary, however, that any equivalent circuit of the rotor meshes should take into account the majority of the above parameters.

The circuit shown within Figure [6.1.1.1] represents the individual rotor meshes which form the N_r bar cage rotor. If the rotor is undamaged the circuit will be perfectly symmetrical, and hence, all N_r rotor bars, end-ring resistances and leakage reactances together with the air-gap field inductance, will be equal. Should the rotor contain an asymmetry, such as a broken bar, then as previously indicated a fault current is considered to exist within the broken bar similar to that shown in Figure [6.1.1.2].

The fault current flowing within the rotor bar containing the asymmetry may be thought of as generating a field curl around the area of the damaged bar. This field component is transmitted in both radial directions into free field waves which are damped after a relatively small fraction of the rotor circumference by the complex damping factor. This damping makes the field effect extremely localised around the area of asymmetry.

The field curl generated by the asymmetry induces small voltages within the stator winding. These voltages contain a fundamental frequency component along with many other high frequency components. These frequency components give rise to oscillatory torques which make the motor run less smoothly, and hence, cause mechanical vibrations to occur.

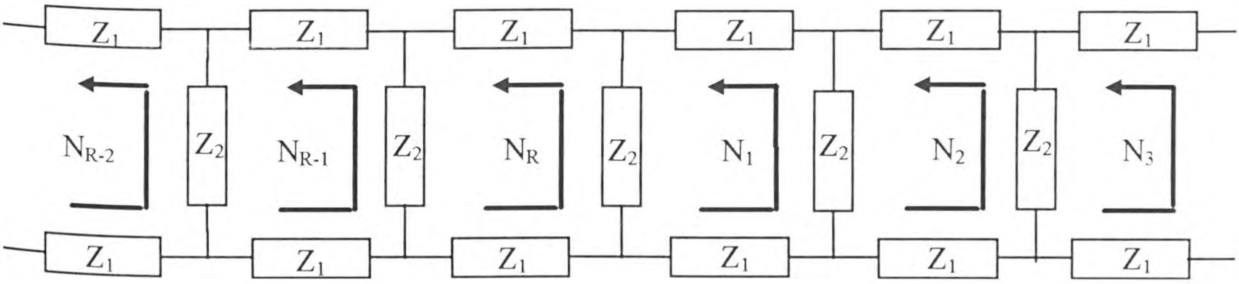

$Z_1 = R_e + js\ X_e$ $\qquad$ $Z_2 = R_b + js\ X_b$

Figure [6.1.1.1] Equivalent Circuit For Squirrel Cage Rotor.

As a means to describe the effects of the broken bar within the rotor, the stator current is assumed to be imposed, hence there is no reaction upon or from the stator current distribution. A further assumption to be made during the calculation is that Superposition or Norton's theorem, which states that the overall performance of the motor may be determined by investigating the effect of the anomaly separately, and then adding the individual results of the effects to the steady state reaction of the undamaged motor, will be employed in the formulation of the expressions describing the current flowing either side of the rotor bar containing the asymmetry. Thus, the theorem may be executed if the current within the rotor bar is assumed to consist of the current flowing in the rotor under normal conditions plus, a fault current of equal magnitude flowing in the opposite direction.

Figure [6.1.1.2] shows a modified example of the rotor equivalent circuit shown in Figure [6.1.1.1]. In this circuit the fault current, I_{Fault}, caused by the introduction of the broken bar is shown to produce two mesh currents, namely $I_{R1} = 1/2\ I_{Fault}$ and $I_{RN} = -\ 1/2\ I_{Fault}$. Since both mesh currents are equal in magnitude, only one side of the broken bar circuit need be analysed, Figure [6.1.1.3].

Using the simplified circuit shown within Figure [6.1.1.3], current equations may be formed utilising Mesh Analysis methods in conjunction with Kirchhoff's voltage laws. This results in a total of N_r equations describing the loop currents within each of the individual rotor meshes.

The rotor loop current will cause flux to cross the air-gap through the loop, returning with even distribution around the remainder of the air-gap periphery. Each rotor loop within the rotor mesh will therefore be consequently inductively coupled with every other loop via this rotor air-gap flux. Over

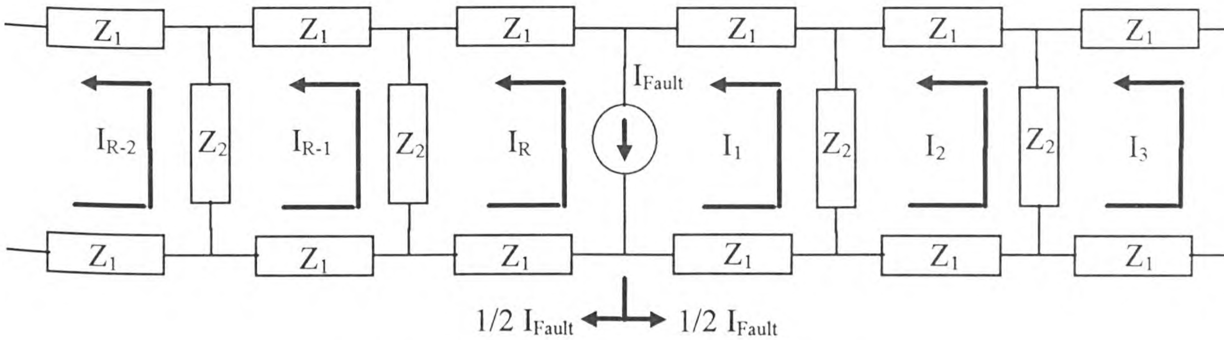

Figure [6.1.1.2] Model of a Broken Rotor Bar.

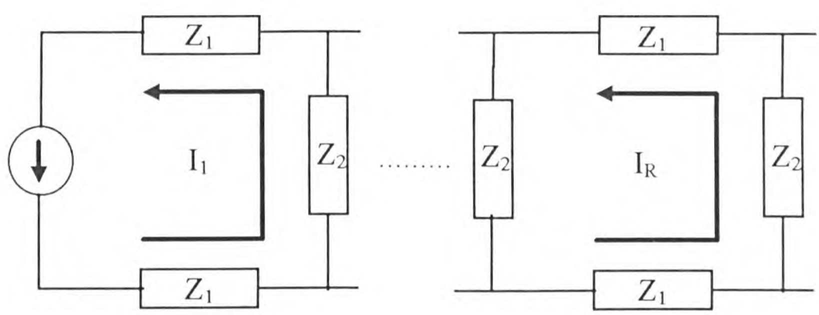

Figure [6.1.1.3] Simplified Mesh Circuit.

and above this, each loop within the rotor mesh model will be coupled to its two immediate neighbouring meshes by virtue of the resistance, R_b, and slot leakage reactance, X_b, of the rotor bars as shown by Figure [6.1.1.1]. Thus the total impedance of a rotor loop will be as shown in eq. (6.1.1.3).

$$Z_{Total} = Z_1 + Z_2 + Z_1 + Z_2 + X_r \qquad \textbf{(6.1.1.1)}$$

$$= R_e + js\,X_e + R_b + js\,X_b + R_e + js\,X_e + R_b + js\,X_b + X_r \qquad \textbf{(6.1.1.2)}$$

$$= \underbrace{2R_b + 2R_e + js\,\{2X_b + 2X_e}_{\text{Self Impedance}} + \underbrace{X_r}_{\text{Mutual Reactance}}\} \qquad \textbf{(6.1.1.3)}$$

For purpose of explanation the rotor under analysis should be considered to contain six meshes. Thus, using KVL around all six meshes results in the expressions shown in eq. (6.1.1.4).

$$\begin{aligned}
V &= I_1Z_1 + I_1Z_2 + I_1Z_1 - I_2Z_2 \\
0 &= I_2Z_2 + I_2Z_1 + I_2Z_2 + I_2Z_1 - I_3Z_2 - I_1Z_2 \\
0 &= I_3Z_2 + I_3Z_1 + I_3Z_2 + I_3Z_1 - I_4Z_2 - I_2Z_2 \\
0 &= I_4Z_2 + I_4Z_1 + I_4Z_2 + I_4Z_1 - I_5Z_2 - I_3Z_2 \\
0 &= I_5Z_2 + I_5Z_1 + I_5Z_2 + I_5Z_1 - I_6Z_2 - I_4Z_2 \\
0 &= I_6Z_2 + I_6Z_1 + I_6Z_2 + I_6Z_1 - I_5Z_2
\end{aligned} \qquad \textbf{(6.1.1.4)}$$

Re-arranging,

$$\begin{aligned}
V &= Z_1 (I_1 + I_1) + Z_2 (I_1 - I_2) \\
0 &= Z_1 (I_2 + I_2) + Z_2 (I_2 + I_2 - I_3 - I_1) \\
0 &= Z_1 (I_3 + I_3) + Z_2 (I_3 + I_3 -I_4 - I_2) \\
0 &= Z_1 (I_4 + I_4) + Z_2 (I_4 + I_4 - I_5 - I_3) \\
0 &= Z_1 (I_5 + I_5) + Z_2 (I_5 + I_5 - I_6 - I_4) \\
0 &= Z_1 (I_6 + I_6) + Z_2 (I_6 + I_6 - I_5)
\end{aligned} \qquad \textbf{(6.1.1.5)}$$

Thus,

$$\begin{aligned}
V &= Z_1 (2I_1) + Z_2 (I_1 - I_2) \\
0 &= Z_1 (2I_2) + Z_2 (-I_1 + 2I_2 - I_3) \\
0 &= Z_1 (2I_3) + Z_2 (-I_2 + 2I_3 - I_4) \\
0 &= Z_1 (2I_4) + Z_2 (-I_3 + 2I_4 - I_5) \\
0 &= Z_1 (2I_5) + Z_2 (-I_4 + 2I_5 - I_6) \\
0 &= Z_1 (2I_6) + Z_2 (-I_5 + 2I_6)
\end{aligned} \qquad \textbf{(6.1.1.6)}$$

Dividing by Z_2,

$$\begin{aligned}
V/Z_2 &= Z_1/Z_2 (2I_1) + (I_1 - I_2) \\
0 &= Z_1/Z_2 (2I_2) + (-I_1 + 2I_2 - I_3) \\
0 &= Z_1/Z_2 (2I_3) + (-I_2 + 2I_3 - I_4) \\
0 &= Z_1/Z_2 (2I_4) + (-I_3 + 2I_4 - I_5) \\
0 &= Z_1/Z_2 (2I_5) + (-I_4 + 2I_5 - I_6) \\
0 &= Z_1/Z_2 (2I_6) + (-I_5 + 2I_6)
\end{aligned} \qquad \textbf{(6.1.1.7)}$$

Grouping the circuit parameters into the complex group defined by $A = Z_1/Z_2$, results in a component dependent upon the slip of the motor.

$$
\begin{aligned}
V/Z_2 &= 2I_1 A + I_1 - I_2 \\
0 &= 2I_2 A + 2I_2 - I_1 - I_3 \\
0 &= 2I_3 A + 2I_3 - I_2 - I_4 \\
0 &= 2I_4 A + 2I_4 - I_3 - I_5 \\
0 &= 2I_5 A + 2I_5 - I_4 - I_6 \\
0 &= 2I_6 A + 2I_6 - I_5
\end{aligned} \qquad \textbf{(6.1.1.8)}
$$

The individual expressions within eq. (6.1.1.8) have the same form and contain the same number of parameters, hence, the equations may be re-written in matrix form, eq. (6.1.1.9).

$$
\begin{bmatrix}
(1+2A)-1 & -1 & 0 & 0 & 0 & 0 \\
-1 & (2+2A) & -1 & 0 & 0 & 0 \\
0 & -1 & (2+2A) & -1 & 0 & 0 \\
0 & 0 & -1 & (2+2A) & -1 & 0 \\
0 & 0 & 0 & -1 & (2+2A) & -1 \\
0 & 0 & 0 & 0 & -1 & (2+2A)
\end{bmatrix}
\begin{bmatrix} I_1 \\ I_2 \\ I_3 \\ I_4 \\ I_5 \\ I_6 \end{bmatrix}
=
\begin{bmatrix} V/Z_2 \\ 0 \\ 0 \\ 0 \\ 0 \\ 0 \end{bmatrix}
$$

(6.1.1.9)

The above matrix may be used to solve the equations for I_1 through to I_6, as is done later in order to show that the mesh current is independent to the number of rotor bars present within the rotor, and that the ratio of the current within two neighbouring meshes is equal to the complex damping factor, 'd'.

On solving the above matrix it may be shown that the current contains two components. One component increasing with increasing mesh number, the other decreasing. When this is considered in terms of air-gap flux, and that of a cylindrical rotor, the rotor asymmetry produces two field waves which travel in opposite directions away from the position of the actual rotor asymmetry with their amplitudes decreasing in a step wise manner, Figure [6.1.1.4].

It is interesting to note that the impedance matrix formed within eq. (6.1.1.9) by the use of the rotor equivalent circuit, forms an integral part of the general matrix expression used to describe the entire induction machine. This expression, eq. (6.1.1.10), developed by Williamson [58] et al. includes all parameters required to successfully model the three phase induction motor. This expression includes a mains frequency stator current component, I_f, a *(1-2s)* times mains frequency component, I_b, a circulating end-ring current component, I_e along with the individual N_b rotor loop currents used within eq. (6.1.1.9). The voltage vector on the left-hand side of eq. (6.1.1.10) contains a single non-zero component, thus reflecting the assumption that the excitation comes from a balanced three phase source.

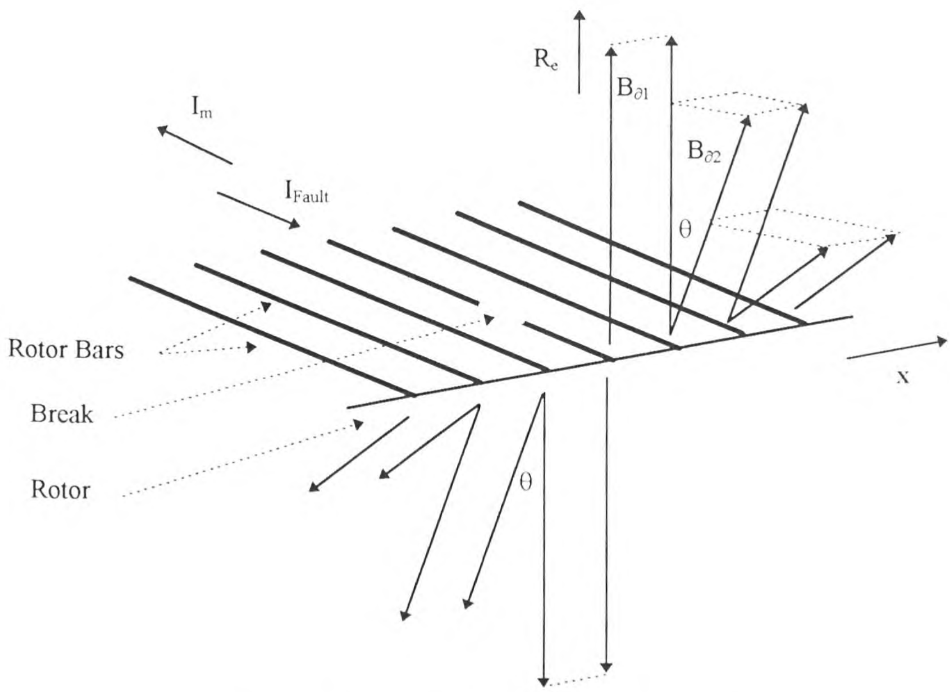

Figure [6.1.1.4] Step-Like Nature of Rotor Anomaly.

$$\begin{bmatrix} Zff & 0 & Zf1 & Zf2 \ldots\ldots & ZfNb & 0 \\ 0 & Zbb & Zb1 & Zb2 \ldots\ldots & ZbNb & 0 \\ Z1f & Z1b & Z11 & Z12 \ldots\ldots & Z1Nb & Z1e \\ Z2f & Z2b & Z21 & Z22 \ldots\ldots & Z2Nb & Z2e \\ . & . & . & . & . & . \\ . & . & . & . & . & . \\ . & . & . & . & . & . \\ ZNbf & ZNbb & ZNb1 & ZNb2 \ldots\ldots & ZNbNb & ZNbe \\ 0 & 0 & Ze1 & Ze2 \ldots\ldots & ZeNb & Zee \end{bmatrix} \begin{bmatrix} If \\ Ib \\ I1 \\ I2 \\ . \\ . \\ . \\ INb \\ Ie \end{bmatrix} = \begin{bmatrix} V \\ 0 \\ 0 \\ 0 \\ . \\ . \\ . \\ 0 \\ 0 \end{bmatrix}$$

(6.1.1.10)

6.1.2 Locus of Complex Damping Factor

Using values of the motor parameters obtained previously by Elder [89], and from expressions derived by Alger [28], it was possible to calculate the value of damping factor for the test-rig motor in question. Calculating the expressions for any two successive mesh currents, using the matrix within eq. (6.1.2.11), it was possible to calculate the respective loop currents, and hence, the complex damping factor for various levels of slip, eq. (6.1.2.1). Approximate values were felt to be adequate, since at this point in time it was only the general trend of complex damping factor which was required and not actual levels. The parameter values used are listed within Table [6.1.2.1]. Using these values and the expressions quoted within eq. (6.1.2.1), the effect of the damping factor when slip is varied may be seen in Figure [6.1.2.1].

Figure [6.1.2.2] shows the locus of the complex damping factor 'd' for various levels of motor slip, 's'. Deleroi reports that when the value of 's' is small, the amplitudes of both 'd' and the phase angle between the additional currents in the neighbouring meshes, 'θ' are small. This results in the rotor anomaly spreading along way over the circumference of the rotor. With higher values of slip, then as may be observed from the diagram, the damping factor 'd' increases resulting in the rotor anomaly becoming more prominent around the rotor bar containing the asymmetry, as it quickly decreases in amplitude with increasing distance from the asymmetry, Figure [6.1.2.3] and Figure [6.1.2.4]. The extent to which the effects of the anomaly are transmitted within the air-gap and the degree of damping obtained are dependant, Deleroi suggests, upon the geometry of the rotor with the excitation of the anomaly being dependant upon the slip of the rotor. The field produced from the asymmetry therefore revolves with the rotor slipping with respect to the main air-gap field.

This additional air-gap field produced by the rotor asymmetry induces voltages within the stator windings of the SCIM, which contain a fundamental frequency a long with many other high frequency components. Deleroi states that the voltages induced will contain frequencies which may be determined by Fourier analysis and can be described by eq. (2.3.3.4).

Thus, when a rotor contains an asymmetry there will be frequency components present within the supply current signal of the SCIM, which may indicate the location of the asymmetry upon the rotor. If these components could be successfully detected, it is theoretically possible to determine the

$$
I_1 = \begin{vmatrix} V/Z_2 & -1 & 0 & 0 & 0 & 0 \\ 0 & (2+2A) & -1 & 0 & 0 & 0 \\ 0 & -1 & (2+2A) & -1 & 0 & 0 \\ 0 & 0 & -1 & (2+2A) & -1 & 0 \\ 0 & 0 & 0 & -1 & (2+2A) & -1 \\ 0 & 0 & 0 & 0 & -1 & (2+2A) \end{vmatrix}
$$

$$
* \frac{1}{\begin{vmatrix} (1+2A)-1 & -1 & 0 & 0 & 0 & 0 \\ 0 & (2+2A) & -1 & 0 & 0 & 0 \\ 0 & -1 & (2+2A) & -1 & 0 & 0 \\ 0 & 0 & -1 & (2+2A) & -1 & 0 \\ 0 & 0 & 0 & -1 & (2+2A) & -1 \\ 0 & 0 & 0 & 0 & -1 & (2+2A) \end{vmatrix}}
$$

$$
I_2 = \begin{vmatrix} (1+2A)-1 & V/Z_2 & 0 & 0 & 0 & 0 \\ -1 & 0 & -1 & 0 & 0 & 0 \\ 0 & 0 & (2+2A) & -1 & 0 & 0 \\ 0 & 0 & -1 & (2+2A) & -1 & 0 \\ 0 & 0 & 0 & -1 & (2+2A) & -1 \\ 0 & 0 & 0 & 0 & -1 & (2+2A) \end{vmatrix}
$$

$$
* \frac{1}{\begin{vmatrix} (1+2A)-1 & -1 & 0 & 0 & 0 & 0 \\ -1 & (2+2A) & -1 & 0 & 0 & 0 \\ 0 & -1 & (2+2A) & -1 & 0 & 0 \\ 0 & 0 & -1 & (2+2A) & -1 & 0 \\ 0 & 0 & 0 & -1 & (2+2A) & -1 \\ 0 & 0 & 0 & 0 & -1 & (2+2A) \end{vmatrix}}
$$

etc .....

(6.1.2.1)

Rotor Bar Resistance	R_b	13mΩ
Bar Leakage Reactance	X_b	0.06Ω
End Ring Resistance	R_e	4mΩ
End Ring Reactance	X_e	0.015Ω
Rotor Mutual Reactance	X_r	4Ω

Table [6.1.2.1] Approximate Motor Parameters.

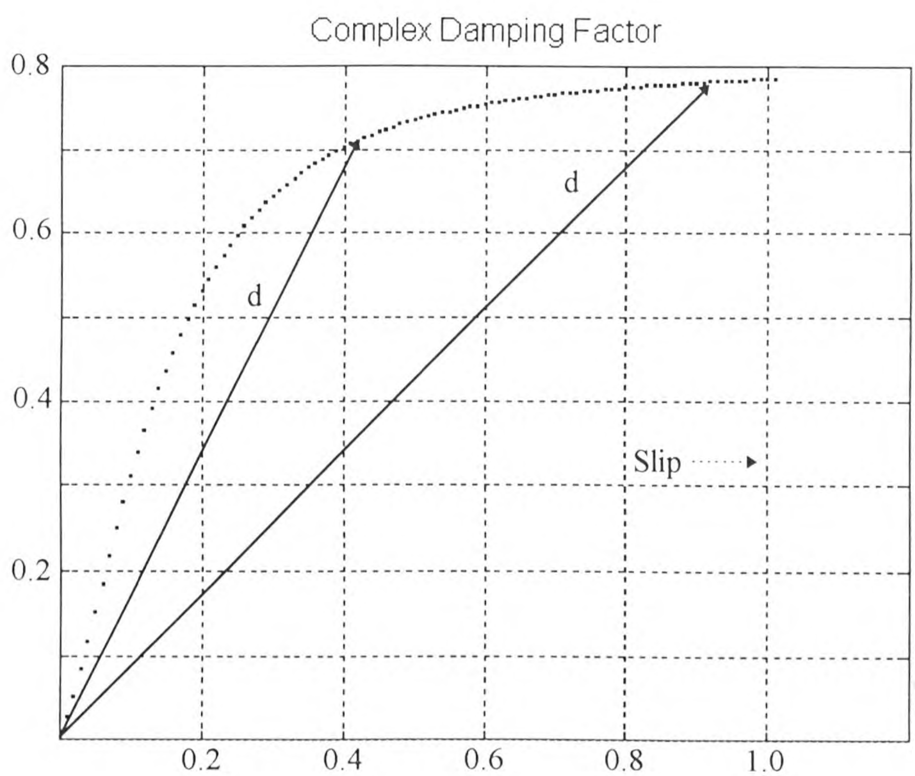

Figure [6.1.2.1] Effect on damping Factor with Varying Slip.

location of the rotor bar fault from the time at which the component takes to occur within the transient. However, due to the damping of the rotor anomaly being dependent upon motor slip, there will come a point within the transient at which the components will no longer be localised around the bar fault.

During the transient, as discussed in Chapter 2, the frequency components are non-stationary in nature. If however, one single particular frequency component is considered within the complete

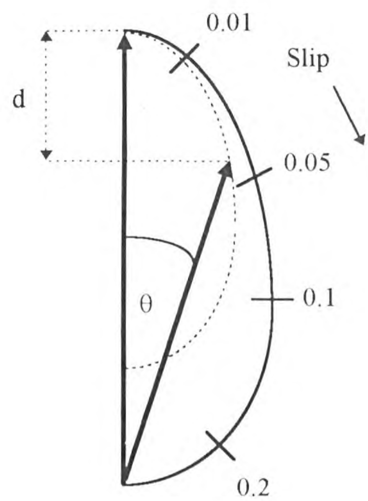

Figure [6.1.2.2] Locus of Complex Damping Factor with varying Slip.

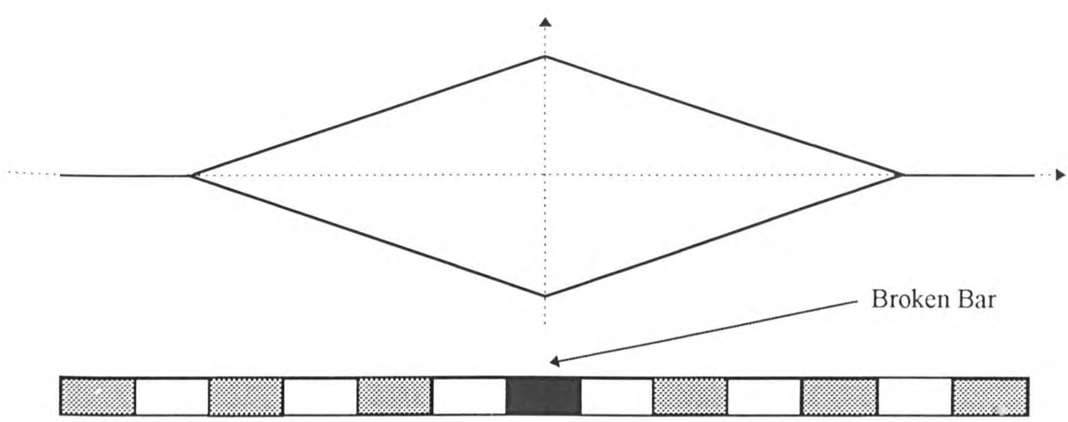

Figure [6.1.2.3] Envelope of Rotor Anomaly. Small Value of 'd'.

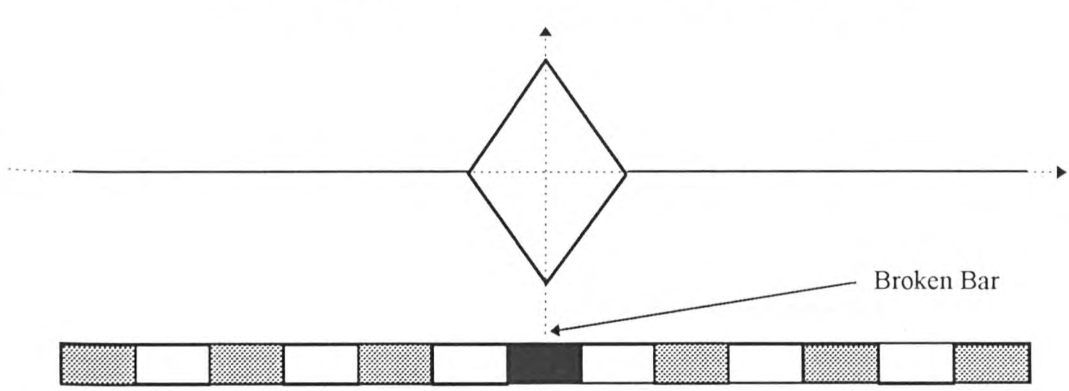

Figure [6.1.2.4] Envelope of Rotor Anomaly. Large Value of 'd'.

transient, then depending upon the location of the faulty bar at the start of the transient, the frequency component should occur at different time periods within the transient.

It is interesting to note that eq. (2.3.3.4) represents the frequency components present due to rotor asymmetries, see Appendix I. This may be observed more clearly when eq. (2.3.3.4) is expanded for various harmonic values, Table [6.1.2.1], with the calculated expressions matching those defined within Table [A.I.1].

It therefore follows that Deleroi is stating that it is the Lower Sideband components, LSB, which will be indicative, for a finite period of time, to the location of rotor bar faults. In conjunction with this and work carried out by Kliman [30], see Chapter 1, the most suitable fault component harmonics for possible fault location would become the 7th, 11th and 13th. Any other harmonics being submerged by other components due to the small levels of amplitude present.

$$F_{deleroi} = (k/p - s (k/p \pm 1))$$

$$= k/p - sk/p \pm s$$

$$= k/p - sk/p - s \quad ; \quad k/p - sk/p + s$$

For the fundamental component, k = p:

$$= p/p - sp/p - s \quad ; \quad p/p - sp/p + s$$

$$= 1 - s - s \quad ; \quad 1 - s + s$$

$$= 1 \quad ; \quad 1 - 2s$$

Harmonic	k	Lower	Upper
3	3p	(3-4s)	(3-2s)
5	5p	(5-6s)	(5-4s)
7	7p	(7-8s)	(7-6s)

Table [6.1.2.1] Harmonics of Deleroi Rotor Fault Components.

6.2 Theoretical Prediction of Rotor Bar Fault Location Technique

In order to obtain information on the physical location of the rotor bar fault, the problem was initially split into two separate problem areas. Firstly, the detection of the frequency components which would yield suitable location information and secondly, to form a methodology where from the location of the broken rotor bars could be obtained from these components.

6.2.1 Detection of Location Frequency Components

The frequency components used within the location work are defined by eq. (2.3.3.4). Initially a spectral search was made upon the steady state supply current to the test-rig in order to see if it were possible to observe the components at known frequencies. This was completed successfully and is reported within Chapter 7.

As the current transient signal contains many harmonic frequencies, both in time and space, it was necessary to obtain some idea of where the fault location frequencies would be in conjunction with the various other frequency components present within the transient signal. A prediction of these harmonic frequencies within a transient was developed using proven expressions, see section (2.3.3). From this prediction, Figure [2.3.3.1], it was found that the optimum search area for the detection of the fault location components would be as indicated, i.e. when the slip of the motor was less than 0.4 and at frequencies greater than 100 Hz. It would be at this point within the transient that the relevant fault location components would be out-with the effects of the larger frequency components present such as the Principal Slot Harmonics and Upper Sidebands.

6.2.2 Methodology behind Broken Bar Location Detection

The location of broken bars within a rotor of a SCIM is dependent upon the successful detection of the frequency components defined by eq. (2.3.3.4). The technique used to detect the location of a bar fault from these components would theoretically require some form of reference point, from where the distance to the faulty bar could then be computed, together with a transducer positioned within the air-gap to detect fault components. A transducer like this would obviously be invasive to the motor in question, hence, the use of the motor stator windings as search transducers within the motor was investigated.

On considering the two pole set-up shown within Figure [6.2.2.1](a), during the acceleration period of the motor, the location frequency component is assumed to occur when the bar is opposite 'A'. This is detected by filtering all three phases of the supply current for one particular frequency, Figure [6.2.2.1](a). This component occurs at a particular time which is easily converted into a distance travelled by a point on the rotor. This is done by extracting slip versus time data, and hence, acceleration data from a plot of the LSB locus during a complete transient analysis similar to Figure [3.7.1.3].

In order to locate the stator winding which would be used as the reference location, all three phases of supply current would be monitored for the particular location frequency, Figure [6.2.2.1](b). The phase which gives the largest filtered output being an indication as to the reference phase, however, as is shown in Figure [6.2.2.1](b), an example of a typical four pole machine, on using the above technique would result in four possible locations being obtained. This, however, was still felt to be useful in at the very least, if successful, would indicate to the operator four possible areas within the rotor in which to concentrate the physical search for rotor faults.

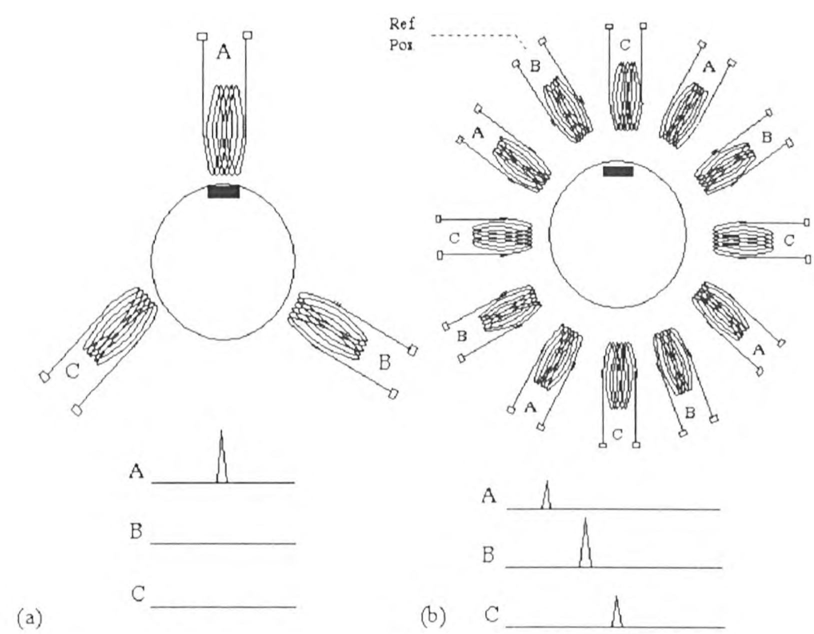

Figure [6.2.2.1] Fault Position Methodology.

6.3 Conclusions

Frequency components reported to be indicative of a squirrel cage rotor bar fault have been discussed in some detail. During this discussion it has transpired that the components in question were in fact the LSB's used previously to indicate the presence of rotor bar faults, see Chapter 4. However, from previous researchers, it was reported that it is the higher harmonics of these components which would be of use with regards to fault location purposes.

The fault components are reported to be indicative to the bar fault due to a damping effect which is prominent during the initial acceleration period from start-up. This damping factor has been shown, with the aid of equivalent circuit methods, to vary with differing levels of motor slip. The larger the slip, the larger the level of damping which occurs upon the magnetic field around the bar fault.

Finally, a non-invasive methodology of using the fault components, once successfully detected, to obtain fault position information has been discussed. The method incorporates the stator winding as a form of search coil and uses this in conjunction with the motor's acceleration data, to compute the approximate location of the bar fault. Information which could not be easily obtained from a steady state analysis of the signal due to the small values of slip present. The acceleration data required for such a technique being available from a complete analysis of the fundamental LSB within the transient signal. Results using the above theories will now be presented within Chapter 7.

Chapter 7

Results of Location Work

7.0 Introduction

The results presented within the following chapter were obtained using the theory and methodologies presented within Chapter 6. They are presented in a logical progression reflecting the thinking processes behind each problem as it presented itself.

7.1 Correlation of Supply Current Signals

The fault frequency components within the transient current signal will be varying in frequency throughout the transient period. If one particular fault component is considered, then depending upon the physical location of the broken bar when the motor is started, the frequency components will occur at different instances in time within the transient signal. As a means to determine this time difference when a rotor with a broken rotor bar is started at different locations, initial investigations involved filtering the transient signals at a particular fault frequency and correlating the signals with similarly filtered signals from other transients obtained with the rotor at different locations upon start-up. In conjunction with these correlation investigations, the various timings of the peaks which occur within the filtered signals were noted in order to observe if they too showed any relationship to the location of the faulted bar upon start-up. All three synchronously sampled phases were analysed.

7.1.1 Correlation Results

Initially the filter frequency of 21 Hz was chosen as the investigation frequency. This frequency was chosen as it had previously been proven to be an excellent indicator to the presence of rotor bar faults, see Chapter 4, and was also a frequency defined by Deleroi in eq. (2.3.3.4).

A transient was sampled from the test-rig which had a fault condition of ten contiguous broken rotor bars. The transient was obtained when the broken bars within the rotor were positioned at a twelve o'clock reference start-up position. This sample was filtered at 21 Hz and correlated with similarly filtered transients obtained from start-ups where broken bars were in different locations upon start-up.

These timings of peaks within the filtered outputs are shown within Figure [7.1.1] and Figure [7.1.2], together with the correlation between the reference transient and other transients, shown within Figure [7.1.3]. Figure [7.1.4] and Figure [7.1.5] show ten samples of the transient with broken bars at the reference position on start-up. These samples were obtained in order to observe the average change which the timings undergo from sample to sample.

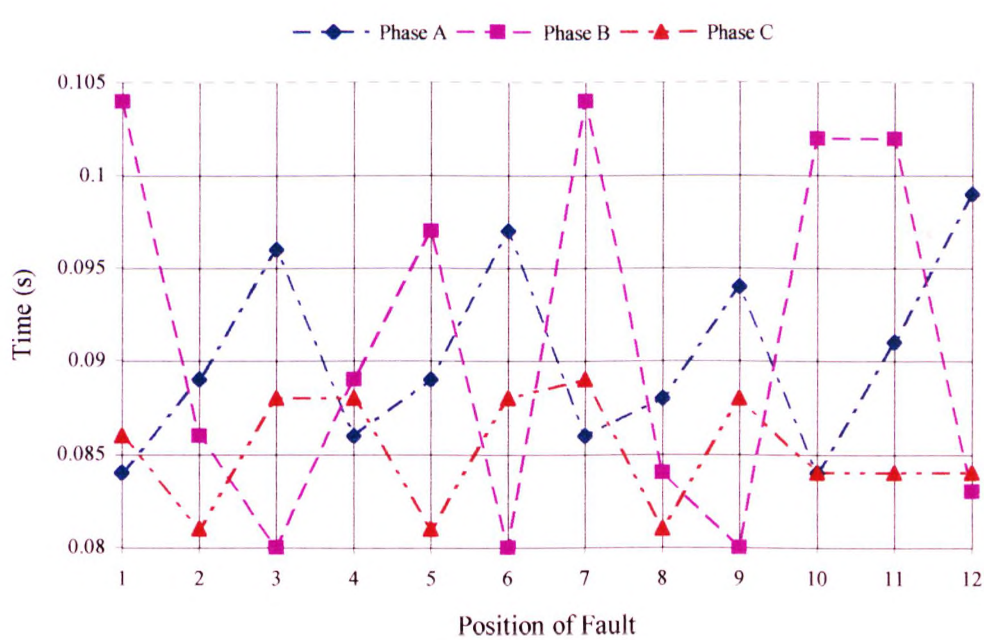

Figure [7.1.1] Time to First Peak, F = 21 Hz.

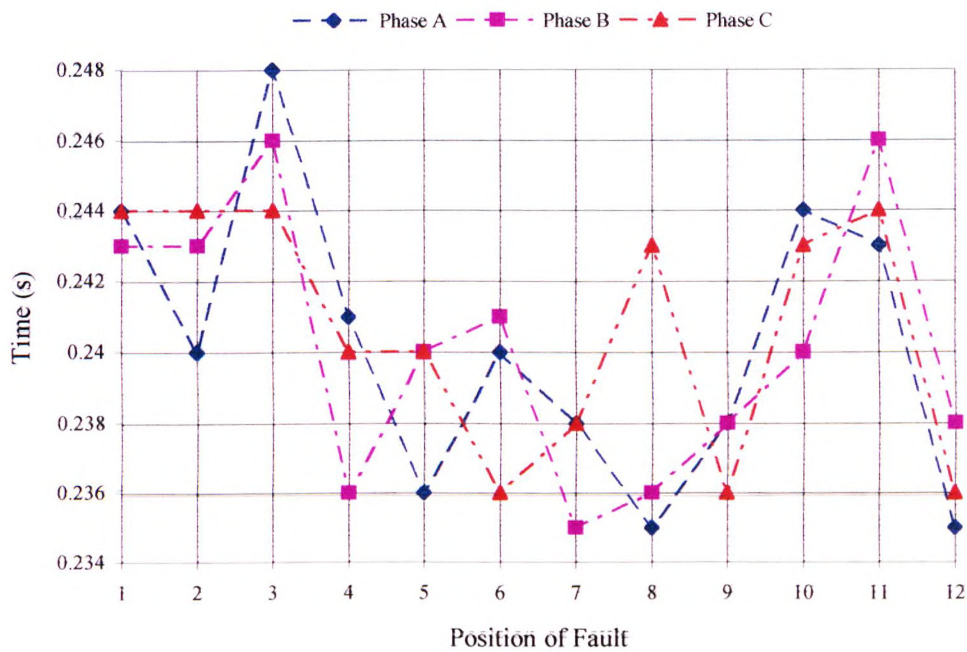

Figure [7.1.2] Time to Second Peak, F = 21 Hz.

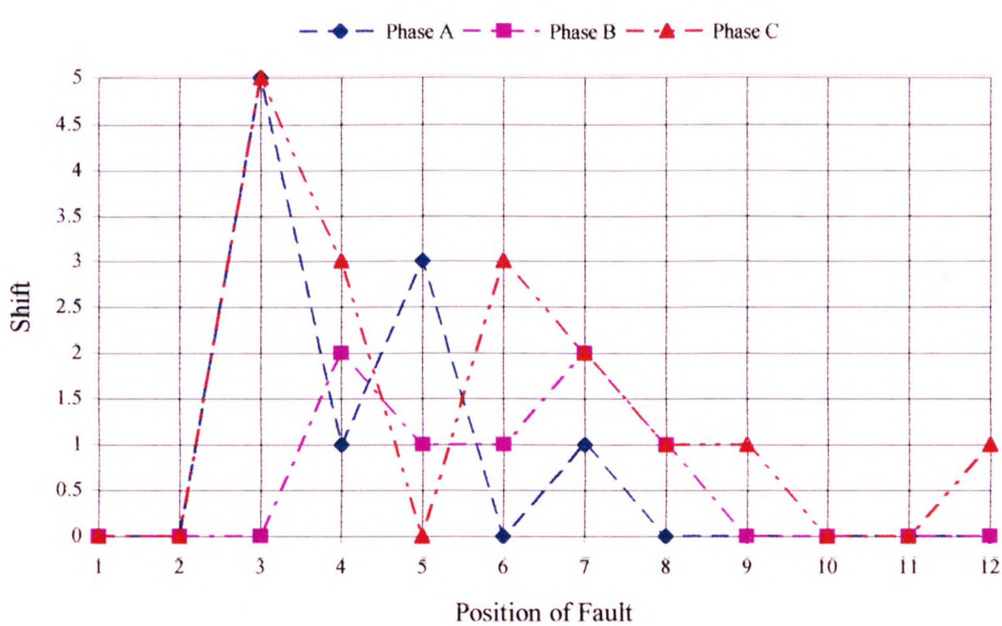

Figure [7.1.3] Correlation Shift, F = 21 Hz.

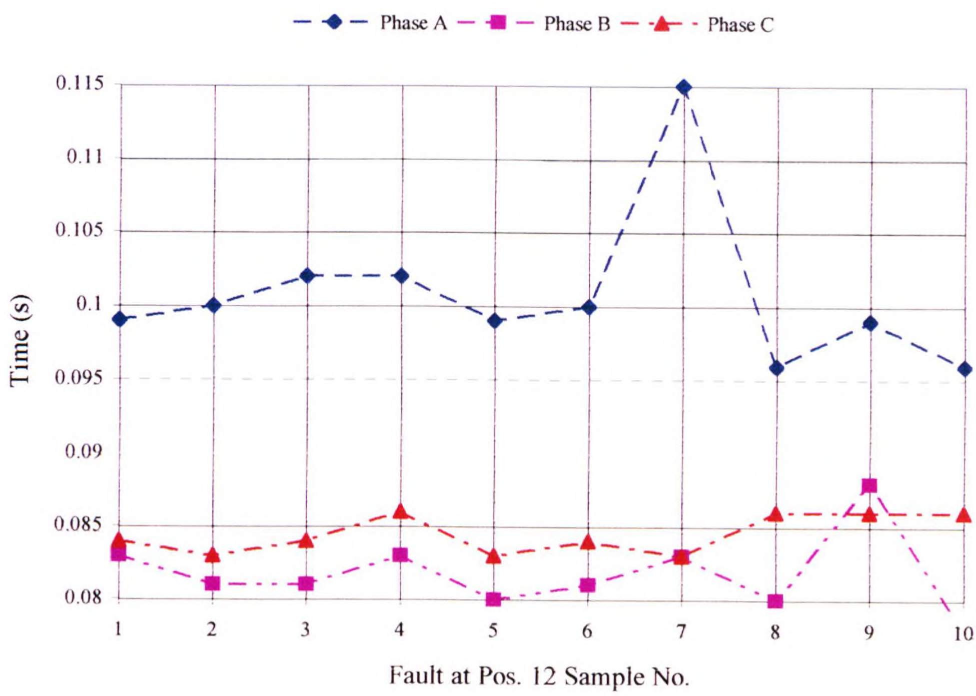

Figure [7.1.4] Time to First Peak, F = 21 Hz.

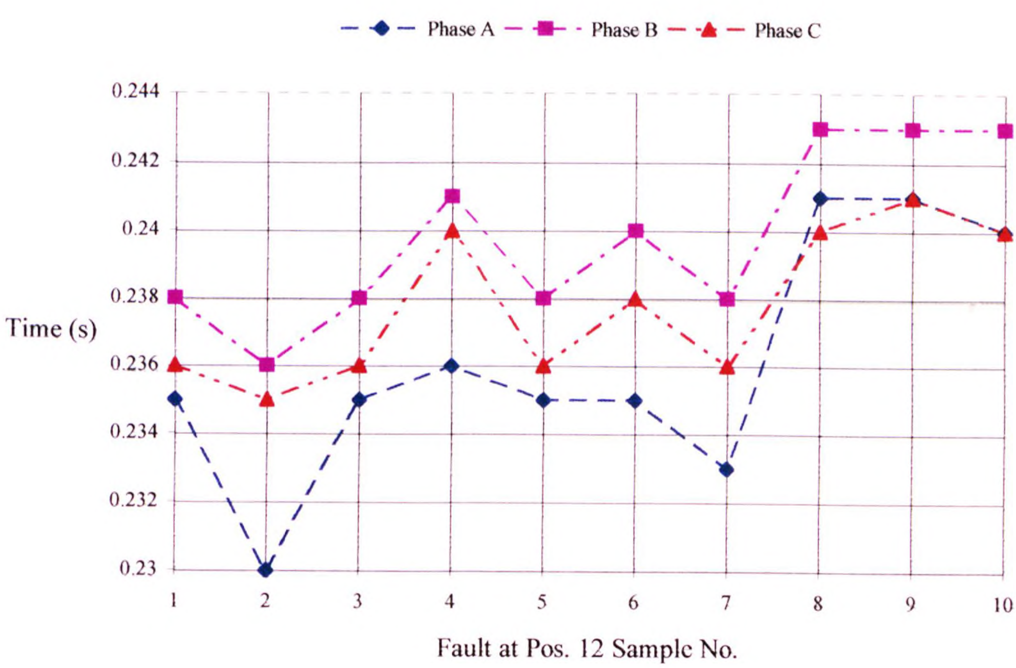

Figure [7.1.5] Time to Second Peak, F = 21 Hz.

Phase A	Phase B	Phase C
0.019	0.01	0.003

Table [7.1.1] Δ Change.

Phase A	Phase B	Phase C
0.01	0.007	0.006

Table [7.1.2] Δ Change.

Figure [7.1.6] to Figure [7.1.7] show results obtained from similar tests using a filter frequency of 75 Hz, with Figure [7.1.8] presenting results from the correlation of data.

Figure [7.1.9] to Figure [7.1.10] present the results from filtering at a frequency of 100 Hz. Figure [7.1.11] showing the correlation results.

The bandwidth of the software filter was then reduced in order to make the filter more frequency selective. A selection of results obtained with this filter is shown within Figure [7.1.12] through to Figure [7.1.14].

7.1.2 Correlation Results - Conclusions

From results obtained within Section (7.1.1), the timings of the individual peaks within the filtered outputs of the transient signals show no connection between their occurrence and the position of the broken rotor bars upon start-up. The observed changes between the times obtained at different bar fault positions all being within the Δ change value observed for ten samples at one location, Table [7.1.1] to Table [7.1.2].

No relevant information could similarly be obtained from the correlations of the filtered data with filtered data obtained from the reference rotor bar fault location.

The lack of satisfactory results indicates that the fault frequency components are far smaller in amplitude than at first anticipated. It therefore became necessary to find a means of amplifying these components over and above the larger components present within the transient signal. The following section describes the selective filtering employed to undertake this task.

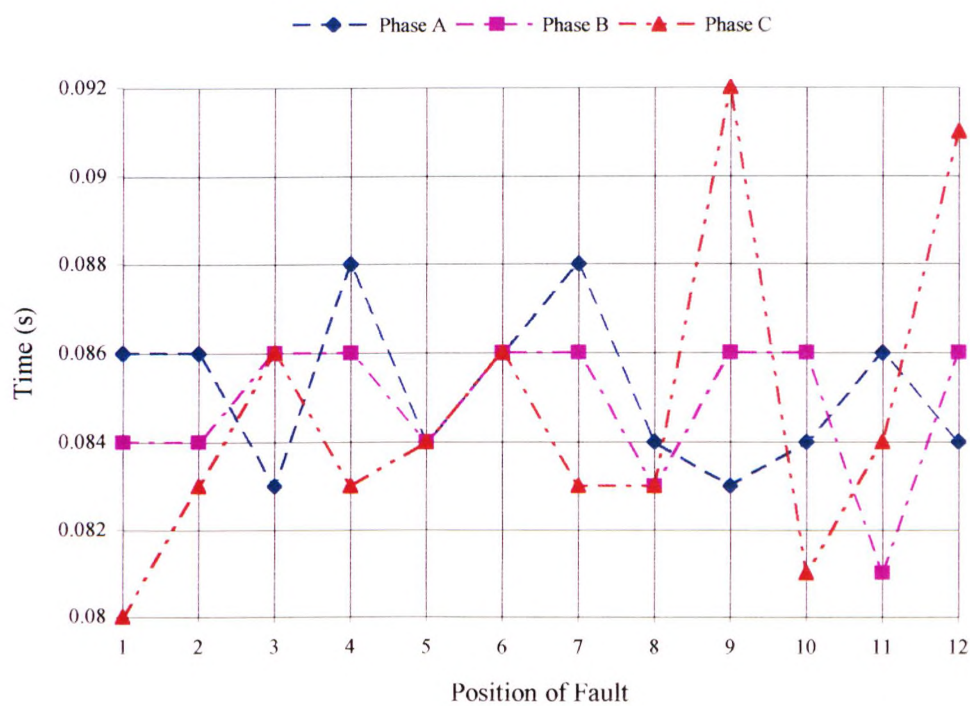

Figure [7.1.6] Time to First Peak, 75 Hz.

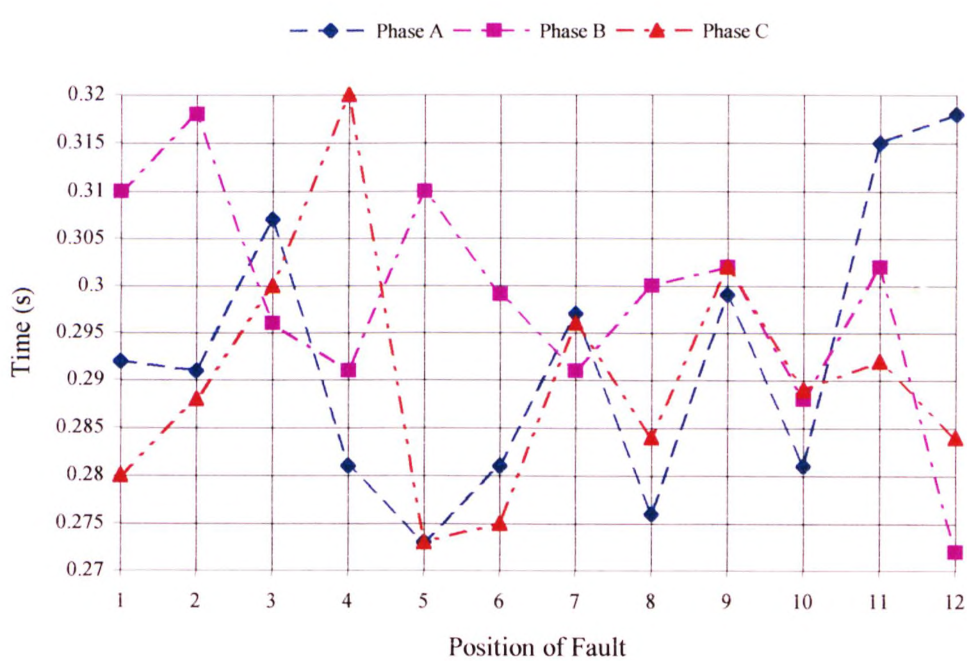

Figure [7.1.7] Time to Second Peak, 75 Hz.

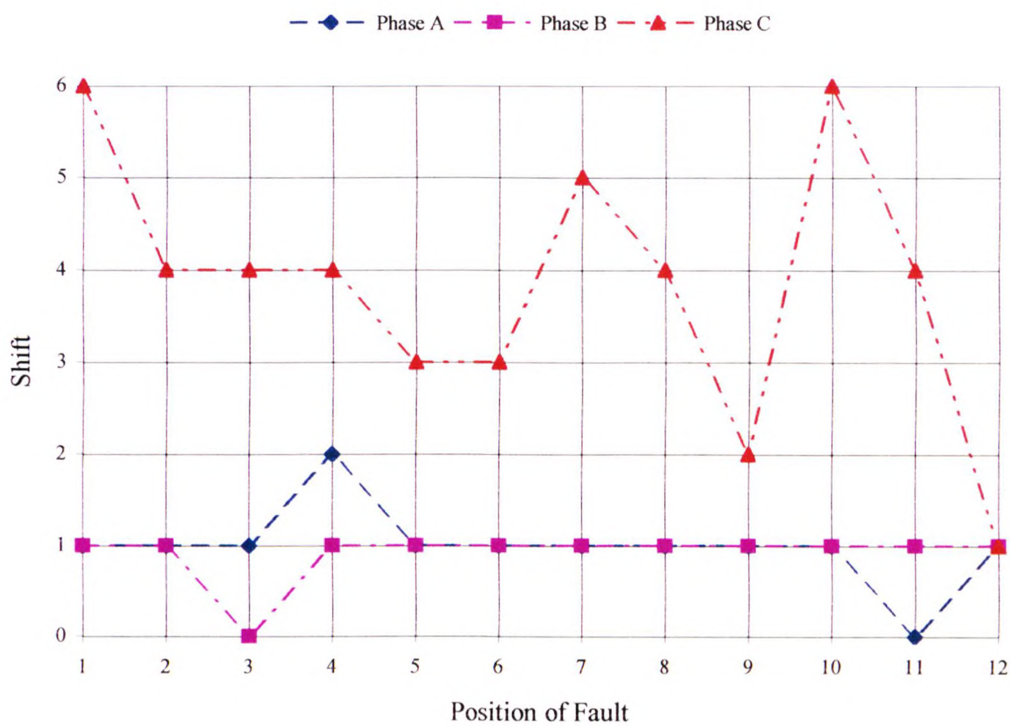

Figure [7.1.8] Correlation Shift, 75 Hz.

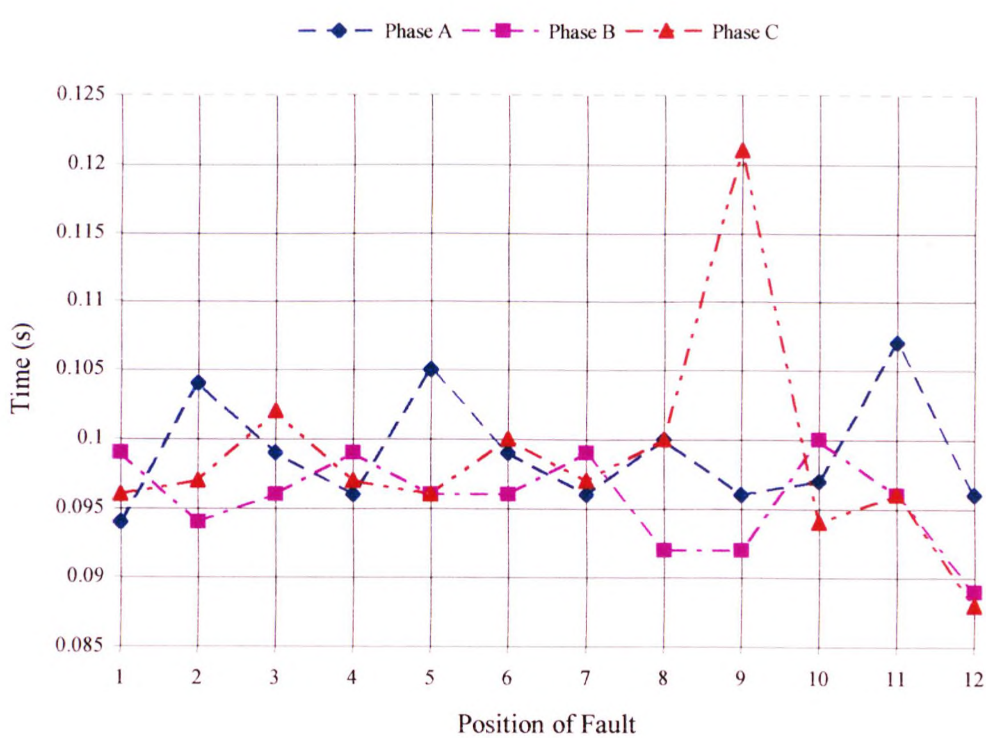

Figure [7.1.9] Time to First Peak, 100 Hz.

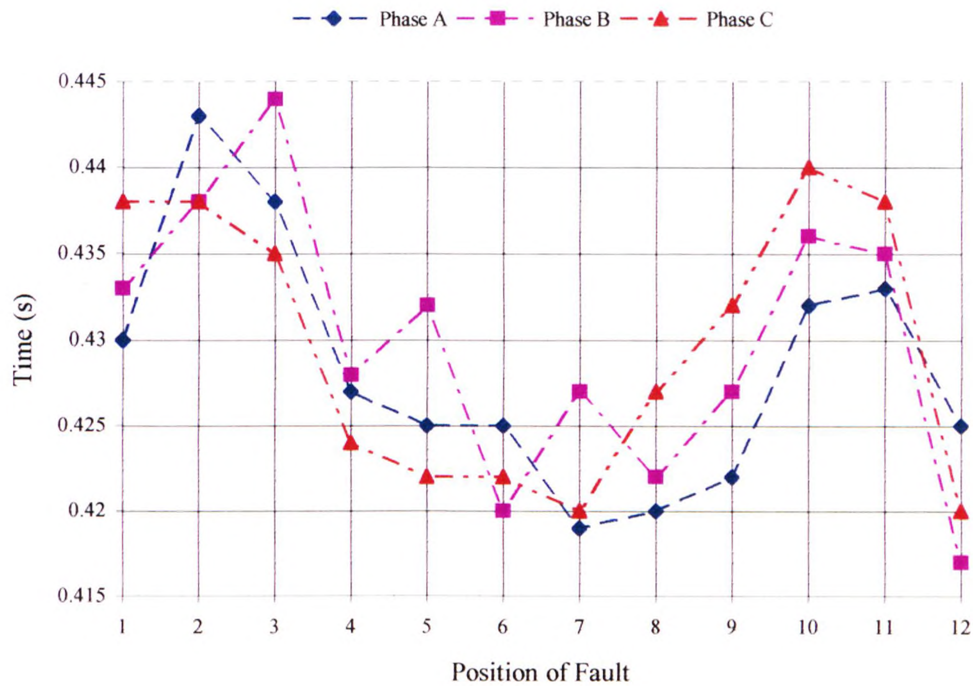

Figure [7.1.10] Time to Second Peak, 100 Hz.

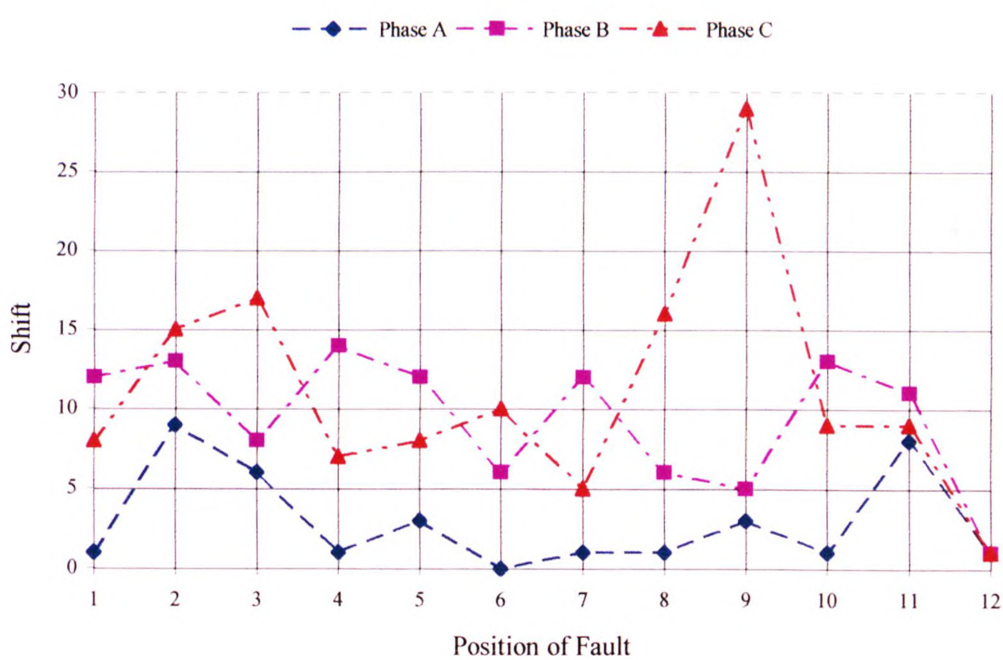

Figure [7.1.11] Correlation Shift, 100 Hz.

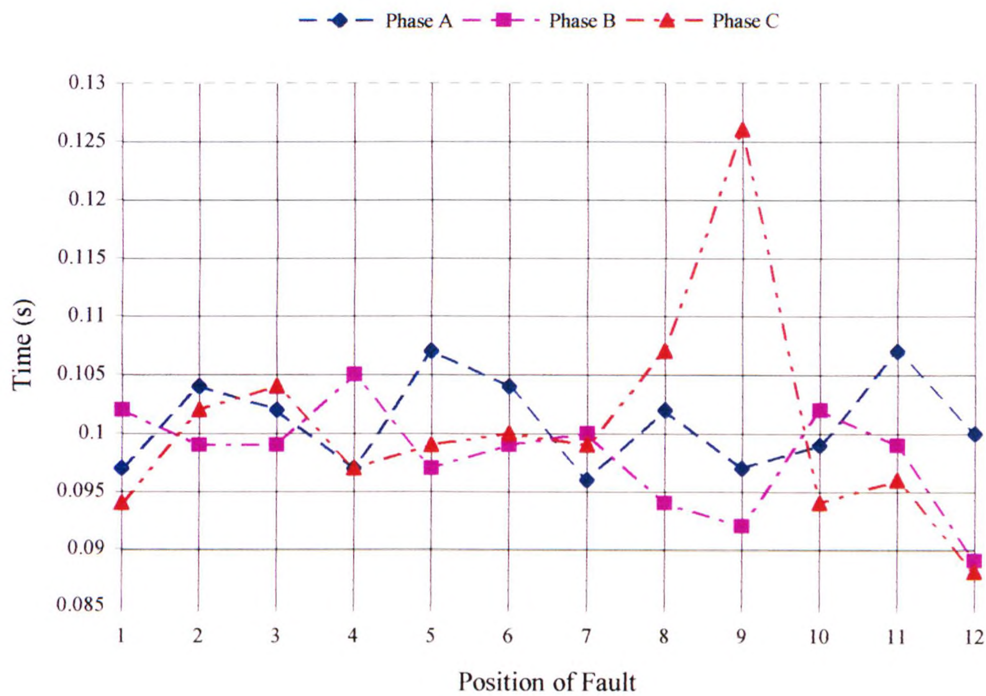

Figure [7.1.12] Time to First Peak, 100 Hz.

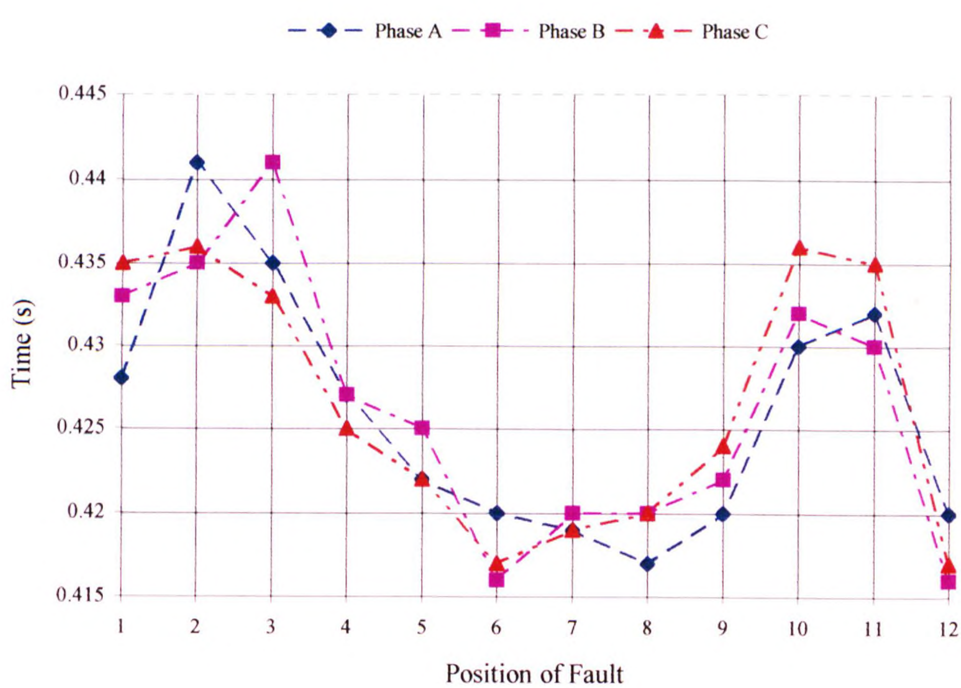

Figure [7.1.13] Time to Second Peak, 100 Hz.

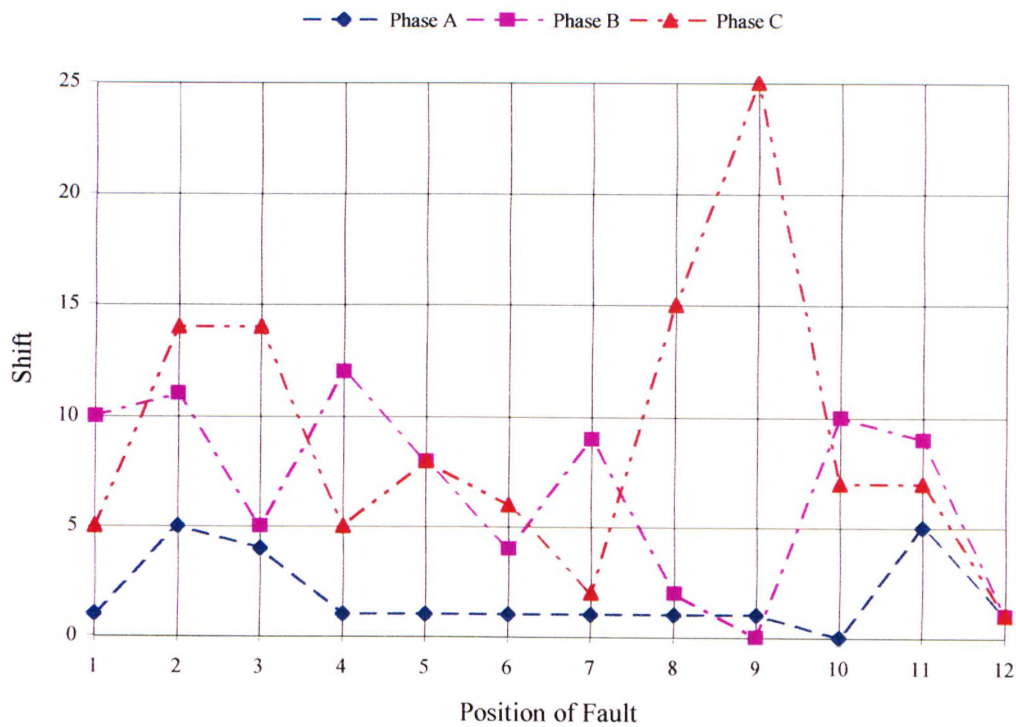

Figure [7.1.14] Correlation Shift, 100 Hz.

7.2 Pre-Filtering of Supply Current Signal

From the prediction of frequency components present within a typical transient current signal, Figure [2.3.3.1], it may be observed that in a relatively short period of time the slot harmonics travel well away from the fault frequency components. From this prediction it is observed that at lower values of slip and at frequencies greater than 100 Hz, the fault frequency components may be distinguishable from other frequency components. Since the large supply fundamental frequency component, 50 Hz, dominated the dynamic range of the data acquisition ADC, it was decided to pre-filter the transient signal prior to any analysis.

From the predicted data the pre-filter required was designed to be a high pass filter with a cut-off frequency higher than 100 Hz. Since the main operation of the filter would be to attenuate the large fundamental component, the designed filter would require a steep roll-off, together with a linear phase response over the frequency range of interest in order to minimise signal distortion.

Several types of filters were tested in order to observe their individual properties and to observe which would be the most favourable for this application. Due to the trade-off between roll-off and phase linearity, the pre-filter most suited to the requirements was found to be a four pole Bessel filter. The cut-off was designed to be 159 Hz with the amplitude response of the filter, Figure [7.2.1], showing that the filter reduces the fundamental frequency component by 26.6 dB. The phase response of the filter, Figure [7.2.2], was also found to be reasonably linear, being similar to a six pole Bessel phase response but slightly more linear.

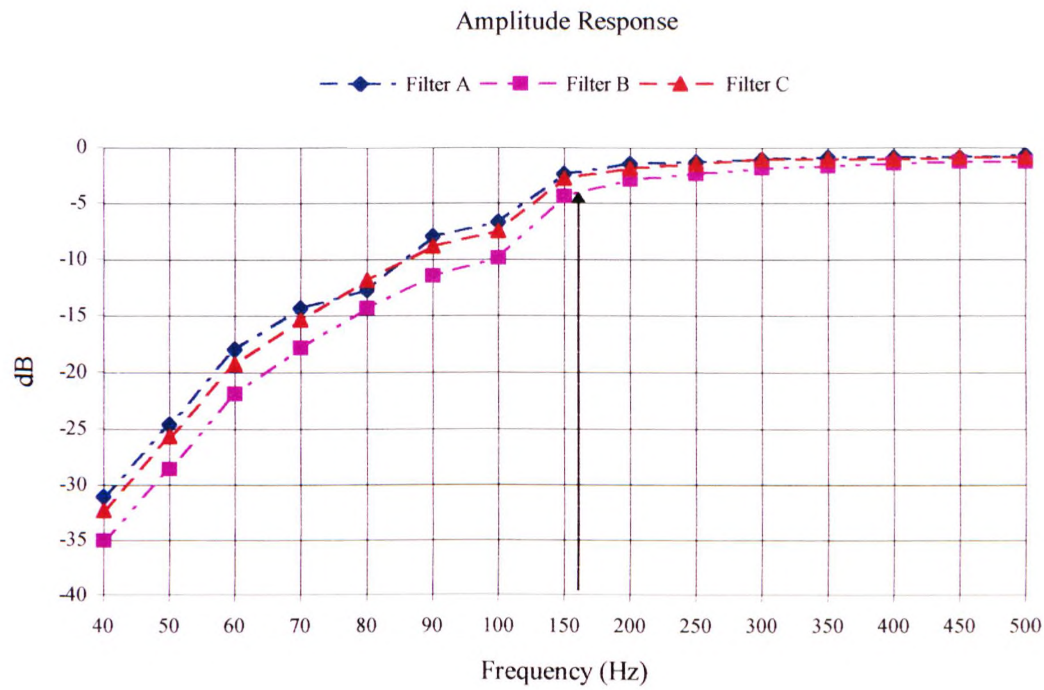

Figure [7.2.14] Pre-Filter Amplitude Response, Phases A,B,C.

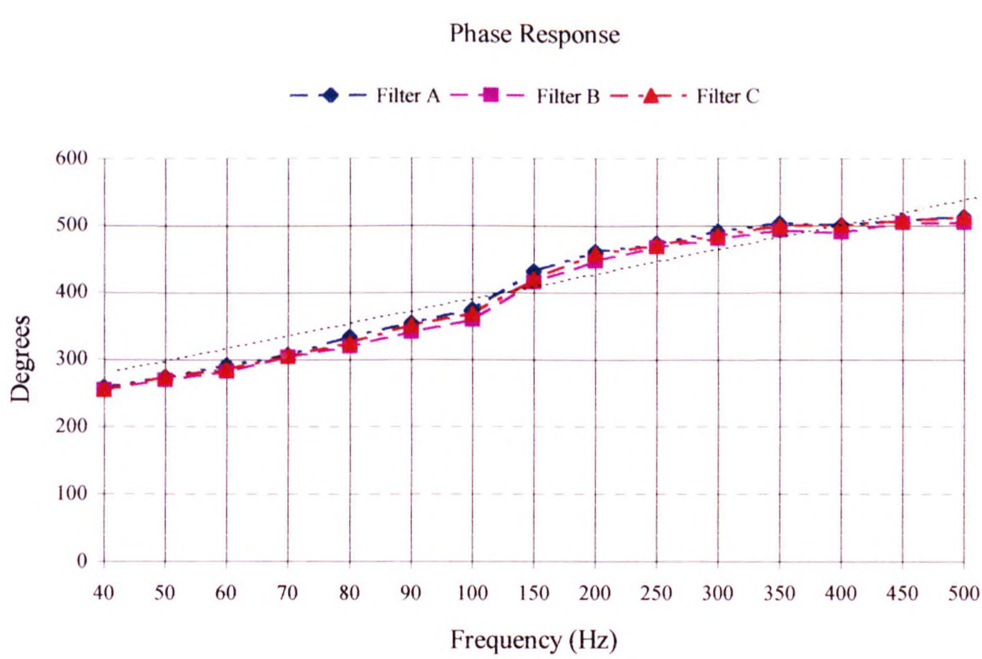

Figure [7.2.15] Pre-Filter Phase Response, Phases A,B,C.

7.3 Detection of Positional Components under Steady State Conditions

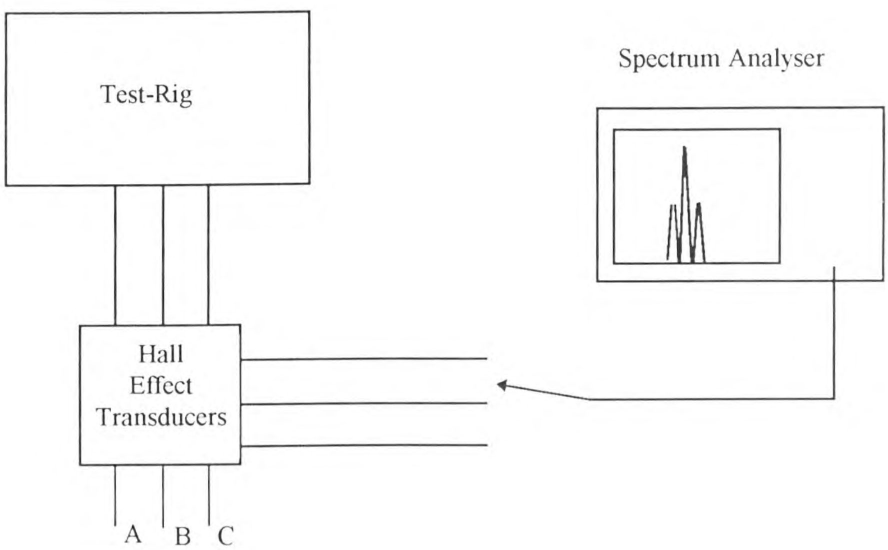

Figure [7.3.1] Steady State Monitoring Set-up.

Initial experiments to detect the positional components within the supply line current were carried out under steady state conditions. Using a Bruël & Kjær two channel spectrum analyser, the three individual phases of the motor supply current were monitored as shown in Figure [7.3.1].

Using eq. (1.3.1) the positional frequency components for the laboratory test-rig, running at a slip of 0.042 were computed. The slip of 0.042 representing a rotor speed of 1439 RPM, measured via a cogged wheel tachometer arrangement as shown within Figure [7.3.2]. The computed fault frequencies being listed within Table [7.3.1].

Using the Bruël & Kjær analyser in ZOOM mode, the frequency components listed within Table [7.3.1] were investigated in order to observe if these components did in fact exist within the current signal under steady state conditions.

The rotor had zero broken bars throughout these initial investigations. The results of a ZOOM spectrum analysis around the 5th and 7th harmonics are shown within Figure [7.3.3] to Figure [7.3.4]

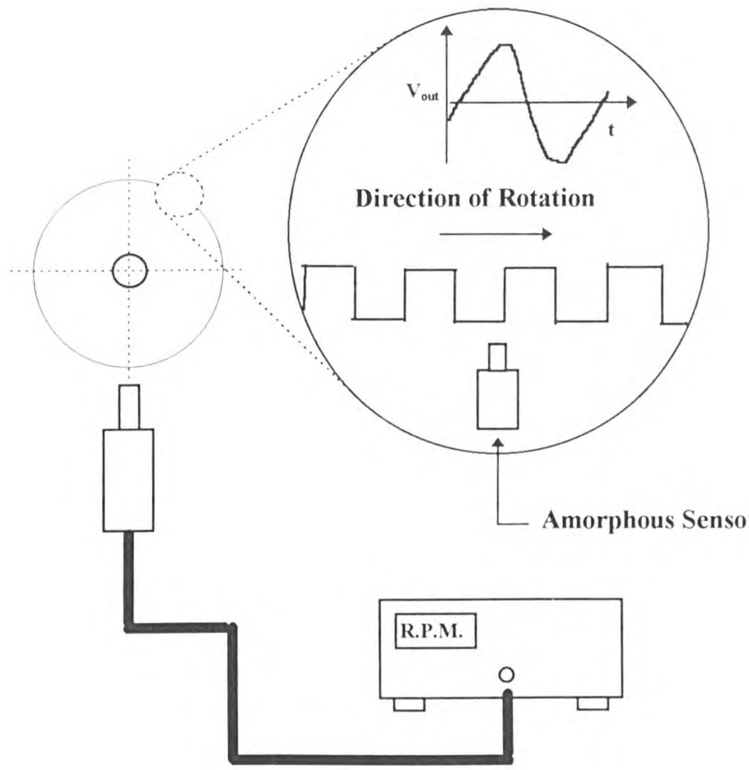

Figure [7.3.2] Analogue Magnetic Pick-up Tachometer.

Harmonic No.	Frequency (Hz)	Frequency (Hz)
1	21.85	26.05
3	69.75	73.95
4	93.70	93.70
5	117.65	121.85
7	165.55	169.75
11	261.35	265.55
13	309.25	313.45

Table [7.3.1] Predicted Positional Frequency Components.

respectively. From these results it is clearly observed that with this level of fault condition there is very little spectral content around the predicted frequency values.

A similar test was re-run using the same rotor, this time with a fault condition of two broken rotor bars. Again, the motor was run at full load, giving a slip of 0.042. The current signal was analysed after pre-filtering around the fault frequency components. The results of the ZOOM spectrums upon the 5th and 7th harmonics may be seen in Figure [7.3.5] and Figure [7.3.6] respectively. Table [7.3.3] shows the dB levels of the components under this fault condition. From these results it is clear that with the introduction of the fault condition, frequency components do become more prominent around the predicted frequency values.

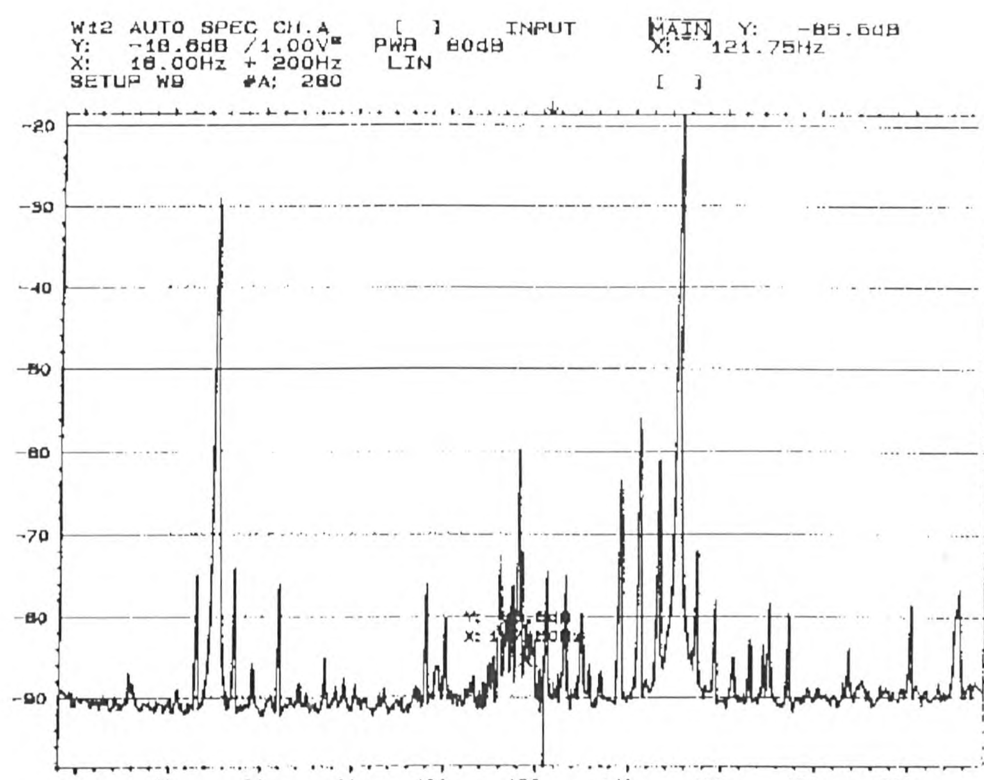

Figure [7.3.3] Zoom Spectrum 5th Harmonic - Zero Broken Bars.

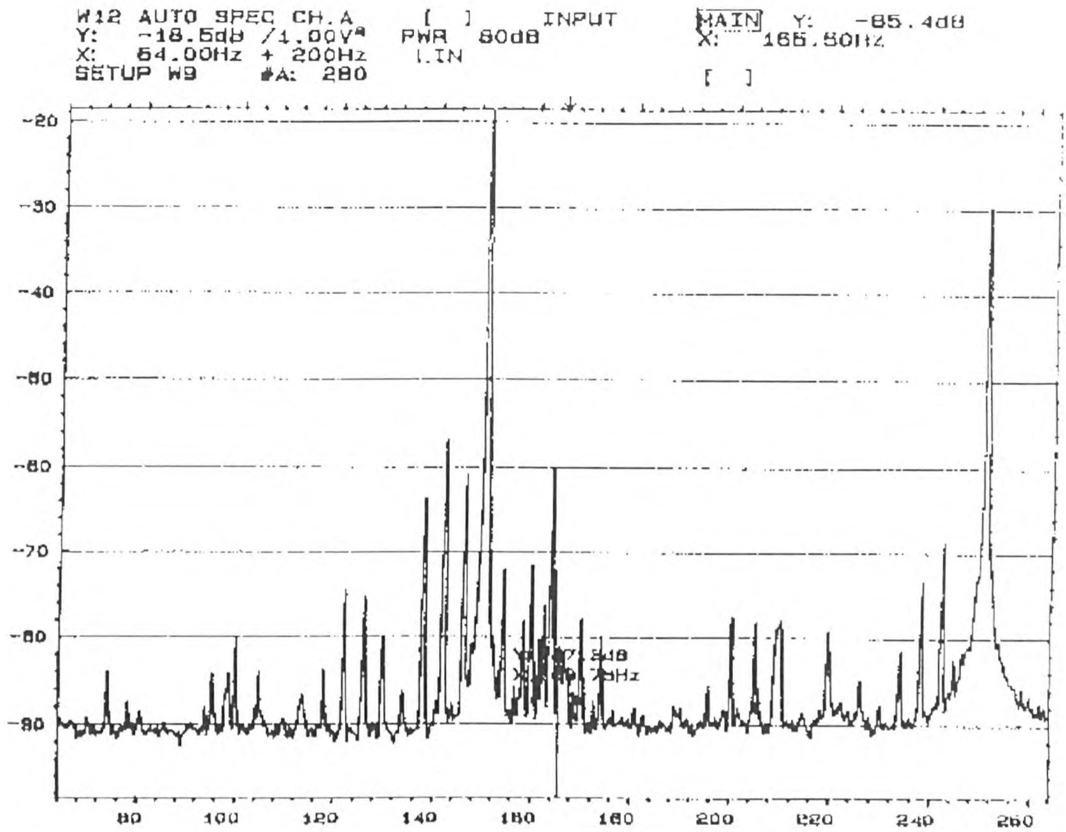

Figure [7.3.4] Zoom Spectrum 7th Harmonic - Zero Broken Bars.

Frequency (Hz)	dB
117.65	-85.5
121.85	-85.6
165.55	-85.4
169.75	-87.3

Table [7.3.2] dB Levels at Predicted Frequencies - Zero Broken Bars.

Frequency (Hz)	dB
117.65	-70.7
121.85	-63.5
165.55	-63.3
169.75	-65.9

Table [7.3.3] dB Levels at Predicted Frequencies - Two Broken Bars.

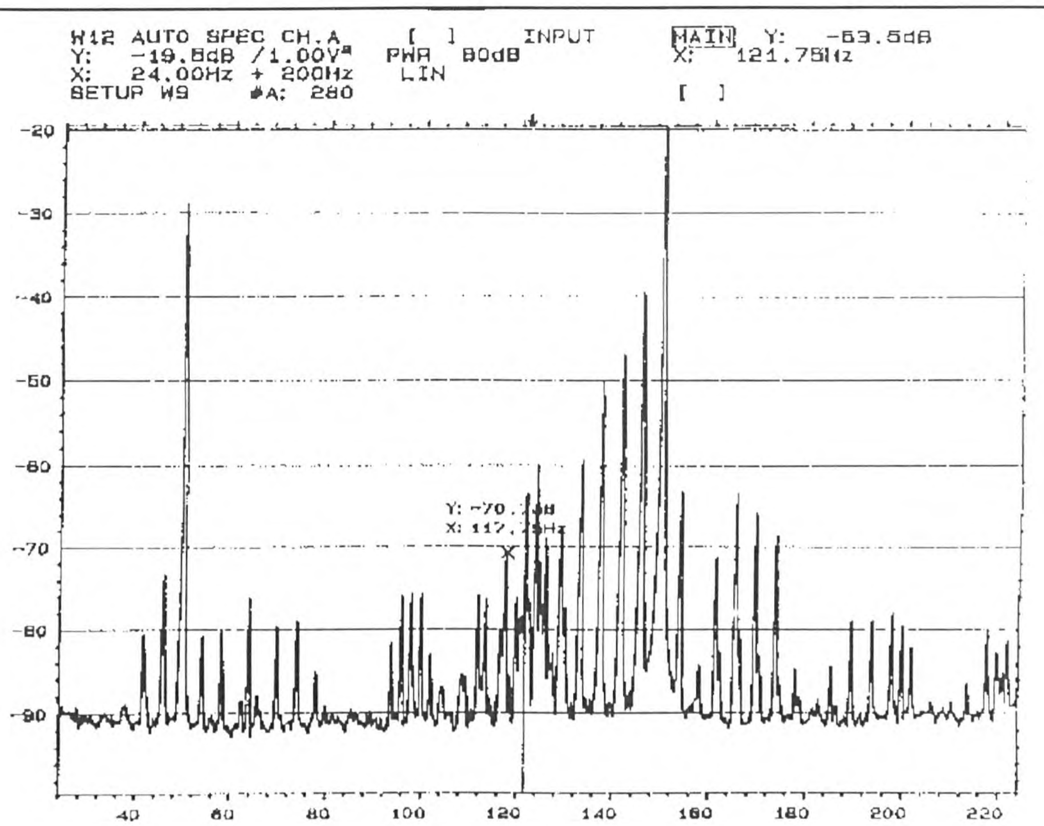

Figure [7.3.5] Zoom Spectrum 5th - Two Broken Bars.

Harmonic No.	dB
5	14.8
7	22.1
11	0.3
13	0.3

Table [7.3.4] dB Level Increase with Fault Condition.

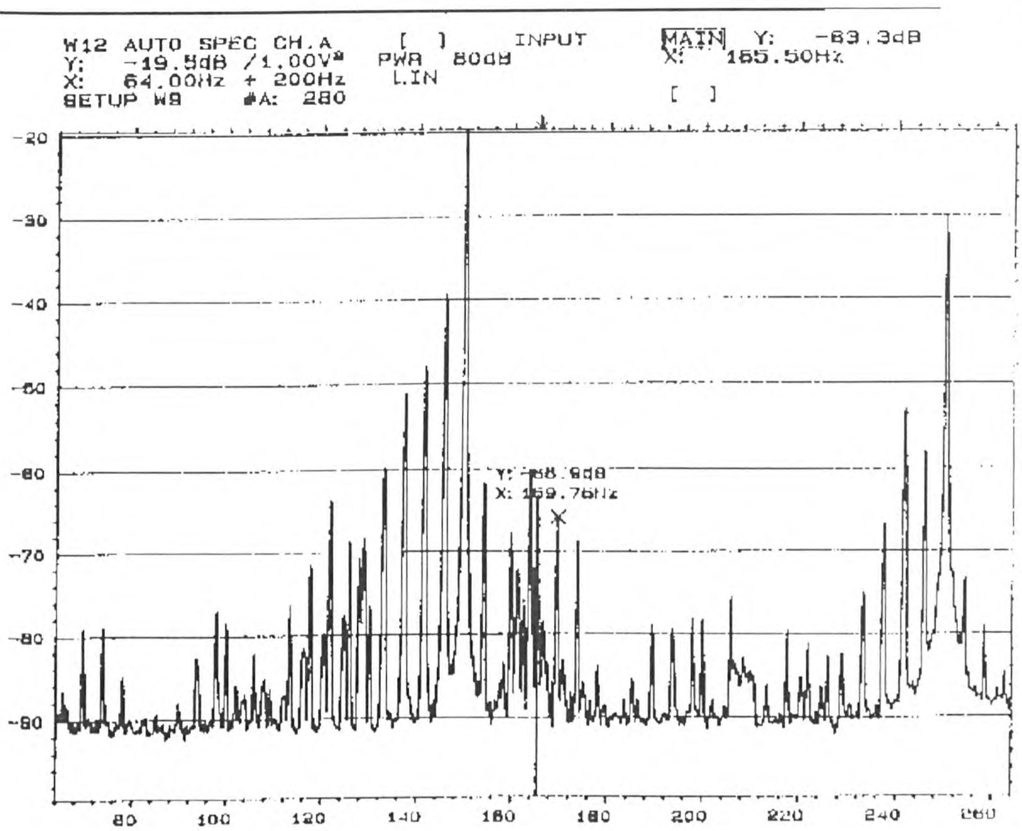

Figure [7.3.6] Zoom Spectrum 7th - Two Broken Bars.

Table [7.3.4] shows the increase in dB levels of the rotor fault frequency components as a result of the introduction of broken rotor bars during steady state operation. From Table [7.3.4] it is clear that the magnitude of the 7th harmonic shows the greatest increase with the presence of broken rotor bars.

The results of these investigations and others using different harmonics of the rotor fault components confirm the theory that with an unfaulted rotor the components are not visible within the steady state spectrum of the supply current. With the introduction of two broken bars the components can clearly be observed, however. It was found that certain harmonics of the components were more responsive to the introduction of faults than others. In particular the 7th harmonic was found to show the greatest change in magnitude with the fault condition of two broken bars, whereas with a rotor containing a group of ten broken bars, the 5th harmonic was found to be the most sensitive.

The steady state investigations of these frequency components clearly verifies that fault frequency components do exist when the rotor contains an asymmetry.

7.4 Location of Stator Coil Slots within SCIM

As the individual phase coils were to be used as a reference location for the rotor bar position, the location of the individual coils were required to be found. A winding diagram for the test-rig was not available however, hence the following tests were carried out in order to determine the locations of the individual coils within the stator core.

The three phase, 11 kW, 51 slot rotor was initially removed from the test-rig in order to gain access to the stator coils. Using a Gauss meter background readings of the flux levels surrounding the 36 windings of the stator were initially obtained. These ambient readings being presented within Figure [7.4.1].

A small AC current was passed through one particular coil of the 'A' phase winding, Figure [7.4.2]. The value of current being 1.8 A. The voltage which drove this current was 20 V obtained from a 3 A Variac. The readings obtained from the Gauss meter are listed in Figure [7.4.3]. The coil which was first investigated here was the first coil within the red phase winding, namely coil s1 - e1.

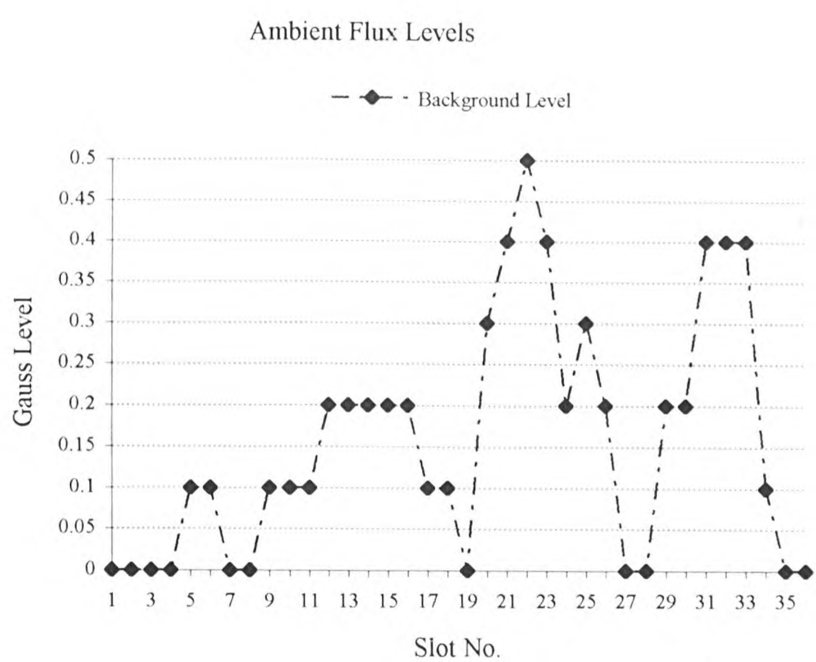

Figure [7.4.1] Ambient Flux Levels.

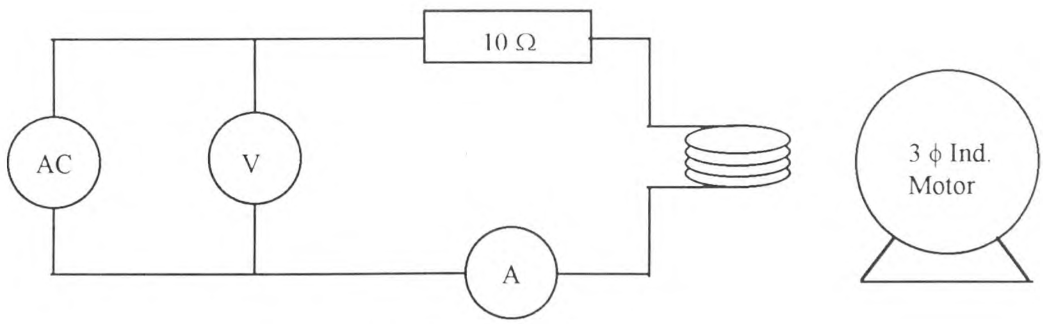

Figure [7.4.2] Simple AC Search Circuit.

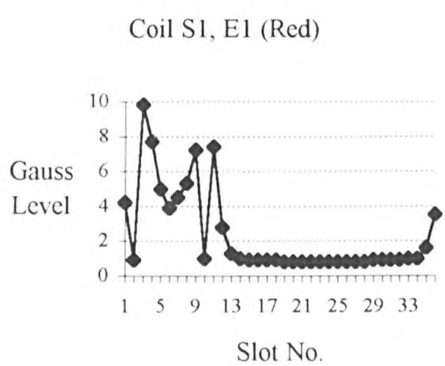

Figure [7.4.3] Gauss Meter Readings, Coil S1 - E1 / Red.

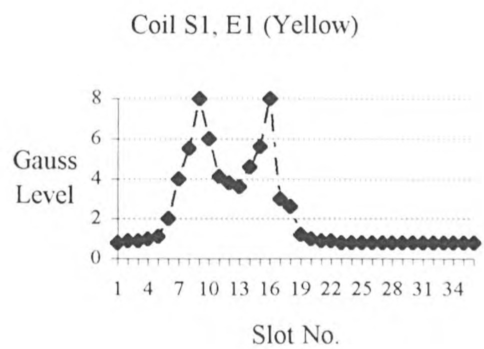

Figure [7.4.4] Gauss Meter Readings, Coil S1 - E1 / Yellow.

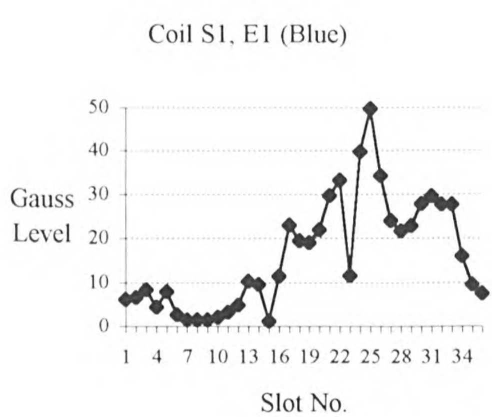

Figure [7.4.5] Gauss Meter Readings, Coil S1 - E1 / Blue.

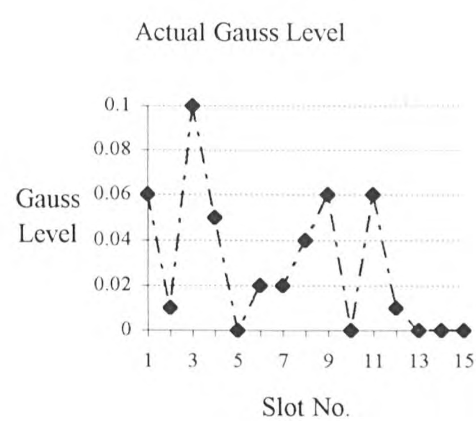

Figure [7.4.6] Actual Gauss Level Readings, Coil S1 - E1 / Red.

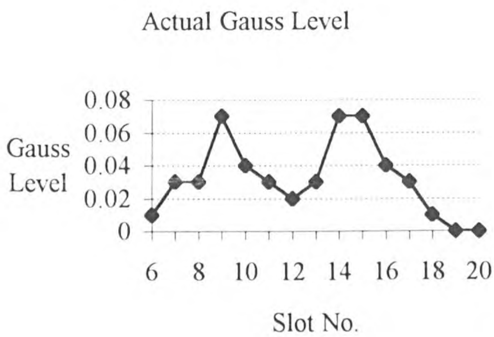

Figure [7.4.7] Actual Gauss Level Readings - Coil S1, E1 / Yellow.

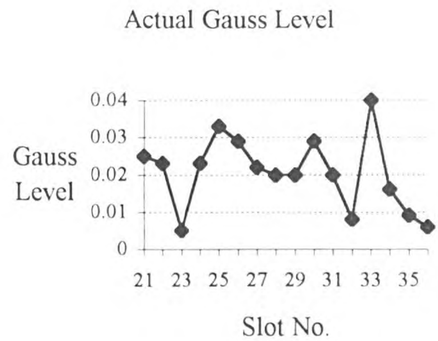

Figure [7.4.8] Actual Gauss Level Readings - Coil S1, E1 / Blue.

Similarly results were obtained from coils in both Yellow and Blue windings. Results of which are shown in Figure [7.4.4] to Figure [7.4.5]. Finally, the results presented within Figure [7.4.6] through to Figure [7.4.8] show adjusted results after compensation for ambient readings and an increased scale within the Gauss meter. From these results, Figure [7.4.3] through to Figure [7.4.8], the following approximation, Figure [7.4.9], may be made on the stator winding layout for the SCIM test-rig.

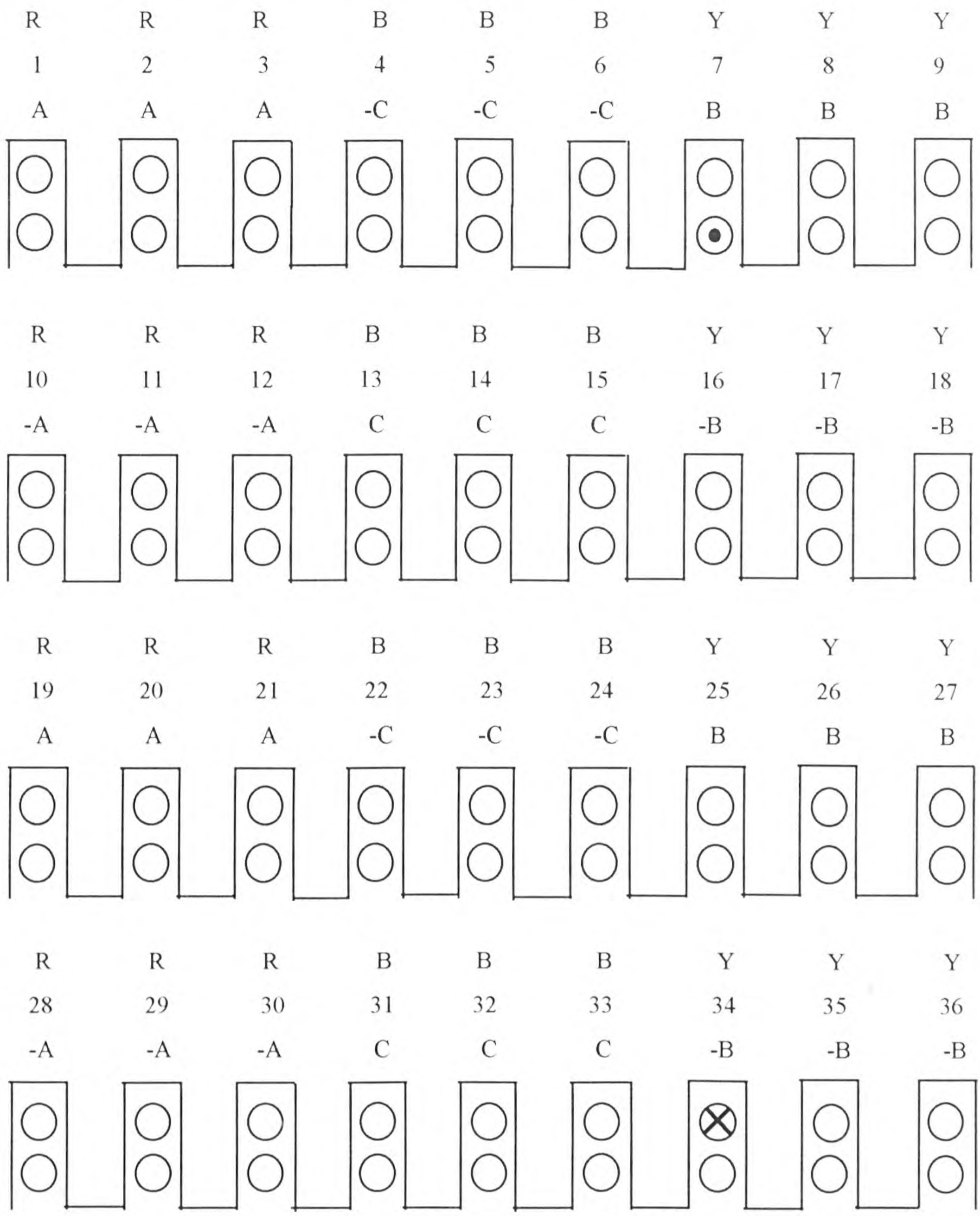

Figure [7.4.9] Laboratory Based SCIM Stator Winding Layout.

7.5 Location of Fault Positional Components

In order to identify the fault location frequency components within the supply current transient signal the frequency range of the decomposition analysis, see Chapter 4, was altered to span the region 90 to 140 Hz. The result of the analysis is shown in Figure [7.5.1]. From the prediction of the fault location frequency components, Figure [2.3.3.1], it may be observed that the main component to be observable in this range is the Upper Sideband. From the results of the scan it may be seen that this is in fact true, with frequency components clearly being observed moving back within frequency, i.e. component 'A'.

Shifting the frequency range of the analysis to that of 125 to 175 Hz, Figure [7.5.2], results in a scan which clearly shows two main frequency components. Component 'A' travels back within frequency and is therefore a harmonic of the Upper Sideband and component 'B', is a group of frequencies which contains either the 11th or 13th harmonics of the fault positional component. This assumption being made due to the fact that the component is in the correct location at the correct time for these components to be in existence.

Figure [7.5.3] shows the result of a further analysis, this time with a frequency range of 170 to 270 Hz. In this analysis there are three points to note. Firstly component 'A', from Figure [2.3.3.1] the prediction suggests that this component is the group of frequencies which contain the mixture of the 11th and 13th harmonics of the fault positional component. This being the same group as component 'B' within Figure [7.5.2]. Secondly, component 'B' of Figure [7.5.3], from Figure [2.3.3.1] the prediction suggests that this is the group of frequencies which contains the 13th harmonic of the positional fault component. Finally, component 'C' which from Figure [7.5.3] can be seen to be stationary. This component, situated at 250 Hz, represents a harmonic of the fundamental supply frequency.

In the above analyses there has been no mention of the Principal Slot Harmonics which from the prediction, Figure [2.3.3.1], may be seen to obtain high values of frequency within a relatively short period of time at the onset of the transient.

An analysis was executed around the range of 185 to 235 Hz. The result of the analysis may be seen in Figure [7.5.4]. Only a small section at the start of the transient has actually been analysed so that the larger components which occur later within the transient do not smother the smaller Principal Slot

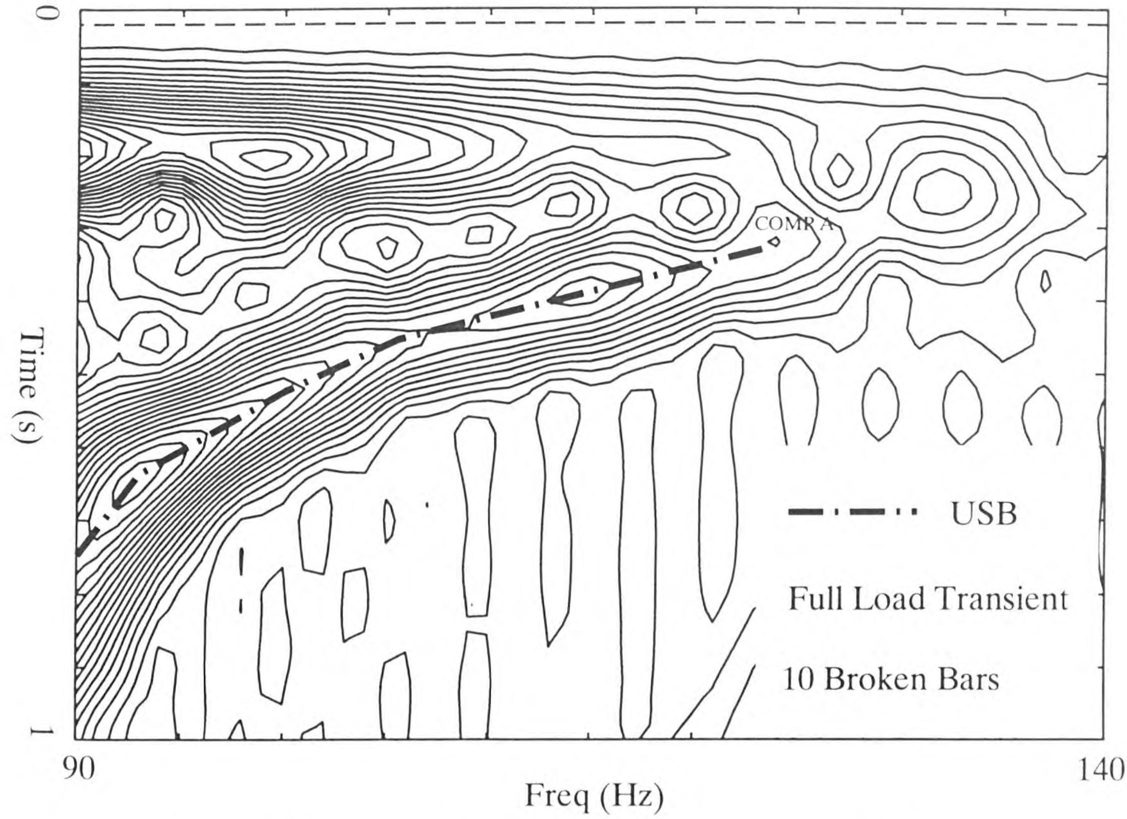

Figure [7.5.1] Contour Plot of Transient Decomposition, 90 - 140 Hz.

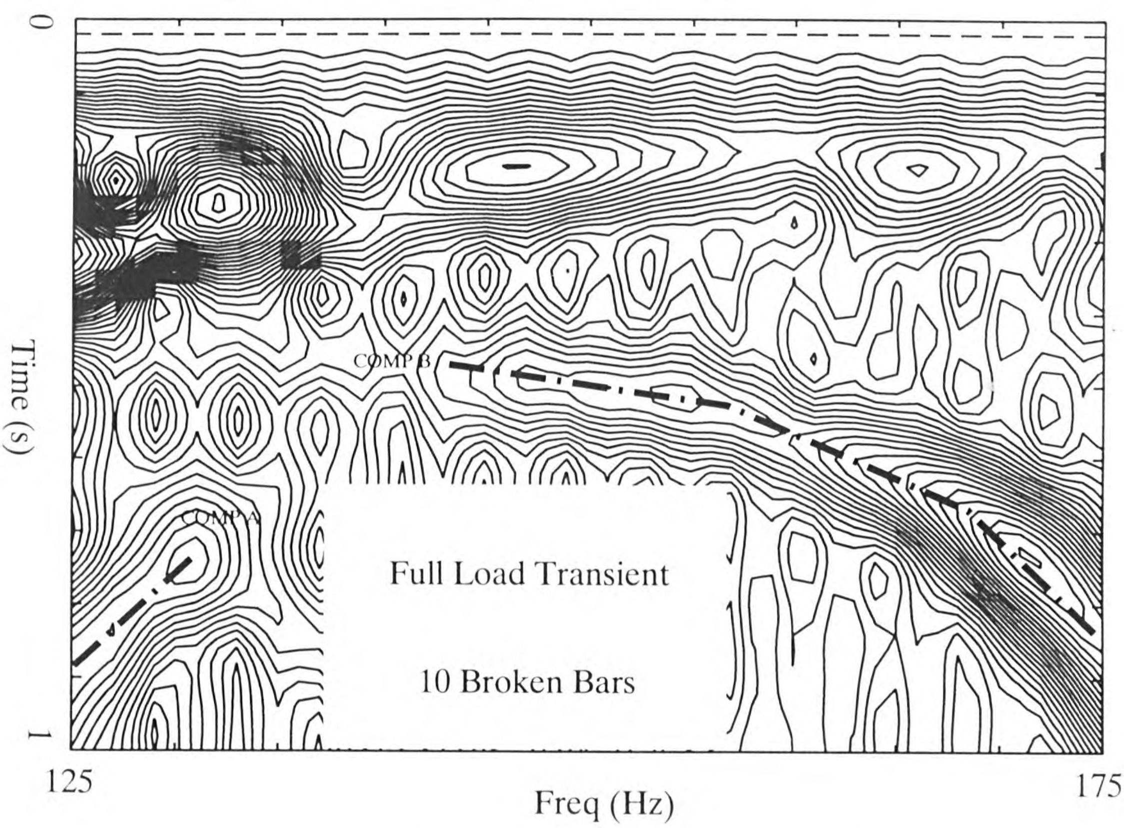

Figure [7.5.2] Contour Plot of Transient Decomposition, 125 - 175 Hz.

Harmonics. Figure [7.5.4] shows the travelling frequency component which tends to peak at various intervals throughout the transient.

The pre-filtered supply current signal from the laboratory test-rig with a two broken bar rotor, previously analysed within steady state, then had its transient signal analysed. This analysis was completed over the frequency range 170 to 270 Hz and may be seen in Figure [7.5.5].

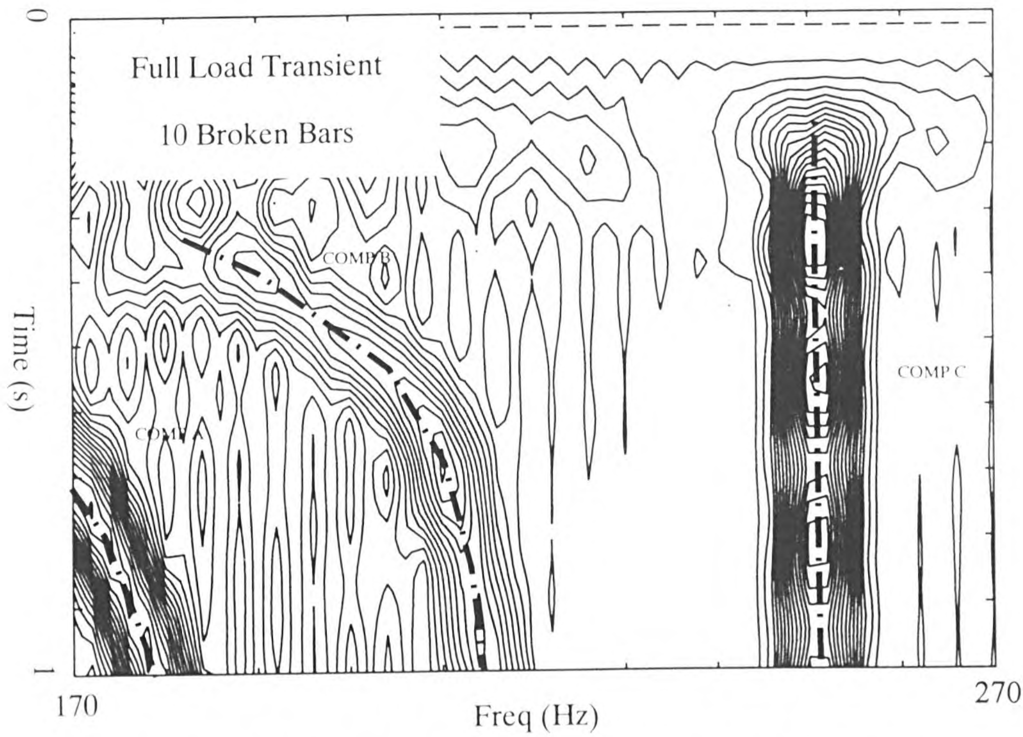

Figure [7.5.3] Contour Plot of Transient Decomposition, 170 - 270 Hz.

From the prediction within Figure [2.3.3.1] the components which should be present within this analysis are the group of frequencies which contain the 13th harmonic of the fault location frequency components and the 150 Hz harmonic of the fundamental supply frequency. From Figure [7.5.5] these components 'A' and 'B' respectively may clearly be observed.

In order to verify that the components being detected in the above analyses were related to the fault location components, and not the Principal Slot Harmonics, which from the prediction within Figure [2.3.3.1] could be the case, an analysis was completed upon a full load transient from the same test-rig as above with a fault condition of ten broken bars present within the rotor, Figure [7.5.6]. If the components previously located were the Principal Slot Harmonics then they would be present within the time-frequency analysis of a transient from the motor with a zero broken bar condition, Figure

[7.5.7]. A comparison between the two analysis results clearly shows the lack of components within the fault free condition, thus proving that the components detected under the fault condition were not related to the Principal Slot Harmonics.

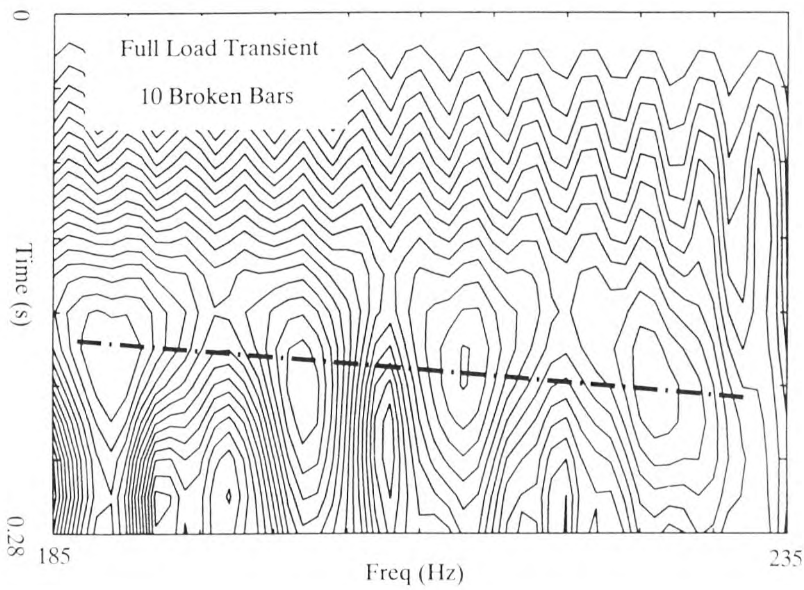

Figure [7.5.4] Contour Plot of Transient Decomposition, 185 - 235 Hz.

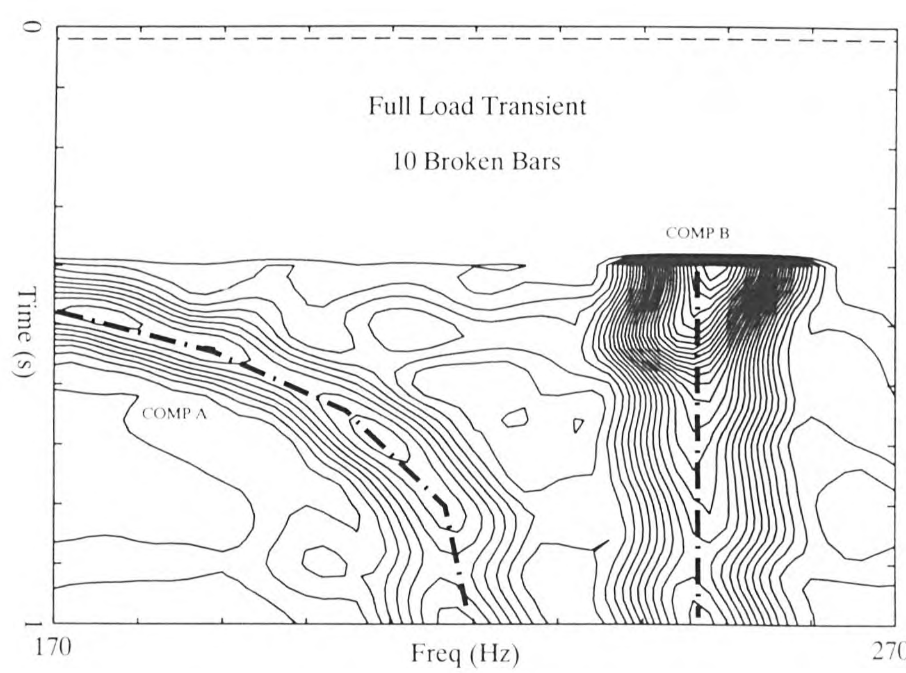

Figure [7.5.5] Contour Plot of Transient Decomposition, 170 - 270 Hz.

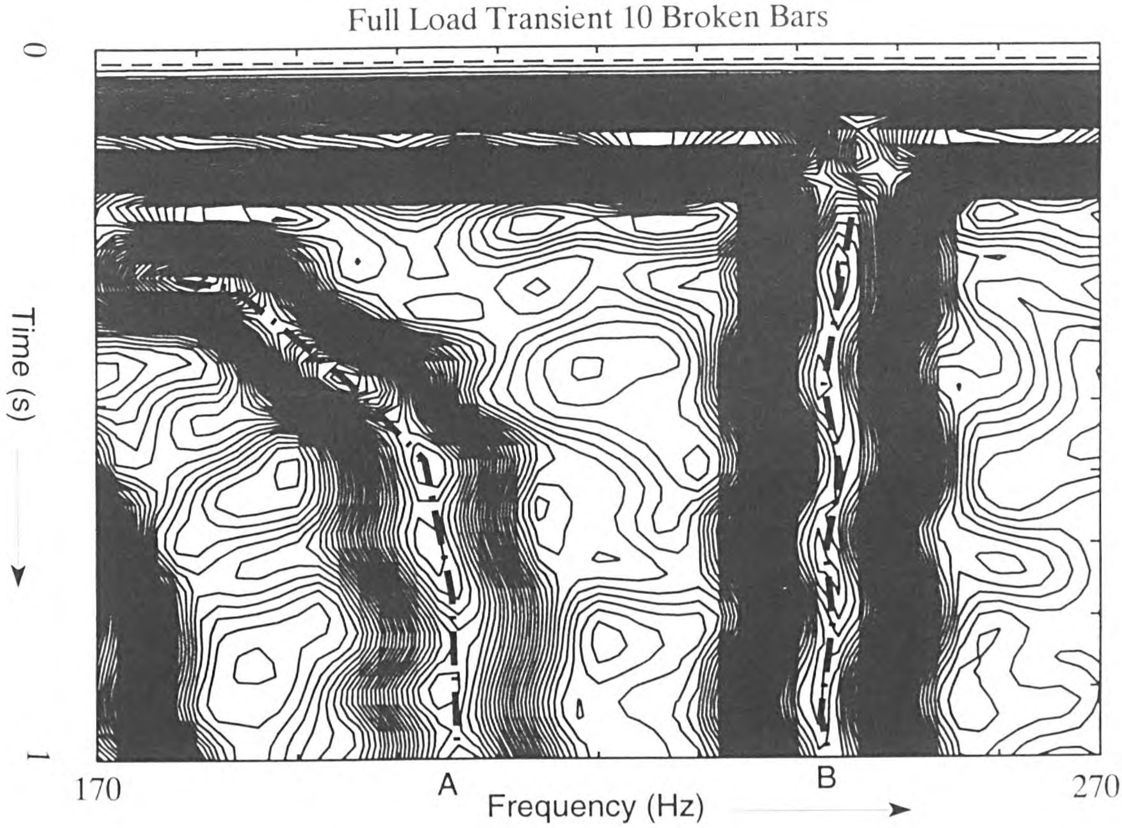

Figure [7.5.6] Transient Decomposition, 10 Broken Rotor Bars.

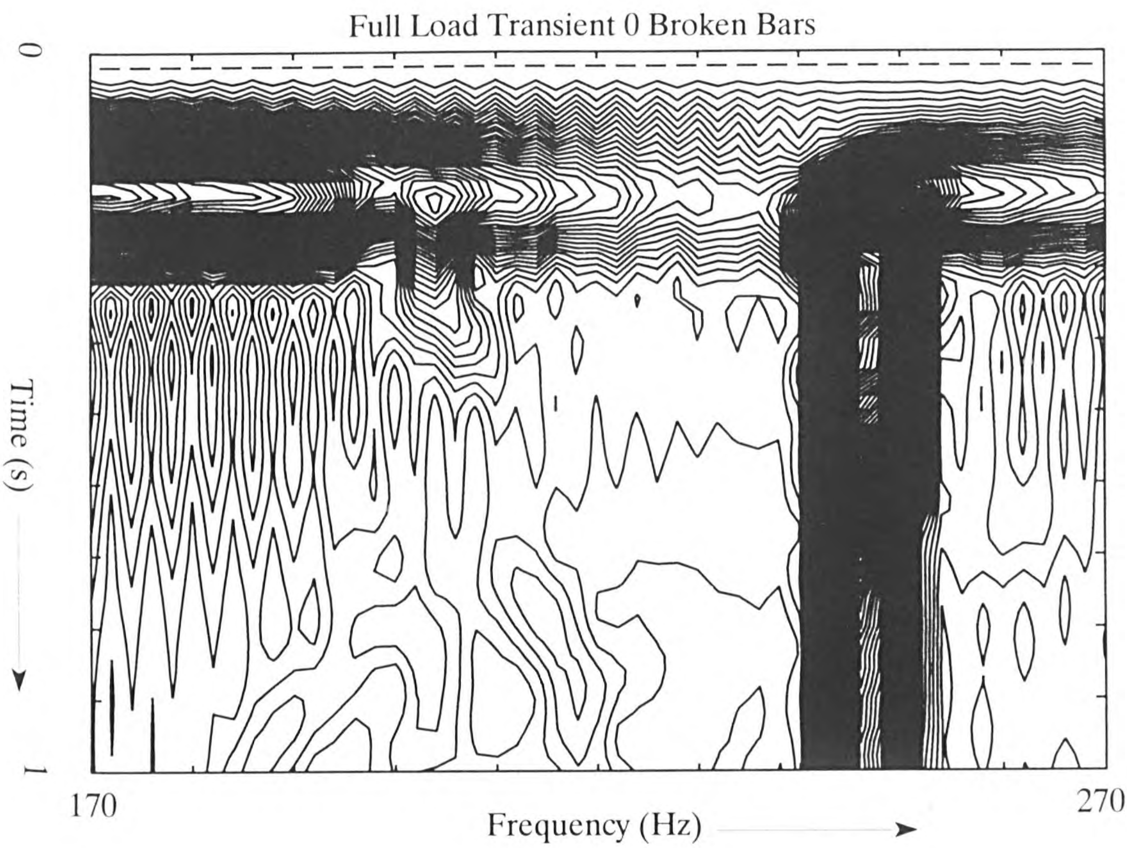

Figure [7.5.7] Transient Decomposition, 0 Broken Rotor Bars.

7.6 Detection of Fault Location Frequency Components

As a means to isolate the fault components which are indicative of cage rotor faults a series of tests were undertaken in order to obtain any correlation between the location of the cage rotor fault and the occurrence of peaks within a signal filtered at specific fault frequencies. The tests involved the recording of peak times within the filtered transient for varying locations of rotor fault upon start-up. The location of the cage rotor fault was varied at start-up in order to allow the fault to be in different locations when the relevant fault frequency occurred, thus simulating a cage rotor with varying fault location. After plotting the various timings of the relevant peaks within the filtered signals, investigations proceeded to detect the areas within the transients where either the 5th, 7th, 11th or 13th harmonic of the fault component could be sufficiently separated in terms of original start-up position. All transient signals were pre-filtered and synchronised. All tests were carried out under full load, ten broken bar conditions in order to amplify any fault effect to a maximum.

7.6.1 5th Harmonic

If the frequencies which make up the 5th harmonic of the fault frequency component are considered, Figure [7.6.1.1] through to Figure [7.6.1.6], then it may be observed that a form of separation may be obtained between the fault locations, particularly within Figure [7.6.1.2] (90 Hz), Figure [7.6.1.3] (95 Hz), Figure [7.6.1.4] (110 Hz), Figure [7.6.1.5] (116.3 Hz) and Figure [7.6.1.5] (121.3 Hz). Figure [7.6.1.7] shows the timing order of the fault locations from the above filter outputs. This was plotted as a means of detecting some form of relationship between the peak occurrence within the transient and fault location upon start-up.

7.6.2 7th Harmonic

Figure [7.6.2.1] through to Figure [7.6.2.6] summarises the results obtained by filtering for the 7th harmonic components. From these results it may be observed that Figure [7.6.2.1] (96.3 Hz), Figure [7.6.2.2] (130 Hz), Figure [7.6.2.3] (131.3 Hz), Figure [7.6.2.4] (150 Hz), Figure [7.6.2.5] (163.8 Hz) and Figure [7.6.2.6] (168.8 Hz) show significant signs of separation between fault locations. Figure [7.6.2.7] reports the order at which the fault locations are found to occur. From this it may be observed that the majority of filter frequencies have a certain order with the best coming from the filter frequencies of 130 and 131.3 Hz.

7.6.3 11th Harmonic

Similar tests were carried out upon the 11th harmonic frequencies, Figure [7.6.3.1] through to Figure [7.6.3.6]. Out of the frequency values tested separation was found to be present within Figure [7.6.3.1] (145 Hz), Figure [7.6.3.2] (185 Hz), Figure [7.6.3.3] (210 Hz), Figure [7.6.3.6] (258 Hz) and Figure [7.6.3.6] (263.8 Hz). The orders of occurrence may be seen in Figure [7.6.3.7].

7.6.4 13th Harmonic

With the 13th harmonic, Figure [7.6.4.1] through to Figure [7.6.4.6], separation may be observed within Figure [7.6.4.1] (175 Hz), Figure [7.6.4.3] (250 Hz), Figure [7.6.4.4] (270 Hz), Figure [7.6.4.5] (306.3 Hz) and Figure [7.6.4.6] (311.3 Hz). Figure [7.6.4.7] shows the occurrence of these components.

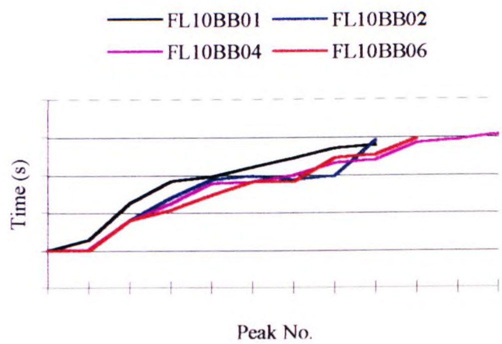

Figure [7.6.1.1] 55 Hz Filter Output Timing (5th).

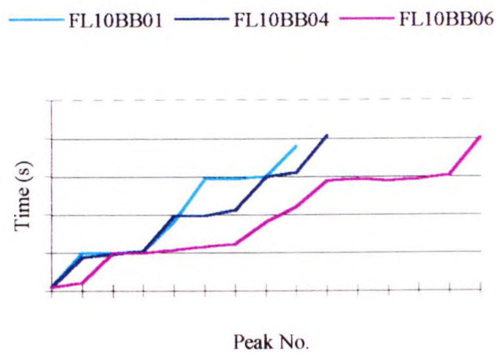

Figure [7.6.1.2] 90 Hz Filter Output Timing (5th).

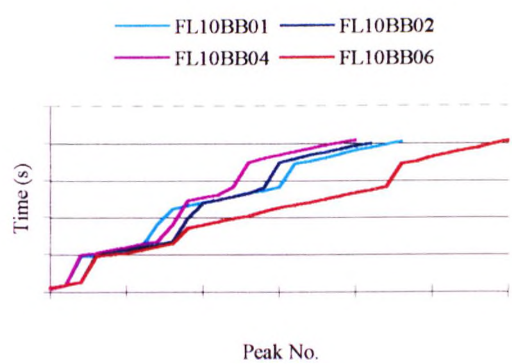

Figure [7.6.1.3] 95 Hz Filter Output Timing (5th).

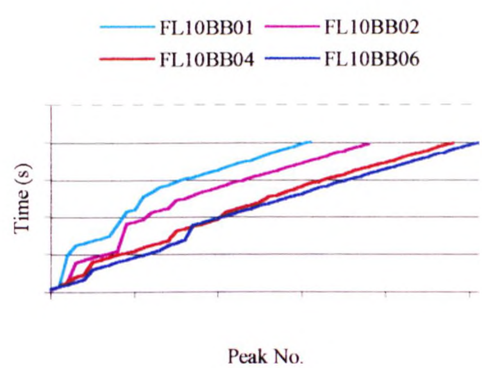

Figure [7.6.1.4] 110 Hz Filter Output Timing (5th).

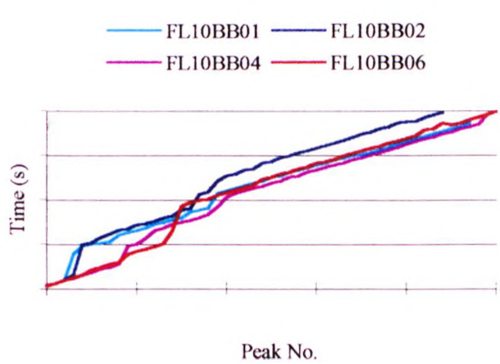

Figure [7.6.1.5] 116.3 Hz Filter Output Timing (5th).

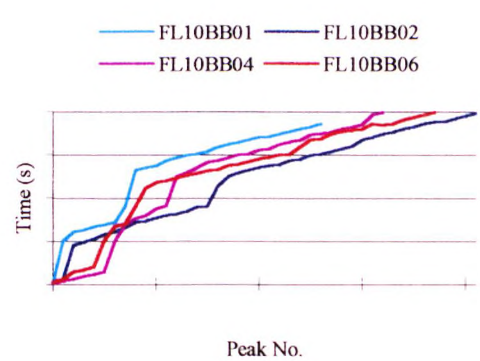

Figure [7.6.1.6] 121.3 Hz Filter Output Timing (5th).

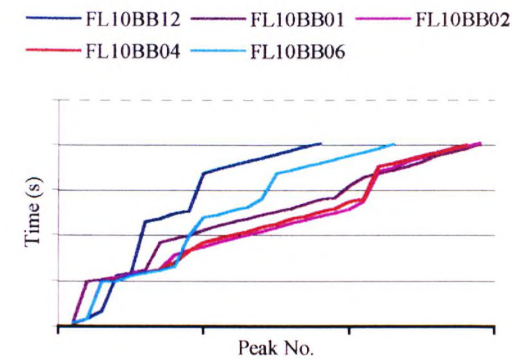

Figure [7.6.2.1] 96.3 Hz Filter Output Timing (7th).

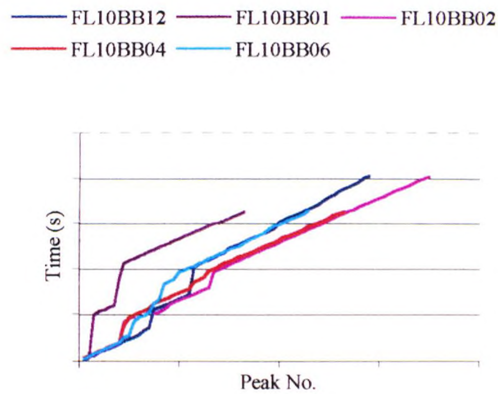

Figure [7.6.2.2] 130 Hz Filter Output Timing (7th).

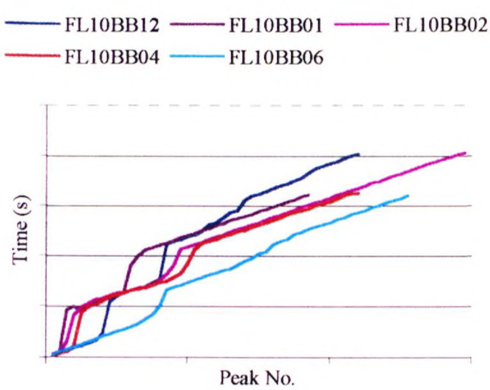

Figure [7.6.2.3] 131.3 Hz Filter Output Timing (7th).

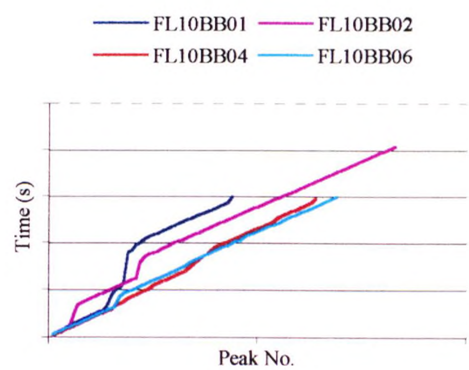

Figure [7.6.2.4] 150 Hz Filter Output Timing (7th).

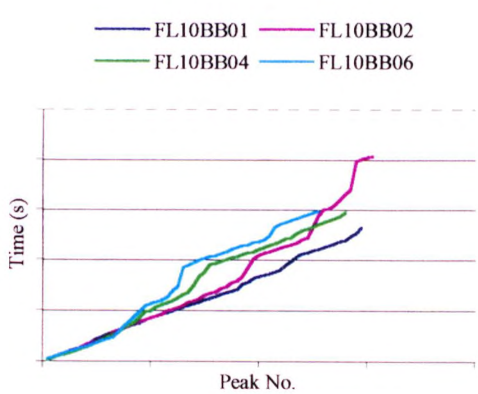

Figure [7.6.2.5] 163.8 Hz Filter Output Timing (7th).

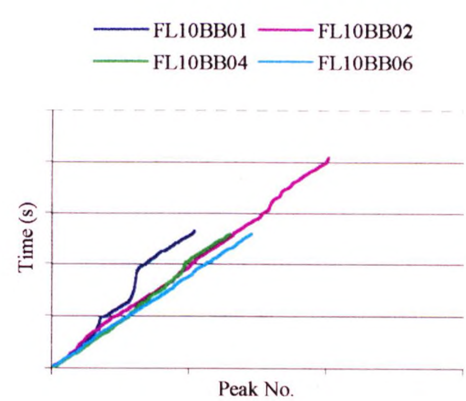

Figure [7.6.2.6] 168.8 Hz Filter Output Timing (7th).

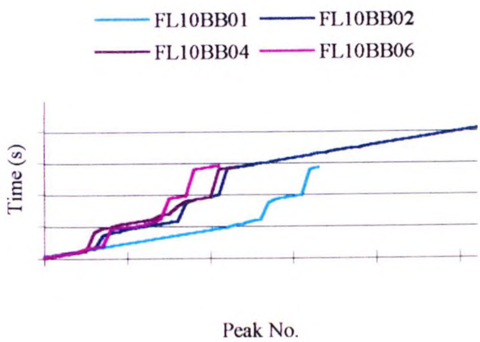

Figure [7.6.3.1] 145 Hz Filter Output Timing (11th).

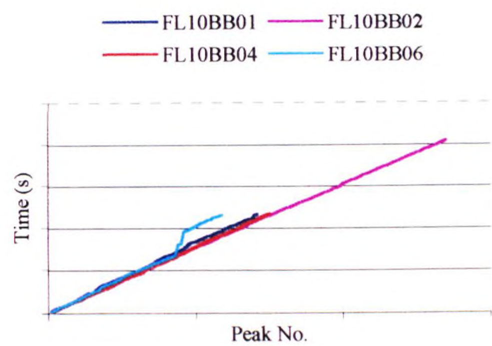

Figure [7.6.3.2] 185 Hz Filter Output Timing (11th).

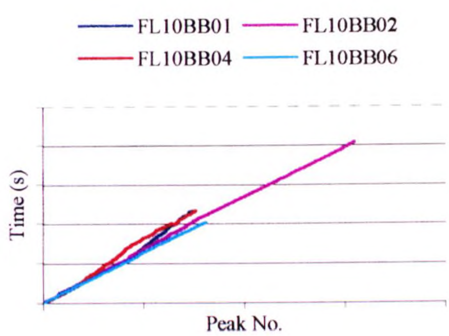

Figure [7.6.3.3] 210 Hz Filter Output Timing (11th).

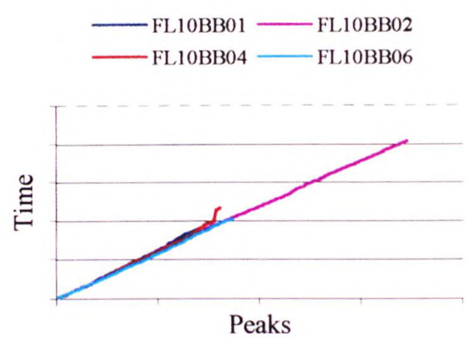

Figure [7.6.3.4] 230 Hz Filter Output Timing (11th).

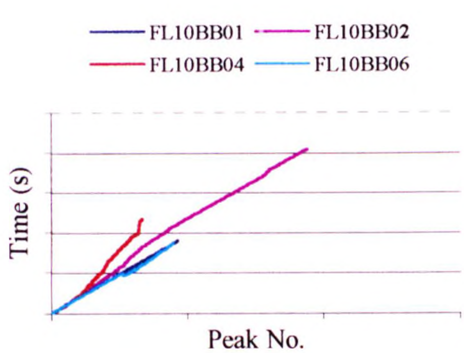

Figure [7.6.3.5] 258.8 Hz Filter Output Timing (11th).

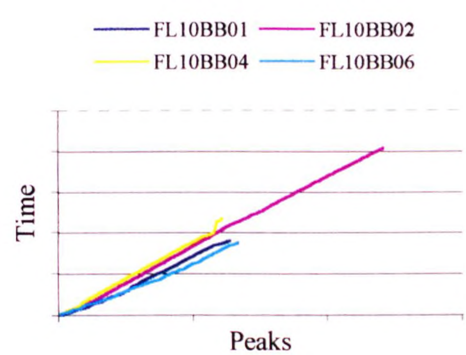

Figure [7.6.3.6] 263.8 Hz Filter Output Timing (11th).

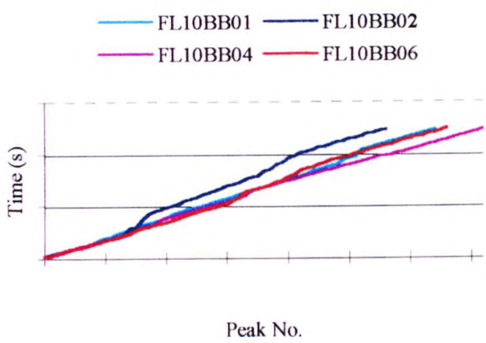

Figure [7.6.4.1] 175 Hz Filter Output Timing (13th).

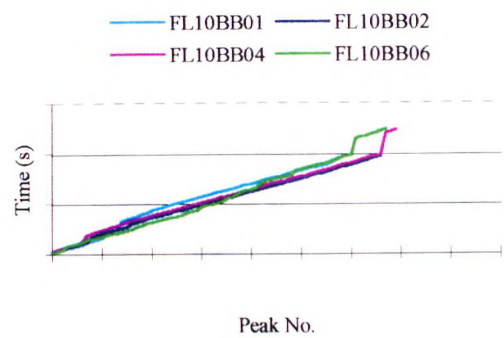

Figure [7.6.4.2] 215 Hz Filter Output Timing (13th).

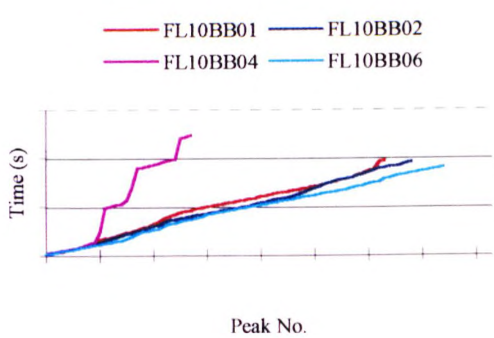

Figure [7.6.4.3] 250 Hz Filter Output Timing (13th).

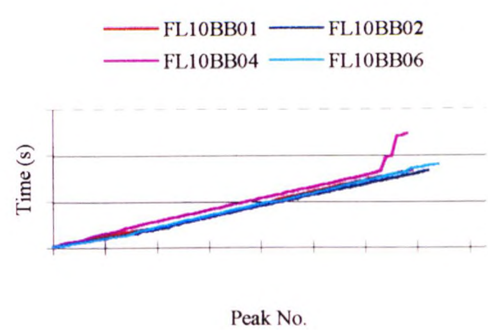

Figure [7.6.4.4] 270 Hz Filter Output Timing (13th).

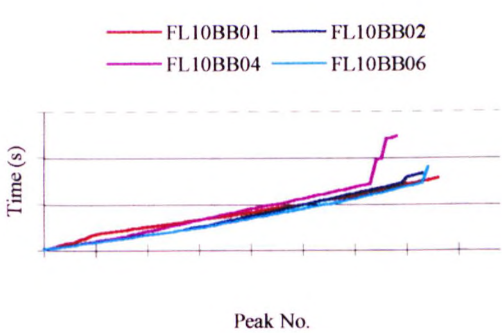

Figure [7.6.4.4] 306.3 Hz Filter Output Timing (13th).

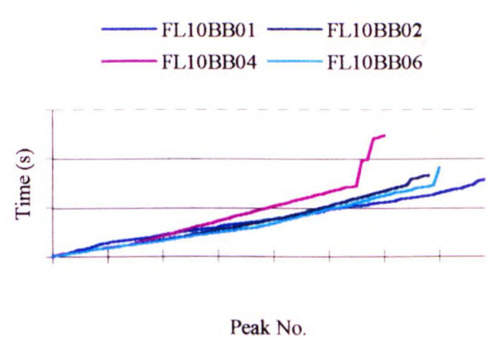

Figure [7.6.4.6] 311.3 Hz Filter Output Timing (13th).

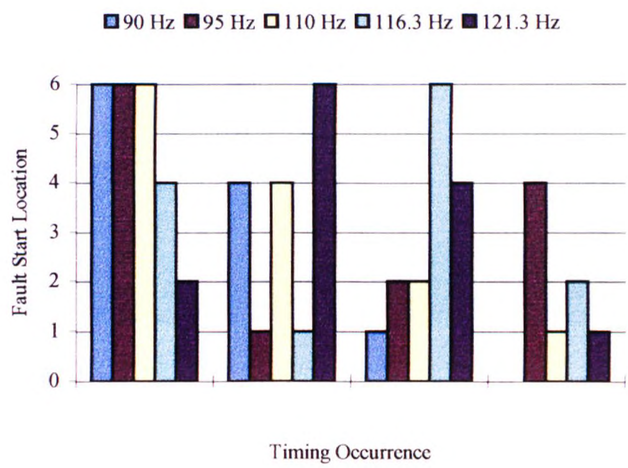

Figure [7.6.1.7] Fault Frequency Occurrence, 5th Harmonics.

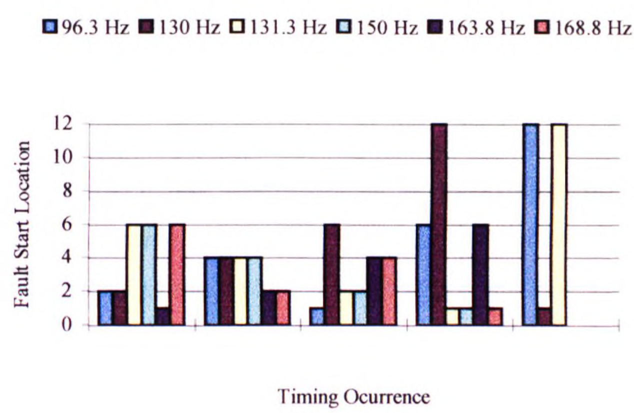

Figure [7.6.2.7] Fault Frequency Occurrence, 7th Harmonics.

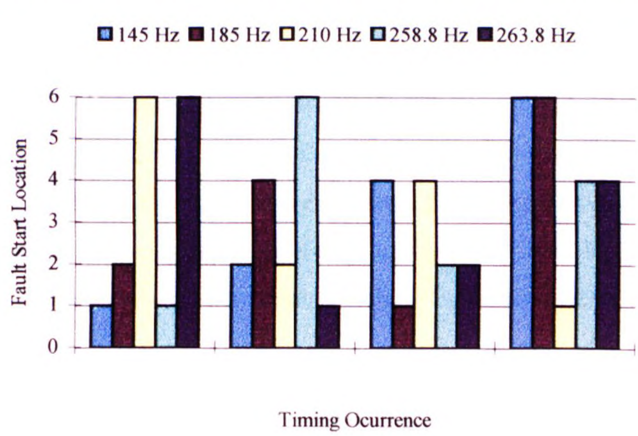

Figure [7.6.3.7] Fault Frequency Occurrence, 11th Harmonics.

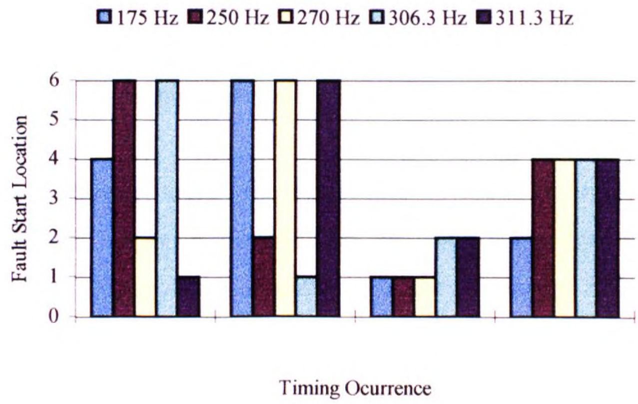

Figure [7.6.4.7] Fault Frequency Occurrence, 13th Harmonics.

7.6.5 Single Scan Analysis Peak Timings

Using a single scan analysis including a low pass filter on the output, (see Chapter 4), various fault frequency components were further tested for correlation between fault location and time of occurrence within the transient. It had been noted, as in previous chapters, that the majority of analysis results contain two or three main peaks within the filtered output. A series of tests was undertaken to find if the timings of these peaks differed for various fault locations within the cage rotor. Again the variation of fault position was simulated using different start-up locations for cage faults. All tests were carried out upon pre-filtered transients obtained from the test-rig with a ten broken rotor bar fault condition. In conjunction to these tests, the timings of the individual peaks for various fault locations was noted as a means of observing any relationships present.

Figure [7.6.5.1] (70 Hz), Figure [7.6.5.3] (100 Hz), Figure [7.6.5.5] (120 Hz) and Figure [7.6.5.7] (210 Hz) show the timings of the peaks within the single scan analysis for the frequencies quoted. From these results it may be seen that there is a separation between the various fault locations upon start up only within the timings of the third and sometimes fourth peaks within the analyses. The first and second peaks almost occurring simultaneously together. This is interesting as it has been previously observed that it is the third peak which was the most observable for detecting fault severity.

Figure [7.6.5.2], Figure [7.6.5.4], Figure [7.6.5.6] and Figure [7.6.5.8] show in a clear format the time differences between the occurrences of the peaks within the analysis for various fault start-up locations. For the first and second peaks the timings are all random in nature, thus giving no indication as to the location of the rotor cage fault. On looking at the third peak in particular, then at first glance no obvious relationship may be observed. However, on closer inspection it may be observed that certain 'quarters' of the plots bear some form of relationship. In that at certain sections the timings follow a linear relationship to the fault start location.

Figure [7.6.5.9] shows in greater detail the occurrence of the fault location peaks for various frequency components tested. It may be observed from the plot that the frequency components which indicate the closest indication to any form of relationship due to the cage fault start location are 120 and 210 Hz.

A correlation between the filter outputs of the single scan analysis was undertaken, the analysis of the transient from the fault start location '12' being used as the reference signal. Figure [7.6.5.10] (a) and (b) report the results of these correlations. It is interesting to note that from this plot four main peaks may be observed both within the correlations for first and second peaks, Figure [7.6.5.10] (a), but not within the correlation results obtained from the third peak, Figure [7.6.5.10] (b).

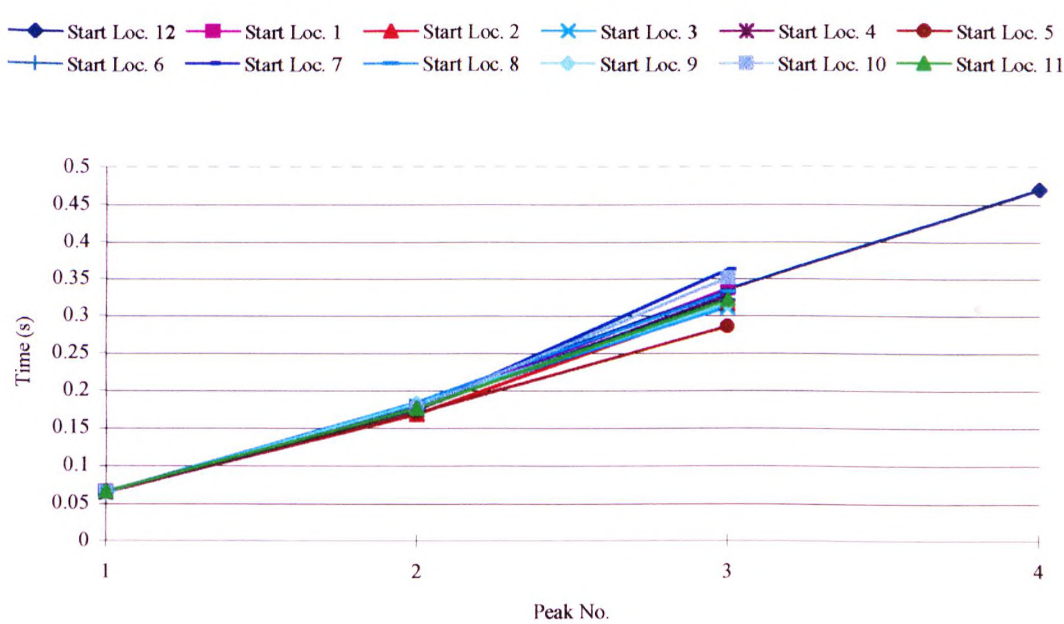

Figure [7.6.5.1] Full Load 10 Broken Bars, 70 Hz.

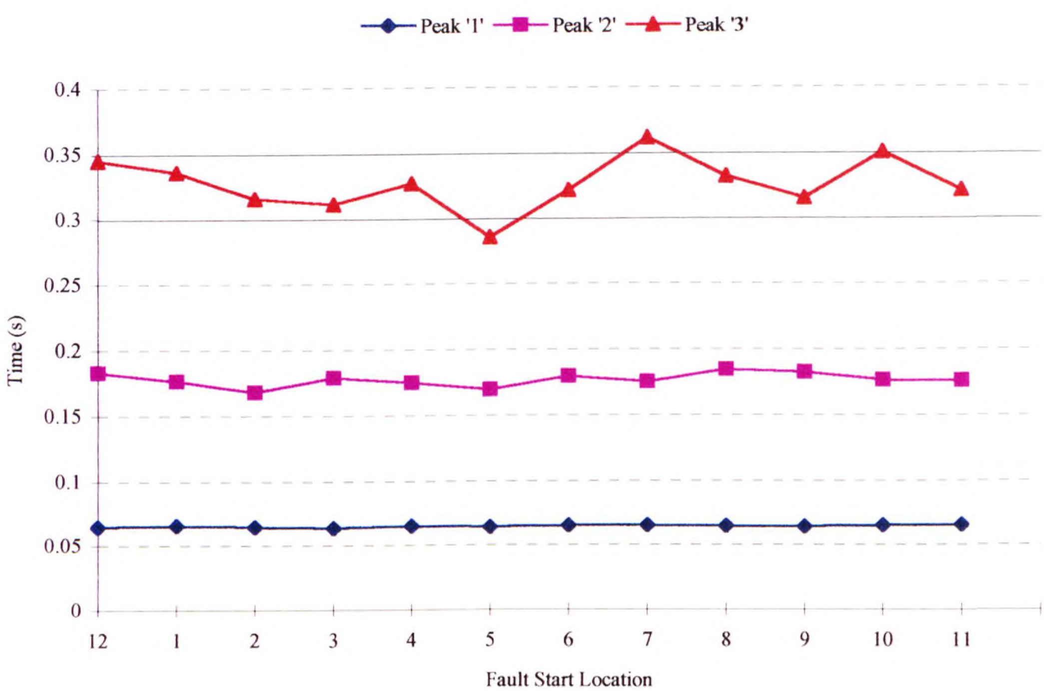

Figure [7.6.5.2] Full Load 10 Broken Bars, 70 Hz.

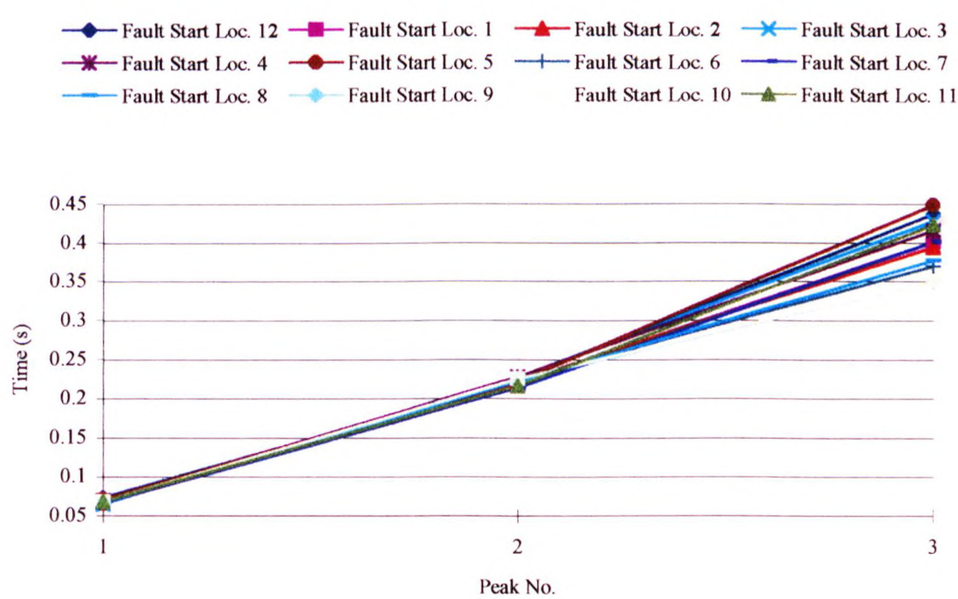

Figure [7.6.5.3] Full Load 10 Broken Bars, 100 Hz.

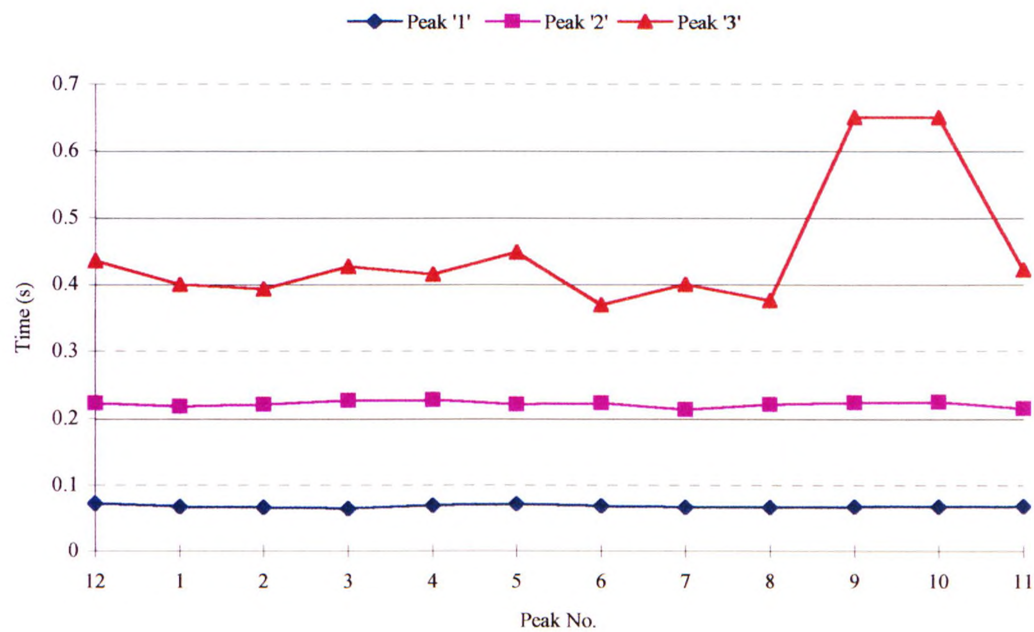

Figure [7.6.5.4] Full Load 10 Broken Bars, 100 Hz.

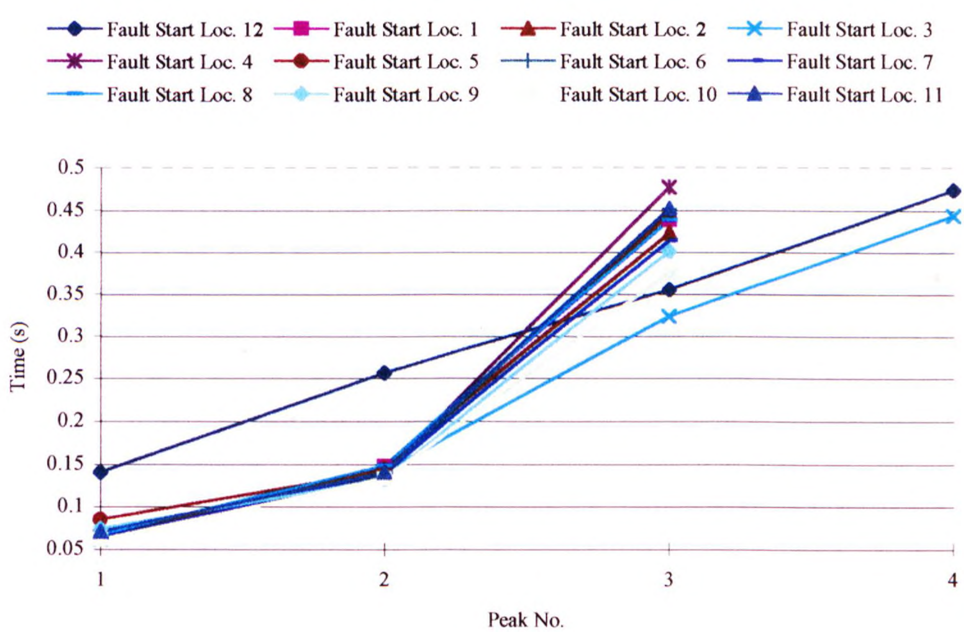

Figure [7.6.5.5] Full Load 10 Broken Bars, 120 Hz.

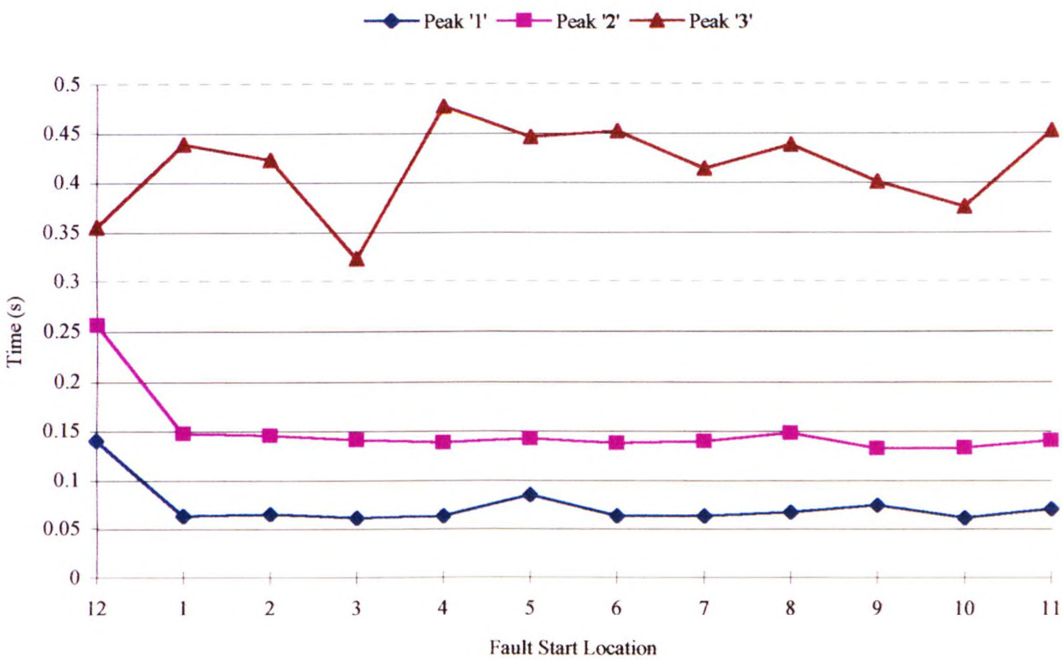

Figure [7.6.5.6] Full Load 10 Broken Bars, 120 Hz.

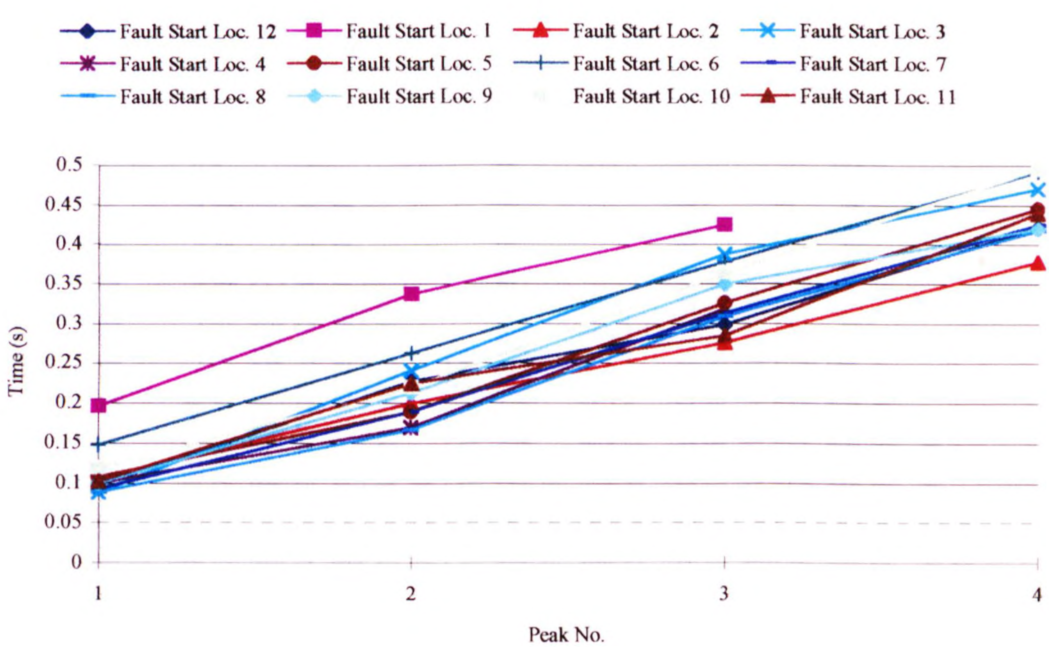

Figure [7.6.5.7] Full Load 10 Broken Bars, 210 Hz.

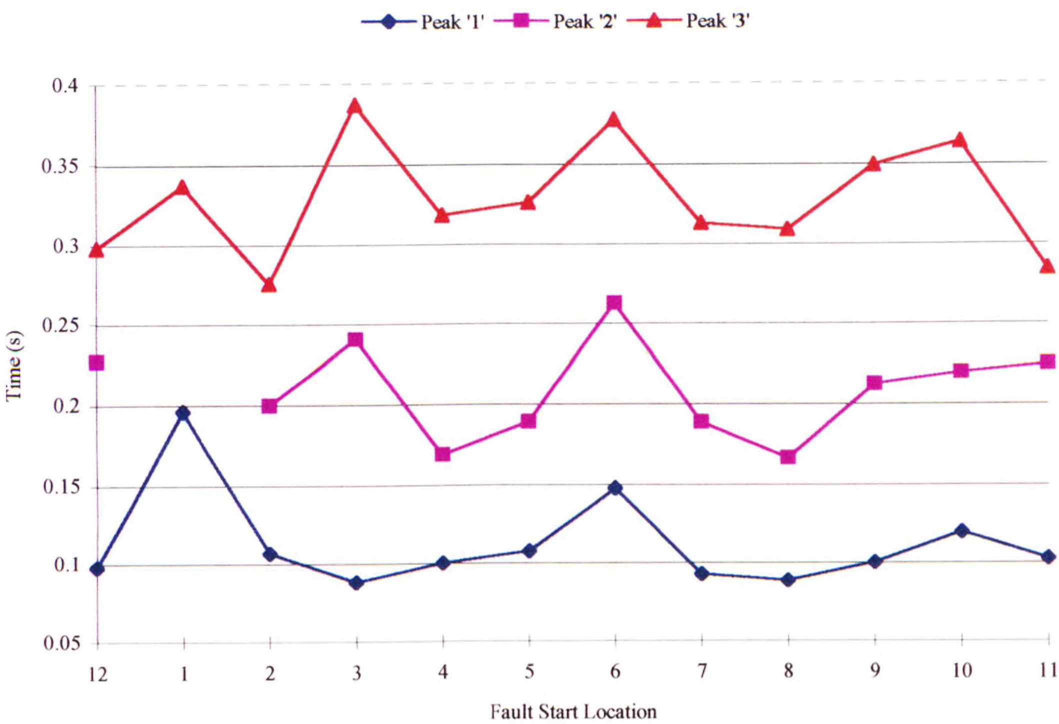

Figure [7.6.5.8] Full Load 10 Broken Bars, 210 Hz.

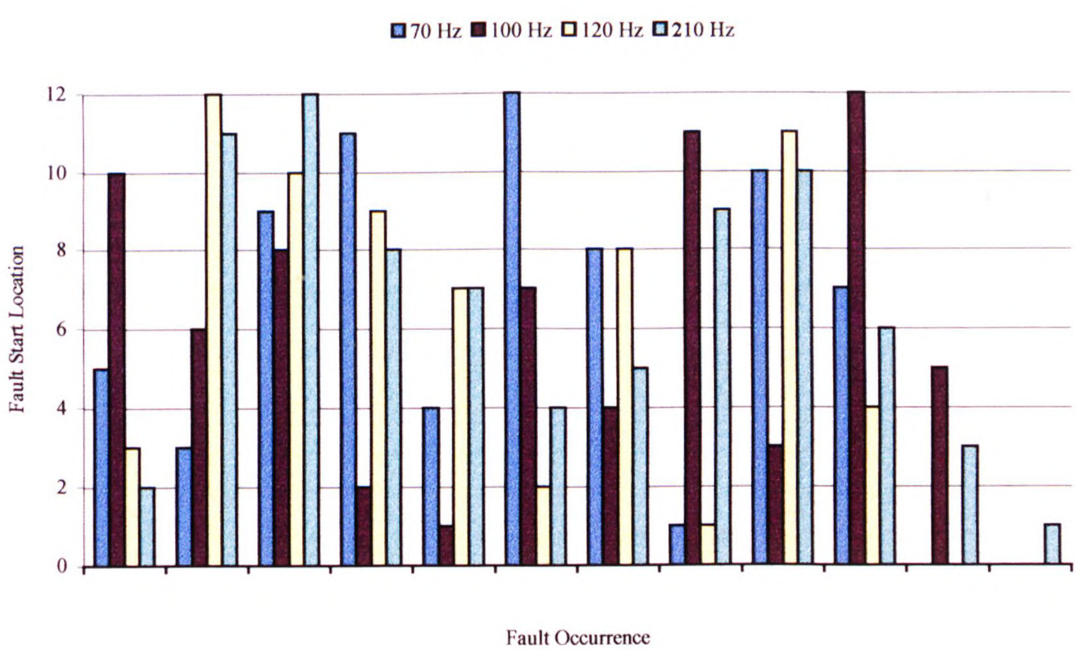

Figure [7.6.5.9] Order of Fault Location Components.

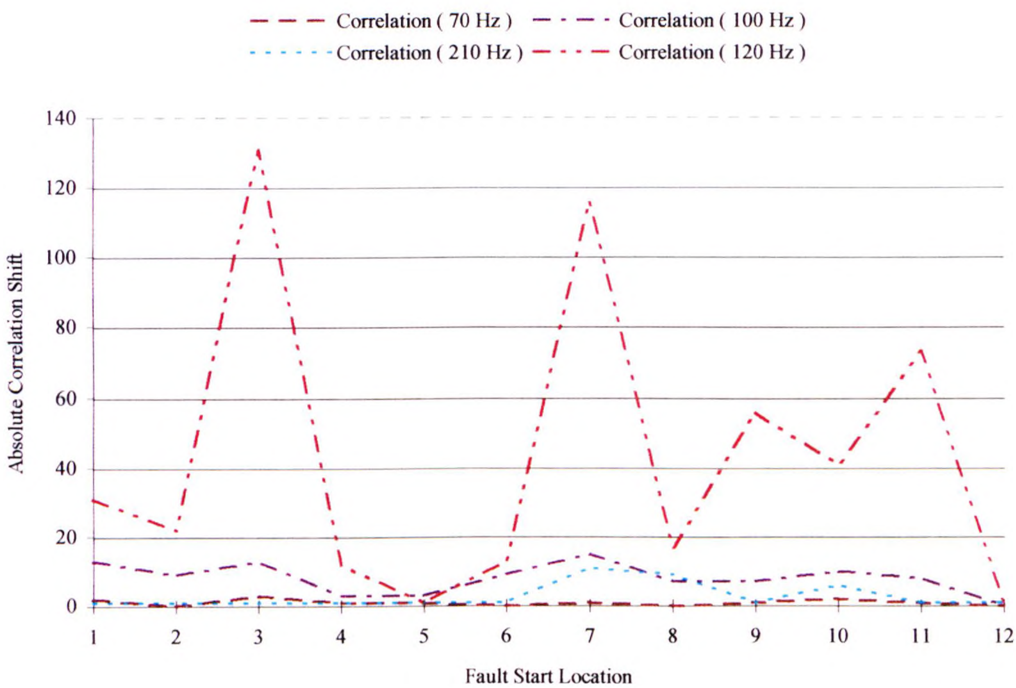

Figure [7.6.5.10] (a) Correlation.

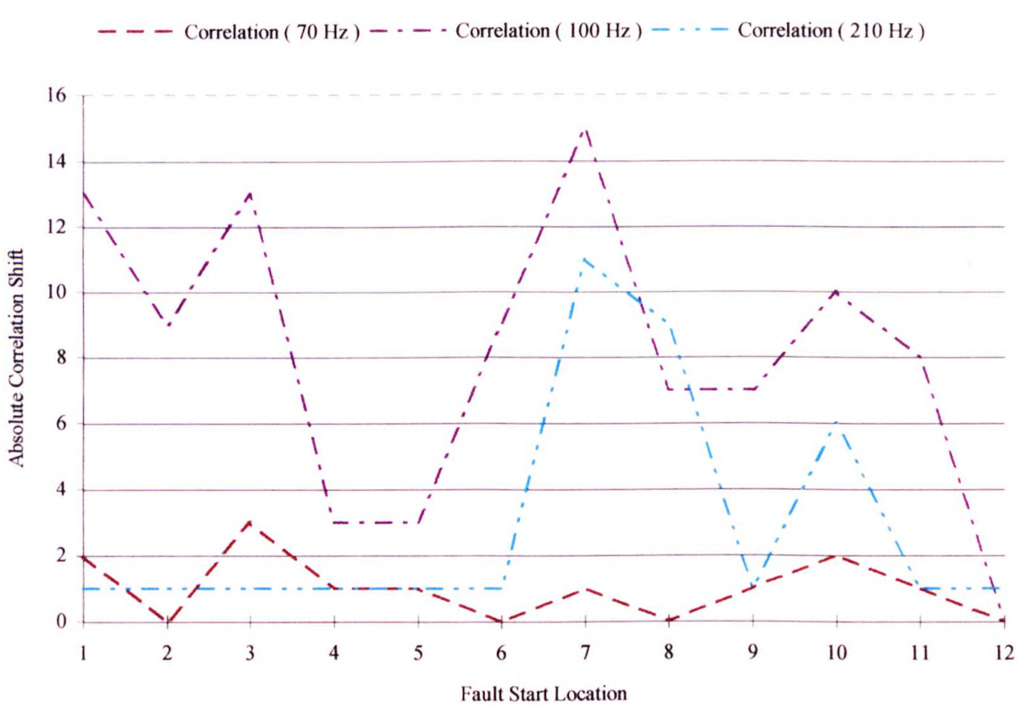

Figure [7.6.5.10] (b) Correlation.

7.7 Obtaining Acceleration Information From Fault Detection Plots

Upon the successful detection of the frequency components indicative of cage rotor faults, it was necessary to use the timings at which these components occur to determine the location of rotor fault. Many algorithms were investigated as to the capability in obtaining this information. The best technique, however, was felt to simply obtain the rotors acceleration. If the start and reference locations are known, then from the methodology described within Section (6.2), the acceleration information may be used to calculate the distance travelled by the fault. As a means to obtain this information a form of rotor speed log was required. This may be implemented by using an accelerometer to record the speed of the rotor via a marked indicator upon the rotor. However, such an approach was not required as from Figure [3.7.1.3], the fault detection plot, the Lower Sideband whose amplitude was shown to determine the severity of rotor fault may be observed, see chapter 3. As this diagram plots the locus of the motor slip dependent frequency components, it is possible to use this data to obtain the required rotor acceleration data. An example of this process which has been developed in software within the Matlab environment is shown within Figure [7.7.1] through to Figure [7.7.2].

Figure [7.7.1] plots the various frequency components within the LSB which are found to occur at various motor slips for differing start locations of rotor fault. Figure [7.7.2] converts this data to slip versus time diagrams where upon it may be shown that the differing start locations give similar plots.

From the obtained time versus slip diagrams the acceleration of a particular rotor may be obtained. From Figure [7.7.1] and Figure [7.7.2] it may be observed that there are slight differences within the individual slip versus time plots for different start-up locations. Therefore, in order to obtain an accurate recording of acceleration it would be advisable to obtain an average of these acceleration plots. From this acceleration information it is possible to calculate the distance covered by any point on the rotor over a certain time period. It is interesting to note that there seem to be two main acceleration rates within the complete acceleration transient, Figure [7.7.2]. The first, from the initial slip of unity accelerates at a constant rate until approximately a slip of 0.4 is obtained, where upon a sudden increase in acceleration is observed. The reason for this may be explained when the torque versus speed characteristic of any typical induction motor is considered. From such a diagram it is clear that two main areas exist, and hence, it follows that this same characteristic will be transferred from the torque to the acceleration characteristic.

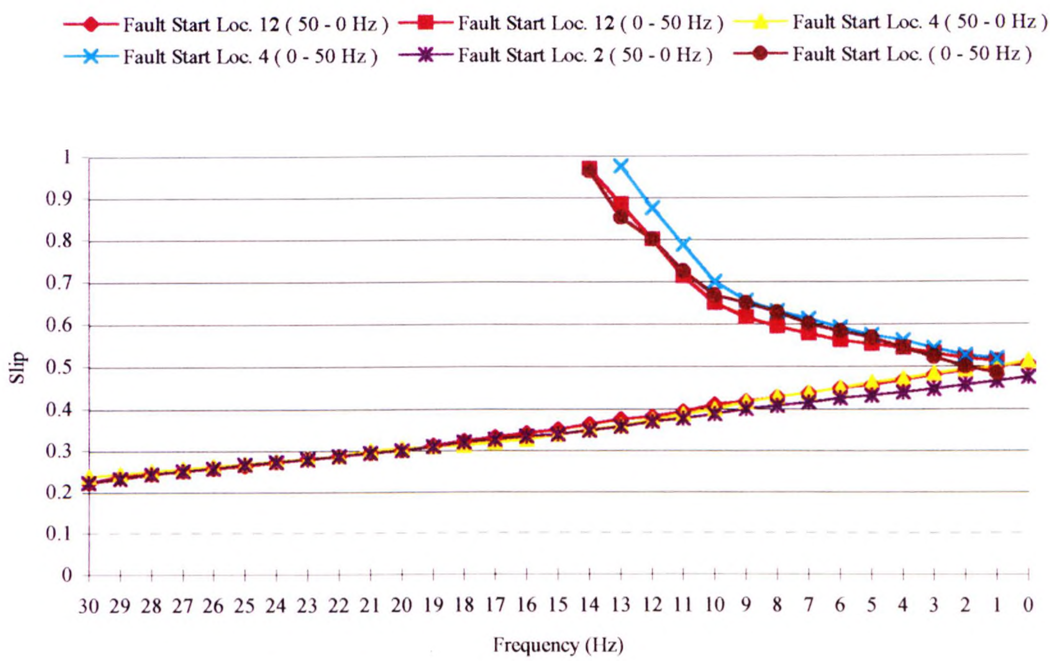

Figure [7.7.1] LSB Frequency v's Slip - Various Rotor Start-up Locations.

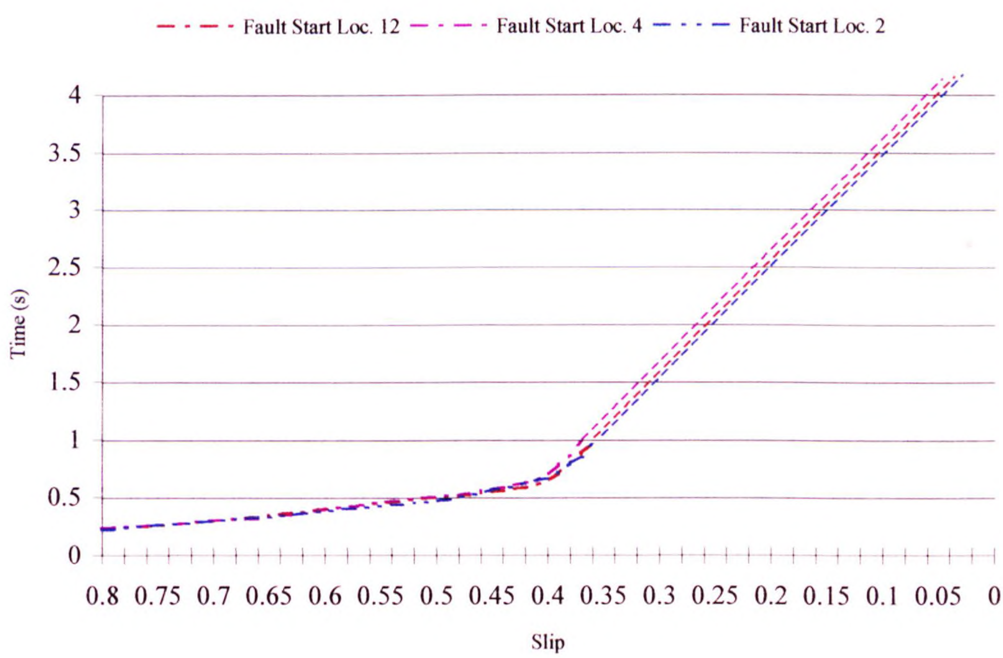

Figure [7.7.2] LSB Slip v's Time - Various Rotor Start-up Locations on Start-up.

7.8 Conclusions

Supply current transients obtained from normal starts of the laboratory test-rig were filtered at various frequencies. These frequencies being calculated from expressions previously shown to be representative of cage rotor faults. Using the filtered output from various starts with the location of the cage fault at different positions, thus simulating varying positions of cage fault, the timings of the peaks present within the filtered outputs were noted. Correlations of the filtered transients with a known reference transient were also obtained in order to find any relationship between the occurrence of the fault location frequency component and the location of the fault upon start-up. Results from these investigations showed that the timings of the first peaks to occur within the filtered outputs were extremely random. However, the timings to the second peaks within the filtered outputs at higher frequencies, and over all three phases, did indicate some form of relationship. In particular the timings to the second peak of the 100 Hz filter output at locations 12-3, 3-6, 6-10 and 10-12.

The transient data was then pre-filtered prior to sampling in order to attempt to reduce the amplitude of the significantly larger fundamental component, and in order to allow the smaller amplitude fault location frequency components to be enhanced within the ADC of the sampling card.

A satisfactory search was made within the steady state period to observe if the fault location frequency components did exist at the predicted frequency values.

A similar set of tests were carried out within the transient signal. Groups of non-stationary frequency components were located which in conjunction with the predicted frequency values in Chapter 2, proved that frequency components were in existence within the transient signal at the predicted areas.

In order to attempt to utilise the stator windings as search coils it was necessary to physically locate the windings. Since no winding diagram for the test-rig used was available, a series of tests involving a flux meter were carried out in order to successfully locate the individual coils which make up the windings.

Investigations using the pre-filtered transient data were next carried out. These investigations took a similar form to those with the normal transients, in that timings of the peaks of filtered transients were noted against varying cage fault start locations. Findings from these results showed that at some frequency values it was possible to observe a relationship between the timing of the fault component and the location of the cage fault upon start-up. However, the findings were found to be variable with filter frequency chosen. The timings of the peaks within single scan analyses of the transients, see Chapter 4, also showed a slight relationship between occurrence and position of fault, although this was very slight and could only be observed with lower frequency values, higher frequency values showing a more random displacement of timings.

From the results of these various investigations it became obvious that some fault frequency components were more representative to fault location detection than others. Although the majority of harmonic components and slip values investigated gave results which were too randomised in order to obtain any sensible information, a few components did give results which suggested some form of correlation between the frequency component occurrence and fault location. It was felt that these components would therefore warrant further investigation using a technique of signal processing which was more selective than that used in the above investigations.

One of the reasons as to the problems being found isolating the frequency components within the transient signal was that during the transient, other frequency components present within the signal were swamping the fault location components. As a means to reduce this, Chapter 8 discusses work carried out on an inverted geometry three phase induction motor. This approach was taken in order to investigate the rotor currents for the suitably transformed fault location frequency components. It was regarded that these components, situated on the rotor side, would be larger since they would not have been attenuated by the air-gap of the motor.

Finally, in order to obtain acceleration information upon the rotor from the transient which is being investigated, software was written which obtains the necessary information from a full analysis of the relevant transient. It was noted that when this is done there are two distinct parts within the acceleration plot. The first from high slip to approximately 0.4 slip which accelerates fairly slowly followed by a second from 0.4 onwards which accelerates rapidly until steady state speed is achieved.

Chapter 8

The Inverted Geometry Induction Motor

8.0 Introduction

Investigations up to this point in time had concentrated upon the analysis of stator phase current, thus conforming to the general requirement of non-invasive monitoring strategy. However, in order to facilitate the location of rotor faults it was decided that a study and analysis of actual rotor bar currents would be useful. It was also felt desirable to study the rotor bar current distribution particularly under normal and faulted operating conditions.

As discussed within the review of rotor bar current analysis techniques, several methods of obtaining rotor bar currents have been tried and tested by past researchers. The overriding problem that all have had to overcome being the obvious difficulties in obtaining access to the bar currents.

After investigating the possibility of several rotor current acquisition techniques, an experimental Inverted Geometry Induction Motor (IGM), was commissioned to aid the investigations.

In the IGM, Figure [8.1.1], motor operation is similar to that of the normal construction of induction motor except that it is the three phase supply winding of the motor which rotates, thus leaving the cage located on the outside of the machine, stationary, in order to provide access to the individual bars.

8.1 Construction of Inverted Geometry Induction Machine Test-Rig

The IGM, Figure [8.1.1], was constructed by the technical staff within the University from a three phase, 7.5 kW, 4 pole Wire Wound Induction Motor and a three phase, 11 kW, 36 rotor, 4 pole Squirrel Cage Induction Motor.

As a means of avoiding confusion, the stator of the IGM will be referred to as the primary and conversely, the cage rotor of the IGM as the secondary within this publication.

The secondary of the IGM, Figure [8.1.2], was constructed from the stator of the original wire wound motor. On removing the distributed three phase winding from the stator, 36 copper rotor bars manufactured specially, Figure [8.1.3], were placed into the individual slots of the stator, each bar being secured via a nut / bolt arrangement to a copper end ring at either end of the secondary, Figure [8.1.4]. The rotor bars, prior to being placed into the slots were fully insulated from the laminations of the secondary, in order to reduce the effects of interbar currents which are prominent when such a motor is operated under faulted conditions [74].

The primary of the IGM was constructed from the original wire wound rotor. This consisted of a double layer star connected winding within 24 slots. The slip-ring mechanism previously used to connect the external resistances of the motor to the wire wound rotor were used to feed the three phase supply to the primary star connected winding.

During the initial investigations the motor was fed via a 25A Variac. Initially the experimental rig was not connected to any load although later investigations were carried out in conjunction with a DC generator acting as a load.

The experimental rig also contained a tachometer consisting of a 60 tooth cogged wheel and analog magnetic pick-up device, Figure [7.3.2]. A cooling fan was also included on the experimental rig in order to maintain some form of temperature control within the motor.

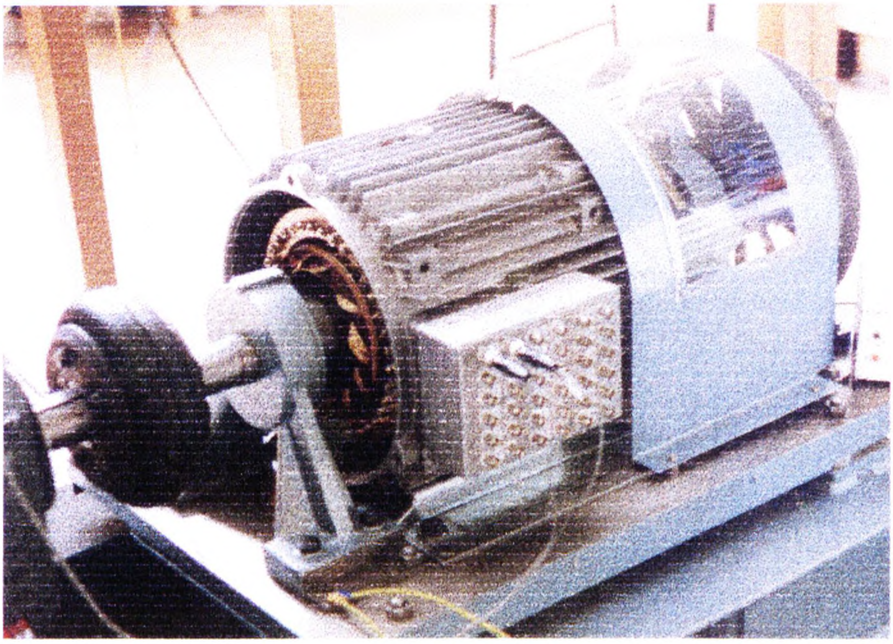

Figure [8.1.1](a) The Experimental Inverted Geometry Induction Motor.

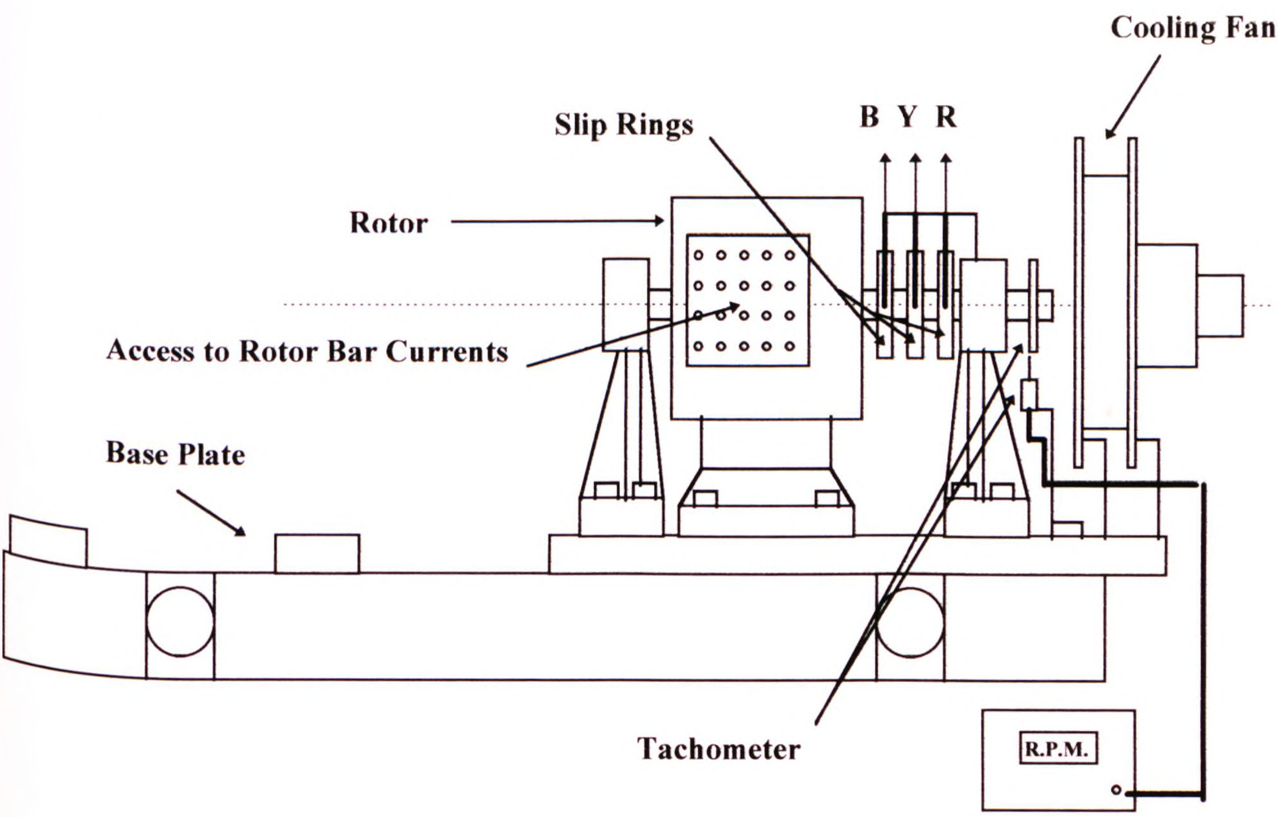

Figure [8.1.1](b) The Experimental Inverted Geometry Induction Motor.

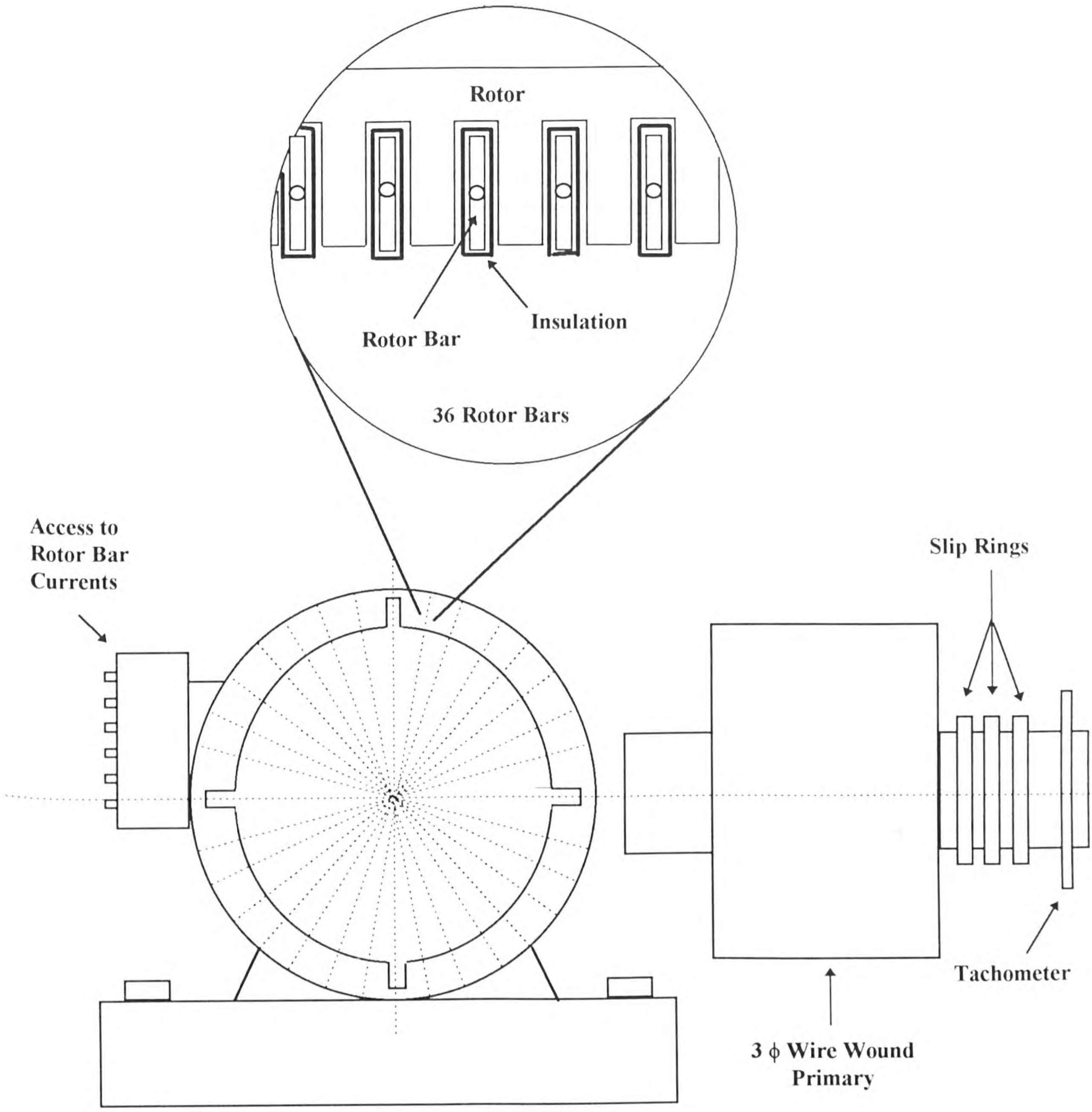

Figure [8.1.2] IGM Secondary Arrangement.

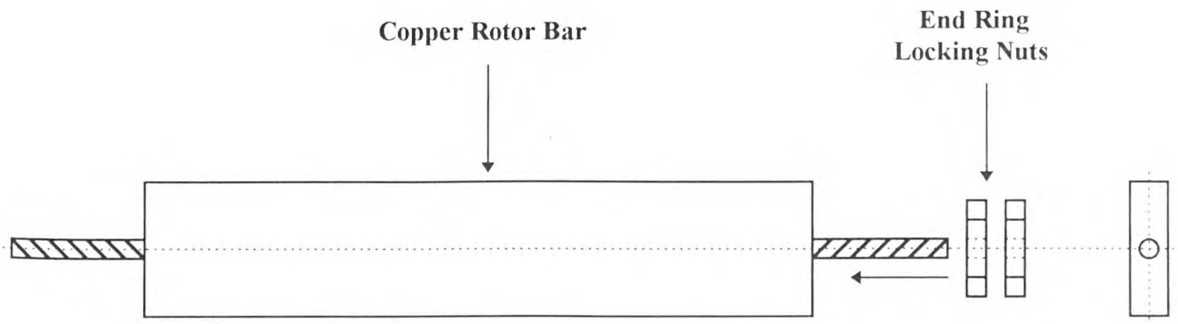

Figure [8.1.3] Copper Rotor Bar.

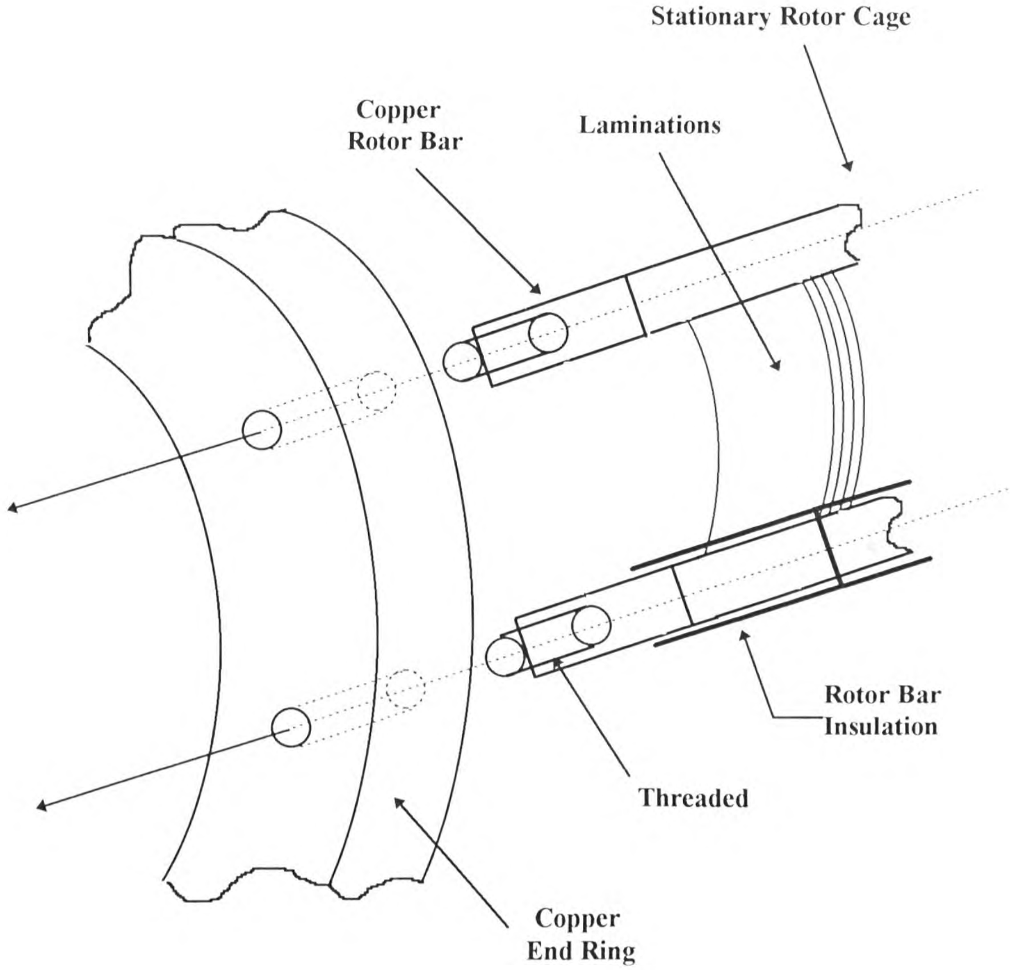

Figure [8.1.4] End-ring Arrangement.

8.2 IGM - Method of Operation

The method of operation for the IGM is not dissimilar to that of the conventional induction motor. A balanced three phase supply is fed to the primary three phase winding which is displaced electrically and mechanically by $2\pi/3$ radians. The supply, in conjunction with the physical set-up, creates a rotating magnetic field around the stationary primary winding in the direction indicated by Figure [8.2.1].

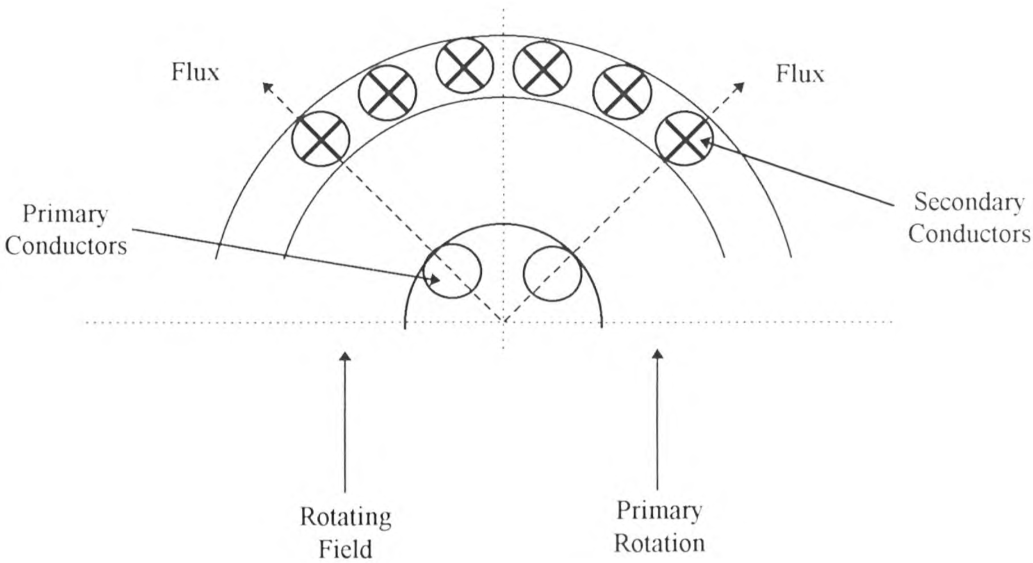

Figure [8.2.1] Induced Rotation within IGM.

A current is now induced in the conductors forming the secondary of the IGM. As the rotation of the magnetic field is clockwise, the secondary conductors travel in an anti-clockwise direction with respect to the rotating field. This develops a current which flows in the direction indicated in Figure [8.2.1] due to Fleming's Right Hand Rule, FRHR.

The secondary conductors are now current carrying conductors in the presence of a magnetic field. As a result these conductors experience a force determined by $F = Bli$. This force, in the direction indicated by Figure [8.2.2], is similar to that of the normal induction machine in that the rotor bars are placed under a force which would make the rotor rotate in the direction of the rotating magnetic field. However, within the IGM the bars which form the secondary cannot move as they are housed within the main body of the motor. Due to Newton's third law of motion which states that every force has an equal and opposite reaction force, it follows that the force acting upon the secondary bars acts to move the primary conductors away, as it is this structure which is free to rotate in the opposite direction to that of the rotating magnetic field.

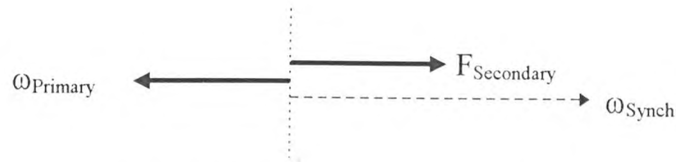

Figure [8.2.2] Direction of IGM Primary Rotation.

8.3 Determination of Rated Supply to IGM

The calculation of required supply voltage and current necessary for efficient operation of the IGM with minimal saturation effects, proved to be a rather more protracted task than initially anticipated.

As the primary of the IGM had been constructed from a previously used D160M three phase slip-ring motor, data associated with the motor was researched and reported within Table [8.3.1]. Using this data in conjunction with several motor design approximations it was possible to calculate the supply voltage and current for the IGM.

Elder [89] had used this motor and carried out both no load and blocked rotor tests upon the slip-ring test-rig. From these tests the equivalent circuit parameters of Table [8.3.2] were obtained for both stator, and more importantly in this case, rotor of the slip-ring motor for the ratings used by Elder.

Category	Value
Pole	4
kW	7.5
RPM	1430
Winding (Rotor) Pitch	1-6
Winding (Rotor) Pitch Factor	0.966
Winding (Rotor) Distribution Factor	0.966
Rotor Resistance (per phase)	0.32
Skew	0.5
Winding (Stator) Pitch Factor	0.960
Winding (Stator) Distribution Factor	0.966

Table [8.3.1] Slip-ring Motor Data.

As a means to calculate the rated supply it was necessary to calculate the number of turns within the primary winding of the IGM. Elder [89] had measured, with some difficulty due to the slip rings, both the stator and rotor resistances of the slip-ring motor to be 1.34 and 0.32 Ω respectively. From these values and that of the equivalent resistance, Table [8.3.2], the referred rotor resistance can be calculated to be 1.81 Ω. In order to calculate the non-referred rotor resistance eq. (8.3.1) must be used. In this equation Elder used $N_{SR}^2 = 6$. With this value of stator to rotor turns ratio, the non-referred rotor resistance can be calculated to be 0.3 Ω. A value which successfully verifies that measured by Elder.

Parameter	Value
R_c	609.3 Ω
I_c	0.41 A
I_m	2.15 A
X_m	j 116.7 Ω
Z_{ph}	7.6 Ω
R_{eq}	3.15 Ω
X_{eq}	j 6.92 Ω

Table [8.3.2] Slip-Ring Motor Equivalent Circuit Data.

$$R_2 = R_2' / N_{SR}^2 = 1.81 / 6 = \mathbf{0.3}\ \Omega \qquad \textbf{(8.3.1)}$$

Sarma [94] defines the turns ratio, N_{SR}^2, to be that shown in eq. (8.3.2). Using the winding factors reported for both the slip-ring motors stator and rotor within Table [8.3.1], the number of turns within the rotor winding can be calculated to be 53 per phase.

$$N_{SR}^2 = [\, m_1 / m_2 \,(k_{w1} / k_{w2} \,.\, N_1 / N_2)^2]^2 \qquad \textbf{(8.3.2)}$$

From the results of the slip-ring motors blocked rotor test, Table [8.3.2], the stator current may be calculated to be 10 A. This value, which represents the current within the stator winding, may be used along with the calculated number of windings within the rotor to compute the equivalent circuits rotor current per phase. Thus, the rotor current of the slip-ring motor during operation at rated values was computed to be 24 A. Similarly, the rated speed together with developed torque under these load conditions for the slip-ring motor, may be calculated to be 149.7 rad/s and 50 Nm respectively.

As a means of verifying these values, Table [8.3.1] indicates that the full load mechanical output power of the slip-ring motor is 7.5 kW. If it is assumed that no mechanical losses take place within the system, then it may be taken that the power developed within the rotor will also equal 7.5 kW. If for practical purposes a full load slip of 5% is assumed, then using eq. (8.3.3), the rotor current can be calculated to be 19.8 A, a value similar to that previously calculated.

$$P_m = P_o = \omega\ T = 3.\ I_2^2\ R_2 / s \qquad \textbf{(8.3.3.)}$$

Using the calculated value of turns and rated load current for the slip-ring rotor, it was then possible to calculate the required ratings for the same rotor within the IGM test-rig.

The slip-ring motor used by Elder had a diameter of 163.8 mm and a length of 146.05 mm. Using this data in conjunction with the average flux density within the air-gap being reported to be 0.6 T, eq. (8.3.4) was used to calculate the flux per pole to be 0.0115 Wb.

$$B = 2\ p\ \phi / \pi\ D\ l \qquad \textbf{(8.3.4)}$$

Using this value of flux per pole together with the motor dimensions of the IGM test-rig, Table [8.3.3], results in an average air-gap flux density of 0.36 T. With the motor design expression shown in eq. (8.3.5), the full load power developed by such a motor with the dimensions given in Table [8.3.3] may be calculated to be 13.7 kW. This results in a full load torque of 91.8 Nm being developed by the motor and together with the data calculated for the wire wound rotor, when in slip-ring motor mode, results in an IGM primary current at full load of 21.2 A. A value of the same order as the slip-ring motors full load rotor current.

Parameter	**Value**
R_2	0.218 Ω
J	≈ 3 A / mm^2
Diameter	210 mm
Length	189 mm
Air-gap Length	2 mm
Rotor Slot Pitch	17 mm
Rotor Bar Width	6 mm
Rotor Bar Height	18.5 mm

Table [8.3.3] IGM Test-rig Data.

$$P = \omega_r\ T = B\ A\ \pi^2\ D^2\ l\ n'' \qquad \textbf{(8.3.5)}$$

A Tinsley Micro Ohmeter (Type 5878) was used to measure the values of rotor bar resistance, Table [8.3.3]. Meter probes were connected to each end of the rotor bar using the nuts used to secure the end-ring. A torque wrench was to be used so that all connections would have an equal torque level. However, such a tool could not be used due to lack of physical access, therefore each nut had to be tightened equally by hand. Each reading for individual bars then required the leads to have good contact with the bar in question together with the meter being zeroed on each measurement. Results from the individual measurements are shown in Figure [8.3.1], the value within Table [8.3.3] representing a per phase value.

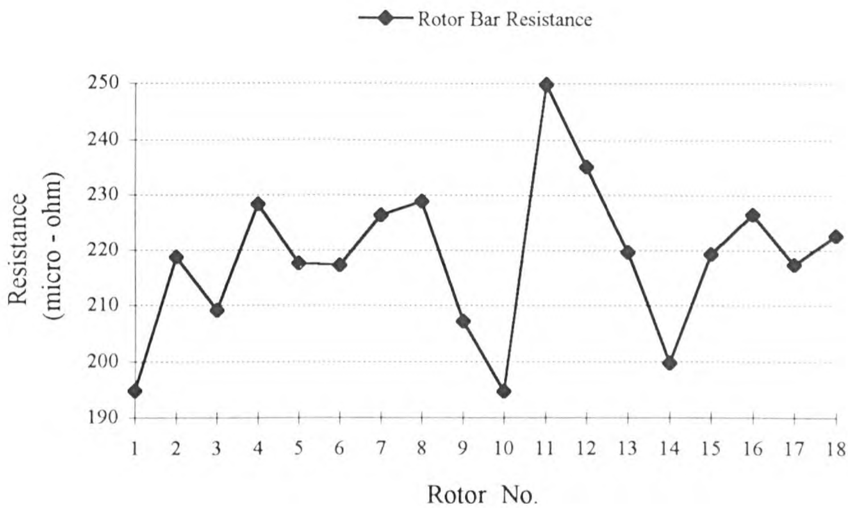

Figure [8.3.1] Inverted Geometry Machines Rotor Bar Resistance's.

Finally, using eq. (8.3.6) it was possible to use the above data to equate the RMS supply voltage for the IGM at the rated level of current. This value, when the primary taken to be star connected, results in a phase supply line voltage of 225 V (rms). Thus, the rated supply voltage to the IGM test-rig to ensure efficient, non-saturated operation will be 320 V.

$$E_1 = 4.44\,(f_s)\,(N_{ph})\,(\phi)\,(k_w) \qquad \textbf{(8.3.6)}$$

8.4 Physical Tests to Determine Inverted Geometry Machine Parameters

As a means to determine the equivalent circuit parameters of the IGM, a series of tests were conducted including light load and blocked rotor tests. The following section presents the results of these tests in addition to other investigatory tests run upon the IGM.

8.4.1 Light Load Test

In this test the motor was supplied at rated line volts and frequency. No mechanical load was connected to the motor whilst input power, line volts, and line current were measured. The results of these tests are presented along with relevant calculated equivalent circuit parameters in Table [8.4.1.1].

V_{ph} (V)	I_{rms} (A)	Power (W)	R_c (Ω)	I_c (A)	I_m (A)	X_m (Ω)
230	8.0	120.0	440.0	0.52	7.98	28.8

Table [8.4.1.1] No Load Data for IGM.

8.4.2 Blocked Rotor Test

In this test the primary of the motor was restricted from rotating using a locking arm. With this in position a small three phase voltage was applied to the IGM at rated frequency until calculated rated load current was flowing. From Section (8.3) it was calculated that the rated current to the IGM was in the order of 20 A. However, due to instrument limitations when carrying out the blocked rotor test, this level of current could not be achieved. A series of blocked rotor tests were carried out over a series of input voltages, Figure [8.4.2.1]. From this, the equivalent impedance could be calculated over the measured range, Figure [8.4.2.2]. From this plot it was observed that the impedance, equivalent resistance and equivalent inductance were constant over the supply range. Hence, a projected value was obtained for power at the rated current value from which the parameters within Table [8.4.2.1] were calculated.

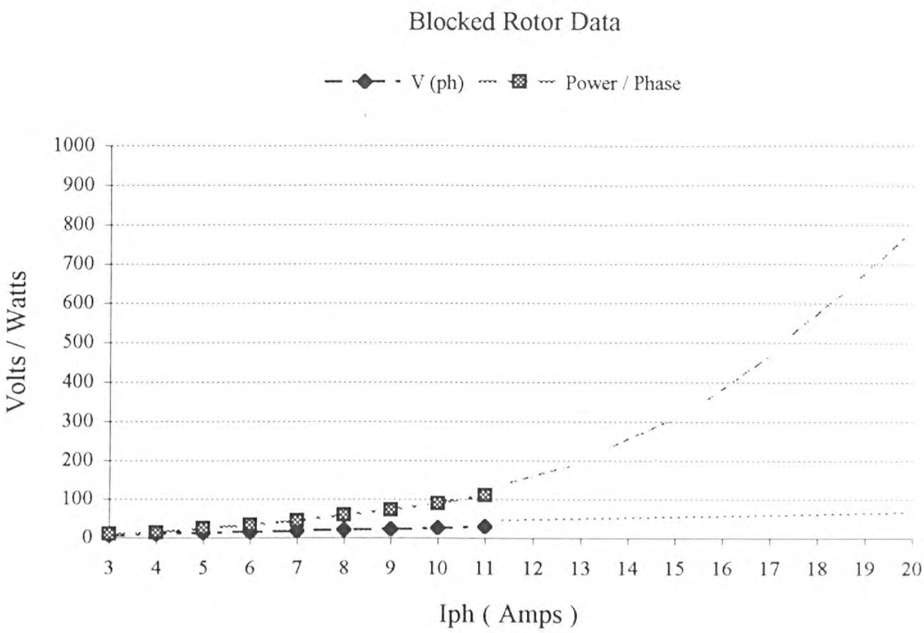

Figure [8.4.2.1] V_{Supply} and Power / phase versus I_{supply}.

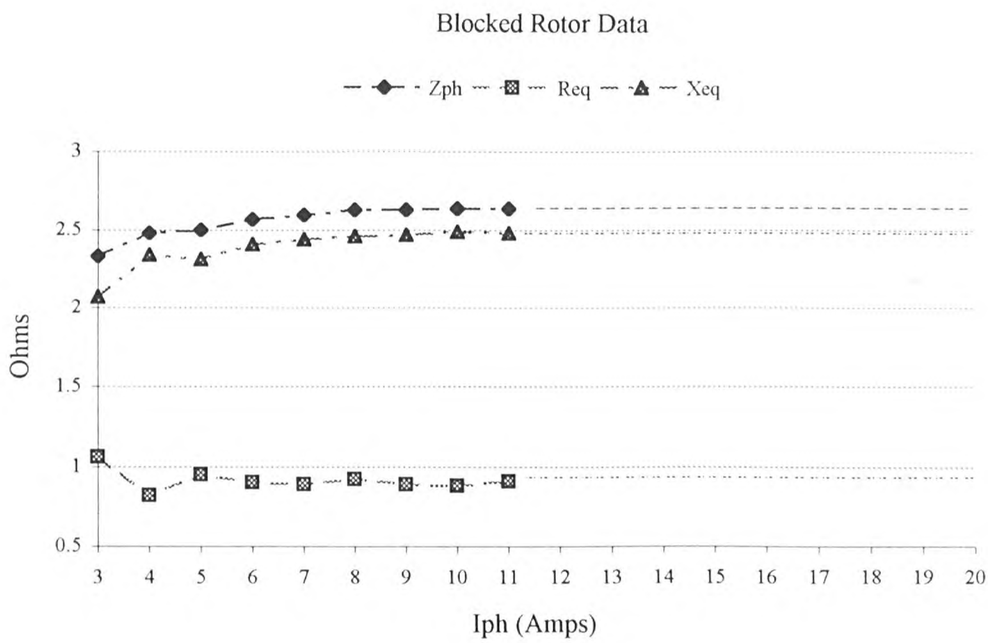

Figure [8.4.2.2] Z_{ph}, R_{eq} and X_{eq} versus I_{Supply}.

I_{ph} (A)	V_{ph} (V)	Power (W)	Z_{ph} (Ω)	R_{eq} (Ω)	X_{eq} (Ω)
20.0	54.0	220.0	2.65	0.9	2.5

Table [8.4.2.1] Blocked Rotor Data.

8.4.3 Measurement of IGM Primary Winding Resistance

In order to measure the resistance of the star connected primary winding a DC meter was used to obtain the resistance between the individual phase windings. It was found that the resistance recorded varied with rotor position, hence several readings were taken and a mean value obtained.

The resistance of the individual slip-rings were then measured, Table [8.4.3.1], and subtracted from the original measured resistance value, giving the average phase resistance as is shown in Table [8.4.3.2]. When divided by two, due to the star configuration of the primary winding, the per phase values are computed to be that shown in Table [8.4.3.3], thus giving an average per phase resistance of 0.29 Ω.

Blue / Yellow	Blue / Red (in ohms)	Yellow / Red
0.875	0.65	0.73

Table [8.4.3.1] Average Phase Resistance.

Blue / Yellow	Blue / Red (in ohms)	Yellow / Red
0.689	0.497	0.563

Table [8.4.3.2] Updated Phase Resistance.

Blue / Yellow	Blue / Red (in ohms)	Yellow / Red
0.34	0.25	0.28

Table [8.4.3.3] Average Resistance per Phase.

8.4.4 Verification of Non Saturation Motor Operation

As a means to verify that the calculated supply voltage and current was not within the saturated area of motor operation, the following tests were implemented. Results were obtained from the IGM running under no load conditions, since at this point in time no loading capability was available. Parameters recorded over a wide range of supply voltage included the line current and primary speed. All tests were completed over all three supply phases with results being presented from the red phase alone.

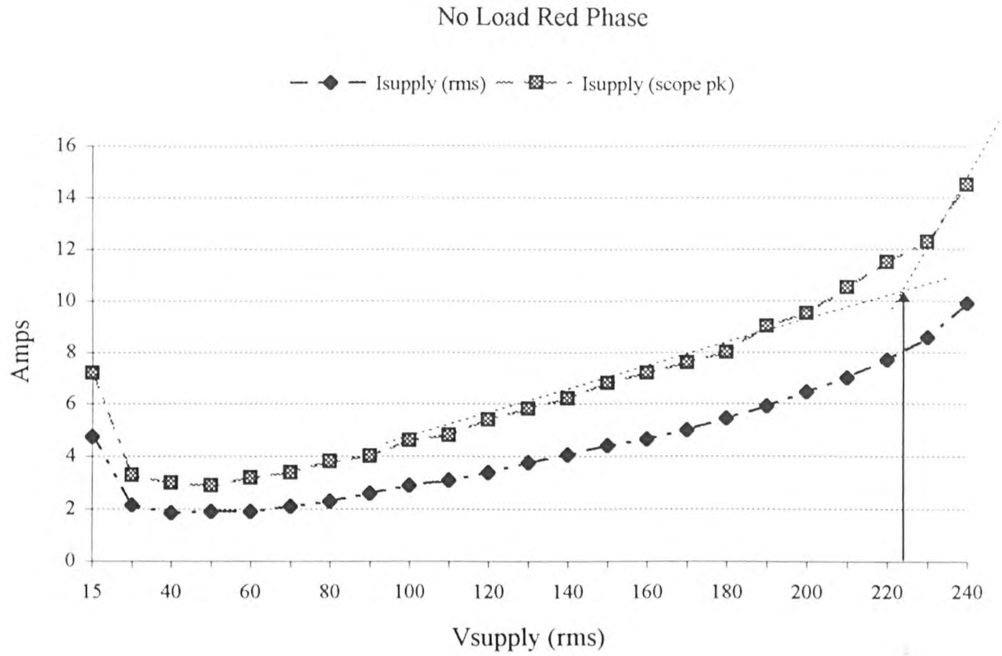

Figure [8.4.4.1] I_{Supply} versus V_{supply}.

Figure [8.4.4.1] shows the current taken by the supply for various supply voltages. The indicator on the plot shows the rated supply voltage. It is interesting to note that at this point the current taken by the supply changes from being a steadily increasing linear component, to a component which dramatically increases. It is at this point that saturation within the IGM system takes place, thus the rated supply is on the edge of the saturation limit. Figure [8.4.4.2] presents the primary speed characteristic for the IGM test-rig. From this it may be observed that the rated voltage occurs within the steady state period of motor operation.

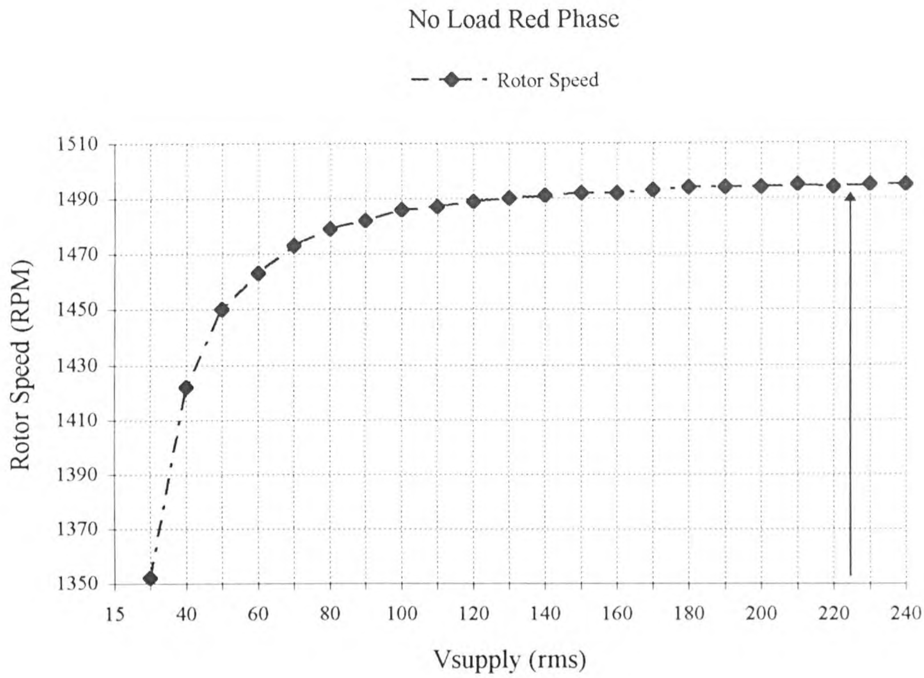

Figure [8.5.4.3] V_{Supply} versus IGM Primary Speed.

8.5 IGM - DC Generator Load

Initial investigations on the IGM were carried out with the IGM run under no load conditions. However, in order that significant currents could flow within the secondary bars, thus allowing significant levels of slip to be developed, it became necessary to load the IGM test-rig with a DC generator - resistive load set-up.

Figure [8.5.1] shows the DC generator employed to load the IGM test-rig with Table [8.5.1] listing the relevant machine data. From the data presented it may be observed that there was an overkill in the power rating of the machine used. This however, was unavoidable due to the lack of available equipment.

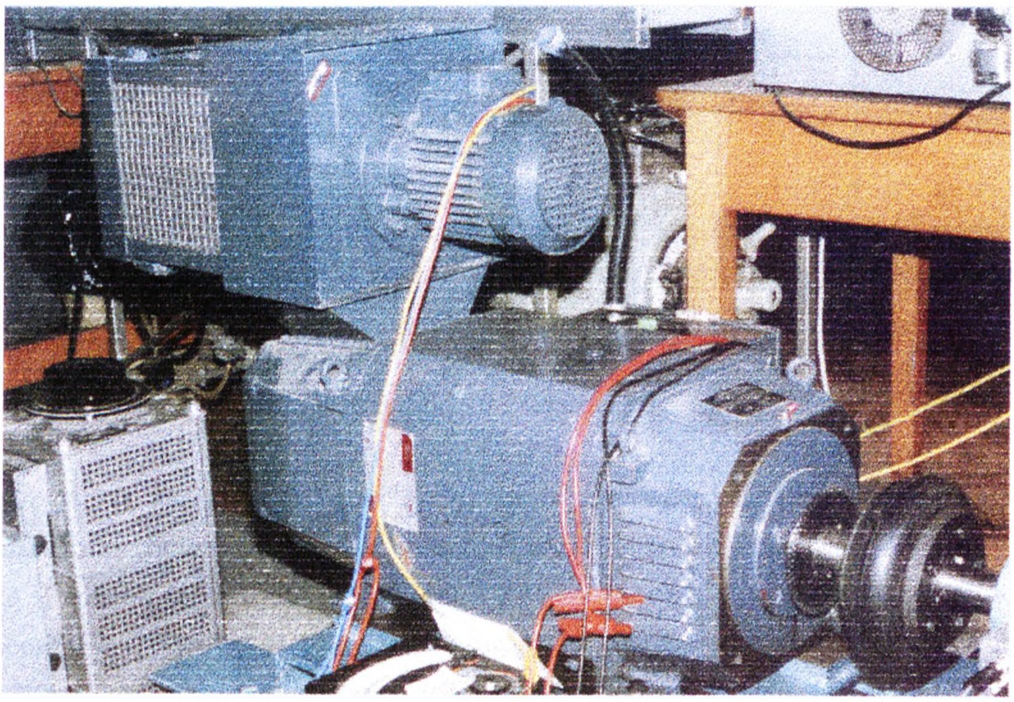

Figure [8.5.1] DC Generator.

FRAME	160 K	TYPE DC MOTOR	BULL ELECTRIC DC
	SER. NO.	033507 WDG SHUNT	MACHINE
	OUTPUT	43 kW RPM 3500	EXCT'N 240 VOLTS
	VOLTS	240 V RATING CONT.	AMPS 2.94
	AMPS	198 A	Ω 20° C 60.0

Table [8.5.1] DC Machine Nameplate Data.

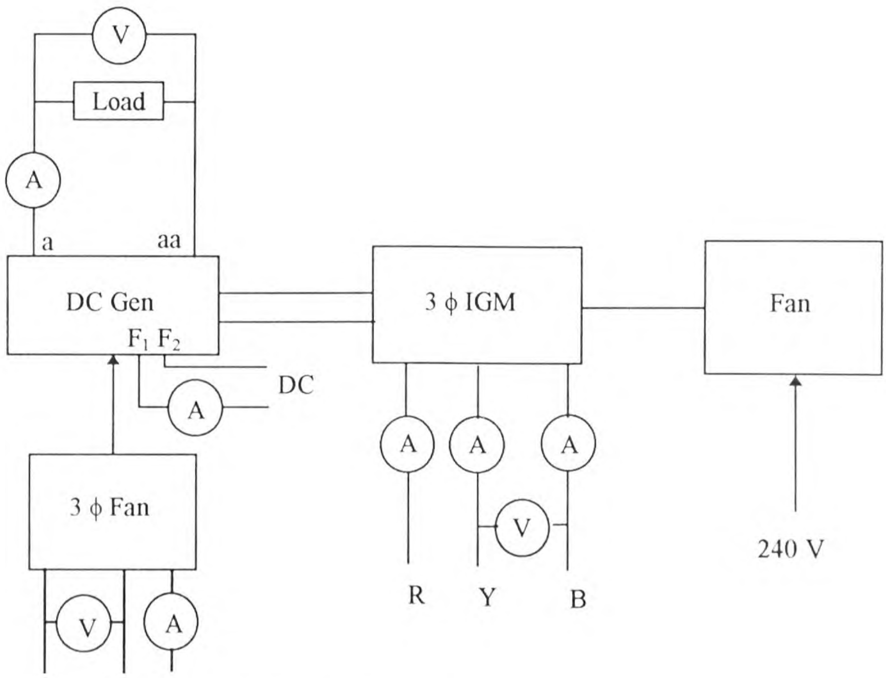

Figure [8.5.2] DC Generator Set-up.

Figure [8.5.2] shows the DC generator set-up in conjunction with the IGM test-rig. From characteristics obtained from the load set-up, and due to limitations in the rating of the DC supply used to energise the field winding, all loaded IGM investigations were undertaken at the settings reported within Table [8.5.2]. This allowed a slip of 0.03 to be developed, thus creating some form of mechanical load for the IGM, and hence, larger secondary currents to flow.

$E_A = 83$ V; $V_{Line} = 200$ V; $I_{Line}^{\ Y} = 8.75$ A; Speed = 1458 - 9 RPM

$I_F = 2.3$ A; $I_{Line}^{\ R} = 7.85$ A; $I_{Line}^{\ B} = 8.8$ A

Table [8.5.2] DC Generator Operating Parameters.

8.6 Rotor Bar Current - Harmonic Content

The magnetic field within a SCIM forms a three phase dimensional quantity which may be described in terms of both electric and magnetic circuit parts. The former describes such effects as EMF's, currents and voltages, the latter describing the MMF's, flux and reluctance of the SCIM. The losses, forces and torques developed within such a motor are found to be dependent upon these quantities with particular dependence upon current and flux densities. The performance of the complete motor is therefore highly dependent upon the distribution of the flux density component within the air-gap.

The flux density within the air-gap of an induction motor is a function of both time and space, i.e. $b = b(\theta, t)$. In a perfect motor the variation is taken to be of a perfectly sinusoidal nature in both time and space. However, in most practical motors it is never possible to achieve such flux densities within the air-gap. Due to slotting which occurs both within the stator and rotor, winding layouts, supplies and many other effects, the distribution and magnitude of flux density within an air-gap will be contaminated by many harmonics of both space and time. Thus, as the stator current within the winding alternates, the MMF of the current is found to consist of a family of rotating waves, each harmonic being associated with a pole number appropriate to its specific harmonic order.

The air-gap MMF produced by positive sequence currents rotates in a manner which is opposite to that of negative sequence air-gap MMF components. Under balanced conditions the fundamental, 7th and 13th are of positive sequence, the 3rd, 9th and 15th are of zero sequence and the 5th, 11th and 17th are of negative sequence.

These harmonic fluxes, besides causing harmonics within the induced EMF's, produce secondary effects within the energy conversion process. As torque is developed when a stator flux component within the air-gap of the motor interacts with a rotor component, should the waves have similar number of poles and a suitable space phase displacement, then it follows that harmonic flux components will develop torque components. These components, known as parasitic torques, are ultimately responsible for machine vibration and extraneous noise, and can, in extreme circumstances, cause the motor to crawl, or cog, at speeds well be low that of the desired synchronous speed, or in the worst case, stop the motor from starting at all by causing the rotor to lock steady at standstill. This has been reported to frequently happen, should the rotor current due to the stator slot MMF harmonics produce waves which have the same order as the principal phase belt harmonic.

Two main parasitic torques are found to occur within the air-gap of the SCIM, these being Asynchronous and Synchronous torques. Asynchronous torques occur when the stator MMF harmonic induces a secondary current which has the same order. The torque produced which is harmonically related to those created by the fundamental, has more poles than that of the fundamental, and hence, a lower synchronous speed resulting in slowing the motor down, the braking affect being similar to that of the backwards rotating component at all forward speeds. Synchronous torques are produced when any two separate harmonics which have the same number of poles react to form a torque. As the harmonic components have a similar number of poles, it follows that when the speeds coincide the fields synchronise and a locking, or Synchronous Torque is obtained producing a form of pulsating torque ripple during steady state periods of operation.

8.6.1 Harmonics Present within Rotor Bar Current

The harmonics present within rotor bar currents were grouped into sections by Binns [70]. Frequency components present within the bar currents include those due to slip frequency components, stator MMF components and slot ripple frequencies together with additional harmonics from both saturation and multiple armature reaction, if present.

Components associated with stator MMF have been defined by Binns to occur at both eq. (8.6.1.1), where 'm' represents the harmonic index which may have values 7, 13, 19, 25, ..., and eq. (8.6.1.2), where 'm' can assume 5, 11, 17, 23, ...

$$[A] = f_s \,|\, 1 - m(1\text{-}s) \,| \qquad \textbf{(8.6.1.1)}$$

$$[B] = f_s \,|\, 1 + m(1\text{-}s) \,| \qquad \textbf{(8.6.1.2)}$$

Slot ripple harmonics are given by eq. (8.6.1.3). It is stated that high order harmonics are quite small in amplitude, (they may be neglected after values of $l > 4$), and that the most troublesome harmonics in existence are those due to belt or phase group harmonics which occur at $2Q_1 \pm 1$, where Q_1 represents the number of phases on the stator, thus for a three phase motor the harmonics, $m = 6 \pm 1 = 5, 7$ ... shall be the worst.

$$f_s \,|\, 2l\, (Z_2 / P\, (1\text{-}\sigma) \pm |\, [A] \text{ or } [B] |\, | \qquad \textbf{(8.6.1.3)}$$

Components may occur due to the effects of saturation, but are reported by Binns to be small compared to the slip frequency components which also occur at that given by eq. (8.6.1.4), where 'k'

$$skf_s \qquad \textbf{(8.6.1.4)}$$

represents the harmonic index, 1,3,5,. The saturation harmonics are only found to occur at odd harmonic orders.

The results of the investigations carried out upon the three phase Inverted Geometry Squirrel Cage Induction Motor are presented within Section (8.8).

8.7 Rotor Bar Transducer - Calibration and Formation

In order to obtain non-invasive access to the individual rotor bar currents within the IGM, a transducer was required which would distinguish between the currents within the bar being monitored from that of bars nearby. The device used would require to be free from any saturation effects and be capable of monitoring fast rising transients. The device chosen, after researching many such devices including that of CT's and potential dividers, was that of the Rogowski Coil. This transducer is simple in nature, is free from saturation problems and operates only from an alternating current normal to the transducer, see Chapter 1. The Rogowski Coil used in the investigations, the worm coil, has also been well documented for this practical application.

8.7.1 Calibration of Coil

The Rogowski Coil used to obtain the rotor bar currents was initially developed from a worm coil of 120 turns of 0.25mm enamelled copper wire. In order to ascertain the output achievable from this prototype, the coil was wrapped singularly around a test rotor bar similar in all respects to that within the IGM. Using the test circuit, Figure [8.7.1.1], various tests were undertaken in order to observe the output and allow the determination of calibration procedures. From Figure [8.7.1.1] it may be seen that the output of the coil was attached across a load resistor prior to being low-pass filtered.

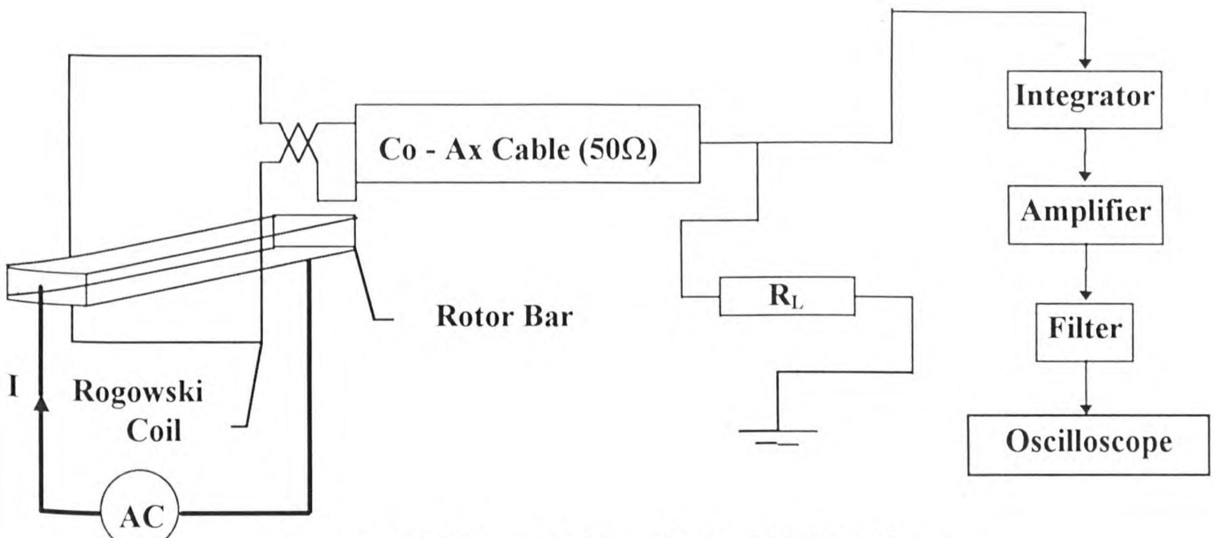

Figure [8.7.1.1] Rogowski 'Worm' Coil Calibration Circuit.

Using the test circuit within Figure [8.7.1.2], the supply was varied in steps of 0.1A between 0 and 2A. This enabled the output of the coil to be obtained along with a projection for higher input currents to be achieved from the obtained results. Figure [8.7.1.3] shows the values obtained for this coil and clearly shows the linear nature of its response.

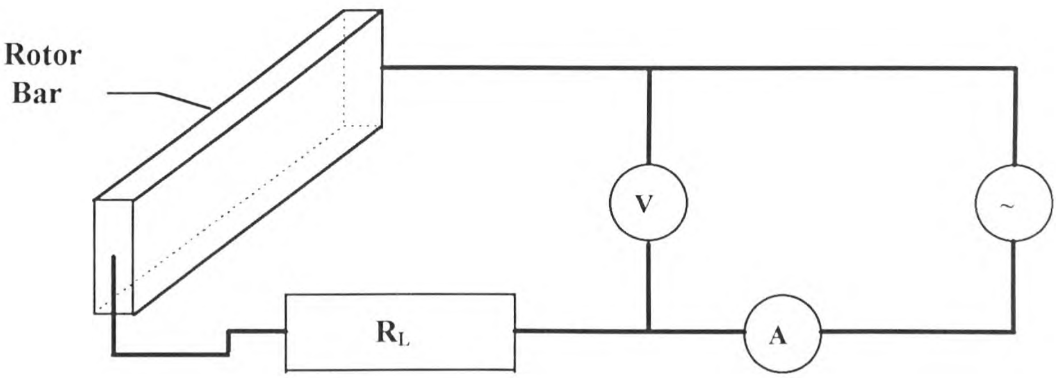

Figure [8.7.1.2] Test Circuit.

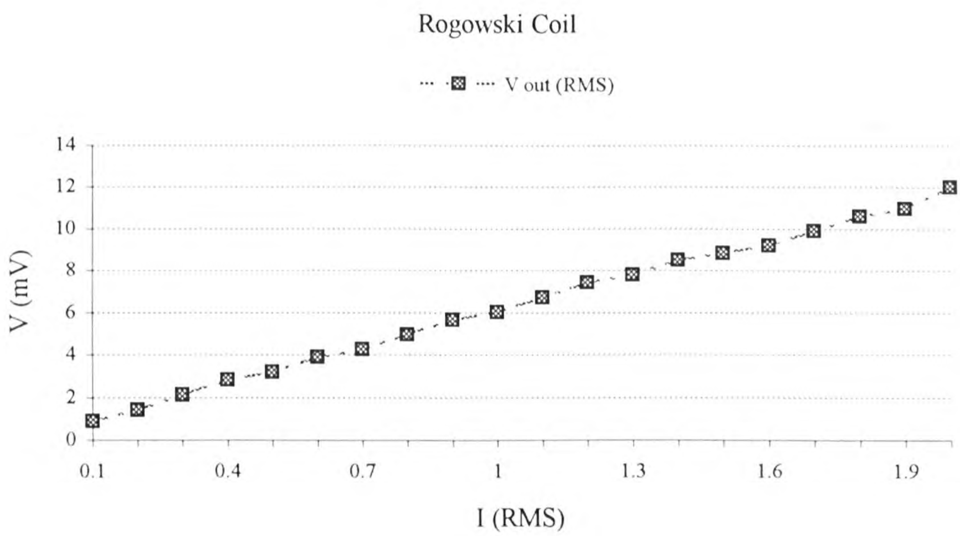

Figure [8.7.1.3] Rogowski Coil Data.

8.7.2 Formation of Coil Former

From the results of the above calibration tests a series of new coils were constructed. Each coil was wound with 100 turns using a wrapping machine, thus enabling a more compact and efficient transducer to be constructed.

In order to improve the mechanical strength, the individual coils were wound initially, upon a Teflon former similar to that in Figure [8.7.2.1]. With this mechanism the rotor bar can pass through a central tunnel within the teflon former and the Rogowski Coil can pass around the bar at the required normal angle to the bar via the grooved trough. This set-up gave full mechanical protection to the coil as the vulnerable lower parts of the coil were now fully protected by the former.

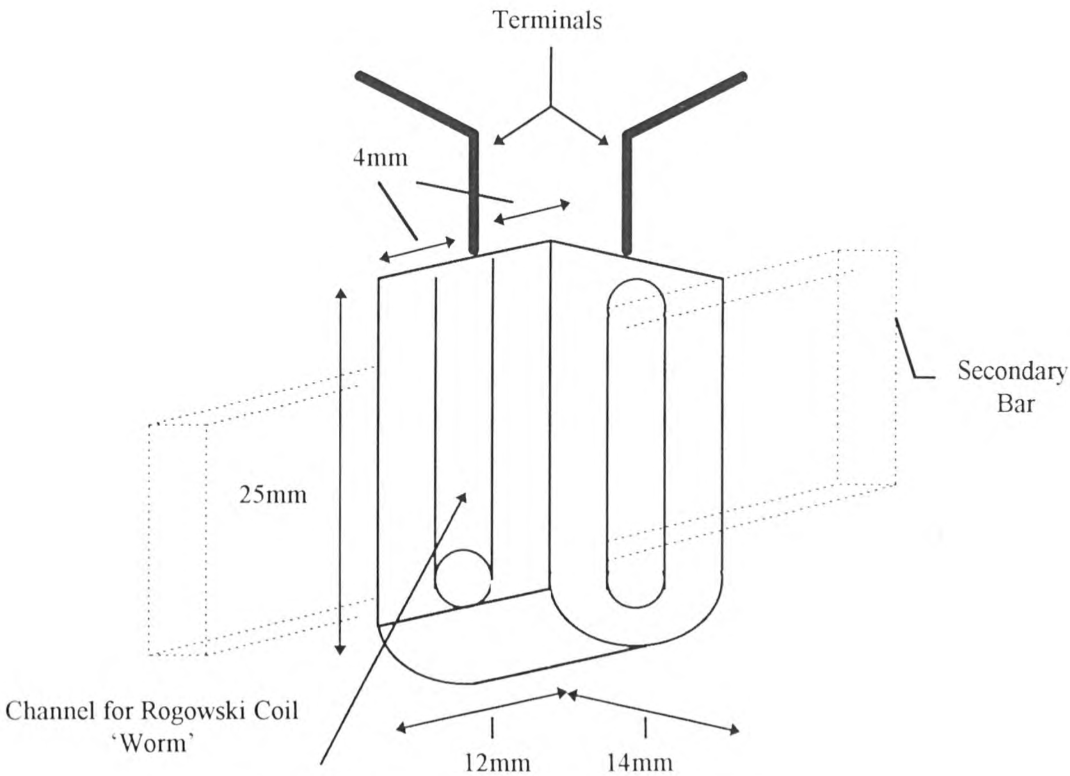

Figure [8.7.2.1] Rogowski 'Worm' Coil Former.

Calibration tests similar to those previously described were carried out, this time with the coil located in-situe upon the IGM. As in previous tests the supply was varied between 0 and 2A in steps of 0.1A, resulting in the output presented within Figure [8.7.2.2].

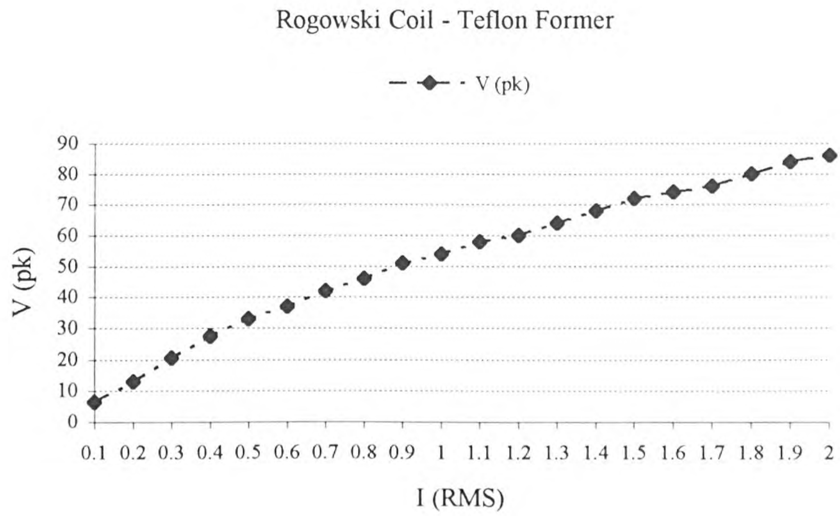

Figure [8.7.2.2] Rogowski Coil Output - Teflon Former.

These results confirmed that the introduction of the former had not altered the output of transducer. It was decided however, to use plastic formers of similar dimensions and shape on the IGM; a plastic former being easier and less time consuming to produce.

Nineteen such plastic formers were produced and wound with the Rogowski Coil. As only 18 of these coils would be required within the IGM, further calibration tests were carried out in order to obtain the 18 best coils which were then placed onto the rotor bars within the IGM, Figure [8.7.2.3].

8.7.3 Transfer of Transducer Signal

Noise in the form of interference, be it coupled to the circuit electro-statically, electro-magnetically or magnetically creates distortion in the original signal so that it no longer represents that being monitored. However, with the use of suitable circuit layout and construction techniques, interference may be reduced to insignificant levels.

As the environment around and particularly within the IGM is a highly electro-magnetically contaminated area, it was imperative that signals from the individual Rogowski Coils were protected. A stator mounted interface panel was designed to bring the two ends of each transducer to an appropriate set of co-axial connectors.

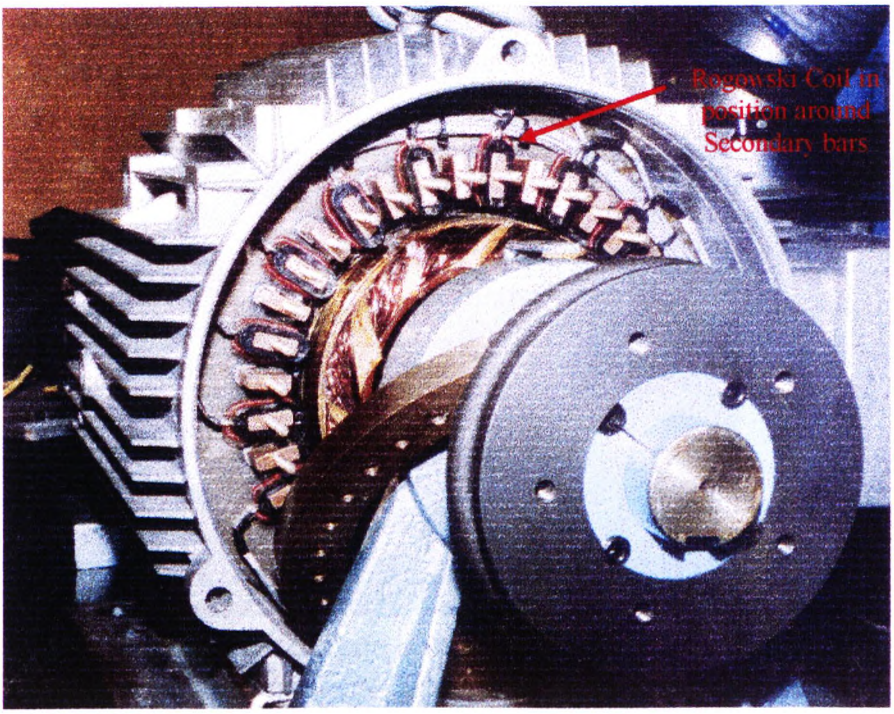

Figure [8.7.2.3] Rogowski 'Worm' Coils in Position within IGM.

This was done in such a way as to allow electrical contact between the body of the panel and test-rig but insulating the co-axial connectors in order to preserve the guard screen of the cabling. Initially a 50Ω cable was used to connect the transducers to the appropriate output. This however, was found not to protect the signals within the IGM, therefore, twin core screened cabling was used for all connections within the motor. This allowed the guard screen to be brought into the IGM itself, thus giving the signal some form of protection within the IGM. The cabling may be seen in Figure [8.7.2.3] and the interface panel itself is shown in Figure [8.7.3.1].

8.7.4 Rogowski Coil Integration

The output of the Rogowski Coil is defined by Amperes law, therefore, in order to obtain true representation of the rotor bar current, it was necessary to integrate the coil output. In order that the integrator does not degrade the signal being monitored it was necessary to design a circuit which would successfully integrate over the frequency range 0.1 to 100 kHz.

As a means of obtaining such a frequency range a compound integrator similar to that shown in Figure [8.7.4.1] was used. This form of integrator has an extended operating bandwidth obtained by combining one integrator with another which has a continuating characteristic. This is achieved by making use of both passive and active integrators.

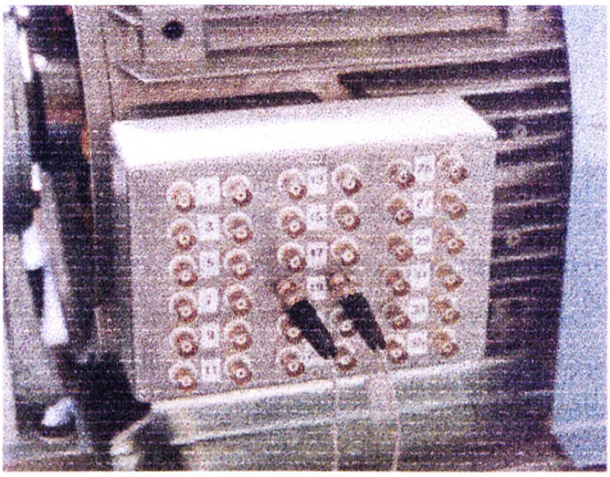

Figure [8.7.3.1] Rogowski Coil Interface Panel.

In addition to the integrator, the co-axial cabling connecting the coil to the integrating system must be treated as part of the entire system. The cable is terminated by its characteristic impedance, 50 or 75Ω. The resulting circuit having a frequency characteristic similar to that shown in Figure [8.7.4.2].

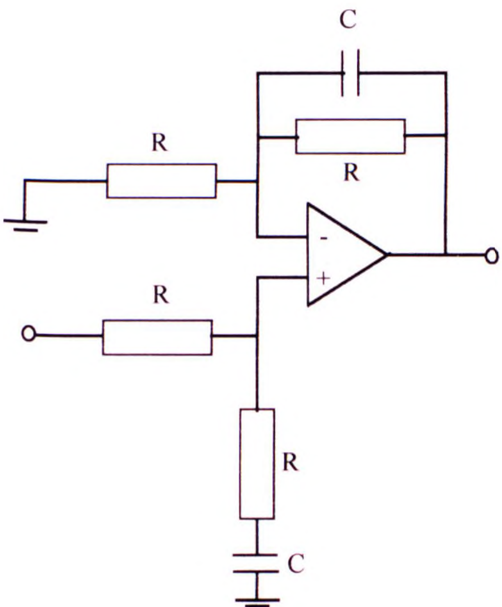

Figure [8.7.4.1] Compound Integrator.

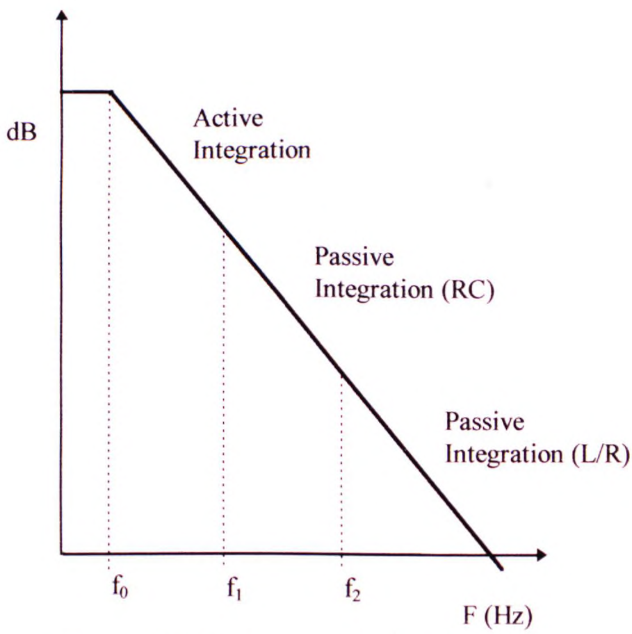

Figure [8.7.4.2] Compound Integrator Characteristic.

8.8 Results of IGM Investigations

8.8.1 Initial IGM Starting Problems

The starting procedure for the IGM test-rig involved supplying the rig from a 15A, 0 - 400V variac. From standstill the supply voltage would be increased until rated supply voltage and primary speed was achieved. Although this was in the main a satisfactory process, it was noted that on numerous occasions the IGM's primary would rotate slightly before coming to a complete standstill even if the supply was removed and re-applied. On achieving this stationary state the primary winding was observed to pulsate slightly. When in this condition, with the IGM acting as a transformer, supply current would rise rapidly due to the lack of opposition caused by the stationary primary not generating any back EMF. However, if the rotor was physically moved to a new location just a few degrees, the motor would begin correct starting. A series of exploratory tests were completed in order to observe any clues as to the reasoning behind such a phenomenon.

As a means to observe the amplitudes of the phase supply currents during non-starting, all three supply lines were monitored using CT's. CT's were used since the Hall effect transducers available had too small a range for monitoring the transient obtained.

The motor was run at three individual times within the steady state condition. With the variac set at 100V, the phase voltages and currents were monitored in order to observe any imbalances within the supply to the IGM.

From the results presented within Table [8.8.1.1] through to Table [8.8.1.3] it may be seen that in phase B the current is approx. 0.5 A less than the other phases. This value represents an imbalance of around 14% of the normal steady state value.

$V_{RY} = 105.0$	$I_Y = 3.5$
$V_{BY} = 102.5$	$I_B = 2.9$
$V_{RB} = 102.5$	$I_R = 3.0$

Table [8.8.1.1] IGM Test No. 1.

$V_{RY} = 100.0$	$I_Y = 3.3$
$V_{BY} = 100.0$	$I_B = 2.8$
$V_{RB} = 99.0$	$I_R = 2.9$

Table [8.8.1.2] IGM Test No. 2.

$V_{RY} = 100.0$	$I_Y = 3.5$
$V_{BY} = 100.0$	$I_B = 2.75$
$V_{RB} = 99.0$	$I_R = 2.8$

Table [8.8.1.3] IGM Test No. 3.

The location of the IGM primary upon start-up was investigated to see if it was possible to obtain some form of correlation between start-up position of the primary and the IGM locking.

Using a reference point on the IGM primary, the motor was put through a series of tests noting whether or not the particular start position was found to lock. The results of which are reported within Table [8.8.1.4].

From Table [8.8.1.4] it may be observed that there was no obvious pattern to emerge from the tests. In fact out of the twelve primary starting locations it was found to lock at least once under all twelve. This therefore being an indication to the fact that there is no positional factor to this particular problem.

The supply currents to the IGM were monitored in order to observe any vast changes within phase displacement between the individual currents. Figure [8.8.1.1] and Figure [8.8.1.2] show the results of these tests under both normal steady state and locked fault conditions. In conclusion from this test it may observed, as previously indicated, that under normal steady state conditions the IGM supply is unbalanced, be this from the supply or due to the slip-ring / primary winding set-up. However, when the primary is in a locked state the backward component is seen to increase slightly.

Primary Location	Test No. 1	2	3	4	5	6	7
1	N	N	Y	Y	-	-	-
2	Y	Y	Y	N	-	-	-
3	N	N	Y	Y	-	-	-
4	N	Y	Y	Y	-	-	-
5	N	Y	N	Y	-	-	-
6	Y	Y	Y	Y	Y	Y	N
7	N	Y	Y	N	-	-	-
8	Y	Y	N	N	-	-	-
9	Y	Y	Y	N	-	-	-
10	Y	Y	Y	Y	N	-	-
11	Y	Y	Y	N	-	-	-
12	Y	N	Y	Y	-	-	-

Table [8.8.1.4] IGM Primary 'Lock' versus Start Location

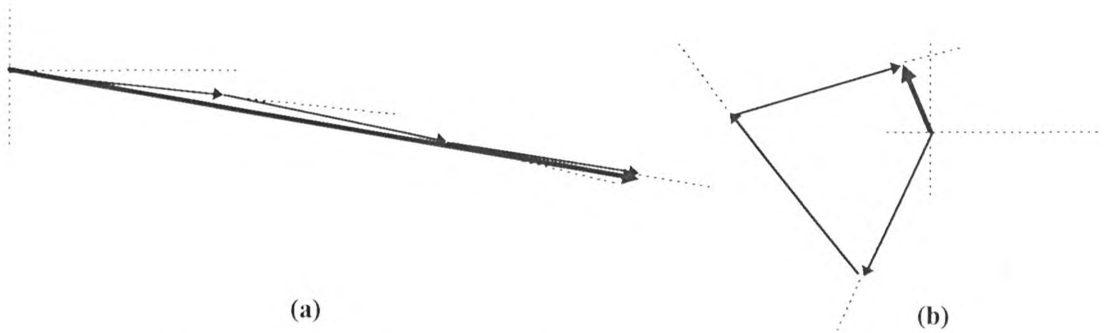

(a) (b)

Figure [8.8.1.1] Forward and Backward Components, Normal Steady State Condition.

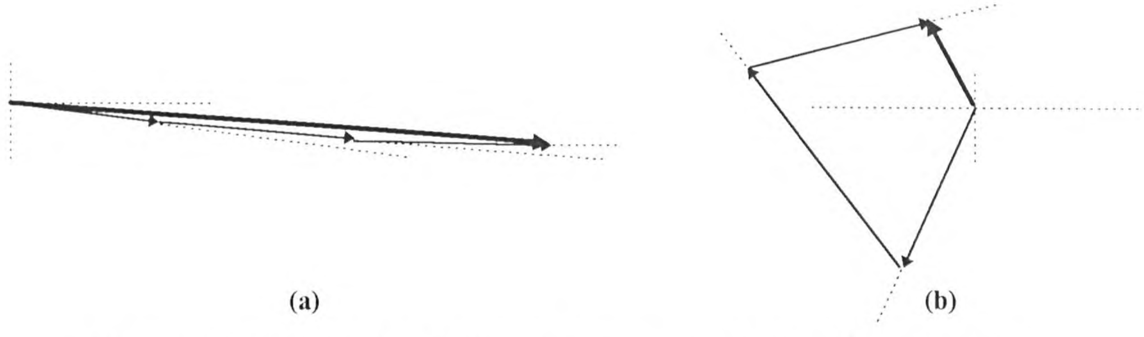

(a) (b)

Figure [8.8.1.2] Forward and Backward Components, Locked Primary Condition.

It was felt that the results from the above tests did not show conclusively any reasoning as to the locking phenomenon. It was felt that perhaps the IGM was suffering from cogging torques. By means of estimating whether or not an induction motor will be prone to such parasitic torques previous researchers had investigated many primary to secondary slot ratios. From these investigations Heller and Hamata [95] produced a table whereby a list of preferred primary to secondary slot ratios for various pole-pairs are listed. This is presented in Table [8.8.1.5] and may be used for small to middle sized squirrel cage motors. The values of slots in round brackets are, because of large synchronous parasitic torques within the braking region, not recommended for reversible drives; the values of slots in square brackets being used only when the rotor slots are skewed by one slot pitch.

From Table [8.8.1.5] it may be observed that the IGM primary to secondary slot ratio of 24:36 for a two pole-pair motor is not recommended. Although the converse ratio, i.e. the original SCIM, is recommended although only when the rotor slots have been skewed by a satisfactory level.

Z_1	Z_2	Pole-Pair
24	(16),[20],([22]),(28),[30]	1
30	(16),[20],(22),[26],[34],[36]	..
36	[24],26,[28],30, ([32]),42,(44),[46]	2
48	(32),34,[36],38,[40], ([44]),(56),58,[60]	..
36	24,[26],[46]	3
54	38,40,[44],[64],66,[68]	..
48	34,[62]	4
72	50,52,54,[56],58,86,88,[90]	..

Table [8.8.1.5] Preferred Primary - Secondary Slot No's.

The following is a comparison of the IGM to SCIM primary to secondary slot ratios and their effects upon the generation of both asynchronous and synchronous torques within the air-gap of the motor.

Asynchronous torques may be limited due to the stator step and slot harmonics [95]. The rotor slots are therefore suggested to be kept within the range of $Z_2 \leq 1.25\ Z_1$. From the IGM primary to secondary ratio it may be observed that this relationship is not obtained, although for the converse, i.e. the SCIM slot ratio, it does hold.

Also, it has been found to be advantageous if the number of rotor slots is kept smaller than that of stator slots. When the primary to secondary ratio is considered it follows that the SCIM relationship holds, the IGM ratio failing to agree with the relationship. Heller and Hamata [95] also state that it has been found that the influence of asynchronous torques is higher the lower the number of primary slots and that a smooth torque curve is difficult to obtain when a four pole machine contains 24 primary slots.

As a means to avoid synchronous torques which may occur at standstill causing the motor to lock, it has been found that the primary slots must not equal $Z_2 = 6pc$, where 'c' represents the harmonic index.

It has also been found that synchronous torques will occur within the motoring region should the rotor slots agree with $Z_2 = 6pc + 2p$, with large torque values occurring, with the risk of causing locking to occur at standstill, should the rotor slots equal $Z_2 = Z_1 - 4p$.

With reference to the asynchronous torques, the primary to secondary slot ratio for the IGM represents the worst case scenario with all 'rules of thumb' failing for the case of the IGM. Synchronous torques are similar in fate, although it is noted that $Z_2 = 6pc$ will fail for both the SCIM and IGM ratios.

In conclusion the ratio of primary to secondary slots used when the test-rig was operated in the SCIM format agrees with most rules developed by [95]. However, when these are reversed, in the case of the IGM format, the majority of the rules and Table [8.8.1.6] point to an incorrect ratio with regards to efficient motor operation.

Further investigations were planned, including the removal of secondary bars in order to improve the primary to secondary ratio. However, before that could be completed a different varaic was used to supply the test-rig. On using this variac no further starting problems have yet been obtained.

8.8.2 Rotor Bar Currents under Normal and Faulted Conditions

With the monitoring techniques previously discussed, it was possible to obtain the rotor bar currents located at either side of a broken bar within the IGM. In order to simulate such a fault condition, one secondary bar of the IGM was removed from the secondary cage. Typical examples of rotor bar currents are presented within Figure [8.8.2.1] to Figure [8.8.2.3].

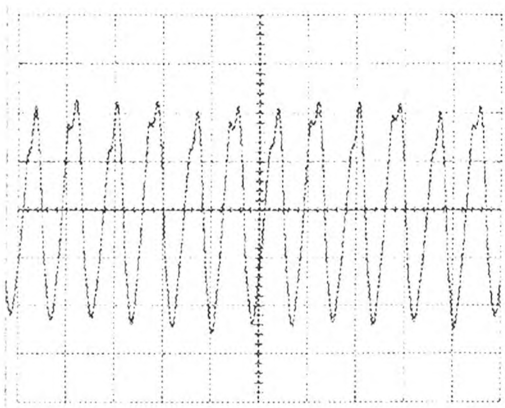

Figure [8.8.2.1] Typical Rotor Bar Current No Load, No Fault, 5V / DIV, 2ms / DIV.

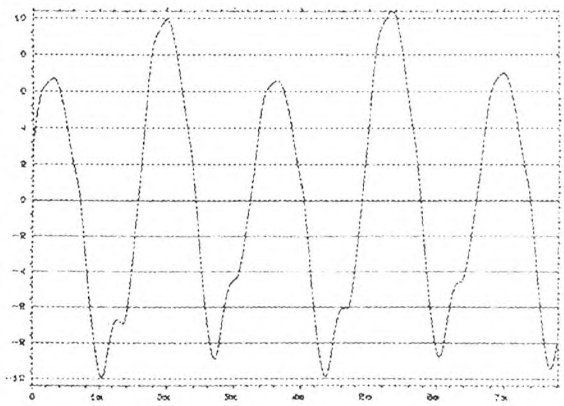

Figure [8.8.2.2] Typical Rotor Bar Current No Load, 1 Broken Bar, 2V / DIV, 1ms / DIV.

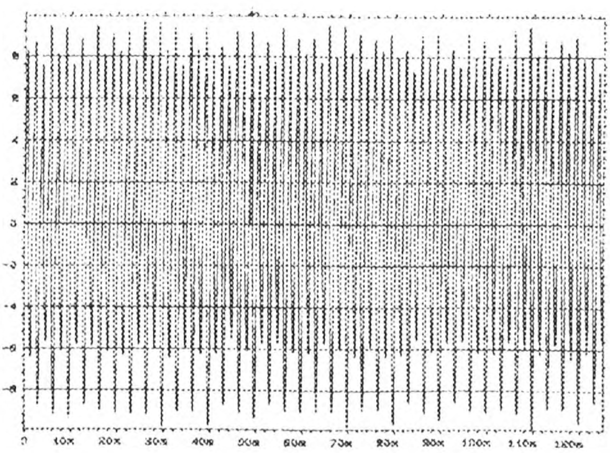

Figure [8.8.2.3] Typical Rotor Bar Current No Load, 1 Broken Bar, 2V / DIV, 10ms / DIV.

Paterson [96] had previously simulated the effects of both normal and faulted operating conditions upon rotor bar currents within a SCIM using a FE package. With this simulation Paterson was able to obtain the difference within rotor bar current densities of each cage bar within the SCIM under both one and zero broken bar conditions. The results showed that the re-distribution of bar current, within bars situated around the broken bar, did not follow an even distribution. In particular it seems that the re-distribution of current density within the bars is biased to one side of the faulted bar.

Figure [8.8.2.4] shows the results obtained from the IGM for the difference between both maximum and minimum values of rotor bar current, under both normal and one broken bar conditions. Two conclusions may be made from these results. They are that under broken bar conditions a general increase in current is observed within all bars situated around the faulty bar and secondly, that in a similar fashion to the simulated results obtained by Paterson, the re-distribution seems to be more heavily located in one area of the cage. This area being the area of cage situated further away from the faulted bar when taken in context to the direction of primary rotation.

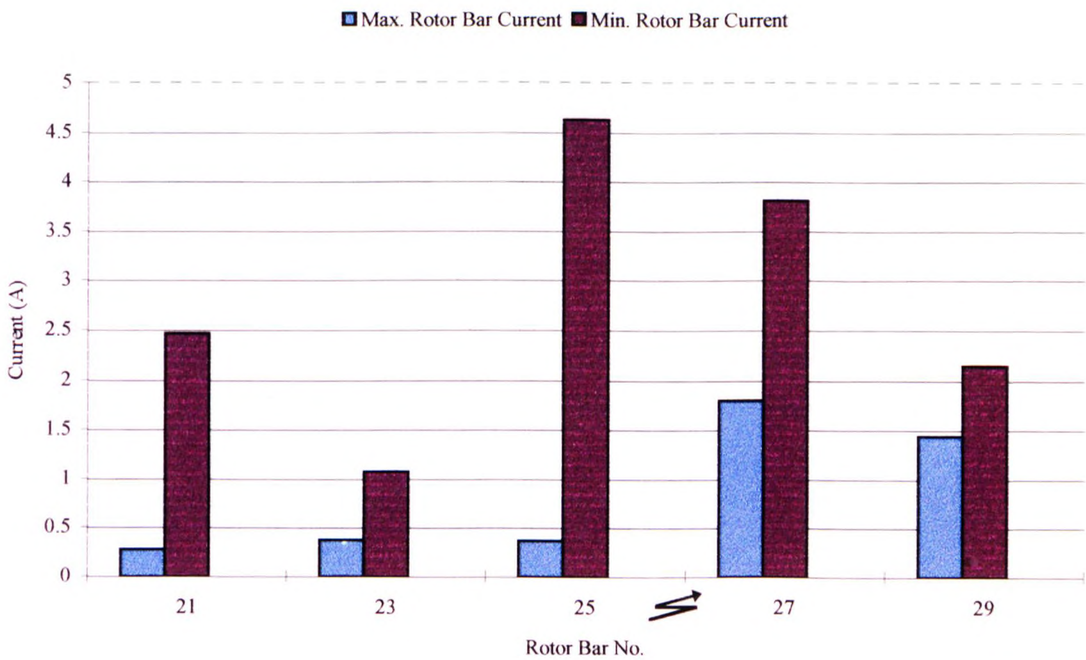

Figure [8.8.2.4] Difference in Rotor Bar Currents between 0 and 1 Broken Bars, No Load.
(Broken Bar Situated between Rotor Bar No. 25 and 27)

Figure [8.8.2.5] shows similar results for both normal and broken bar conditions during semi loaded, s = 0.03, conditions. Conclusions from the results presented in Figure [8.8.2.5] are similar to those in Figure [8.8.2.4] with the greater change in bar current amplitudes being observed with the minimum values, i.e. that a general increase in current takes place in the bars surrounding the broken bar, bars

25 and 27, and that a heavier dissipation in bar current seems to take place at one side of the broken bar, bar 27 onwards.

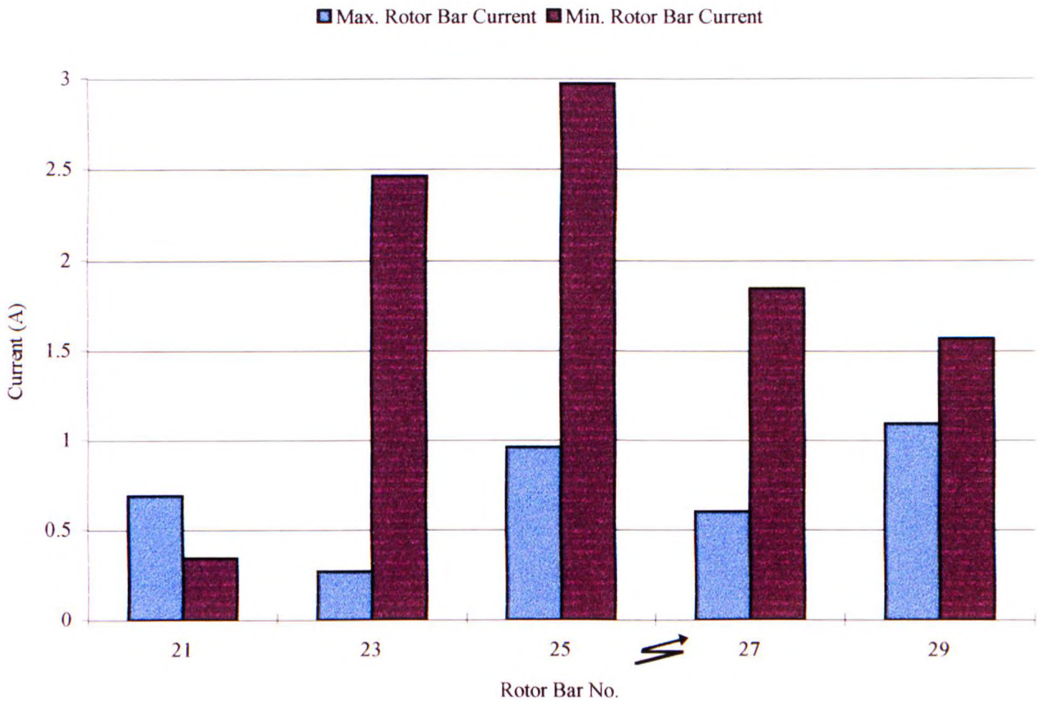

Figure [8.8.2.5] Difference in Rotor Bar Currents between 0 and 1 Broken Bars, Loaded.
(Broken Bar Situated between Rotor Bar No. 25 and 27)

8.8.3 Typical Rotor Bar Current Frequency Spectrum

Figure [8.8.3.1] through to Figure [8.8.3.3] show typical examples of the frequency content within the rotor bar current of the IGM. The spectra shown within this section were all obtained from rotor bar No. 21 under loaded (s = 0.03), no broken bar conditions. Figure [8.8.3.1], 0 - 6 Hz, clearly shows the first few slip frequency components present within the bar current. Since the level of slip is small, then it follows that these components are quite closely situated beside one another. Figure [8.8.3.2], 0 - 200 Hz, clearly shows the harmonic components of the slip frequencies and saturation components, with Figure [8.8.3.3], 0 - 3.2 kHz, presenting the slot ripple components with the 4th order harmonics still being of an appreciable magnitude. The frequency components caused due to the applied stator MMF may also be observed, the amplitude of these possibly being due to the slot ripple components occurring at similar frequencies.

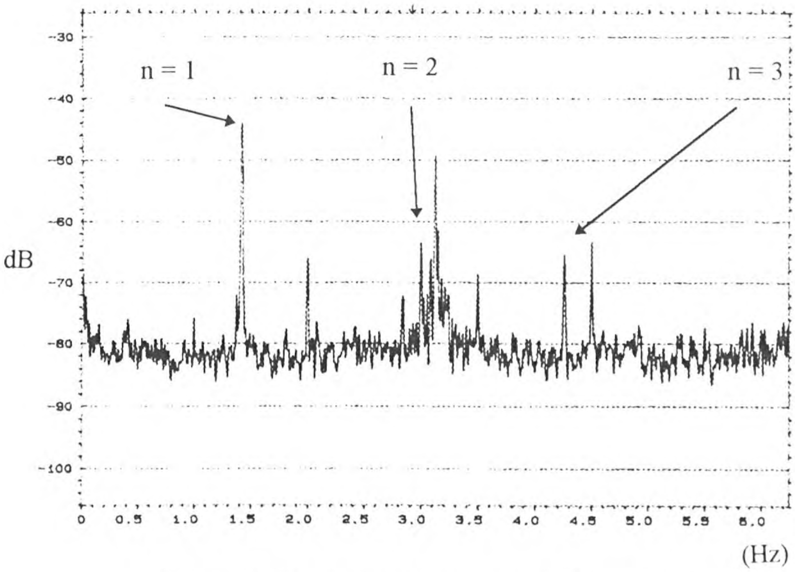

Figure [8.8.3.1] Zoom Spectrum Coil No. 21.

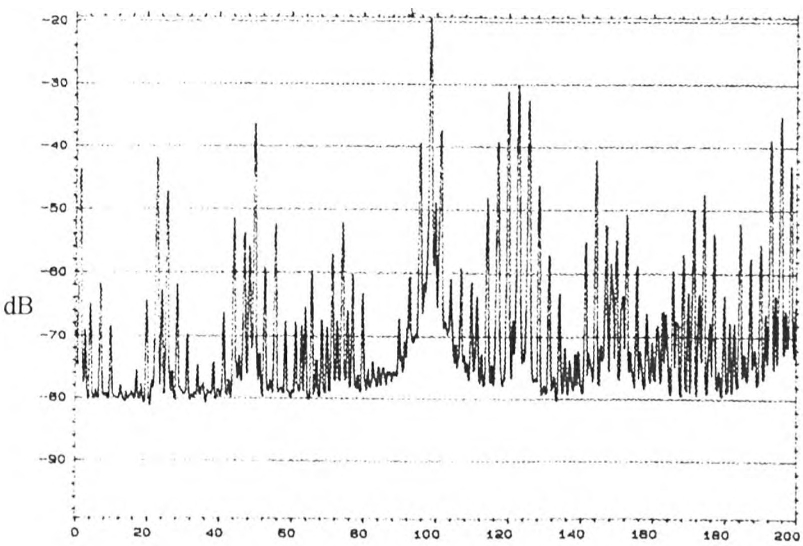

Figure [8.8.3.2] Zoom Spectrum Coil No. 21.

The slot ripple harmonic components stand out clearly within Figure [8.8.3.3], with the 4th order components, (l= 4), still being of an appreciable level. The phase belt components, m = 5, 7, 11, 13 ... may also be observed. The high amplitude of these components possibly being due to the slot ripple components coinciding with the phase belt components.

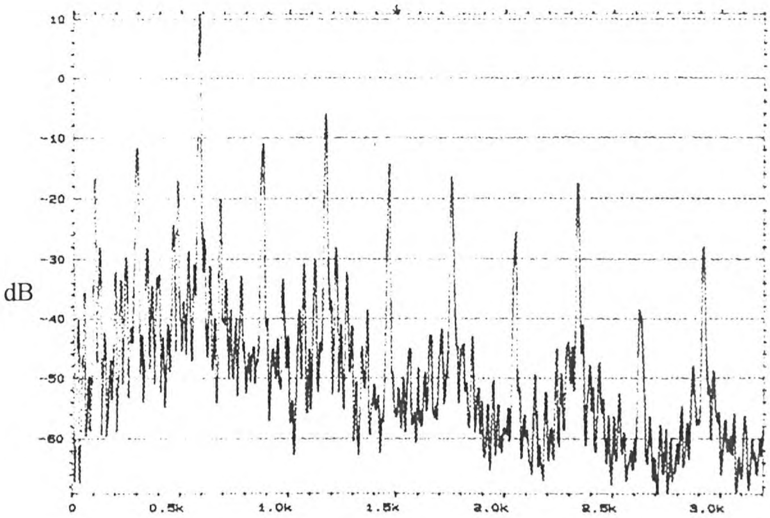

Figure [8.8.3.3] Zoom Spectrum Coil No. 21.

m = { 5 / 7 11 / 13 } l = 0

m = { 5 / 7 1 5 / 7 11 / 13 } l = 1

m = { 11 / 13 5 / 7 1 5 / 7 11 / 13 } l = 2

m = { 11 / 13 5 / 7 1 5 / 7 11 / 13 } l = 3

m = { 11 / 13 5 / 7 1 5 / 7 11 / 13 } l = 4

8.8.4 Effects on Rotor Bar Current Frequency Content due to Single Broken Rotor Bar.

An investigation was carried out into the effects upon frequency content of the rotor bar currents due to broken bar conditions. A single broken bar condition was implemented upon the IGM test-rig, with the frequency content of the rotor bar current being monitored during both no load and loaded conditions. The frequency components monitored included the slip frequency, the applied stator MMF and the slot ripple components. Six bars in total were investigated with three either side of the bar to be broken, i.e. between bar No's 25 and 27.

Figure [8.8.4.1] and Figure [8.8.4.2] show the effects of introducing the single broken rotor bar fault upon the frequency content of the surrounding rotor bar currents. It is interesting to note that in rotor bar No.'s 27 to 31, a greater change within the entire range of monitored frequencies is observed. Figure [8.8.4.2] also clearly shows a change with the introduction of the bar fault, but does not show the increased frequency levels within bar No.'s 27 through to 31.

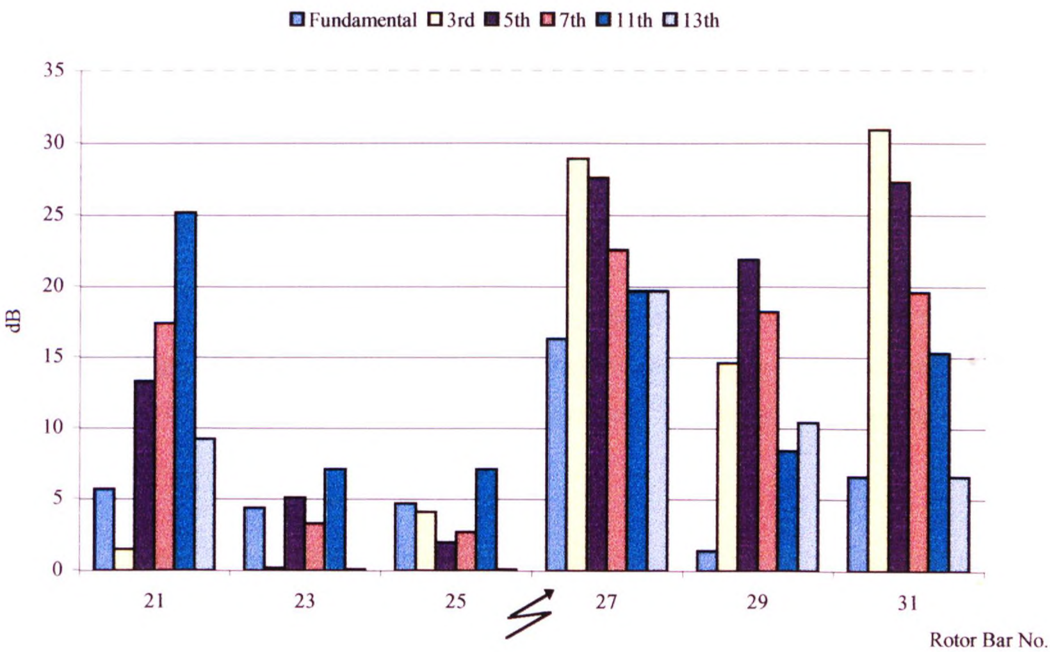

Figure [8.8.4.1] Slip Frequencies - dB change with 1 Broken Cage Rotor Bar, No Load.

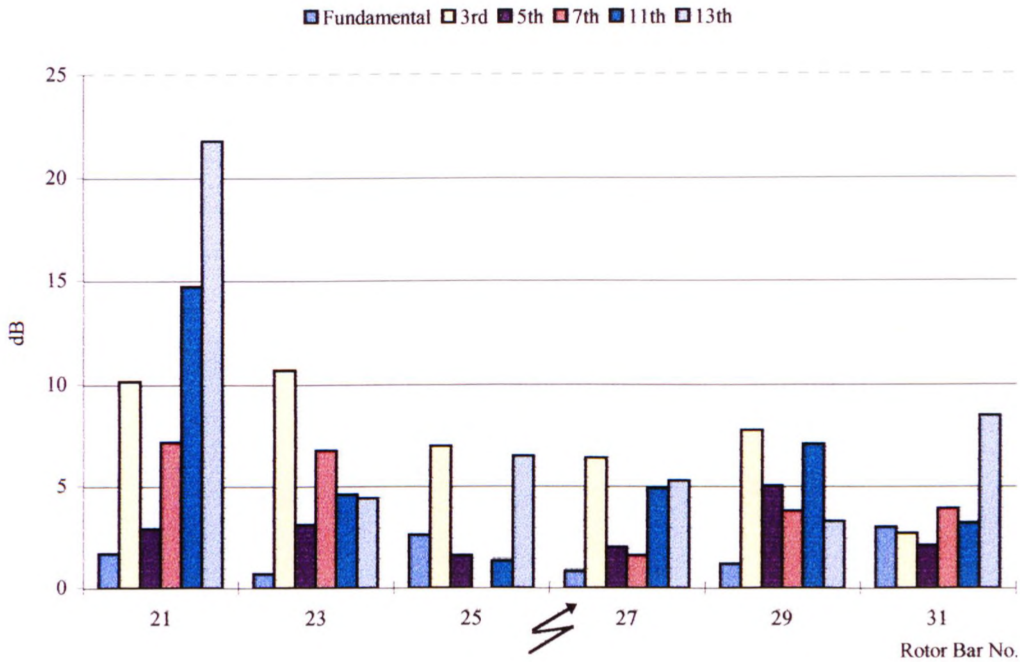

Figure [8.8.4.2] Slip Frequencies - dB change with 1 Broken Cage Rotor Bar, Loaded.

Figure [8.8.4.3] and Figure [8.8.4.4] show the results of monitoring the frequency components due to applied stator MMF for the same two load conditions. In both cases the levels of frequency component were found to reduce with the introduction of the rotor bar fault. In the case of the no load investigation, Figure [8.8.4.3], the reduction of the dB level is constant apart from that around rotor bar No.'s 25 and 27, where a slight increase in the frequency level is found to occur. With the loaded investigation, Figure [8.8.4.4], all components are found to decrease, in particular the harmonics l = 2, l = 3 (m = 11, 13) and l = 4 (m = 5, 7). The remaining harmonics decreasing in a reduced but constant manner.

Figure [8.8.4.5] and Figure [8.8.4.6] report the results of monitoring the slot ripple components under both no load and loaded conditions. From the results obtained from the no load investigation, it may be observed that the components remain constant on the introduction of the rotor bar fault, particularly from rotor bar No. 27 onwards. However, from rotor bar No. 25 to No. 21, the increased frequency level may be observed to reduce the further away from the rotor bar fault the frequency content is monitored from.

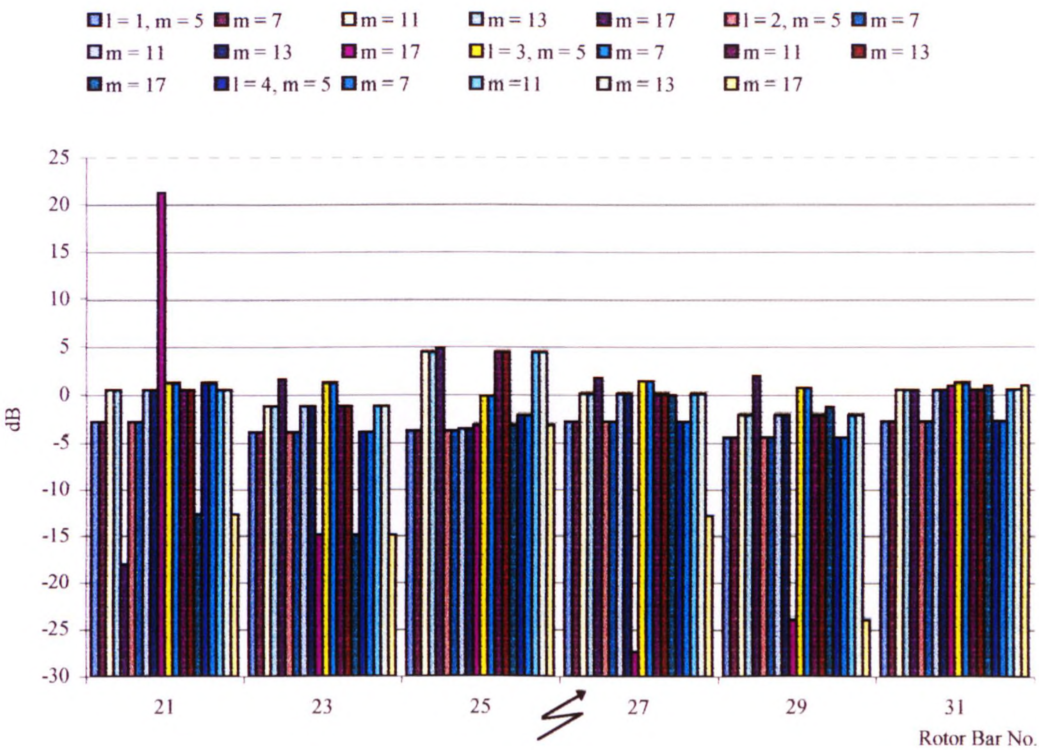

Figure [8.8.4.3] Applied Stator MMF Components - No Load.

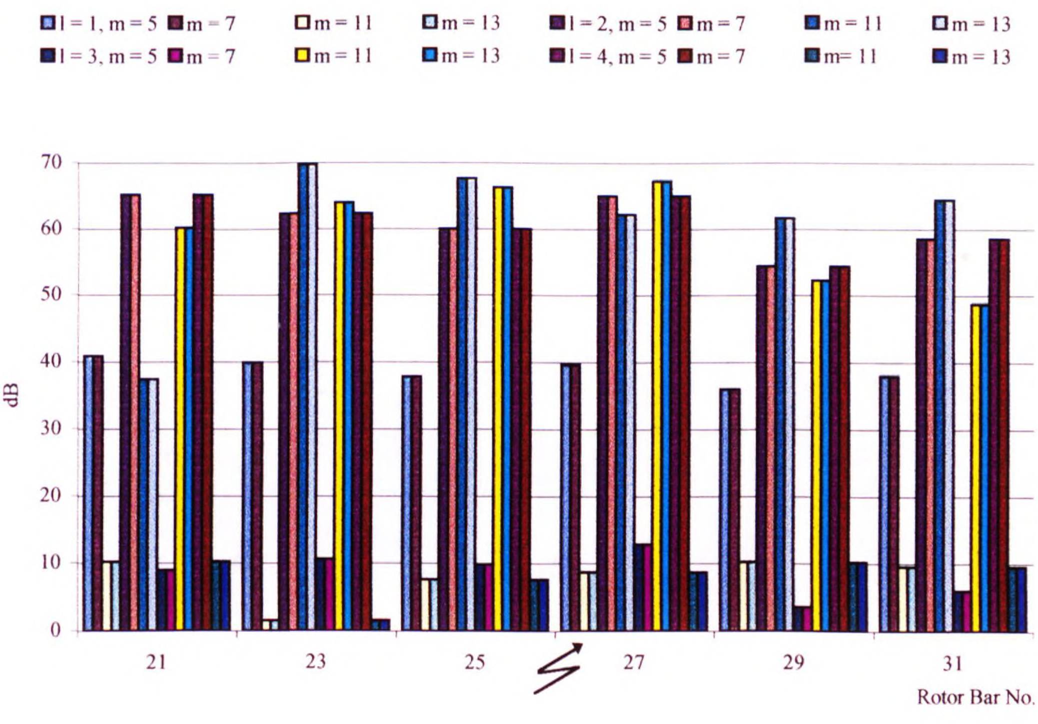

Figure [8.8.4.4] Applied Stator MMF Components - Loaded.

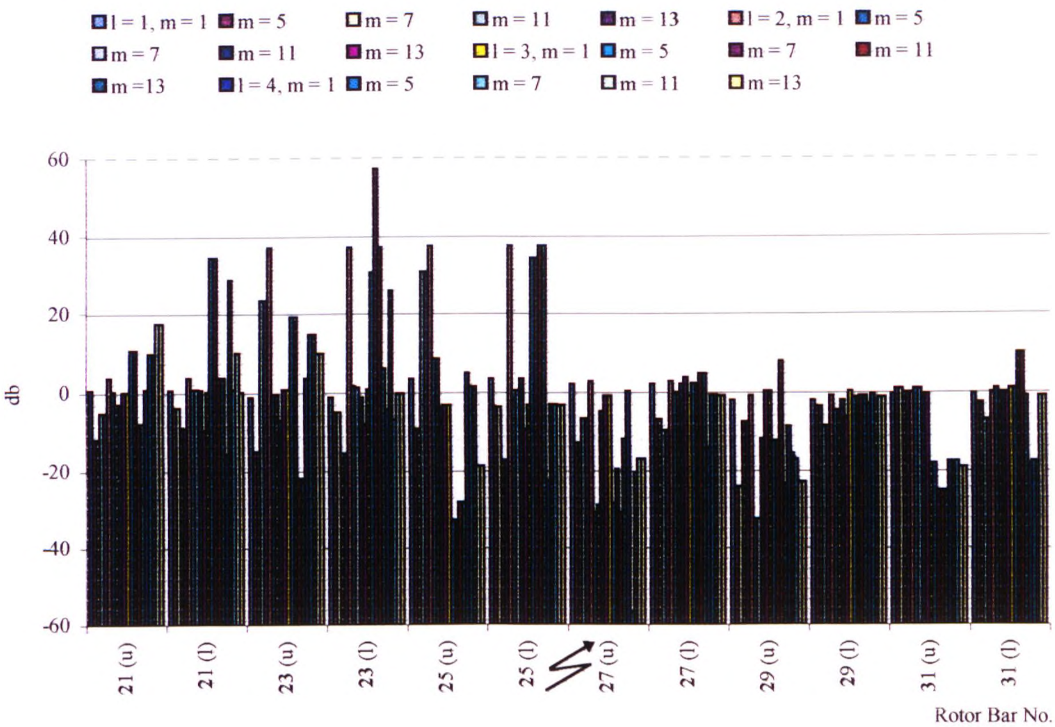

Figure [8.8.4.5] Rotor Bar Slot Ripple Frequency Content - No Load.

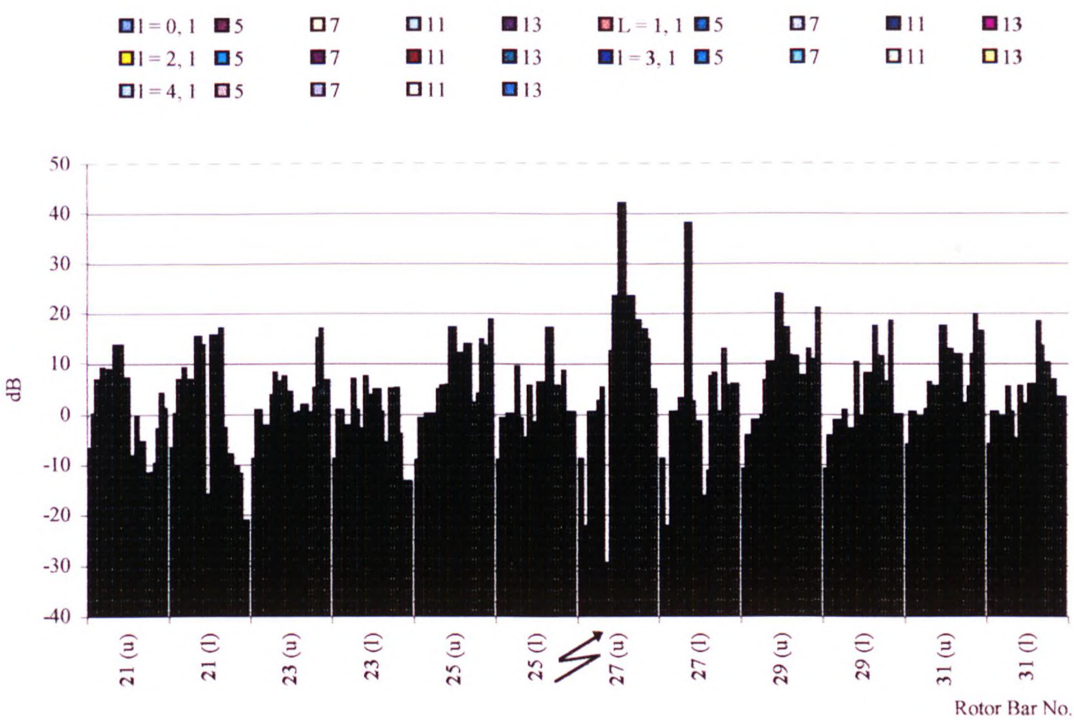

Figure [8.8.4.6] Rotor Bar Slot Ripple Frequency Content - Loaded.

From the results of the loaded investigations, Figure [8.8.4.6], it may be observed that a general increase in the slot ripple components is present with the introduction of the rotor bar fault, with a slight increase in this change being situated around the areas of rotor bar No.'s 27 and 29.

Within Section (8.8.2) it was shown that upon the introduction of a single rotor bar fault, an overall increase in bar current was observed with an increase bias seeming to take place on one side of the broken bar. On investigating the frequency content of these rotor bar currents it was found that under loaded conditions, an expected increase in the level of slip frequency components took place. The increase however, suggests that a greater increase in bias takes place on the other side of the bar fault from that detected by monitoring current magnitude. The frequency components due to the applied stator MMF were found to decrease in level upon the introduction of the rotor bar fault. The decrease in frequency level however, was not constant through the entire harmonic range monitored. On monitoring the slot ripple harmonic components, a general increase in frequency level was found to exist, with the increased frequency component level bias, this time, agreeing in favour with the results obtained from that of the monitored current magnitude data.

8.8.5 Rotor Bar Current Transient Analysis

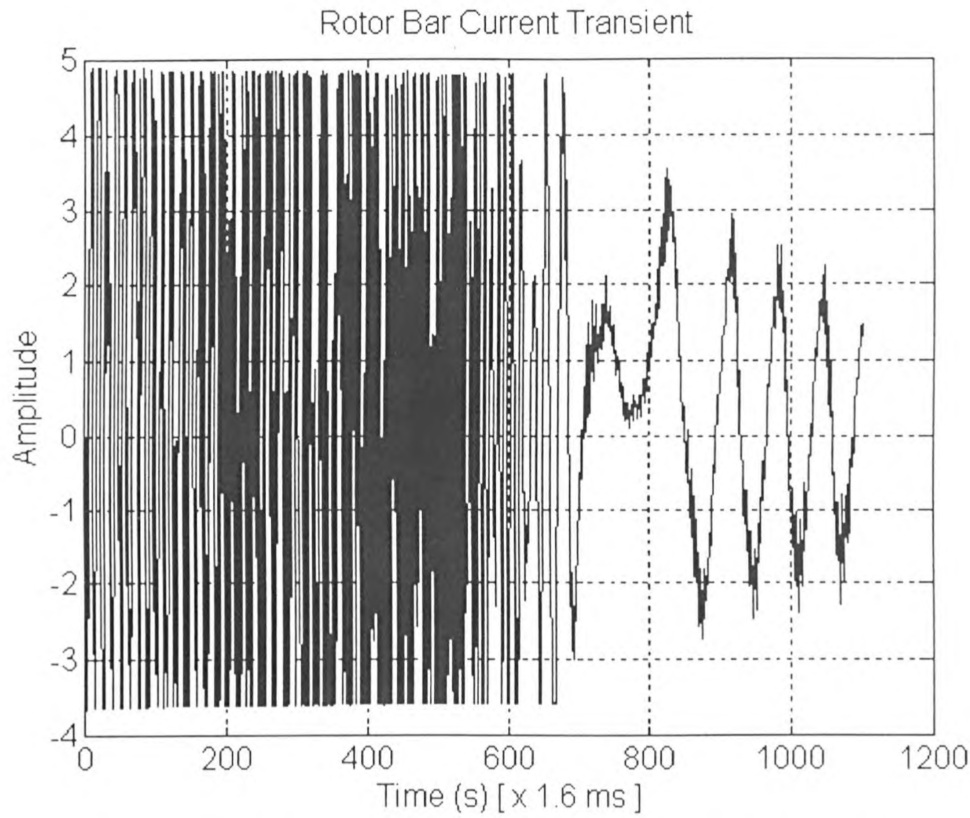

Figure [8.8.5.1] Typical Rotor Bar Current Transient, 1 Broken Bar, Reduced Voltage Start, 1V = 0.8 A.

Figure [8.8.5.1] presents approximately 2 seconds of a typical example of a no load rotor bar transient. Several transients were obtained from a series of reduced voltage starts with the IGM under a fault condition of one broken cage rotor bar. From a series of such transients obtained from several bars around the broken bar, an investigation was carried out into the detection of the timings of the fault location frequency components once suitably referred to the stationary rotor frame of reference. As it was impossible to monitor the rotor bar currents and detect location information from the currents, the investigation concentrated in determining any correlation between the occurrence of the fault frequency components and location of the bar under investigation from the broken cage rotor bar. The fault frequencies to be investigated are shown in Table [8.8.5.1]. These frequencies all represent the fault frequency components for a slip of 0.4. This value of slip was chosen as lower slips would not be valid due to the fault location field effect only being present at large slips, see Chapter 6.

Harmonic	Frequency (Hz)
Fundamental	20
5th	100
7th	140
11th	220
13th	260

Table [8.8.5.1] Fault Frequency Components.

Figure [8.8.5.2] presents the results obtained from monitoring the frequencies shown in Table [8.8.5.1]. The results of the timings at which these frequency components occur at during the transient are presented for six rotor bar transients around the broken rotor bar. The broken bar being situated between rotor bar No.'s 25 and 27.

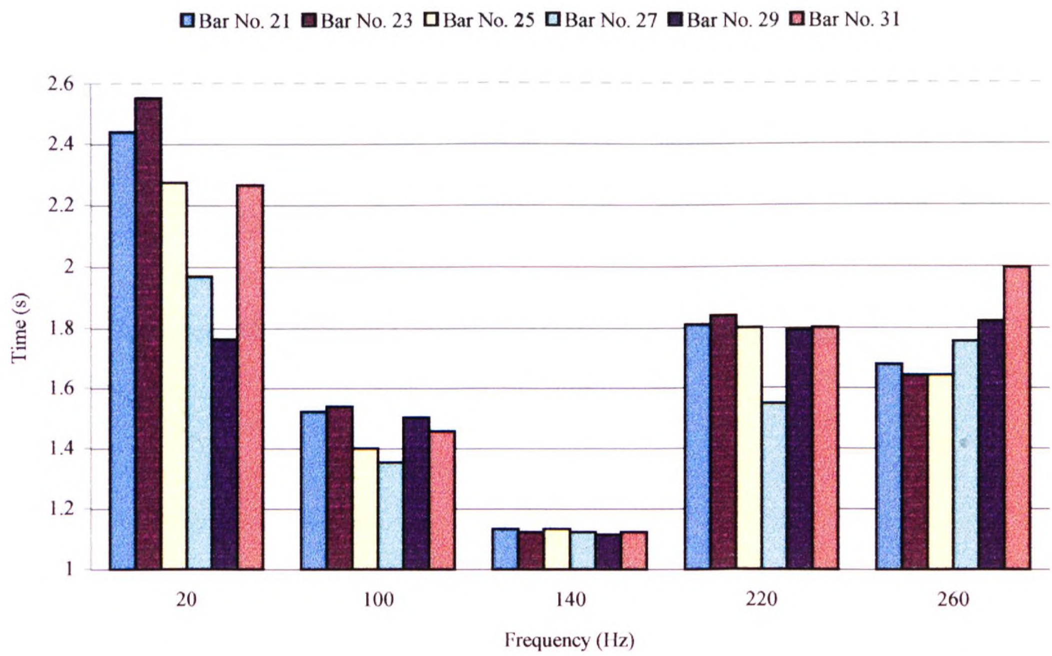

Figure [8.8.5.2] Timings of Fault Frequency Components within Rotor Bar Current Transient.

From Figure [8.8.5.2] it can be observed that the frequencies which show some form of relationship between occurrence of frequency component and the location of the rotor bar are 100 Hz, 220 Hz and 260 Hz.

In order to see if the fault frequency components under investigation occurred at constant times within the transient signals which had all been synchronised, a series of tests were carried out upon one bar. The fault components were monitored within the rotor bar current transient obtained from rotor bar No. 21. The results of this are presented within the Figure [8.8.5.3]. From Figure [8.8.5.3] it can be observed that the fault frequency which gives the most constant result is that of 220 Hz.

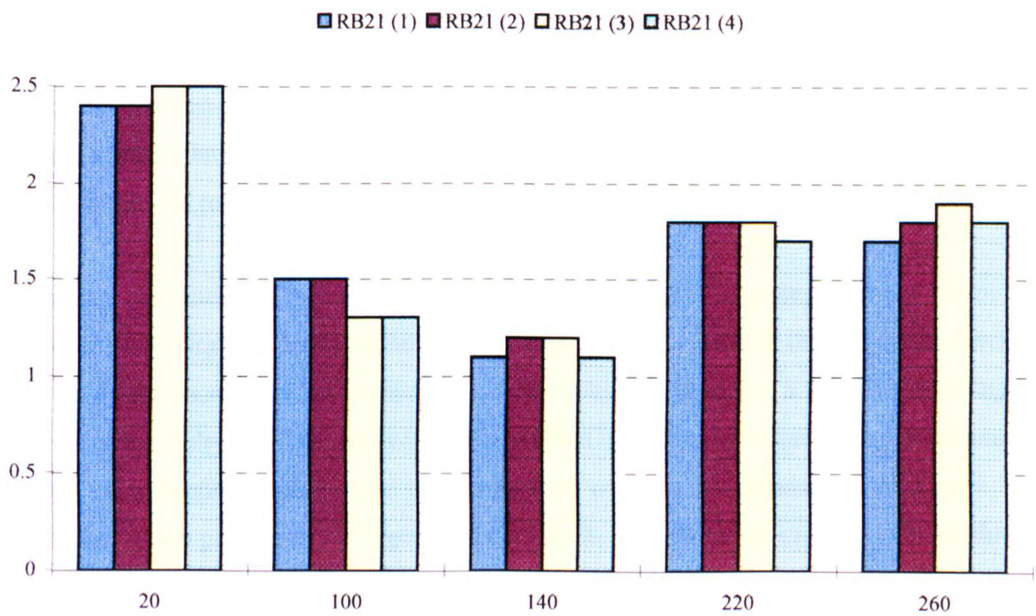

Figure [8.8.5.3] Fault Component Occurrence within Four samples from Rotor Current No. 21.

8.9 Conclusions

The inverted geometry three phase squirrel cage induction motor (IGM), used throughout these investigations was initially discussed in detail. Along with a description of the basic operation and construction of the test-rig used, the Rogowski Coil current transducers used to obtain the rotor bar current signals from the stationary cage rotor bars are described.

Motor parameters were obtained which allowed the rated supply current and voltage levels to be calculated. The test-rig was then operated in conjunction with a DC generator load as a means to produce a greater level of slip, and hence, easier detection of the slip frequency components which are present within the rotor bar currents.

Results are presented which show the effects of the introduction of a single broken bar on both the magnitude and frequency levels of the rotor bar currents. The results of the magnitude investigations show an overall increase in bar current around the faulty bar. However, a heavier bias is suggested at one side of the faulty bar. This effect is further verified by one set of frequency investigations. Further analysis of such effects was deemed best undertaken within a synchronised environment. Thus, the acquisition set-up previously developed, see Chapter 4, was altered in order to achieve this. Such a set-up was designed to allow all 18 rotor bar currents to be sampled in a synchronous fashion. In order to achieve this the hardware set-up described within Appendix VIII was designed.

Finally, results are presented with regards to the detection of the fault location frequency components within the transient signal of a rotor bar current. It had been previously thought that such components would be easier to locate on the rotor side, rather than the stator side due to the lack of attenuation caused by the air-gap when these components are monitored from the stator side. Using a reduced voltage start, in order to keep the signal levels within the range required by the acquisition circuitry, several fault location frequencies were monitored. The results presented show that it is the higher harmonics of the fault location frequency components which show any form of correlation with regards to the location of the faulty bar and the time of occurrence.

Chapter 9

Project Conclusions and Future Work

This project started with a general overview of a typical induction motor. Through a brief resume of three phase induction motor theory together with a brief description of the various formats of motor available, the reader was introduced to the most commonly used industrial prime mover. A discussion was presented on common faults found to occur within the three phase Squirrel Cage Induction Motor (SCIM), followed by a resume of historical methods detecting these faults.

From results of a survey completed by past researchers at The Robert Gordon University [10], and from discussions with industrial operators, one of the most common faults to occur within such motors, due to the general operation of the motor, was identified to be cracked or broken cage rotor bars. These faults, if left undetected, may cause further stress problems to occur within other areas of the cage rotor, which may result in parts of the motor cage breaking off, due to the centrifugal forces present, causing harm to both operating personnel and other machinery.

A more in-depth discussion of relevant theories was presented with regards to the latest steady state and transient health monitoring techniques used within the area of machine Condition Monitoring. Particular emphasis was placed upon techniques which employ the supply line current parameter, of the motor under investigation, as the main parameter of interrogation.

In conjunction with past theories and theories previously not connected with Condition Monitoring, frequency components were identified which theoretically will not only indicate the presence of only SCIM broken bar faults, but also indicate the location upon the cage rotor of such a fault.

As a means to locate these non-stationary frequency components within the supply current transient signal of the SCIM, several signal processing techniques that result in the formation of a signals time-frequency plane were investigated. The signal processing strategies included within the investigations were the STFT, the Wigner Ville Decomposition and Wavelet Decomposition, together with interference reducing variations of the latter two.

Using various test signals, both synthesised and actual signals obtained from a SCIM laboratory test-rig, the individual signal processing methods were investigated as to their individual ability to detect the non-stationary components representative of bar faults. From the investigations reported it was shown that for this particular practical application the latter of the techniques was found to respond the best.

Using this signal processing strategy, a portable supply current transient, machine health monitoring system has been successfully developed and tested. The system which at the moment comprises of a portable PC, thus allowing data sampling to take place on-site, together with assorted data acquisition circuitry and transducers, allows the operator to acquire, analyse and record the results of a motor supply current health investigation.

The system is shown to give favourable results under both laboratory and industrial conditions, with two case studies being reported that present to the reader results obtained from both faulted and fault free industrially sized three phase, 5 MW, SCIM's.

Upon monitoring the non-stationary frequency components representative of cage rotor bar faults, it had been noticed by previous researchers, and again verified by the time-frequency representations obtained from the chosen signal processing strategy, that as the rotor fault components move through the frequency domain the amplitude of the components came to a pronounced peak midway between a slip of 0.5 and zero.

Investigations using a unified theory three phase induction motor simulation were carried out as a means to obtain a reason behind such a phenomenon. The investigations carried out upon the simulation comprised mainly of monitoring the response of varying several parameters within the simulation. The timings and occurrences of any peaks which may occur within the chosen parameters were noted. However, on completing an extensive series of tests, no precise conclusions behind this interesting phenomenon could be made.

Results were then presented on the work carried out towards the objective of locating the frequency components shown to be indicative to the location of cage rotor bar faults. It was shown that frequency components were found to exist at the predicted frequencies during steady state motor operation although, from various filtering and correlation results presented there is still no clear indication as to the observability of the frequency components during the transient period of the supply current signal.

In conjunction with this work, a methodology was created which would allow the detection of the rotor fault location to be pin-pointed to an area within four locations, (should the motor under investigation be a two pole-pair machine). The methodology requires the detection of the fault location frequency components together with acceleration information of the motor under investigation during the transient run-up to steady state speed.

These investigations were extended to include results obtained from an inverted geometry squirrel cage induction motor. The idea behind such a move being that it would be possible to analyse the rotor bar currents for these particular fault location frequency components, which by their very nature are small in amplitude, before being further attenuated by the air-gap. Results presented do show that at some frequency values, some form of correlation between the location of the fault and the time of frequency component occurrence does exist.

A secondary objective from the inverted SCIM was to investigate the rotor bar currents under both faulted and fault free conditions. From the results presented, both of rotor bar current magnitude and frequency level, it is clear that the bars situated at either side of the broken bar do undergo an increase of current. However, from particularly the frequency component investigations it is clear that not all frequency components increase with the introduction of the fault condition. Also, the results seem to suggest a bias in the amount of increase due to rotor bar fault upon one side of the faulty bar location.

Future areas of further work may be summarised into four areas, these being improvements made to the Transient Monitoring System; Fault Location; IGM Investigations; and Sideband Amplitude Determination.

One such future development has already been undertaken and is now in a prototype stage. This involves using the transient monitoring system to create a 'finger-printing' device. A further discussion of this is presented within Section (9.1).

As discussed within Chapter 4 the hardware within the instrumentation of the transient monitoring system must be improved in order to solve the problems caused by the large power glitches when used within an industrial environment. Other long term improvements which should be made to the system are an improved man-machine interface, the calculation of some form of broken bar level, as in the case of 'Motormonitor', and the introduction of a modem facility in order to facilitate the transfer of industrial machine data from the industrial site to the University.

The results presented within Chapter 7 and Chapter 8 do suggest that at some frequency levels some form of correlation does exist between the occurrence of fault frequency components and the location of the broken cage rotor bar. In order to take this further it would be best to continue using such a signal processing technique as was implemented within this project, but with a more selective format of wavelet, also some form of band filtering would be useful since it would no longer be required to monitor such a wide frequency range, all further investigations taking place at one of the frequency components indicated by Chapter 7.

In addition to fault location work, Chapter 8 also presented investigations from the IGM. As previously mentioned any further work, in order to obtain more accurate results, would be best undertaken using the synchronised acquisition methods designed and reported within Appendix VIII. It is felt that the test-rig still has a lot of research potential, as other common cage faults may be investigated from the rotor side.

Finally, with regards to the reasoning behind the amplitude of the Lower Sideband components, Chapter 5, and ultimately to use any conclusions from this work to obtain a form of broken bar factor within the transient monitoring system, it is felt that any further analysis using the induction motor model employed within this project would not produce any further relevant information. Work has been started, by other researchers within the department, using Finite Element techniques and it is hoped that this form of technology will give further indications as to the reasoning behind this phenomenon.

To summarise the main research objectives of this project a technique of monitoring the supply current of a three phase squirrel cage induction motor has been successfully transferred from the mainframe to the portable computer. Using various hardware and software techniques a monitoring system, which is still in a development stage in order to fine tune it to the operators wishes, was produced. The system which initially was developed in the laboratory was successfully tested with industrially sized motors. In conjunction with this work, investigations were undertaken to locate frequency components which were thought to be indicative to the location of a cage rotor bar fault. The results of these investigations resulted in the conclusion that although the majority of frequency components tested gave random results, some frequency components did give some form of information and would therefore warrant further investigations.

9.1 Prototype *'finger-printing'* Exercise

A future development feature within the monitoring system has been developed latterly. This is a facility known as 'finger-printing', whereby the condition of the motor under investigation is monitored and recorded at a certain point in time, commonly on the installation of the motor. This signal would then be kept as a signature signal for that particular motor. At regular intervals further analyses would be taken from the motor under similar operating conditions to that of the original. The signals then being compared with the signature in order to observe any problem situation occurring.

This is a typical monitoring technique in a wide range of systems from modern day military sonar ship identification systems to motor monitoring systems, as any differences, or similarities, which may occur are easily detected when the two signals are compared with one another.

The 'finger-printing' facility has been developed to be used in conjunction with the results obtained from the transient monitoring system. The facility, whose essential model is shown within Figure [9.1], allows the difference between any two synchronised transient analyses, along with the cross correlation of the same analyses, to be computed.

Using the results obtained from the industrial verification Case Studies, Section (4.3.3), as the source of signature and latest monitored data signals, the results presented in Figures [9.2] through to Figure [9.4] show successfully how such a system could be operated.

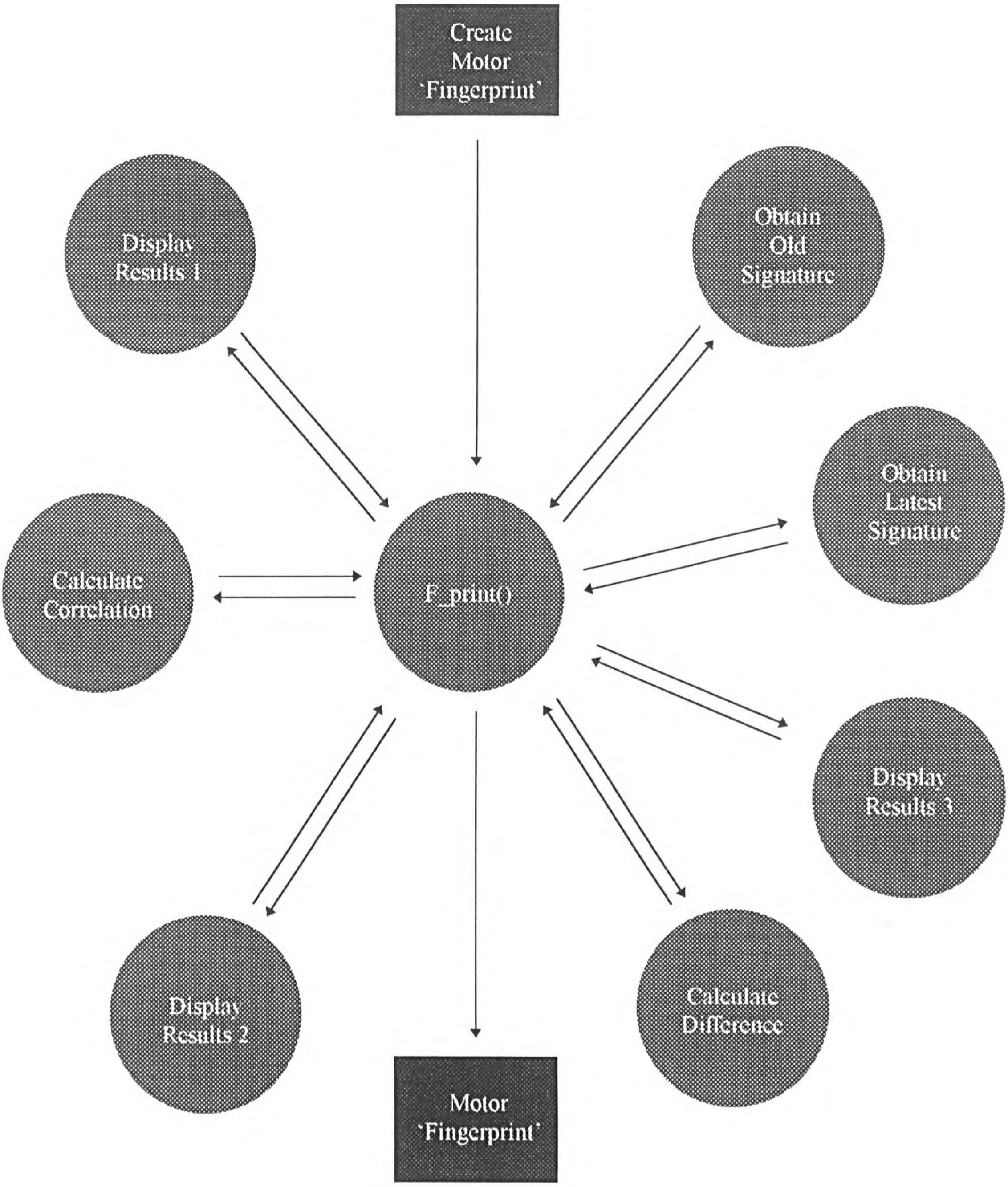

Create Motor 'Fingerprint'
Display Results 1
Obtain Old Signature
Obtain Latest Signature
Calculate Correlation
F_print()
Display Results 3
Display Results 2
Calculate Difference
Motor 'Fingerprint'

(a)

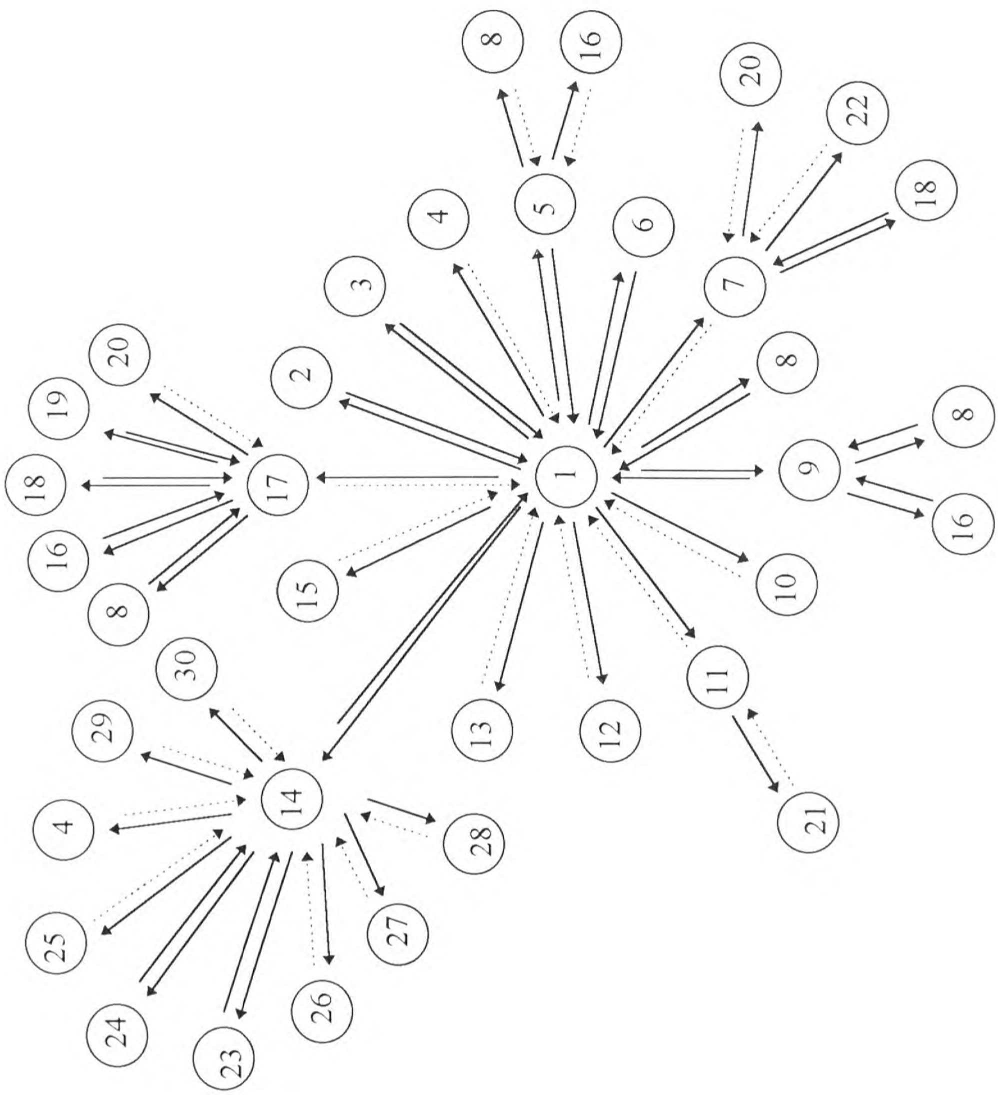
1
2
3
4
5
6
7
8
9
10
11
12
13
14
15
16
17
18
19
20
21
22
23
24
25
26
27
28
29
30

(b)

Essential Model - Function List

1 - F_print();	11 - Correl_data();	21 - Rxy();
2 -ComfirmPopup();	12 - Free();	22 - Fread();
3 - LoadMenuBar();	13 - UnloadMenuBar();	23 - LoadPanel();
4 - GetUserEvent();	14 - Display();	24 - DisplayPanel();
5 - Load_Signature_File();	15 - CloseInterfaceManager();	25 - SetActivePanel();
6 - Calloc();	16 - FileSelectPopup();	26 - GetCtrlVal();
7 - Load_Data();	17 - Save_Data();	27 - SetInputMode();
8 - MessagePopup();	18 - Fopen();	28 - Deleteplots();
9 - Load_new_file();	19 - Fwrite();	29 - UnloadPanel();
10 - Calc_Diff();	20 - Fclose();	30 - Ploty();

(c)

Figure [9.1] Essential Model for 'finger-printing' Software.

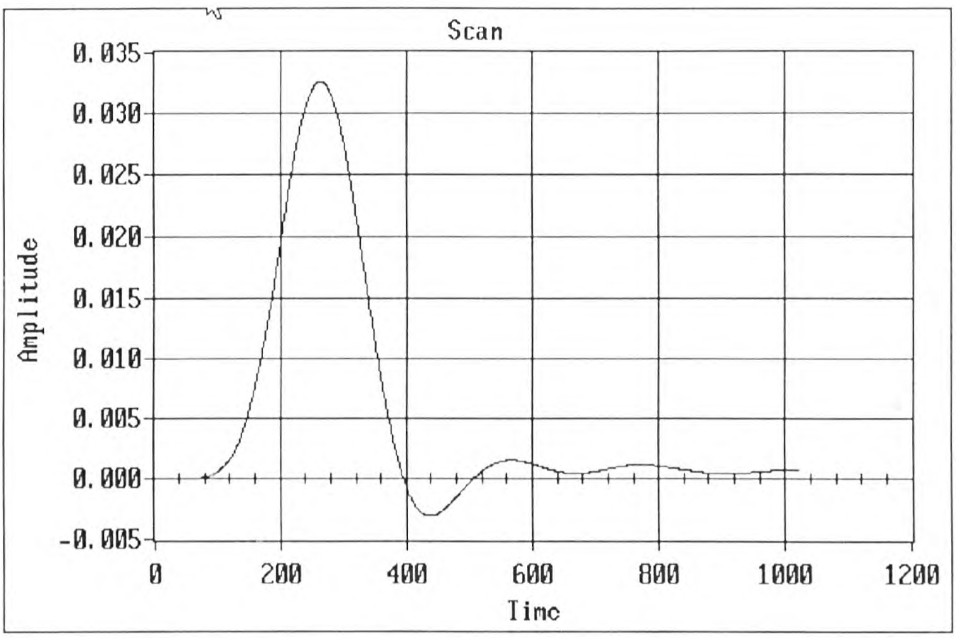

Figure [9.2] Hypothetical Motor Signature to be compared with Latest Analyses.

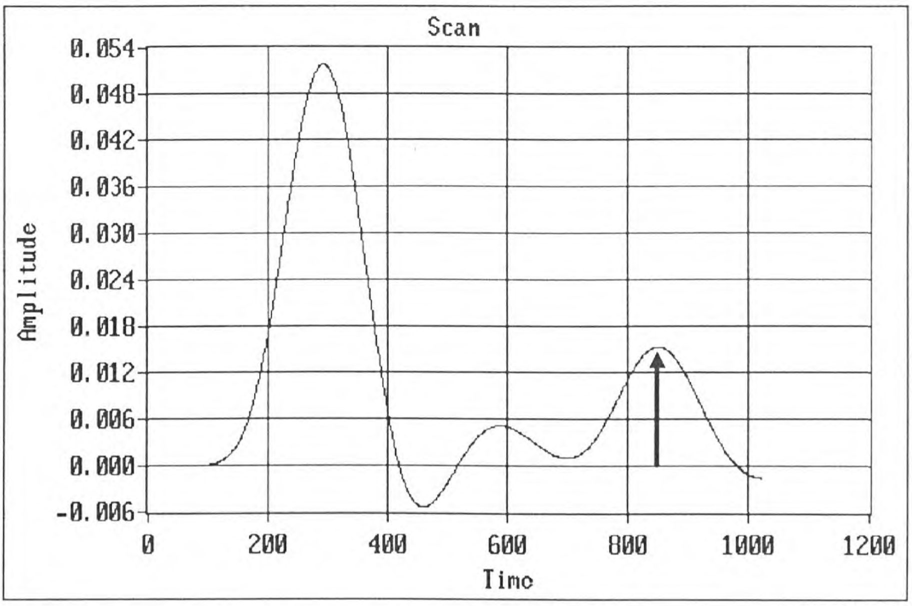

Figure [9.3] Latest Hypothetical Analysis from motor under investigation.

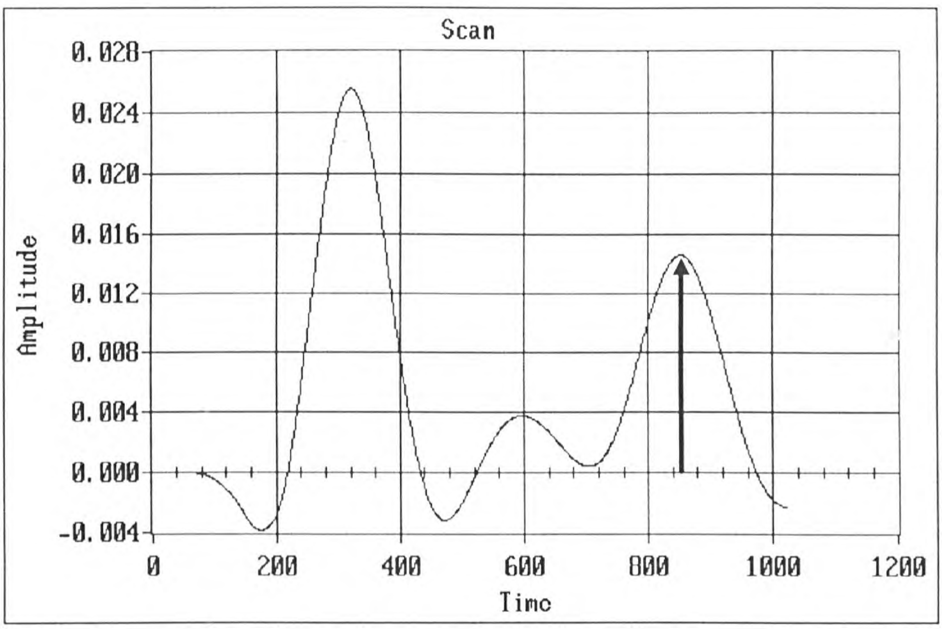

Figure [9.4] Hypothetical Difference indicating Fault Presence.

Chapter 10

References

[1] M. Faraday, "A treatise on the theory of alternating currents", *Cambridge University Press*, Vol II, p325 - 360.

[2] Ferraris, "A treatise on the theory of alternating currents", *Cambridge University Press*, Vol II, p325 - 360.

[3] N. Tesla, "A new system of alternating current motors and transformers", American Institute of Electrical Engineers, 1888.

[4] Dobrowolsky, "A treatise on the theory of alternating currents", *Cambridge University Press*, Vol II, p325 - 360.

[5] A.M. Armour and J.W. Walley, "A magneto-electric method for detecting defects in cast aluminium rotor windings for squirrel cage motors", *The MV Gazette*, October 1956, p 314 - 317.

[6] D. Rankin, "An expert eye on machine health", *Electrical Review*, Vol. 222, No. 8.

[7] R. Nailen, "Detecting and correcting open rotor bars", *Electrical Apparatus*, July 1986.

[8] B.G. Gaydon and D.J. Hopgood, "Faltering pulse can reveal an ailing motor", *Electrical Review*, Vol. 205, No. 14, October 1979, p 37 - 38.

[9] A. H. Bonnet and G. C. Soukup, "Analysis of rotor failures in squirrel cage induction motors", *Trans. IEEE on Ind. Appl.*, Vol. 24, No. 6, Nov. / Dec. 1988.

[10] W.T. Thomson, N. D. Deans, R. A. Leonard and A.J. Milne, "Condition monitoring of induction motors for availability assessment in offshore installations", *4th Eurodata Conf.*, Venice, Italy, 1983.

[11] W.T. Thomson and C.J. McRae, "On-line current monitoring to detect inter-turn stator winding faults in induction motors", *Proc. of the 24th University Power Engineers Conf.*, Belfast, p477 - 480, Sept. 1989.

[12] D.G. Dorrell, W.T. Thomson and S. Roach, "Analysis of air-gap flux, current and vibration signals as a function of the combination of static and dynamic air-gap eccentricity in 3-phase induction motors", *IEEE Industry Applicat. Soc.*, p563 - 570, Oct. 1995.

[13] W.T. Thomson and D. Rankin, "Case histories of rotor winding fault diagnosis in induction motors", *2nd International Condition Monitoring Conf.*, Swansea, Mar. 1987.

[14] R. L. Burns, "Rotor bar failures in large AC squirrel cage motors", *Electrical Engineering*, Oct. 1977, p11 - 14.

[15] S. Williamson and A.C. Smith, "Steady state analysis of 3 phase cage motors with rotor bar and end ring faults", *IEE Proc. Pt. B, Vol. 129*, May 1982.

[16] M.S. Bhattacharyya, M.S. Zoha and S. Chatterjee, "Shop-floor testing of 190 kW, 6 kV squirrel cage induction motor", *IE - Journal EL*, Vol. 63, Oct. 1982.

[17] G.B. Kliman, R.A. Koegl, J. Stein, R.D. Endicott and M.W. Madden, "Non invasive detection of broken rotor bars in operating induction motors", *IEEE Trans. on Energy Conv.*, Vol. 3, No. 4, Dec. 1988.

[18] C. Hargis, B.G. Gaydon and K. Kamash, "The detection of rotor defects in induction motors", *IEE Int. Conf. on Elec. Mach. Design and Applications*, July 1982.

[19] B.G. Gaydon, "An instrument to detect induction motor rotor circuit defects by speed fluctuation measurements", *Testmex 79 Conf. Papers*, p5 - 8, 1979.

[20] I. Morita, "Air gap flux analysis for cage rotor diagnosis", *Electrical Engineering in Japan*, Vol. 112, No. 3, 1992.

[21] J. Penman, M.N. Dey, A.J. Tait and W.E. Bryan, "Condition monitoring of electrical drives", *IEE Proc.*, Vol. 133, Pt. B, No. 3, May 1986.

[22] A.G. Carr and A. Neil, "A new concept in low cost diagnostic monitoring and protection for three phase ac induction motors", *ERA Technology Ltd.*

[23] R.A. Leonard and W.T. Thomson, "Vibration and stray flux monitoring for unbalanced supply and interturn winding fault diagnosis in induction motors", *Conf. on Condition Monitoring*, Swansea, April 1984.

[24] W.T. Thomson, N.D. Deans, R.A. Leonard and A.J. Milne, "Monitoring strategy for discriminating between different types of rotor defects in induction motors", *18th UPEC Proc. Univ. of Surrey*, Guildford, U.K.

[25] J.R. Cameron, W.T. Thomson and A.B. Dow, "Vibration and current monitoring for detecting air gap eccentricity in large induction motors", *IEE Proc.*, Vol. 133, Pt. B, No. 3, May 1986.

[26] A. Gaylard, A. Meyer and C. Landy, "Acoustic evaluation of faults in electrical machines", *IEE Conf. on Electrical Machines and Drives*, Univ. of Durham, Sept. 1995.

[27] A.J. Marques Cardoso and E. de Sousa Saraiva, "The use of park's vector in the detection of electrical failures on three phase induction motors", *Proc. of Int. AMSE Conf. 'Modelling and Simulation'*, Vol. 2C, p99 - 109, Cairo, March 2 - 4, 1987.

[28] P.L. Alger, "The nature of induction machines", *Gordon and Breach Science Pub.*, 1965.

[29] C.V. Jones, "Unified theory of Electrical Machines", *Butterworth*, 1967.

[30] G.B. Kliman, "The detection of faulted rotor bars in operating induction motors", *GEC Corporate Research and Development*, NY.

[31] M.E. Steele, R.A. Ashen and L.G. Knight, "An electrical method for condition monitoring of motors", *Conf. Proc. Electrical Machines - Design and Application IEE*, London, July 1982.

[32] W.T. Thomson and S.J. Chalmers, "New developments in on line fault diagnosis of large ac drives", *R.G.I.T.*, Aberdeen.

[33] S.L. Ho and K.M. Lau, "Detection of faults in induction motors using artificial neural networks", *IEE Conf. on Electrical Machines and Drives*, Univ. of Durham, Sept. 1995.

[34] F. Filippetti and P. Vas, "A fuzzy logic approach to on-line induction motor diagnostics based on stator current monitoring", *IEE Conf. on Electrical Machines and Drives*, Univ. of Durham, Sept. 1995.

[35] S. Elder, J.F. Watson and W.T. Thomson, "Fault detection in induction motors as a result of transient analysis", *R.G.I.T.*, Aberdeen.

[36] J. Jianguo, Z. Zhiping, S. Penshang and W. Xiangheng, "Time frequency spectrum (TFS) of line current during starting process - a tool for diagnosing failure of induction motor", *Dept. of Electrical Engineering, Tsinghua Univ.*, Beijing, China.

[37] J.F. Watson and F. Nour, "The monitoring and analysis of transient vibration signal as a means of fault detection in 3 phase induction motors", *Proc. 28th Universities Power Engineering Conf.*, Staffordshire University, 1993.

[38] S. Elder, J.F. Watson and W.T. Thomson, "the analysis of transient currents in induction motors for the purposes of detecting rotor faults", *Conf. Proc. UPEC*, p691 - 694, 1990.

[39] W. Deleroi, "Squirrel cage motor with broken bar in the rotor - physical phenomena and their experimental assessment', *Delft Univ. of Tech. Dept. of Elec. Eng.*, Delft, Netherlands.

[40] W. Deleroi, "Überwachen, analsieren und orten von elektrischen ungleichenförmigkeiten in käfigläufern", *Etz Archive*, Vol. 5, Pt. 3, p95 - 101, 1983.

[41] N.M. Elkasabgy, A.R. Eastham and G.E. Dawson, "Detection of broken bars in the cage rotor on an induction machine", *IEEE Trans. in Ind. Appl.*, Vol. 28, No. 1, Jan. / Feb. 1992.

[42] J.E. Brown and O.I. Butler, "The zero sequence parameters and performance of three phase induction motors", *Proc. of IEE*, Vol. 101, Pt. 4, 1954.

[43] P. Vas, "Performance of three phase squirrel cage induction motors with rotor asymmetries", *Periodical Polytechnica Elec. Eng.*, Vol. 19, 1975.

[44] P. Vas, "Steady state and transient performance of induction motors with rotor asymmetry", IEEE Trans. on Power Apparatus and Systems, Vol. PAS 101, No. 9, Sept. 1982.

[45] I.R. Smith and S. Sriharan, "Transient performance of the induction motor", *Proc. of IEE*, Vol. 113, No. 7, July 1966.

[46] M.R. Lloyd, "Transient performance of induction motors in electro-mechanical systems", *Laurence, Scott and Electromotors Ltd*, U.K.

[47] A.K. de Sarkar and G.J. Berg, "Digital simulation of three phase induction motors", *IEEE Trans. on Power App. and Sys.* Vol. PAS - 89, No. 6, July / Aug. 1990.

[48] F. Ishibashi and K. Kobayashi, "Experimental study of harmonic magnetic flux of small squirrel cage induction motors", *Elec. Eng. in Japan*, Vol. 110, No. 6, Aug. 1990.

[49] J.J. Campbell, P.E. Clark, I.E. McShane and K. Wakeley, "Strains on motor end windings", *IEEE Trans. on Ind. Apps.*, Vol. IA - 20, No. 1, Jan. / Feb. 1984.

[50] S.C. Ho, C.G. Hong and G.C. Hwang, " Transient and steady state performance of a squirrel cage induction motor", *IEE Proc.* , Vol. 136, Pt. B, No. 3, May 1989.

[51] S. Williamson, L.H. Lim and A.C. Smith, "Transient analysis of cage induction motors using finite elements", *IEEE Trans. on Magnetics*, Vol. 26, No. 2, March 1990.

[52] T. Tsuji, "Measurement of squirrel cage rotor current by twin stator induction motors", *Dept. Elec. Eng. Kyushu Institute of Tech.*, Kitakyushu, Japan.

[53] C. Uenosono, Y. Inoue, Y. Ueda and K. Kaneko, "Measurement and analysis of flux distribution and bar current in a cage - type induction motor", *Electrical Engineering in Japan*, Vol. 103B, No. 2, p69 - 76, Feb. 1983.

[54] Y. Yoshida, K. Mohri, K. Kasai, t. Kondo and N. Iwabuchi, " Novel rotor current detection using amorphous core magnetometer", *9th annual Conf. on Industrial Electronics IEEE*, San Francisco, Nov. 1983.

[55] R. and L. Kreindler, "Off line and on line squirrel cage induction motor parameter identification", *Polytechnic Institute of Bucharest, Dept. of Elec. Eng.*, Romania.

[56] R. Magureanu, L. Kreindler, D. Floriceau and C. Solacolu, "Current versus voltage control of the induction motors operating at constant motor flux", *Polytechnic Institute of Bucharest, Research Institute for elect. Eng. I.C.P.E.*, Bucharest, Romania.

[57] R. Magureanu, A. Fransua and I. Kreindler, "A new squirrel cage rotor current transducer and its applications in motor parameter identification and optimal control", No Reference Available.

[58] S. Williamson and A.C. Smith, "Steady state analysis of 3 phase cage motors with rotor bar and end ring faults", *IEE Proc.*, Vol. 129, Pt. B, No. 3, May 1982.

[59] C.F. Landy, "Analysis of rotor bar currents as a means of evaluating torque produced in a squirrel cage induction motor", No Reference Available.

[60] R.L. Stoll, "Method of measuring alternating currents without disturbing the conducting circuit", *IEE Proc.*, Vol. 122, No. 10, Oct. 1975.

[61] D.H. Ellison, J.L.T. Exon and D.A. Ward, "Protection of slip ring induction motors", *Conf. Proc. Developments in Power system protection, IEE*, London, June 1980.

[62] D.A. Ward and J. La Exon, "Using the rogowski coils for transient current measurements", *Eng. Science and Education Journal*, p105 - 113, June 1993.

[63] Anonymous, "Electronics revives the rogowski coil c.t.", *Electricity Council Research Centre*.

[64] J.A. Pettinga and J. Siersema, "A Polyphase 500 kA current measuring system with rogowski coils", *IEE Proc.*, Vol. 130, Pt. B, No. 5, Sept. 1983.

[65] P.H. Trickey, "Field harmonics in induction motors", *Electrical Engineering*, Vol. 50, p939 - 941 Dec. 1931.

[66] J.S. Gault, "Rotor-bar currents in squirrel cage induction motors", *Electrical Engineering*, p784 - 791, Jul. 1941.

[67] M.M. Liwshitcz, "Field harmonics in induction motors", *Electrical Engineering*, p797 - 803, Nov. 1942.

[68] C.H. Lee, "Saturation harmonics of polyphase induction machines", *Electrical Engineering*, p597- 603, Oct. 1961.

[69] A.K. Wallace, E.S. Ward, A. Wright, "Sources of harmonic currents in slip-ring induction motors", *Proc. IEE*, Vol. 121, No. 12, p1495 - 1500, Dec. 1974

[70] K.J. Binns and E. Schmid, "Some concepts involved in the analysis of the magnetic field in cage induction machines", *Proc. IEE*, Vol. 122, No. 2, p169 - 175, Feb. 1975.

[71] F. Smikál, "induction machines with interrings", *Conf. Proc. of Int. Conf. on Electrical Machines*, Brussels, Sept. 1978.

[72] I. Kerzenbaum and C.F. Landy, "The existence of large inter bar currents in three phase squirrel cage motors with rotor bar and / or end ring faults", *IEEE Trans. on Power Apparatus and Systems*. Vol. PAS 103, No. 7, July 1984.

[73] R.F. Walliser and C.F. Landy, "The role of interbar currents in squirrel cage motors having broken bars", *Trans. of the South African Elec. Engineers*. p78 - 86, June 1992.

[74] C.F. Landy and R. Moore, "Further success in the detection of broken and / or cracked rotor bars in large squirrel cage induction motors", *Conf. Proc. 3rd Int. Conf. on Electrical Machines and Drives, IEE*, London, Nov. 1987.

[75] T.H. Barton and B.C. Doxey, "The operation of three phase induction motors with unsymmetrical impedance in the secondary circuit", Feb. 1955.

[76] Z. Janda, "New approach for broken rotor bars detection in induction motors", *Int. Conf. on Electrical Machines*, Paris, Sept. 1994.

[77] S. Ferkolj, "On-line fault diagnostic techniques of induction motor drives", *IEEE/KTH Stolkholm Power Tech. Conf.*, Stolkhom, June 1995.

[78] A.P. Russell and I.E.D. Pickup, "An analysis of the induction motor Part 1 - Steady state operation", *IEE Proc. Pt. B. Vol. 129*, Sept. 1982.

[79] W.T. Thomson, S.J. Chalmers and D. Rankin, "On-line current monitoring fault diagnosis in HV induction motors - case histories and cost savings in offshore installations", *Offshore Europe '87 Conf.*, Sept. 1987, Aberdeen, Scotland.

[80] R.R. Scheon and T.G. Habetler, "Effects of time varying loads on rotor fault detection in induction machines", *IEEE Trans. on Indust. Applic.*, Vol. 31, No. 4, July/August 1995.

[81] D. Rankin and D. Leith, "Keeping motors turning", *Electro Technology*, Feb. / March 1993, p16 - 17.

[82] D. Rankin, "The industrial application of phase current analysis to detect rotor winding faults in squirrel cage induction motors", *IEE Power Engineering Journal*, April 1995.

[83] H.C. Stanley, "An analysis of the induction machine", *AIEE Trans.*, Vol. 57, pp. 751 - 757, 1938.

[84] R. Fiser, S. Ferkolj and H. Solinc, "Steady state analysis of induction motor with broken rotor bars", *IEE Conf. on Electrical Machines and Drives*, Univ. of Durham, Sept., 1995.

[85] A.V. Oppenheim, IEEE Spectrum, p57 - 62, Aug. 1970.

[86] T.A.C.M. Claasen and W.F.G. Mecklenbraüker, "The wigner distribution - a tool for time frequency signal analysis", *Parts I,II,III, Phillips Journal of Research*, Vol. 35, 1980.

[87] D. Gabor, " Theory of communication", *IEE*, London, Vol. 93, 1943, p 429.

[88] H. Choi and W.J. Williams, "Improved time-frequency representation of multi-component signals using exponential kernals", *IEEE Trans. on Acoustics, Speech, and Signal Processing*, Vol. 37. No. 6, Jun. 1989.

[89] S. Elder, "The monitoring of induction motor starting transients with a view to early fault detection", *PhD Thesis*, School of Electronic and Electrical Engineering, The Robert Gordon University, Aberdeen.

[90] "Motor Monitor", Entek Corporation, Cincinnati, Ohio.

[91] L. Cohen, "Generalised phase space distribution functions", *Math. Phys.* Vol. 7, p781 - 786, 1966.

[92] A.P. Chattock, "On a magnetic potentiometer", *Philos. Mag*, Vol. 5, p94 - 96, 1887.

[93] W. Rogowski and W. Steinhaus, "Die messung der magnetischen spannung", *Arch. Elektrotech*, Pt. 4, p141 - 150, 1912.

[94] M.S. Sarma, "Electric machines steady state theory and dynamic performance", *West*, P300 - 307.

[95] B. Heller and V. Hamata, "Harmonic field effects in induction machines", *Elsevier Scientific Publishing Company*, New York, 1977.

[96] N.C. Paterson, "The analysis and detection of rotor faults in three phase induction machines using finitic element methods", *Research Conference '96 - Engineering Monitoring and Maintenance*, The Robert Gordon University, Aberdeen, p47 - 57, April 1996.

[97] Matlab, Mathematical Package, User Manual.

[98] National Instruments, Lab PC+ Data Acquisition Card, User Manual.

[99] Toshiba T6400 DX Series Portable Personal Computer, User Manual.

[100] National Instruments, LabWindows for DOS Software, User Manual.

[101] Borland Turbo C, User Manual.

Appendix I

Frequency Components Present due to Rotor Asymmetries

A.I.1 Introduction

From the poll of three phase SCIM operators carried out by Thomson [10] et al., it was reported that one of the most frequent faults to occur within a cage induction motor was the general wear and tear of rotor bars leading to actual breakages. These breakages, as previously described, being due to the high levels of both mechanical and electro-mechanical stress present within the rotor bars of the motor. In particular, from an electro-mechanical point of view, the levels of current which flow in the bars is particularly high, both during the transient period of the motor when accelerating from standstill to operating velocity and during fully loaded steady state operation.

A.I.2 Fault Components

The currents which flow during steady state operation may be modelled as the set of loop currents I_r ....I_{r-n}, where n is the number of meshes present within the rotor cage, Figure [A.I.1].

In the event of a bar breaking, ignoring the effects of interbar currents, then it is no longer possible for the rotor current to flow along the relevant bar. This effect may be modelled by two additional equal loop currents flowing within the adjacent bars in an opposite manner to the normal currents, Figure [A.I.2].

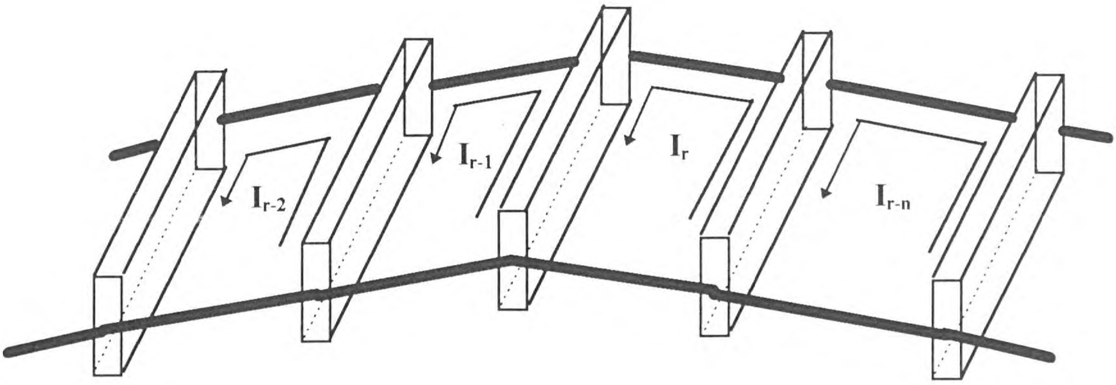

Figure [A.I.1] Currents Present Within Rotor Mesh.

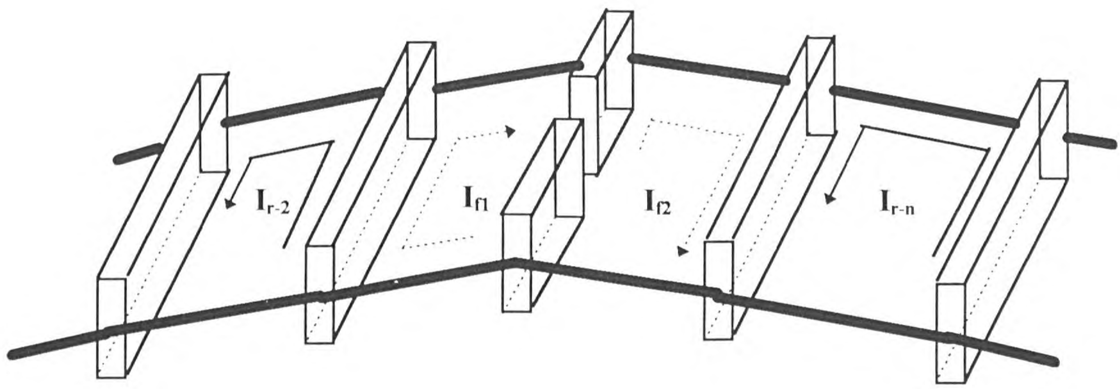

Figure [A.I.2] Model of Rotor Fault Condition.

A magnetic field is created around the adjacent bars to the broken bar which is produced from the two additional fault currents, Figure [A.I.3].

If this additional field is now considered within the rotor frame of reference, then at any instant in time, the flux emitted by the current component leaves the rotor core between the two conductors and returns via the air-gap circumference as shown in Figure [A.I.4].

The effect of the stator rotating magnetic field passing the rotor conductors is to induce currents within the rotor conductors which have the frequency $s\omega_s$ Hz. As these currents are sinusoidal in distribution, the field waveform shown in Figure [A.I.4] pulsates at slip frequency. The effect of this can be seen in Figure [A.I.5] where at different instants in time the level of generated MMF is different. However, it should be noted that at all instants in time the magnetic system must be equalised, as all flux that leaves the rotor must re-enter the core at some point. Hence, the areas above and below the x-axis within Figure [A.I.4] and Figure [A.I.5] must equal one another.

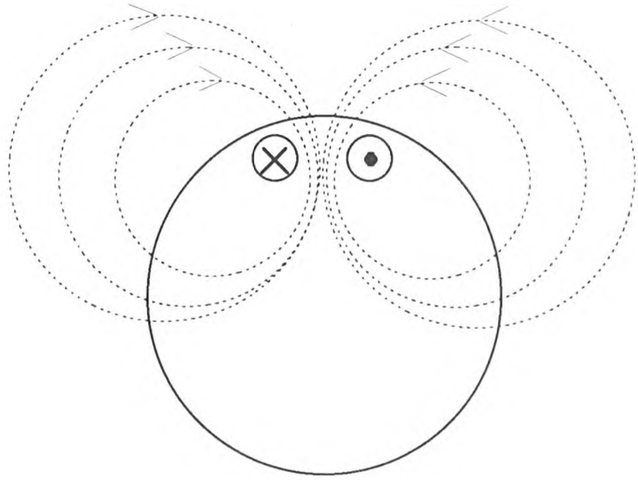

Figure [A.I.3] Additional Magnetic Field Component Due to Rotor Fault.

The waveforms show the distribution of the fault component air-gap field around the circumference of the air-gap. The distribution can be seen to form an approximate square wave, where the wave may be broken down into its Fourier series by computing a Fourier analysis upon the waveform. A Fourier series is defined by eq. (A.I.1).

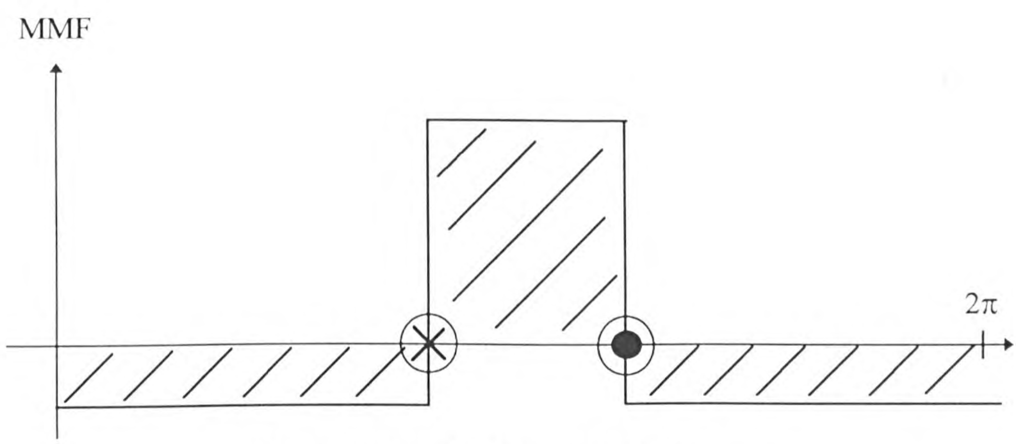

Figure [A.I.4] MMF Due to Fault Component.

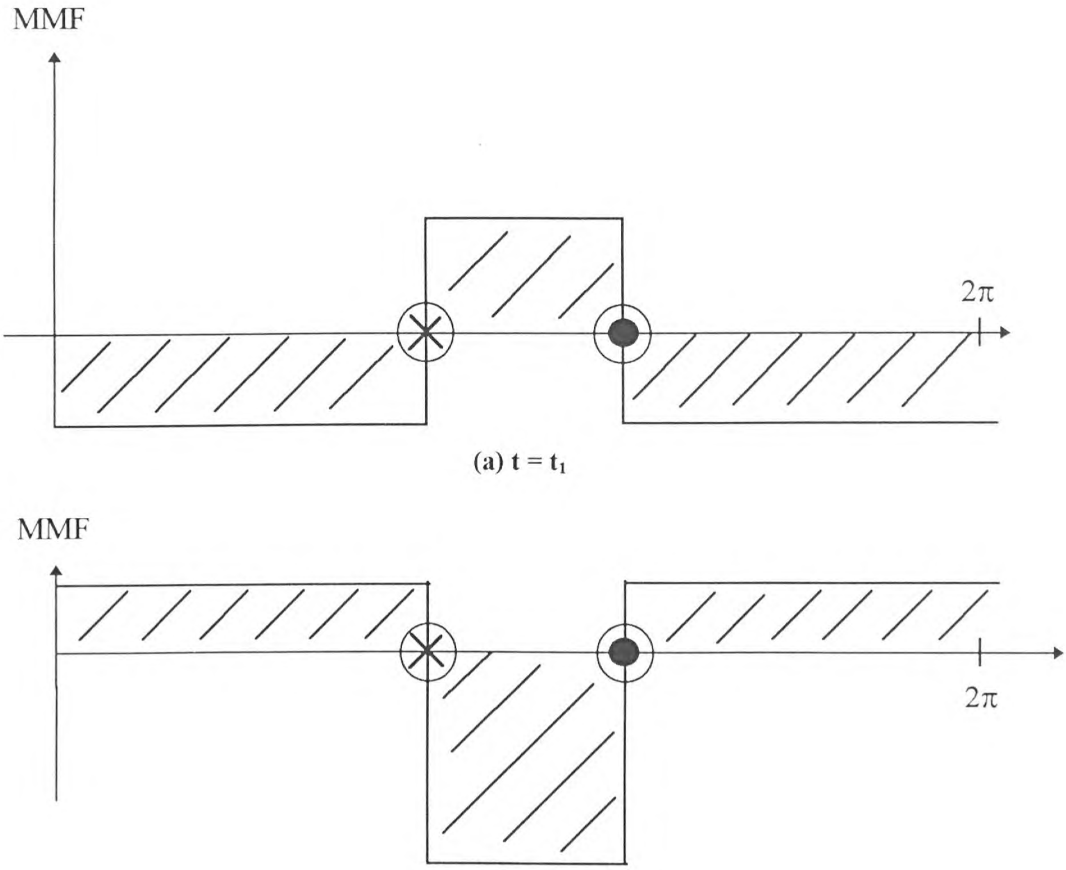

(a) t = t_1

(b) t = t_2

Figure [A.I.5] MMF Due to Fault Component.

$$F(x) = 1/2\,A_0 + \sum_{n=1}^{\infty}\{A_n \cos nx + B_n \sin nx\} \qquad \textbf{(A.I.1)}$$

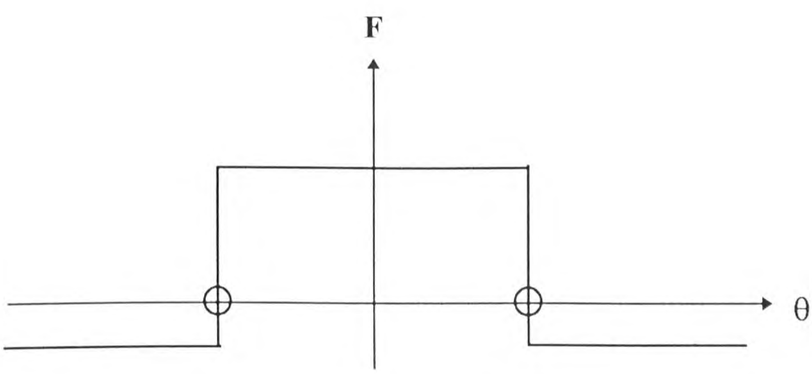

Figure [A.I.6] An Even Function.

The waveform shown in Figure [A.I.6] is an example of an even function as it is symmetrical around the Y - axis. Due to this the sine terms within the Fourier series can be shown to cancel as $B_n = 0$.

Also, as the MMF which leaves the rotor between the two conductors will return to the rotor at some point within the circumference of the rotor, the waveform above the X - axis will equal that below. Due to this the D.C. level of the wave in Figure [A.I.6], and hence, that of the MMF due to the faulty bar, will equate to zero. Hence, the term $1 / 2 \; A_0 = 0$. The field within the air-gap will therefore be represented by the Fourier series shown in eq. (A.I.2).

$$F(\theta) = \sum_{n=1}^{\infty} An \cos n\theta \qquad \textbf{(A.I.2)}$$

As 'θ' indicates the position around the circumference of the air-gap with reference to the rotor frame of reference, the series shown in eq. (A.I.2) represents the spacial breakdown of the field due to the fault condition.

As the rotating magnetic field due to the stator is constantly passing the rotor conductors at a velocity of $s\omega_s$ the spacial representation of the field pulsates at slip frequency. In order to include this within the Fourier series representation eq. (A.I.2) is multiplied, or modulated, by the pulsating term $\cos s\omega_s t$.

$$F(\theta, t) = \sum_{n=1}^{\infty} An \cos s\omega s t \cos n\theta \qquad \textbf{(A.I.3)}$$

Eq. (A.I.3) gives the Fourier series for the field component introduced by the fault condition within the rotor. This expression is, however, with respect to the rotor reference location. This point is obviously rotating, hence, in order to express the effect in terms of a stationary frame of reference, the stator reference frame, the expression must be transformed. This can be done by substituting the rotor angle θ with its equivalent within the stator reference frame, eq. (A.I.4).

$$\theta = \vartheta - \omega r t \qquad \textbf{(A.I.4)}$$

Substituting eq. (A.I.4) into eq. (A.I.3).

$$F(\theta, t) = \sum_{n=1}^{\infty} An \cos(s\omega s\, t) \cos(n(\theta - \omega r\, t)) \quad \textbf{(A.I.6)}$$

$$\omega r = (1 - s) / p(\omega s\, t) \quad \textbf{(A.I.7)}$$

As eq. (A.I.6) includes a mechanical angle term, the transformation eq. (A.I.7) is required in order that the Fourier series can be completely expressed in terms of electrical degrees. The effect of the fault condition is therefore to introduce a field term within the stator winding which contains a Fourier series of the form shown in eq. (A.I.8).

$$F(\theta, t) = \sum_{n=1}^{\infty} An \cos(s\omega s\, t) \cos(n(\vartheta - (1-s)/p(\omega s\, t)))$$

$$= \sum_{n=1}^{\infty} An/2 \left[\cos(s\omega s\, t + n\theta - n(1-s)/p(\omega s\, t)) + \cos(s\omega s\, t - n\theta + n(1-s)/p(\omega s\, t))\right]$$

$$= \sum_{n=1}^{\infty} An/2 \left[\cos((s - n(1-s)/p)\omega s\, t + n\vartheta) + \cos((s + n(1-s)/p)\omega s\, t - n\vartheta)\right] \quad \textbf{(A.I.8)}$$

A.I.3 Conclusions

For a 'p' pole-pair machine, the harmonics are identified by the fundamental n = p, 3rd harmonic n = 3p, 5th harmonic n = 5p, etc. Considering a 2 pole-pair machine, (p = 2), the expression for the fundamental component is computed using eq. (A.I.8). It is shown in eq. (A.I.9) that this series equates to two components. One component which represents the original fundamental, and a second which is (1-2s) times the fundamental frequency.

$$F(\theta, t) = \sum_{n=1}^{\infty} An/2 \left[\cos (s-1+s)\omega s t + n\vartheta + \cos (s+1-s)\omega s t - n\vartheta\right]$$

$$(s-1+s)\ \omega s t = (-1+2s)\ \omega s t$$

$$= (1-2s)\ \omega s t$$

$$(s+1-s)\ \omega s t = (1)\ \omega s t \qquad \textbf{(A.I.9)}$$

Similarly, the 3rd, 5th and 7th harmonics are listed within Table [A.I.1].

Harmonic No.	n	Sideband 1	Sideband 2
3	6	$(3-4s)\omega_s t$	$(3-2s)\omega_s t$
5	10	$(5-6s)\omega_s t$	$(5-4s)\omega_s t$
7	14	$(7-8s)\omega_s t$	$(7-6s)\omega_s t$

Table [A.I.1] Harmonics of Rotor Fault Component.

Appendix II

Frequency Components Present due to the Effects of Torque Variations

A.II.1 Torque Variation

It has been shown in Appendix I that when a rotor contains an asymmetry frequency components will be generated at $(1\text{-}2s)f_s$ Hz. The following shows how these components will cause the speed of the motor to vary along with inducing components to occur at $(1+2s)f_s$ Hz.

If the current density of the fault component for a two pole motor is considered to rotate at $(1\text{-}2s)f_s$ Hz, the expression which defines the density may be written as that in eq. (A.II.1.1).

$$J_r^{(1\text{-}2s)} = J_R^{(1\text{-}2s)} \cos[(1\text{-}2s)\,\omega s\, t - 2\theta - \alpha] \qquad \textbf{(A.II.1.1)}$$

$$b_{main} = B_{main} \cos[\omega s\, t - 2\theta - \beta] \qquad \textbf{(A.II.1.2)}$$

The main air-gap field of the motor can be considered to be eq. (A.II.1.2), hence, any torque ripple obtained by the interaction of the above two components can be obtained from eq. (A.II.1.3).

$$T = l\, r \int b_{main}\, j_r^{(1\text{-}2s)}\, d\theta$$
$$= l\, r \int B_{main} J_r^{(1\text{-}2s)} \cos[(1\text{-}2s)\,\omega s\, t - 2\theta - \alpha] \cdot \cos[\omega s\, t - 2\theta - \beta]\, d\theta$$

(A.II.1.3)

Using the trigonometric identity defined by eq. (A.II.1.4), eq. (A.II.1.3) may be reduced to that shown in eq. (A.II.1.5).

$$\cos(A).\cos(B) = 1/2\,[\cos(A+B) + \cos(A-B)] \qquad \textbf{(A.II.1.4)}$$

$$= 1/2 \cos[(1-2s)\,\omega s\,t - 2\theta - \alpha + \omega s\,t - 2\theta - \beta]$$

$$+ 1/2 \cos[(1-2s)\,\omega s\,t - 2\theta - \alpha - (\omega s\,t - 2\theta - \beta)]$$

$$= 1/2 \cos[\omega s\,t - 2s\omega s\,t - 2\theta - \alpha + \omega s\,t - 2\theta - \beta]$$

$$+ 1/2 \cos[\omega s\,t - 2s\omega s\,t - 2\theta - \alpha - \omega s\,t + 2\theta + \beta]$$

$$= 1/2 \cos[2\omega s\,t - 2s\omega s\,t - 4\theta - \alpha - \beta]$$

$$+ 1/2 \cos[-2s\omega s\,t - \alpha + \beta]$$

$$= 1/2 \cos[2(1-s)\omega s\,t - 4\theta - \alpha - \beta]$$

$$+ 1/2 \cos[2s\omega s\,t + \alpha - \beta] \qquad \textbf{(A.II.1.5)}$$

This results in an expression being formed for the torque developed by the *(1-2s)* fault component, eq. (A.II.1.6).

$$T = l\,r / 2\, B_{main}\, J_r^{(1-2s)} \int \cos[2(1-s)\omega s\,t - 4\theta - \alpha - \beta]$$

$$+ \cos[2s\omega s\,t + \alpha - \beta] \qquad \textbf{(A.II.1.6)}$$

From eq. (A.II.1.6) the torque due to the fault component contains a term which is independent of any spacial positioning and is comprised of a frequency component which is 2s times the fundamental of the supply. It is this component of torque which causes a 2s oscillation within the overall torque of the motor.

A.II.2 Production of (1+2s) component due to Torque Ripple

Considering the 2s torque ripple caused by the fault component, it is then possible to calculate the effects which this has upon the speed of the rotor.

$$D\, d\omega_{Ripple} / dt = T_{rot}^{(2s)} \qquad \textbf{(A.II.2.1)}$$

(Assuming D is the inertia of the rotor and that a constant load torque is applied)

$$d\omega_{Ripple} / dt = T_{rot}{}^{(2s)} / D$$

$$\omega_{Ripple} = \int T_{rot}{}^{(2s)} / D\, dt$$

$$= T/D \int \cos (2s\omega_s t + \alpha - \beta)\, dt$$

$$= T/2Ds\omega_s \sin (2s\omega_s t + \alpha - \beta) \qquad \textbf{(A.II.2.2)}$$

The mean rotor speed may now be considered to comprise of the average rotor speed along with the effects of the speed ripple, eq. (A.II.2.2). The complete rotor speed expression being shown in eq. (A.II.2.3).

$$\omega_r = (1\text{-}s) \omega_s / 2 + \delta / s \sin (2s\omega_s t + \alpha - \beta) \qquad \textbf{(A.II.2.3)}$$

The rotor main field may now be expressed within the rotor reference frame. Where θ' and β' represent the rotor reference frame.

$$b_r = B_r \cos (s\omega_s t - 2\theta' - \beta') \qquad \textbf{(A.II.2.4)}$$

In order for the above to be considered in the stationary stator reference frame, a conversion of the form of eq. (A.II.2.5) is used resulting in eq. (A.II.2.6).

$$\theta_{Stator} = \theta_{Rotor} + \int \omega_r\, dt$$

$$\theta_{Rotor} = \theta_{Stator} - \int \omega_r\, dt$$

$$\theta_{Rotor} = \theta_{Stator} - \int (1\text{-}s) \omega_s / 2 + \delta / s \sin (2s\omega_s t + \alpha - \beta)\, dt$$

$$\theta_{Rotor} = \theta_{Stator} - (1\text{-}s) \omega_s t / 2 - \delta / 2s^2 \omega_s \cos (2s\omega_s t + \alpha - \beta)$$

(A.II.2.5)

$\theta_{Stator} = \theta$ and $\theta_{Rotor} = \theta'$;

$$b_r = B_r \cos [s\omega_s t - 2 (\theta - (1\text{-}s) \omega_s t / 2 - \delta / 2s^2 \omega_s \cos (2s\omega_s t + \alpha - \beta)) - \beta']$$

$$= B_r \cos [s\omega_s t - 2\theta + (1\text{-}s) \omega_s t + \delta / s^2 \omega_s \cos (2s\omega_s t + \alpha - \beta) - \beta']$$

$$= B_r \cos [s\omega_s t - 2\theta + \omega_s t - s\omega_s t + \delta / s^2 \omega_s \cos (2s\omega_s t + \alpha - \beta) - \beta']$$

$$= B_r \cos [\omega_s t - 2\theta - \beta' + \delta / s^2 \omega_s \cos (2s\omega_s t + \alpha - \beta)] \qquad \textbf{(A.II.2.6)}$$

Using Euler's identity, $e^{j\theta} = \cos \theta + j \sin \theta$, and only considering the real part, it is possible to express eq. (A.II.2.6) in terms of exponentials.

$$b_r = B_r \cos\ [\ \omega_s t - 2\theta - \beta' + \delta / s^2\ \omega_s \cos(\ 2s\omega_s t + \alpha - \beta\ )]$$

$$=> Br\ [\ e^{j(\omega s\ t - 2\theta - \beta' + \delta / s2\ \omega s \cos(\ 2s\omega s\ t + \alpha - \beta\ ))}\ ]$$

$$=> Br\ [\ e^{j(\omega s\ t - 2\theta - \beta')}\ e^{j(\delta / s2\ \omega s \cos(\ 2s\omega s\ t + \alpha - \beta\ ))}\ ] \quad \textbf{(A.II.2.7)}$$

If the series $e^x = 1 + x / 1! + x^2 / 2! + x^3 / 3! + ...$ is considered to the first harmonic, $e^{j(\delta / s2\ \omega s \cos(\ 2s\omega s\ t + \alpha - \beta\ ))}$ may be re-written as eq. (A.II.2.8).

$$1 + j\delta / s^2\ \omega_s \cos(\ 2s\omega_s t + \alpha - \beta\ ) \quad \textbf{(A.II.2.8)}$$

Replacing eq. (A.II.2.8) into the rotor field expression, eq. (A.II.2.7), and taking the converse of Euler's identity results in eq. (A.II.2.10) being obtained.

$$=> B_r\ [\{\ \cos(\ \omega_s t - 2\theta - \beta'\ ) + j \sin(\omega_s t - 2\theta - \beta')\ \}.$$
$$\{\ 1 + j\delta / s^2\ \omega_s \cos(\ 2s\omega_s t + \alpha - \beta\ )\ \}] \quad \textbf{(A.II.2.9)}$$

$$=> B_r\ [\ \cos(\ \omega_s t - 2\theta - \beta'\ ) + j \sin(\omega_s t - 2\theta - \beta')$$
$$+ j\delta / s^2\ \omega_s \cos(\ 2s\omega_s t + \alpha - \beta\ ) \cos(\ \omega_s t - 2\theta - \beta'\ )$$
$$+ j^2\delta / s^2\ \omega_s \sin(\omega_s t - 2\theta - \beta') \cos(\ 2s\omega_s t + \alpha - \beta\ )\ ]$$

$$=> B_r\ [\ \cos(\ \omega_s t - 2\theta - \beta'\ ) - \delta / s^2\ \omega_s \sin(\omega_s t - 2\theta - \beta') \cos(\ 2s\omega_s t + \alpha - \beta\ )$$
$$+ j\ \{\ \sin(\omega_s t - 2\theta - \beta') + \delta / s^2\ \omega_s \cos(\ 2s\omega_s t + \alpha - \beta\ ) \cos(\ \omega_s t - 2\theta - \beta'\ )\ \}]$$

(A.II.2.10)

Considering again only the real part of eq. (A.II.2.10), and making use of the trigonometric identity, eq. (A.II.2.11), results in eq. (A.II.2.12) being formed.

$$\sin A \cos B = 1/2\ \{\ \sin(\ A+B\ ) + \sin(\ A-B\ )\ \} \quad \textbf{(A.II.2.11)}$$

$$=> B_r\ [\ \cos(\ \omega_s t - 2\theta - \beta'\ ) - \delta / s^2\ \omega_s \sin(\omega_s t - 2\theta - \beta') \cos(\ 2s\omega_s t + \alpha - \beta\ )]$$

$$=> B_r\ [\ \cos(\ \omega_s t - 2\theta - \beta'\ ) - \delta / 2s^2\ \omega_s \{\ \sin(\omega_s t - 2\theta - \beta' + 2s\omega_s t + \alpha - \beta\ )$$
$$+ \sin(\ \omega_s t - 2\theta - \beta' - 2s\omega_s t - \alpha + \beta\ )\ \}]$$

$$=> B_r\ [\ \cos(\ \omega_s t - 2\theta - \beta'\ ) - \delta / 2s^2\ \omega_s \{\ \sin((\ 1+2s\ )\omega_s t - 2\theta + \alpha - (\ \beta'+\beta\ ))$$
$$+ \sin((\ 1-2s\ )\omega_s t - 2\theta - \alpha + (\ \beta-\beta'))\ \}] \quad \textbf{(A.II.2.12)}$$

$$b_r^{(2s)} = B_r \cos(\omega_s t - 2\theta - \beta') - \delta B_r / 2s^2 \omega_s [\sin((1+2s)\omega_s t - 2\theta + \alpha - (\beta'+\beta)) + \sin((1-2s)\omega_s t - 2\theta - \alpha + (\beta-\beta'))\}] \quad \textbf{(A.II.2.13)}$$

From eq. (A.II.2.13) it can be seen that the effect of a speed ripple caused by the 2s torque oscillation which in turn is caused by the presence of the $(1\text{-}2s)f_s$ fault component, is to create a component within the air-gap field which contains both a $(1\text{-}2s)f_s$ component in addition to a new component at $(1+2s)f_s$. Thus, the oscillations due to a rotor anomaly will cause additional *(1-2s)* components to occur and a new set of components at *(1+2s)* to be present.

Appendix III

Modulation due to Fault Component Third Harmonic

Hargis [18] et al. state that due to third harmonic components within the stator caused by saturation effects or supply imbalances, a component will be generated at $(1+2s)f_s$ Hz which enhances the frequency components already in existence should the rotor contain any form of asymmetry.

If the rotor contains an asymmetry, then from Appendix I it was shown that frequency components will occur at $(1-2s)f_s$ Hz. The third harmonic of this fault component will therefore occur at eq. (A.III.1).

$$(1 - 2s_3)f_3 \qquad \textbf{(A.III.1)}$$

Where $s_3 = (3\omega_s - \omega_r) / 3\omega_s$,

$$= (3 - \omega_r / \omega_s) / 3$$

$$= [2 + (1 - \omega_r / \omega_s)] / 3$$

$$= (2 + s) / 3 \qquad \textbf{(A.III.2)}$$

Replacing eq. (A.III.2) in eq. (A.III.1),

$$= [1 - 2.(2 + s) / 3] 3f_s$$

$$= [3 / 3 - 2.(2 + s) / 3] 3f_s$$

$$= [1 - (4 / 3) - (2s / 3)] 3f_s$$

$$= [(3 / 3) - (4 / 3) - (2s / 3)] 3f_s$$

$$= [(-1 / 3) - (2s / 3)] 3f_s$$

$$= [(1 / 3) + (2s / 3)] 3f_s$$

$$= [\ 1 + 2s\ ]f_s \qquad \textbf{(A.III.3)}$$

In conclusion, third harmonics present within the supply voltage will cause a modulation of the supply component, which ultimately enhances the frequency components occuring at $(1+2s)f_s$, eq. (A.III.3).

Appendix IV

Fault Frequency Component Induction and Interaction

When a balanced three phase supply is placed onto the terminals of a three phase stator winding, a rotational field rotates at the angular velocity of ω_s radians / sec. This field, which has a frequency of F_s Hz, similar to the source creating it, induces EMF's within the rotor circuit at a frequency of, sF_s Hz, Figure [A.IV.1]. Should an asymmetry be present within the rotor, the currents which are then present cause two counter rotating magnetic fields to be present. These fields, in turn induce frequencies at $\pm sF_s$ Hz. The positive rotating component interacts with the stator field, Figure [A.IV.2], whereas the negative component induces EMF's within the stator with the frequency of $(1\text{-}2s)\ F_s$ Hz. These EMF's now interact with the rotor currents of frequency $-sF_s$ Hz, Figure [A.IV.2]. The interaction between the $(1\text{-}2s)F_s$ Hz currents and the fundamental magnetic field can be shown via simple mathematical relationships to produce an oscillatory torque which has an oscillation frequency of $2s$ Hz, Figure [A.IV.2]. The oscillation within the torque, and hence, the speed of the rotor, causes both a reaction current at a frequency of $(1\text{-}2s)F_s$ Hz and a new component to occur at a frequency of $(1+2s)F_s$ Hz. The currents which now flow within the stator circuit at a frequency of $(1+2s)F_s$ Hz consequently produce a rotating magnetic field which rotates at $3sF_s$ Hz with respect to the rotor, Figure [A.IV.3]. If a similar procedure is repeated with a broken bar present within the rotor, the currents which are generated by the corresponding EMF's will produce two rotating fields, this time at frequencies of $\pm 3sF_s$ Hz. Again, the $+3sF_s$ component will react with the originator, Figure [A.IV.2]. Similarly, the $(1\text{-}4s)F_s$ Hz component will now result in a torque ripple which as is shown within Figure [A.IV.2] oscillates at $4sF$ Hz, thus producing a $(1+4s)F_s$ Hz component back within the stator.

In conclusion, a rotor which contains an asymmetry will produce *(1 - 2s)*F_s Hz components within the stator circuit. The resulting $2sF_s$ Hz oscillations within the torque will then cause a further *(1-2s)*F_s Hz and a new *(1+2s)*F_s Hz component to be present within the stator winding. The resultant *(1-2s)*F_s Hz component being a combination of effects from both the rotor asymmetry and the resulting torque ripple. Finally, due to interactions, similar reactions will take place thus producing further harmonic components within the air-gap of the motor which will either improve or hinder the operation of the induction motor.

$F_s = N_s\, p;$

$F_r = N_r\, p;$

$s = (\omega_s - \omega_r) / \omega_s;$

$s\omega_s = \omega_s - \omega_r;$

$sF_s = F_s - F_r;$

$F_r = F_s (1-s);$

Now,

$$
\begin{aligned}
F_r &= (\omega - \omega)\, p \\
&= (s\omega_s)\, p \\
&= s\, N_s\, p \\
&= \mathbf{sF_s}.
\end{aligned}
$$

or

$$
\begin{aligned}
\omega \text{ (w.r.t.r)} &= \omega_s - \omega_r \\
&= F_s - (F_s (1-s)) \\
&= F_s - F_s + sF_s \\
&= \mathbf{sF_s}.
\end{aligned}
$$

Figure [A.IV.1] Supply Frequency with respect to Rotor.

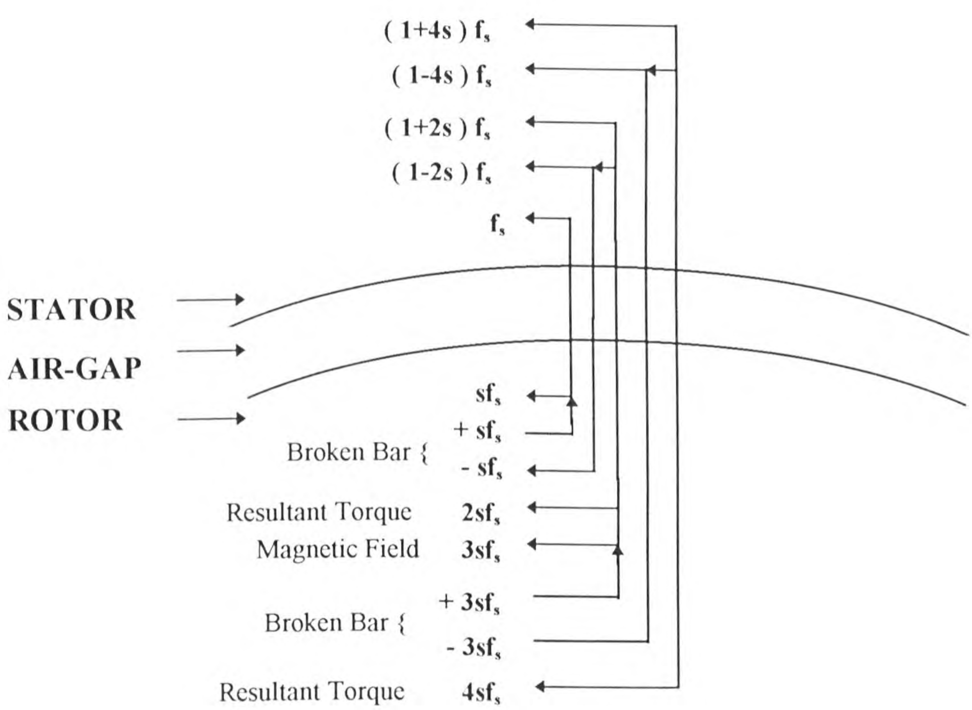

Figure [A.IV.2] Frequency Components Present due to Rotor Asymmetry.

$$\text{Stator Frequency} = (1+2s)\, f_s$$

$$\omega\ (\text{w.r.t.r}) = \omega_s - \omega_r$$

$$= (1+2s)\, F_s - (F_s\,(1-s))$$

$$= F_s + 2sF_s - F_s + sF_s$$

$$= \mathbf{3sF_s}$$

Figure [A.IV.3] Production of 3sf Component from Fault Component.

Appendix V

The Generalised Expression

The Wigner Distribution is not the only Time-Frequency representation available. As mentioned previously another Time-Frequency representation is that of the Short Time Fourier Transform, STFT. As will be shown there is a link between the STFT and the WD through a generalised expression which links the Time-Frequency distributions.

The generalised class of Time-Frequency signal representations was introduced by Cohen [91], eq. (A.V.1).

$$Cf(t,\omega\,;\,\phi) =$$

$$1\,/\,2\pi \int_{-\infty}^{\infty}\int_{-\infty}^{\infty}\int_{-\infty}^{\infty} e^{j(\xi t\,-\,\tau\omega\,-\,\xi u)}\,\phi(\xi\,-\,\tau)\,f(u+\tau/2)\,f^{*}(u-\tau\,/\,2)\,du\,d\tau\,d\xi$$

(A.V.1)

Where Φ is an arbitrary kernel function which determines the particular representation of the class.

Introducing the functions $\zeta_f(t,\tau) = f(t+\tau/2)f^{*}(t-\tau/2)$ and $\Gamma_f(\xi,\omega) = F(\omega+\xi/2)F^{*}(\omega-\xi/2)$ the WD can be re-written as that in eq. (A.V.2).

$$WD(t,\omega) = \int_{-\infty}^{\infty} x(t + \tau / 2)\, x^*(t - \tau / 2)\, e^{-j\omega\tau}\, d\tau$$

$$= \int_{-\infty}^{\infty} e^{-j\omega\tau}\, \zeta f(t,\tau)\, d\tau$$

(A.V.2)

This may also be expressed within the frequency domain as that shown in eq. (A.V.3).

$$WD(\omega, t) = 1 / 2\pi \int_{-\infty}^{\infty} F(\omega + \xi / 2) F^*(\omega - \xi / 2)\, e^{j\xi t}\, d\xi$$

$$= 1 / 2\pi \int_{-\infty}^{\infty} e^{j\xi t}\, \Gamma f(\xi, \omega)\, d\xi$$

(A.V.3)

Another form of Time-Frequency representation is the Ambiguity Function, eq. (A.V.4).

$$Ax(\omega, \tau) = \int_{-\infty}^{\infty} x(t + \tau / 2) x^*(t - \tau / 2)\, e^{-j\omega t}\, dt \qquad \textbf{(A.V.4)}$$

Using the above definitions, eq. (A.V.4) may be defined in time and frequency as follows.

$$Af(\xi, \tau) = \int_{-\infty}^{\infty} e^{-j\xi t}\, \zeta f(t, \tau)\, dt$$

(A.V.5)

$$= 1 / 2\pi \int_{-\infty}^{\infty} e^{j\omega t}\, \Gamma f(\xi, \omega)\, d\omega$$

From these expressions it is clear that the Wigner Distribution and the Ambiguity Function are related by a two dimensional Fourier Transform. Using this definition of Ambiguity Function within the Generalised Equation, eq. (A.V.1) may be written as eq. (A.V.6).

$$Cf(t,\omega;\phi) = 1/2\pi \int_{-\infty}^{\infty}\int_{-\infty}^{\infty} e^{j(\xi t - \omega\tau)}\,\Phi(\xi,\tau)Af(\xi,\tau)\,d\xi\,d\tau$$

(A.V.6)

Alternatively using the definition of the Wigner Distribution, C_f may be written as:

$$Cf(t,\omega;\Phi) = 1/2\pi \int_{-\infty}^{\infty}\int_{-\infty}^{\infty} \theta(t-\tau,\omega-\xi)\,Wf(\tau,\xi)\,d\tau\,d\xi$$

(A.V.7)

$$\theta(t,\omega) = 1/2\pi \int_{-\infty}^{\infty}\int_{-\infty}^{\infty} e^{j(\xi t - \omega\tau)}\,\Phi(\xi,\tau)\,d\xi\,d\tau \qquad \textbf{(A.V.8)}$$

If the WD kernel = 1, then this will lead to the WD via eq. (A.V.1). Similarly, the AF kernel to depend upon t and ω, then using eq. (A.V.1) the AF, eq. (A.V.4), may be obtained.

By definition a Spectrogram is obtained from the Short Time Fourier Transform, STFT. The STFT is calculated via eq. (A.V.9).

$$Ft(\omega) = \int_{-\infty}^{\infty} e^{-j\omega t}\,f(\tau)\,h(\tau - t)\,d\tau \qquad \textbf{(A.V.9)}$$

The Spectrogram of the signal under analysis, S(t,ω), is obtained by taking the magnitude squared of the obtained STFT, for all values of t.

$$S(t,\omega) = |F(\omega)|^2 \qquad \textbf{(A.V.10)}$$

As the WD law 2.39 [86] states,

$$\int_{-\infty}^{\infty} Wf(t,\omega)\,dt = |F(\omega)|^2 \qquad \textbf{(A.V.11)}$$

The definition of the STFT, eq. (A.V.10), can therefore be re-written taking account of this WD law, eq. (A.V.12).

$$S(t, \omega) = \int_{-\infty}^{\infty} Wf(\tau, \omega)\, d\tau \qquad \textbf{(A.V.12)}$$

As the Spectrogram in reality will make use of windows in order to obtain finite data lengths, the WD of a windowed signal will be given by eq. (A.V.13).

$$S(t, \omega) = 1/\, 2\pi \int_{-\infty}^{\infty} \int_{-\infty}^{\infty} Wf(\tau, n) Wh(\tau - t, \omega - n)\, d\tau\, dn$$

(A.V.13)

This equation is obviously of the same nature to the generalised Time-Frequency expression developed by Cohen, eq. (A.V.1). In fact eq. (A.V.13) may be obtained from the General Equation if the following kernel is used in eq. (A.V.1).

$$\theta s(\tau, \xi) = Wh(-\tau, \xi) \qquad \textbf{(A.V.14)}$$

Therefore the Spectrogram of a signal is a special representation of the Generalised Equation, eq. (A.V.1), generated by the use of a kernel which is in fact a Wigner Distribution.

Appendix VI

Three Phase Simulation Model

A.VI.1 Background Theory

The three phase simulation, De Sarkar [47], represents a far more computationally intensive technique than that of the previous two phase simulation. The basic form of the program is the direct solution of the three phase induction motor equations which describe the nature of the voltages induced within the individual windings of the motor.

Taking eq. (A.VI.1), commonly known as Maxwell's circuit equation, and applying it to each individual phase within a three phase induction motor, Figure [A.VI.1], results in the six equations defined by eq. (A.VI.2).

$$e = p\psi + Ri \qquad \textbf{(A.VI.1)}$$

The resulting matrix of equations may further be expressed in terms of the individual winding flux linkages. Neglecting any core losses, saturation effects, and space harmonics, the voltage balanced equations for the three phase wire-wound rotor induction motor are given by eq. (A.VI.3), with eq. (A.VI.4) defining the expressions in terms of matrix algebra.

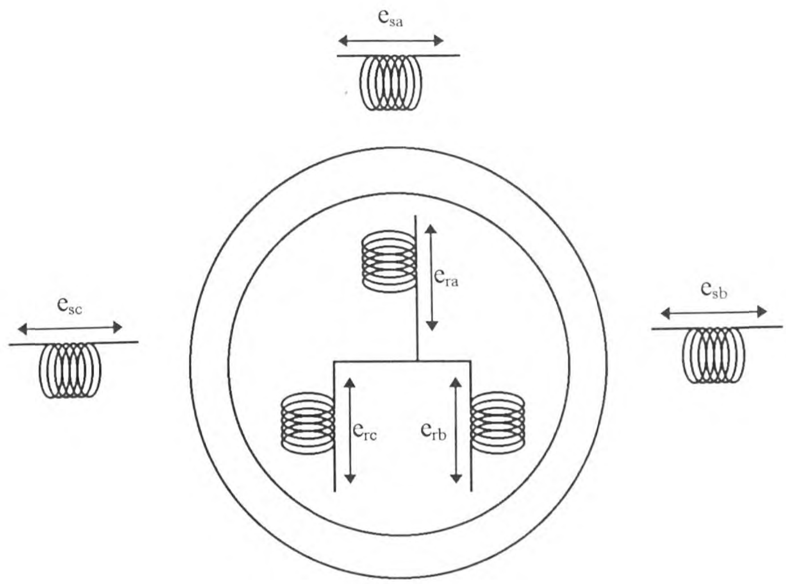

Figure [A.VI.1] Three Phase Induction Motor Simulation Model.

$$
\begin{aligned}
e1 &= Ri11 + p\left[L11i1 + M12i2 + M13i3 \ldots M16i6\right] \\
e2 &= Ri11 + p\left[L21i1 + M22i2 + M23i3 \ldots M26i6\right] \\
e3 &= Ri31 + p\left[L31i1 + M32i2 + M33i3 \ldots M36i6\right] \\
e4 &= Ri41 + p\left[L41i1 + M42i2 + M43i3 \ldots M46i6\right] \\
e5 &= Ri51 + p\left[L51i1 + M52i2 + M53i3 \ldots M56i6\right] \\
e6 &= Ri61 + p\left[L61i1 + M62i2 + M63i3 \ldots M66i6\right]
\end{aligned}
\qquad \textbf{(A.VI.2)}
$$

$$
\begin{aligned}
e1 &= esa = p\psi_{sa} + Rsisa \\
e2 &= esb = p\psi_{sb} + Rsisb \\
e3 &= esc = p\psi_{sc} + Rsisc \\
e4 &= era = p\psi_{ra} + Rrira \\
e5 &= erb = p\psi_{rb} + Rrirb \\
e6 &= erc = p\psi_{rc} + Rrirc
\end{aligned}
\qquad \textbf{(A.VI.3)}
$$

$$[e] = p[\psi] + [R][i] \qquad \textbf{(A.VI.4)}$$

Re-arranging eq. (A.VI.4) in order to obtain an expression for flux linkage, results in eq. (A.VI.5). By taking the general expression for flux linkage, eq. (A.VI.6), and solving for the phase current results in eq. (A.VI.7), where the flux linkages are defined by eq. (A.VI.8) and are equated from eq. (A.VI.5). The phase currents being defined by eq. (A.VI.9) and the inductance matrix by eq. (A.VI.10).

$$p[\psi] = [e] - [R][i] \qquad \textbf{(A.VI.5)}$$

$$[\psi] = [L][i] \qquad \textbf{(A.VI.6)}$$

$$[i] = [L]^{-1}[\psi] \qquad \textbf{(A.VI.7)}$$

$$[\psi] = [\psi sa,\ \psi sb,\ \psi sc,\ \psi ra,\ \psi rb,\ \psi rc]^{t} \qquad \textbf{(A.VI.8)}$$

$$[i] = [isa,\ isb,\ isc,\ ira,\ irb,\ irc]^{t} \qquad \textbf{(A.VI.9)}$$

$$\begin{bmatrix} Lss & Mss & Mss & Msr\cos(\theta) & Msr\cos(\theta) & Msr\cos(\theta) \\ Mss & Lss & Mss & Msr\cos(\rho) & Msr\cos(\theta) & Msr\cos(\theta) \\ Mss & Mss & Lss & Msr\cos(\phi) & Msr\cos(\rho) & Msr\cos(\theta) \\ Msr\cos(\theta) & Msr\cos(\rho) & Msr\cos(\phi) & Lrr & Mrr & Mrr \\ Msr\cos(\phi) & Msr\cos(\theta) & Msr\cos(\rho) & Mrr & Lrr & Mrr \\ Msr\cos(\rho) & Msr\cos(\phi) & Msr\cos(\theta) & Mrr & Mrr & Lrr \end{bmatrix}$$

(A.VI.10)

where,

$$\phi = \theta + 2\pi / 3 \text{ and } \rho = \theta - 2\pi / 3$$

The calculated values of phase current are used within the simulation to obtain predicted values of the electrical torque, eq. (A.VI.11).

$$Te = -polepairs \begin{bmatrix} (isa\, ira + isb\, irb + isc\, irc)\sin(\theta) + \\ (isa\, irb + isb\, irc + isc\, ira)\sin(\theta + 2\pi/3) + \\ (isa\, irc + isb\, ira + isc\, irb)\sin(\theta - 2\pi/3) \end{bmatrix} Msr$$

(A.VI.11)

The dependence of M_{rs}, within the inductance matrix, [L] eq. (A.VI.10), upon the value of rotor electrical angle, θ, is unlike any of the previous two phase simulations, where the two axes transformed equations have their dependence on θ changed to a dependence on rotor speed, ω_r. Due to this, the inductance matrix must be solved via a step by step approach, and hence, requires the level of rotor electrical angle to be calculated at each step.

Such a value is obtained by the integration of the general speed equation, eq. (A.VI.12). On separating this 2nd order differential expression into its two first order components, eq. (A.VI.13) and eq. (A.VI.14), the resulting expression, eq. (A.VI.15), represents that which is required to obtain the level of rotor electrical angle.

$$J \frac{d^2\theta m}{dt^2} + \Im \frac{d\theta\, m}{dt} + Tm = Te \qquad \textbf{(A.VI.12)}$$

$$\frac{d\omega\, m}{dt} = \frac{1}{J}(Te - Tm - \Im(\omega\, m)) \qquad \textbf{(A.VI.13)}$$

$$\frac{d\theta\, m}{dt} = \omega\, m \qquad \textbf{(A.VI.14)}$$

$$\theta\, m = \theta / polepairs \qquad \textbf{(A.VI.15)}$$

A.VI.2 Conclusion

Since the equations used within the three phase simulation which describe the induction motor are dependent upon rotor electrical angle and time, then it follows that during the transient period in which the simulation is to be operated, the expressions become non-linear differential expressions.

The solution of these expressions is obtained by a suitable step by step mathematical approach which contains a sufficiently small step length. Two general methods of this type of solution are firstly, a multi-step method whereby values of previously calculated ordinates are required further to the calculation of further ordinates and secondly, a one step method whereby the values of previously calculated ordinates are not required within the calculation of further ordinates.

The Runge Kutta method, employed as the integration method by Elder [89] within the simulation belongs to the latter classification. The consideration between the selection of the individual numerical techniques being the overall numerical stability achieved by the technique, the simplicity of the respective algorithm, and finally the nature of the problem to be solved.

Appendix VII

The Rogowski Coil

A.VII.1 Introduction

The Rogowski Coil was first used by Chattock [92] in 1887 when a long flexible coil of conducting wire was used as a magnetic potentiometer in order to make magnetic reluctance measurements. This technique was further investigated by Rogowski and Steinhaus [93] in the early 1900's.

The Rogowski Coil operates using a simple principle whereby an air-cored uniformly wound coil is placed around a conductor in a toroidal fashion. The magnetic field emanating from the current within the conductor induces a voltage via Faraday's Law which is then proportional to the currents rate of change.

A.VII.2 Review of Current Transducers

A current signal may be obtained from an electrical system by one of three main techniques. These methods being that of a Potentiometer, Current Transformer or Rogowski Coil. Although the Current Transformer (CT) has been well documented to be a successful current transducer it has been found to contain certain properties and restrictions which limit the number of applications to which such a device can be employed. Limitations with which the Rogowski Coil, as will be discussed, are not applicable.

The Rogowski Coil consists of a toroidal wound coil of wire which contains no iron core within the device. Due to the lack of a high permeability iron core the coil is no longer open to saturation problems which are ever present within the CT set-up. In a CT the saturation which is caused via the iron core causes the output of the secondary winding to fall to such levels as gross inaccuracies in the current ratio become probable. In order for the CT to overcome the possibility of saturating when monitoring the current signal, the iron core within the CT must be designed so that it is of sufficiently high quality and large proportions, thus rendering the CT far to bulky in terms of physical size, weight and overall expenditure.

As the Rogowski Coil draws no output current it is possible to design a coil which is manufactured with thin core wire, therefore making the Rogowski Coil a light weight and compact transducer. The Rogowski Coil is also a more practically orientated current transducer than that of a potentiometer system or CT, in that it may be fitted to a system after the systems installation. The worm coil being a typical example of this form of portable Rogowski Coil. This leads to easy use within on-site measurements where temporary fittings of transducers are required. A CT is more suited to fitting on a permanent basis although portable CT's have been used in the past. These CT's, however, require a split core set-up and as any amount of air-gap within the CT's iron path severely reduces the output of the device, accurately machined core faces are required along with some form of locking clamp mechanism. This obviously increases the overall cost of the device and although there is a split within the core the devices are still cumbersome to install.

Another limitation of the CT is that in order to obtain a flexible ratio of primary to secondary currents a tap must be introduced into the secondary circuit of the transducer. The Rogowski Coil ratio, however, depends upon the number of times that the coil is wound around the required conductor. With this property it is possible to monitor conductors which are of different dimensions without the necessity of splitting the monitoring device.

The Rogowski Coil is found to have a wider operating bandwidth and a greater accuracy than the CT, thus allowing currents ranging from milli-amps to millions of amps to be monitored. The coil gives a low harmonic distortion to the monitored signal and has a good phase integrity. For calibration purposes, as the coil produces a linear output it is possible to calibrate the transducer once the device has been installed. The device is found to be damage free from almost any overload and is capable of measuring fast rising transients.

A.VII.3 Rogowski Coils - Industrial Applications

Some typical industrial applications of various forms of Rogowski Coils are as slip current measuring devices within wound rotor induction motors, current detectors on generator main output connectors, the monitoring and testing of uninteruptable power supplies, partial discharge measurements and the detection of spurious currents within transformer pipework.

A.VII.4 Physical Description

A Rogowski Coil may be generally classified into one of two basic formats. Those being a rigid toroidal coil which are more suited to permanent monitoring applications and those with a flexible worm coil which due to their nature are perfect in design for semi-permanent and portable applications.

A.VII.4.1 The Rigid Toroidal Coil

The rigid toroidal coil is formed by winding the transducer coil on a non-ferrous rigid former. This results in a monitoring device which is both very stable and accurate, but is less versatile than the worm coil format. As mentioned this form of coil is best suited to applications whereby a high degree of performance is involved.

A.VII.4.2 The Flexible Worm Coil

This form of Rogowski Coil is formed by wrapping a thin coil of wire around the current carrying conductor in a normal fashion. The coil may be wrapped around the conductor any amount of times as the sensitivity of the overall transducer will increase with the number of times with which the coil is wrapped around the conductor. The main advantage of this coil is that it is able to fit a conductor of virtually any dimension or shape and may be easily used when access to conductors is restricted.

In general, both formats of Rogowski Coil should have their coils positioned at an angle which is normal to the current carrying conductor, thus reducing the sensitivity with which the coil may have to any external sources of magnetic fields. Should external magnetic fields be a problem then metal shields may be placed around the coils to reduce the effects on the induced voltage from interfering conductors.

A.VII.5 Theory of Operation

The operation of the Rogowski Coil relies upon the coil sensing the magnetic field which is emitted from a current carrying conductor. The mathematical relationship which defines the theoretical operation of the coil is known as Ampère's Law, however, any derivation of this law is outwith the scope of this thesis.

Appendix VIII

Rotor Bar Current Acquisition

A.VIII.1 Introduction

In order to investigate the nature of the rotor bar currents, both in terms of frequency content and amplitude when under normal and faulted periods of operation, it was necessary to develop an acquisition system which would enable the digitisation of 18 out of the 36 individual rotor bar currents. Using a Rogowski worm coil the method of obtaining the rotor bar currents followed two main avenues of development. The first, Single Bar Acquisition, was similar to that previously developed for acquiring data within the *CAPro* health monitoring system. The main difference between the two being a change in current - voltage transducer. The second acquisition method involved a more complicated set-up. In this system an acquisition system which allowed synchronous Multi Bar Acquisition was developed.

A.VIII.2 Single Bar Acquisition

As a means to obtain a single rotor bar current, a signal conditioning circuit in conjunction with the individual 18 transducers via the interface panel was developed. Since the Rogowski coils give a voltage dependent upon the alternating current flowing through the rotor bars at the terminals of the coil, a conditioning circuit which has the capability of obtaining a differential voltage was required. Utilising an instrumentation amplifier along with signal protection techniques, the signal conditioning circuit shown in Figure [A.VIII.2.1] along with acquisition software developed via LabWindows was developed.

Since the pick-up transducer and necessary transferring cabling pass through areas which are highly contaminated with EMC, i.e. the inside of the IGM and within the general area of the laboratory environment, it was felt that some form of signal protection would be required for the conditioning circuitry as the amplitude of the signal, prior to any form of conditioning, would be small and prone to any distortion.

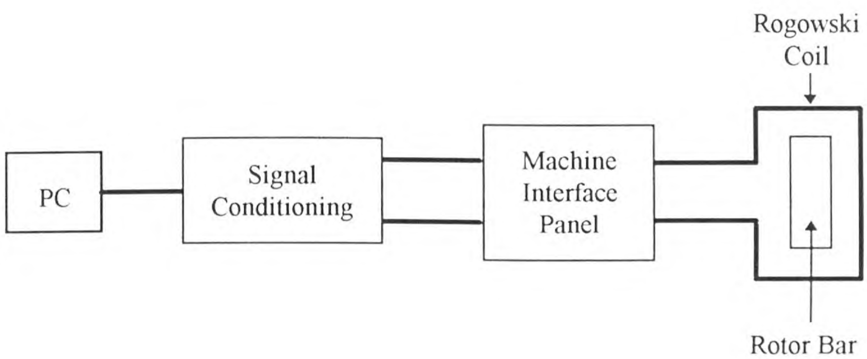

Figure [A.VIII.2.1] Single Current Acquisition Conditioning Set-up.

Several techniques involving signal protection techniques were investigated, including the careful choice of earth connections and use of different forms of cabling between the machine interface panel and conditioning circuitry aswell as within the IGM itself.

The technique, however, which was found to reduce the effects of interference the most in this application can be seen in Figure [A.VIII.2.2]. Here the use of twin core screened cable feeds the signal into a high precision instrumentation amplifier which produces and amplifies the necessary differential signal. The circuitry, the screened cores and the circuitry container are all protected via a guard voltage. This produces an easier path for noise interference to travel to ground and reduces the effects of capacitance between the signal wire and the signal screen causing stray paths to occur. The guard voltage is supplied via the instrumentation amplifier used.

The circuit shown in Figure [A.VIII.2.3] shows the complete circuit including guard voltage for the single bar acquisition set-up. Figure [A.VIII.2.4] shows the hardware required for successful acquisition of single bar currents. The acquisition software required was developed from that previously used by the *CAPro* monitoring system, see Chapter 4.

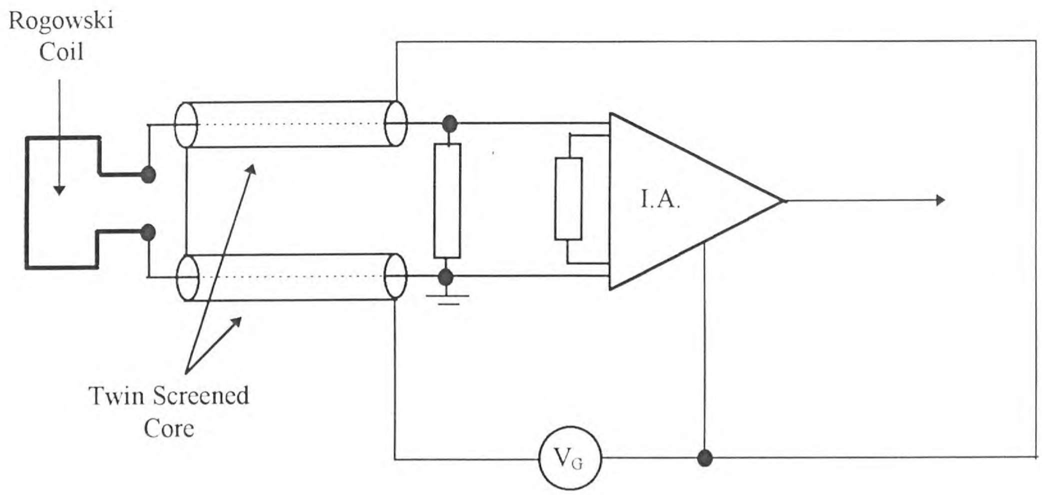

Figure [A.VIII.2.2] Guard Voltage Technique.

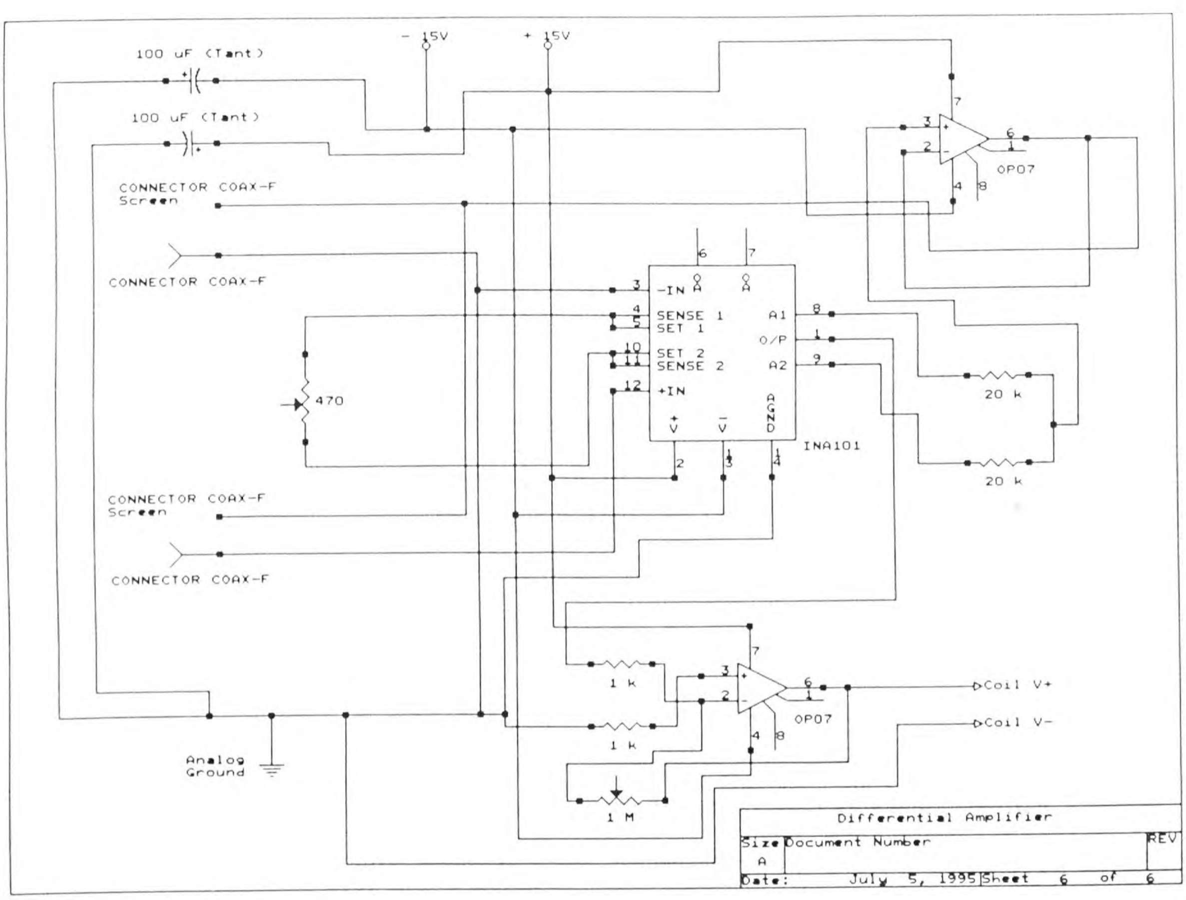

Figure [A.VIII.2.3] Complete Single Bar Current Acquisition Circuitry.

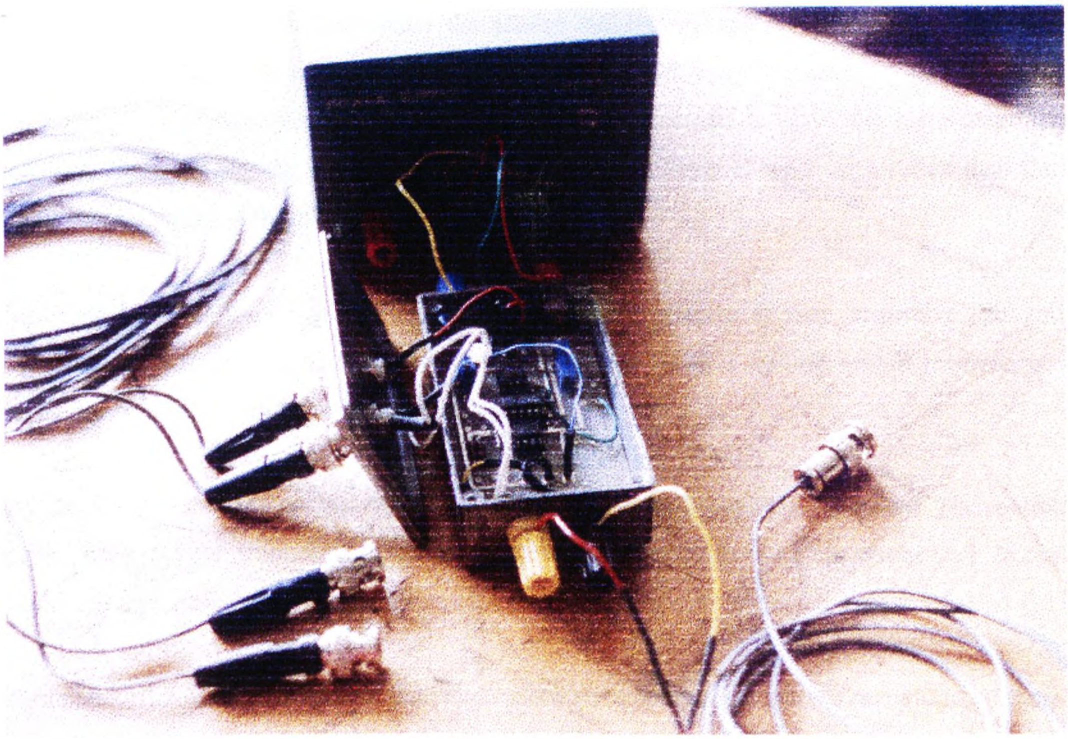

Figure [A.VIII.2.4] Single Bar Acquisition Set-up.

A.VIII.3 Multi Bar Acquisition

Only 18 out of the 36 rotor bar currents would be digitised so as to reduce the problems associated with physical space within the IGM. The first basic acquisition system to be developed allowed the currents picked up by individual Rogowski worm coils to be fed to analog multiplexers which, via a control section, act like a switch accessing the individual 18 rotor currents in turn and passing the associated voltages to an instrumentation amplifier which derives a differential voltage for the particular worm coil, amplifies it, and passes it onto the P.C. via a LabWindows acquisition card.

This method of acquisition however did not allow synchronous acquisition to be achieved. In order for this to occur the addition of sample and hold IC's was required to allow the rotor bar currents to be frozen in time, thus allowing the P.C. to store synchronised data following a suitable choice of sample rate. The introduction of the S/H capability within the acquisition system therefore resulted in another section to be controlled via the control section.

Results using this acquisition circuit however were not satisfactory. The levels of current being used as test signals were not picked up sufficiently outwith background noise levels. In order to introduce a certain amount of amplification before the analog multiplexer, the instrumentation amplifier was brought to the input side of the analog switch, this signifies a marked increase in the amount of components required within the design but was deemed necessary to allow the extra amplification required, thus allowing the S/H and multiplexer a decent voltage to work with rather than the low levels currently used within the previous designs.

Figure [A.VIII.3.1] shows all 18 Rogowski worm coils connected to their respective S/H and IA circuits. The diagram shows how the formation of the 18 to 1 analog switch mechanism was developed using standard 8 dual channel devices.

In order for the system to operate correctly a substantial level of control was required. The controlling signals are generated from digital clocks and undertake many controlling operations such as timing, counting and handshaking.

Figure [A.VIII.3.2] summarises the individual subsections of the main control section. In all there are seven such subsections each of which are discussed within the following sections.

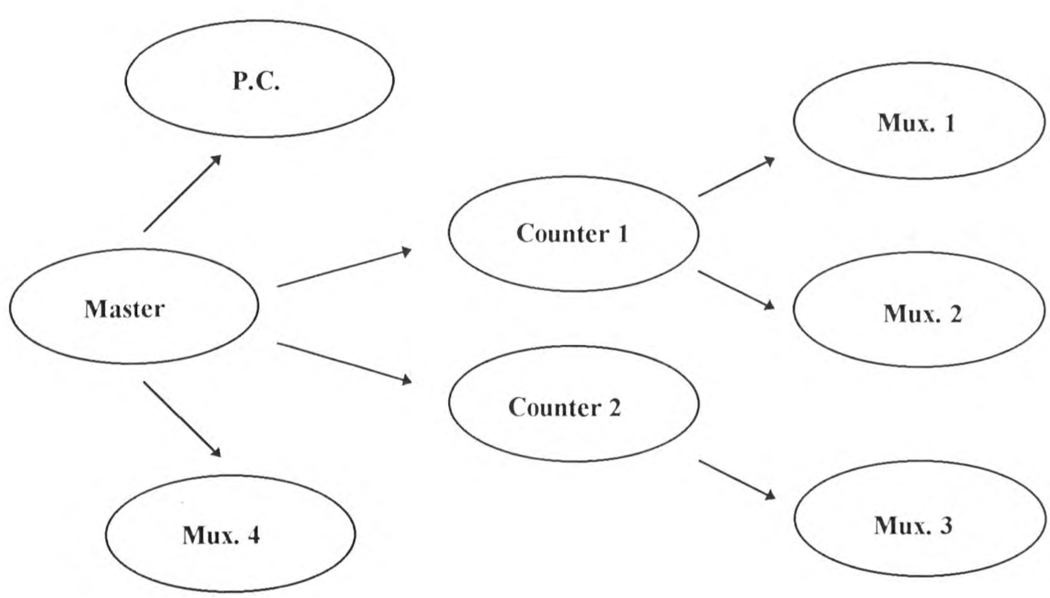

Figure [A.VIII.3.2] Sub-sections within Control Section.

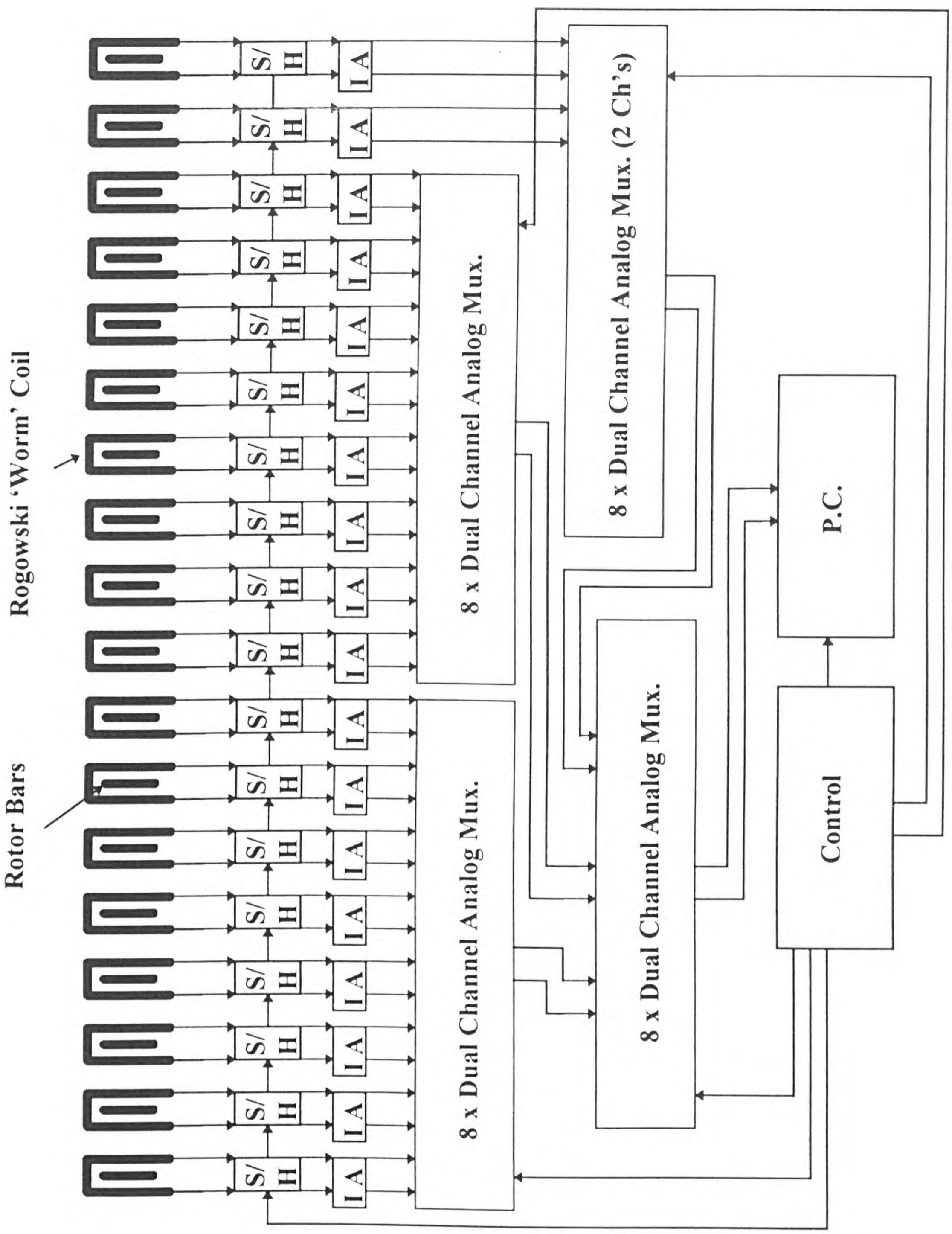

Figure [A.VIII.3.1] Multi Bar Acquisition Set-up.

A.VIII.3.1 Mux. 1, Mux. 2, Mux. 3 and Mux. 4

These are the four analog multiplexers used within the design of the acquisition system. In order to control these switches four signals were required to be sent to the individual ic, these signals being an Enable and three Address lines.

Three 8 x dual channel switches are used to access the 18 individual rotor bar currents. The outputs of these three switches are brought to a single differential output via the fourth switch as can be seen in Figure [A.VIII.3.1.1].

A.VIII.3.2 Sub-Controller 1 (Counter 1)

This is the control circuit which allows the first two analog multiplexers, Mux. 1 and Mux. 2, to access all 8 of their differential channels in a sequential order. This control circuit has three outputs: the address lines that count from 0 through to 7, and one input, a signal sent from the master control circuit to this sub-circuit indicating that counting should proceed.

A.VIII.3.3 Sub-Controller 2 (Counter 2)

This control circuit does a similar task as to Counter 1 in that it controls the third remaining analog multiplexer, Mux. 3. As 18 rotor bar currents are digitised then only 2 dual channels are required in this switch. The control circuit therefore only requires to count from 0 to 1. The circuit contains two output lines: the address lines and one input line, the line indicating that counting should proceed.

A.VIII.3.4 Sub-Controller 3 (PC)

As the PC acquisition circuit is similar to that used in the *CAPro* system only one input is required, the *Extconv** signal. This signal indicates to the PC that a conversion of current data should be executed, and is required to be supplied from an external source. The master control circuit is therefore required to generate this signal.

A.VIII.3.5 Master Controller

The Master controller dictates to the three other sub-controllers when, and when not, to operate. The Master controller also has a task of operating the fourth analog multiplexer, Mux. 4. This being the final step in multiplexing the 18 analog inputs down to one singular input, which is then placed into the input of the LabWindows acquisition card within the PC.

A.VIII.4 Control System - Timing

In order for this control section to operate correctly, the design must be made around a series of synchronised timings and handshaking events. Figure [A.VIII.4.1] shows the timing required prior to correct operation of the control section. Table [A.VIII.4.1] presents a glossary of the signals used within the control section.

A.VIII.5 Master Controller

Figure [A.VIII.5.1] through to Figure [A.VIII.5.5] show the finished circuits of the developed multi-bar acquisition system. It should be noted that the 18 individual instrumentation amplifiers are similar to that used within the single bar acquisition. The clock circuitry is also similar, in that a schmitt trigger set-up is used, the difference between the two applications being a faster clocking rate within the multi bar acquisition.

The software developed to acquire the data from the output of Mux. 4 was developed from that of the acquisition software within the *CAPro* monitoring system. The program developed enables the operator to acquire both single and multi-bar data, the operator being only required to select the appropriate clock timing for the required application. The essential model for this software is shown in Figure [A.VIII.5.6] (a), (b) and (c).

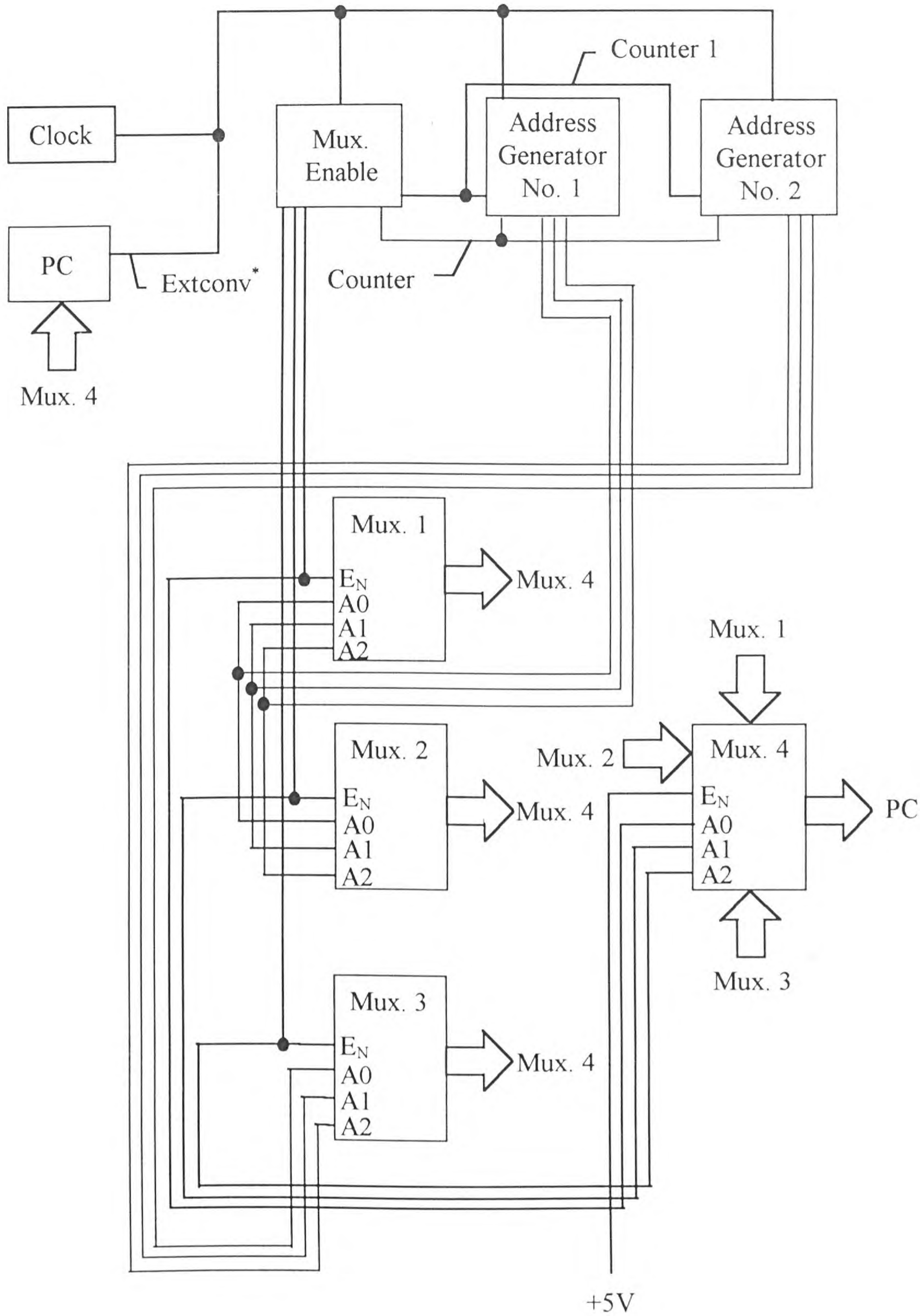

Figure [A.VIII.3.1.1] Multi Bar Acquisition Set-up.

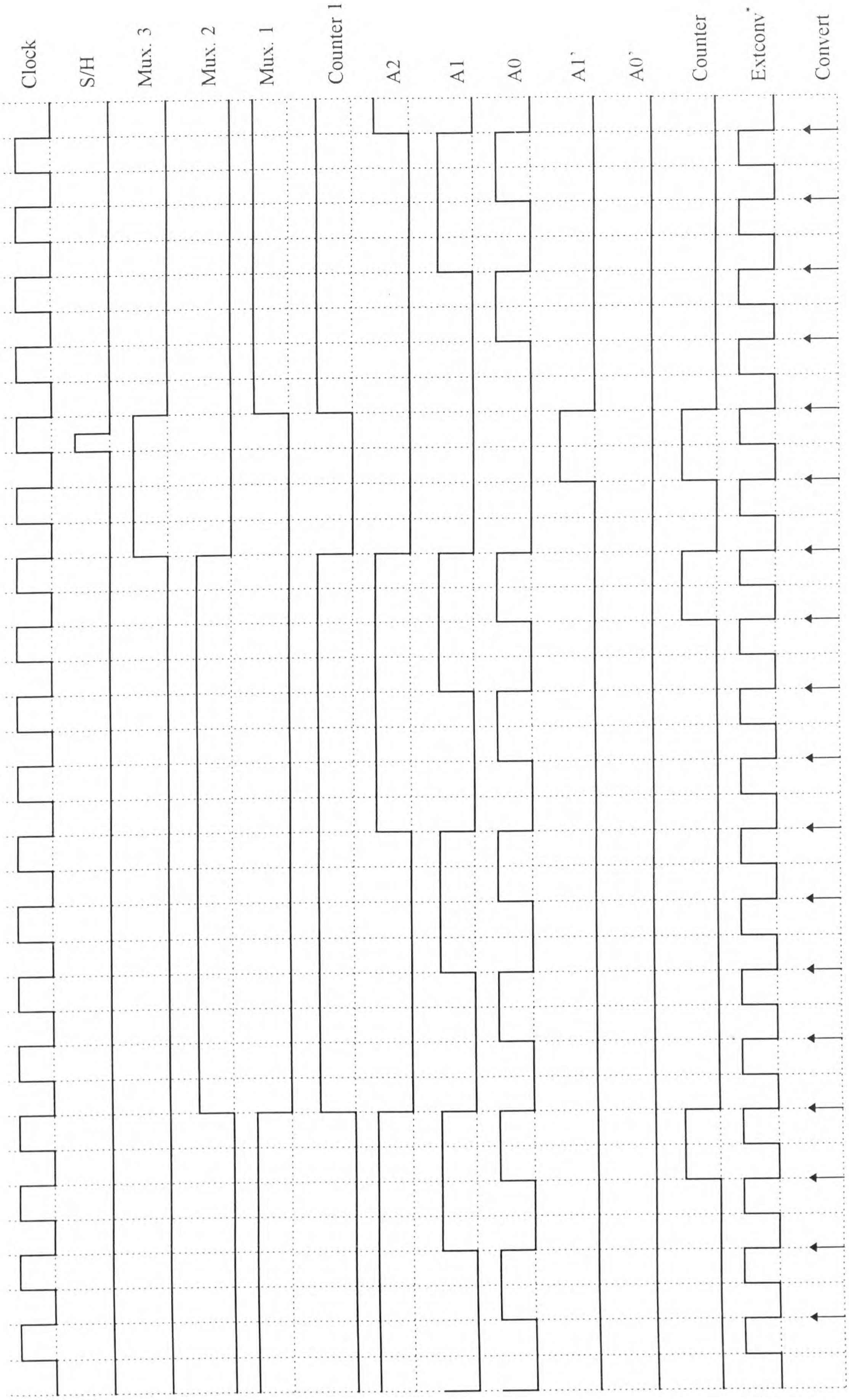

Figure [A.VIII.4.1] Multi Bar Acquisition Timing.

Clock:	Signal developed from a schmitt trigger circuit which is used to generate the pulse which is used to synchronise all operations within the multi bar current acquisition system.
S/H:	A pulse generated from Extconv* and used to trigger Sample and Hold IC.
Mux. 3, Mux. 2, Mux. 1:	Enable signals for the analog switch multiplexers.
Counter_1, Counter:	Enable signals for counter circuits.
A2, A1, A0:	Address lines for Counter 1.
A1',A0':	Address lines for Counter.
ExtConv*:	Signal required by LabWindows acquisition board to begin conversion.
Convert:	Conversion undertaken on falling edge.

Table [A.VII.4.1] Glossary of Timing Signals.

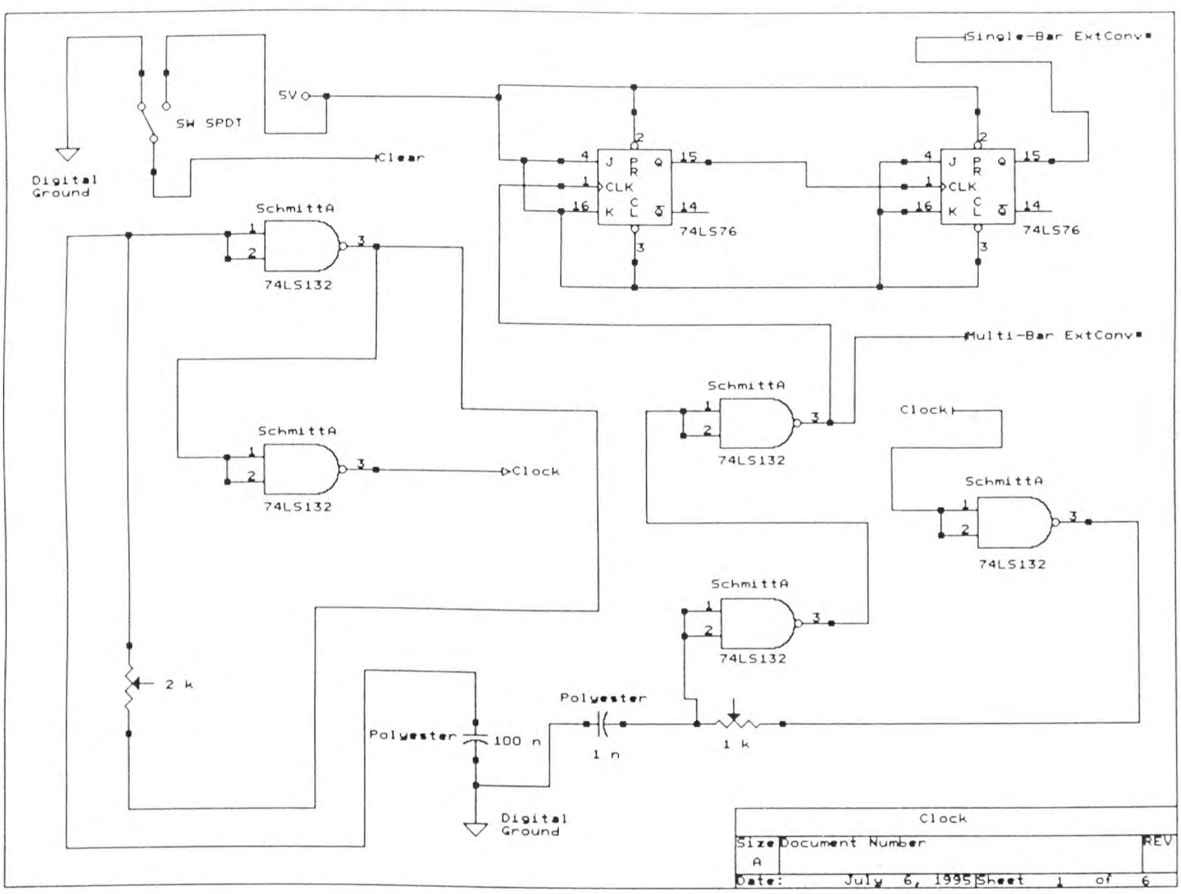

Figure [A.VIII.5.1] Clock Circuitry - Single and Multi Bar Acquisition.

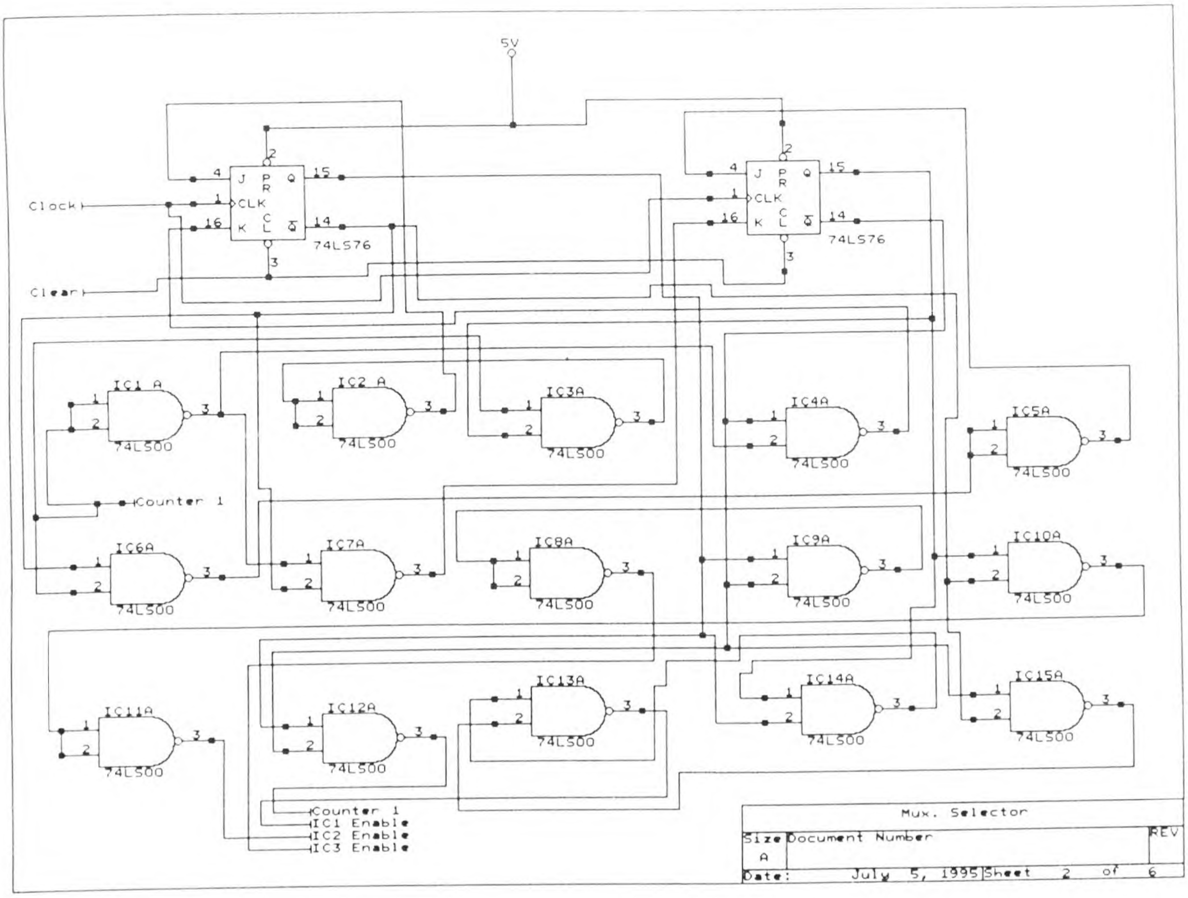

Figure [A.VIII.5.2] Mux. Selector Circuitry.

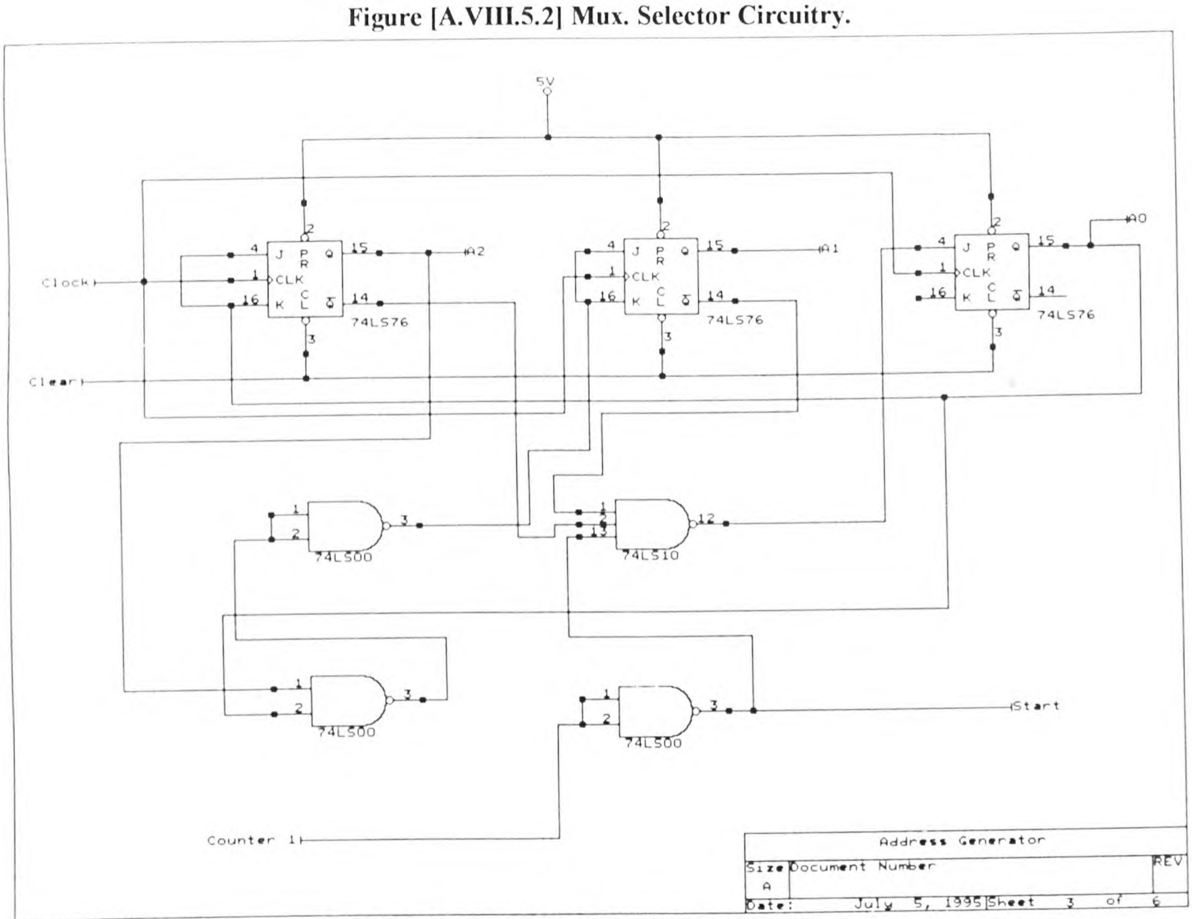

Figure [A.VIII.5.3] Address Generator No. 1.

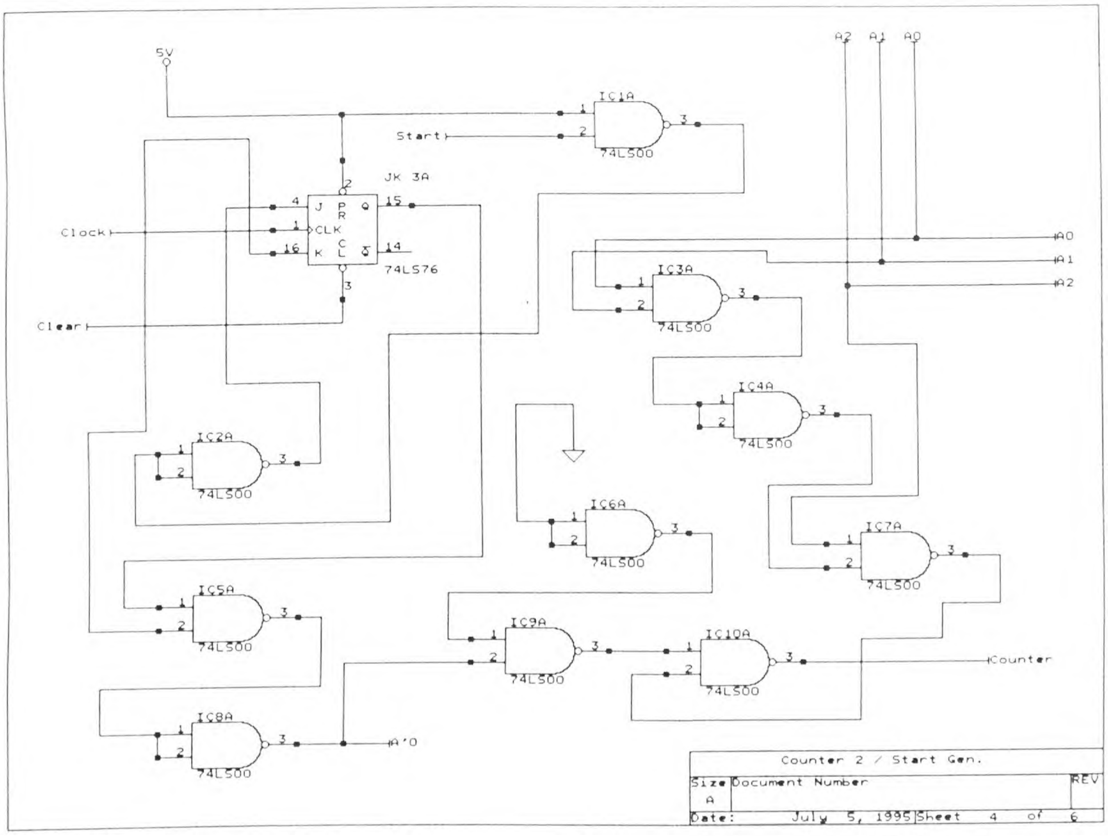

Figure [A.VIII.5.4] Address Generator No. 2.

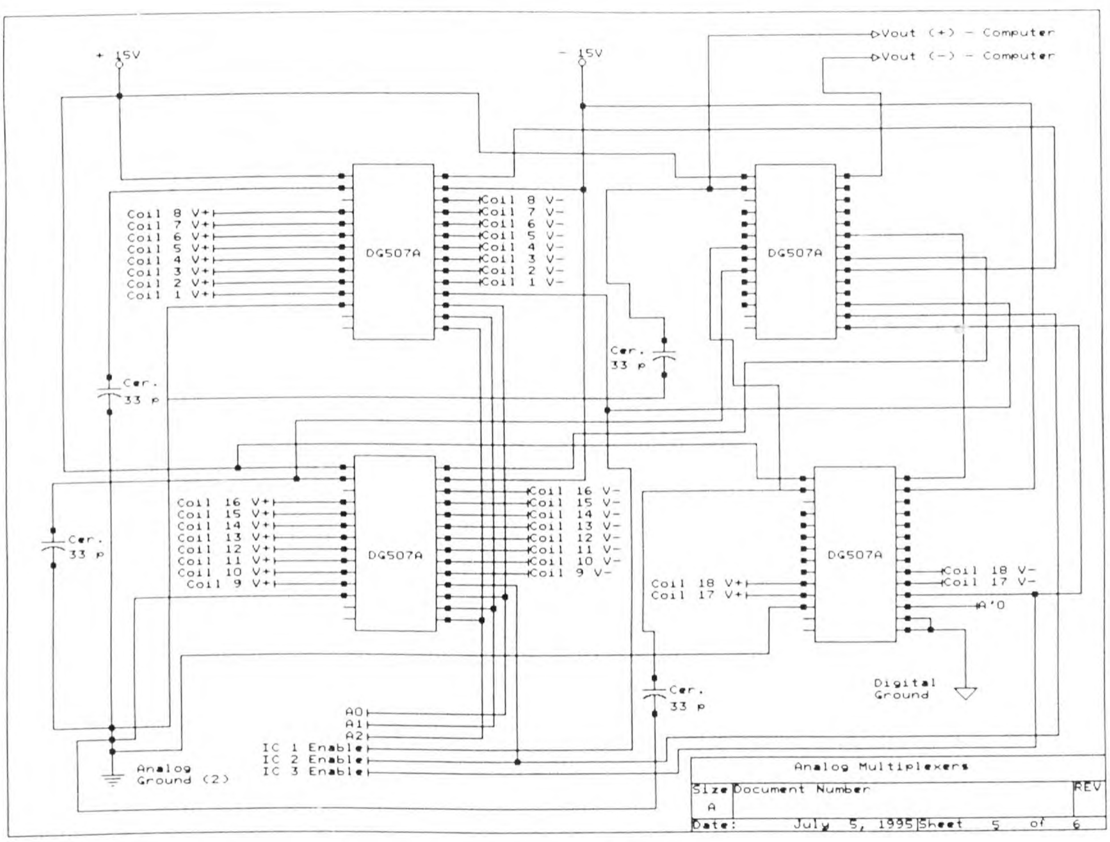

Figure [A.VIII.5.5] Analog Multiplexers.

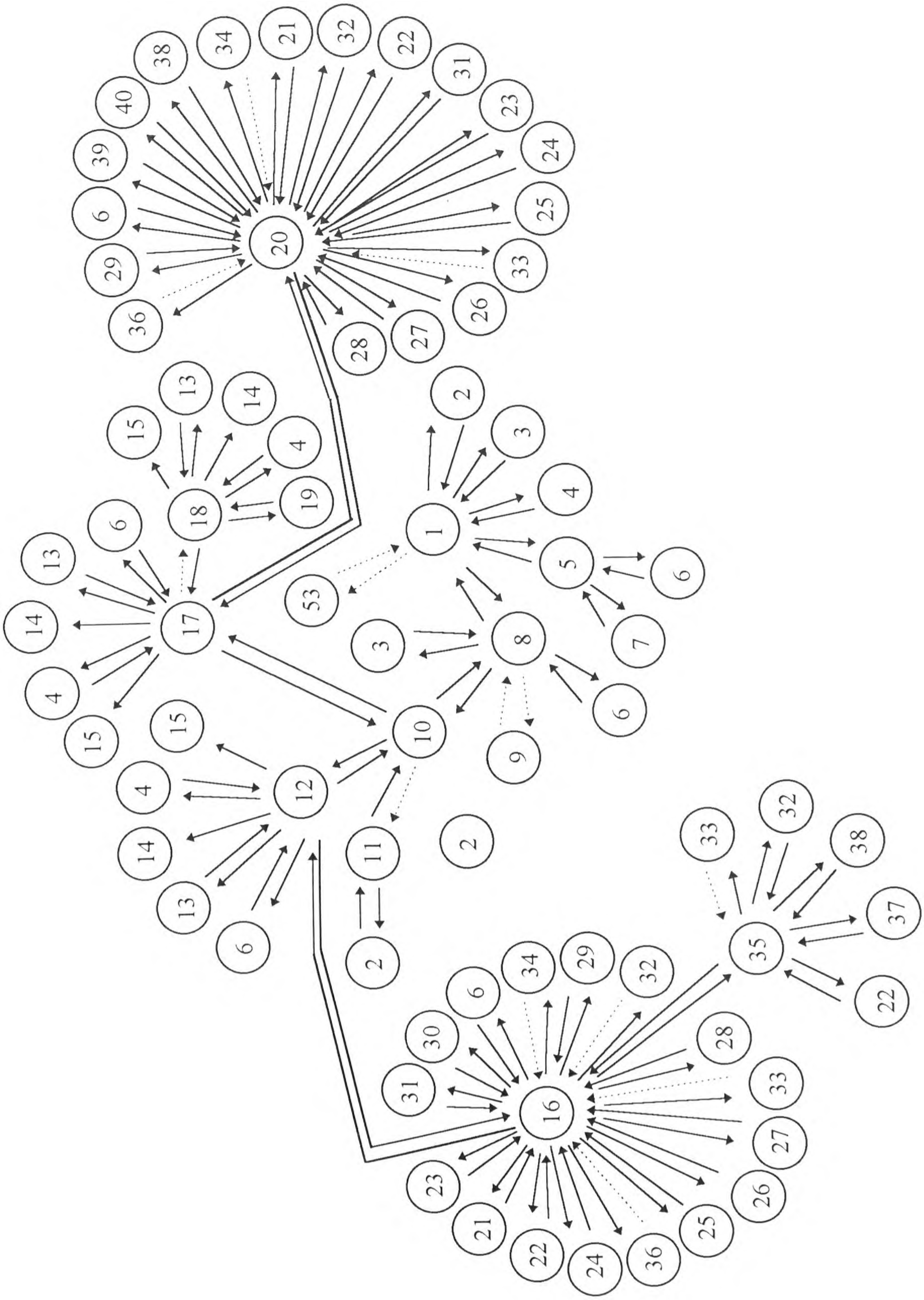

Figure [A.VIII.5.6] (a) Rotor Bar Current Acquisition Essential Model.

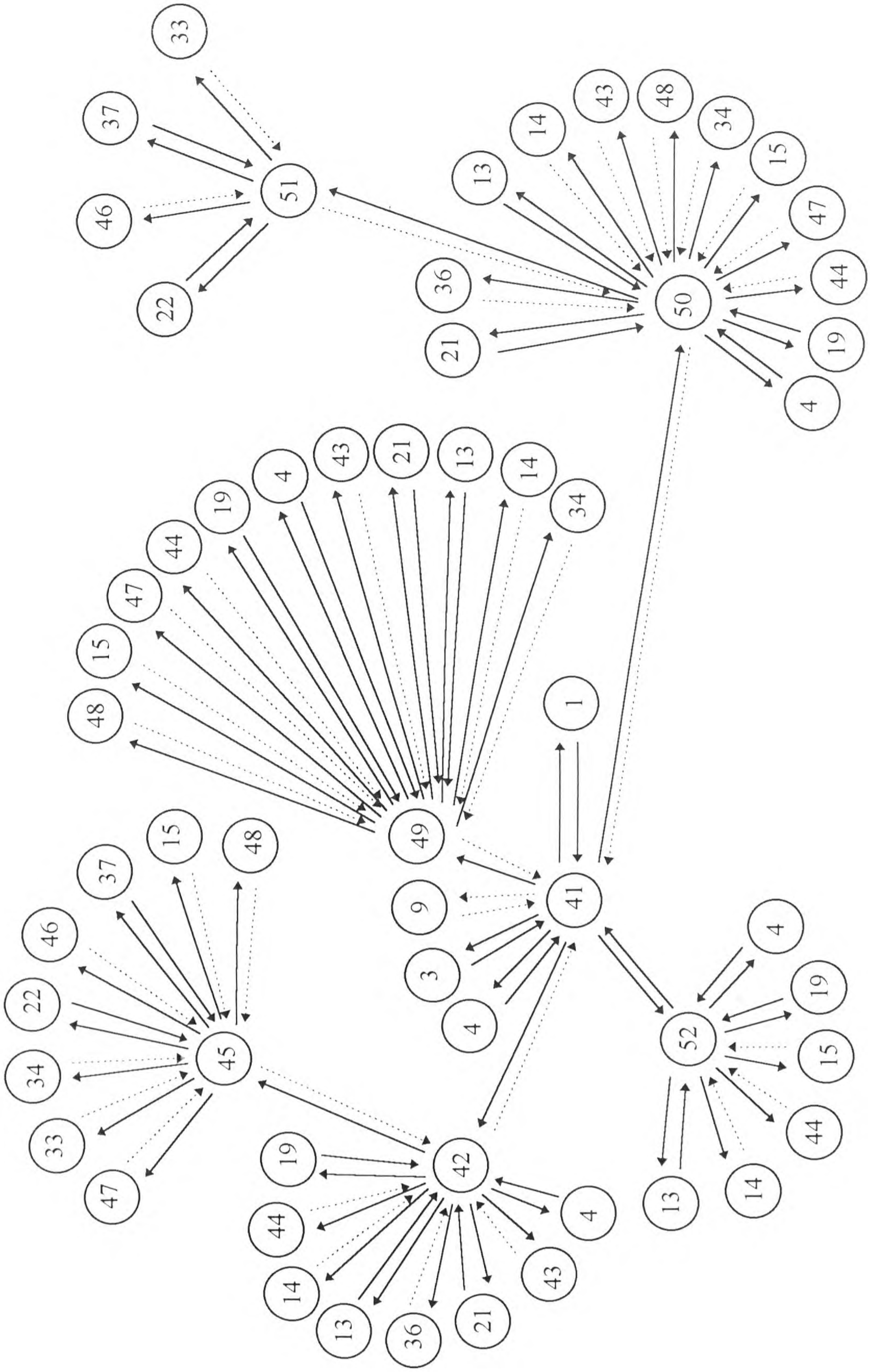

Figure [A.VIII.5.6] (b) Rotor Bar Current Acquisition Essential Model.

1 - Rotor ();
2 - ConfirmPopUp ();
3 - LoadMenuBar ();
4 - GetUserEvent ();
5 - SelectDataFile ();
6 - MessagePopUp ();
7 - FileSelectPopUp ();
8 - Sample ();
9 - UnLoadMenuBar ();
10 - Data_Acquisition ();
11 - Rotor_Current_Selection ();
12 - Single_Acquire ();
13 - LoadPanel ();
14 - DisplayPanel ();
15 - UnLoadPanel ();
16 - Grab_Data ();
17 - Tri_Acquire ();
18 - Sample_Length ();
19 - GetCtrlVal ();
20 - Grab_Tri_Data ();
21 - Calloc ();
22 - Fopen ();
23 - AI_Configure ();
24 - DAQ_Config ();
25 - DAQ_Trigger_Config ();
26 - DAQ_DB_Config ();
27 - Timeout_Config ();
28 - DAQ_Rate ();
29 - DAQ_Start ();
30 - DAQ_Check ();
31 - DAQ_Clear ();
32 - Fwrite ();
33 - Fclose ();
34 - Free ();
35 - Conversion ();
36 - ClearGraphics Screen ();
37 - Fread ();
38 - DAQ_Vscale ();
39 - DAQ_DB_Halfready;
40 - DAQ_DB_Transfer ();
41 - Display_Currents ();
42 - Display_Range ();
43 - SetActivePanel ();
44 - SetInputMode ();
45 - Load_Single_Currents;
46 - Fseek ();
47 - DeletePlots ();
48 - Ploty ();
49 - Display_Range_2 ();
50 - Display_Range_3 ();
51 - Load_Single_Samp_Currents ();
52 - Enter_Offset ();
53 - CloseInterface Manager ();

Figure [A.VIII.5.6] (c)
Essential Model Glossary.

Appendix IX

Published Papers

ICEM '94, PARIS, SEPTEMBER 1994.

*

IMTC '95, IEEE INSTRUMENTATION / MEASUREMENT TECHNOLOGY CONFERENCE, BOSTON, APRIL 1995.

*

7TH INTERNATIONAL CONFERENCE ON ELECTRICAL MACHINES AND DRIVES, UNIVERSITY OF DURHAM, SEPTEMBER 1995.

*

EUROPEAN SIGNAL PROCESSING JOURNAL, EURASIP, No. 49, Vol.1, MARCH 1996.

*

THE DETECTION AND LOCATION OF ROTOR FAULTS WITHIN THREE PHASE INDUCTION MOTORS.

LA DETECTION ET LA LOCALISATION DES DEFAULTS ROTORIQUES DANS LES MOTEURS A INDUCTION TRIPHASES.

R.Burnett J.F.Watson S.Elder
The Robert Gordon University
Aberdeen, Scotland, U.K

Abstract

It has been shown that rotor faults such as broken rotor bars can be detected as a result of an analysis of the line current under starting transient conditions. Signal processing strategies, appropriate to handling time-varying signals, have been used to further refine the detection technique and to track and analyse current components which provide information on the location of any fault. This paper explains the techniques developed and provides some initial results of their application.

Keywords:

Condition Monitoring
Transient Analysis
Fault Location

Introduction

A variety of faults can occur within three phase induction motors during the course of normal operation. Several, such as rotor-stator eccentricity and broken rotor bars can, if undetected, lead to a potentially catastrophic failure. Consequently, a variety of condition monitoring techniques have been developed which allow the health of a motor to be assessed. The onset of potential faults can be detected and their development monitored, thus using planned maintenance to prevent plant failures.

Over the years a number of machine parameters have been monitored; line current [1][2], leakage flux, along with core and bearing vibration [6] being the most common. The majority of these techniques require the machine in question to be operating under full load, steady state conditions before a reliable diagnosis can be carried out. Certain machines however, as a result of their operational environment, or perhaps because they have been removed to a workshop for repair, cannot be tested under loaded conditions. Furthermore, certain machine designs such as double rotor cage construction can develop faults which only manifest themselves during starting and are undetectable during steady state analysis.

It was principally for these reasons that work was initiated some five years ago at The Robert Gordon University to determine whether machine faults could be detected by analysing the line current under a single, no load, starting transient. The initial premise was that the high current and severe mechanical stresses experienced by the machine throughout this period would allow faults to be detected on no-load and at an earlier stage in their development.

Previous Work

It has previously been shown that a frequency spectrum analysis of the line current under steady-state operating conditions yields components indicative of broken rotor bars (and/or rotor-stator eccentricity). These components manifest themselves as sidebands at ± 2sf centred on the fundamental of the supply frequency. The magnitude of these components is proportional to the degree of severity of the rotor faults.

The initial premise of the transient analysis was to monitor these same components, but during the acceleration of the machine they are changing in both frequency and magnitude. The work to date has shown that it is possible to detect faults such as broken rotor bars by monitoring a single no-load starting transient. The technique has been successfully applied to machines in both laboratory and industrial environments [2][3].

Signal processing techniques have been developed whereby the transient line current is passed through a series of digital bandpass filters. If the output of the filters between 0 and 50 Hz is monitored the sidebands, indicative of rotor faults, can be seen progressing in frequency as the transient develops. The peak of the sideband energy is found to correlate well with the number of broken rotor bars. Examples of this technique are shown in Figures 6 and 7. Figure 6 corresponds to a staring transient on a laboratory motor with 3 out of 51 rotor bars broken. The sideband can clearly been seen as it moves from 0 Hz (at approximately ½ speed) to close to 50 Hz under steady state conditions.

Further work was required to improve the resolution of the technique and to quantify the degree of fault detected. A further problem arises in that occasionally a fault is detected yet on examination no immediate physical evidence is obvious. This is particularly true on machines with cast rotors or in cases of high resistance joints between rotor bars and end-rings.

For these reasons it is desirable to be able not only to detect a rotor fault but also to have the ability to locate it. Preliminary work suggested that fault detection and analysis during starting transients may provide the required information. It is this work which is described in this paper.

Frequency Components Resulting From Rotor Asymmetries

Deleroi [4] states that when a Squirrel Cage Induction Motor, or SCIM, has a rotor which contains a broken bar, then the rotor can be considered as having an extreme amount of asymmetry. The distortion in the symmetry is assumed to produce a fault current within the rotor bar which contains the asymmetry, in addition to the current which would flow under normal *symmetrical conditions.*

Deleroi shows that the ratio of the additional current in the two neighbouring meshes to the rotor bar with the asymmetry, is equal to the complex damping factor, 'd'. This ratio is also present within the air gap flux density around the bar and is found to be independent of the number of bars which are present in the rotor. The air gap flux density contains two components, one which increases with increasing distance from the bar with the asymmetry, the second decreasing. Hence, the air gap flux when considered in relation to a cylindrical rotor which contains an asymmetry, produces two field waves which travel in opposite directions away from the location of the rotor asymmetry. The amplitudes of the waves decreasing in a stepwise manner, Figure 1.

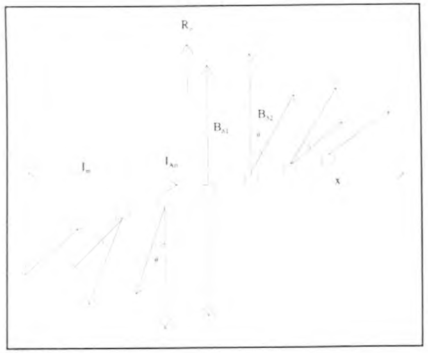

Figure 1

Figure 2 shows the locus of the complex damping factor, 'd', for various values of motor slip, 's'. Deleroi shows that when the value of 's' is small, then the amplitudes of both 'd' and the phase angle between the additional current in neighbouring meshes, 'θ', are small. This results in the rotor anomaly spreading out a long way around the circumference of the rotor. With higher values of slip, then from Figure 2 the damping factor, 'd', increases, resulting in the rotor anomaly becoming more prominent around the rotor bar which contains the asymmetry, as it quickly decreases in amplitude with increasing distance from the asymmetry, Figure 3. The extent to which the effects of the anomaly are transmitted in the air gap and the degree of damping which is obtained are dependent upon the rotor geometry, with the excitation of the anomaly being dependent on the slip of the rotor. The field produced from the asymmetry therefore revolves with the rotor, slipping with respect to the main air gap field.

This additional air gap field, produced by the rotor asymmetry, induces voltages within the stator windings of the SCIM, which contain a fundamental frequency, along with many other high frequency components. According to Deleroi, the voltages which are induced will contain frequencies which can be determined by Fourier analysis, and can be described by the following expression:

$$F_{Deleroi} = f(k/p - s(k/p \pm 1)) \qquad (1)$$

Thus, when a rotor contains an asymmetry, then from Deleroi's theory, there will be frequency components present in the supply current signal of the SCIM which may indicate the location of the asymmetry on the rotor. It is felt, that if these components can be detected within the transient signal, then it should be possible to obtain fault location information. Information which could not be easily obtained from a steady state analysis of the current signal, due to the small values of slip present.

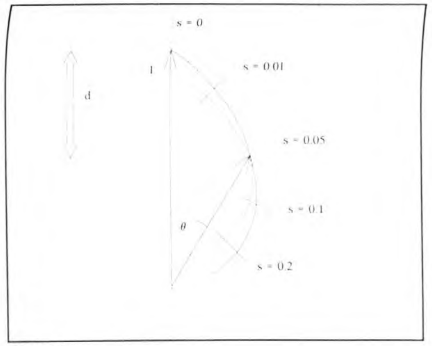

Figure 2

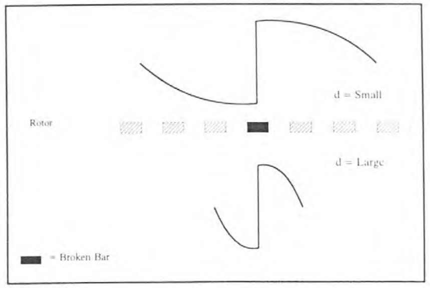

Figure 3

Prediction of Deleroi Frequency Components

From the expression describing the Deleroi components, equation (1), it is clear that the components are dependent on the slip of the machine. This means that during the transient period, the frequency values of the Deleroi components will be changing with respect to slip.

In order to observe the locus of the Deleroi components, whilst the value of slip is moving from unity towards zero, a plot of frequency versus slip was created for a 3 phase, 11kW, 4 pole, 51 slot laboratory machine.

Along with the Deleroi components, the Upper and Lower sidebands, the Principal Slot Harmonics, and the fundamental of the supply frequency, with harmonics thereof, were plotted onto the same 'map' of frequencies.

Once the components were plotted, it was possible to observe how the different components travelled in relation to one another, as the value of slip changed throughout the transient period. The plot of frequencies would also serve as an indication to the optimum detection range for the Deleroi components; i.e. the areas deemed to be clear of interference from dominating frequency components.

All components were calculated for different values of slip using proven equations.

For the Upper and Lower sidebands, the formula used to calculate the components was that which had been proven by Hargis et al [5].

$$F_{ULS} = f(1 \pm 2s) \qquad (2)$$

The Principal Slot Harmonics were calculated using the formula which had been verified by Thomson et al [6].

$$F_{PSH} = f(n \pm R(1-s)/p) \pm 2sf \qquad (3)$$

The fundamental frequency of the supply was taken to be 50 Hz, with harmonics of this value being displayed. The Deleroi components were calculated using equation (1).

Figure 4 shows the resulting map of frequencies for a rotor with 51 bars. The significant features of this diagram are firstly, the Principal Slot Harmonics increase to high values of frequency in a relatively short space of time, and secondly, that it is the 7th and higher harmonics of the Deleroi components, which will be clear of the dominating Upper and Lower sidebands (USB, LSB).

As indicated in Figure 4, the optimum area within the transient for detecting the Deleroi components, would appear to be when the slip of the machine is less than 0.4, and at values of frequency higher than 100 Hz.

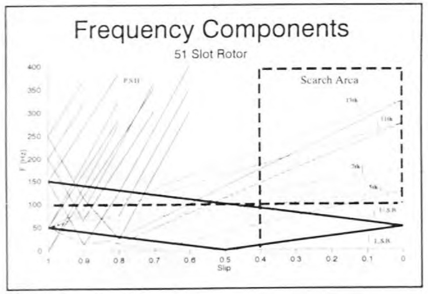

Figure 4

Verification of Steady State Components

Prior to the detection of the Deleroi components during the transient period of the SCIM's supply current signal, the existence of the components during steady state conditions was investigated.

Table 1.0 shows the frequencies of the Deleroi components, calculated by equation (1), for a full load slip value of 0.042.

Using a 3 phase, 11 kW, 4 pole, 51 slot rotor, SCIM, one phase of the supply current signal was analysed, whilst the motor was at full load, using a zoom spectrum analyzer. The current signal was first analysed under a zero broken bar condition, followed by an analysis of a two broken bars condition.

The results of the zoom analysis on the supply current signal, showed that at steady state, the Deleroi components were present when the motor was under a broken bar condition.

Table 2.0 shows the change in decibels which occurs in the 5th, 7th, 11th and 13th harmonics of the Deleroi component between the zero and broken bar conditions.

The results of monitoring the steady state current signal, verified the existence of frequency components at the frequencies given by the Deleroi expression, equation (1), whilst the value of slip was at a known constant value. It was also found that certain harmonics of the Deleroi component increased in amplitude by a larger amount than others with the introduction of the broken bar condition.

DELEROI FREQUENCY COMPONENTS

HARMONIC No.	SIDEBAND 1 (Hz)	SIDEBAND 2 (HZ)
1	21.85	26.05
3	69.75	73.95
5	117.65	121.85
7	165.55	169.75
11	261.35	265.55
13	309.25	313.45

TABLE 1.0

COMPONENT INCREASE WITH FAULT

HARMONIC No.	dB CHANGE (dB's)
5	14.8
7	22.1
11	0.3
13	0.3

TABLE 2.0

Correlation of Transient Signals

When a rotor contains an asymmetry, then due to Deleroi's theory, the supply current transient should contain frequency components which are indicative of the location of the asymmetry on the rotor. If the position of the asymmetry is then moved to a different location on start up, the transient signal obtained, from this start up, will contain similar frequency components to the previous transient, except now the components have been time shifted due to the change in position of the fault.

The 3 phase currents from several transients were filtered at various Deleroi frequencies before correlating with their respective phases from a reference transient. In addition, the timings of the peaks within the filtered transients were also noted.

The result of monitoring the peak timings within the filtered transients, and the correlating of the filtered transients with a reference position transient, unfortunately showed little connection with the location of the fault on the start up of the machine. This was thought to be due to the larger Upper and Lower sidebands dominating the contents of the filtered transients.

Time Frequency Representation of Transient

The supply current transient was then converted into its time frequency representation. This was done in order to observe if it would be possible to detect the Deleroi components, travelling in frequency, with increasing time, as predicted by Figure 4.

Several signal processing techniques which result in the production of a signals time frequency representation, were investigated in order to obtain the most efficient technique *suitable for the class of signal which was being analysed, namely a time varying signal.*

The Spectrogram is a popular method of displaying the time frequency representation of a time varying signal. The Spectrogram displays the time frequency representation of the signal under analysis by obtaining a short time spectrum of the signal, via implementation of a Fourier Transform equation, a process known as a Short Time Fourier Transform, or STFT.

The STFT is calculated by the expression shown in equation (4), with equation (5) showing how the STFT is used in the formation of a Spectrogram.

$$F(k) = \sum_{n=0}^{N-1} w(nT)f(nT + rMT)\, e^{-j(2\pi/N)nk} \qquad (4)$$

$$S(t,\omega) = |F(k)|^2 \qquad (5)$$

The Smoothed Wigner Ville Distribution of a signal, SWVD, is calculated by the expression shown in equation (6).

The SWVD is calculated using the analytic representation of the signal under analysis. The analytic signal is obtained by transforming the signal under analysis using the Hilbert

$$SWVD(n,m) = 2 \sum_{k=-N}^{N} r_n(k)\, e^{-jkm2\pi/K} \qquad (6)$$

$$r_n(k) = [\sum_{i=-R}^{R} w(i)\, xa(n+i+k)xa^*(n+i-k)]\, |h(k)|^2$$

transformation, in either the frequency or time domain. This transformation, coupled with the use of the appropriate windowing, again in both time and frequency, minimises the effects of spectral interference. One particular form of interference, known as 'crossterms', is a result of the bilinear nature of the distribution, resulting in interference terms occurring midway between the actual frequency components of a multicomponent signal. These interference terms can be up to twice the size of the original frequency components. However, if these interference components can be reduced to a manageable size by the use of windowing, then the SWVD is a far more efficient method of obtaining the time frequency representation of a signal, as the SWVD can be calculated, using an FFT algorithm, in half the amount of operations as is required by the STFT.

One of the first time frequency representations of a signal was introduced by Gabor [7]. This representation of a signal in the time frequency plane is known as the Gabor decomposition of the signal. In this decomposition, the signal under analysis, r(t), is broken down into a two variable function $R(t,\omega)$. This function is obtained by the convolution of the signal r(t) with a wavelet signal, h(t).

The wavelet signal, h(t), has its centre frequency on the current frequency under investigation. A typical example of such a wavelet is that of a Gaussian wavelet, which has a constant duration regardless of the centre frequency.

After investigation of the above techniques, the latter time frequency representation of wavelet decomposition, was found to give the best results for a supply current transient of an SCIM.

Verification of Signal Processing Technique

In order to observe the correct operation of the wavelet decomposition technique, a supply current transient, which was obtained from a no load start of a motor with 3 out of the 51 *bars in the rotor broken, was investigated over the frequency range of 0 Hz to 42 Hz.*

The prediction shown in Figure 4 suggests that in this range of the frequency spectrum, the Lower sidebands will be the most prominent components. Figure 5 shows a contour plot of the transients time frequency representation. From this plot, the Lower sideband components can be seen moving from 50 Hz towards 0 Hz and then returning to 50 Hz as predicted. The amplitudes of the sidebands can be seen more clearly in Figure 6. Again in this figure, the Lower sidebands can be seen to be moving through frequency as time increases. When this figure is compared to that of Figure 7, a time frequency representation of a transient from the same motor with a zero broken bar condition, then it can be seen that the Lower sidebands increase in amplitude with the introduction of the fault condition.

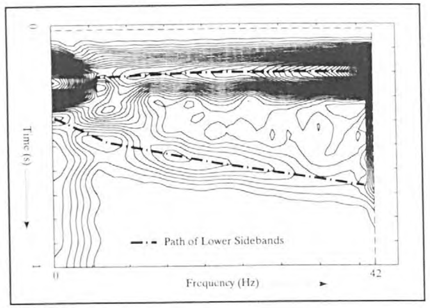

Figure 5

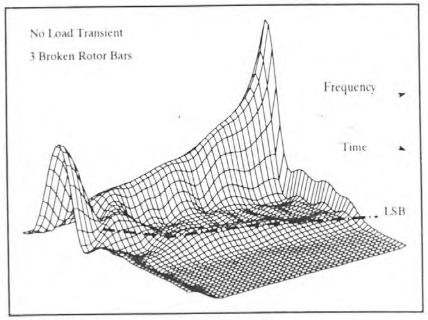

Figure 6

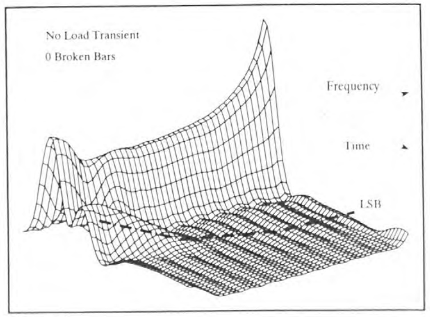

Figure 7

Figures 5 and 6 verify the correct operation of the decomposition technique, as the results compare favourably to the prediction shown in Figure 4.

Search for Deleroi Frequency Components

The supply current transients which were to be analysed were obtained from the motor supply lines by sampling at a rate of 4kHz. The signals, before sampling, were pre-filtered using a 4^{th} order Bessel filter, which reduced the fundamental supply frequency component by 30 dB. The signals were filtered in order that the dynamic range of the samplers ADCs would not be smothered by dominating frequency components such as, the supply frequency and the Upper and Lower sidebands.

Using transient signals from a full load start, in order to increase the amplitude of the Deleroi components which were to be detected, a transient from a ten broken bar condition was first investigated. The investigation took the form of obtaining the time frequency representation of the transient, via the decomposition method, for frequency bands of 100 Hz, from 70 Hz up to a frequency level of 270 Hz. The results of which are shown in Figures 8 and 9.

Figure 8 shows the decomposition of the transient over the frequency range 70 Hz to 170 Hz. If this figure is compared to the prediction, Figure 4, then there are two main points to be obtained. Firstly, component 'A' can clearly be seen travelling

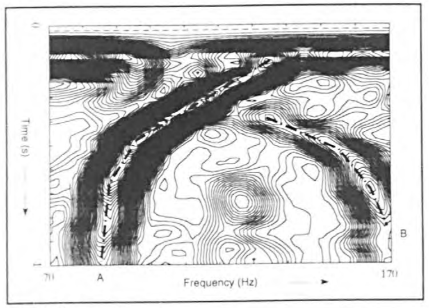

Figure 8

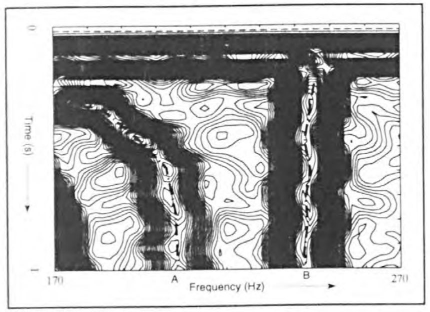

Figure 9

down in frequency, with increasing time. From the prediction in Figure 4, this component represents the Upper sideband. If the slip of the motor is calculated for the frequency which occurs at the end of the analysis, in Figure 8, using equation (2) in reverse, then a value of 0.36 is obtained, hence the end of the plot, in Figure 8, does not represent a slip of zero, as in Figure 4. With *this in mind, component 'B', in Figure 8, when compared with Figure 4, represents one of the harmonics of the Deleroi component. A similar assumption can be given to component 'A'* in Figure 9. It should be noted that the components do not move in a linear fashion due to the non linear acceleration of the rotor. The second point to note is that, component 'B', in Figure 9, which remains static in frequency as time increases, is the 5^{th} harmonic of the fundamental supply frequency.

Initially, there was doubt whether component 'B' in Figure 8 and component 'A' in Figure 9 were Deleroi components. On comparison with the prediction in Figure 4, the components which had been located could also have been Principal Slot Harmonics. Due to this doubt, a time frequency representation of a transient from the same motor with a zero broken bar condition was obtained. If the components which had been located above were Principal Slot Harmonics, then they would be present in the time frequency analysis of the zero broken bar transient.

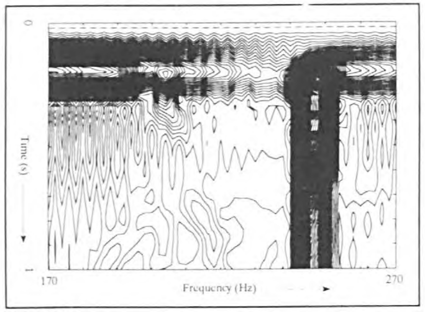

Figure 10

Figure 10 shows the result of the analysis over the frequency range 170 Hz to 270 Hz. If Figure 10 is compared with Figure 9, the only component present is the static 5^{th} harmonic of the fundamental frequency. This verifies that the components which were located in Figures 8 and 9 were the Deleroi components, as predicted by Figure 4.

Location of Broken Bars

Using the time frequency representation of the Lower sidebands, Figure 5, it is possible to obtain the slip versus time information of the rotor under analysis. This is calculated by using equation (2) in reverse. From this slip information, a speed versus time graph can easily be obtained.

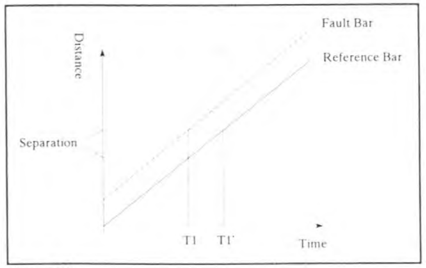

Figure 11

With this slip information, the acceleration of the rotor can be

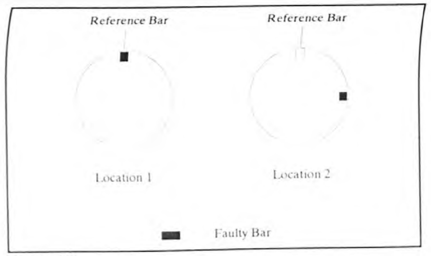

Figure 12

calculated, and hence a plot of time versus the angular distance covered by a reference point can be obtained, Figure 11. If the rotor is started from a known point, for example, a reference rotor bar opposite a reference point in the stator, then the slip data obtained from Figure 5 can be thought of as corresponding to the reference bar in particular.

If an analysis for a particular Deleroi frequency is carried out on a transient, from a motor with the faulty bar in line with the reference bar, location 1, Figure 12, then the particular Deleroi frequency, $Fdel_{REF}$, will take T1 seconds to occur, as predicted by Figure 4. If the position of the fault is moved to location 2, Figure 12, then again the Deleroi frequency under investigation, Fdel, will take T1 seconds to occur, assuming comparable accelerations. However, the frequency takes T1 seconds with respect to the faulty bar. From Figure 11 it can be seen that T1 seconds with respect to the faulty bar, corresponds to T1' seconds with respect to the reference bar, to which we have access. Figure 11 shows that when the difference in times is converted to distance, then the resulting distance corresponds to the distance between the reference bar and the location of the faulty bar.

As an estimation to the resolution which would be obtained, data obtained from the 11 kW SCIM shows that the rotor achieves a speed of 900 RPM in approximately 0.66 seconds. This gives an acceleration of 0.022 revolutions per millisecond, or 7.92 angular degrees per millisecond. This estimation suggests that if the Deleroi frequencies were to occur at intervals separated by 1 millisecond, then it would be possible to determine the location of the faulty bar to within 8 degrees.

Conclusions

The supply current signal of an SCIM will contain frequency components which are indicative of the location of a fault within the rotor of the SCIM. These components, when mapped out with the other frequency components which are present in the supply currents transient, should be detectable at frequencies of 100 Hz or higher, once a slip of 0.4 or less has been obtained. The components have been detected in the steady state signal. In order to obtain fault location information, the components will have to be detected within the transient signal. Using the signal processing technique of wavelet decomposition, the components have been located in the supply current transient signal of an 11 kW, 4 pole, 51 slot rotor, SCIM. As the location of a fault within the rotor is moved, with respect to a reference position, then a particular Deleroi frequency will be shifted in time. This time shift can be converted to a distance using the slip versus time *information, which is obtained from a similar analysis on the Lower sidebands of the motor. The calculated distance will then be the distance between the reference point on the rotor and the* location of the rotor's asymmetry. Initial Correlations between transients obtained from start up's with different fault locations showed little connection between the location of the fault and the results of the correlations. This however, was probably due to the large Upper and Lower sidebands, which were present in the transient signals when correlated, smothering the Deleroi components. Future investigations into the connection between the Deleroi components and the location of the fault, shall use signals which have been pre-filtered in order to reduce the dominance of the Upper and Lower sidebands, along with the fundamental supply frequency component.

Acknowledgement

The authors would like to acknowledge the sponsorship of this work by Scottish Nuclear Ltd.

References

[1] J.R.Cameron, W.T.Thomson, A.B.Dow, 'Vibration and current monitoring for detecting airgap eccentricity in large induction motors', Proc IEE, Vol 133, Pt B, 3 May 1986.

[2] S. Elder, ' Condition monitoring of three phase induction motors as a result of transient analysis', PhD Thesis, CNAA, RGIT, 1992.

[3] J.F.Watson, S.Elder, 'Transient analysis of the line current as a fault detection technique for three phase induction motors', ICEM Conf, Manchester, Sep 1992.

[4] W. Deleroi, ' Squirrel Cage Motor with Broken Bar in the Rotor - Physical Phenomena and their Experimental Assessment', ICEM, Budapest, 1982.

[5] C. Hargis, B. G. Gaydon, K. Kamash, ' The Detection of Rotor Defects in Induction Motors ', IEE Int. Conf. on Electrical Machines - Design and Applications, July 1982, pp 216 - 220.

[6] W.T.Thomson, N.D.Deans, R.A. Leonard, A. J.Milne, 'Monitoring Strategy for Discriminating Between Different Types of Rotor Defects in Induction Motors', 18th UPEC Proc., Univ. of Surrey, Guildford, UK, 1983, pp 241 - 246.

[7] D. Gabor, ' Theory of communication ', IEE, London, Vol. 93, 1943, p 429.

Description of Signal Processing Symbols

F(k)............STFT Spectral Point.
N............Sample Length.
w(nT)............Sampled Smoothing Window.
f(nT)............Sample of Signal Under Analysis.
rMT.........Length of Overlap Between Successive STFT's.
s(t,ω)............Spectrogram.
R............Length of Time Window.
w()............Time Window.
h()............Frequency Window.
xa()............Analytic Signal.
xa*()............Complex Conjugate of Analytic Signal.

The Application of Modern Signal Processing Techniques to Rotor Fault Detection and Location within Three Phase Induction Motors

R. Burnett, J. F. Watson, S. Elder
School of Electronic and Electrical Engineering
The Robert Gordon University
Aberdeen, AB9 1FR, Scotland, U.K.
Tel (0) (1224) 262400 Fax (0) (1224) 262444 E-Mail: R.Burnett@rgu.ac.uk

Abstract - Previous work at The Robert Gordon University has shown that faults within the rotors of large three phase Induction Motors, such as broken rotor bars, can be detected by monitoring and analysing the line current taken by the machine during a no-load starting transient [1] [2].
This line current has been shown to contain frequency components which are indicative of these fault conditions. Under transient conditions these components are however non-stationary in both the time and frequency domains.
A variety of signal processing strategies applicable to time variant data such as The Spectrogram, The Wigner Ville Distribution and Wavelet Decomposition have been implemented and their success in detecting these non-stationary components evaluated.
The most suitable of these techniques has been used to determine the occurrence and severity of motor faults. Preliminary work suggests that these techniques may also be used to detect frequency components indicative to the location of the fault.

I. INTRODUCTION.

The Squirrel Cage Induction Motor (SCIM) is the most commonly used prime mover in industry today. Whether fed from single or three phase supplies, its relatively simple, rugged construction and general robustness ensure its use in a wide variety of industries. Large SCIM's are commonly used as auxiliary drives in the electricity supply industries and as drives for gas compressors, sea water injection and oil exporting pumps in the oil and gas production industries.
Under normal operating conditions the induction motor is under considerable thermal, electrical and mechanical stress. These stresses become even more exaggerated when the machine is operated under abnormal or transient conditions. Such transients are a regular operational feature in some applications and the resultant stresses can lead to catastrophic failures if developing faults are not detected and corrected timeously.
Consequently, a number of techniques have been developed over the years which monitor specific induction motor parameters with a view to allowing the health of the motor to be determined and hence maintenance schedules planned. Unnecessary plant failures and consequential damage and/or loss of revenue thus being avoided. These monitoring techniques are all examples of what has become known as *CONDITION MONITORING.*
The work reported in this paper uses the stator line current [3] as the monitored machine parameter. Line current can be monitored 'non-invasively' in that there is no requirement to fit dedicated transducers or to interrupt the operation of the machine whilst carrying out the monitoring process.

A. Motor Fault Detection

The parameter fundamental to the operation of an induction motor, Fig. 1, is the magnetic flux within the air-gap between the stator and rotor of the machine.
In a healthy, well designed machine this is essentially a sinusoidal function of both time and angular position. Multiple harmonics of the fundamental frequency exist due to the nature of the machine design.

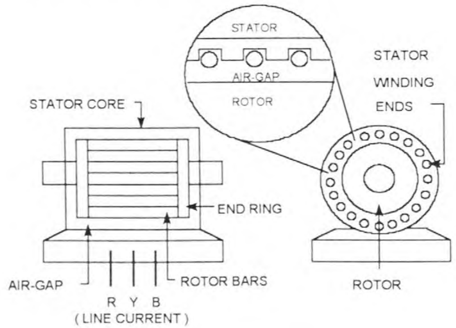

Fig. 1. Induction motor glossary.

Rotor faults within the motor produce local aberrations in the air-gap magnetic field and since this field is essentially produced by the stator current such anomalies are reflected in this parameter. It has been shown [3] that a rotor fault such as broken rotor bars (a relatively common problem) will produce specific components within the frequency spectrum of the stator line current. These components appear as sidebands located at ±2s Hz around the fundamental supply frequency, f_0. [Where 's' signifies a machine term known as 'slip' which is used to define the difference between the speed of the rotating magnetic field within the air-gap of the motor and the actual rotor speed].

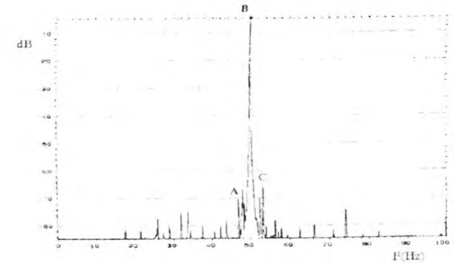

Fig. 2. Current spectrum - no broken bars.

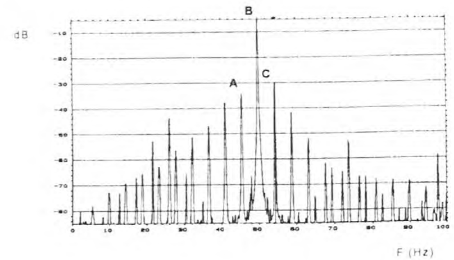

Fig. 3. Current spectrum - 10 broken bars.

Fig. 2 shows a spectrum zoom analysis of the supply line current from a 11 kW, 51 slot rotor SCIM with 0 broken rotor bars operating under steady state conditions. The frequency component 'B' represents the fundamental supply frequency. The zoom analysis shown in Fig. 3 was obtained from the same motor with 10 broken rotor bars (an exaggerated error introduced to amplify the effect). If the two spectra are compared an increase in amplitude of sidebands 'A' and 'C' within the spectrum of the faulty motor is observed.
This technique (which forms the basis of a commercially available motor monitoring system [4]) is applied to machines operating under steady state conditions and has a basic requirement that for reliable diagnosis a substantial current must flow; i.e. the motor must be operating at or near full load conditions. There are certain situations however when this requirement is impractical, i.e. if the motor has been removed from service and taken to a workshop for repair. Under such circumstances the motor can only be tested under no load conditions. This is the principle reason why work was initiated at RGU to detect faults within motors whilst operating under no load conditions by monitoring the supply line current during the starting period. On starting the motor is under severe electrical and mechanical stress and it was hoped that the rotor faults might be detected at a much earlier stage in their development.

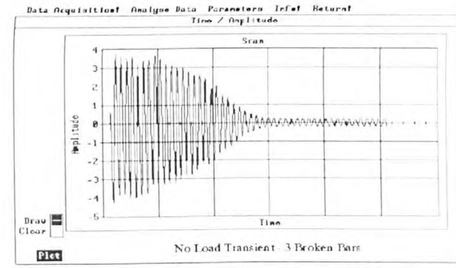

Fig. 4. Current transient signal.

As the rotor accelerates during the transient from rest to near steady state speed (several seconds in the case of larger machines) the stator line current can be as high as 5 - 8 times the full load current, even when started under no load conditions, Fig. 4.
The transient current will contain the **(f_0 ± 2s)** Hz components indicative of any rotor fault but since these frequencies are functions of slip and hence speed, they are non-stationary in the frequency domain.

B. Motor Fault Location

Previous research has shown that when a SCIM contains a broken rotor bar, the rotor of the motor can be considered as having a certain degree of asymmetry.
The additional field produced by the asymmetry (which is more prominent at high values of slip) induces voltages and hence currents within the stator windings. These voltages have been shown to have frequencies defined by (1).

$$F = f (k / p - s (k / p \pm 1)) \quad (1)$$

These components, if detected and tracked, contain data which may be used to indicate the location of the rotor fault. This is the direction of the present work and will form the basis of future publications.

II. SIGNAL ACQUISITION.

In order to obtain the transient current signals from the SCIM a data acquisition system was specifically developed. Although current need only be monitored on 1 phase for reliable diagnosis the acquisition system was designed to incorporate synchronous monitoring of all three phases. It was felt that this would prove necessary in future fault location work.
The acquisition system, Fig. 5, comprises three Hall Effect transducers with associated circuitry which supply a

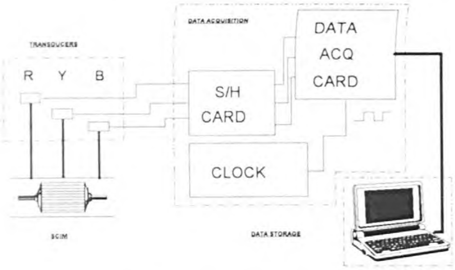

Fig. 5. Data acquisition system.

voltage signal that is proportional to the supply current.
A LAB WINDOWS PC+ Data Acquisition card allows four differential bipolar channels to be sampled via a 12 bit successive approximation ADC. Three of the differential channels are fed from the second card within the Data Acquisition section. This card was specifically designed to contain the required sample and hold circuitry along with the associated timing circuitry which enables the three phases to be sampled simultaneously at a rate of 4 kHz. The software which controls the acquisition of the signals is written in 'C' and has been developed as a sub-part of a motor health software tool.
A portable Toshiba 6400 DX PC is used to store the sampled data. This is a 486 based 33 MHz PC with 4 mega bytes of on-board RAM. A 200 mega byte hard disk allows numerous sampled transients to be acquired. A portable system was developed in order to enable the operator to acquire data from motors in industrial situations.

III. SIGNAL PROCESSING STRATEGIES.

In order to detect the non-stationary components several signal processing techniques capable of representing a waveform in the Time-Frequency plane were investigated.

A. The Spectrogram

The Spectrogram obtains the Time-Frequency representation of the signal under analysis by computing the Short Time Fourier Transform (STFT), via implementation of a Fourier Transform algorithm.
If the excitation of the time varying signal under analysis is relatively slow, then it may be assumed that the signal is stationary throughout the calculation of the STFT. The number of STFT calculations required being dependant upon the signal sample length and the size of the time window used to partition the signal.

Computation of the STFT is achieved via the Fast Fourier Transform algorithm (FFT), which is a software tool used to calculate the Discrete Fourier Transform (DFT), (2).

$$F(k) = \sum_{n=0}^{N-1} f(nT)\exp^{-j(2\pi/N)nk} \quad (2)$$

The data obtained by (2), for values of k = 0 to N - 1, corresponds to the set of outputs from a bank of filters, each having a Gaussian characteristic whose centre frequency is defined by (3).

$$\omega = (2\pi k) / (NT) \quad (3)$$

On computation of (2), a single spectral section will be calculated. In order to obtain a complete analysis it is necessary to repeat this computation over successive instants of time (4), where each computation is separated by MT seconds.

$$F(k) = \sum_{n=0}^{N-1} w(nT) f(nT+rmT) e^{-j(2\pi/N)nk} \quad (4)$$

It should be noted that when (2) is calculated using a finite amount of data, a rectangular time window of width, NT, is automatically imposed onto the signal. Hence, by using other types of window in (4), it may be possible to obtain an improved spectral representation.
Once the STFT has been calculated by (4), a **Spectrogram** can be obtained as is shown in (5).

$$S(t,\omega) = |f(k)|^2 \quad (5)$$

With this technique any increase in the size of the time window employed will result in an increase in the time resolution and a decrease in the frequency resolution of the computed representation. The opposite occurring when the time window is reduced in size.

B. The Wigner Distribution

The discrete Auto-Wigner Distribution (DAWD) [5] is defined in (6), where the time index, n, is discrete and the frequency index, θ, is continuous.

$$AWD(n,\vartheta) = 2 \sum_{k=-\infty}^{\infty} f(n+k) f^*(n-k) e^{-j2k\vartheta} \quad (6)$$

In order to improve the spectral representation of the AWD, it is usually necessary to introduce a window in the frequency direction, a rectangular window being automatically imposed in the time direction due to the finite length of sampled data. This form of AWD is known as the Pseudo Wigner Distribution (PWD).

$$PWD(n,\vartheta) = 2 \sum_{k=-\infty}^{\infty} w(k) f(n+k) w^*(-k) f^*(n-k) e^{-j2k\vartheta} \quad (7)$$

Due to the interaction between the positive and negative frequencies of a signal, low frequency artefacts will be present within the Wigner Distribution. These components, *containing no useful information can be reduced by using the analytic representation of the signal. The AWD which* analyses the analytic signal in place of the real signal is known as the Wigner Ville Distribution (WVD), (8).

$$WVD(t,\omega) = \int_{-\infty}^{\infty} z(t+\tau/2) z^*(t-\tau/2) e^{-j\omega\tau} d\tau \quad (8)$$

The analytic signal, z(t), can be computed both in the time and frequency domains. In the time domain the analytic version is obtained via the Hilbert transformation, whereas in the frequency domain the signal may be obtained via the Fourier transform, with the time domain signal being recovered from z(f) via the Inverse Fourier Transform (IFT). Using this it can be shown that the discrete WVD can be obtained via (9).

$$WVD(t,f) = \underset{m \to 2k}{2\,DFT} [z(n+m) z^*(n-m)] \quad (9)$$

The Wigner Distribution and its many variants contain several desirable properties when representing a signal in the Time-Frequency plane: the distribution of any real or complex function will be real; a shift in the time signal will result in an equal time shift in the distribution and, the total energy in the signal is equal to the integral of the distribution over the whole plane. However, along with these favourable properties the Wigner Distribution possess a single property which limits the practical applications to which the distribution can be used. This being the presence of **Crossterms**.
These crossterm components are caused by the bilinear nature of the distribution causing interference terms to appear between the individual components of a multi-component signal.
In order to reduce the amplitude of the interference components (which can be up to twice that of the original frequency terms) windowing in both the frequency and time directions is employed.
The result of windowing in both directions on the WVD is to produce a Wigner Distribution known as the Smoothed Wigner Ville Distribution (SWVD).
It can be shown that the SWVD can be calculated via one DFT operation for each 'n' value as is shown in (10).

$$SWVD(n,m) = 2 \sum_{k=-L}^{L} r_n(k) e^{-jkm2\pi/K} \quad (10)$$

$$r_n(k) = [\sum_{i=-R}^{R} w(i) x_a(n+i+k) x_a^*(n+i-k) |h(k)|^2 \quad (11)$$

Taking this computation property into consideration, the SWVD can be computed up to twice as fast as the Spectrogram technique.

C. Wavelet Decomposition

One of the first Time-Frequency representations of a signal was introduced by Gabor [6]. This representation of a signal *in the Time-Frequency domain is known as the Gabo* Decomposition of the signal, (12).

$$R(\tau,\omega) = 1/2\pi(2\pi\sigma^2)^{-1/4} \int_{-\infty}^{\infty} \exp(-(t-\tau)^2/4\sigma^2 \exp(-j\omega(t-\tau)) r(t) dt \quad (12)$$

On analysis of the above equation, it is found that the Time Frequency representation, R(τ,ω), is obtained by th convolution of the signal r(t) with a signal h(t). This signal h(t), is a wavelet and is of Gaussian form.
The two variables in (12), τ and ω, are used as translation into the time and frequency domains respectively.
For a fixed time, τ, the calculated function represents th instantaneous energy partition along the frequency spectrum
For a fixed ω, it is representative of the energy partition at particular frequency along the time axis.
The decomposition of the signal under analysis is therefor obtained by convolving the signal with a wavelet similar t that described above. The wavelet having its centr frequency on the current frequency under investigation.

IV. EVALUATION OF SIGNAL PROCESSING TECHNIQUES.

In order to confirm the theoretical predictions and evaluat the performances of the individual techniques whe analysing multi-component signals, the above technique were subjected to a series of tests using both simulated an actual current signals obtained by the developed acquisitio system. The signals were obtained from a laboratory base test rig which comprised of a 3 phase, 11 kW, 51 slo SCIM. The rotor was removable in order to introduc various degrees of fault. A summary of the results fro these tests now follows.

A. The Wigner Distribution

The Wigner Distribution and several of its variants wer investigated using both simulated and actual signals. Th technique and its smoothed variants were found to give goo frequency and time resolution in the respective directions o the Time-Frequency plane.
When analysing actual multi-component signals th technique, including the smoothed versions, was found t suffer considerably from crossterms. Several methods o crossterm reduction (over and above that of using th SWVD) were investigated, including the Exponenti Distribution [7]. These reduction techniques however di not entirely eliminate the presence of crossterms within th Time-Frequency representation, resulting in this techniqu being the poorest of the three Time-Frequenc representations.

B. The Spectrogram

The Spectrogram was found to give reasonable results when analysing both mono and multi-component signals. The technique was found to give average resolution control in both the time and frequency directions by either increasing / decreasing the time between the individual analyses and the size of window length respectively.
The effect of different window types on the technique was investigated. Out of the windows which were used the HANNING window was found to give the best results when analysing the simulated and actual signals.
The Spectrogram was however found to suffer from the predicted resolution problem, which could be a significant problem in this particular application.

C. Wavelet Decomposition

Analysing simulated and actual signals with the Wavelet Decomposition results in good frequency and time resolutions being obtained. There are no problems with crossterm interference when multi-component signals are analysed and hence frequency component identification within a signal can easily be executed. This technique was found to give the best representation of the transients under investigation and was thus deemed to be the most appropriate for obtaining the fault detection and location information from the motors transient supply current signal.

V. FAULT DETECTION.

Analysing a no load transient signal obtained from the test rig with 3 broken rotor bars using the Wavelet Decomposition method over the frequency range of 0 Hz to 42 Hz, in steps of 1 Hz, results in the Time-Frequency representation shown in Fig. 6.
From this diagram the ±2s frequency components can be observed travelling from 50 Hz at start-up towards 0 Hz, returning to 50 Hz at steady state. (The components travel from -50 Hz to 50 Hz but in these analyses it is the absolute value of frequency which is displayed). When Fig. 6 is compared to the Time-Frequency representation in Fig. 7, obtained from the test rig with 0 broken rotor bars, again from a no load starting condition, an amplitude change in the non-stationary components can observed. It is this change in amplitude which has been found to be proportional to the degree of severity of rotor fault. A further example of this can be seen in Fig. 8 whereby a transient from the test rig has been obtained, again under no load conditions, whilst the motor has the exaggerated fault of 10 broken rotor bars. (Due to auto-scaling the amplitudes in Fig. 8 look as if they are smaller than those in Fig. 7. In reality Fig. 7 required several magnitudes of

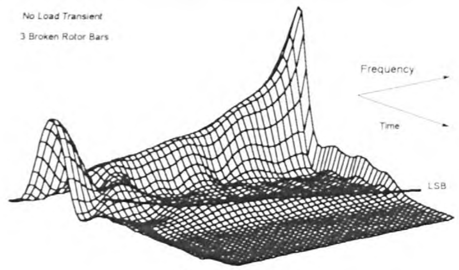

Fig. 6. Wavelet decomposition.

amplification whereas Figure 7 did not). Observations of Fig. 6 and 8 show that as the non-stationary components travel back towards the 50 Hz component in the latter stages of the transient the amplitude of the sidebands pass through a peak value. The frequency at which this peak occurs forms the basis of a simplified fault detection technique as described below. Work has been carried out in order to determine the reasoning behind the occurrence of this peak in the sideband amplitude, but this is beyond the scope of this paper.

VI. TRANSIENT MONITORING PACKAGE.

This fault detection theory has been transferred successfully onto a machine health package, whereby the transient signal from a SCIM is filtered at the optimum frequency. This analysis technique has been incorporated along with the acquisition software, thus allowing the acquisition and analysis of data to be completed by a single software package.
For the case of the test rig the optimum frequency was found to occur at 21 Hz. The result of a single frequency analysis on a transient obtained from the test rig on a no load start with 10 broken bars present is shown in Fig. 9.

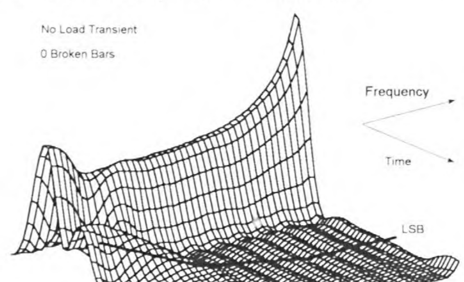

Fig. 7. Wavelet decomposition.

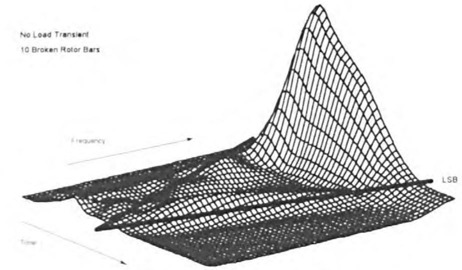

Fig. 8. Wavelet decomposition.

The sideband 'B' represents the large fault condition via its amplitude. Comparing this to the analysis of a transient, Fig. 10, obtained from the same test rig on a no load start with 3 broken rotor bars, then the amplitude of both the sidebands 'A' and 'B' are clearly reduced in size.
This single frequency approach is also being used to detect the fault location components within the transient signal. The components have been successfully detected at steady state and work is being carried out in order to detect the components within the transient. These location components are significantly smaller in amplitude than the fault detection components and are consequently more difficult to detect.
The detection of these components and the methodology which has been adopted to obtain the location information form the basis of a future paper.

VII. CONCLUSIONS.

It has been shown that by using a signal processing technique which obtains the Time-Frequency representation of multi-component non-stationary signals, it is possible to detect the presence of the non-stationary components within the transient line current of a 3 phase induction motor supply which are indicative of rotor faults , such as broken

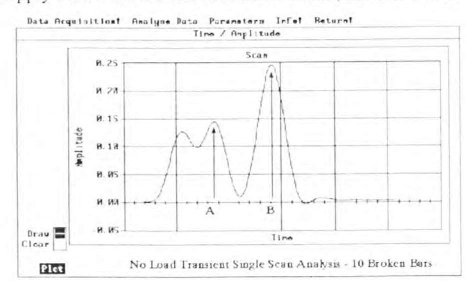

Fig. 9. Simplified analysis approach.

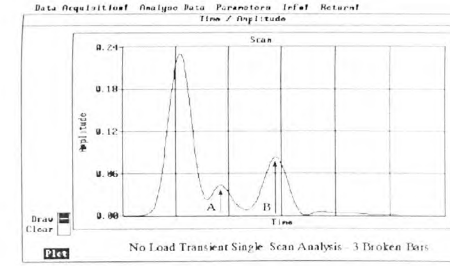

Fig. 10. Simplified analysis approach.

rotor bars. The amplitude of these non-stationar components is proportional to the severity of the fault. Thi processing technique has been simplified and installed on a portable PC along with a specifically developed acquisitio system. This forms the basis of a portable motor monitorin system which enables the operator to determine the health o the motor by monitoring the supply current transient unde no load conditions.

ACKNOWLEDGMENT

The authors would like to acknowledge the sponsorship o this work by Scottish Nuclear Ltd.

REFERENCES

[1] J.F. Watson and S. Elder, "Transient analysis of the lin current as a fault detection technique for 3-phase inductio motors", *International Conference on Electrical Machine* UMIST, September 1992.
[2] S. Elder, J.F. Watson and W.T. Thomson, "The analysis o transient currents in induction motors for the purposes o detecting rotor faults", *Conf. Proc. UPEC*, p691-694, R.G.I.T Aberdeen, 1990.
[3] W.T. Thomson, N.D. Deans, R.A. Leonard and A.J Milne, "Monitoring strategy for discriminating betwee different types of rotor defects in induction motors", *18t UPEC Proc. Univ. of Surrey, Guildford, U.K.*, pp241-24 1983.
[4] "Motor Monitor", Entek Corporation, Cincinnati, Ohio.
[5] T.A.C.M. Claasen and W.F.G. Mecklenbraüker, "The wign distribution - a tool for time frequency signal analysis - Parts I II, III ", *Phillips Journal of Research*, Vol. 35, 1980.
[6] D. Gabor, "Theory of Communication", *IEE*, London, Vo 93, 1943, p429.
[7] H. Choi and W.J. Williams, "Improved time frequen representation of multi-component signals using exponenti kernels", *IEEE Trans. on Acoustics, Speech and Sign Processing*, Vol. 37, No. 6, June 1989.

THE CURRENT ANALYSIS PROGRAM - A SOFTWARE TOOL FOR ROTOR FAULT DETECTION IN THREE PHASE INDUCTION MOTORS

R. Burnett J.F. Watson

The Robert Gordon University, Aberdeen.
United Kingdom.

1.0 INTRODUCTION

Several parameters within a three phase induction motor have been monitored by researchers as a means of obtaining useful health information. The parameters, which are monitored non-invasively, have included: the axial leakage and airgap flux, [Thomson et al (1)], and core / bearing vibration, [Cameron et al (2)].

Another parameter which has been proven to yield sufficient health information is the supply current to the motor. Hargis et al (3) has shown that when an induction motor contains a broken rotor bar during steady state operation, the amplitude of the frequency components which exist at ±2s around the fundamental supply frequency are found to increase. This amplitude change has been found to be dependant upon the severity of the rotor fault. The detection of this increase in sideband amplitude forms the basic theory behind commercial current monitoring motor health packages such as "Motor Monitor" (4).

Although current monitoring techniques are widely used in industry due to their success in the detection of broken rotor bars and their ability to report findings in a non-technical format, these systems do inherently have drawbacks.

In order to facilitate successful detection of rotor faults during steady state operation a large supply current is required to flow. This large current usually being obtained by monitoring the motor whilst running under full load conditions.

The necessity of requiring a large current in some cases may not be appropriate nor achievable if, for example, the motor has been taken off line or removed to a workshop environment.

In addition to requiring a large current these monitoring techniques also have difficulty in detecting other common rotor faults over and above simple broken bars. These faults include: damaged end rings or broken bars within a double bar rotor machine.

In reply to this, work was initiated several years ago at The Robert Gordon University to investigate the possibility of utilising the large supply current which flows during the initial acceleration period of the motor at start-up. It was hoped that this transient current would yield the relevant health information and perhaps be capable of detecting other rotor faults without the necessity of the motor being operated under full load conditions.

This paper describes the transient monitoring system which has been developed to-date. Results are presented which show the successful operation of the system on a laboratory based test rig.

2.0 THEORETICAL BACKGROUND

2.1 Machine supply current transient

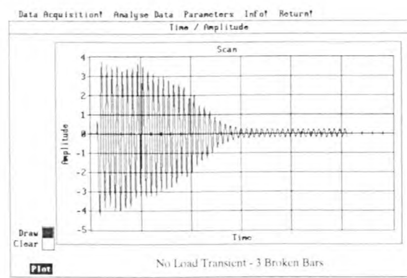

Figure 1: Induction motor supply current transient

During the motors acceleration period, (between standstill and operational speed), it is observed that the supply current to the motor, Figure 1, is far larger than the steady state values. This current which can be up to 5 - 8 times the full load steady state current, can flow for periods of time greater than 10s for large machines. It is this area of the current signal which was investigated for the health information found during the steady state period.

2.2 Rotor bar fault frequency components

During a steady state analysis, as executed in standard current monitoring packages, the fault components which are found to yield health information are situated at ±2s around the fundamental frequency. Due to the *constant value of slip, s, these frequencies are stationary in value.* However, during the transient period the machine is accelerating and hence, the slip is no longer constant. Due to this the fault frequency components are non-stationary in nature, Figure 2.

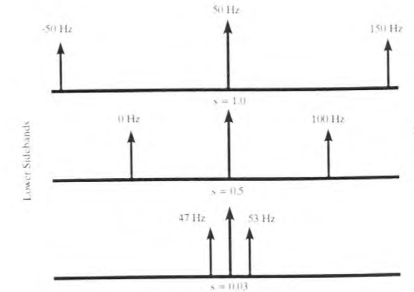

Figure 2: Non-stationary sidebands

The frequency components which are of interest when detecting broken rotor bars are the lower sidebands. From Figure 2 it is observed that during the transient period the components travel from -50 Hz to 0 Hz (at half speed) and approach 50 Hz once steady state speed has been achieved. (Negative sign indicating that there is a phase shift on the components. It should be noted that in this paper the absolute values of frequency are displayed).

2.3 Signal processing

In order to detect the non-stationary components a signal processing technique which can monitor a multi-component non-stationary signal was required. Several signal processing techniques capable of monitoring such signals were investigated. Of the numerous techniques tested using both actual and simulated signals, the technique known as Wavelet Decomposition was found to give the most suitable results for this particular application.

In this technique a Gaussian wavelet is convolved with the signal under investigation. The result of which produces a Time-Frequency representation of the signal. Initially all frequencies between 0Hz and 50Hz were monitored in steps of 1Hz. However, it was found that monitoring a single optimum frequency could yield sufficient information for the purpose of fault diagnosis.

2.4 Laboratory test rig

The laboratory test rig used throughout the investigations was a three phase, 11 kW, 4 pole, 51 slot rotor squirrel cage machine. A selection of cage rotors were at hand in order to simulate different levels of fault condition.

Although all results shown in this paper were obtained from the above test rig, the technique has been used on motors as large as 5 MW in an industrial environment. The results of these tests showing an excellent correlation with the laboratory data.

3.0 TRANSIENT CURRENT MONITORING SYSTEM

3.1 Overview of Monitoring System

The transient current monitoring system which has been developed to-date consists of three main sub-sections. These include: transducers, data acquisition and data analysis, Figure 3. All three sections are accessed by a controlling software package run from a portable TOSHIBA T6400 DX. A portable system has been developed in order to allow on site health analyses to be obtained.

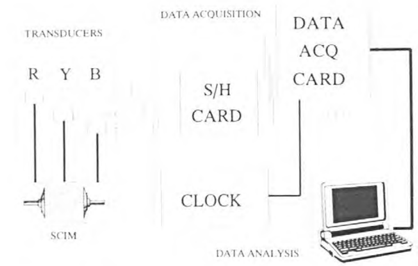

Figure 3: Acquisition system

3.2 Data Acquisition

Figure 3 shows the hardware required to obtain the supply current for analysis purposes. The system is capable of acquiring both single and three phase data as it is envisaged that the latter will be required for future fault location work.

The acquisition setup consists of three sub areas. Initially, three Hall Effect transducers or Rogowski coils produce voltages proportional to the supply current. Conventional current transformers were not used here due the likelihood of the CT's saturating with the large currents flowing during the transient period.

These signals are then sampled and held for the final section, data acquisition. The data acquisition section comprises of a LABWINDOWS LAB PC+ card which allows three differential channels to be sampled via a

12 bit successive approximation ADC. This section also contains all the relevant timing and control circuitry required to enable synchronous data sampling when acquiring three phase data.

The controlling software allows the operator of the system to store the data in user defined data files for future processing.

3.3 Data Analysis

Having acquired the data some simple processing must be carried out prior to the main analysis. Initially, the software removes one phase of data from the data file which may contain single or three phase data. With the single phase of data the D.C. offset is removed and the data is decimated by a factor of two. The data is now in the correct format for the main analysis to be completed. This entails the convolution of the data using the Wavelet Decomposition method with a Gaussian window of pre-determined bandwidth and centre frequency.

The optimum centre frequency which has been found to give the best results during the tests carried out on the test rig is 21 Hz.

After convolution the data is rectified and low pass filtered. The processed data is then displayed on the screen prior to being saved again in a user defined file thus enabling record keeping (in particular finger printing of the motor condition) to be achieved.

3.4 Parameters

A feature of the current monitoring system allows the operator to modify the values of the defaults which the controlling software uses.

A summary of the parameters which can be modified and their use within the complete monitoring system now follows.

3.4.1 Offset. This has been incorporated to allow the removal of any noise data from the start of the transient prior to processing. This is necessary as the early versions of the system do not have any triggering facility allowing the acquisition to start on the detection of the transient signal.

3.4.2 Bandwidth. Here the bandwidth of the Gaussian wavelet which is used may be altered. The default bandwidth is 1Hz but this may be altered in order to change the resolution of the analysis.

3.4.3 Sample Frequency. The sampling frequency for both single and three phase data acquisition is defaulted to 2 kHz and 4 kHz respectively. This facility allows *the sample frequency used within the analysis section of the monitoring system to be altered.*

3.4.4 Filter Cut Off. The final part of the analysis comprises a low pass filter. The cut off frequency at which the low pass filter's 3dB point is situated is defaulted to 6 Hz but may be altered to be between 2Hz and 12Hz.

3.4.5 Filter Order. The order of the above low pass filter may also be altered.

3.4.6 No. of Points Displayed. The amount of data points which are displayed on the display screen may be altered. The maximum amount of data points to be displayed by the current version of the monitoring system is 1024.

4.0 RESULTS OF CURRENT MONITORING SYSTEM

4.1 Detection of non-stationary components

Figure 4 shows the Time-Frequency representation of a no load supply current transient obtained from a motor with 10 broken rotor bars using the Wavelet Decomposition method. The bars are present in a group and represent an exaggerated fault condition in order to amplify the effect. (Single broken bars are also easily detected using this technique). Analysing the representation from 0 Hz to 50 Hz, Figure 4, it is possible to observe the non-stationary fault components travelling through frequency as the motor accelerates towards steady state speed.

As previously mentioned the current monitoring system only requires one 'slice' of this Time-Frequency representation to be able to detect the presence of broken bars.

For the laboratory test rig used throughout these investigations the optimum frequency used to obtain the 'slice' was 21 Hz. The result of which can be seen in Figure 5. Here a single 'slice' of frequency 21 Hz has been produced from the same transient signal which produced the Time-Frequency representation in Figure 4.

From this diagram (the main analysis results screen of the monitoring system) we can see that there are three peaks. The initial peak is produced due to the sudden input of energy produced in the transient with the two remaining peaks, 'A' and 'B' being of importance in determining the health of the motor. Peak 'A' represents the non-stationary sideband as it travels from 50 Hz to 0 Hz. Peak 'B' represents the sideband as it returns back to 50 Hz from 0 Hz. If Figure 5 is compared to Figure 6, a similar analysis obtained from a motor with only three broken bars on the rotor, then an amplitude difference can be observed in the sidebands. It is this amplitude change that has been found, as in the steady state condition, to be proportional to the degree of severity of the rotor fault. It has been found that in the case of the transient analysis it is peak 'B' which is the more sensitive to rotor fault conditions.

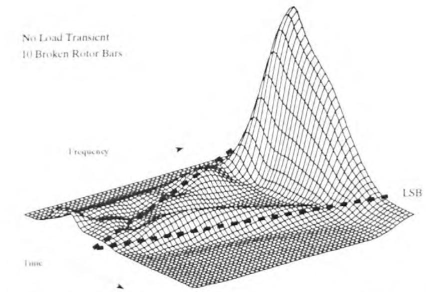

Figure 4: Detection of non-stationary Lower Sidebands (LSB)

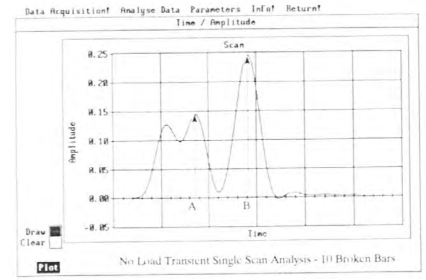

Figure 5: Transient current analysis

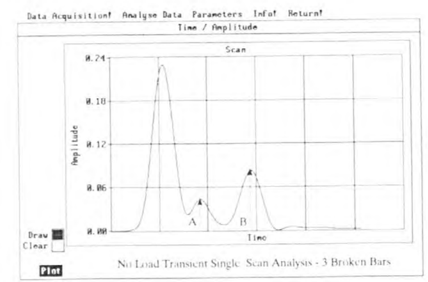

Figure 6: Transient current analysis

5.0 REVIEW OF FAULT LOCATION WORK

5.1 Overview of fault location problem

The above monitoring system allows the detection of broken bars by monitoring the supply current to the motor when the machine under investigation is started under no load. As a further aid to fault detection the possibility of obtaining information on the location of the fault from the transient signal has been investigated. If this were possible then not only would the operator be able to detect the presence of a broken rotor bar but they would also be given its location on the rotor. Thus saving on valuable and costly down times carrying out physical searches for faulty areas of rotor.

In order to obtain this information the problem was first split into two sections. The first being the detection of the frequency components which would yield this information and secondly, to obtain a methodology in order to obtain the location from these components.

5.2 Fault location

Deleroi (5) has shown that when a rotor contains a single broken bar an air gap field is set up around the area of the faulty bar. This air gap field anomaly has been shown to rotate with the rotor thus inducing small voltages within the stator windings of the motor. This field is complex in nature and undergoes an amount of damping depending on the value of rotor slip. At high levels of slip the anomaly is damped severely, reducing as the slip tends towards zero at steady state operation. This results in the anomaly being localised around the area of the broken bar at high values of slip.

The voltages which are induced into the stator windings due to this anomaly have frequencies which are defined by (1).

$$f_{bb} = f_o(k/p - s(k/p \pm 1)) \qquad (1)$$

5.3 Detection of location frequency components

The frequency components which give the location information are defined by (1). Initially a spectral search was made on the steady state supply current to the test rig in order to see if it were possible to observe the components at a known frequency. This was completed successfully in that at a slip of 0.03 frequency components were detected at the frequencies predicted by (1).

As a current transient contains many harmonic frequencies it was necessary to obtain some idea of where about the fault location frequencies would be in conjunction with the other frequencies present within the transient. A prediction of the harmonic frequencies *within a transient was developed using proven* equations. From this prediction it was found that the optimum search area for the detection of the fault location components would be when the slip of the motor was less than 0.4 and at frequencies greater than 100 Hz. It is at this point within the transient that the fault location components are out with the effects of the larger harmonics such as the Upper and Lower sidebands.

Using the Wavelet Decomposition method work is being carried out in order to observe any correlation between the occurrence of these fault location components and the position of the rotor on start up.

5.4 Methodology behind broken bar location detection.

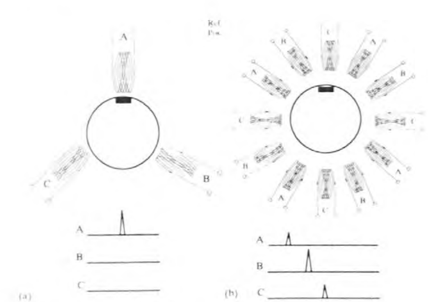

Figure 7: Location methodology

The location of broken bars within a rotor of an induction motor is dependant on the successful detection of the frequency components defined by (1). The technique used to detect the location involves using the motor's stator windings as reference locations within the motor from where the distance travelled by the broken bar can be computed.

Considering the two pole setup shown in Figure 7(a), during the acceleration period of the motor, the location frequency component is assumed to occur when the bar is opposite 'A'. This is detected by filtering all three phases of the supply current for one frequency, Figure 7(a). This component occurs at a particular time which is easily converted into a distance travelled by a point on the rotor. This is done by extracting slip v's time data and hence, acceleration data, from a plot similar to Figure 4.

In order to locate the stator winding which can be used as the reference location, all three phases of supply current would be monitored for the location frequency, Figure 7(b). The phase which gives the largest filtered output is an indication to the reference phase, however, as is shown in Figure 7(b) - an example of a typical 4 *pole machine - using the above technique would result in four possible locations being obtained. Further work* is being carried out to develop this fault location technique.

6.0 CONCLUSION

This paper shows that it is possible to monitor the supply current to an induction motor during the motors acceleration period and be able to detect the non-stationary frequency components previously monitored whilst stationary during the motors steady state operation. Results show that the increase in component amplitude observed with a faulty rotor when monitoring in steady state under full load conditions can clearly be observed when monitoring the transient signal under no load conditions. Using a signal processing technique known as Wavelet Decomposition it is shown that the sidebands may be tracked during the transient period. This technique has been simplified and implemented along with a data acquisition system to form a complete current transient health monitoring system which determines the health of the motor from its no load supply current transient signal. The software which controls both the acquisition and analysis part of the monitoring system has been developed so that the operator has access to all main parameters used within the analysis.

7.0 ACKNOWLEDGEMENT

The authors would like to acknowledge the sponsorship of this work by Scottish Nuclear Ltd.

8.0 REFERENCES

1. Thomson W.T., Deans, N.D., Leonard R.A. and Milne A.J., 1983, "Monitoring Strategy for Discriminating Between Different Types of Rotor Defects in Induction Motors", Proc. UPEC, Guildford, 241-246

2. Cameron J.R., Thomson W.T. and Dow A.B., 1986, "Vibration and Current Monitoring for Detecting Airgap Eccentricity in Large Induction Motors", Proc. IEE, 133, Pt B

3. Hargis C., Gaydon B.G. and Kamash K., 1982, "The Detection of Rotor Defects in Induction Motors", IEE Int. Conf. on Electrical Machines - Design and Applications, 216-220

4. Entek Corporation, "Motor Monitor", Cincinnati, Ohio

5. Deleroi W., 1982, "Squirrel Cage Motor with Broken Bar in the Rotor - Physical Phenomena and their Experimental Assessment", ICEM, Budapest

SIGNAL PROCESSING

An International Journal
A publication of the European Association for Signal Processing (EURASIP)

Editorial Policy. SIGNAL PROCESSING is an Interdisciplinary Journal presenting the theory and practice of signal processing. Its primary objectives are the following:
Dissemination of research results and of engineering developments to all signal processing groups and individuals.
Presentation of practical solutions to current signal processing problems in engineering and science.
The editorial policy and the technical content of the Journal are the responsibility of the Editor-in-Chief and the Editorial Board. The Journal is self-supporting from subscription income and contains a minimum amount of advertisements. Advertisements are subject to the prior approval of the Editor-in-Chief. The journal welcomes contributions from every country in the world.

Scope. SIGNAL PROCESSING incorporates all aspects of the theory and practice of signal processing (analogue and digital). It features original research work, tutorial and review articles, and accounts of practical developments. It is intended for a rapid dissemination of knowledge and experience to engineers and scientists working in signal processing research, development or practical application.

Subjects. Subject areas covered by the Journal include: Signal Theory, Stochastic Processes, Detection and Estimation, Spectral Analysis, Filtering, Signal Processing Systems, Software Developments, Image Processing, Pattern Recognition, Optical Signal Processing, Digital Signal Processing, Multi-dimensional Signal Processing, Communication Signal Processing, Biomedical Signal Processing, Geophysical and Astrophysical Signal Processing, Earth Resources Signal Processing, Acoustic and Vibration Signal Processing, Data Processing, Remote Sensing, Signal Processing Technology, Speech Processing, Radar Signal Processing, Sonar Signal Processing, Special Signal Processing, Industrial Applications, New Applications.

Membership and Subscription Information:
Signal Processing (ISSN 0165-1684) is published in eight volumes (24 issues) a year. For 1996 Volumes 48 55 are scheduled for publication. Subscription prices are available upon request from the publishers. Subscriptions are accepted on a prepaid basis only and are entered on a calendar year basis. Issues are sent by surface mail except to the following countries where air delivery (S.A.L. Surface Air Lifted) is ensured: Argentina, Australia, Brazil, Canada, Hong Kong, India, Israel, Japan, Malaysia, Mexico, New Zealand, Pakistan, People's Rep. of China, Singapore, South Africa, South Korea, Taiwan, Thailand, USA. For the rest of the world, airmail charges are available upon request. Claims for missing issues will be honoured free of charge if made within six months after the publication date of the issues. Mail orders and inquiries to: Elsevier Science B.V., Journals Department, P.O. Box 211, 1000 AE Amsterdam, The Netherlands. For full membership information of the Association, possibly combined with a subscription at a reduced rate, please contact: EURASIP, P.O. Box 134, CH-10000 Lausanne 13, Switzerland.

US mailing notice Signal Processing (ISSN 0165-1684) is published semimonthly by Elsevier Science B.V., Molenwerf 1, Postbus 211, 1000 AE Amsterdam, The Netherlands. Annual subscription price in USA US $1793 (subject to change), including air speed delivery. Second class postage rate is paid at Jamaica, NY 11431.
USA POSTMASTERS, Send address changes to Signal Processing, Publications Expediting, Inc., 200 Meacham Avenue, Elmont, NY 11003. Airfreight and mailing in the USA by Publication Expediting.

ⓘ The paper used in this publication meets the requirements of ANSI/NISO 239.48-1992 (Permanence of Paper).

Published 24 times a year 0165-1684/96/$15.00 Printed in The Netherlands

ELSEVIER

Signal Processing 49 (1996) 57–70

SIGNAL PROCESSING

The application of modern signal processing techniques for use in rotor fault detection and location within three-phase induction motors

R. Burnett, J.F. Watson*, S. Elder

The Robert Gordon University, Schoolhill, Aberdeen, AB9 1FR, Scotland, UK

Received 28 November 1994; revised 13 November 1995

Abstract

A commonly used technique for the detection of faults which may occur in three-phase induction motors is to carry out a spectral analysis of the supply current to the motor under investigation. The presence of certain frequency components within the spectral analysis has been shown to be indicative of a fault condition (Hargis et al., 1982). Such techniques are becoming well established and are used regularly to monitor the health of large induction motors which are operated in critical applications within, for example, the nuclear and oil industries. This technique is generally applied to machines when they are operated under steady-state conditions. Recent work however has suggested that greater information may be obtained from a faulty motor if the same parameters which are monitored in the steady state are measured and analysed during transient conditions, such as the initial starting and acceleration periods of the motor. The frequency components which are indicative of motor faults are functions of speed, and hence, under these transient conditions are non-stationary in nature. This paper presents a review of modern signal processing techniques applicable to the analysis of signals whose frequency content is non-stationary. The individual techniques are compared using both test and actual data. Results are presented which identify the technique most appropriate for the task of fault detection in an induction motor under transient conditions. This technique is further investigated with regard to the possibility of locating as well as detecting machine faults.

Zusammenfassung

Eine gängige Technik zur Detektion von Fehlern, die in Dreiphasen-Induktionsmotoren auftreten können, besteht in einer Spektralanalyse des Versorgungsstroms des untersuchten Motors. Das Vorhandensein bestimmter Frequenzkomponenten im Spektrum hat sich als Fehleranzeige-Kriterium erwiesen (Hargis et al., 1982). Derartige Techniken haben sich durchgesetzt und werden regelmäßig zur Überwachung der Funktionstüchtigkeit großer Induktionsmotoren in kritischen Anwendungen benutzt wie z.B. in der Kern- und Ölindustrie. Sie werden allgemein auf Maschinen während ihres Dauerbetriebes angewandt. Neuere Arbeiten legen jedoch den Schluß nahe, daß man über einen fehlerhaften Motor mehr erfahren kann, wenn man dieselben Parameter, die man sonst im eingeschwungenen Zustand beobachtet, unter Einschwingbedingungen mißt und analysiert: in Frage kommen die Anfahr- und Beschleunigungsperioden des Motors. Die Frequenzanteile, welche auf Motorfehler hinweisen, hängen von der Geschwindigkeit ab und sind daher unter diesen Einschwingverhältnissen von instationärer Natur. Dieser Beitrag stellt eine Übersicht moderner

* Corresponding author. Tel.: (0) 1224 262472; fax: (0) 1224 262444; e-mail: r.burnett@rgu.ac.uk.

SSDI 0165-1684(95)00146-8

Signalverarbeitungstechniken vor, die zur Analyse von Signalen mit nichtstationärem Spektralgehalt brauchbar sind. Die einzelnen Methoden werden auf der Basis sowohl von Testsignalen als auch von realen Daten verglichen. Vorgelegt werden Ergebnisse, welche die zur Fehlerdetektion an Induktionsmotoren im Übergangsverhalten am besten geeignete Technik herausstellen. Dieses Verfahren wird im Hinblick auf die Möglichkeit einer Detektion wie einer Lokalisierung von Maschinenfehlern weiter untersucht.

Résumé

Une technique souvent utilisée pour la détection de défauts qui peuvent se produire dans les moteurs à induction triphasés est d'effectuer une analyse spectrale du courant d'alimentation du moteur etudié. La présence de certaines composantes fréquentielles dans l'analyse spectrale s'est révélée être un indicateur de défauts. De telles techniques commencent a être bien établies et sont utilisées régulièrement pour surveiller la santé de grands moteurs à induction qui sont utilisés dans des applications critiques dans le cadre, par exemple, des industries nucléaire et pétrolière. Cette technique est en général appliquée aux machines lorsqu'elles fonctionnent en conditions de régime stationnaire. Toutefois, des travaux recents ont suggéré qu'une information plus importante peut être obtenue d'un moteur défectueux si les mêmes paramètres qui sont surveillés en régime stationnaire sont mesurés et analysés en conditions transitoires, comme la mise en marche initiale et les périodes d'accélération du moteur. Les composantes de fréquence qui sont indicatives de défauts du moteur sont alors fonction de la vitesse, et de ce fait, sont non-stationnaires par nature en régime transitoire. Cet article passe en revue les techniques de traitement moderne du signal qui sont applicables à l'analyse de signaux dont le contenu en fréquence est non-stationnaire. Les techniques sont comparées en utilisant des données de test aussi bien que des données réelles. Des résultats sont présentés, qui identifient la technique la plus appropriée à la détection de défauts dans un moteur à induction en régime transitoire. Cette technique est etudiée plus à fond quant à la possibilité de localiser aussi bien que de détecter les défauts.

Keywords: Time-frequency distributions; Signal analysis; Non-stationary; Transient analysis; Machine condition monitoring; Fault detection

1. Introduction

The three-phase *squirrel cage induction motor* (SCIM) is the workhorse of modern industrial prime movers due to its high level of reliability and simple, rugged construction. Common applications for these motors are as gas circulators in the electricity generating industry and as drives for gas compressors, sea water injection pumps, and oil exporting pumps within the oil and gas exploration industries.

Under certain operating conditions however, the induction motor can be under immense physical, thermal and electromechanical stresses which may last for considerable periods of time. This can result in the motor being susceptible to failures which may result in the most catastrophic of problems should the failure not be detected and cured.

Consequently, a number of techniques have been developed which monitor certain parameters within the induction motor, allowing its health to be determined and therefore maintenance schedules planned in order to prevent plant failures and costly shut-downs. These monitoring techniques are all examples of what has become known as *machine condition monitoring*.

Condition monitoring techniques can often be separated into two main categories, those being *invasive* and those being *non-invasive*. *Invasive* monitoring, as the name suggests, involves the disassembly of the motor in question for the purpose of introducing specific transducers, or to conduct a visual inspection, whereas *non-invasive* techniques allow the health of the motor to be obtained whilst the motor is still in normal operation. Machine parameters which have been monitored via the *non-invasive* category over the past years include: line current [8], leakage flux [7] and core/bearing vibration [1].

Previous research [8] has shown that when monitoring the supply line current to the motor under steady-state conditions, it is possible to detect the presence of faults by observing the amplitude of the frequency sidebands which occur at

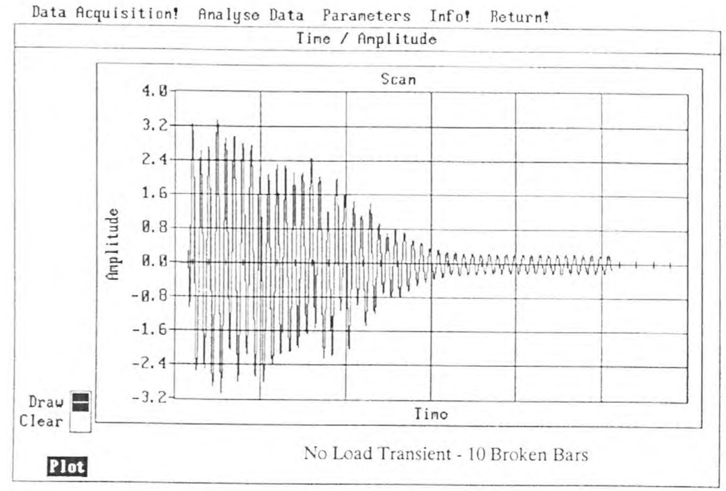

Fig. 1. Typical no-load transient supply current signal. Time base = 85 ms/div, amplitude = 1/20th original value.

$\pm 2s$[1] around the fundamental supply frequency. Faults which can be detected include the presence of broken rotor bars and rotor/stator eccentricity. As mentioned previously, this technique can only give suitable diagnostic information when the motor under investigation is operated under fully loaded, steady-state conditions.

However, during the starting period of a SCIM, a large current transient flows for a relatively long period of time, even when the motor is operated under no-load conditions. A typical example of an induction motor supply current transient signal is shown in Fig. 1. Due to this increased amplitude, which may be as high as 5–10 times the normal steady-state value, the no-load supply current transient should, theoretically, yield the required health information. As with steady-state monitoring, the frequency sidebands which occur at $\pm 2s$ around the supply frequency are monitored. However, within the current transient signal of the motor, these frequency components are of a non-stationary nature, travelling from −50 to 50 Hz due to the value of motor slip changing from unity to near zero during the initial acceleration period of the motor. It is for these reasons that the signal processing techniques which are described in this paper are investigated.

Several techniques exist today which enable a signal to be represented within the *time–frequency* plane. This paper makes a comparison of three such techniques in order to find the most suitable technique for the detection of the non-stationary frequency components required for the purpose of fault detection within a three-phase induction motor.

The techniques are initially investigated using mono-component, multi-component and non-stationary test signals. Comparison is made on both the effects of sample length and the use of different window types on the individual analyses' ability to detect non-stationary components over a frequency range of 50 Hz. Finally, the techniques are investigated as to their suitability for analysing a real

[1] Slip is given the symbol 's', and is a term used to define the relative difference between the speed of the rotating magnetic field within the air gap of the motor and the rotor speed.

transient current signal obtained from a laboratory based three-phase induction motor.

2. Review of possible signal processing strategies

The following techniques, which enable the *time frequency* representation of a signal to be computed, were considered in order to determine the most appropriate for the detection of the non-stationary components under investigation.

2.1. The spectrogram – background theory

The Spectrogram obtains the *time frequency* information of the signal under analysis by computing its short time spectrum, the short time Fourier transform (STFT), via implementation of a Fourier transform algorithm. If the excitation of the time varying signal under analysis is relatively slow, then it may be assumed that the signal is stationary throughout the calculation of the STFT, the number of STFT calculations being dependent upon the signal sample length and the size of the time window used to partition the signal.

Computation of the STFT is achieved via the fast Fourier transform algorithm (FFT), which is a software tool used to calculate the discrete Fourier transform (DFT) defined in (1).

$$F(k) = \sum_{n=0}^{N-1} f(nT)\exp^{-j(2\pi/N)nk}. \quad (1)$$

If the signal to be analysed is sampled in order to preserve Nyquist's law, it can be shown that the value which is computed for $F(k)$ is similar to the magnitude of the signal obtained at a time $t = (N-1)T$, when the samples of the analog signal, $f(t)$, are passed through an analog filter having a frequency response characteristic similar to that shown in Fig. 2.

The data obtained by (1), for values of $k = 0$ to $N-1$, corresponds to the set of outputs from a bank of filters, each having a similar characteristic to that shown in Fig. 2, with centre frequencies defined by (2).

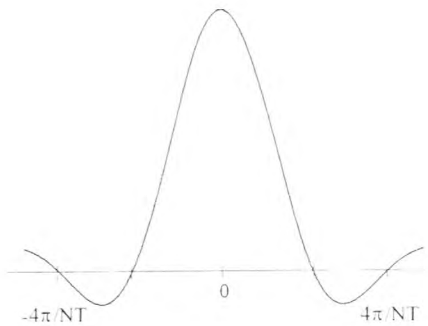

Fig. 2. Filter frequency response characteristic.

On computation of (1), a single spectral section will be calculated. In order to obtain a complete analysis it is necessary to repeat this computation over successive instants of time (3), where each computation is separated by MT seconds.

$$\omega = (2\pi k)/(NT), \quad (2)$$

$$F_r = \sum_{n=0}^{N-1} w(nT)f(nT + rMT)\exp^{-j(2\pi/N)nk}. \quad (3)$$

It should be noted that when (1) is calculated using a finite amount of data, a rectangular time window of width, NT, is automatically imposed onto the signal. Hence, by using other types of windows in (3), it may be possible to obtain an improved spectral representation.

Once the STFT has been calculated by (3), a *spectrogram* can be obtained as is shown in (4).

$$S(t,\omega) = |F(k)|^2. \quad (4)$$

Past researchers have found with this technique that any increase in the size of the time window employed will result in an increase in the time resolution and a decrease in the frequency resolution of the computed representation, the opposite occurring when the time window is reduced in size.

2.2. The wigner distribution – background theory

The auto-wigner distribution (AWD) of a continuous signal is defined by Claasen and Mecklenbraüker [3] as that shown in (5), where $x(t)$ represents the continuous signal which is under analysis, τ is a shift component and $x^*(t)$ indicates the complex conjugate of $x(t)$.

$$\mathrm{AWD}(t,\omega) = \int_{-\infty}^{\infty} x(t+\tau/2)x^*(t-\tau/2)\mathrm{e}^{-j\omega\tau}. \quad (5)$$

The discrete form of (5) can be obtained from this expression and is defined by Claasen and Mecklenbraüker [3] as that shown in (6), where the time index, n, is discrete and the frequency index, θ, is continuous.

$$\mathrm{AWD}(n,\theta) = 2\sum_{k=-\infty}^{\infty} f(n+m)f^*(n-m)\mathrm{e}^{-j2k\theta}. \quad (6)$$

In order to improve the spectral representation of the AWD, it is usually necessary to introduce a window in the frequency direction, a rectangular window being automatically imposed in the time direction due to the finite length of sampled data. This form of AWD is known as the pseudo-Wigner distribution (PWD) and is shown in (7).

$$\mathrm{PWD}(n,\theta) = 2\sum_{k=-\infty}^{\infty} w(k)f(n+k)w^*(-k) \times f^*(n-k)\mathrm{e}^{-j2k\theta}. \quad (7)$$

When sampling the signal to be analysed by the AWD, or a variant such as the PWD, the preservation of Nyquist's law is necessary in order to reduce the effects of aliasing. However, low frequency artefacts will still be present within the Wigner distribution. These components, containing no useful information, are not caused by the incorrect selection of the sampling rate, but by the interaction between the positive and negative frequencies of the signal.

Reduction of these components is obtained via the analytic representation of the signal. The AWD which analyses the analytic signal in place of the real signal is known as the Wigner Ville distribution (WVD) (8).

$$\mathrm{WVD}(t,\omega) = \int_{-\infty}^{\infty} z(t+\tau/2)z^*(t-\tau/2)\mathrm{e}^{-j\omega\tau}\,\mathrm{d}\tau. \quad (8)$$

The analytic signal, $z(t)$, can be computed both in the time and frequency domains. In the time domain the analytic version is obtained via the Hilbert transformation, whereas in the frequency domain the signal may be obtained via the Fourier transform, with the time domain signal being recovered from $z(f)$ via the inverse Fourier transform (IFT).

It can be shown that the AWD can be calculated via the use of the FFT algorithm. When this is taken into consideration the WVD, in discrete form, can be obtained via (9).

$$\mathrm{WVD}(t,f) = 2\,\underset{m\to 2k}{\mathrm{DFT}}[z(n+m)z^*(n-m)]. \quad (9)$$

The Wigner distribution and its many variants contain several desirable properties when representing a signal in the *time-frequency* plane. These properties include: the distribution of any real or complex function shall be real; a time shift in the time signal will result in an equal time shift in the distribution; and the total energy in the signal is equal to the integral of the distribution over the whole plane (t,ω). However, along with these favourable properties the Wigner distribution possesses one single property which limits the practical applications to which the distribution can be used, this being the presence of *crossterm interference* or *crossterms*. These crossterms are caused by the bilinear nature of the distribution causing interference terms to appear between the individual components of a multi-component signal.

In order to reduce the amplitude of these interference components, which can be up to twice that of the original, windowing in both the frequency and time directions is employed. The result of windowing in both directions on the WVD is to produce a Wigner distribution known as the smoothed Wigner Ville distribution (SWVD).

It can be shown that the SWVD can be calculated via one DFT operation for a certain 'n' value, as is shown in (10).

$$\mathrm{SWVD}(n,m) = 2\sum_{k=-L}^{L} r_n(k)e^{-jkm2\pi/K}, \quad (10)$$

where

$$r_n(k) = \left[\sum_{i=-R}^{R} w(i)x_a(n+i+k) \times x_a^*(n+i-k)\right]|h(k)|^2. \quad (11)$$

$r_n(k)$ is referred to as the smoothed complex kernel which is complex symmetrical, i.e. $r_n(k) = r_n(-k)$. Due to this property it is only necessary to compute half of the sequence as the DFT of a complex symmetrical sequence is real, thus the DFT of $jr_n(k)$ will be imaginary, hence, it is possible to compute two slices of the SWVD with only one DFT calculation by combining the two complex kernels into a composite complex kernel, $R_n(k)$ (12).

$$R_n(k) = r_n(k) + jr_{n+1}(k). \quad (12)$$

The two WVD time slices thus come from the real and imaginary parts of the composite kernel. Taking this computation property into consideration, the SWVD can be computed up to twice as fast as the spectrogram technique. This is one of the main reasons why the Wigner distribution is used as a method of obtaining a signals *time–frequency* representation, although for multi-component signals the technique is limited by the presence of crossterms.

2.3. *The wavelet decomposition – background theory*

One of the first *time–frequency* representations of a signal was introduced by Gabor [4]. This representation of a signal in the *time–frequency* domain is known as the Gabor decomposition of the signal. In this decomposition, the signal, $r(t)$, is broken into a two-variable function $R(\tau,\omega)$. This is achieved by the Gabor decomposition (13).

$$R(\tau,\omega) = 1/2\pi(2\pi\sigma^2)^{-1/4}\int_{-\infty}^{\infty} \exp(-(t-\tau)^2/4\sigma^2)\exp(-j\omega(t-\tau))r(t)\,dt. \quad (13)$$

On analysis of the above equation, it is found that the *time–frequency* representation, $R(\tau,\omega)$, is obtained by the convolution of the signal $r(t)$ with the signal $h(t)$. The signal $h(t)$ is known as a wavelet which can assume a *Gaussian* form and can be obtained from the following expression.

$$h(t) = 1/2\pi(2\pi\sigma^2)^{-1/4}\exp(-t^2/4\sigma^2)\exp(j\omega t). \quad (14)$$

The two variables in (13), τ and ω, are used as translations into the time and frequency domains, respectively, of the wavelet, $h(t)$.

For a fixed time, τ, the calculated function, $R(\tau,\omega)$, represents the instantaneous energy partition along the frequency spectrum. For a fixed ω, it is representative of the energy partition at this particular frequency along the time axis. The decomposition of the signal under analysis, $R(\tau,\omega)$, is therefore obtained by convolving the signal with a wavelet similar to that described above, the wavelet having its centre frequency on the current frequency under investigation.

A typical example of a *Gaussian* wavelet, which has a constant duration regardless of the centre frequency, unlike the Wavelet transform representation [6], is shown in Fig. 3.

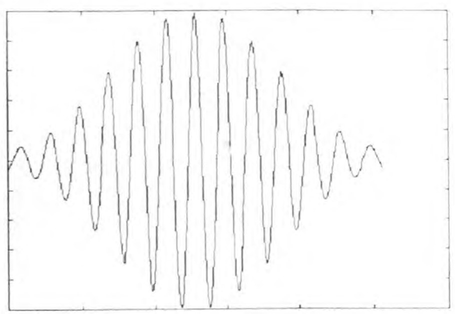

Fig. 3. Typical example of a Gaussian wavelet.

Table 1
Description of test signals

Test signal no.	$f(t)$
1	$f(t) = 10\sin(2\pi(23.4375\,\mathrm{Hz})t)$
2	$f(t) = 10\sin(2\pi(15.625\,\mathrm{Hz})t)$
3	$f(t) = 10\sin(2\pi(7.8125\,\mathrm{Hz})t) + 10\sin(2\pi(23.4375\,\mathrm{Hz})t))$
4	$f(t) = 10\sin(2\pi(7.8125\,\mathrm{Hz})t) + 10\sin(2\pi(15.625\,\mathrm{Hz})t) + 10\sin(2\pi(23.4375\,\mathrm{Hz})t))$
5	$f(t) = 10\sin(2\pi(7.8125\,\mathrm{Hz})t)$ + non-stationary sinusoidal varying from 10 to 100 Hz
6	$f(t) = 10\sin(2\pi(78.125\,\mathrm{Hz})t)$
7	$f(t) = 10\sin(2\pi(78.125\,\mathrm{Hz})t) + 10\sin(2\pi(234.375\,\mathrm{Hz})t))$
8	$f(t) = 10\sin(2\pi(21.0\,\mathrm{Hz})t)$
9	$f(t) = 10\sin(2\pi(21.0\,\mathrm{Hz})t) + 10\sin(2\pi(42.0\,\mathrm{Hz})t))$

3. Evaluation of techniques using test signals

In order to confirm the theoretical predictions and performances of the three techniques when analysing multi-component signals, a program of tests incorporating four mono-component test signals, four multi-component test signals and one test signal containing both stationary and non-stationary frequency components was initiated.

The details of the individual test signals are listed in Table 1. All signals are sampled at a rate of 1 kHz and were simulated using the mathematical software package MATLAB (Ver. 4.0).

3.1. *Results of evaluation with test signals*

The spectrogram, formed from the computation of the short time Fourier transform (STFT), was found to give reasonable results when analysing test signals nos. 1, 2 and 3. The technique allows average resolution control both in the time and frequency directions by either increasing/decreasing the time between the individual analyses and the size of window length, respectively. When used to locate the non-stationary components within test signal no. 5, Fig. 4, the Spectrogram was found to be very successful.

$$F_{\mathrm{res}} = f_s/N. \quad (15)$$

In the analysis a sample length, N, of 128 samples and a time of 16 ms between each individual sample length were used. This results, due to (15), in a frequency resolution of 7.8125 Hz being obtained.

The effect of different window types on the technique was then investigated. The window which had been used in the above tests was a *Hamming* window. Using a *Kaiser* window the effects on the analyses were found to include an increased sensitivity in the frequency direction. The spectrogram was however found to suffer from a resolution problem in that when one resolution is increased, the other automatically decreases, as predicted theoretically.

The Wigner distribution and several of its smoothed variants were then investigated. Using test signals nos. 7 and 4, the technique was found to give good resolution control in both frequency and time directions. When analysing test signal no. 4, both the WVD and the SWVD techniques were investigated. However, in both versions of the WVD crossterm interference was found to occur. Several methods of crossterm interference reduction, over and above that of using the SWVD, were investigated, including that of the Exponential distribution [2]. These reduction techniques however did not eliminate entirely the presence of crossterm interference within the *time–frequency* representation.

$$F_{\mathrm{res}} = f_s/2N. \quad (16)$$

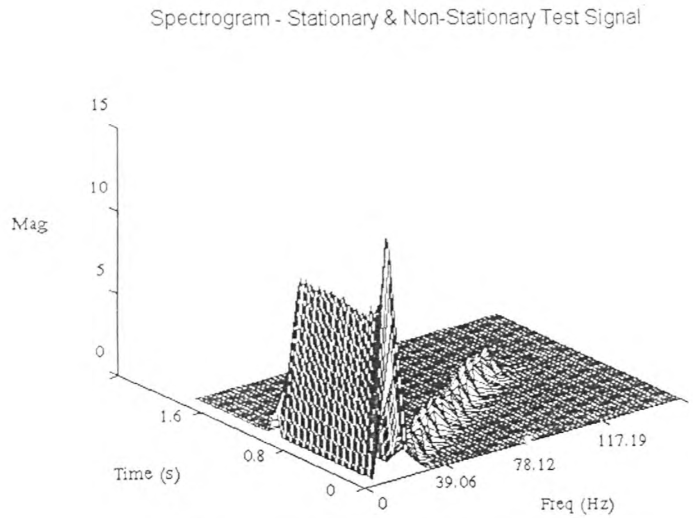

Fig. 4. A Spectrogram representation of test signal no. 5.

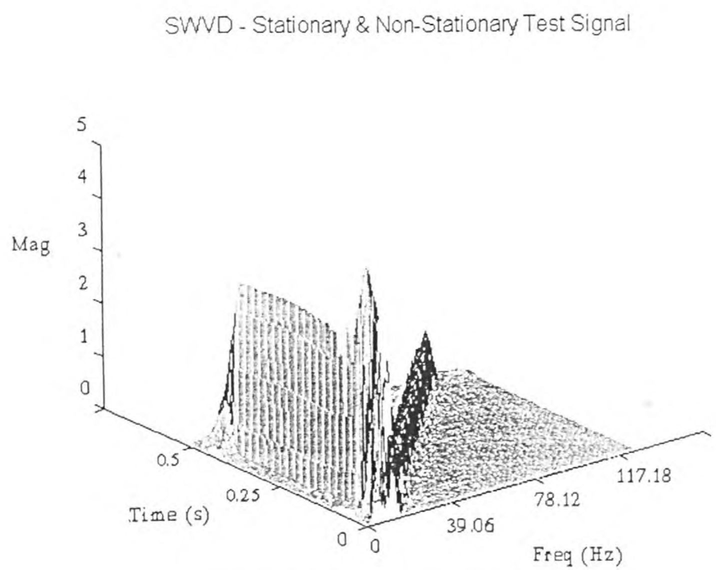

Fig. 5. A smoothed Wigner Ville distribution of test signal no. 5.

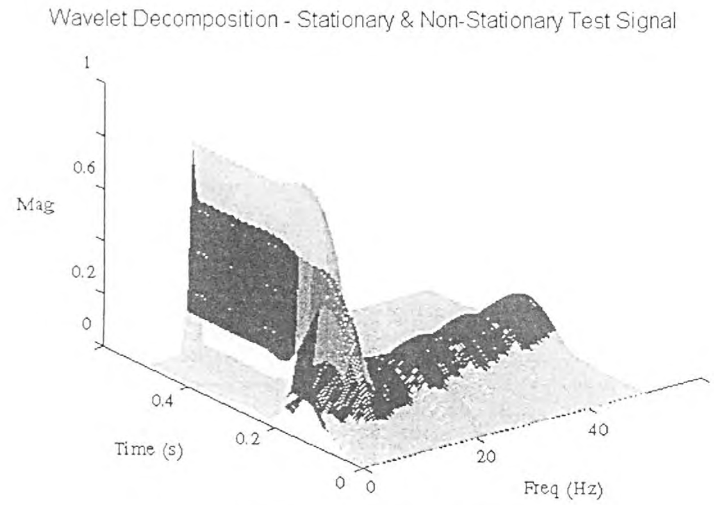

Fig. 6. A Wavelet decomposition of test signal no. 5.

Using a *Kaiser* window of 256 samples in the frequency direction, then from (16) the frequency resolution obtained in the SWVD analysis is 1.953 Hz. Along with a *rectangular* window of 64 samples, test signal no. 5 was analysed with the results being shown in Fig. 5. The stationary and non-stationary components can clearly be seen. The crossterm interference is located midway between the two components and hence cannot be seen in this analysis.

When analysing test signals nos. 2, 3 and 6 with the Wavelet decomposition method, good frequency and time resolutions were obtained. There are no problems with interference when multi-component signals are analysed, and when the decomposition of test signal no. 5 is obtained using a *Gaussian* window, the results, Fig. 6, show an extremely clear *time–frequency* representation.

4. Acquisition of real test data

Real test data were obtained from the supply lines to a laboratory-based three-phase, 11 kW, four-pole, 51-slot SCIM. The signals of particular interest are the transient supply current signals

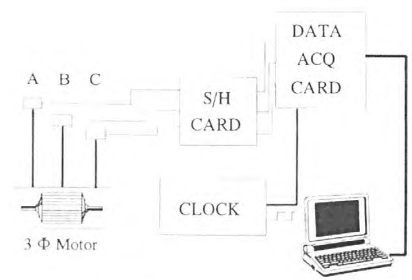

Fig. 7. The transient current acquisition set-up.

obtained when the motor is started under no-load conditions, these signals being obtained physically by the acquisition arrangement shown in Fig. 7.

In this scheme, three Hall effect transducers, A, B and C, pick up the transient supply current to the motor and present the signal as a proportional voltage to the acquisition circuitry. This is sampled at a rate of 2 kHz via the sample and hold (S/H) card which has been specifically developed in order to allow synchronous sampling of all three phases. The S/H card feeds the data values into a portable

PC for analysis purposes via a LabWindows PC+ data acquisition card. An external timing circuit has been developed in order to control the entire acquisition process.

Using the acquired data, the individual signal processing techniques were investigated in order to find the most appropriate one for detecting the non-stationary components within the practical signals.

The suitability of the individual techniques is determined by their ability to locate the non-stationary components within a 50 Hz bandwidth ranging from 0 to 50 Hz. This size of bandwidth is required as the non-stationary components during the acceleration period of the motor vary from – 50 to 50 Hz. This is due to the value of slip changing from unity to near zero at steady state, the negative frequency component denoting a phase shift which occurs within the non-stationary components. As the individual analyses detect the absolute values of the frequency, a search area of bandwidth 50 Hz is all that is required.

Another factor which will determine a technique's suitability will be the frequency resolution which is obtained. A small frequency resolution is required due to the fact that the non-stationary components are several magnitudes smaller than the fundamental of the supply frequency, 50 Hz, even when amplified under fully loaded conditions. A small frequency resolution is therefore necessary in order to separate the large 50 Hz component from the smaller non-stationary components.

5. Evaluation of techniques using real data

A 1024 sample of the transient data, obtained by the manner described in Section 4, with the SCIM running under no-load conditions and 10 broken rotor bars present was obtained. The fault condition of 10 broken rotor bars is in fact an extreme fault condition which was used initially in order to see if the fault conditions could be detected by the analysis methods. A more typical level of fault severity, three broken rotor bars, will be analysed later by the technique found to be most suitable.

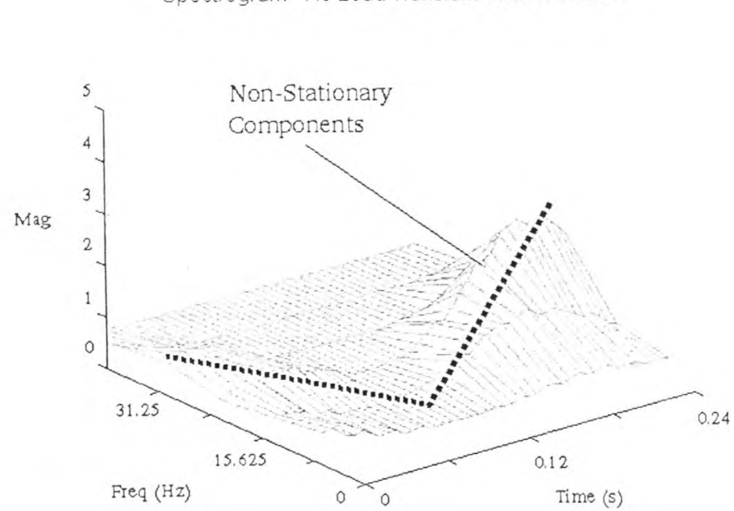

Fig. 8. A Spectrogram of a no-load transient supply current signal (10 broken rotor bars).

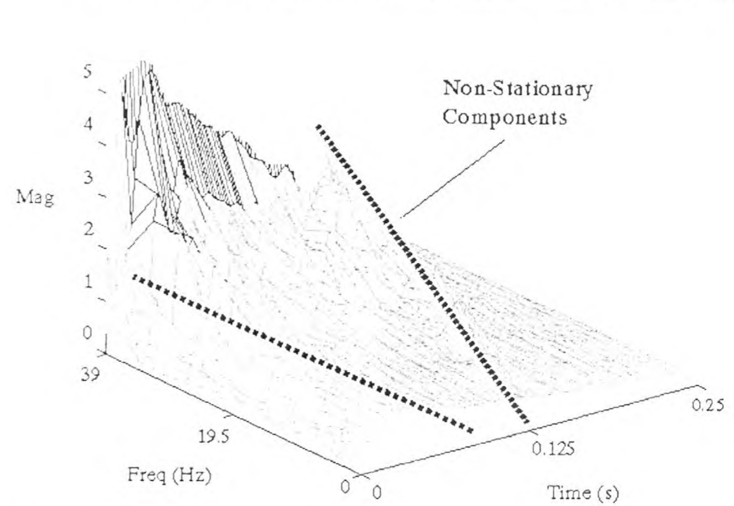

Fig. 9. A smoothed Wigner Ville distribution of a no-load transient supply current signal (10 broken rotor bars).

The most favourable *time–frequency* representation using the Spectrogram technique was achieved by employing a 512-sample *Hamming* window. As the data were sampled from the supply lines of the motor at a rate of 2 kHz, then from (15), the frequency resolution of the spectrogram is 7.8125 Hz. The results of the analysis are shown in Fig. 8. From the spectrogram, the non-stationary frequency components which are contained within the transient signal of the motor can clearly be observed.

Fig. 9 shows the results of the smoothed Wigner Ville distribution analysis of the same current transient. The frequency window used in this analysis was of the *Kaiser* type, length 256 samples, and the time window was of the *rectangular* type, length 64 samples. These types and lengths of windows were found to give the best results for tracking the non-stationary components. As a result of (16), the frequency resolution of the SWVD analysis is 3.9 Hz. Again, the non-stationary components within the transient signal can be observed, although the components with this technique are no longer as clearly evident as they were with the spectrogram analysis.

Fig. 10 shows the result of analysing the transient signal using the Wavelet decomposition method. In this analysis a *Gaussian* wavelet of bandwidth 1 Hz has been convolved with the transient signal under investigation in order to obtain the decomposition of the signal. As the wavelet assumes the frequency of the investigation, a frequency resolution of 1 Hz can be obtained.

From the results of the three *time–frequency* representations, it is clear that all three successfully detected the non-stationary components within the transient current signal. The poorest analysis of the three investigated was found to be the WVD. Although a number of crossterm interference suppression techniques were investigated within the analysis, including the SWVD, the presence of the interference components hinders the successful detection of the non-stationary components.

The next most successful technique was found to be the Spectrogram. Using this technique the non-stationary components can clearly be located, although the technique does suffer from a resolution problem in that when the time resolution is

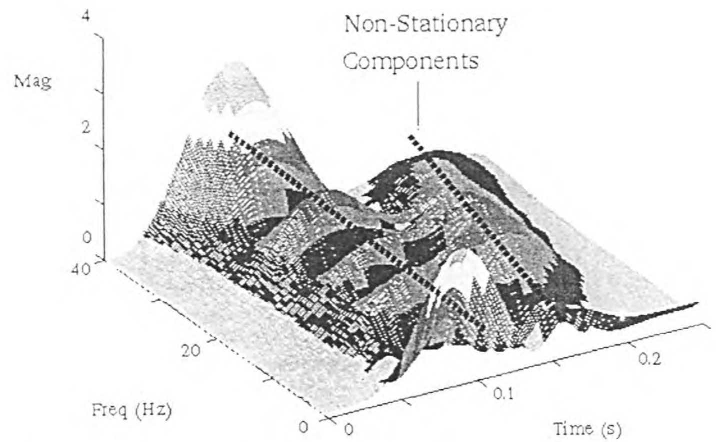

Fig. 10. A Wavelet decomposition of a no-load transient supply current signal (10 broken rotor bars).

increased the frequency resolution automatically reduces and vice versa. This however can be solved if two tests are done on the one signal, the first having a high time resolution followed by a second test having a high frequency resolution.

The *time–frequency* representation technique which gave the best results when applied to real data obtained from the motor was found to be the decomposition via a wavelet. In this technique the non-stationary components can clearly be observed travelling in the frequency direction. Consequently, this technique was used to investigate the possibility of fault detection using the transient current signal obtained from the motor.

6. Rotor fault detection using chosen signal processing technique

The analysis shown in Fig. 11 is obtained by computing the Wavelet decomposition of the transient supply current signal from a three-phase, 11 kW, four-pole, 51-slot SCIM starting under no-load conditions over the frequency range of 0–50 Hz. The motor within this example contains three broken bars.

The results of the analysis clearly show the non-stationary components travelling from 50 Hz at motor start-up to 50 Hz at steady state. Comparison of this analysis with the result of another obtained from the same motor under fault-free conditions, Fig. 12, results in an obvious reduction in the amplitude of the sidebands occurring.

It is this difference in sideband amplitude which has been shown to be proportional to the degree of rotor fault severity. This technique has now been transferred to a portable PC, thus providing a motor health monitoring system which enables the data to be immediately accessible, without the need for data transfer to larger mainframe computers.

Work has now been initiated in order to determine if it is possible to obtain positional information in addition to detection information on motor faults. It is postulated that this information can be

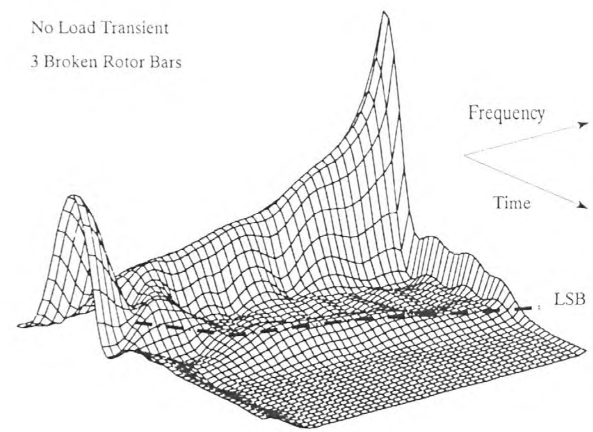

Fig. 11. A Wavelet decomposition of a no-load transient supply current signal (three broken rotor bars).

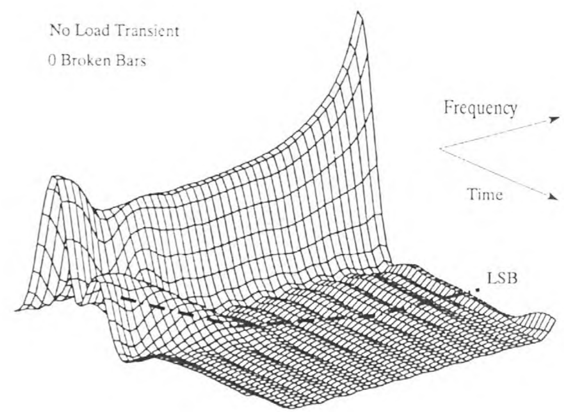

Fig. 12. A Wavelet decomposition of a no-load transient supply current signal (0 broken rotor bars).

obtained from the frequency content of the supply line current transient using the *time–frequency* representation of the signal.

Frequency components indicative of the location of a rotor fault have been theoretically predicted and detected during steady-state conditions. Current work is aiming to detect these components during the transient period of the signal using the *time–frequency* representation. Once detected, a technique has been developed whereby the position of the rotor's fault can be determined.

7. Conclusion

This paper compares the suitability of three *time–frequency* analysis techniques towards a particular practical application; namely the detection of rotor faults within a three-phase induction motor.

On investigation, using both test and real signals, the real signals being obtained from a laboratory-based motor, it was found that the non-stationary frequency components within the motor supply current transient, which are indicative of the presence of rotor faults, can be detected using a decomposition technique. In this technique a 512-sample *Gaussian* wavelet of bandwidth 1 Hz convolved with the transient signal thus producing an extremely clear *time–frequency* representation of the motor's transient supply current signal.

Using this technique to monitor the progress of the non-stationary frequency components, investigations were carried out in order to establish whether the increase in amplitude due to the severity of fault, as found when monitoring the components in steady state, could be detected within the transient *time–frequency* representation of the signal.

Several levels of fault were introduced into the laboratory motor. It has been successfully proven that the decomposition technique does enable the severity of the fault to be determined via the amplitude of the non-stationary components.

The technique, which is PC based, uses software to calculate the required signal processing operations. It is perfectly feasible that the technique could be realised using a dedicated DSP board/facility. The ethos of the research project however was to investigate the effectiveness of the various signal processing strategies, and to determine if in fact rotor bar failures could be detected using such PC-based technology. As such it could readily be incorporated into existing monitoring and control instrumentation systems.

Since the system monitors the supply current transient, which is only present for a finite period of time, there is no practical requirement for such a monitoring system to be capable of on-line monitoring. The transient monitoring system, which is now in an advanced prototype stage, is a complementary diagnostic system to the well-proven steady-state supply current monitoring systems available. The technique would be of particular use to industrial applications where motors are frequently started on no load, or have been removed to a workshop environment where fully loaded conditions are neither practical nor achievable.

The *time–frequency* technique is now being investigated further with a view to determining the physical location of the motor fault over and above mere fault detection.

Acknowledgements

The authors would like to acknowledge the sponsorship of this work by Scottish Nuclear Ltd.

References

[1] J.R. Cameron et al., "Vibration and current monitoring for detecting air-gap eccentricity in large induction motors", *Proc. IEE*, Vol. 133, Pt. B, No. 3, May 1986, pp. 153–163.

[2] H. Choi and W.J. Williams, "Improved time–frequency representation of multicomponent signal using exponential kernels", *IEEE Trans. Acoust. Speech Signal Process.*, Vol. 37, No. 6, June 1989, pp. 862–871.

[3] T.A.C.M. Claasen and W.F.G. Mecklenbraüker, "The Wigner distribution – A tool for time–frequency signal analysis Parts I, II, III", *Phillips J. Res.*, Vol. 35, 1980.

[4] D. Gabor, "Theory of communication", *IEE* (London), Vol. 93, 1943, p. 429.

[5] C. Hargis et al., "The detection of rotor defects in induction motors", *IEE Internat. Conf. on Electrical Machine Design and Applications*, July 1982.

[6] R. Kronland-Martinet and A. Grossmann, "Application of time–frequency scale methods (wavelet transforms) to the analysis, synthesis and transformation of natural sounds", in: *Representations of Musical Sounds*, MIT Press, Cambridge, MA, 1991.

[7] J. Penman et al., "Condition monitoring of electrical drives", *Proc. IEE*, Vol. 133, Pt. B, No. 3, May 1986, pp. 142–148.

[8] W.T. Thomson et al., "Monitoring strategy for discriminating between different types of rotor defects in induction motors", *18th UPEC Proc.*, Univ. of Surrey, Guildford, UK, 1983, pp. 241–266.

Instructions to authors

General. *Prospective authors are encouraged to submit manuscripts within the scope of the Journal. To qualify for publication, papers must be previously unpublished and not be under consideration for publication elsewhere.* All material should be sent in quadruplicate (original plus three copies) to the Editor-in-Chief. Contributors are reminded that once their contribution has been accepted for publication, all further correspondence should not be sent to the Editor, but directly to the publishers (Editorial Department, Elsevier Science B.V., P.O. Box 1991, 1000 BZ Amsterdam, The Netherlands).
All manuscripts will be assessed by at least two (anonymous) referees.
Upon acceptance of an artice, the author(s) will be asked to transfer copyright of the article to the publisher. This transfer will ensure the widest possible dissemination of information.
Accepted languages are English (preferred), French and German. The text of the paper should be preceded by abstracts of no more than 200 words in English, and, if possible, in French and German. Abstracts should contain the substance of the methods and results of the paper. Page proofs will be sent to the principal author with an offprint order form. Fifty offprints of each article can be ordered free of charge. Costs arising from alterations in proof, other than of printer's errors, will be charged to the authors.
All pages should be numbered. The first page should include the article title and the author's name and affiliation, as well as a name and mailing address to be used for correspondence and transmission of proofs. The second page should include a list of unusual symbols used in the article and the number of pages, tables and figures. It should also contain the keywords in English.
Figures. All illustrations are to be considered as figures, and each should be numbered in sequence with Arabic numerals. The drawings of the figures must be originals, drawn in black india ink and carefully lettered, or printed on a high-quality laser printer. Each figure should have a caption and these should be listed on a separate sheet. Care should be taken that lettering on the original is large enough to be legible after reduction. Each figure should be identified. The approximate place of a figure in the text should be indicated in the margin. In case the author wishes one or more figures to be printed in colour, the *extra* costs arising from such printing will be charged to the author. In this case 200 offprints may be ordered free of charge. More details are available from the Publisher.
Tables. Tables should be typed on separate sheets. Each table should have a number and a title. The approximate places for their insertion in the text should be indicated in the margin.
Footnotes in text. Footnotes in the text should be identified by superscript numbers and listed consecutively on a separate page.
References. References must be *in alphabetical order* in the style shown below:

Book [1] A.V. Oppenheim et al., *Digital Signal Processing*, Prentice Hall, Englewood Cliffs, NJ, 1975, Chapter 10, pp. 491–499.
Journal [2] F.J. Harris, "On the use of windows for harmonic analysis with the discrete Fourier transform", *Proc. IEEE*, Vol. 66, No. 1, January 1978, pp. 53–83.
Conference Proceedings [3] D. Coulon and D. Kayser, "A supervised-learning technique to identify short natural language sentence", *Proc. 3rd Internat. Joint Conf. on Pattern Recognition*, Coronado, CA, 8–11 November 1976, pp. 85–89.
Contributed Volume [4] E.F. Moore, "The firing squad synchronization problem", in: E.F. Moore, ed., *Sequential Machines, Selected Papers*, Addison Wesley, Reading, MA, 1964, pp. 213–214.

Fast Communications. Papers for the Fast Communications section should be submitted by electronic mail to the Editor-in-Chief: Professor M. Kunt. Papers should be a maximum of 2,500 words in length (approximately 6 printed journal pages for Signal Processing). Submissions will be subject to the same editorial selection criteria as regular papers. Reviews will be dispatched electronically and decisions will be binary (yes/no) to avoid publication delays. Please ensure your complete postal and e-mail address are indicated on the title page. As no page proofs will be sent to the authors, the presentation should be very clear. For Fast Communications, the figures should be provided in Encapsulated Postscript (eps) format.
To ensure fast publication, the manuscript should be written in LaTeX using the document styles of Elsevier Science B.V. Move all files needed (TeX source, eps-files, style and bibliography files) into one directory. Remove all compilation files (*.log, *.lof, *.dvi, *.aux, . . .). Rename the main TeX source into *review.tex* and archive (tar), compress and uuencode this directory, and e-mail the uuencoded file to: fastcom@ltssun17.epfl.ch. Authors who comply with the above conditions will have their Fast Communication published on the EEE-Alert Server within three weeks of acceptance.

LaTeX files of papers that have been accepted for publication may be sent to the Publisher by e-mail or on a diskette (3.5" or 5.25" MS-DOS). If the file is suitable, proofs will be produced without rekeying the text. The article should be encoded in ESP-LaTeX, standard LaTeX, or AMS-LaTeX (in document style 'article'). The ESP-LaTeX package, together with instructions on how to prepare a file, is available from the Publisher. It can also be obtained through the Elsevier WWW home page (http://www.elsevier.nl) or using anonymous FTP from the Comprehensive TeX Archive Network (CTAN). The host-names are: ftp.dante.de, ftp.tex.ac.uk, ftp.shsu.edu; the CTAN directory is: /tex-archive/macros/latex/contrib/supported/elsevier. *No changes* from the accepted version are permissible, without the explicit approval by the Editors. The Publisher reserves the right to decide whether to use the author's file or not. If the file is sent by e-mail, the name of the journal, *Signal Processing*, should be mentioned in the subject field of the message to identify the paper. Authors should include an ASCII table (available from the Publisher) in their files to enable the detection of transmission errors. The files should be mailed to: Ineke Kolen, Elsevier Science B.V., P.O. Box 103, 1000 AC Amsterdam, Netherlands. Fax: +31 20 4852829. E-mail: c.kolen@elsevier.nl.
For the purpose of further correspondence the manuscript should end with a complete mailing address, preferably including e-mail address, of at least one of the authors.